

NOVEMBER 1, 1991

# Analytical

## CHEMISTRY



**INVESTIGATING THE EFFECT  
OF HYDROGEN PEROXIDE ON  
NORWAY SPRUCE TREES**

1047 A

# Finding The Right Solution To Environmental Analysis Problems Can Be Puzzling...

*But it's really quite simple.*

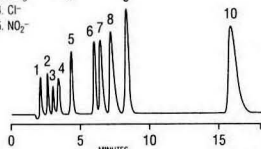
Dionex provides better custom fit solutions. From complex environmental matrices to routine applications, Dionex tailors IC, HPLC, and Supercritical Fluid technology to fit your specific needs.

## Inorganic analysis – fast, sensitive, and accurate

Common anions and oxyhalides by manual or automated wet chemistry can be tedious and costly. Dionex ion chromatography does the job with greater speed, sensitivity, and accuracy.

### Anions in Water

- |                                  |                                  |                                   |
|----------------------------------|----------------------------------|-----------------------------------|
| 1. F <sup>-</sup>                | 6. Br <sup>-</sup>               | 9. HPO <sub>4</sub> <sup>2-</sup> |
| 2. ClO <sub>3</sub> <sup>-</sup> | 7. ClO <sub>2</sub> <sup>-</sup> | 10. SO <sub>4</sub> <sup>2-</sup> |
| 3. BrO <sub>3</sub> <sup>-</sup> | 8. NO <sub>3</sub> <sup>-</sup>  |                                   |
| 4. Cl <sup>-</sup>               |                                  |                                   |
| 5. NO <sub>2</sub> <sup>-</sup>  |                                  |                                   |



Dionex Chemically Suppressed IC is specified worldwide for the analysis of anions and cations in acid rain, ground water, drinking water, waste water, and waste extracts. (U.S. EPA Method 300.0)



*We provide the perfect fit in separation technology.*

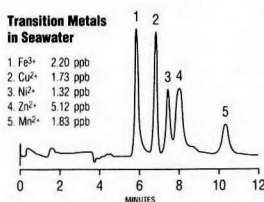


## New metals analysis capability lets you crash the ppb barrier

Use Dionex Chelation IC to determine fractional ppb levels of transition metals – easily – even in seawater.

### Transition Metals in Seawater

- |                     |          |
|---------------------|----------|
| 1. Fe <sup>3+</sup> | 2.20 ppb |
| 2. Cu <sup>2+</sup> | 1.73 ppb |
| 3. Ni <sup>2+</sup> | 1.32 ppb |
| 4. Zn <sup>2+</sup> | 5.12 ppb |
| 5. Mn <sup>2+</sup> | 1.83 ppb |



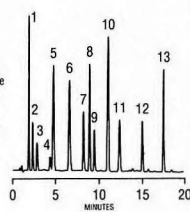
Speciation and total metals analysis in complex matrices, such as hazardous waste incinerator emissions, is no problem. Even hexavalent chromium can be accurately determined, interference-free, down to the ppt level.

## Powerful new organics analysis capability

Reliable, trouble-free performance of all approved HPLC methods is possible with Dionex metal-free HPLC systems. For difficult sample preparation problems, the Dionex Supercritical Fluid Extraction system provides a simple and fast solution.

### Polar and Ionic Organics

- |                                     |                                     |
|-------------------------------------|-------------------------------------|
| 1. Benzoate                         | 10. 1,3,5-Benzenetricarboxylate     |
| 2. Benzenesulfonate                 | 11. 2,5-Dihydroxybenzoate           |
| 3. <i>p</i> -Toluenesulfonate       | 12. 1,3,5-Benzenetricarboxylate     |
| 4. <i>p</i> -Chlorobenzenesulfonate | 13. 1,2,4,5-Benzenetetracarboxylate |
| 5. <i>p</i> -Bromobenzoate          |                                     |
| 6. 3,4-Dinitrobenzoate              |                                     |
| 7. <i>o</i> -Benzenedicarboxylate   |                                     |
| 8. <i>p</i> -Benzenedicarboxylate   |                                     |
| 9. <i>p</i> -Hydroxybenzoate        |                                     |



Additionally, Dionex unique OmniPac<sup>®</sup> resin technology, which combines ion exchange and reversed-phase adsorption mechanisms, delivers rapid analysis of highly water-soluble pollutants such as chlorinated aromatic sulfonates.

## Not just solutions, perfect fit solutions

Find out how Dionex IC, HPLC, and SFE technology can be tailored to fit your specific environmental analysis problems. Contact your local Dionex representative. Or call **1-800-227-1817 ext. 438** today. Outside the U.S. call the Dionex office nearest you.

**DIONEX**  
A BETTER SOLUTION

Dionex Corporation, P.O. Box 3603, Sunnyvale, CA 94088-3603 **Canada** Dionex Canada Ltd., (416) 855-2551 **United Kingdom** Dionex (UK) Ltd., (0276) 691722 **Germany** Dionex GmbH (06126) 6036  
**France** Dionex S.A., (1)46216666 **Italy** Dionex S.r.l., (06) 371-5454 **Japan** Nippon Dionex K.K., (06) 885-1213 **Netherlands** Dionex B.V., (076) 714-800. OmniPac is a registered trademark of Dionex Corporation.

CIRCLE 28 ON READER SERVICE CARD



# How we made a better HPLC system for QC/QA analysis



## We started by eliminating the computer

Our new programmable 307 Pump is at the heart of the system. It controls other system components: an auto-injector, detector and integrator or data analysis system. This system is less expensive than most computer-based QC/QA systems and much easier to operate, too. All the information you need to start a run flashes on the front panel display.

Another key feature of the 307 is that it provides extremely smooth flow rates for repetitive retention times. And flow accuracy is unaffected by pressure changes or by the nature of the liquid.

## Then we added an auto-injector that ensures accurate, reproducible results

The Gilson 231/401 Auto-Sampling Injector is another key component in the system. It automates the preparation and injection of up to 120 samples. (A larger capacity unit is available that can handle up to 540 samples.) A built-in rinsing function virtually eliminates cross-contamination due to carry-over. And because the 231/401 loads the sample directly into the injection valve, sample consumption is reduced.

## Plus, all these benefits for QC/QA applications

- System requires less than 2 sq. ft. of bench space. Ideal for labs with multiple systems and minimal space.
- Quick system set-up. You can assemble the QC/QA system in 30 minutes or less. All connections are easily accessible.
- Simplifies compliance with GLP guidelines. 307 Pumps have built-in functions for tracking pump head usage.

To learn more about these and other advantages of the Gilson HPLC system for QC/QA analysis, contact your local Gilson representative. Or call us toll-free.

 **GILSON®**

Call 800-445-7661

Gilson Medical Electronics, Inc., Box 27, 3000 W. Beilene Hwy., Middleton, WI 53562 USA, Tel: 608-836-1551, TLX: 26-5478, FAX: 608-831-4451  
Gilson Medical Electronics (France) S.A., 72 rue Gambetta, B.P. No. 45, 95400 Villiers-le-Bel, France, Tel: (33) 1 34.29.50.00, TLX: 606682, FAX: (33) 1 34.29.50.80

CIRCLE 50 ON READER SERVICE CARD

# BAKERBOND spe\* columns: There's more to solid phase extraction than you see on the surface.

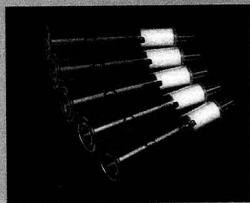


With only 1/8 of its mass visible, a sharply-cleaved iceberg drifts off the west coast of the Antarctic Peninsula.

## Simplify your sample preparation with J.T. Baker's Technical Support Program combined with BAKERBOND spe columns.

You've come to expect consistent, outstanding quality from BAKERBOND spe solid phase extraction columns. But for optimum results, you also need technical information and assistance to help you tailor column use to your specific applications.

That's why J.T. Baker has developed a four-part technical support program:



- A growing collection of over 100 pre-developed, step-by-step Application Notes virtually eliminates method development time.
- Our manual, **Solid Phase Extraction for Sample Preparation**, provides detailed information on theory, method development and troubleshooting.
- An experienced solid phase extraction Application Specialist is only a phone call away to provide additional personal assistance.
- A Report of Analysis in each box of BAKERBOND spe columns provides you with actual data for those parameters critical to column performance. Sometimes it's what you can't see that makes all the difference.

To learn more about how we can help you, contact J.T. Baker Inc., 222 Red School Lane, Phillipsburg, NJ 08865. 1-800-JTBAKER. (1-800-582-2537). FAX: 201-859-9318.

**1-800-JTBAKER**



\*BAKERBOND spe is a trademark of J.T. Baker Inc.  
Photo: © Gordon Wilsie/Adventure Photo, 1989

CIRCLE 14 ON READER SERVICE CARD



NOVEMBER 1, 1991  
VOLUME 63  
NUMBER 21

**ANCHAM**  
The Audit Bureau  
63(21) 1009A-1060A/2401-2544 (1991)  
ISSN 0003-2700

Registered in U.S. Patent and Trademark Office;  
Copyright 1991 by the American Chemical Society

ANALYTICAL CHEMISTRY (ISSN 0003-2700) is published semimonthly by the American Chemical Society at 1155 16th St., N.W., Washington, DC 20036. Editorial offices are located at the same ACS address (202-872-4570; fax 202-872-4574; Bitnet rmi96@cas; TDD 202-872-8733). Second-class postage paid at Washington, DC, and additional mailing offices. Postmaster: Send address changes to ANALYTICAL CHEMISTRY Member & Subscriber Services, P.O. Box 3337, Columbus, OH 43210. Canadian GST Reg. No. R127571347

Claims for missing numbers will not be allowed if loss was due to failure of notice of change of address to be received in the time specified; if claim is dated (a) North America: more than 90 days beyond issue date, (b) all other foreign: more than one year beyond issue date, or if the reason given is "missing from files."

**Copyright Permission:** An individual may make a single reprographic copy of an article in this publication for personal use. Reprographic copying beyond that permitted by Section 107 or 108 of the U.S. Copyright Law is allowed, provided that the appropriate per-copy fee is paid through the Copyright Clearance Center, Inc., 27 Congress St., Salem, MA 01970. For reprint permission, write Copyright Administrator, Publications Division, ACS, 1155 16th St., N.W., Washington, DC 20036.

**Registered names and trademarks, etc.,** used in this publication, even without specific indication thereof, are not to be considered unprotected by law.

**Advertising Management:** Centcom, Ltd., 500 Post Rd. East, Westport, CT 06880 (203-226-7131)

**1991 subscription rates include air delivery outside the U.S., Canada, and Mexico**

	Members	Nonmembers (personal)	Nonmembers (institutional)
U.S.	31	69	289
Canada and Mexico	67	105	325
Europe	112	210	370
Other countries	131	229	389

**Nonmembers rates in Japan:** Rates above do not apply to nonmember subscribers in Japan, who must enter subscription orders with Maruzen Company Ltd., 3-10, Nihonbashi 2-chrome, Chuo-ku, Tokyo 103, Japan. Tel: (03) 272-7211.

**For multi-year and other rates,** call toll free 800-227-5558 in the U.S. and Canada; in the Washington, DC, metropolitan area and outside the U.S., call 202-872-4363; fax 202-872-4615.

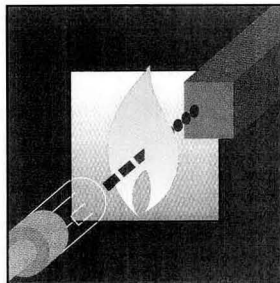
**Subscription orders by phone** may be charged to VISA, MasterCard, or American Express. Call toll free 800-333-9511 in the continental U.S.; in the Washington, DC, metropolitan area and outside the continental U.S., call 202-872-8065. Mail orders for new and renewal subscriptions should be sent with payment to American Chemical Society, Department L-0011, Columbus, OH 43268-0011

**Subscription service inquiries and changes of address** (include both old and new addresses with ZIP code and recent mailing label) should be directed to the ACS Columbus address noted above. Please allow six weeks for changes to become effective.

**ACS membership information:** Lorraine Bowlin (202-872-4567)

**Single issues,** current year, \$13.00 except review issue, \$26.00, and LabGuide, \$50.00; **back issues and volumes and microform editions** available by single volume or back issue collection. For information or to order, call the number listed for subscription orders by phone; or write the Microform & Back Issues Office at the Washington address.

# Analytical CHEMISTRY®



## REPORTS 1024 A & 1033 A

**1991 Waters symposium on atomic absorption spectroscopy.** In the second two of four articles from this year's symposium, S.R. Koirtyohann of the University of Missouri-Columbia discusses the development of AAS from an academic perspective and Walter Slavin of Perkin Elmer explores the reasons for the success of AAS



## ANALYTICAL APPROACH 1047 A

**On the cover.** Investigating the effect of hydrogen peroxide on Norway spruce trees. Elevated levels of ozone in ambient air, combined with acid precipitation, are believed to play a major role in forest decline in Europe and North America. A.A.F. Kettrup and colleagues at the University of Paderborn describe the use of microscopy and chromatographic methods to investigate the relationship between the amount of H<sub>2</sub>O<sub>2</sub> in the air and forest decline

## BRIEFS

1014 A

## EDITORIAL

1021 A

**The curious value of research.** The research community serves as a resource and role model to society when we successfully convey the reasons, rewards, and pervasiveness of intellectual curiosity that we know so well

## NEWS

1023 A

**New Division of Analytical Chemistry officers elected.** • Nobuhiko Ishibashi, former Advisory Board member, dies. • IUPAC nomenclature for chromatography

## NEW PRODUCTS & MANUFACTURERS' LITERATURE

1040 A

## AUTHOR INDEX

2401

## Articles

### Monitoring of Formation Rates of Thin Films in Laser-Induced Chemical Vapor Deposition 2402

Comparison between acoustic wave, photoacoustic response, transmittance, reflectance, and quartz crystal microbalance measurements is performed for in situ laser-induced chemical vapor thin-film deposition.

**Ho-ming Pang and Edward S. Yeung\***, Ames Laboratory-USDOE and Department of Chemistry, Iowa State University, Ames, IA 50011

### Fundamentals of Sinusoidal Flow Sequential Injection Spectrophotometry 2407

The design of the sequential injection analyzer is based on the mutual penetration of sample and reagent zones, which are sequentially stacked into a tubular conduit, injected into a reactor, and transported to the detector.

**Thomas Gübeli**, Alitea U.S.A., P.O. Box 26, Medina, WA 98039 and **Gary D. Christian and Jaromir Ruzicka\***, Department of Chemistry, BG-10, University of Washington, Seattle, WA 98195

### Determination of the Diffusion Coefficients of Iodine in Porphyrin Thin Films by Utilization of the Battery Effect in Schottky Barrier Devices 2414

By analyzing the time evolution of the device's dark current, the diffusion coefficient of iodine in a series of tetraphenylporphyrins is determined to be approximately  $10^{-15}$  cm<sup>2</sup>/s (increasing in order of central substituent Mg < Cu < Zn < H<sub>2</sub> < Ni).

**W. Andrew Nevin**, Department of Electrical and Electronic Engineering, Trent Polytechnic, Burton Street, Nottingham NG1 4BU, England

### Multichannel Amperometric Detection System for Liquid Chromatography and Flow Injection Analysis 2418

A 16-working electrode electrochemical detector in a parallel configuration and a computer-controlled multichannel potentiostat are developed. When used for the detection of catecholamines separated by LC, the response is linear over the range  $10^{-5}$ – $10^{-9}$ , and a detection limit of ~0.1 pg epinephrine injected is achieved.

**Johan C. Hoogvliet\***, **Johannes M. Reijn**, and **Wouter P. van Bennekom**, Faculty of Pharmacy, Utrecht University, P.O. Box 80.082, 3508 TB Utrecht, The Netherlands

### Development of the H-Point Standard-Additions Method for Ultraviolet-Visible Spectroscopic Kinetic Analysis of Two-Component Systems 2424

The H-point standard addition method is extended to kinetic analysis; time is included as an additional measurement dimension. Good results are obtained for analyte concentration in the presence of a complex matrix and for binary mixtures.

**Francisco Bosch-Reig, Pilar Campins-Falcó\***, **Adela Sevillano-Cabeza, Rosa Herráez-Hernández**, and **Carmen Molins-Legua**, Departamento de Química Analítica, Facultad de Química, Universidad de Valencia, Burjassot (Valencia), Spain

### Simultaneous Determination of Elemental Ratios in Coal by Direct Powder Injection into a Helium Microwave Induced Plasma 2430

C, H, Cl, and S are determined by direct solid sampling. C/H ratios are determined to within ~10% accuracy when simultaneous measurements are performed and standards are similar in composition.

**Jay M. Gehlhausen and Jon W. Carnahan\***, Department of Chemistry, Northern Illinois University, DeKalb, IL 60115

### Automated Model Selection for the Simulation of Carbon-13 Nuclear Magnetic Resonance Spectra of Cyclopentanones and Cycloheptanones 2435 ■

A method to select appropriate regression models for the prediction of <sup>13</sup>C NMR chemical shifts is developed. Models are selected from a database containing previously reported equations and newly generated ones developed for cyclopentanones and cycloheptanones. The models yield a mean standard error of 1.12 ppm.

**Jon W. Ball, Lawrence S. Anker**, and **Peter C. Jurs\***, Department of Chemistry, The Pennsylvania State University, 152 Davey Laboratory, University Park, PA 16802

### Scanning Electrochemical Microscopy. 11. Improvement of Image Resolution by Digital Processing Techniques 2442

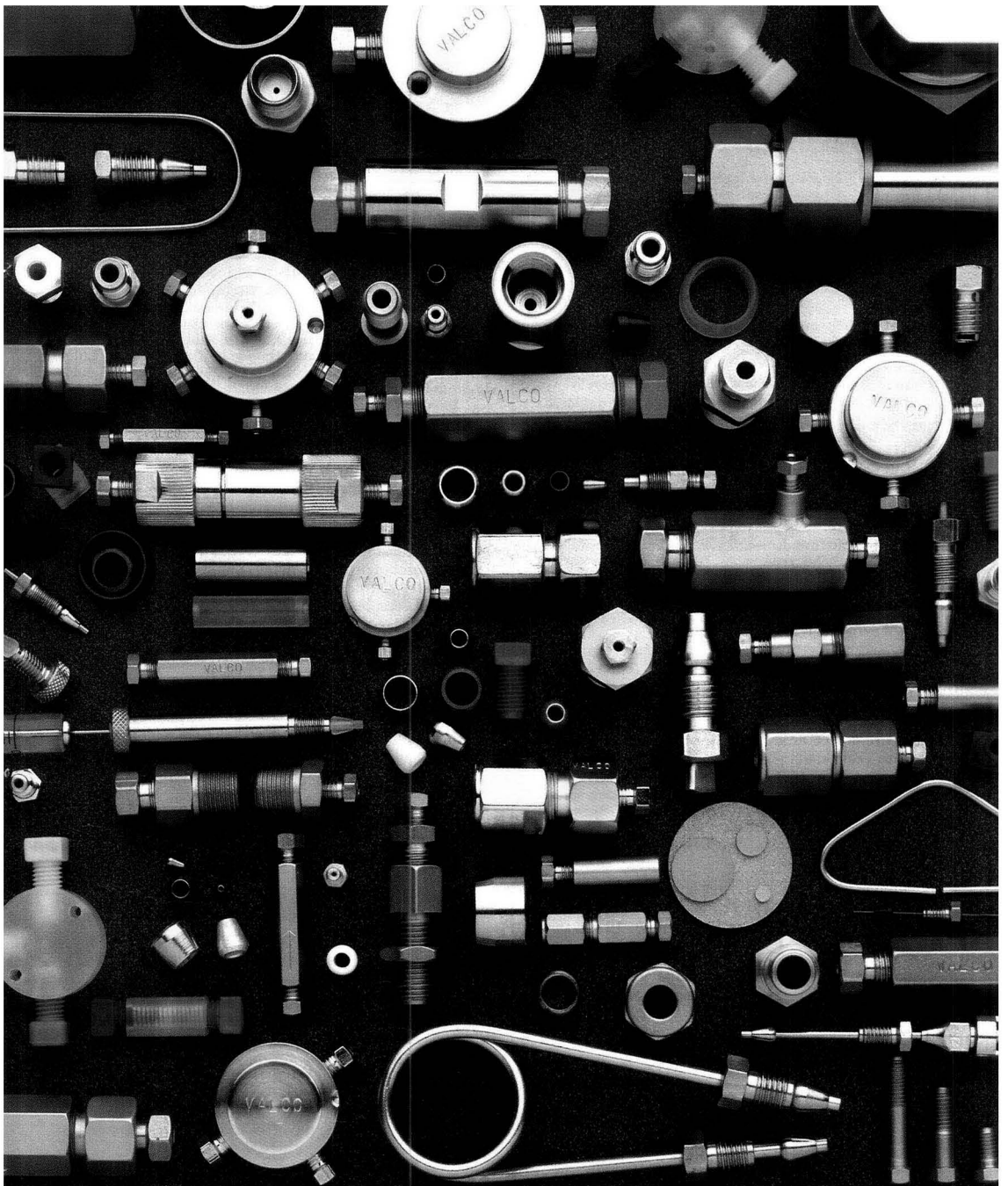
A linear combination of Laplacian and Gaussian filters applied to scanning electrochemical microscope images provides processed images with improved resolution (comparable to the resolution obtained with tips three to four times smaller).

**Chongmok Lee, David O. Wipf**, and **Allen J. Bard\***, Department of Chemistry and Biochemistry, The University of Texas at Austin, Austin, TX 78712 and **Keith Bartels and Alan C. Bovik**, Department of Electrical and Computer Engineering, The University of Texas at Austin, Austin, TX 78712

\*Corresponding author

■ Supplementary material available





**MORE HIGH PRECISION FITTINGS THAN ANYWHERE ELSE IN THE WORLD.**

**VICI**

Valco Instruments Co. Inc.  
P.O. Box 55603, Houston, TX 77255 USA  
Telephone (713) 688-9345  
Telefax (713) 688-8106 Telex 79-0033 VALCO HOU

**VICI**AG

Valco Europe  
Untertannberg 7 CH-6214 Schenkon, Switzerland  
Telephone (045) 21 68 68  
Telefax (045) 21 30 20 Telex 868342 VICI CH

CIRCLE 149 ON READER SERVICE CARD

**Quantitative Surface Analysis of Organic Polymer Blends Using a Time-of-Flight Static Secondary Ion Mass Spectrometer 2447**

Surface compositions of bisphenol-A polycarbonate/polystyrene and tetramethylcarbonate/polystyrene polymer blends are determined using TOF-SSIMS and XPS. Accuracy for both TOF-SSIMS and XPS is within  $\pm 0.1$  monomer fraction, whereas the typical precision of the TOF-SSIMS results is primarily determined by counting statistics and is generally better than that of the XPS results.

**Patrick M. Thompson**, Surface Science Section, Research Laboratories, Eastman Kodak Company, Rochester, NY 14650-2132

**Determination of the Concentration and Stable Isotopic Composition of Nonexchangeable Hydrogen in Organic Matter 2456**

Multiple isotopic equilibrations of exchangeable hydrogen with isotopically different water vapors, subsequent bulk  $\delta D$  determinations, and mass balance calculations reveal the concentration and D/H ratio of nonexchangeable hydrogen.

**Arndt Schimmelmann**, University of California at San Diego, Scripps Institution of Oceanography, La Jolla, CA 92093-0215

**Theoretical Analysis of Probe Dynamics in Flow Injection/Membrane Introduction Mass Spectrometry 2460**

A mathematical analysis is performed on membrane pervaporation used in conjunction with FIA. The effects of flow rate, injection time profile, mixing in the flow chamber, partitioning onto the membrane surface, diffusion through the membrane, and membrane thickness and temperature on the analyte flux are discussed and compared with experimental results.

**Gow-Jen Tsai**, **Glen D. Austin**, **Mei J. Syu**, and **George T. Tsao**, Laboratory of Renewable Resources Engineering, Purdue University, West Lafayette, IN 47907 and **Mark J. Hayward**, **Tapio Kotiaho**, and **R. Graham Cooks\***, Department of Chemistry, Purdue University, West Lafayette, IN 47907

**Supercritical Fluid Chromatography and Time-of-Flight Secondary Ion Mass Spectrometry of Poly(dimethylsiloxane) Oligomers in the Mass Range 1000–10 000 Da 2466**

SFC and TOF-SIMS give similar results when determining the average molecular weights and the shape of oligomer distributions in the mass range up to 3000 Da. Differences occur at higher masses because of mass discrimination effects.

**Birgit Hagenhoff**, **Alfred Benninghoven\***, **Herbert Barthel**, and **Wolfgang Zoller**, Physikalisches Institut der Universität Münster, Wilhelm-Klemm-Strasse 10, D-4400 Münster, F.R.G.

**Matrix-Assisted UV-Laser Desorption/Ionization Mass Spectrometric Analysis of Monoclonal Antibodies for the Determination of Carbohydrate, Conjugated Chelator, and Conjugated Drug Content 2470**

Methods are described for estimating carbohydrate content and determining quantity and distribution of chelators and drugs bound to monoclonal antibodies using matrix-assisted UV-laser desorption/ionization MS. Results are compared with currently used methods.

**Marshall M. Siegel\***, **Irwin J. Hollander**, **Philip R. Hamann**, **John P. James**, and **Lois Hinman**, American Cyanamid Company, Medical Research Division, Lederle Laboratories, Pearl River, NY 10965, **Bryan J. Smith**, **Andrew P. H. Farnsworth**, **Alison Phipps**, and **David J. King**, Celtech, Ltd., Slough SL1 4EN Berkshire, U.K., and **Michael Karas**, **Arndt Ingendoh**, and **Franz Hillenkamp**, Institute of Medical Physics, University of Münster, D-4400 Münster, F.R.G.

**Direct Introduction of Large-Volume Urine Samples into an On-Line Immunoaffinity Sample Pretreatment-Capillary Gas Chromatography System 2481**

An immunoaffinity precolumn containing immobilized antibodies raised against the synthetic steroid hormone  $\beta$ -19-nortestosterone is used for the automated sample pretreatment of 5–25 mL urine samples containing  $\beta$ -19-nortestosterone, norethindrone, and norgestrel. The 19-norsteroids can be determined at the ppt level.

**A. Farjam**, **J. J. Vreuls**, **W.J.G.M. Cuppen**, **U.A.Th. Brinkman\***, and **G. J. de Jong**, Department of Analytical Chemistry, Free University, De Boelelaan 1083, 1081 HV Amsterdam, The Netherlands

**Tandem Mass Spectrometry of Very Large Molecules: Serum Albumin Sequence Information from Multiply Charged Ions Formed by Electrospray Ionization 2488**

Limited primary sequence information is obtained for intact 66 kD serum albumin proteins from 10 different species by electrospray ionization tandem MS.

**Joseph A. Loo**, **Charles G. Edmonds**, and **Richard D. Smith\***, Chemical Sciences Department, Pacific Northwest Laboratory, Richland, WA 99352

**Nondependence of Diffusion-Controlled Peak Dispersion on Diffusion Coefficient and Ionic Mobility in Capillary Zone Electrophoresis without Electroosmotic Flow 2499**

The single analyte-specific property responsible for peak broadening is the charge number, not the diffusion coefficient,  $D$ , or the ionic mobility,  $u$ . This result is derived theoretically by substituting the ratio  $u/D$ , occurring in the conventional expression for the plate number, with the relation between these parameters as given by Einstein.

**Ernst Kenndler\*** and **Christine Schwer**, Institute for Analytical Chemistry, University of Vienna, Währingerstrasse 38, A 1090 Vienna, Austria





## THE WORLD'S BEST MASS SPECTROMETER IS NOW WITHIN YOUR REACH.

If you think Finnigan MAT is beyond your laboratory's reach, you've got a nice surprise coming.

The SSQ® 710 *Advantage*™ now fits easily within your MS budget, while delivering twice the performance and quality of HP's MS Engine. Compare:

We deliver as standard: 2000 amu mass range, 20 kV dynode multiplier, turbomolecular pumping, easy-to-use Instrument Control Language™ and the most complete

and powerful data system in mass spectrometry. And you get complete inlet options, including Electrospray.

With MS Engine, you'll pay extra for extended mass range, and money just can't buy *Advantage's* other features on that instrument.

For complete details, call your Finnigan MAT office below. Or FAX (408) 433-4823.



A subsidiary of Thermo Instrument Systems, Inc.

California (408) 433-4800 • Georgia (404) 424-7850 • Ohio (513) 891-1255 • Illinois (708) 310-0140 • New Jersey (201) 740-9177  
Maryland (301) 698-9760 • Germany (0421) 54 93-0 • UK (0442) 233555 • France (01) 69 41 98 00 • Italy (02) 66011742 • Netherlands (08385) 27266  
Sweden (08) 6800101 • Japan (03) 3372-3001

CIRCLE 44 ON READER SERVICE CARD

## BRIEFS

### Migration Behavior of Cationic Solutes in Micellar Electrokinetic Capillary Chromatography 2503

Migration of cationic solutes in MECC is quantitatively described through mathematical models that allow the prediction of solute behavior based on a limited number of experiments and facilitate the optimization of separations.

**Joost K. Strasters and Morteza G. Khaledi\***, Department of Chemistry, North Carolina State University, P.O. Box 8204, Raleigh, NC 27695

### High-Speed Countercurrent Chromatography Used for Alkylbenzene Liquid-Liquid Partition Coefficient Determination 2508

Partition coefficients of alkylbenzenes from benzene to dodecylbenzene are measured by CCC in seven methanol-rich compositions (water  $\leq 20\%$  v/v) of the heptane-methanol-water biphasic liquid system.

**Alain Berthod\* and Madeleine Bully**, Laboratoire des Sciences Analytiques, UA CNRS 435, Université de Lyon 1, 69622 Villeurbanne Cedex, France

### Real-Time Principal Component Analysis Using Parallel Kalman Filter Networks for Peak Purity Analysis 2512

A recursive algorithm for performing principal component analysis on multivariate data sets is described. The procedure, based on principles of the adaptive Kalman filter, is used to determine the rank of multiwavelength chromatographic data.

**Stephen J. Vanslyke and Peter D. Wentzell\***, Trace Analysis Research Centre, Department of Chemistry, Dalhousie University, Halifax, Nova Scotia, Canada B3H 4J3

### Concentration of Hydrophobic Organic Compounds and Extraction of Protein Using Alkylammoniosulfate Zwitterionic Surfactant Mediated Phase Separations (Cloud Point Extractions) 2520

The synthesis and evaluation of the phase separation behavior of two zwitterionic surfactants, 3-[nonyl- (or decyl-) dimethylammonio]propyl sulfate, is reported. Results indicate that such surfactants can be used for the extraction/preconcentration of hydrophobic species in a manner similar to that reported for nonionic surfactants.

**Tohru Saitoh and Willie L. Hinze\***, Department of Chemistry, Laboratory for Analytical Micellar Chemistry, Wake Forest University, P.O. Box 7486, Winston-Salem, NC 27109

## Correspondence

### Quadrupole Fourier Transform Mass Spectrometry of Oligosaccharides 2526

**James A. Carroll, Lambert Ngoka, Sési McCullough, Eric Gard, A. Daniel Jones, and Carlito B. Lebrilla\***, Department of Chemistry and Facility for Advanced Instrumentation, University of California, Davis, CA 95616

### Separation and Determination of Copper, Zinc, Palladium, Iron, and Manganese with *meso*-Tetrakis(3-bromo-4-sulfophenyl)porphine and Reversed-Phase Ion-Pair Liquid Chromatography 2529

**Xue-Jun Xu, Hua-Shan Zhang, Chuan-You Zhang, and Jie-Ke (Jai-Kai) Cheng\***, Department of Chemistry, Wuhan University, Wuhan 430072, China

## Technical Notes

### Determination of Total and Free Sulfur Dioxide in Wine by Flow Injection Analysis and Gas-Diffusion Using *p*-Aminoazobenzene as the Colorimetric Reagent 2532

**Jordi Bartroli\*, Manel Escalada, Cecilia Jimenez Jorquera, and Julian Alonso**, Department de Química, Universitat Autònoma de Barcelona, 08193 Bellaterra, Spain

### Bulk-Electrolysis Flow-Cell System for UV-Visible and X-ray Absorption Spectroelectrochemical Analysis 2535

**David H. Igo, R. C. Elder\*, and William R. Heineman\***, Department of Chemistry, University of Cincinnati, Cincinnati, OH 45221-0172 and **Howard D. Dewald**, Department of Chemistry and Condensed Matter and Surface Science Program, Ohio University, Athens, OH 45701-2979

### On-Line Preconcentration and Volatilization of Iodine for Inductively Coupled Plasma Atomic Emission Spectrometry 2539

**Scott P. Dolan, Scott A. Sinex, and Stephen G. Capar**, Division of Contaminants Chemistry, Food and Drug Administration, Washington, DC 20204 and **Akbar Montaser\* and Robert H. Clifford**, Department of Chemistry, George Washington University, Washington, DC 20052

### Determination of Small Amounts of Water in Dimethylformamide and Dimethylsulfoxide Using Luminescence Lifetime Measurements of Europium (III) 2542

**Stefan Lis and Gregory R. Choppin\***, Department of Chemistry, The Florida State University, Tallahassee, FL 32306-3006

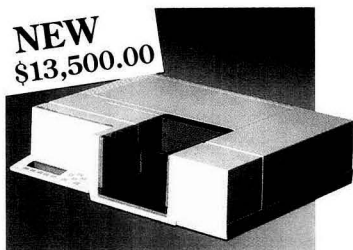
### Correction. Horizontal Touch Voltammetric Analysis—Determination of Insoluble Electroactive Species in Films at the Air/Water Interface 2544

**Cary J. Miller and Allen J. Bard\***, Department of Chemistry, The University of Texas at Austin, Austin, TX 78712



# Why Are More And More FTIR Users Buying Mattson?

## Low Cost



Workhorse FTIR for QC or teaching applications.

- High return on investment quickly justifies purchase.
- Gets analysis routines on line fast—short operator learning curve.
- Survives harsh lab environments with sealed and desiccated optical system.

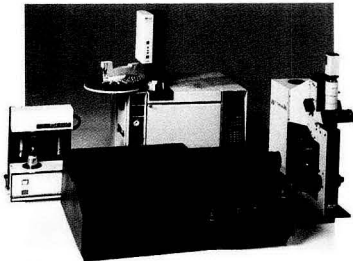
## Analytical Spectroscopy



Flexible systems for analytical spectroscopy.

- Unparalleled flexibility—high resolution and the fastest scan speed of any FTIR.
- GC-FTIR includes full automation and control of GC autosampler with real-time IR acquisition and display.
- Full range of IR-Microscopy systems; both in-compartment and external bench TGA interfaces.

## Research Spectroscopy



Spectroscopy for research applications.

- Spectral range coverage from 25,000 to 225  $\text{cm}^{-1}$  at 0.25  $\text{cm}^{-1}$  resolution.
- High-intensity fluid-cooled source and continuously adjustable computer controlled iris aperture.
- Two external beams for mounting external bench experiments and accessories.



**Mattson**

**Mattson Instruments, Inc.**  
1001 Fourier Drive  
Madison, WI 53717  
Tel. (608) 831-5515  
Fax: (608) 831-2093

Mattson, Orion, and Unicam are operating divisions of Analytical Technology, Inc

**Free personal computer with  
Galaxy™ Series 5000, 7000 and  
Research Series™ FTIR Spectrometers!  
Limited time offer.**

CIRCLE 80 ON READER SERVICE CARD

# Phone (800)228-4250 and discover new solutions to your analysis problems

## Capillary Electrophoresis

CE is a powerful new tool for separation and analysis of proteins, peptides, organic acids, nucleotides, and other sample mixtures.

Isco's two CE systems give you femtomole detection sensitivity with nanoliter samples.

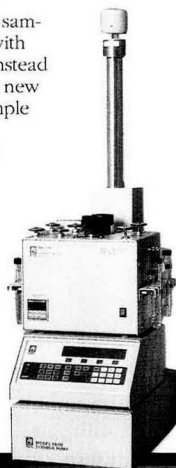
One system is automated with computer data management; the other is a compact, affordable "personal CE".



CIRCLE 64 ON READER SERVICE CARD

## SFE Sample Prep

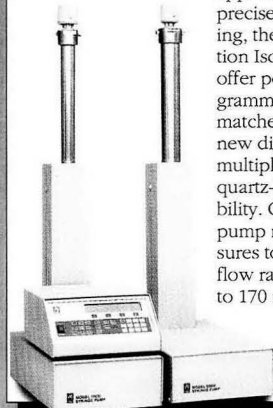
Prepare your GC or HPLC samples quickly and cleanly with low-cost, non-toxic CO<sub>2</sub> instead of organic solvents. These new extraction systems cut sample prep time to minutes and eliminate solvent disposal problems. The extractor uses finger-tight sample cartridges and handles two samples at once—ideal for busy environmental, industrial, and contract-analysis labs.



CIRCLE 65 ON READER SERVICE CARD

## Precision fluid metering

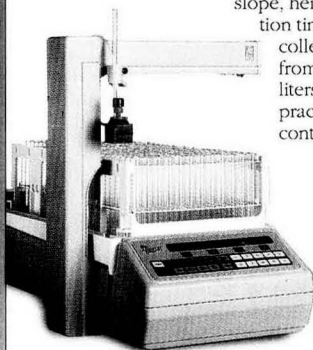
For reactant feed and other applications requiring precise, pulse-free metering, these fourth-generation Isco syringe pumps offer powerful new programmability and unmatched performance. A new digital controller runs multiple pumps with quartz-locked flow stability. Choose from three pump modules with pressures to 10,000 psi and flow rates from 0.1  $\mu$ l/min to 170 ml/min.



CIRCLE 66 ON READER SERVICE CARD

## Foxy 200 fraction collector

Improve your preparative LC with the smartest fraction collector available. Foxy 200 makes it easy to collect just the peaks you want – by slope, height, or retention time. Reliably collect anything from drops to liters/minute in practically any containers.



CIRCLE 67 ON READER SERVICE CARD

**Call toll-free today for your copy of  
our big, 120-page catalog.**

Isco, Inc., P.O. Box 5347  
Lincoln NE 68505 U.S.A.  
Tel. (800)228-4250  
Fax (402)464-0318

Isco Europe AG, Brüschstr. 17  
CH8708 Männedorf, Switzerland  
Fax (41-1)920 62 08



**ISCO**

## The Curious Value of Research

The prevailing attitude of researchers in chemistry, indeed almost a basic tenet, is that research—the pursuit of knowledge—is an intrinsically good profession. Seeking new knowledge and understanding, a clearer vision of fact, and the invention of new modes of thought about chemical phenomena, is viewed as a desirable thing. New knowledge should not be refused or eschewed; ignorance is not bliss; and the innate curiosity of the human species requires scratching.

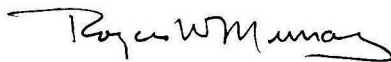
A great segment of modern society tends to take a more practical view of research. What good does this curiosity-scratching do? What are the motivations of those who pursue it? Who decides how the results are to be used? And how are they used? Should society consume resources to support research activities? These and other questions have been raised repeatedly over the years. They seem loudest and most persistent in times of greatest worldwide stress.

These are all reasonable questions that deserve attention and response, not silence or evasion, from the academic, government, and industrial research communities—including their analytical chemists. There are many forms of answers. Certainly the most important individual and personal motivation for research is intellectual curiosity. What are the chemical phenomena around us that affect our lives? How can we control chemical phenomena in useful ways? These are perhaps the clearest and easiest questions for society to answer because most segments of society have their own very basic brands of intellectual curiosity. How does my lawnmower work? What makes the weather? What are the best spice ingredients for a particular dinner? How do you judge where the fish lie? These questions begin to illustrate the diversity of curiosities. Nurturing our children's curiosity, and conveying to them in home, school, college,

and university a sense of the excitement of scientific thought, experiment, and deduction, are important parts of an education that prepares them to live and work successfully in our technological age. The research community serves as a resource and role model to society when we convey the reasons, rewards, and pervasiveness of intellectual curiosity that we know so well.

There are of course many other motivations for intellectual curiosity, both individual and collective. The corporate curiosity is a collective one, with a motivation of seeking originality and innovation in products and processes with an end goal of economic success. Individuals participating in the corporate curiosity derive added satisfaction from seeing their research efforts leading to products valued and used by society. In colleges and universities, researchers are teaching young chemists about the use of curiosity at a very sophisticated level, to seek new chemical knowledge. Professors derive a different satisfaction, that of seeing their products—these young chemists—become useful parts of the world of chemistry. Whether or not the motivations of particular individuals are to serve society, their products—the materials and goods of a technological age and the trained young minds to help advance it—offer clear societal benefits.

History also teaches us that a regrettable but major motivation for national collective chemical research is to acquire the offensive and defensive paraphernalia of armed conflict. It is hoped that the changes occurring on the world scene do not waste the intellectual energies that have been consumed in this area but instead redirect those energies to the needs of peaceful societies.



## Low dead volume SWAGELOK® Tube Fittings for Chromatography

- █ Leak-free sealing provides consistency in liquid or gas systems
- █ Optimum size, capability and selection
- █ Minimum dead space for reduced purge time and precise repeatability
- █ 316 stainless steel construction for use with a wide range of carrier gases and solvents

Immediate delivery from your Local Authorized Sales & Service Representative.

© 1989 Swagelok Co., all rights reserved PG-2-084



SWAGELOK Co.  
Solon, Ohio 44139  
SWAGELOK Canada Ltd., Ontario



CIRCLE 125 ON READER SERVICE CARD

## SWAGELOK® Tube Fittings for polyethylene tubing

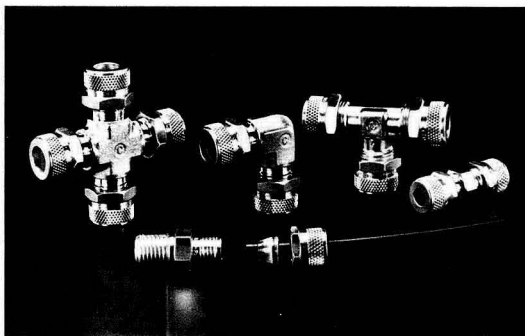
- █ Leak-tight seal on polyethylene tubing, even in dynamic applications
- █ Easy installation — 1-1/4 turns with wrench
- █ Finger-tight remake with knurled nut
- █ Brass and 316SS, with nylon or TFE ferrules
- █ Male connectors, unions, union tees, 90° elbows, crosses
- █ Sizes 1/4" to 1/2"

Immediately available from your local Authorized Sales & Service Representative.

© 1989 Swagelok Co. all rights reserved PG-2-086



SWAGELOK Co.  
Solon, Ohio 44139  
SWAGELOK Canada Ltd.  
Ontario



CIRCLE 126 ON READER SERVICE CARD

Whether you are in research, development, management, or all three . . .

**CHEMTECH** is the publication you should be reading!



**CHEMTECH** is so stimulating, so wide-ranging, so idea-packed, it's guaranteed! Once you've seen an issue of CHEMTECH, you'll want to use it every day.

### ARTICLES

You'll welcome regular access to wide-ranging authoritative articles on management . . . legal issues . . . new chemical technologies . . . chemical effects within the environment . . . development of new materials . . . new engineering techniques . . . education . . . business strategies . . . uses of computers and robotics . . . just to name a few.

**CHEMTECH** also contains regular features that will undoubtedly become your favorite reading . . .

### VALUED HIGHLIGHTS

*Heart Cut* points the way to new products, processes, research, or simply that odd fact you wouldn't see anywhere else . . . highlights from current literature.

### EYE-OPENING OPINIONS

View from the *Top* gives CEO's, legislators, and other top-ranking industry leaders a chance to speak out. The *Guest Editorial* is one person's opinion on important issues of all kinds. And each month the founding editor, *B.J. Luberoff*, provides a provocative look at today's world.

**CHEMTECH** also looks at the world with a lighter eye in *The Last Word* and original cartoons.

### See for yourself . . . Subscribe today!

ISSN:0009 2703	Volume: 21	U.S.	Canada & Mexico	Europe**	All Other Countries**
1991 Rates					
Members*	One Year	\$ 41	\$ 50	\$ 57	\$ 61
	Two Years	\$ 69	\$ 87	\$101	\$109
Nonmembers (Personal)	One Year	\$ 75	\$ 84	\$ 91	\$ 95
	Two Years	\$127	\$145	\$159	\$167
Nonmembers (Institutional)	One Year	\$325	\$334	\$341	\$345
	Two Years	\$552	\$570	\$584	\$592

\*For personal use only. \*\*Air Service included.

Foreign payment must be made in U.S. dollars by international money order, UNESCO coupons, or U.S. bank draft. Orders accepted through your subscription agency. For nonmember rates in Japan, contact Maruzen Co., Ltd.

Subscriptions to CHEMTECH will begin when order is received and will expire one year later unless specific start date is requested. Please allow 45 days for delivery of your first issue.

To subscribe, contact: American Chemical Society, Marketing Communications Dept., 1155 Sixteenth Street, NW, Washington, DC 20036. Telex: 440159 ACSP UI or 89 2582 ACSPUBS

In a hurry? Call TOLL FREE (800) 227-5558 (U.S. and Canada) and charge your order! In D.C. or outside the U.S. and Canada call (202) 872-4363. Or FAX your order: (202) 872-4415. Please send FAX to the attention of the Marketing Communications Department.



## Division Officers Elected



**Joseph L. Glajch**, research manager of the New Product Chemistry Group of the DuPont Merck Pharmaceutical Company, North Billerica, MA, was recently elected chairman-elect of the ACS Division of Analytical Chemistry.

Glajch received his A.B. degree from Cornell University and a Ph.D. in analytical chemistry from the University of Georgia in 1978, working under the direction of L. B. Rogers. He then joined the Central Research and Development Department at E. I. du Pont de Nemours & Co. in Wilmington, DE, where he worked in a process research/catalysis group developing chromatographic methods for on-line measurement before becoming a supervisor in the molecular biology section, where he was responsible for separations research, protein characterization, and oligonucleotide synthesis. In 1985 he moved to the analytical section as the supervisor of a separations research group and continued work on column packing development and optimization of phase systems in HPLC.

Glajch currently is responsible for formulation and analytical methods development of radiopharmaceuticals. He has 33 publications and three patents in the field of analytical chemistry. He has served as president of the Chromatography Forum of the Delaware Valley and helped initiate collaboration among chromatography discussion groups in the mid-1980s. In 1982 he was program chairman of the International Symposium on Column Liquid Chromatography, on whose organizing committee he continues to serve. Glajch is a past member of the Executive Committee of the Separations Subdivision of the ACS Division of Analytical Chemistry and has served the Delaware Section of ACS as a staff member of its local publication, the *Del-Chem Bulletin*. He currently holds memberships on the Executive Committee of the New England Chromatography Council and the Division of Analytical Chemistry Graduate Fellowship Committee. He is also chairman of the 1991 Gordon Conference on Analytical Chemistry.

Other officers elected were Sarah Rutan of Virginia Commonwealth University, secretary; William Heine-man of the University of Cincinnati, counselor; and Roland Hirsch of the National Institutes of Health, alternate counselor. Charles Wilkins of the University of California-Riverside assumed the 1991 chairmanship in October. David Curran of the University of Massachusetts will continue to serve as treasurer.

Continuing to serve as counselors are Edward Yeung of Iowa State University, Jeanne Pemberton of the University of Arizona, and Galen Ewing, formerly of Seton Hall University. Ted Williams of the College of Wooster, Margaret Merritt of Wellesley College, and Robert Osteryoung of the State University of New York at Buffalo will continue to serve as alternate counselors.

## Nobuhiko Ishibashi—Spectroscopist



The JOURNAL regrets to report the death of Nobuhiko Ishibashi of the School of Engineering, Kyushu University, Fukuoka, Japan, on Aug. 23, 1991. Ishibashi was a distinguished scholar and leader in Japanese analytical chemistry and served on the Advisory Board of ANALYTICAL CHEMISTRY from 1987 to 1989.

## Chromatography

The International Union of Pure and Applied Chemistry (IUPAC) Commission on Analytical Nomenclature is seeking comments on a document entitled "Nomenclature for Chromatography." This document lists all the terms and definitions used in the major chromatographic techniques, such as gas, liquid, supercritical fluid, column, planar, partition, adsorption, ion-exchange, and size-exclusion chromatographies.

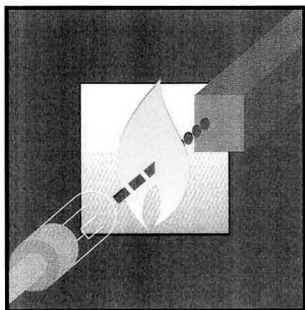
A copy of the document is available from the ACS Journals Department, P.O. Box 3330, Columbus, OH 43210. Comments should be sent by June 30, 1992, to C. A. Cramers, Eindhoven University of Technology, Laboratory of Instrumental Analysis, Department of Chemistry, 5600 MB Eindhoven, The Netherlands.

## For Your Information

*Graduate School and Beyond*, a booklet from the U.S. Department of Energy's Argonne National Laboratory, provides college women interested in science careers with practical, how-to advice from women scientists. Based on a panel discussion at the Laboratory's annual "Science Careers in Search of Women" conference, the booklet offers personal experience and guidance on selecting a graduate school, supporting oneself through school, choosing a thesis advisor, combining a career and family life, planning for the future, and fulfilling unspoken requirements such as preparing and giving seminar talks. To order, contact the Division of Educational Programs, Argonne National Laboratory, 9700 S. Cass Ave., Argonne, IL 60439.

The Joint Committee on Atomic and Molecular Physical Data (JCAMP) is organizing a round-robin program exchange of JCAMP-DX data files. Software developers and instrument vendors are invited to submit files prior to Jan. 1, 1992. Each participating user will receive an IBM PC-compatible diskette and a request for a report on how well the software reads the files. Results will be reported at Pitcon '92. For further information, contact Robert S. McDonald, 9 Woodside Dr., Burnt Hills, NY 12027 (518-399-5145, fax 518-399-6868).

# A HISTORY OF ATOMIC ABSORPTION SPECTROMETRY



The Second James L. Waters Annual Symposium Recognizing Pioneers in the Development of Analytical Instrumentation was held at the 1991 Pittsburgh Conference and Exposition in Chicago. This year's symposium honored four pioneers in the field of atomic absorption spectroscopy: Alan Walsh, Boris L'vov, S. R. Koirtyohann, and Walter Slavin. In the October 1 issue, L'vov and Walsh recounted their efforts in developing AAS as an analytical method. Here Koirtyohann discusses these developments from an academic perspective and Slavin explores the reasons for the success of AAS.

## S. R. Koirtyohann

Department of Chemistry  
University of Missouri-Columbia  
Columbia, MO 65211

Viewed from a 35-year perspective, atomic absorption spectroscopy (AAS) is a tremendous success story. It is easy to forget that this success did not happen as soon as the idea was introduced. Individuals and companies had to invest considerable amounts of time, money, and talent, and not everyone who sought to take advantage of this new technology was equally successful. The purpose here is to review the historical facts and consider reasons for the variability in the degree of success achieved.

### Early history

If history were concerned only with *what* happened, we could begin by considering two papers published in 1955 (1, 2). However, because the intent here is to understand (or at least speculate about) *why* certain things happened, we must look briefly at earlier years. Historical chapters in books by Twyman (3) and Slavin (4) are particularly helpful.

Optical spectroscopy can be traced to 1672, when Newton observed that sunlight could be separated into colors upon passage through a prism. Indeed, the word spectrum comes from Newton's attempt to describe the ghostly appearance of dispersed sunlight. The first person to observe spectral features other than simple colors was Wollaston, who in 1802 described (but made no attempt to explain or characterize) numerous dark lines in the sun's spectrum. Starting in 1817, Fraunhofer carefully mapped these lines that bear his name and designated some of the more prominent ones by letters, starting with A at the red end of the spectrum. Even today, one sees reference to the sodium D lines, using Fraunhofer's original designation. His observations also laid the groundwork for spectral observations in astronomy. Fraunhofer noted that light from Venus looked much like that from the Sun but that light from the bright star, Sirius, had a very different spectrum.

Kirchhoff and Bunsen explained the origin of Fraunhofer lines in a classic series of papers published in 1859 and 1860. They not only explained that Fraunhofer lines were caused by atomic absorption in the Sun's atmosphere; they also established the general laws of emission and absorption of light and described the conditions needed for earthbound analytical observations using flames in both emission and atomic absorption. Flame analysis became common in Bunsen's lab, and several new elements were discovered by spectral analysis in the early 1860s. However, the full analytical potential of both flame emission and atomic absorption remained unexploited for many years.

Other significant events in the development of spectral analysis, to be discussed in greater detail below, include:

- The first quantitative spectral analyses by Lockyer in 1873
- Hartley's work on the quantitative analysis of solutions, beginning in about 1884 at the University of Dublin and continued by Pollok and Leonard well into this century
- de Gramont's studies at the Sorbonne in the early 1900s
- Twyman's design of the first convenient commercial spectrographs at Adam Hilger Ltd. from 1909 through 1912
- The first U.S. journal paper on spectral analysis by Meggers in 1922
- The development of flame spectral analysis by Lundegårdh in Sweden starting in 1929
- Direct electrical detection of flame emission spectra by Jansen, Hayes, and Richter in the mid-1930s
- Introduction of the Beckman DU spectrophotometer (the instrument generally credited with converting chemists to spectral thinking) in 1941 and the photomultiplier attachment for that instrument in 1953.

### Modern AAS

We begin with a "thumbnail" history covering the first three and a half decades of flame AAS. There were several distinct periods, as indicated in the box on p. 1026 A.

The induction period is best characterized by what did not happen.

# FROM AN ACADEMIC PERSPECTIVE

Atomic absorption—the technique that soon would revolutionize elemental analysis—was ignored by nearly all practicing analytical chemists. Walsh and a mere handful of people down under developed the method and demonstrated its utility time and time again—and still people stayed away in droves. Walsh traveled extensively, trying to promote AAS, and was often frustrated by his inability to generate wide interest. His American friends have not let him forget that he once accurately described the United States as a country “underdeveloped” in AAS.

From 1962 through 1969 explosive growth occurred as AAS caught on and surged to the forefront of elemental analysis. The period opened, at least from my perspective, with the 10th Colloquium Spectroscopicum Internationale in College Park, MD, in June 1962 and closed with the 2nd International Conference on Atomic Spectroscopy in Sheffield, England, in July 1969.

My own active participation in atomic absorption research nearly coincides with the beginning of this explosive period, which may explain why I think of it as the “fun time.” AAS symposia were spiced by frequent (usually polite) arguments about the best sources and atomizers. New techniques and applications were suggested almost as rapidly as most of us could follow. This high level of interest made a heady brew for those fortunate enough to be involved at that time.

Such explosive growth could hardly be sustained, and 1969–76 was a period of relative stability (i.e., relative to that of the previous years). AAS put on its work clothes and began to generate data for other fields. Research was still being done, and improvements were still being made, but for anyone who had participated in the exciting growth period the slower pace was obvious.

In about 1976 the revolution in solid-state electronics began to make an impact on chemical instrumentation, and there appears to be no end in sight. Most AAS customers today are at least as interested in software as in hardware. Instrument throughput and, to a lesser extent, instru-

ment capabilities have been enhanced whereas much of the tedium of routine analysis has been removed. One disadvantage of this revolution is that AAS systems are much more difficult to learn to use, especially for an old fogey like me. With older instruments, I could start with reasonably bright but totally untrained college freshmen and have them generating AAS data in 10–30 minutes, depending on the complexity of the work. Today 30 minutes hardly suffices for an introduction to the software manual, and without a working knowledge of the software, you can't even turn the #@%\$&%“\_+ thing on!

Now let us return briefly to the fun time, because much of what we see in AA instruments today is a consequence of arguments resolved then. At least in certain areas of the midwestern United States, flames continued to emit. Velmer Fassel and co-workers at Iowa State University (5) and Ed Pickett and I at the Univer-

## REPORT

sity of Missouri (6), along with a few others, pointed out repeatedly that the emission mode of operation had certain advantages and should not be abandoned. In the intervening years we have not changed our minds, but we seem to have made little progress in convincing others. Few people use flame emission today, even in cases where the advantages are significant and easily demonstrated.

During the fun time, detection limits were a source of great pride and it seemed that nearly every conference paper included a claim to have established a new record in the quest for zero. A discussion of interferences was sure to spark instant debate; many researchers argued that AAS was much less prone than atomic emission to effects from chemical interferences. The very existence of spectral interferences in AAS was vigorously denied by proponents of the technique. The confusion concerning interferences can perhaps be best conveyed by quoting from a publication of the period (7): “Atomic ab-

sorption spectroscopy does not suffer from chemical interferences but (the) presence of large amounts of anions and cations can cause pronounced effects on absorption.”

In other words, it is not the chemicals, but those blasted anions and cations that cause the problems. The authors of the above statement should be defended, because they were not writing in their native tongue and undoubtedly had a language problem. The fact that such a statement got past two reviewers and a journal editor is harder to understand and is indicative of the confusion that prevailed.

By 1969 most misconceptions about AAS had been resolved. Spectral interferences, although relatively rare, were acknowledged, and chemical interferences were known to be primarily a function of the atomizer, not the mode of observation. Atomic fluorescence had been introduced, and people already were beginning to wonder why it was not more popular. Automated background correction systems for AAS were available and, in an important advance, the nitrous oxide–acetylene flame had nearly doubled the number of elements to which AAS was applicable. The evolution of flame AAS was essentially complete. Furnaces had been introduced and their evolution was just beginning, but that is another story.

### Ideas that did not succeed

This evolution did not proceed along a smooth pathway. Although numerous approaches to doing AAS were tried, most eventually were discarded. A few of these, listed below, will be discussed in detail.

- Total consumption nebulizer–burners
  - Multipass optical systems
  - Heated spray chambers
  - Hot gas nebulization
  - The tantalum boat
  - Premixed oxygen–acetylene flames
  - Flame-in-tube designs

In the 1950s emission flame photometry in the United States was dominated by the use of a combination nebulizer–burner marketed by Beckman Instruments. The combus-

## REPORT

tion gases were mixed only after they exited the burner, and solution aerosol was sprayed directly into the resulting turbulent flame. Because the gases were not premixed, nearly any fuel-oxidant combination could be used safely. Oxygen-hydrogen and oxygen-acetylene flames were quite popular for emission work.

It is not surprising that when AAS arrived on the scene many people tried to retain the simple and familiar burner. The short absorption pathlength was a disadvantage, however, and workers tried various ways to overcome this deficiency. An optical system that passed light from the primary source through the flame from a tandem array of three such burners as many as five times was developed commercially. The sound level was roughly comparable to that of a jet plane taking off.

This and other attempts to use total consumption burners failed not because of the short absorption pathlength, however, but because large aerosol droplets were injected into the flame rather than separated in a spray chamber. Gradually it was shown that incomplete vaporization of analyte contained in large droplets, rather than the emission mode of operation, was the cause of many chemical interferences.

Conventional AAS burners waste about 90% of the sample solution. Many people sought ways to avoid that loss and enjoy an instant 10-fold improvement in detection limits. Heating the spray chamber to vaporize much of the solvent increased sample transport and was successful if only detection limits were considered. Unfortunately, memory effects were quite severe, and this method never became popular. Heating the nebulizing gas resulted in greater sensitivity, but at the cost of severe nebulizer clogging problems. (The hot gas caused salts to build up on the nebulizer tip because of solution evaporation.)

An attachment designed to improve detection limits by increasing the rate at which sample was introduced into the flame was marketed for a time. The sample solution was put into a tantalum boat with about a 1-mL capacity. The boat was moved close to the flame for solvent evaporation and then inserted into the flame just below the light beam. Volatile analytes, such as lead, were quickly vaporized and atomized, resulting in a transient signal of a few seconds' duration. Detection limits improved dramatically, but matrix effects also increased. The fatal flaw,

however, was instability in the shape and position of the boat. Repeated heating caused distortion of the boat and its holders. With each distortion increment came a change in atomization efficiency. More time was spent in recalibrating the system (chasing the working curve) than in running samples.

Before the nitrous oxide flame was introduced, several attempts were made to exploit the higher temperature of the oxygen-acetylene flame in a premixed burner. The problem was the high burning velocity of the mixture, which caused those flames to have the nasty habit of flashing back into the spray chamber. The resulting explosion caused a loud report and often damaged the system.

Probably the most successful development was by Fassel's group (8). The burner was water cooled, massive, and rather complex, but it worked quite well. Indeed, the design

probably would have gained acceptance had a better idea, the nitrous oxide-acetylene flame, not come along. The paper describing the work contains a most unusual acknowledgment (8): "The authors would like to thank . . . Mr. J. O. Rasmuson for his timely confirmation that oxy-acetylene flashbacks in this burner cause no serious damage to the burner or its surroundings." One wonders if the undamaged "surroundings" were defined to exclude the eardrums of the operator.

The flame-in-tube design first described by Fuwa and Vallee (9) was not successful but led to another development that did succeed (10). Both are shown in Figure 1. In the original design (Figure 1a), a quartz or Vycor tube about 1 cm in diameter and 10–100 cm in length was placed on the optical axis, and the flame from a Beckman burner was directed into one end from a slight angle. The system gave extremely good sensitivity but suffered from high background absorption, as shown in Figure 2. There was an obvious need to compensate for the background, and this led to the development of the continuum source background correction system (Figure 1b), which was later automated and incorporated into many commercial instruments. The original flame-in-tube design failed not because of background absorption but because of the same matrix interference problems that plagued the total consumption burner.

### Some unusual aspects of AAS history

One of the most striking things about the history of AAS is the degree to which the method was "born mature." The operating principles of today's flame AAS units are indistinguishable from those of the one that Walsh first described. To be sure, refinements have been made and computer technology has had significant impact. However, hollow cathode sources, the premixed air-acetylene flame formed on a slot burner, and double-beam optics with modulation and ac amplification were all a part of the earliest instruments. Many attempts were made to improve on these conditions, but most were gradually shown to be steps away from the optimum.

Contributions to the early development of AAS from the academic community are conspicuous by their absence. In the United States, only Pickett was active (to my knowledge) prior to the beginning of the explosive growth period, and his early

### A Brief History of Flame AAS

**1955** Method described independently by Walsh and by Alkemade and Milatz

**1955–62** The induction period—development down under while United States remains an "underdeveloped country"

**1962–69** Explosive growth—the "fun time" for those of us fortunate enough to have been there in person

**1969–76** Relative stability—AAS puts on its work clothes

**1976–present** Electronic revolution—microprocessor and computer enhancement of instrumental capabilities

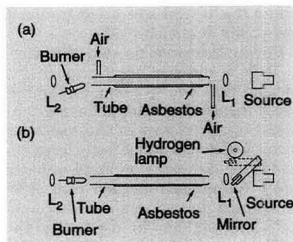


Figure 1. Flame-in-tube designs.

(a) Simplification of arrangement used by Fuwa and Vallee using only a hollow cathode source. (b) Continuum source background correction system using both a hydrogen lamp and a hollow cathode lamp. L<sub>1</sub> and L<sub>2</sub> are lenses. (Adapted from Reference 10.)



work was never published. Jim Robinson probably was the first in the United States to do AAS, and certainly he was the first to publish extensively in this country (11, 12). He did his early work at Esso Research before moving to Louisiana State University in 1964. Both Robinson and Pickett used homemade, or at least home-assembled, AAS units that gave satisfactory performance. My own experience with the equipment at Missouri will be discussed later.

There are a few examples where the early commercial development of a technique was so totally associated with a single manufacturer when several others seemed to be in equally strong initial positions. Perkin Elmer quickly dominated the market, especially in the United States, and largely through the company's efforts AAS became an accepted technique. I will elaborate on P-E's contributions in a later section.

Once accepted, AAS replaced competitive methods for elemental analysis to an unprecedented degree. An atmosphere prevailed in which legitimate problems with AAS were underestimated and its advantages over other methods overestimated. The confusion mentioned earlier regarding interferences prevailed for a time, and the virtual exclusion of flame emission continues today. Colorimetric and polarographic methods are used for routine analyses only in special cases.

The replacement went beyond the optimum, at least in principle. It is legitimate to ask why. Operational simplicity for a laboratory seems to be a major part of the answer. AAS was the obvious choice for elements such as Zn, Cd, Hg, and Mg. It was also quite satisfactory, though perhaps not optimal, for a long list of others. The lab manager could simplify the operation by using this one technique for the broadest possible range of applications. In practice, it seems to have worked rather well.

#### Some disagreements with conventional wisdom

It has been suggested that AAS should have been developed years, even decades, before it was. I disagree. It is true that the conditions for observation of atomic absorption were described in 1859, that astronomers routinely used AA spectra in establishing the composition and motion of stars, that self-absorption and self-reversal were well known to emission spectroscopists as troublesome phenomena to be avoided at all costs, and that an AA instrument for determination of mercury vapor concentrations was described in the late 1930s. Why, then, did the advantages of AAS as a general analytical technique remain unappreciated until 1953 when Walsh started the work that was published in 1955?

The answer, or at least one answer, lies in the area of supporting technology. All new developments require

supporting materials that often come from seemingly unrelated areas. Two examples will illustrate the point. First, Kirchhoff's observations on atomic spectra were made possible by the burner that Bunsen had invented a few years earlier. For the first time, spectral behavior could be observed in a nonluminous, nearly transparent flame. The beginning of spectrochemical analysis and a series of related developments were made possible, or at least much easier, by the lowly burner that has been used by every chemist since Bunsen's time. Second, the highly efficient diffraction gratings, on which modern instruments depend, were made possible by industrial-scale high-vacuum technology, which developed because of the tremendous commercial success of radio in the 1930s.

The development of AAS had to await the availability of photomultiplier (PM) tubes. True, in principle it is possible to do AAS photographically, but it is not nearly as convenient as emission (and goodness knows, that was bad enough). Other detectors were available, but hollow cathodes are rather feeble light sources that would not have been very practical without the sensitive detection capability of PM tubes and their associated electronics, which were developed in the late 1930s. However, World War II intervened and PM tubes did not become routinely available to chemists until the late 1940s. As an example, the battery-powered PM attachment for the Beckman DU spectrophotometer was introduced, even later, in 1953 (13). Thus Walsh's work followed, without great delay, the time when supporting technology became available.

Was the seven-year period needed for AAS to really catch on an excessive length of time? It undoubtedly seemed so to those who realized its tremendous potential but were unable to generate interest in the scientific community. However, if we look at how long it took for other methods to gain acceptance, we might reconsider. The utility of arc-spark emission spectroscopy for quantitative analysis was demonstrated as early as 1873 and was well established in several laboratories in the opening years of the twentieth century. Quality commercial instruments were available only a few years later (1909-12), but it was 1922 before the first paper on the method was published in the United States. Slavin (4) comments on the situation:

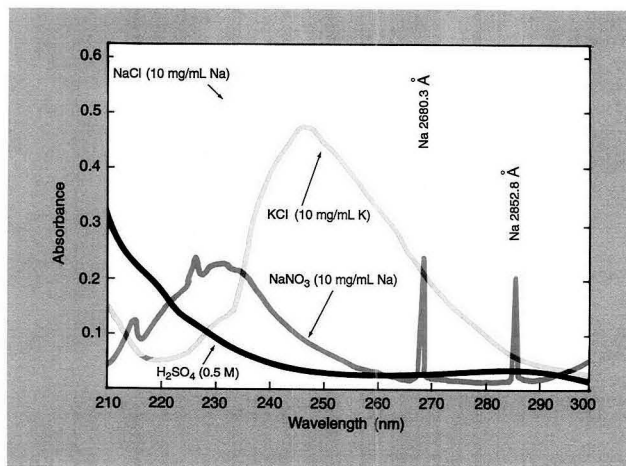


Figure 2. Absorption spectra of solutes in a long-path flame.

(Adapted from Reference 10.)

## REPORT

Thus by 1920 all the conditions needed for a system of chemical analysis by spectroscopy existed. We had excellent instruments, good photographic emulsions, a power distribution network, and basic theory. However, chemists were very slow to take advantage of this powerful tool, even for simple qualitative identifications. They still relied on the classical instruments, the test tube, the blowpipe, the eye, and the nose.

Emission spectroscopy did not become popular until well over a decade later and, again, Slavin (4) does a better job of describing the situation than I could hope to:

Impetus for growth of the field, at least in this country, was given by a series of summer conferences organized by G. R. Harrison at the Massachusetts Institute of Technology. Beginning in 1933 and continuing to 1940 . . . these meetings were held for five days . . . in a small lecture hall seating about 80 persons. Only toward the end of

the period were there enough participants to fill the room, and more than half were organic chemists working with the spectrophotometer, not emission workers. . . . It was a truly egalitarian group; everyone was equal in his ignorance.

The story is much the same for flame emission analysis. Lundegårdh started work in 1929 and eventually developed a completely automated system. Electrical detection of flame emission was described in the late 1930s. Developments undoubtedly were delayed by World War II, but a full 20 years after Lundegårdh's work, Meggers would write (14): "the flame photometer appears *suddenly* (my emphasis) to have come into vogue for the quantitative determination of sodium, potassium, and calcium in almost anything."

After 20 years, the scientific community suddenly woke up to the value of flame emission analysis. Thus the induction period for AAS probably was no longer than should have been expected.

Adam Hilger Ltd. was the first major instrument company to market

atomic absorption equipment under an exclusive license to Walsh's patent. This unit took the form of a kit consisting of a hollow cathode lamp and power supply and a premixed nebulizer-burner assembly. It was designed to mount on one of the company's existing UV spectrophotometers, which used dc electronics. In this system, any flame emission would be detected and cause an error in the absorption measurement.

The electronics are often cited as the fatal flaw in the Hilger kit. Based on my experience, I disagree. The second atomic absorption unit I ever used was a modified Hilger kit mounted on a Beckman DU (dc electronics) spectrophotometer in Pickett's lab. The modification was important. The kit came equipped for an air-propane flame, which proved to be totally unsatisfactory. Within weeks after delivery, Pickett, who had used a Lundegårdh flame, made a new burner head, following Walsh's design, and started burning acetylene.

By the time I arrived on the scene in 1963, the instrument was in routine daily use and was at least as convenient to operate as the P-E Model 303, which eventually re-

Sample preparation for XRF-AA-ICP-CHEM.

## To Bis! or not to Bis!

That is the question!

**claisse**  
PLAXIER BIS!

The most sophisticated automatic microprocessor controlled fusion apparatus that...

- processes almost all kinds of samples
- prepares glass disks and solutions
- makes six samples at one time
- can be modified to make 100 solutions per hour
- uses propane or butane, no oxygen.

Most competitive pricing.

With sale, free training trip to Quebec City.



Call or write to the most experienced people on fusion for information.



corporation  
scientifique  
claisse inc.

2522, chemin Sainte-Foy  
Sainte-Foy (Québec)  
Canada G1V 1T5  
Tel: (418) 656-8453  
Fax: (418) 656-1169  
Telex: 051-31731

**The First and Finest in Fusion**

CIRCLE 24 ON READER SERVICE CARD

## Trends in Chemical Consulting

Restructuring in the chemical industry has created a wealth of opportunities for consultants. Companies are now more willing to seek outside help than in the past as they recognize the value of experienced specialists.

But what constitutes the efficient use of a consultant? And is consulting for you? *Trends in Chemical Consulting* explores these issues through contributions from chemical consultants, those who have used the services of a consultant, and participants in cooperative arrangements. Presentations focus on those considerations specific to consulting relationships between scientific professionals.

Chemists, chemical engineers, and other scientific professionals in support areas to the chemical industry will find this an indispensable resource of information on chemical consulting.

### Contents

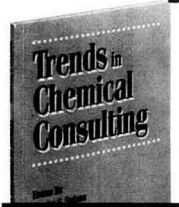
- Consulting to the Chemical Industry
- Industrial Expectations for Consultants and Consulting Services
- Understanding, Selecting, Managing, and Compensating Consultants
- An Academic Perspective on Consulting
- University-Industrial Relationships
- Accessing Federal Laboratories Know-How
- What Consulting Practices Look Like
- Defining and Marketing Your Consulting Specialty
- Opportunities for Retired Chemists
- Using Consultants to Interpret Regulatory Initiatives
- Major Chemical Company Retirees as Consultants and Market Developers
- Robotic Servicing on the Space Station
- Freedom
- Consultation in Sensory Evaluation
- Chemical Information Consultants

Charles S. Sodano and David M. Sturmer, *Editors*

174 pages (1991) Paperbound  
ISBN 0-8412-2106-5  
\$29.95

Order from: American Chemical Society, Distribution Office, Dept. 11  
1155 Sixteenth St., N.W., Washington, DC 20036

or CALL TOLL FREE **800-227-5558**  
(in Washington, D.C. 872-4363) and use your credit card!



placed it. Its primary use was for the determination of nutritionally significant elements (Ca, Mg, Cu, Zn, Fe, and Mn) in biological materials. Na and K were determined by emission, as they still should be today. The point here is not that dc electronics were desirable but that the modified Hilger unit worked well enough for enough elements that it could have been successful. It certainly outperformed most methods commonly used at that time for the above elements.

If this kit worked so well, why did it not succeed? The most serious deficiency probably was the flame. Few users would have had the insight and inclination to modify the kit as Pickett did, and all reports indicate very poor performance using air-propane. In addition, Hilger made a limited investment in a marketing effort and the kit arrived on the market a bit too early. The induction period had not yet run its course.

#### The Perkin Elmer success

Just a few years after the Hilger kit was introduced, the company agreed to a nonexclusive patent license, clearing the way for other businesses to enter the market. Several did, and

P-E was far more successful than the others. Why? Other companies that attempted to compete made one or more serious design errors, especially with dc electronics and total consumption burners. P-E, however, by consulting extensively with Walsh and others at CSIRO, as well as with the few experienced users in this country, was able to produce the first optimized commercial atomic absorption instrument.

This success was followed by aggressive marketing and a willingness to fill the education vacuum left by academia. Customer seminars, the *Atomic Absorption Newsletter*, a methods manual unofficially but universally called the AAS "Cookbook," and field product specialists assisting customers with problems were important components not only of the P-E success but of the success of AAS in general. Another reason for success was fortuitous timing. The induction period had run its course. Scientists had heard of AAS often enough from the group down under, and from a few other groups around the world, to be more receptive to the idea. Also, several companies that were in a position to become major

competitors concentrated on ideas from the "did not succeed" list discussed earlier.

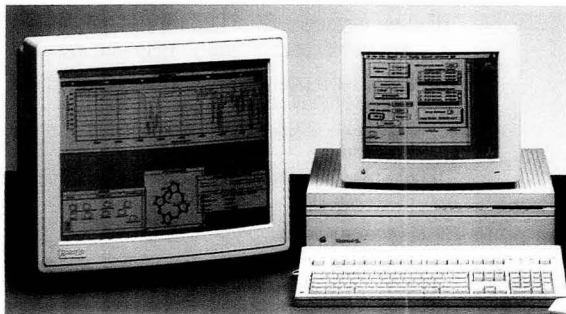
As significant as these factors are, they do not reach the heart of the matter. The real difference at P-E was the small number of talented and dedicated people who truly believed in AAS and had the courage of their convictions. I hesitate to mention names because of the risk that equally deserving people will be excluded. But fools rush in . . . ! In the early days, Dick Reiss was an important member of this group until he left P-E. Herb Kahn also eventually left P-E, but not until after its successes and his contribution thereto were well established. Walter Slavin, the son of Morris Slavin (whose work has been quoted extensively here), was in the thick of the early development and remains a major player in the still successful AAS business at the company. There may have been others but, if so, they were less visible from my perspective.

What about the success of AAS as an analytical method? Why did it become so popular? The best simple explanation comes from Lundell's paper, "The Chemical Analysis of

Why Are More and More People Buying Mattson FTIR Spectrometers?

# MacFIRST™ FTIR Software for Macintosh!

**New!**



Full data acquisition and evaluation software for FTIR spectroscopy—incorporating all the ease-of-use of a Macintosh.

- Full multiple windowing of infrared spectra with multitasking.
- Complete support of file export for desktop publishing.
- Cut, copy and paste infrared spectra and reports.
- On-screen editing of annotations and comments.
- On-screen expansion, roll, zoom and overlay of infrared spectra.



**Mattson Instruments, Inc.**  
1001 Fourier Drive  
Madison, WI 53717  
Tel: (608) 831-5515  
Fax: (608) 831-2093

**Mattson**

Mattson, Orion and Unicam are operating divisions of Analytical Technology, Inc.

MacFIRST™ is a trademark of Mattson Instruments, Inc.  
Macintosh® is a registered trademark of Apple Computer, Inc.

CIRCLE 77 ON READER SERVICE CARD

## REPORT

Things as They Are," published two decades before Walsh started his work (15): "There is no dearth of methods that are entirely satisfactory for the determination of elements when they occur alone. The rub comes in because elements never occur alone, for nature and man both frown on celibacy."

These noncelibate elements could be measured more quickly, more reliably, and less expensively by AAS than by methods commonly used in the late 1950s. AAS did a superior job of analyzing "things as they are."

### How were elemental analyses done before AAS?

This question was asked by Zoe Grosser at a preliminary presentation of this paper to people at P-E. Her question is a good one because a generation of fortunate analysts has grown up without being forced to consider some of the old problems. The answer depends on many specifics, of course, and my perceptions come from experience in the analysis of agricultural and biological materials.

First, many fewer analyses were done, especially at trace levels. Those that were done usually required con-

siderably more chemical manipulation than is common today. Consider major constituents. Potassium in fertilizer was measured gravimetrically after separation from interferences and precipitation as  $K_2PtCl_6$ . It was a laborious procedure even if the need to recover and reuse the platinum was not considered. The flame photometer was used for potassium in most other sample types, and later flame methods were refined to yield acceptable results for fertilizers. Calcium and magnesium were normally measured by two EDTA titrations, the first to measure calcium and the second to determine calcium plus magnesium. Magnesium was obtained by difference. Good results usually were obtained for calcium, but those for magnesium left much to be desired—especially for cases of large Ca/Mg ratios. If I were to pick a single element for which AAS made the greatest difference, it would be magnesium.

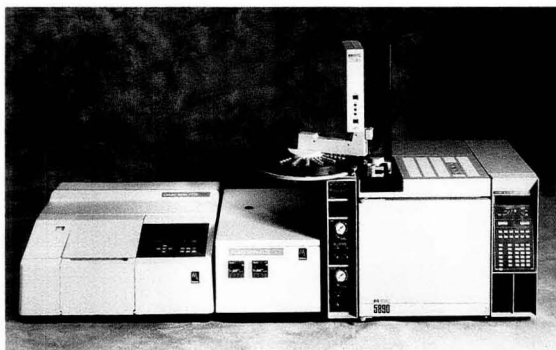
For determination of trace elements, the emission spectrograph was used extensively in large laboratories that could afford one. Polarographic methods were used for a few elements, notably Pb, Cu, Zn, and Cd. However, probably more trace

determinations were done spectrophotometrically or colorimetrically than by any other class of methods. Many books dealing exclusively with such methods were published; the classic work of Sandell (16) is one example. The methods lacked the specificity inherent in the atomic spectrum, and extensive manipulations—including pH control, extraction, back extraction, distillation, and addition of masking agents—were the norm. In many cases, chemical separations were required to enhance sensitivity and to control interferences. Keep in mind, too, that certified biological reference materials for quality assurance did not exist. A skilled and patient analyst who had the ability to devise and carry out a quality-control scheme from the ground up was essential for reliable results. Contamination was an ever-present problem because of the number of reagents and the amount of manipulation required. Indeed, high blanks probably were responsible for more profanity per hour in labs of the day than any other single factor. Today, even though we typically work at concentration levels 1–2 orders of magnitude lower, the simplicity of

Why Are More and More FTIR Users Buying Mattson FTIR Spectrometers?

# The Only Complete MS-DOS Based GC-FTIR System!

**New!**



High-performance GC-FTIR with all the features you expect in a fully integrated system.

- Full control of HP 5890 GC, HP 7673A autosampler and FTIR with a single MS-DOS based PC.
- Real-time spectral acquisition with both infrared and GC-FID chromatograms.
- On-the-fly infrared functional group analysis to classify GC peaks.
- 3-D and 2-D contour run display.
- Direct access to powerful spectral identification routines.



**Mattson Instruments, Inc.**  
1001 Fourier Drive  
Madison, WI 53717  
Tel: (608) 831-5515  
Fax: (608) 831-2093

Mattson, Orion and Unicam are operating divisions of Analytical Technology, Inc.

MS-DOS® is a registered trademark of Microsoft Corporation.

CIRCLE 78 ON READER SERVICE CARD



highly specific procedures and the availability of prepurified reagents make blank control much easier.

Reliable results were obtained in spite of the problems. I recall a group of food samples in about 1970 from which AAS and colorimetric results for lead were compared. Large disagreements were resolved in favor of the colorimetric values because workers using AAS had failed to correct for background absorption.

#### The situation today

The success of AAS continues. My feeling is that more elemental analyses currently are done by AAS than by any other method. Its only close competitor would be inductively coupled plasma emission. Instruments of ever-increasing complexity are selling like hot cakes, and there appears to be no end in sight. The situation described by Slavin (4) is even more true today than it was in 1971, especially if one includes the computer system with which the instruments interact: "In fact the possession of spectroscopic instruments (not necessarily their wise use) has become a status symbol. . . . A pecking order is developing among laboratory work-

ers on the basis of the size, number and elaborateness of optical apparatus. Affluence breeds strange fruits."

#### References

- (1) Walsh, A. *Spectrochim. Acta* **1955**, *7*, 108.
- (2) Alkemade, C.T.J.; Milatz, J.M.W. *J. Opt. Soc. Am.* **1955**, *45*, 583.
- (3) Twyman, F. *The Spectrochemical Analysis of Metals and Alloys*; C. Griffin & Co. Ltd.: London, 1941; Chapter 1.
- (4) Slavin, M. *Emission Spectrochemical Analysis*; Wiley-Interscience: New York, 1971; Chapter 1.
- (5) Fassel, V. A.; Golightly D. W. *Anal. Chem.* **1967**, *39*, 466.
- (6) Pickett, E. E.; Koirtzyhann, S. R. *Anal. Chem.* **1969**, *41*(14), 28 A.
- (7) Chan, Y. K.; Wong, P. Y. *Talanta* **1968**, *15*, 867.
- (8) Fiorino, I. A.; Kniseley, R. N.; Fassel, V. A. *Spectrochim. Acta* **1968**, *23B*, 413.
- (9) Fuwa, K.; Vallee, B. L. *Anal. Chem.* **1963**, *35*, 942.
- (10) Koirtzyhann, S. R.; Pickett, E. E. *Anal. Chem.* **1965**, *37*, 601.
- (11) Robinson, J. W. *Anal. Chem.* **1960**, *32*(8), 17 A.
- (12) Robinson, J. W. *Anal. Chem.* **1961**, *33*, 1067.
- (13) Jarnutowski, R. J. Beckman Instruments, Inc., personal communication, 1991.
- (14) Meggers, W. F. *Anal. Chem.* **1950**, *22*, 18.
- (15) Lundell, G.E.F. *Ind. Eng. Chem. Anal. Ed.* **1933**, *5*, 221.

(16) Sandell, E. B. *Colorimetric Determination of Traces of Metals*, 2nd ed.; Wiley-Interscience: New York, 1950.

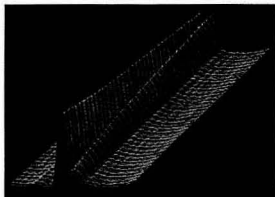


S. R. Koirtzyhann earned his M.S. degree and Ph.D. from the University of Missouri-Columbia, where he has been a faculty member since 1966. He joined Oak Ridge National Laboratory in 1958, working in emission spectroscopy with Cyrus Feldman and becoming active in AA research. He has published about 75 research papers and book chapters on AAS. His contributions include the definition of the nature of background spectra in flames and the development of continuum source background correction. He has also contributed to the understanding of atom formation in flames and furnaces and has worked throughout his career on the application of AA methods to practical problems.

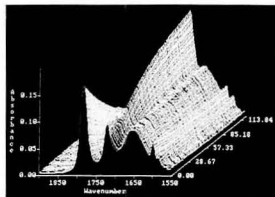
Why Are More and More FTIR Users Buying Mattson FTIR Spectrometers?

# Time Evolved Analysis for Kinetics and Reaction Monitoring!

**New!**



Gas phase hydrolysis of Acetyl Chloride with  $D_2O$ . Run of 2.5 seconds at  $16\text{ cm}^{-1}$  resolution.



Base-catalyzed esterification of Benzoic Anhydride. Two hour run at  $4\text{ cm}^{-1}$  resolution with MIR fiber optic probe.

Full, turnkey system for analysis of reaction kinetics—as fast as 25 spectra each second.

- Continuous data acquisition—up to capacity of the hard disk.
- Multiple event trigger input to accurately initiate reactions.
- Real-time spectral acquisition with allowing observation of changes in up to eight wavelength regions.
- Absorbance vs. time plots in ASCII for direct input to spreadsheets.
- 3-D and 2-D contour run display.
- Time-base programming to match time to reaction rate decay.



**Mattson Instruments, Inc.**  
1001 Fourier Drive  
Madison, WI 53717  
Tel: (608) 831-5515  
Fax: (608) 831-2093

**Mattson**

Mattson, Orion and Unicam are operating divisions of Analytical Technology, Inc.

CIRCLE 79 ON READER SERVICE CARD

# EM SEPARATIONS

... a High Performance

# ChromaSource™

*(Krō'mə-sōrs)* n: A combination of experienced companies, advanced technology and proven products uniquely integrated to provide a single resource for chromatography technology transfer.

**E. Merck**  
Chromatography Products

**SepTech**  
Separations Technology

**Interaction Chemicals Inc.**

**We are EM Separations.** Your direct source for high performance chromatography products — your working partner for separations technology transfer from analytical to process scale. We have the products and the technology to perform the toughest separation as well as the hands-on experience to make it work ... and we are supported by the worldwide resources of E. Merck, a company whose history is synonymous with the development of chromatography.

**E. Merck chromatography products now available directly from EM Separations.**

**ORDER DIRECT**



## EM SEPARATIONS

A Division of EM Industries, Inc.

480 Democrat Road • Gibbstown, New Jersey 08027  
(609) 224-0742 • (800) 922-1084 • FAX: (609) 423-4389

Sample Preparation • Thin Layer Chromatography • Analytical HPLC • Prep Scale HPLC • High Performance Biochromatography • Process Scale Chromatography

# ATOMIC ABSORPTION SPECTROSCOPY: WHY HAS IT BECOME SUCCESSFUL?

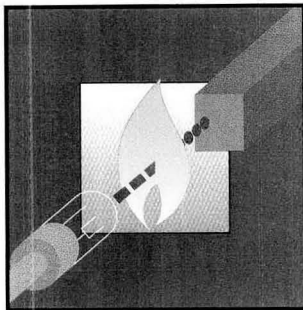
Walter Slavin

The Perkin-Elmer Corporation  
761 Main Ave.  
Norwalk, CT 06859-0237

The reasons for the success of a new analytical technique can be oversimplified if one tries to find a single explanation; these rare successes in fact depend on many things. The underlying technical reason for the success of atomic absorption spectroscopy (AAS) was Sir Alan Walsh's realization that the use of a light source of the element to be determined provided resolution equivalent to that of a very large spectrometer, thus effectively removing the spectral interferences that had been the most difficult problem in emission spectroscopy. Walsh also realized that small changes in the temperature of the atomizing device produced a very large change in the emission signal but had only a small effect on the absorption signal.

Subsequently, however, many workers have shown that other techniques can be very competitive with flame AAS from a purely technical point of view. Therefore, to explain the success of AAS, we must look also to other factors. At the time flame AAS was being developed, flame atomic emission spectroscopy (AES) was being promoted and used quite extensively. Walsh chose, and Perkin Elmer retained, the Lundegårdh premix air-acetylene burner for AAS while those using AES struggled with the much less convenient total consumption burner. Had the Lundegårdh burner been widely used for AES, the potential for AAS would have been considerably diminished.

A new analytical technique is not accepted until it can be shown to solve practical analytical problems. Thus the first users of AAS were also a critical part of the success of the



technique. Most potential purchasers wanted P-E to tell them, in some detail, how to analyze their own particular samples. This led us to develop the *Analytical Methods Book for AAS*, which we call the "Cookbook." We believe it was an important ingredient for success. The core of early users of AAS also benefited from the rapid communication of new methods and techniques resulting from the early introduction of the *Atomic Absorption Newsletter*, now called *Atomic Spectroscopy*.

But even these support mechanisms were not fully adequate; a sales organization that supported different analytical techniques could not be expected to stay current with the technical literature and recent developments in all these techniques. Therefore a network of product specialists with backgrounds in atomic spectroscopy had to be developed. These techniques are now widely used in the support of analytical instrumentation, but we believe they were first used in the support of flame AAS.

## Sociology

The purpose of the Waters Symposium is to explore the reasons for the success of specific analytical tech-

niques. It is hoped that this will eventually help to guide research workers and instrument developers in what they must do to make new techniques successful. Business sociologists have developed extensive theories on "innovation," and two sociological studies have been performed to evaluate the reasons for the success of AAS (1, 2).

In this REPORT I will try to identify the factors that in my judgment have been most influential in the success of AAS, with heavy emphasis on the word "judgment." The sociologists recognize the need for judgment by distinguishing between "invention" and "innovation." Invention conveys the concept of temporal priority and legal patents, whereas innovation suggests the establishment of new ways of doing something. Despite the usefulness of patents, successful innovation in analytical instrumentation is very often not directly associated with temporal priority or with patents.

There is also a problem of objectivity. I was one of many people interviewed by the sociologists studying AAS. I was warned that, as a participant, I could not be objective in my judgment of the relative importance of different factors in the success of AAS. In fact, however, the sociologists also depend on their judgment of the reported facts and their relative importance. Simply collecting the opinions of the people may not produce a valuable assessment of the real situation.

## Early work in AAS

Physicists have understood the concept of atomic absorption for almost two centuries, dating back at least to the work of Wollaston in 1802. In 1817 Fraunhofer observed dark absorption lines in the spectrum of the sun located at the same wavelengths as characteristic radiation emitted

by certain elements on Earth. Talbot and Brewster published papers on emission and absorption spectra in the 1820s and 1830s, but it was the work of Bunsen and Kirchhoff around 1860 that clearly established the roles of both emission and absorption spectroscopy. Figure 1 shows Kirchhoff's experiment as it appeared in a book published in 1898 (3). Bunsen, a chemist, recognized the potential of both emission and absorption for determining the elements in materials, and emission spectroscopy applied to analytical chemistry developed gradually over the next 100 years.

During that period and into the first half of the twentieth century, absorption methods were widely used

by astronomers to study the elemental composition of the stars. It would be misleading to select 1955, the date of Walsh's first publication (4), as the date of the "invention" of AAS. An AA instrument for the determination of mercury was described in 1939 (5) and, still earlier, an instrument for the determination of mercury appeared in the German literature (6). In the early 1900s the great American physicist R. W. Wood performed numerous atomic absorption experiments. Thus chemical applications of AAS certainly did not have to be discovered.

Nevertheless, for most of us, the key date is 1955 when, at opposite ends of the earth, Walsh (4) in Australia and Alkemade (7) in Holland

independently published the concept of analytical AAS in much the same form as it is practiced today. Although I consider the idea as having come from Alkemade, most scholars, including Alkemade (8), credit Walsh with the innovation of AAS because he took the time and energy to overcome resistance to this new idea.

I saw the Alkemade paper in 1955 because it was published in the *Journal of the Optical Society of America*, which I have read for many years. Although the first publication was no more than a letter to the editor, a longer paper appeared the same year in an obscure journal (9). The Walsh paper was published in *Spectrochimica Acta*, a journal that in those days was not widely read in the United States.

The management of the small instrument company at which I was then employed was not very interested in AAS, as was typical in the early days following these two pioneering publications. In November 1956 I joined P-E, and in December of that year I wrote a "new product suggestion" based on the Alkemade paper. Alkemade used a flame burning the element of interest as a source and another flame as the atomizing device (Figure 2), and my product suggestion read in part: "Obviously, if the source flame is replaced by a Na lamp, an absorption photometer results. The apparatus seems like a fine approach to . . . producing a flame photometer useful for materials other than Na and K." I was not told until later that Walsh, a P-E consultant in IR spectroscopy at that time, had already approached the company about his AAS work.

Walsh's proposal, in his very thorough and far-sighted paper, suggested that hollow cathode lamps, which he had learned to make in his laboratory, be used as the light source. He noted clearly, as did Alkemade, that the source must be ac and the detector must be tuned to the same ac frequency in order to avoid confusion with the emission signal from the flame. For the flame atomizer he chose the premixed burner designed originally by Lundegårdh in Sweden and usable with air-propane and air-acetylene flames. His instrument design was thus not very different from modern instrumentation intended for flame AAS.

Although his paper did not appear until 1955, Walsh had been negotiating with Hilgers in England since 1953 to build an AAS instrument. The fact that commercial instruments were not made available until

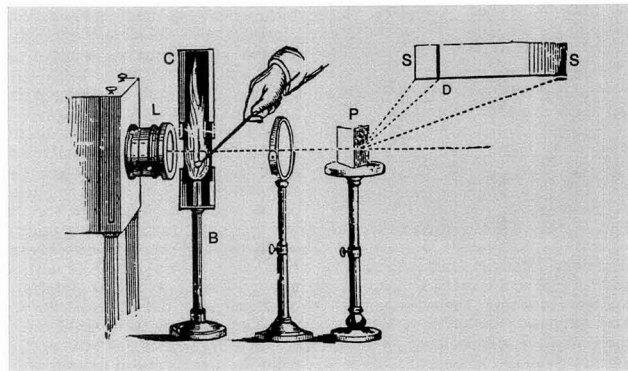


**Figure 1.** The Kirchhoff AA experiment as illustrated in a book by Tyndall.

Light from the sun enters the room from the left through a slit cut in a curtain and the lens, L, images the slit onto a screen, SS. In passing through the prism, P, the light is dispersed into the spectrum and the familiar Fraunhofer spectrum of the sun is observed. Introduction of a sodium salt into the flame, C, of the Bunsen burner, B, provides an atomic vapor of sodium and greatly intensifies the sodium D absorption.

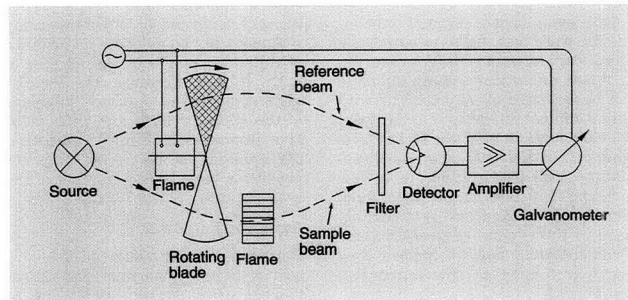


**Figure 2.** The Alkemade proposal for an AA flame photometer.

A flame source is imaged through an analytical flame and a filter to a detector. To distinguish the light from the two flames, the source flame is chopped by a rotating blade and the signal is amplified. The sample signal is separated from the reference beam signal, and the ratio is displayed on a galvanometer. (Adapted with permission from Reference 7.)



about 1959 caused Walsh considerable frustration (10). This apparent lack of interest can be contrasted, however, to the activity at P-E during that period. Ray Sawyer, an applications chemist at P-E in the late 1950s, wrote a detailed research department report in which he reviewed P-E AAS activity up to that date (11). Beginning in May 1956 there were internal memoranda between various technical people and Van Zant Williams, the developer of IR spectroscopy at P-E and director of technical activities at that time. Memos and reports were being written at the rate of about two or three per month into 1958. My own new product suggestion was written in that period, but most of the material referenced in the Sawyer report came from numerous other people, including some workers outside P-E.

There were also discussions with scientists at Esso Research in Baton Rouge in April 1958. The first reference in Sawyer's report to Jim Robinson, now a professor of chemistry at Louisiana State University, is in January 1959. Until 1958, when the first applications papers in AAS appeared from Eric Allan (12) in New Zealand and John David (13) in Australia, there were no actual analytical applications of AAS, although there were several oral suggestions that the technique was being applied.

Surely, one major lesson to be learned from this part of the history is that five years should not have elapsed from the time that Walsh had an instrument that worked until real applications were published. The first two applications papers used instruments assembled from available parts in the laboratories of the authors. In 1960 Robinson (14) published the first paper from an American laboratory on AAS. Also in 1960, P-E built a prototype AA instrument for Esso. Robinson (15) has claimed to be the first worker in the United States to use AAS and to have been the stimulant behind the P-E entry into AAS. Although his claim certainly has validity, the record shows that many researchers were active and interested in AAS in this early period.

The truly critical point in these activities occurred in February 1959 when CSIRO offered P-E a license to build AA instruments under the Walsh patent. (Until that time Hilgers had an exclusive license from CSIRO.) Although the Sawyer report indicated that P-E was interested in a license, the legal situation was not resolved for five or six years. A li-

cence was granted to P-E in November 1959, and I believe a license was also granted to Jarrell-Ash at about the same time.

This suggests another strong recommendation to academic or research laboratory innovators that is almost never mentioned in the several sociological studies. Exclusive licenses are sometimes of value, especially when considerable expense is required to convert an idea into a commercial product, but an exclusive license reduces the effectiveness of the innovator in promoting an idea to fellow scientists. Despite the influence of Allan, Robinson, and many others who saw the potential opportunity for AAS, development had to wait for the commercial opportunity, which in the case of AAS required non-exclusive licenses.

Sawyer gave the first P-E paper on AAS at a September 1959 symposium in Ottawa. He also attended the Australian Spectroscopy Conference that fall, where he heard Allan, David, and others speak.

In 1961, P-E began shipments of an AA instrument, the Model 214 (Figure 3). It was designed by E. H. Siegler and J. Borden with considerable input from J. Atwood and applications support from D. C. Manning. Some 35 units were built through mid-1963, and many of these are still in operation.

Nineteen sixty-three was a key year in the development of AAS because it was then that P-E began to sell the Model 303, the first really

successful AA instrument. More will be said below about the Model 303, but I want first to discuss why it took 10 years from Walsh's first approach to a manufacturer until a successful instrument became commercially available.

The sociologists working on the Sappho Project at the University of Sussex in England (1) compared the AAS activity at Hilgers with that at P-E. (The purpose of the Sappho Project was to compare successful and unsuccessful companies in the exploitation of innovation. By doing this for several innovations in different technologies, they hoped to uncover the clues to success.) Their detailed study of what happened in the two companies provides considerable insight into why Hilgers was unsuccessful in AAS.

Project Sappho (1), Encel (2), and Walsh (10) give Menzies, then president of Hilgers and a very competent physical spectroscopist, great credit for accepting the AAS idea. As Encel said, "Dr. Menzies was convinced of the value of the process (the first and only man to be so convinced during the next five years)."

Both Walsh and Alkemade clearly understood the necessity of encoding the radiation from the light source as an ac signal so that suitable ac electronics could distinguish that radiation from the dc emission of the analyte in the flame. But because the Hilgers molecular spectroscopic instrumentation was dc, it was easier to adapt their dc hardware than to

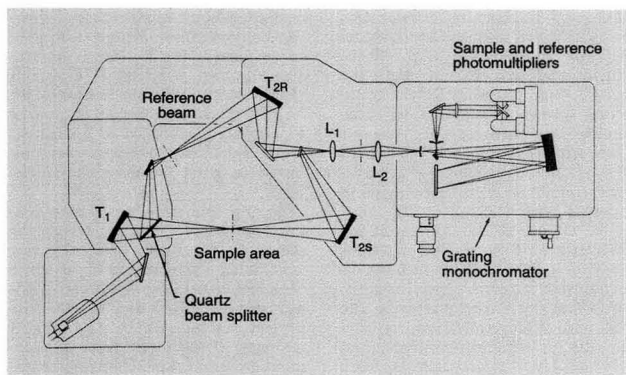


Figure 3. The optical system of the Model 214 AA instrument.

The source lamp is imaged onto the sample area by toroidal mirror  $T_1$ . A reference beam is extracted by the quartz beam splitter, and toroidal mirror  $T_{2R}$  reimages the reference beam through field lens  $L_1$  and lens  $L_2$  onto the entrance slit of the grating monochromator. Toroidal mirror  $T_{2S}$  images the sample beam onto the entrance slit, and the two signals are measured by the sample and reference photomultipliers after leaving the monochromator.

design a completely new system for AAS (16). Hilgers developed its own method for making hollow cathode lamps (HCLs) without taking much advantage (if any at all) of the work already done in Walsh's lab. The only person from Hilgers to visit CSIRO during this 10-year period was Menzies, and he only once. The Hilgers scientists also designed their own burner assembly with little regard to the work at CSIRO.

Although I do not have much insight into the work at Jarrell-Ash during this period, it seems very similar to the experience at Hilgers. Jarrell-Ash also used a dc molecular spectroscopy system they happened to be manufacturing, and they used the Beckman total consumption burners. There was very little interaction with CSIRO. I must strongly emphasize that, during this entire period, the technical people at CSIRO were very willing—and actually quite anxious—to cooperate with any company that obtained a license.

Perhaps I sound overly critical of my spectroscopy competitors' use of what happened to be available and their failure to fully appreciate the technical requirements of the new technique. They failed to take advantage of the research innovator's (Walsh's) offer to help. Those mistakes are critical lessons of this study and should be remembered well by those contemplating innovation.

I can make these criticisms so strongly because, a few years later, we at P-E were to make the same mistake in our efforts to develop graphite furnace AAS! We adapted the furnace to our flame AA instruments with inadequate consideration of the different system requirements of flame and furnace AAS. Where Hilgers and Jarrell-Ash made the flame AA an accessory for their molecular spectrophotometers, we made our furnace an accessory for our flame AA instruments. It took about 15 years to undo that error and rescue furnace AAS from the oblivion to which it was heading in the mid-1970s. Of course, in defense of my colleagues at P-E, we did not have access to a "Walsh." Our furnace innovator was a Soviet physicist working in a secret Soviet agency on the other side of an intellectual iron curtain. But, as in the case of Walsh, not only did L'vov know that we were making a mistake, he also knew what the mistake was, and he eventually helped to correct the situation.

#### Technical marketing

Until now I have focused on the neg-

ative side of innovation, the things that prevent success even when one starts with a good idea. We must now discuss the things that made AAS successful within P-E. Over the years Alan Walsh and I have often discussed this point, perhaps even argued it. I think he believes our success was the result of the design of the Model 303 instrument. Although this was surely very important, I attribute our continued success to what I have called "technical marketing." By this I mean the fusion of all the technical issues in physics, engineering, and chemical applications that makes it possible to solve the problems of the analytical chemist.

In 1961 we started to sell the Model 214. It was competent but certainly more expensive than it needed to be for its function. In October of that year my close colleague Herbert Kahn and I completed a long and very thorough engineering report that outlined the design and application of an AA instrument that became the Model 303 (17). We talked several times not only to Walsh but also to several of his specialized colleagues from CSIRO, and we recruited Walsh to help convince the P-E management to let us proceed in developing the Model 303. We also had a lively meeting with P-E managers that produced the now-famous interchange between our president, Chester Nimitz, and Walsh (15). To Nimitz' challenge, "If this technique is as useful as you say it is, why isn't it being used right here in the United States?," Walsh responded "[We] have to face up to the fact that, in many ways, the United States is an underdeveloped country!" John David, the Australian chemist who published one of the two first applications papers, visited P-E senior management in Connecticut in 1961, helping to support our estimates for a potential market for an AA instrument. By March 1962 we were allowed to start building the Model 303.

During this time we were selling the Model 214, mostly through the efforts of Dick Riess, while Manning was doing experiments in a small chemical laboratory. Kahn and I split our duties when the Model 303 project started. He became project manager of the instrument development program, and I started to assemble an applications laboratory.

Also in March 1962 we started the *Atomic Absorption Newsletter*, without which we could never have succeeded. The *Newsletter* was used to rapidly distribute analytical information and

methods developed by users. At the same time we began to hire a few people, one of whom was Sabina Sprague, who came to us directly from graduate school.

A year after we started the development project, we introduced the Model 303 at the Pittsburgh Conference in March 1963 and started shipments to customers a few months later. By P-E standards, that was a very rapid program! For the first several years we could not build enough Model 303s because the market developed so rapidly.

We realized very soon that new and potential customers needed to know in full detail how to accomplish their analyses. We began to prepare the "Cookbook." The first edition appeared in late 1963 and was distributed free to all users of Models 214 and 303. It was then included with every AA instrument shipped from P-E, and it has been updated periodically over the last 28 years.

We will further address customer support but, to remain chronological, we must now discuss the actual process of the AAS development program. Many instrumentation issues had to be addressed immediately, for example, the light sources (the HCLs recommended by Walsh). By that time Westinghouse had responded to the early interest in AAS by making HCLs for a limited number of elements. We told them we needed lamps for all elements, including difficult ones (such as Ca, Na, and K) and toxic ones (such as Ti, As, and Se). There were heated discussions, the outcome of which was that they would not do it. Incredibly, we had a wonderful new analytical technique but some critical elements could not be determined because the manufacturer did not want to make the sources. We decided to make the lamps ourselves and spent several weeks in Australia learning how to do it.

Despite comments in some of Walsh's reminiscences, making HCLs was not an easy task. HCLs for a few of the elements have always been fairly easy to make, but most have required a great deal of effort. (There are more names associated with these efforts than I can fully report.) In Walsh's lab, our constant support was Jack Sullivan, the guru of the CSIRO lamp efforts. The photo opposite shows Sullivan with Allan and Walsh in the CSIRO laboratory during our 1963 visit to Australia. Carl Sebens, now deceased, became our expert, and John Vollmer, a young engineer at the time, learned the art from Sebens, carrying on to

the present day. Manning learned how to tell good lamps from bad and taught our manufacturing organization quality control.

In AAS we have always gotten help wherever it was available. We will be forever indebted to John Wulff, then professor of metallurgy at MIT and for several fruitful years a hollow cathode metallurgy consultant for us. He came to Norwalk once a month and made our heads spin with incredible detail on intermetallic compounds, eutectic alloys, sintered metallurgy, and gas absorption by metals. It was one of our most satisfying consulting relationships, and most of our HCLs still bear the mark of his contributions. The important improvements in the internal electrical design of our lamps were largely attributable to the efforts of Vollmer, who holds several patents for these designs.

The burner used in the Model 214 deserves some discussion. The P-E engineers had designed a new burner and nebulizer, but when Manning used the system as a whole to confirm the published experiences of Allan (12) and David (13), he found interferences that the literature said were not present. Allan and David were using burner assemblies built to CSIRO design in Melbourne. I notified John Willis, Walsh's assistant on the CSIRO team, of these results the same day that Manning finished his experiments. That same day Willis air-mailed to us a tested burner assembly manufactured in CSIRO. The interferences were gone, and we completely confirmed the published results of Allan and David. Since that day we have used essentially the same burner and nebulizer design that came to us by rush air mail! There are very recent improvements, and the materials have changed, but the design looks remarkably similar to the original design used at CSIRO.

This burner permitted only air-

acetylene and cooler flames; the more refractory elements were inaccessible to AAS. Robinson published work with a cyanogen flame (18), and by 1963 we had shown that we could determine Al, Ti, and some other refractory metals in an oxygen-acetylene flame using a Beckman burner (19). This work was published alongside a paper by Fassel and Mossotti (20) with almost identical results.

The Beckman burners were not very attractive for routine laboratory use because they were terribly noisy, both audibly and signal-wise. Manning and I attempted to premix oxygen and acetylene, and spent many late hours (usually after others had left) behind shock-resistant glass barricades because our design attempts usually ended in powerful explosions.

By 1966 the real breakthrough came from Amos and Willis (21), who used premixed nitrous oxide-acetylene flames. This was second in importance only to Walsh's original work. The simplicity and convenience of flame AAS was now available for all metals except a very few highly refractory ones, which are still outside the capability of AAS. Allan conceived the use of nitrous oxide-acetylene flames more than a year before the Amos and Willis experiments. However, the nitrous oxide available to Allan in New Zealand was impure and he did not achieve the necessary high temperatures.

#### Technical resources

By 1965 the growing complexity of the technical information in AAS and the difficulty of teaching it to all of our sales engineers, who also had to learn equivalent material in IR and GC, had become major problems. We proposed to the sales manager what has become the product specialist role—people trained in chemistry whose job it is to support our users of AAS. They work out of our regional



Eric Allan (left), Alan Walsh (center), and Jack Sullivan (right) in Walsh's laboratory in Melbourne in 1963.

# Required Reading

FOR ANALYTICAL AND QUALITY CONTROL CHEMISTS

#### Polymers:

##### Analysis of Polymer Pellets with no sample preparation

Now, whole pellets can be analyzed without solvents or mechanical sample prep. Accurate determination of comonomers is now available. Polyolefins, butylenes, butadienes, polyesters, acrylics, rubber, and many other polymers can be analyzed in seconds!

Circle 95 for more information



#### Pet Food:

##### Protein, Fat and Moisture in dry dog food

Rapid, multi-component analysis of extruded dry dog food for protein, fat and moisture is described. All three components were analyzed simultaneously with results available in less than 20 seconds. Actual spectra, derivative spectra and math treatments are covered.

Circle 96 for Food Application Note #011



#### Pharmaceuticals:

##### At-Line, On-Site, In-the-Container Analyzers

Rapid-ID™ Analyzers identify actives, excipients and impurities without sample preparation or reagents. Application-tailored versions test in bulk storage containers or directly through sample bag or vial walls. Identification is infrared-specific with automatic regulatory recordkeeping.

Circle 97 for more information



## NIRSystems

A Perstora Analytical Company

12101 Tech Road, Silver Spring, MD 20904 (301) 680-9600

1990's

# VersaStat™

Versatile Potentiostat



The Premium Quality  
You Expect from EG&G PARC  
— at an Unexpected Price

We're proud to introduce the VersaStat — a premium potentiostat in the tradition of our model 273, at under half the price.



1970's  
The Model 273  
Potentiostat

How were we able to do this?

Our free HeadStart software functions as a versatile front panel, letting you tap the full power of our unique Electrochemical Command Set. Plus, the VersaStat



1980's  
The Model 273  
performs research

electrochemistry smoothly under the control of our time-tested Model 250 software, specially adapted from our widely-used Model 270 research package.

Finally, to keep hardware costs down, we limited the VersaStat's specifications, but still designed it to perform as a premium potentiostat in most applications.

So if you're looking for the best cost/performance value to hit the potentiostat market, try the VersaStat.

You'll find out the apple hasn't fallen far from the tree.



**EG&G PARC**

P.O. BOX 2565 • PRINCETON, NJ 08543-2565  
(609) 530-1000 • TELE: 843409 • FAX: (609) 883-7259

CIRCLE 32 ON READER SERVICE CARD

## REPORT

sales offices but receive technical guidance from Connecticut. They assist our sales people by running samples for potential customers in laboratories around the country, answering detailed applications questions from customers, training customers in the operation of their instruments, and helping with applications problems that arise after instrumentation has been purchased and installed in the customer's laboratory.

We hired the first four AAS product specialists in 1965. One of them, Jack Kerber, is now the manager of our AAS business in the United States. The product specialist concept was gradually expanded and extended to other P-E product lines and eventually introduced into other instrument companies. But this concept, organized with Kahn and subsequently expanded by him, was originally conceived as part of our AAS plans.

We could add to this discussion many more details of instrument design and marketing technique, including electrodeless discharge lamps, which Kahn has entertainingly described (22). Background correction was also important, but that is Koirtyhann's story (23).

I hope that my intention in undertaking this chronology is by now quite clear. To be successful in a new technology, it takes much more than just a good original idea. The good idea is absolutely necessary, but (in mathematical jargon) it is not sufficient. Success requires a small group of imaginative people with enough resources and sufficient freedom from constraint to address every problem and opportunity as they arise. The people cannot be compartmentalized into engineering and chemistry cubicles, and success cannot be achieved overnight. They are likely to fail if they depend only on their own intellectual resources. Conversely, their greatest opportunity is found in the scientific community throughout the world, which wants to make new analytical opportunities available to all. It seems an easy formula for success, but few are the companies that put this formula into practice.

In this short article I have mentioned only a few of the many people who have caused flame AAS to become so useful. All of us who benefit from the technique owe a great debt of gratitude to the people, named and unnamed, who have made all of this possible. Walsh was certainly the prime innovator for flame AAS, and

he came to the rescue whenever and wherever there was need. It has been one of the privileges of my life to have had the pleasure of associating with him over the many years.

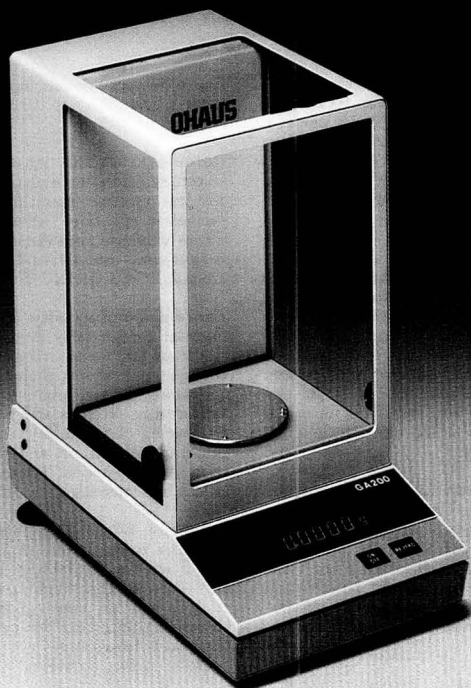
## References

- (1) "Success and Failure in Industrial Innovation," University of Sussex Project Sappho.
- (2) Enzel, S. *Int. Soc. Sci. J.* **1970**, *22*, 42–53.
- (3) Tyndall, J. *Six Lectures on Light*; Appleton: New York, 1898.
- (4) Walsh, A. *Spectrochim. Acta* **1955**, *7*, 108–17.
- (5) Woodson, T. T. *Rev. Sci. Instrum.* **1939**, *10*, 308.
- (6) Muller, K.; Pringsheim, P. *Dis Naturwissenschaften* **1930**, *18*, 364.
- (7) Alkemade, C.T.J.; Milatz, J.M.W. *J. Opt. Soc. Am.* **1955**, *45*, 583.
- (8) Alkemade, C.T.J. *Spectrochim. Acta* **1950**, *35B*, 671–76.
- (9) Alkemade, C.T.J.; Milatz, J.M.W. *Appl. Sci. Res. Sec. B* **1955**, *4*, 289.
- (10) Walsh, A. *Anal. Chem.* **1974**, *46*, 698 A.
- (11) Sawyer, R. R. Research Report No. 2, Oct. 1959; Perkin Elmer: Norwalk, CT.
- (12) Allan, J. E. *Analyst (London)* **1958**, *83*, 466.
- (13) David, D. J. *Analyst (London)* **1958**, *83*, 655.
- (14) Robinson, J. W. *Anal. Chem.* **1960**, *32*, 17 A–25 A.
- (15) Robinson, J. W. *Anal. Chem.* **1980**, *52*, 1368 A–1370 A.
- (16) Menzies, A. C. *Anal. Chem.* **1960**, *32*, 898–904.
- (17) Kahn, H. L.; Slavin, W. *Appl. Opt.* **1963**, *2*, 981–96.
- (18) Robinson, J. W. *Anal. Chem.* **1961**, *33*, 1067.
- (19) Slavin, W.; Manning, D. C. *Anal. Chem.* **1963**, *35*, 253.
- (20) Fassel, V. A.; Mossotti, V. G. *Anal. Chem.* **1963**, *35*, 252.
- (21) Amos, M. D.; Willis, J. B. *Spectrochim. Acta* **1963**, *22*, 1325.
- (22) Kahn, H. L. *Spectrochim. Acta* **1984**, *39E*, 167–70.
- (23) Koirtyhann, S. R. *Anal. Chem.* **1991**, *63*, 1024 A–1031 A.



Walter Slavin is a senior scientist at Perkin Elmer specializing in atomic spectroscopy. He is a 1949 graduate of the University of Maryland in physics and math. He has led P-E's efforts in the field of AAS and has made extensive contributions to the development of atomic absorption techniques and applications. Slavin is the author of two books on AAS as well as over 200 papers in the fields of analytical chemistry and instrumentation.

# A Perfectly Balanced Offer



Buy one GA Series Analytical and receive either a \$75 rebate or a FREE Ohaus C305.

Model	GA110	GA200	GA200D
Capacity (g)	110	200	200/40
Readability (g)	0.0001	0.0001	0.0001/ 0.00001
Platform size (in/mm)	3.5/90 dia.		
Tare range	Full Capacity		
Display (in/mm)	.5/12.7 Fluorescent		
Temperature range	50° - 104°F, 10° - 40°C		
Calibration	Internal		
Weigh Below	Yes		
Dimensions (in) (L x W x H)	12.8 x 7.5 x 13.7	17.5 x 8.1 x 12.1	
RS-232	Optional		

For a limited time, when you purchase an Ohaus GA Analytical balance, you can have an Ohaus C305 portable balance FREE.

Or you can receive \$75. It's your choice, but either way, your laboratory budget's well on its way to being well-balanced. Call Ohaus today for the name of your nearest dealer. This offer ends December 31, 1991.

Ohaus Corporation, 29 Hanover Road,  
Florham Park, NJ 07932-0900

800-672-7722

# OHAUS®



# NEW PRODUCTS



**GC-8IAEC**, an isothermal, single-injector, single-detector gas chromatograph, is designed to prevent column effluent from contacting the nickel-63 foil or electrode, thus eliminating contamination from the sample or stationary phase. It is ideally suited for analysis of PCBs in transformer oils. Shimadzu **401**

## Instrumentation

**Moisture analysis.** TURBO2 blending volumetric titrator incorporates a sample blending mechanism that allows users to measure moisture in solids and viscous liquid samples without the need for extensive sample preparation. Orion **402**

**pH.** PHH-90-series handheld pH meters measure the entire pH range with a resolution of 0.01 pH unit. Automatic temperature compensation is featured, and a three-in-one electrode, 9-V battery, buffer packets, electrolyte fill solution, and plastic beakers are included. OMEGA **403**

**Petroleum.** Automatic distillation analyzer MP-626 evaluates petroleum samples according to ASTM D-86, D-850, D-1078, DIN 51751, and IP-123 methods. Temperature and volume measurements are automatically calibrated. Walter Herzog **404**

**HPLC.** Model 738 universal autosampler, designed for HPLC and ion chromatography, can perform precolumn derivatization before sample injection and can dilute samples with reagents before injection. The autosampler holds up to 96 samples and can inject 1-1000  $\mu$ L from small volumes. Alcott **405**

**Helium-cadmium lasers.** Positive-column metal vapor discharge lasers use naturally abundant Cd as both the excitation and optical gain medium, and He as the start gas. All three plasma tube sizes (56, 74, and 112 cm) are available in single-line violet (442 nm), UV (325 nm), and multiline (442/325 nm) wavelengths. Omnichrome **406**

**Amino acids.** LC 3000 is designed for automated amino acid analysis in a wide range of samples. Detection limits better than 30 pmol are achieved using the ninhydrin technique; detection limits better than 10 pmol are achieved using the optional fluorescence method. Eppendorf **407**

**Zeta potential.** EKA electrokinetic analyzer measures the zeta potential of solids of any shape, including fibers, plates, foils, strips, and granules. Conductivity and pH sensors are built in, and an automatic burette system facilitates the measurement of zeta potential as a function of pH surfactant concentration. Brookhaven Instruments **408**

**Semiconductors.** SPM-400 sputter process monitor, designed for semiconductor industries, detects contaminants such as water, oxygen, and other compounds down to ppb levels at sputter process pressures of  $10^{-3}$  to  $10^{-2}$  torr. The design of the ion source permits sampling of gases directly from the process chamber. Balzers **409**

**Oxygen.** Model 755R paramagnetic oxygen analyzer is equipped with a variety of field-selectable ranges, alarm and current output options, and a small rugged sensing unit. The analyzer is designed for both process control and monitoring and combus-

tion efficiency monitoring and features a sensitivity of 0.01% oxygen. Rosemount **410**

**Detectors.** ULTRA ion-implanted silicon detectors for alpha spectroscopy feature close mounting for high geometric efficiency, ultra-thin entrance windows for enhanced energy resolution, and ultra-low background. EG&G ORTEC **411**

**Thermal conductivity.** Model 235 thermal conductivity analyzer provides on-line monitoring of gases. Typical applications include hydrogen analysis in petroleum refinery hydrocarbon streams and gas purity monitoring of argon, oxygen, hydrogen, nitrogen, helium, and other gases in air liquefaction. Teledyne Analytical Instruments **412**

**Balances.** RC-series balances have weighing ranges of 0-60 g and 0-250 g with a readability range of 0.01-0.1 mg. The weighing chamber is accessed by turning the draft shield and adjusting the opening to the most convenient position for sample loading. Sartorius **413**

**Detection.** Dynamax Model FL-1 scanning fluorometer, designed for HPLC detection, uses programmable excitation and emission monochromators, enabling wavelength changes from 190 to 650 nm. The optics feature a blazed concave holographic diffraction grating to minimize stray light. Rainin Instruments **414**

**Furnace.** Heavy-duty 1200 °C box furnace is designed for ashing, heat treating, sintering, brazing, glass annealing, and materials testing research applications. The furnace features firebrick insulation, a counter-weighted door that moves upward, and four embedded heating elements. Barnstead/Thermolyne **415**

---

Companies interested in a listing in this department should send their releases directly to ANALYTICAL CHEMISTRY, Attn: New Products, 1155 16th Street, N.W., Washington, DC 20036.

---

ACETONITRILE

METHANOL

TETRAHYDROFURAN

WATER



## One filter fits all.

The new Millex®-LCR Filter Unit is compatible with all common aqueous or organic-based HPLC solvents—from water to methanol to tetrahydrofuran.

Its special membrane produces no organic or inorganic contaminants. So risk of introducing unwanted variables and artifacts into your work is eliminated.

Particulates are reduced

below detectable limits, which keeps frits from plugging and extends column life.

Test the HPLC-certified Millex-LCR Filter Unit yourself. Send in the coupon, or call 800-225-1380 (in Mass., call 617-275-9200) for a free sample and technical brief.

### Try the Millex-LCR Unit. Free.

Send to: Joe Peters  
Millipore Corporation  
80 Ashby Road  
Bedford, MA 01730

Name \_\_\_\_\_  
Title \_\_\_\_\_  
Co./Inst. \_\_\_\_\_  
Department \_\_\_\_\_  
Address \_\_\_\_\_  
City \_\_\_\_\_  
State \_\_\_\_\_ Zip \_\_\_\_\_  
Phone ( ) \_\_\_\_\_ Best time to call \_\_\_\_\_  
PA 900008 © 1990 Millipore Corporation



MILLIPORE

CIRCLE 87 ON READER SERVICE CARD

## NEW PRODUCTS

**Water treatment.** Series E-Plus reverse osmosis water treatment systems feature high recovery rates, modular membrane construction, internal connections that eliminate bulky external piping, and high-performance membranes. In addition, a waste flow control valve and a low feedwater pressure shutdown control are included. Culligan **416**

**DNA.** Genetic thermal cycling systems, designed for DNA and gene amplification, enzyme digestion, enzyme catalysis, and DNA denaturing, consist of a GTC-2 thermal cycler and a low-temperature cooling module. The unit holds up to 48 0.5-mL microfuge tubes in the sample block, which provides uniform temperatures ( $\pm 0.5^\circ\text{C}$ ) between sample wells. Precision Scientific **417**

**Detector.** Model 7215 UV detector for HPLC features a motor-driven monochromator, low baseline noise ( $< 5 \times 10^{-5}$  ABU/hr at 250 nm), autozero, and variable outputs for a variety of recorders and integration systems. Applied Chromatography Systems **418**

**IgM purification.** ImmunoPure IgM purification kit uses mannan-binding protein to selectively bind IgM. HPLC analysis shows that the eluted IgM product is at least 90% pure. Each run isolates  $\sim 3$  mg of mouse IgM. The kit provides enough IgM purification buffers to perform 10 purifications. Pierce **419**

## Software

**Database.** REGMAT database allows regulatory references of chemicals to be retrieved by chemical name, CAS registry number, or UN hazard class number. Records can also be searched by a regulatory program or agency. Chemical Information Systems **420**

**Data management.** Facilities information reporting systems technology (FIRST) software monitors and reports processes as required by the hazardous waste treatment storage and disposal facilities organic air emission standards for process vents and equipment, as well as the impending national emissions standard

for hazardous air pollutants. Orr Safety **421**

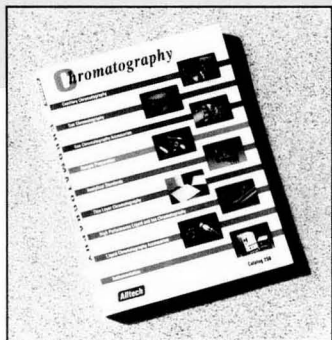
**Spreadsheet.** DataTalk software version 2.0 collects information from two RS-232 instruments simultaneously, imports the data into a spreadsheet, and exports it in a customized format. Labtronics **422**

## ACS Publications and Services

**Intern program—information for students.** Brochure describes the application, selection, and placement processes of the 1992 Summer Intern Program for college students sponsored by the ACS Division of Analytical Chemistry. **423**

For more information on instrumentation and software products, and/or to obtain the free available information on other listed items, please circle the appropriate numbers on one of our Readers' Service Cards.

## Alltech's NEW Catalog!



the new Alltech catalog contains  
700 pages of products and  
applications for chromatography

● GC ● HPLC ● IC ● TLC ● Sample Prep  
● Filtration ● Standards ● Instrumentation

Alltech

Alltech Associates, Inc.  
2051 Waukegan Road Deerfield, IL 60015  
Phone: 1-800-255-8324 Fax: 708-948-1078

CIRCLE 1 ON READER SERVICE CARD

## From Caveman to Chemist Circumstances and Achievements

What was the connection between early chemistry and magic? What was the logic that made alchemists think they could make gold out of lead? Why were gases not recognized until the 17th century? Why did it take 49 years before Avogadro's hypothesis was accepted?

In *From Caveman to Chemist*, author Hugh Salzberg traces the oddities of chemistry, examining cultural and political influences on the ideas of chemists. He follows the evolution of chemistry from the Stone Age beginnings of ceramics and metallurgy, through the rise and decline of alchemy, to the culmination of classical chemistry in the late 19th century.

Chapters 1 through 9 lead from prehistoric technology, through ancient and medieval science to the study of chemicals and reactions that resulted in the 16th century birth of scientific chemistry. Subsequent chapters focus on key chemists such as Sala, Boyle, Black, Lavoisier, Dalton, Berzelius, Laurent, and Arrhenius as they developed the ideas that led to classical chemistry and the concepts of molecules, chemical reactions, homology, valence, and molecular formulas and structures, among others.

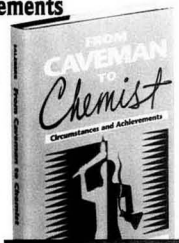
Twenty topical illustrations enhance the text. Six timelines and two maps help readers understand the influences of early history on chemistry.

Hugh W. Salzberg, Editor

300 pages (1991)

Clothbound: ISBN 0-8412-1786-6  
\$24.95

Paperbound: ISBN 0-8412-1787-4  
\$14.95

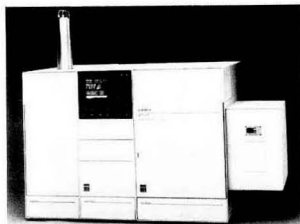


Order from: American Chemical Society, Distribution Office, Dept. 88  
1155 Sixteenth St., N.W., Washington, DC 20036

or CALL TOLL FREE **800-227-5558**

(in Washington, D.C. 872-4363) and use your credit card!

## NEW PRODUCTS



**SFE/50M, a multiple-vessel supercritical fluid extraction system,** can perform serial or parallel extractions in addition to static and dynamic extractions. Pressure, density, temperature, and flow can be programmed. Suprex 424

**Intern program—information for employers.** Employers looking for summer help can participate in the 1992 Summer Intern Program sponsored by the ACS Division of Analytical Chemistry. Brochure describes the program and contains a Sponsor Application Form on which available positions can be listed. 425

**College Chemistry Consultants.** Written to provide academic institutions and other organizations with access to expert advice on scientific and educational issues, this booklet describes C<sub>3</sub>S, the ACS College Chemistry Consultants Service. An application for consulting services is included. 426

**Chemists in the Classroom.** This booklet contains suggestions for chemists who visit an elementary or middle school classroom as visiting scientists. Advance planning, safety considerations, and follow-up activities are described. 7 pp. 427

### Manufacturers' Literature

**Chromatography.** Brochure highlights the capabilities of the 715 HPLC system controller software for gradient system control and data analysis. 4 pp. Gilson Medical Electronics 428

**Temperature control.** Brochure outlines how temperature-controlled systems are designed, engineered,

and manufactured. Systems described include ovens, environmental chambers, and thermal shock and environmental stress screening systems. 9 pp. Blue M Electric 429

**GC/MS.** Application note describes the analysis of air samples containing ppb levels of CFCs using the HP MS engine mass spectrometer with cryogenic trapping, subambient gas chromatograph, oven control, and micropacked GC column. 6 pp. Hewlett-Packard 430

### Catalogs

**Electrodes.** Catalog features 48 types of pH and oxidation-reduction potential electrodes and 27 types of ion-selective electrodes. A detailed selection guide for specific applications is included. pHoenix Electrode 431

**Laboratory products.** Catalog lists high-performance laboratory products, including labware, tubing, fitting and valves, and environmental sampling products. 57 pp. Norton 432

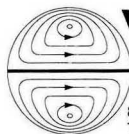
# Absolute Macromolecular Analysis In Minutes!

Our DAWN® laser light scattering instruments can tell you more about your macromolecules in a few minutes than *any* other analytical technique. A lot more! By coupling a DAWN to your existing GPC line, you'll be determining absolute molecular weights, sizes and distributions without having to resort to universal column calibrations, assumptions, or "fudge-factors." And if that isn't enough, you'll be able to predict physical properties such as flex life, brittleness and tear strength.

Whether you're using the DAWN instruments for GPC, or off-line for static measurements, our ASTRA and AURORA software make absolute macromolecular characterizations for molecules from a few-thousand to tens-of-millions of Daltons in just minutes!

At Wyatt Technology, we've been producing state-of-the-art instruments for over seven years. And we back those products with service, training, seminars and consulting.

Jump light-years ahead of the competition; call us at (805) 963-5904. It won't take us long to show you just how much you've been missing!



**Wyatt  
Technology**  
CORPORATION

802 E. Cota St • Santa Barbara, CA 93103  
Tel: (805) 963-5904 • Fax: (805) 965-4898

© 1990 Wyatt Technology Corporation

CIRCLE 148 ON READER SERVICE CARD

ANALYTICAL CHEMISTRY, VOL. 63, NO. 21, NOVEMBER 1, 1991 • 1045 A

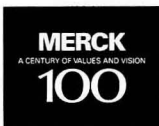
Over 140,000 sold  
Now in its second printing

**THE MERCK INDEX:**  
**Classic.**  
**Concise.**  
**Contemporary.**

TO ORDER, CALL TOLL-FREE  
**1-800-659-6598, EXT 750**  
(VISA OR MASTERCARD ONLY) OR COMPLETE THE COUPON

**The Eleventh/Centennial Edition—More Essential than Ever**

- Information on more than 10,000 significant drugs, chemicals, and biologicals
- New entries: pharmaceuticals with novel mechanisms of action, unique naturally occurring compounds, and chemicals of environmental concern
- New indices: therapeutic category/bioactivity, CAS Registry Numbers



Merck & Co., Inc., a research-intensive company, publishes *The Merck Index* as a nonprofit service to the scientific and medical communities.

Enclosed is my payment of \$35.00 for the Eleventh/Centennial Edition of THE MERCK INDEX. I will not be charged for shipping (U.S. only).

Merck & Co., Inc.  
Professional and Consumer Publishing  
P.O. Box 2000  
WBS-435  
Rahway, NJ 07065

- Check enclosed. Make check payable to Merck & Co., Inc.  
 VISA     MasterCard

Card No. \_\_\_\_\_ Exp. Date \_\_\_\_\_  
Signature \_\_\_\_\_  
Name \_\_\_\_\_  
Address \_\_\_\_\_ City \_\_\_\_\_  
State \_\_\_\_\_ Zip \_\_\_\_\_  Residence  Business (check one)

Please allow four to six weeks for delivery.

CIRCLE 85 ON READER SERVICE CARD

# CHEMTECH

*inspires  
the innovator*

**Why do so many innovators in all chemical fields turn to CHEMTECH each month?**



... One of the best condensed technical news sources I get ... Outstanding melding of social, political, and scientific literature ... The fresh glibness and tongue-in-cheek style are unique and welcomed ... I am impressed with the quality, scope and personal touch of the articles ... I almost dread it when each issue arrives because I know I will take the time, whether I have it to spare or not, to read it from cover to cover.

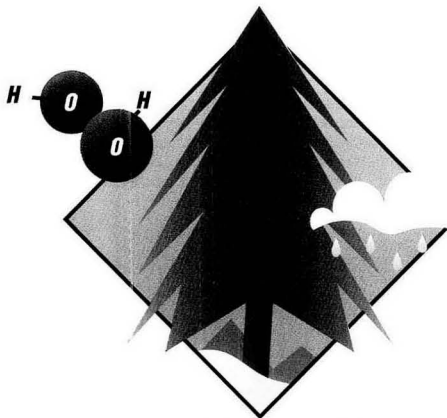


**Join your satisfied colleagues and subscribe to the innovator's magazine ...**



**Call now to order:  
800-227-5558**





## Investigating the Effect of Hydrogen Peroxide on Norway Spruce Trees

A.A.F. Kettrup<sup>1</sup> and H. G.  
Kicinski

Department of Applied Chemistry  
University of Paderborn  
P.O. Box 1621, 4790 Paderborn  
Germany

Georg Masuch

Department of Applied Botany  
University of Paderborn  
P.O. Box 1621, 4790 Paderborn  
Germany

<sup>1</sup> Also affiliated with the Institute of Ecological Chemistry, GSF Munich, Ingolstädter Landstraße 1, 8040 Neuherberg, Germany

The widespread forest decline throughout central and northern Europe and northeastern America is a well-documented phenomenon (1, 2). Elevated levels of ozone in ambient air, combined with the direct and indirect effects of acid precipitation and acid mists, are believed to play a major role in the decline of high-elevation forests in both Europe and North America (3). However, the "acidification theory" and the "ozone theory" do not provide satisfactory

explanations for the full extent of the dieback of forests that has been observed.

Some researchers have tried to link damage patterns to the occurrence of fog and clouds to which the tree crowns are exposed. Laboratory experiments have shown that some of the effects of fog can be attributed to the presence of acidic compounds within the fog itself. Because of their large relative surface area, water droplets in fog are efficient collectors of pollutants (e.g., SO<sub>2</sub> and NO<sub>x</sub>). Strong acids (e.g., H<sub>2</sub>SO<sub>4</sub> and HNO<sub>3</sub>) are thus formed, and pollutants can be contained in fog at concentrations that are 10 to 100 times higher than those found in rainwater (4). Acidic fogs with extreme pH values of 2.2 and 1.8 have been reported (5, 6).

Although the role of acidic compounds and photooxidants (especially ozone) in plant damage is now widely accepted, questions still remain. For example, in some regions with high ozone concentrations, tree damage is absent (7). To explain this situation, one must recall that oxidizing agents other than ozone and peroxyacetyl

nitrate (PAN) are present in the atmosphere. For instance, hydrogen peroxide is considered to be the most important oxidant of SO<sub>2</sub> in atmospheric water droplets. It converts SO<sub>2</sub> to SO<sub>4</sub><sup>2-</sup> at low (<5.0) pH (8), and thus has an important role in the acidification of rainwater and moisture in clouds and fog.

A dominant source of aqueous phase H<sub>2</sub>O<sub>2</sub> is believed to be the dissolution of gaseous H<sub>2</sub>O<sub>2</sub> from the air (9). An important source of atmospheric H<sub>2</sub>O<sub>2</sub> may be solid surface generation, which involves photosensitized generation of H<sub>2</sub>O<sub>2</sub> at the surface of certain sunlight-absorbing solids suspended in clouds (10). Atmospheric H<sub>2</sub>O<sub>2</sub> is generated by photochemical reactions involving radical species (i.e., OH<sup>•</sup>, RH<sup>•</sup>, HO<sub>2</sub><sup>•</sup>, and RO<sub>2</sub><sup>•</sup>) (11). The concentration of H<sub>2</sub>O<sub>2</sub> in air is recognized to be relatively low, < 4–5 ppb (v/v) (12).

High concentrations of H<sub>2</sub>O<sub>2</sub> can occur in the liquid phase. Results of the determination of H<sub>2</sub>O<sub>2</sub> in cloud water collected during several flights in July 1982 range from 850 ppb to 3000 ppb at 150–2000 m above sea

level in Rotterdam and Den Helder, The Netherlands, and Hull, U.K.  $H_2O_2$  concentrations measured above the continent and at ground level indicate that the concentration is markedly reduced because of reactions with precursors ( $NO_x$  and  $SO_2$ ) (13).

Trees in elevated areas are frequently exposed to clouds of fog. The occurrence of fog increases with height above sea level. In Germany fog is present ~120 days per year at

60 m and more than 200 days per year at altitudes over 800 m (14). The concentration of  $H_2O_2$  in acid mist in contact with spruce needles is normally < 1 ppm (15).

Histological investigations of current-year spruce needles from healthy and damaged forest stands in Germany revealed that vacuoles of mesophyll cells (the cells between epidermal/hypodermal and endodermal layers of a needle) contained different amounts of phenols (16, 17).

We were interested in investigating the possible relationship between the location and concentration of these phenolic compounds within the needle and the degree of pollution of the forest stand. Although it is possible to localize phenol accumulation in the needle tissues by light microscopy and electron microscopy, and to identify some phenolic compounds by special staining procedures (18, 19), these techniques do not provide quantitative data.

Historically, TLC and paper chromatography (20) as well as HPLC have been useful for the study of plant phenolic compounds. We recently identified and quantified some of these compounds (Figure 1) as bio-indicators for forest decline possibly caused by acid mist containing  $H_2O_2$  as an air pollutant (21). Because of the complex chromatograms that arise when these plant extracts are analyzed, we chose to develop a method involving HPLC coupled with UV-vis spectroscopy using a photodiode array detector. Simultaneous detection at different wavelengths and measurement of the UV spectra of each separated compound during elution permits rapid identification of the derivatives of benzoic acid, *o*-coumaric acid, *p*-hydroxyacetophenone, stilbenes, and flavonoid compounds, as well as several catechins.

Peaks present in the chromatogram can be identified by comparing retention times and UV-vis spectra with those of standard samples. However, for compounds having closely related structures, this technique might be insufficient for an unambiguous identification. The phenolic compounds can be derivatized by enzymatic or acidic hydrolysis, and if the UV spectra of the resulting monomeric nonglycosidated phenolic forms are known, a more quantitative determination of the constituents can be obtained.

#### Nebulization experiments

Experimental outdoor fog chambers were used to treat three-year-old spruce trees (*Picea abies* Karst) with acidic fog (pH 4.0) containing  $864 \pm 250$  ppb  $H_2O_2$ . Fog containing  $H_2O_2$  was sprayed four days a week from 4 a.m. to 7 a.m. over a period of eight weeks during June and July 1987. During the remaining time, the chambers were open and the trees were exposed to natural climatic conditions (21). Reference series spruce trees were treated with acidic fog (pH 4.0) that did not contain  $H_2O_2$ . The spray solution composition was

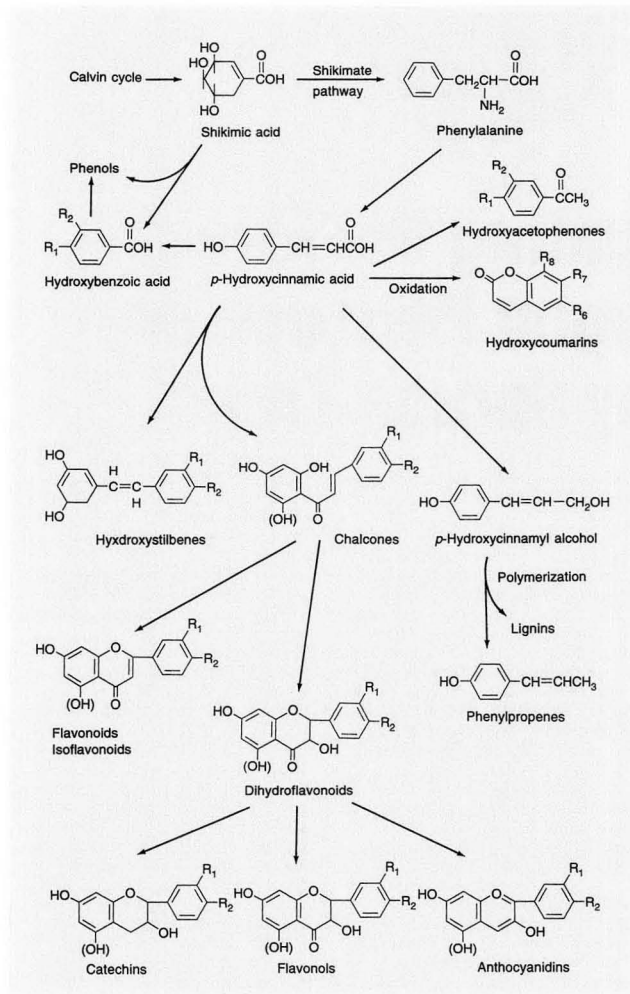


Figure 1. Typical plant phenolic compounds.

R indicates hydroxyl or alkyl groups.

comparable to the moisture found naturally in clouds (pH 4.0) and included the following ions:  $\text{Cl}^-$  (770  $\mu\text{mol/L}$ ),  $\text{SO}_4^{2-}$  (280  $\mu\text{mol/L}$ ),  $\text{NO}_3^-$  (135  $\mu\text{mol/L}$ ),  $\text{H}^+$  (105  $\mu\text{mol/L}$ ),  $\text{Na}^+$  (630  $\mu\text{mol/L}$ ),  $\text{NH}_4^+$  (357  $\mu\text{mol/L}$ ),  $\text{Ca}^{2+}$  (73  $\mu\text{mol/L}$ ),  $\text{Mg}^{2+}$  (90  $\mu\text{mol/L}$ ), and  $\text{K}^+$  (47  $\mu\text{mol/L}$ ).

#### Sample preparation

**Light microscopy.** Spruce needles were taken randomly out of the middle of the current-year twigs from 10 different trees of each experimental series. They were cut into 1-mm slices (one slice out of the middle of each needle) and fixed for 3 h at room temperature in a solution of 1%  $\text{OsO}_4$  and 2.5%  $\text{K}_2\text{Cr}_2\text{O}_7$  with 0.1 M phosphate buffer (22). After a dehydration sequence in ethanol, the fixed slices were embedded in styrene-methacrylate polymer (23). Sections of 1- $\mu\text{m}$  thickness were cut with an LKB-Ultratome III and stained with toluidine blue (24). A Leitz-Orthomat microscope was used for light microscopic studies. Quantitative measurements of the micrographs were made with the aid of a digitizer tablet connected to a microcomputer.

**Scanning electron microscopy.** After polymerization the block was trimmed and 1- $\mu\text{m}$  sections were cut until the internal structures of interest were localized by light microscopy. For examination of phenolic droplets inside the vacuoles of spruce mesophyll cells, the resin was removed from the sectioned block with amyl acetate. Correlation of information obtained from a specific section by light microscopy with information obtained from surface analysis of the cut needle block by scanning electron microscopy was thus possible (25, 26). After extracting resin from the embedded tissue, the spruce needle block was dried, affixed to aluminum support stubs with colloidal silver adhesive, and coated with gold by sputtering. Specimens were examined with a Hitachi H-3010 scanning electron microscope.

**Plant material extraction.** After the nebulization experiment, current-year needles were taken from the reference series trees treated with acidic fog and from trees of the experimental series sprayed with acidic fog containing  $\text{H}_2\text{O}_2$ . The needles were frozen immediately in liquid nitrogen to avoid any biological change. Once in the laboratory, they were stored at  $-70^\circ\text{C}$  until processed.

Purified needle extracts were obtained by extracting 1 g of triturated

and lyophilized needle material (see Figure 2). This procedure yields ~70% of the total needle phenols; the remaining condensed phenolic compounds are irreversibly bound to proteins within the cell (27). Cell wall bound phenols were isolated by using a method described by Strack (28). The enzymatic hydrolysis of the glycosides and the acid hydrolysis of the procyanidins (flavan-3-ols) were carried out as described in the literature (29, 30).

#### HPLC apparatus and conditions

The HPLC system comprised an HP 1050 liquid chromatograph (Hewlett-Packard, Waldbronn, Germany)

equipped with a UV-vis diode array detector and 40 MByte data station. Separations were performed on a 10- $\mu\text{m}$  LiChrosorb RP-18 column (250  $\times$  4.6 mm i.d., Merck, Darmstadt, Germany), equipped with a 5- $\mu\text{m}$  LiChrosorb RP-18 precolumn (4  $\times$  4 mm i.d., Merck). For the elution two solvents were used: A, glacial acetic acid-water (0.5:99.5, v/v); B, methanol. The elution profile was: 0–2 min, 7% B in A (isocratic); 2–8 min, 7–15% B in A (linear); 8–25 min, 15–75% B in A (linear); 25–27 min, 75–80% B in A (linear); 27–29 min, 80% B in A (isocratic). The temperature of the oven thermostat was set at 40  $^\circ\text{C}$ . The flow rate was 1.5

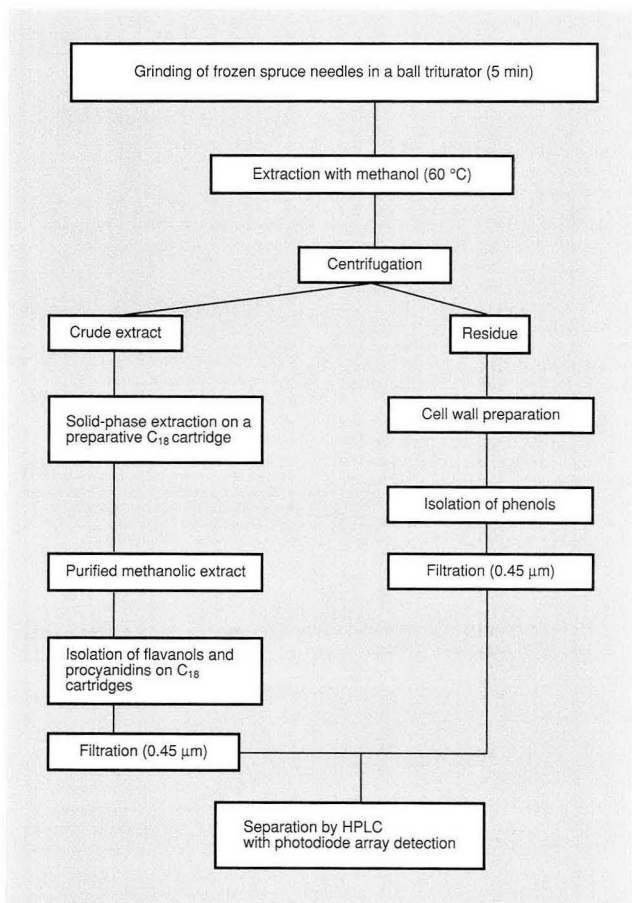


**Figure 2.** Schematic for sample extraction and cleanup of methanolic soluble and cell wall bound phenolic compounds from Norway spruce needles.

mL/min and the column back pressure was 150–180 bar. The diode array detector wavelengths were 250 nm, 280 nm, and 330 nm; optical bandwidth was 8 nm.

### Macroscopic and histological results

The color of healthy spruce needles during mid-summer of their first year is a vivid, intense green, reflecting their exposure to full sunlight. Needles treated with  $H_2O_2$  have color deviations from the green reference needles. Apart from normal color variations, a marked color change to light green or greenish yellow on all needle sets is observed. Pigments from both series of needles were analyzed, and the results appear in Table I.

After exposure to  $H_2O_2$ , the length of current-year twigs and current-year needles decreases significantly. The tissue areas of the needle transverse sections are reduced in those needles exposed to  $H_2O_2$  (Table II). The mean volumes of the current-year needles were calculated; reference needles revealed a mean volume of  $4.0 \pm 0.2 \text{ mm}^3$ , whereas those of the experimental series treated with  $H_2O_2$  had a mean volume of  $2.5 \pm 0.5 \text{ mm}^3$ . Volumes of needle tissues and the intercellular space were also reduced under the influence of  $H_2O_2$ . The reduction of tissue volume per needle is due both to a reduced number of cells per needle and to a reduced cell size.

One symptom observed in the treated spruce needles is the increase of phenolic compounds in the central vacuoles of the mesophyll cells, as well as in the cells of the epidermal and endodermal layers bordering the mesophyll tissue. These compounds

can be stained with  $FeCl_3$  for light microscopic observation. When observed with the scanning electron microscope, phenolic compounds occur as fairly densely packed globular bodies. Phenolic bodies or droplets can be found in the needles of both the reference series and the  $H_2O_2$  se-

ries. The concentration of phenols differs in the cells of the mesophyll tissue. There is an increasing phenolic content in the mesophyll cells from the central layer near the endodermis to the peripheral layer underlying the epidermis and hypodermis.

In the reference series the innermost mesophyll cells are generally free of phenols (Figure 3a) and the central vacuoles are translucent. The large background bodies are packed chloroplasts, overlaid by the vacuolar membrane. In the  $H_2O_2$ -treated series it is difficult to find mesophyll cells without phenols. Cells with low concentrations of phenols contain loosely arranged droplets, aggregated in short strings (Figure 3b).

In some reference needle mesophyll cells the phenolic droplets occur loosely packed in the central vacuoles, are relatively large in size, and are partly in contact with each other (Figure 4a). Compared with the reference series, mesophyll cells of the  $H_2O_2$  series with a medium content of phenols show small droplets (Figure 4b). Near the external surface of the reference series needles mesophyll cells contain higher concentrations of phenolic droplets; they are smaller than those in Figure 4a and are crowded together (Figure 5a). In the peripheral mesophyll cells of needles exposed to acidic mist and  $H_2O_2$ , phenolic droplets are packed extremely close together; the central vacuole is nearly filled with phenolic material (Figure 5b).

The distribution of phenols in the different mesophyll cells of the needle is also dependent on the lighting conditions to which the needles were subjected. Light-exposed parts of the needle contain higher amounts of phenols in the mesophyll cells than

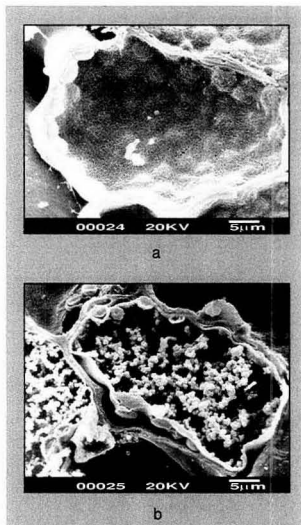


**Figure 3.** Comparison of mesophyll cells of Norway spruce current-year needles taken from the reference series and  $H_2O_2$ -treated trees.

(a) The central vacuole is translucent in the reference series needles. The large background bodies are packed chloroplasts, overlaid by the vacuolar membrane. (b) Loosely arranged phenolic droplets are aggregated in short strings in the  $H_2O_2$ -treated series needles.

**Table I.** Pigment composition of current-year spruce needle chloroplasts<sup>a, b</sup>

Pigment	Reference series	$H_2O_2$ -treated series
Chlorophyll a	$3.43 \pm 0.47$	$2.85 \pm 0.61$
Chlorophyll b	$1.21 \pm 0.09$	$1.15 \pm 0.07$
$\beta$ -Carotin	$0.98 \pm 0.13$	$0.75 \pm 0.05$
Lutein	$0.61 \pm 0.09$	$0.87 \pm 0.05$
Xanthophylls	$1.12 \pm 0.10$	$1.52 \pm 0.33$

<sup>a</sup> Data are expressed as mg/g (dry wt).

<sup>b</sup> Values are reported as the mean  $\pm 1 \sigma$  for three replicates.

**Table II.** Tissue areas of current-year spruce needles as seen in transverse needle sections<sup>a, b</sup>

Tissue area	Reference series	$H_2O_2$ -treated series
Total transverse section area	$396\ 894 \pm 1950$	$315\ 002 \pm 70\ 620$
Epidermis	$33\ 870 \pm 2760$	$29\ 030 \pm 3760$
Hypodermis	$30\ 320 \pm 2840$	$21\ 840 \pm 4900$
Endodermis	$7340 \pm 950$	$6320 \pm 1150$
Vascular bundle	$20\ 740 \pm 3100$	$14\ 700 \pm 4180$
Intercellular space	$98\ 260 \pm 22\ 900$	$76\ 330 \pm 25\ 600$
Mesophyll cell area	$197\ 300 \pm 28\ 900$	$162\ 650 \pm 35\ 975$

<sup>a</sup> Data are expressed in  $\mu\text{m}^2$ .

<sup>b</sup> Values are reported as the mean  $\pm 1 \sigma$  for 10 replicates. Level of significance ( $p$ ) is calculated by applying the student  $t$ -test, and  $p < 0.05$ .



"I hear your new product is ready."

"Yep. Mmm, the lasagne looks tasty!"

"Patents checked?"



"Wouldn't have tested otherwise."

"And regulatory compliance?"

"It checks out..."



...which is more than I can say about that meatloaf."

"Hey, where're you getting so much help?"

## The answer is in Dialog.

*Information*—complete, precise, up-to-the minute. It's your most powerful research tool. Find exactly what you need to know fast in Dialog® the world's first and largest electronic library. We offer over 400 diverse, detailed databases readily accessible online via computer and modem, many even

on compact disc. You probably won't have to look anywhere else. See your Information Specialist about Dialog. Or call for a free kit on Dialog information for your industry.

**1-800-3-DIALOG**

Outside U.S., 415-858-3785. Fax 415-858-7069.

*Dialog Tools for Chemistry: Research and industry news, plus chemical substructures and properties, patent, trademark, safety, regulatory, environmental, and competitive data. Full text and/or abstracts from newspapers, newsletters, journals, conference proceedings, citations, handbooks, encyclopedias. Some sources updated as often as daily, even continuously.*

**DIALOG INFORMATION SERVICES, INC.**  
A KNIGHT-RIDDER COMPANY

© 1991 Dialog Information Services, Inc., 3460 Hillview Avenue, Palo Alto, California 94304. All rights reserved. DIALOG is a servicemark of Dialog Information Services, Inc., Registered U.S. Patent and Tradem.

CIRCLE 30 ON READER SERVICE CARD



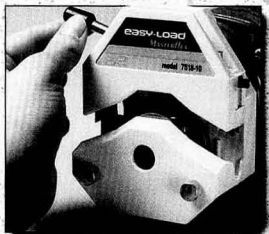
## NEW Pump heads!

# MASTERflex® L/S EASY-LOAD

as  
easy  
as...

①

OPEN



②

INSERT  
TUBING

③

CLOSE  
AND  
START  
PUMPING

IT'S  
EASY!



For fast and easy tubing changes, your choice is **EASY**. Easy-Load™ pump heads open and close with the flip of a lever. Masterflex® L/S Easy-Load pump heads mount directly to Masterflex L/S drives, accept the same tubing and produce the same flow rates (up to 2280 ml/min) as your current Masterflex L/S pump heads. When several Easy-Load pump heads are stacked on a single drive, you can change the tubing in one Easy-Load without interrupting the other pump heads. Add Easy-Load to your Masterflex peristaltic system today. **Your choice is EASY!**

Easy-Load™—TM Cole-Parmer Instrument Co.  
Masterflex—Reg TM Cole-Parmer Instrument Co.



**Cole-Parmer® Instrument Co.**  
7425 N. Oak Park Ave., Chicago, IL 60648  
FAX: 1-708-647-9660  
DIAL: 1-800-323-4340 or  
1-708-647-7600

CIRCLE 22 ON READER SERVICE CARD.

**Supplementary  
Material  
is available  
for this journal!**

**Need more information  
than is provided in an article?  
Need tables? Diagrams?**

**Supplementary Material  
is the answer!**

Articles with Supplementary Material available have a black box by the page number in the table of contents. And, a notice of its availability will appear at the conclusion of the paper.

**To order your Supplementary Material . . .**

**Send your order with payment for either  
photocopies or 24X microfiche to:**

American Chemical Society  
Microforms and Back Issues Office  
1155 Sixteenth St., N.W.  
Washington, D.C. 20036

**The rates are:** \$10 for microfiche (add \$1 for postage outside the U.S. and Canada)

\$10 for photocopies up to 3 pages, plus  
\$1.50 per page for each additional  
page (Add \$2 for postage outside the  
U.S. and Canada)

Please give complete title of article, authors' names, journal, issue date, and page numbers.

Or, call 202-872-4554 and charge your order to your MasterCard, VISA, or American Express.

**An annual subscription to Supplementary  
Material is available . . .**

If you want all the Supplementary Material as it is published, why not enter an annual subscription to Supplementary Material? Annual subscription rates (available in microfiche only) are listed on the masthead page. Or, subscribe to the package plan, where you will receive all Supplementary Material (those with subscriptions and those without subscriptions) for \$400 (U.S.) or \$550 (for all other countries).

do sheltered parts (Figure 6). This phenomenon can also be observed in the epidermal cells. It is possible to detect different amounts of phenols by comparing histological specimens, but no quantitative data can be obtained using this method.

#### Analytical results

The HPLC measurements of phenolic compounds in current-year needles indicate an average of 36.15 mg phenols per gram needle (dry wt) for the reference series and 85.95 mg phenols per gram needle (dry wt) for the  $H_2O_2$  series. Second-year needles contain 61.45 mg phenols per gram needle (dry wt) in the reference series and 227.8 mg phenols per gram needle (dry wt) in the  $H_2O_2$  series. It can be concluded that  $H_2O_2$  in acid mist is a stress factor that causes accumulations of phenols in the central vacuoles of mesophyll cells of spruce needles. For more details concerning the quantitative speciation of phenolic compounds in Norway spruce needles, we must use HPLC with diode array detection.

In choosing a method for isolation

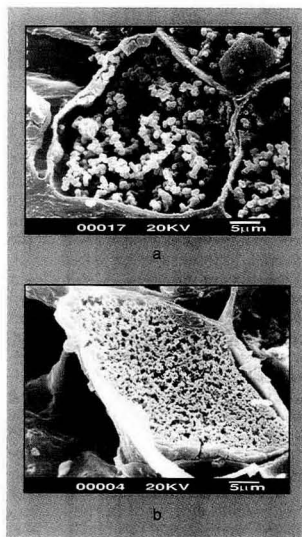


**Figure 4.** Phenolic droplets in mesophyll cells of Norway spruce current-year needles taken from the reference series and  $H_2O_2$ -treated trees.

- (a) Phenolic droplets occur loosely packed in the central vacuole in the reference series needles. (b) Increased amounts of small phenolic droplets occur in the  $H_2O_2$ -treated series needles.

of spruce needle phenolics, one must take into consideration not only the properties of the compounds but also the chemical composition of the biological source. Needle material is composed mainly of insoluble cellulose and lignin as well as soluble chlorophyll, waxes, fats, terpenes, esters, salts, sugars, amino acids, and phenolic compounds. The extraction procedure developed seems to be a powerful tool for isolation and purification of needle phenolics. Although extraction procedures may vary somewhat for different plant species and tissues, the same procedure for separation and identification is applicable and has been used successfully for a variety of plant and tree tissues. By being able to extract and isolate phenolics for use in particular studies, we can observe their presence and the quantities and combinations in which they occur throughout the physiological growth and development of the plant.

Reversed-phase liquid chromatography on octadecylsilyl-bonded columns with methanol-water has been successfully employed in many separations of polar flavonoid aglycones

and flavonoid glycosides (31–33). Because needle extracts of *Picea abies* usually contain phenolic compounds of different polarity and oxidation states, elution with acidified water-methanol gradients turned out to be an ideal solution system. Chromatograms representing the separation of purified primary spruce needle extracts from trees that were slightly injured are shown in Figures 7–9. The complexity of secondary spruce needle products such as phenols is documented in the literature by observation of at least 50 soluble compounds; about 20 structures could be identified by our group using HPLC. They include benzoic acids, acetophenones, cinnamic acids, coumaric acids and stilbenes as well as several different flavonoids such as catechin and flavonols (Table III).

The availability of a photodiode array detector for HPLC enables a remarkable improvement in peak identification. As can be seen in Figure 7,  $\beta$ -hydroxybenzoic acid glycoside can be detected only at 250 nm. Shikimic acid, the most important intermediate of phenolic biosynthesis, can be

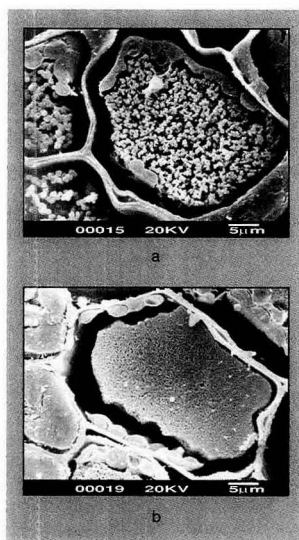


**Figure 5.** Mesophyll cells from reference series and  $H_2O_2$ -treated trees.

- (a) Cell near the external surface of the reference series needle contains higher concentrations of phenolic droplets. (b) Peripheral cell from the  $H_2O_2$ -treated series needle with closely packed phenolic droplets nearly filling the central vacuole.



**Figure 6.** Transverse section of a current-year Norway spruce needle from the reference series exposed to acidic fog (pH 4.0).

Phenol distribution in the central vacuoles of mesophyll cells is dependent on the lighting conditions. The upper part of the needle was exposed to sunlight and contains relatively high amounts of phenols. The lower part of the needle was sheltered and is nearly free of phenols; chloroplasts can be seen through the translucent central vacuoles.

detected only below 220 nm. Compounds 1 and 3–11 (Table III) can be identified by comparison of their retention times and UV spectra with those of authentic compounds from the reference mixture.

With the exception of compounds 4,

5, 6, 8, and 10, all extracted phenols were in their natural glycoside linkage, ester linkage, or procyanidin B/C (dimeric/trimeric) form. To identify the presence of compounds 12–19, separation was repeated after enzymatic hydrolysis and hydrochloric

acid hydrolysis of the sample.

The retention, peak area, and UV wavelength data of the identified "new" monomeric compounds may be directly correlated with the unhydrolyzed glycosides, although the sugar compound was not analyzed. The following needle phenols have been identified in this manner: *p*-hydroxybenzoic acid glycoside, *p*-coumaric acid glycoside, *o*-coumaric acid glycoside, kaempferol-3-glycoside, quercetin-3-glycoside as glycoside compounds, and the procyanidins B-3, B-4, B-6, and C-2 (31).

Needle phenols accumulate predominantly in the form of hydrophilic conjugates in the vacuoles. There are reports, too, on their extraprotoplasmic location (e.g., exudates or cell wall components) (28). The latter include the polymer lignin as well as monomeric hydrolyzable phenols, which are mainly hydroxycinnamic acids or kaempferol-3-glycoside linked to polysaccharides and/or lignin. In the course of studies on identification of phenols and their metabolism in Norway spruce needles, the insoluble material resulting from methanolic extractions of soluble phenols for the presence of hydrolyzable ester-bound phenolic compounds was examined. The released compounds were readily identified as *p*-coumaric acid and kaempferol-3-glycoside (Figure 9).

The relatively high concentration of cell wall bound phenols (amounting to ~0.2% of total needle fresh weight), especially kaempferol-3-glycoside, raises the question of metabolism and the importance of cell wall bound phenols as well as the possible influence of air pollution on formation of phenols. A significant alteration in the amount of cell wall bound phenols was not observed in current-year and second-year Norway spruce needles from both reference trees and those exposed to acidic fog containing H<sub>2</sub>O<sub>2</sub>. These nebulation chamber results are in good agreement with data of several forest stands in Germany that are slightly or severely damaged (34).

In contrast to these observations, a remarkable difference in the amount of the methanolic soluble fractions obtained from current-year and second-year needles was observed. Compared with reference needles (not damaged), slightly and severely injured needles from forest stands show higher amounts of picein (5–12 fold) and catechin (2–5 fold) as well as decreasing amounts of *p*-hydroxyacetophenone and isorhapontin (up

Table III. Identified phenolic compounds

Compound	Index	<i>t<sub>R</sub></i> (min)	<i>K'</i> <sup>a</sup>	Wavelength (nm)
Quinic acid	0	1.50	0.11	< 220
Shikimic acid	1	1.80	0.33	< 220
Gallic acid	2	3.90	1.89	280
Procataechnic acid	3	4.90	2.63	250
Picein	4	8.80	5.52	250
<i>p</i> -Hydrobenzoic acid	5	9.70	6.19	250
<i>d</i> -Catechin	6	11.20	7.80	280
Chlorogenic acid	7	12.50	8.26	330
Caffeic acid	8	13.20	8.78	330
(-)-Epicatechin	9	13.70	9.15	280
<i>p</i> -Hydroxyacetophenone	10	14.00	9.37	280
Piceatannol glycoside	11	14.70	9.89	280
<i>p</i> -Coumaric acid	12	15.40	10.41	330
3-Indoleacetic acid	13	16.50	11.20	280
Benzoic acid	14	17.00	11.60	280
<i>o</i> -Coumaric acid	15	18.00	12.33	330
Cinnamic acid	16	20.50	14.19	330
Quercetin	17	21.45	14.89	330
Kaempferol-3-glycoside	18	23.00	16.04	330
Isorhapontin	19	24.50	17.15	280

<sup>a</sup> *t<sub>0</sub>* = 1.35 min

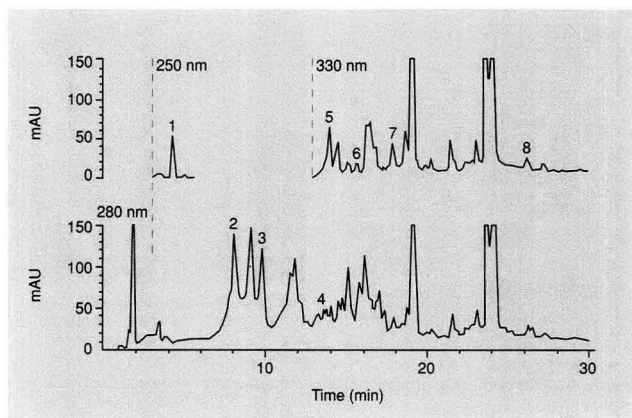


Figure 7. Multisignal plot of a purified Norway spruce needle extract.

Compounds identified: (1) *p*-hydroxybenzoic acid glycoside; (2) picein; (3) catechin; (4) *p*-hydroxyacetophenone; (5) kaempferol-3-glycoside; (6) piceatannol glycoside; (7) kaempferol-7-glycoside; (8) isorhapontin.

**Table IV. Quantitative amounts of phenolic compounds in current- and second-year spruce needles<sup>a, b</sup>**

Phenolic compound	Current-year needles		Second-year needles	
	Reference series	H <sub>2</sub> O <sub>2</sub> -treated series	Reference series	H <sub>2</sub> O <sub>2</sub> -treated series
Quinic acid	3300 ± 118	4952 ± 107	5846 ± 215	7416 ± 200
Shikimic acid	16 170 ± 947	27 435 ± 1047	14 190 ± 263	23 980 ± 270
Catechin	5010 ± 241	9480 ± 38	10 400 ± 200	32 152 ± 456
<i>p</i> -Hydroxyacetophenone	325 ± 10	200 ± 12	824 ± 17	390 ± 15
Picein	8155 ± 500	40 201 ± 1080	16 419 ± 418	16 0218 ± 3458
Picetannol-glucoside	590 ± 10	705 ± 37	1050 ± 41	1157 ± 45
Isorhapontin	2400 ± 17	2709 ± 19	2722 ± 15	2520 ± 40
Kaempferol-3-glucoside	202 ± 7	269 ± 10	40 ± 10	47 ± 10

<sup>a</sup> Data are expressed as mg/g (dry wt).

<sup>b</sup> Values are reported as the mean ± 1  $\sigma$  for three replicates.

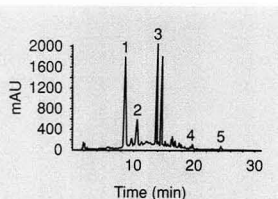


**Figure 8.** Liquid chromatogram of phenolic compounds of a purified methanolic spruce needle extract.

Compounds: (1) picein; (2) catechin; (3) *p*-hydroxyacetophenone; (4) kaempferol-3-glucoside; (5) isorhapontin.

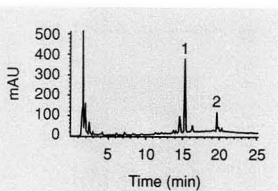


**Figure 9.** Liquid chromatogram of cell wall bound compounds.

(1) *p*-coumaric acid; (2) kaempferol-3-glucoside.

to 60%) (Table IV) (21, 34).

HPLC coupled with a UV-vis diode array detector is a suitable method for the screening of polyphenolic compounds in the needle extracts. Comparing retention times and UV spectra of compounds with those of authentic samples in a database al-

lows fast and easy identification. The simple method of using hydrolysis to provide monomeric phenolic compounds improves the reliability of peak identification. On-line HPLC-UV-vis spectroscopy appears to be useful for studying the effects of air pollution on the distribution of needle phenols. However, the method has limitations, especially if no authentic samples are available for comparison. In such a case it should be combined with LC/MS.

We are now beginning to gain an understanding of the physiological and biochemical mechanisms of phenolic compounds in conifer needles. It has been reported that production of phenols increases the plant's resistance to transpiration (35) and drought (36). The "active" phenols occur exclusively as aglycones (nonglycosidated phenols); they are toxic to microorganisms (37). The majority of phenols, however, are present as glycosidic derivatives. Glycoside formation detoxifies aglycones and leads to a decrease in chemical activity (38).

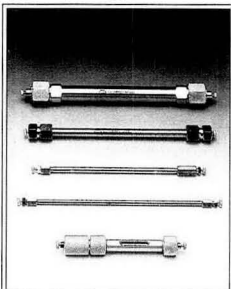
The authors thank J.-T. Franz for SEM assistance. The authors are indebted to J. Slanina and R.K.A.M. Mallant of the European Commonwealth of Nations, Petten, The Netherlands, for help in creating fog and determining H<sub>2</sub>O<sub>2</sub>.

#### References

- (1) Blank, L. W. *Nature (London)* **1985**, *314*, 311-14.
- (2) McLaughlin, S. B. *J. Air Pollut. Control Assoc.* **1985**, *35*, 512-52.
- (3) Barnes, J. D.; Eamus, D.; Brown, K. A. *New Phytol.* **1990**, *114*, 713-20.
- (4) Waldmann, G. *Allg. Forst. Jagdztg.* **1985**, *156*, 204-21.
- (5) Munger, J. W.; Jacob, D. J.; Waldmann, J. M.; Hoffmann, M. *J. Geophys.*

## Chromatography Specialists

### Liquid Chromatography



#### Packings

- Silicas NUCLEOSIL® and POLYGOSIL®
- Aluminium oxide
- Cellulose, Polyamide

#### Packed columns

- Guard columns
- Cartridge system
- Preparative columns
- Columns for special applications

#### Accessories

- Valves and fittings
- Micro syringes
- Vials and accessories and many more

Please ask for further information.



MACHERY-NAGEL GmbH & Co. KG  
P.O. Box 101352 · D-5160 Düren · W. Germany  
Tel. (02421) 698-0 · Telefax (02421) 62054

Switzerland: MACHERY-NAGEL AG  
P.O. Box 224 · CH-4702 Oensingen  
Tel. (062) 762066 · Telefax (062) 762864

CIRCLE 92 ON READER SERVICE CARD

## SAMPLE PREPARATION BOMBS FOR TRACE METAL ANALYSIS



Available in a variety of sizes and styles, our teflon-lined Acid Digestion Bombs are designed for microwave and convection

heating. Use them to treat inorganic samples in HF, HCl and other strong mineral acids. Or to digest organic samples in strong alkali or oxidizing acid at elevated temperatures and pressures.

Our Oxygen Bomb decompose any combustible solid or liquid — quickly and completely.



The sealed bomb contains and converts materials to a soluble form while allowing complete recovery of all elements. Now available in a new longer-lasting material for high halogen-containing substances.

For complete details ask for our free Brochure #4700.



**PARR INSTRUMENT COMPANY**  
211 Fifty-Third Street  
Moline, IL 61265  
309-762-7716  
Telex: 270226  
Fax: 309-762-9453

CIRCLE 108 ON READER SERVICE CARD

## ANALYTICAL APPROACH

- Res. Atmos.* **1983**, *88*, 5109-21.
- (6) Sigg, L.; Stumm, W.; Zobrist, J.; Zurcher, F. *Chimia* **1987**, *41*, 159-65.
- (7) National Meetnet voor Luchtverontreiniging, NML-RIVM No. 26, Report No. 228216020, Rijksinstituut voor Volksgezondheid en Milieuhygiene, Bilthoven, The Netherlands, 1984.
- (8) Mohnen, V. A. *Sci. Am.* **1988**, *259*, 4-22.
- (9) Schwartz, S. E. *J. Geophys. Res. Atmos.* **1984**, *89*, 11589-98.
- (10) Bahnemann, D. W.; Hoffmann, M. R.; Hong, A. P.; Kormann, C. In *The Chemistry of Acid Rain*; Johnson, R. W.; Gordon, G. E., Eds.; American Chemical Society: Washington, DC, 1987; pp. 120-32.
- (11) Finayson, B. J.; Pitts, J. N., Jr. *Atmospheric Chemistry*; Wiley Interscience: New York, 1986; p. 1098.
- (12) Sakugawa, H.; Kaplan, I. R. Presented at the 196th National Meeting of the American Chemical Society, Los Angeles, CA, Sept. 1988; paper ENVR 85.
- (13) Römer, F. G.; Viljeer, J. W.; van den Beld, L.; Slangewal, H. J.; Veldkamp, A. A. *Atmos. Environ.* **1985**, *19*, 1847-58.
- (14) Georgii, H. W.; Schmitt, G. *Staub Reinhalt. Luft* **1985**, *45*, 260-64.
- (15) Düm, W. Ph.D. Thesis, University of Paderborn, 1989.
- (16) Vogels, K.; Guderian, R.; Masuch, G., In *Acidification and Its Policy Implications*; Schneider, T., Ed.; Elsevier: Amsterdam, 1986; pp. 171-86.
- (17) Soikkeli, S. *Can. J. Bot.* **1977**, *56*, 1932-40.
- (18) Frohne, D. *Anatomisch-mikrochemische Drogenanalyse*. Thieme: Stuttgart, 1974.
- (19) Hoque, E. *Biochemie und Physiologie erkrankter Fichten*; Ecomed: Landsberg 1990.
- (20) Evans, M. V. *J. Liq. Chromatogr.* **1983**, *6*(5-2), 153-78.
- (21) Masuch, G.; Kicinski, H. G.; Dülma, W.; Kettrup, A. *Int. J. Environ. Anal. Chem.* **1989**, *37*, 161-85.
- (22) Senser, M.; Schötz, F.; Beck, E. *Planta* **1975**, *126*, 1.
- (23) Kushida, H. *J. Electron Microsc.* **1961**, *10*, 16.
- (24) Trump, B. F.; Smuckler, E. A.; Benditt, E. *J. Ultrastruct. Res.* **1961**, *5*, 343.
- (25) Jarvis, L. R. *J. Microscopy* **1975**, *105*, 115-17.
- (26) Erlandsen, S. L.; Thomas, A.; Wendelschafer, G. *Scanning Electron Microscopy 1973*; IIT Research Inst: Chicago, IL, 1973; Part III, pp. 349-56.
- (27) Harborne, J. B. *Phytochemical Methods*; Chapman and Hall: London, 1987.
- (28) Strack, D. Z. *Naturforsch.* **1988**, *43C*, 37-41.
- (29) Siewek, F.; Galensa, R. *J. Chromatogr.* **1984**, *294*, 385-89.
- (30) Endres, H. *Habilitation*, University of Munich, 1962.
- (31) Costeale, K.; Geiger, H.; Van Sumere, C. F. *J. Chromatogr.* **1982**, *240*, 31.
- (32) Niemann, G. J.; Koerselmann-Koody, J. W. *Planta Med.* **1977**, *31*, 297.
- (33) Daigle, D. J.; Con Kerton, R. J. *J. Chromatogr.* **1982**, *240*, 202-05.
- (34) Masuch, G.; Franz, J. T.; Kicinski, H. G.; Kettrup, A. *Environ. Exp. Bot.*, in press.
- (35) Fahn, A. *Plant Anatomy*; Pergamon Press: Oxford, 1982; p. 42.
- (36) Parker, J. *Nature* **1971**, *234*, 231.
- (37) Levin, D. A. *Am. Nat.* **1971**, *105*, 157-68.
- (38) Pridham, J. B. *Annu. Rev. Plant Physiol.* **1965**, *16*, 13-36.



A.A.F. Kettrup holds a Ph.D. from the University of Münster. He has held positions at the University of Bochum, the University of Paderborn, and the University of Cape Town. In 1990 he was appointed director of the Institute of Ecological Chemistry of the GSF National Research Center for Environment and Health, where he is involved with specimen banking and the study of indoor chemicals. He holds a simultaneous appointment in the department of applied chemistry at the University of Paderborn.



H. G. Kicinski is a group leader and lecturer in environmental chemistry in the Höhere Berufsfachschule Chemie (HBFS) (Bielefeld, Germany). He received his D.Sc. degree from the University of Paderborn. Before joining HBFS, he was group leader in the analytical department of applied chemistry at the University of Paderborn, where he developed methods for the determination of trace nonvolatile organic compounds in water and biochemical compounds in spruce needles.



Georg Masuch is professor of biological sciences at the University of Paderborn. After receiving the D.Sc. degree in botany from the University of Münster (1967), he joined the University of Paderborn, where his early research interests involved cell biology and digital image analysis. More recently he has been working in the areas of light and electron microscopy, computer-aided image analysis, and proton NMR imaging analysis in environmental applications.



# PAPERED OVER?



## Let CA SELECTS Uncover You!

Subscribe to CA SELECTS. We will free you from mounds of extraneous papers...and uncover the information you need.

CA SELECTS is a series of 237 different current-awareness bulletins. These printed bulletins give you the same bibliographic information, abstracts, and structure diagrams (when available) that you find in CHEMICAL ABSTRACTS, only focused on specialized topics.

With CA SELECTS, you can relax while a computer

profile searches for current literature relevant to your interests. The information you need will flow effortlessly across your doorstep.

All this is yours for just \$180.00 a year—\$6.92 a biweekly issue—only pennies per abstract! Ask for our FREE catalog.

Let CA SELECTS strip away your mounting mass of papers!

**YES!** Please send me the descriptions of all 237 topics.

NAME \_\_\_\_\_

JOB TITLE \_\_\_\_\_

ORGANIZATION \_\_\_\_\_

ADDRESS \_\_\_\_\_

STATE \_\_\_\_\_

ZIP \_\_\_\_\_

CITY \_\_\_\_\_

COUNTRY \_\_\_\_\_

PHONE NUMBER \_\_\_\_\_

For faster response, complete the coupon, and FAX this ad to 614/447-3713!

CAS

Marketing Dept. 47991  
2540 Olentangy River Road  
P.O. Box 3012  
Columbus, Ohio 43210-0012, U.S.A.

# LABORATORY SERVICE CENTER

## ELECTRODE FABRICATION

- To Your Specifications
  - All Sizes/Applications
  - Prompt Delivery
  - HPLC Electrodes Our Specialty
  - Low Cost
  - Problem Solving
  - Since 1966
- KOSLOW Scientific Co., Edgewater, NJ 07020  
201-941-4484 800-556-7569

## FREE CATALOG

GRAPH: great for scientific plotting and standard curve calculations, MINSQ: non-linear curve fitting and modeling, EQUIL: solution chemical equilibrium calculations, and more! Prices from \$150.

**1-800-942-MATH**  
MicroMath, Salt Lake City, UT 84121-0550

## LOWEST COST-HIGHEST PERFORMANCE

**GAS CHROMATOGRAPHS AND INTEGRATORS**  
SEVEN DETECTORS FOR ALL EPA/ASTM METHODS  
**FID TCD ECD FPD**  
**PID ELCD NPD**  
COMBINE ANY OR ALL  
**SRI INSTRUMENTS**  
213-214-5090 fax 5097

FIELD PORTABLE TEMP. PROG.  
DATA SYSTEMS-INTEGRATORS  
PURGE AND TRAP  
GAS SAMPLING VALVES  
THERMAL DESCORBERS  
AUTOSAMPLERS

GCs STARTING AT \$2495.00  
RENTALS AT 0.5% PER DAY  
TRAINING CLASSES  
TWO YEAR WARRANTY

## CLASSIFIED—HELP WANTED

### PROJECT LEADER

Biosensor Research: Conduct & oversee an exploratory research program in biosensors, employing optical & electrochemical means, aimed at providing future marketable products. Pos req'd M.S. or equiv. in Analytic/Bio Chemistry & 5 yrs in pos or as Electrochem or Optical Sensing Research Scientist. Candidates must have acquired the following thru educ/work achievements: exp in original research to develop chemical instrumentation employing electrochemical & optical sensing methods; exp utilizing sensing elements that include enzyme, multi-enzyme systems, antibodies, receptors, nucleic acids, micro-organisms & tissues; exp utilizing transducer elements that include electrochemical, optical & acoustic; exp directing subordinate research scientists over the length of a project; research exp employing reagents containing bilirubin oxidase enzyme in test solutions such as biological fluids; research exp employing fluoride ion-selective membrane containing fluoride ion-selective material in an electrically insulating material; research exp employing electrode devices for the determination of ionic activity in aqueous samples by means of ion-selective electrodes comprised of organic plastic material; research exp employing dry electrochemical reference half-cells for use as internal reference w/ion-selective electrodes for composing an organic polymeric substance having a substantially planar surface; research exp employing analytical processes/means for measuring immunochemical reactions in which one of the immunochemical binding reagent molecules is labelled to a particle of metal or semiconductor mtrl that has resulting measurable optical properties; exp recording experimental data in an acceptable manner, making appropriate calculations as req'd, maintaining accurate records of work performed, analyzing data in terms of basic math/statistical procedures, communicating/interpreting experimental results, contributing suggestions for modifying research techniques & preparing mfg protocols/specifications; and, exp providing critical analysis of emerging new technologies to forecast future trends & determine/allocate budgets for specific R&D programs. Must have published research & obtained patents in connection w/biosensor technology & be willing to sign employer's standard agreement dealing w/inventions, works of authorship & the handling of confidential information. Yrly salary for 40 hr wk: \$82,104. Job site/interview: Fullerton, CA. Must have proof of legal authority to work permanently in the U.S. Send ad and detailed resume to job #DC16284, P.O. Box 9560, Sacramento, CA 95823-0560 no later than November 15, 1991.

### Analytical Chemists— Quality Assurance

San Antonio, TX

We need three professionals to help us develop and monitor quality assurance activities in a major environmental restoration program. Individuals will be responsible for interpretation of environmental data, which characterize potential sources and identify the extent of contamination from hazardous waste sites. In addition, selected individuals will review sampling and analysis plans, work plans and statements of work, and recommend modifications or additions to the documents to meet objectives of project and program requirements. On-site evaluations of environmental laboratories providing analytical services will be conducted by our staff chemists. ■ Qualifications for these integral positions include an MS or PhD in Chemistry and 8–10 years' hands-on experience in analyzing environmental samples for both organic and inorganic analytes and using SW-846 methods. U.S. citizenship, willingness to travel, and expertise in quality assurance and quality control in chemical measurements are required. Experience in conducting laboratory audits and data validation is highly desirable. ■ An independent, not-for-profit organization, MITRE works in the public interest, solving complex technical problems by providing system engineering, technical assistance, system integration and acquisition support to government and civil agencies. In addition to competitive salaries, we offer a comprehensive benefits package.

**For confidential consideration, please forward your resume to: The Office of Human Resources, Section M11, The MITRE Corporation, 7525 Colshire Drive, McLean, VA 22102.**

MITRE is proud to be an equal opportunity/affirmative action employer and is committed to diversity in our workforce. MITRE's Corporate Offices are located in Bedford, MA and McLean, VA.

# MITRE

### HELP WANTED ADS

ROP display at ROP rates. Rate based on number of insertions within contract year. Cannot be combined for frequency.

Unit	1-TI	6-TI	12-TI
1" (25 mm)	\$200	\$180	\$170
	24-TI	48-TI	72-TI
	\$160	\$150	\$140

**ANALYTICAL CHEMISTRY**  
500 Post Road East  
P.O. Box 231  
Westport, CT 06880  
203-226-7131/FAX: 203-454-9939

### LABORATORY SERVICE CENTER

(Equipment, Materials, Services, Instruments for Leasing). Maximum space — 4 inches per advertisement. Column width, 2-3/16"; two column width, 4-9/16". Artwork accepted. No combination of directory rates with ROP advertising. Rates based on number of inches used within 12 months from first date of first insertion. Per inch: 1" — \$175; 12" — \$170; 24" — \$165; 36" — \$160; 48" — \$155.

**ANALYTICAL CHEMISTRY**  
500 Post Road East  
P.O. Box 231  
Westport, CT 06880  
203-226-7131  
FAX: 203-454-9939

## INDEX TO ADVERTISERS IN THIS ISSUE

CIRCLE INQUIRY NO.	ADVERTISERS	PAGE NO.	CIRCLE INQUIRY NO.	ADVERTISERS	PAGE NO.
1.....	*Alltech Associates, Inc. Chromad	1042A	125, 126 .....	*Swagelok Company Falls Advertising Company	1022A
14.....	*J. T. Baker, Inc. Stiegler, Wells & Brunswick, Inc.	1012A	140.....	*Valco Instruments Company, Inc. Technical Advertising Associates	1015A
16.....	Bio-Rad Digilab Division Digilab	OBC	148.....	*Wyatt Technology Corporation	1045A
22.....	Cole-Parmer Instrument Company C-P Advertising	1052A			
24.....	Corporation Scientifique Claisse, Inc.	1028A			
30.....	*Dialog Information Services, Inc. Grey Advertising	1051A			
28.....	*Dionex Corporation Dionex Advertising & Design	IFC			
32.....	*EG&G Princeton Applied Research Kilgore Associates	1038A			
34.....	EM Separations Scientific Marketing Services, Inc.	1032A			
44.....	Finnigan MAT, Inc. Pinne/Herbers Advertising, Inc.	1017A			
50.....	*Gilson Medical Electronics, Inc.	1011A			
64-67.....	*Isco, Inc. Farneaux Associates	1020A			
92.....	Macherey-Nagel GmbH & Co. KG MP Design Werbeagentur	1055A			
77-80.....	*Mattson Instruments, Inc. Fourier Court Advertising	1019A, 1029A-1031A			
85.....	Merck & Company, Inc. William Douglas McAdams, Inc.	1046A			
87.....	*Millipore Corporation Mintz & Hoke, Inc.	1041A			
95-97.....	NIRSystems Barrett Advertising	1037A			
104.....	*Ohaus Corporation Francioli Richartz Weiman & Fliss	1039A			
108.....	*Parr Instrument Company FBA Marketing/Communications	1056A			

*Classified advertising section, see page 1058A.*

*Directory section, see page 1058A.*

*\* See ad in ACS Laboratory Guide.*

*Advertising Management for the American Chemical Society Publications*

### CENTCOM, LTD.

*President*

**James A. Byrne**

*Executive Vice President*

**Benjamin W. Jones**

**Robert L. Voepel, Vice President**

**Joseph P. Stenza, Production Director**

500 Post Road East  
P.O. Box 231  
Westport, Connecticut 06880  
(Area Code 203) 226-7131  
Telex No. 6433 10  
Fax No. 203-454-9939

### ADVERTISING SALES MANAGER

**Bruce E. Poorman**

### ADVERTISING PRODUCTION MANAGER

**Jane F. Gatenby**

### SALES REPRESENTATIVES

Philadelphia, PA... CENTCOM, LTD. GSB Building, Suite 405, 1 Belmont Ave., Bala Cynwyd, PA. 19004. Telephone: 215-667-9666, FAX: 215-667-9353

New York/New Jersey... Dean A. Baldwin, John F. Rafferty, CENTCOM, LTD., Schoolhouse Plaza, 720 King Georges Post Road, Fords, NJ 08863, Telephone: 908-738-8200, FAX: 908-738-6128

Westport, CT... Edward M. Black, CENTCOM, LTD., 500 Post Road East, P.O. Box 231, Westport, CT 06880. Telephone: 203-226-7131, Telex 643310, FAX: 203-454-9939

Cleveland, OH... Bruce E. Poorman, CENTCOM, LTD., 325 Front St., Suite 2, Berea, OH 44017. Telephone: 216-234-1333, FAX: 216-234-3425

Chicago, IL... Michael J. Pak, CENTCOM, LTD., 540 Frontage Rd., Northfield, Ill. 60093. Telephone: 708-441-6383, FAX: 708-441-6382

Houston, TX... Michael J. Pak, CENTCOM, LTD. Telephone 708-441-6383

San Francisco, CA... Paul M. Butts, CENTCOM, LTD., Suite 808, 2672 Bayshore Frontage Road, Mountain View, CA 94043. Telephone: 415-969-4604, FAX: 415-969-2104

Los Angeles, CA... Paul M. Butts, CENTCOM, LTD. Telephone: 415-969-4604

Boston, MA... Edward M. Black, CENTCOM, LTD. Telephone: 203-226-7131

Atlanta, GA... CENTCOM, LTD. Telephone 216-234-1333

Denver, CO... Paul M. Butts, CENTCOM, LTD. Telephone: 415-969-4604

United Kingdom  
Reading, England... Malcolm Thiele, Technomedia Ltd., Wood Cottage, Shurlock Row, Reading RG10 0QE, Berkshire, England. Telephone: 0734-343302, Telex #848800, FAX: 0734-343848

Continental Europe... Andre Jamar, International Communications, Inc., Rue Mallar 1, 4800 Verviers, Belgium. Telephone: (087) 22-53-85, FAX: (087) 23-03-29

Tokyo, Japan... Sumio Oka, International Media Representatives Ltd., Room 100, 21 Bldg., 2-2-22 Okusawa, Setagaya-ku, Tokyo 158 Japan. Telephone: 502-0656, Telex #22633, FAX: 5706-7349

# Explore Landmark Organic Chemistry Achievements With the Chemists That Made Them Happen!

## Profiles, Pathways, and Dreams Autobiographies of Eminent Chemists

Jeffrey I. Seeman, Editor

This new multi-volume series is a virtual "Who's Who" of award-winning organic chemists, highlighting the history of organic chemistry through the eyes of some of its most noted researchers. The lifetime achievements of these acclaimed scientists are chronicled in their own words, along with fascinating photos depicting both their professional and private lives. Their autobiographies provide candid portrayals of themselves, their personal philosophies, and their contributions to the world of chemistry.

*Profiles, Pathways, and Dreams* not only examines the most important developments of the past 50 years, but also gives insight into the humanistic side of organic chemistry's most famous researchers. Readers interested in the history of organic chemistry will find these volumes highly entertaining.

**The Concept and Development of  
Solid-Phase Peptide Synthesis**

**Bruce Merrifield**  
Profiles, Pathways, and Dreams  
200 pages. (1991) Cloth.  
ISBN 0-8412-1842-0

\$24.95

**Enjoying Organic Chemistry 1927-1987**

**Egbert Havinga**  
Profiles, Pathways, and Dreams  
234 pages. (1990) Cloth.  
ISBN 0-8412-1774-2

\$24.95

**Explorations with Sugar:  
How Sweet It Was**

**Raymond U. Lemieux**  
Profiles, Pathways, and Dreams  
185 pages. (1990) Cloth.  
ISBN 0-8412-1777-7

\$24.95

**A Fifty-Year Love Affair with  
Organic Chemistry**

**William S. Johnson**  
Profiles, Pathways, and Dreams  
200 pages. (1991) Cloth.  
ISBN 0-8412-1834-X

\$24.95

**Fifty Years of Free Radicals**

**Cheves Walling**  
Profiles, Pathways, and Dreams  
200 pages. (1991) Cloth.  
ISBN 0-8412-1830-7

\$24.95

**Following the Trail of Light:  
A Scientific Odyssey**

**Melvin Calvin**  
Profiles, Pathways, and Dreams  
200 pages. (1991) Cloth.  
ISBN 0-8412-1828-5

\$24.95

**From Cologne to Chapel Hill**

**Ernest L. Eliel**  
Profiles, Pathways, and Dreams  
138 pages. (1990) Cloth.  
ISBN 0-8412-1767-X

\$24.95

**From Design to Discovery**

**Donald J. Cram**  
Profiles, Pathways, and Dreams  
146 pages. (1990) Cloth.  
ISBN 0-8412-1768-8

\$24.95

**From Small Organic Molecules to  
Large: A Century of Progress**

**Herman Mark**  
Profiles, Pathways, and Dreams  
234 pages. (1990) Cloth.  
ISBN 0-8412-1776-9

\$24.95

**From the Ivy League into the Honey Pot**

**Paul von Rague Schleyer**  
Profiles, Pathways, and Dreams  
200 pages. (1991) Cloth.  
ISBN 0-8412-1844-7

\$24.95

**A Lifetime of Synergy with Theory and  
Experiment**

**Andrew Streitwieser, Jr.**  
Profiles, Pathways, and Dreams  
200 pages. (1991) Cloth.  
ISBN 0-8412-1836-6

\$24.95

**Mechanisms, Novel Reactions, Synthetic  
Principles**

**Rolf Huisgen**  
Profiles, Pathways, and Dreams  
200 pages. (1991) Cloth.  
ISBN 0-8412-1832-3

\$24.95

**My 132 Semesters of Studies of  
Chemistry**

**Vladimir Prelog**  
Profiles, Pathways, and Dreams  
234 pages. (1990) Cloth.  
ISBN 0-8412-1772-6

\$24.95

**Organometallic Chemistry**

**F.G.A. Stone**  
Profiles, Pathways, and Dreams  
200 pages. (1991) Cloth.  
ISBN 0-8412-1826-9

\$24.95

**The Right Place at the Right Time**

**John Roberts**  
Profiles, Pathways, and Dreams  
299 pages. (1990) Cloth.  
ISBN 0-8412-1766-1

\$24.95

**A Semiempirical Life**

**Michael J.S. Dewar**  
Profiles, Pathways, and Dreams  
234 pages. (1990) Cloth.  
ISBN 0-8412-1771-8

\$24.95

**Seventy Years in Organic Chemistry**

**Tetsuo Nozoe**  
Profiles, Pathways, and Dreams  
234 pages. (1990) Cloth.  
ISBN 0-8412-1769-6

\$24.95

**Some Recollections of Gap Jumping**

**Derek H.R. Barton**  
Profiles, Pathways, and Dreams  
234 pages. (1990) Cloth.  
ISBN 0-8412-1770-X

\$24.95

**Steroids Made it Possible**

**Carl Djerassi**  
Profiles, Pathways, and Dreams  
234 pages. (1990) Cloth.  
ISBN 0-8412-1773-4

\$24.95

**To Catch the Interesting While  
Running**

**Teruaki Mukaiyama**  
200 pages. (1991) Cloth.  
ISBN 0-8412-1838-2

\$24.95

**To See the Obvious**

**Arthur J. Birch**  
Profiles, Pathways, and Dreams  
200 pages. (1991) Cloth.  
ISBN 0-8412-1840-4

\$24.95

**A Wandering Natural Products Chemist**

**Koji Nakanishi**  
Profiles, Pathways, and Dreams  
234 pages. (1990) Cloth.  
ISBN 0-8412-1775-0

\$24.95

Purchase these volumes individually, or enroll in the Profiles, Pathways, and Dreams standing order plan. With the standing order plan, you'll automatically receive each book as it becomes available, with a 15% discount off the list price of each title. Approved credit must be established prior to placing a standing order. Please call for availability of individual titles.

To order these and other ACS products, call TOLL FREE 1-800-227-5558. In Washington, DC call 202-872-4363. Or fax your order to 202-872-6067.

EDITOR: ROYCE W. MURRAY

ASSOCIATE EDITORS: Catherine C. Fenselau,  
Georges Guiochon, Walter C. Herlihy, Robert  
A. Osteryoung, Edward S. Yeung**Editorial Headquarters**1155 Sixteenth St., N.W.  
Washington, DC 20036  
Phone: 202-872-4570  
Telefax: 202-872-4574  
Bitnet: rmh96@cas

Managing Editor: Mary Warner

Senior Editor: Louise Voress

Associate Editor: Grace K. Lee

Assistant Editors: Jane K. Baker, Felicia Wach

Contributing Editor: Marcia Vogel

Director, Operational Support: C. Michael  
PhillippeHead, Production Department: Leroy L.  
Corcoran

Art Director: Alan Kahan

Composition Systems Administrator: Vincent L.  
Parker

Designers: Peggy Corrigan, Robert Sargent

Production Editors: John W. Laine, Elizabeth  
Wood

Circulation: David Schulbaum

Editorial Assistant, LabGuide: Joanne Mullican

Journals Dept., Columbus, Ohio

Associate Head: Marianne Brogan

Editorial Office Manager: Mary Scanlan

Journals Editing Managers: Kathleen E. Duffy,  
Joseph E. Yurvati

Associate Editor: Terri Bailey

Assistant Editor: Stephanie R. Harrell

Advisory Board: Michelle V. Buchanan,  
M. Bonner Denton, Bernard J. Bulkin, Renaat  
Gijbels, William S. Hancock, Timothy D. Harris,  
Thomas L. Isenhour, James W. Jorgenson,  
Philip D. LaFleur, Alan G. Marshall, John F.  
Rabolt, Debra R. Rolison, Shigeru Terabe, Mi-  
chael Thompson, George S. Wilson, Richard N.  
Zare

Ex Officio: Sam P. Perone

Instrumentation Advisory Panel: Daniel W.  
Armstrong, Anna Brajter-Toth, Thomas L.  
Chester, R. Graham Cooks, Jack D. Henion,  
Sanford P. Markey, Dallas L. Rabenstein, Bren-  
da R. Shaw, Gary W. SmallPublished by the  
AMERICAN CHEMICAL SOCIETY1155 16th Street, N.W.  
Washington, DC 20036**Publications Division**

Director: Robert H. Marks

Journals: Charles R. Bertsch

Special Publications: Randall E. Wedin

Manuscript requirements are published in the  
January 1, 1991 issue, page 89. Manuscripts  
for publication (4 copies) should be submitted  
to ANALYTICAL CHEMISTRY at the ACS Washing-  
ton address.The American Chemical Society and its editors  
assume no responsibility for the statements  
and opinions advanced by contributors. Views  
expressed in the editorials are those of the  
editors and do not necessarily represent the  
official position of the American Chemical  
Society.

- Alonso, J., 2532  
Anker, L. S., 2435  
Austin, G. D., 2460
- Ball, J. W., 2435  
Bard, A. J., 2442, 2544  
Bartels, K., 2442  
Barthel, H., 2466  
Bartroli, J., 2532  
Benninghoven, A., 2466  
Berthod, A., 2508  
Bosch-Reig, F., 2424  
Bovik, A. C., 2442  
Brinkman, U. A. T., 2481  
Bully, M., 2508
- Campins-Falcó, P., 2424  
Capar, S. G., 2539  
Carnahan, J. W., 2430  
Carroll, J. A., 2526  
Cheng, J.-K., 2529  
Choppin, G. R., 2542  
Christian, G. D., 2407  
Clifford, R. H., 2539  
Cooks, R. G., 2460  
Cuppen, W. J. G. M., 2481
- de Jong, G. J., 2481  
Dewald, H. D., 2535  
Dolan, S. P., 2539
- Edmonds, C. G., 2488  
Elder, R. C., 2535  
Escalada, M., 2532
- Farjam, A., 2481  
Farnsworth, A. P. H., 2470
- Gard, E., 2526  
Gehlhausen, J. M., 2430  
Gübeli, T., 2407
- Hagenhoff, B., 2466  
Hamann, P. R., 2470  
Hayward, M. J., 2460  
Heineman, W. R., 2535  
Herráez-Hernández, R., 2424  
Hillenkamp, F., 2470  
Hinman, L., 2470  
Hinze, W. L., 2520  
Hollander, I. J., 2470  
Hoogvliet, J. C., 2418
- Igo, D. H., 2535  
Ingendoh, A., 2470
- James, J. P., 2470
- Jimenez Jorquera, C., 2532  
Jones, A. D., 2526  
Jurs, P. C., 2435
- Karas, M., 2470  
Kenndler, E., 2499  
Khaledi, M. G., 2503  
King, D. J., 2470  
Kotiaho, T., 2460
- Lebrilla, C. B., 2526  
Lee, C., 2442  
Lis, S., 2542  
Loo, J. A., 2488
- McCullough, S., 2526  
Miller, C. J., 2544  
Molins-Legua, C., 2424  
Montaser, A., 2539
- Nevin, W. A., 2414  
Ngoka, L., 2526
- Pang, H.-m., 2402  
Phipps, A., 2470
- Reijn, J. M., 2418  
Ruzicka, J., 2407
- Saitoh, T., 2520  
Schirmmelmann, A., 2456  
Schwer, C., 2499  
Sevillano-Cabeza, A., 2424  
Siegel, M. M., 2470  
Sinex, S. A., 2539  
Smith, B. J., 2470  
Smith, R. D., 2488  
Strasters, J. K., 2503  
Syu, M. J., 2460
- Thompson, P. M., 2447  
Tsai, G.-J., 2460  
Tsao, G. T., 2460
- van Bennekom, W. P., 2418  
Vanslyke, S. J., 2512  
Vreuls, J. J., 2481
- Wentzell, P. D., 2512  
Wipf, D. O., 2442
- Xu, X.-J., 2529
- Yeung, E. S., 2402
- Zhang, C.-Y., 2529  
Zhang, H.-S., 2529  
Zoller, W., 2466



# Monitoring of Formation Rates of Thin Films in Laser-Induced Chemical Vapor Deposition

Ho-ming Pang and Edward S. Yeung\*

Ames Laboratory-USDOE and Department of Chemistry, Iowa State University, Ames, Iowa 50011

**Acoustic analysis for in situ laser-induced chemical vapor thin-film deposition is described. It shows that the transient acoustic signal due to the density change from the photodissociation process can be used to monitor the deposition rate. The acoustic signal is compared with transmittance, reflectance, and quartz crystal microbalance measurements. The observed deposition rate at the initial moment of film formation is also examined by photoacoustic measurements. The contributions from surface absorption and surface-induced dissociation can thus be assessed independently.**

## INTRODUCTION

UV laser-induced photodissociation (1-3) has received wide attention for thin-film deposition because of its unique features such as low-temperature photochemical processes and localized deposition for microelectronic fabrication. Much attention is concentrated on the study of photodissociation mechanisms in the gas phase and for surface-related decomposition (4, 5). The deposition rate is one of the critical parameters for elucidating the mechanisms of laser-induced chemical vapor deposition. Several techniques have been used frequently for determining the deposition rate in situ. Quartz-crystal microbalance (QCM) (6, 7) is a sensitive method for determining the absolute mass deposited. However, applications of this method have been limited to available coated electrode surfaces and to samples with relatively large surface areas. Also, QCM has to be built right on the surface of interest. Optical methods provide independent, noncontact real-time measurement of deposition rates. Among optical methods are reflectance (8), transmittance (9), and profilometry (10). Reflectance measurements produce complicated responses because the technique depends on interference patterns which in turn depend on the refractive index of the film. Transmittance measurements can only be applied to transparent substrates and to films with limited thickness. It also requires extensive calibration for absolute deposition rate determination because of unknown absorption coefficients. Real-time profilometry is restricted to a minimum film thickness on the order of a few micrometers, which makes it difficult for studying thin-film formation at the initial stages.

We report here a noncontact transient acoustic technique for the in situ measurement of relative laser-induced chemical vapor deposition rates. It has been demonstrated earlier that the acoustic signal generated from the photodissociation process in the gas phase is directly proportional to the total molar number of fragments produced (11). This acoustic signal is derived mainly from the density wave instead of the thermal wave (12). Therefore, one should also be able to use this acoustic signal to study the phenomenon related to photodissociation processes on the surface and the corresponding thin-film deposition. The acoustic signal will be compared with other in situ deposition rate measurement methods including transmittance, reflectance, and QCM. Moreover, photoacoustic (photothermal) measurements on the surface will be performed in order to understand the

mechanism at the initial moment of film formation, since these measurements reflect the surface absorption characteristics (13).

## EXPERIMENTAL SECTION

The basic experimental arrangement is shown schematically in Figure 1. An excimer laser (Lumonics, Model HyperEx-460) operated at the 308-nm XeCl transition with a 25-ns pulse duration and 4-Hz repetition rate was used to photodissociate the reagent gas for thin-film deposition. An amplitude stability of 5% (peak to peak) from this laser output was observed. A 50-mm focal length quartz lens was used to focus the excimer laser beam into a  $2 \times 3$  mm spot with the focal point located behind the substrate surface. Typical laser energies used were varied between 5 and 17 mJ/pulse and controlled by suitable combinations of attenuation neutral density filters and high-voltage settings of the excimer laser. About 5% of the excimer laser energy was reflected by a quartz flat and directed onto an energy meter (Moletron J3-09) for monitoring. No damage on the irradiated substrate surface was observed at these laser energy levels when buffer gas only was used.

The substrates studied include quartz plate, molybdenum plate, or quartz crystal coated with gold. The surface was mounted normal to the incident laser beam inside a Pyrex gas cell which contained quartz windows for coupling the laser beams. The gas cell pressure was monitored by a pressure gauge (MKS Baratron 221A HS-F-100). The gas cell was initially evacuated with a two-stage mechanical pump. Then, He was introduced near the laser beam entrance and exit windows, so that the inner faces of the windows were purged continuously throughout the entire experiment in order to minimize deposition on the window surface. Also, He was used as the buffer gas to facilitate acoustic measurements. The pressure in the gas cell was kept at  $\sim 50$  Torr. The excimer laser was then allowed to fire several hundred times in order to preclean the substrate surface. Then, the substrate surface facing the excimer laser beam was continuously purged with saturated carbonyl vapor. This carbonyl vapor was produced by passing a small amount of He over the solid carbonyl sample in the sample reservoir at room temperature. The carbonyl sample ( $\text{Cr}(\text{CO})_6$  or  $\text{Mo}(\text{CO})_6$ ) was obtained directly from Aldrich and used without any further purification. By this arrangement, the final pressure inside the gas cell was maintained at  $\sim 53$  torr. The actual partial pressure of the reagent on the reaction surface was not determined. In this arrangement, contamination from oxygen in the air due to the use of a relatively primitive vacuum system is minimized because the reaction surface was continuously purged with reagent vapor. Upon UV irradiation, a green and blue luminescence could be clearly seen along the excimer laser beam path from the dissociation of  $\text{Cr}(\text{CO})_6$  and  $\text{Mo}(\text{CO})_6$ , respectively. This is a result of emission from the excited-state chromium atoms formed via gas-phase photodissociation (11).

For QCM measurement, an AT cut, 13 mm in diameter, 6-MHz quartz crystal with gold-coated electrodes (Maxtek) was employed and the gold surface served as the substrate surface. The QCM crystal was driven at its fundamental frequency by a crystal-controlled oscillator. A photon counter (EG&G ORTEC, model 9315) operated as a frequency counter was used to measure the frequency of the QCM.

For transmittance and reflectance measurements, a quartz plate was used as the substrate and was mounted at the Brewster's angle relative to the p-polarized incident light from a linearly polarized HeNe laser (Uniphase, Model 1105P, 8 mW). This laser was aligned through the center of the UV laser beam at the irradiated

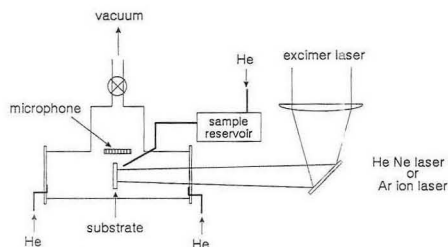


**Figure 1.** Experimental setup for laser-induced chemical vapor deposition with simultaneous transient acoustic, photoacoustic, transmittance, and reflectance monitoring.

surface. The HeNe laser beam was focused to produce a spot slightly smaller than the reaction surface. By this arrangement, natural reflection by the bare quartz surface was nearly completely eliminated. This should enhance the sensitivity of the reflectance signal especially at the very early stage of film formation. The low-power HeNe laser did not participate in the photodissociation process. The transmitted HeNe light intensity was monitored by a photodiode. The reflected light from the deposited surface was collected and detected by a photomultiplier tube. Both signal outputs were recorded with digital multimeters.

For measurement of the transient acoustic signal generated from photo-dissociation on a single pulse basis, an electret microphone (Knowles, BT-1759) was mounted inside the gas cell above the substrate at a distance  $\sim 8$  mm away from the laser irradiation spot. The microphone was powered by a 6-V battery. Output from the microphone was measured by a waveform analyzer (Data Precision, Model D6000 with Model 630 vertical amplifier and D1000 dual-channel preamplifier). Each data point was the result of averaging over 20 laser pulses in order to minimize the effects of laser power fluctuations and to match the integration times from the other probes. Deposits on the microphone from the gas-phase photodissociation process were minimal even after over tens of thousands of laser pulses.

A cw Ar ion laser (Uniphase Corp, Model 2013) was used to produce a photoacoustic signal so that absorption by the film can be monitored. The laser power was  $\sim 15$  mW before entering the cell. At this power density, no photodissociation or film deposition caused by the Ar ion laser was observed. The Ar ion laser beam was slightly defocused in order to cover the entire film deposition region. The beam also was chopped with a mechanical chopper at a frequency of 341 Hz. The photoacoustic signal was detected by the same microphone used for transient acoustic measurements. The signal output from the microphone was demodulated through a lock-in amplifier (EG&G PARC, Model 5209) with preamplification by an oscilloscope (Tektronix 7904 with differential amplifier 7A22).

Except for the measurement of the transient acoustic signal generated from the laser photodissociation process, all other measurements were performed when the excimer laser was not fired, i.e. between laser pulses.

## RESULTS AND DISCUSSION

**Film Morphology.** In the case of thin-film deposition on a quartz substrate from  $\text{Cr}(\text{CO})_6$ , the use of different laser power density for deposition substantially affected the quality and the composition of the film. When the laser energy was lower than 7 mJ/pulse, only brown, powdery deposits were observed. These deposits can be peeled off by a Q-tip or Scotch tape. However, when the UV laser energy increased, a greenish deposit was formed at the center, surrounded by the brown powder. As the laser energy increased into a level before laser ablation occurred ( $\sim 20$  mJ), the greenish deposit covered most of the reaction surface and the amount of brown powder was reduced but not totally eliminated. This green film cannot be peeled off by Q-tip or Scotch tape. The film formation may be explained by the fact that multiphoton absorption was required to completely dissociate the carbonyl.

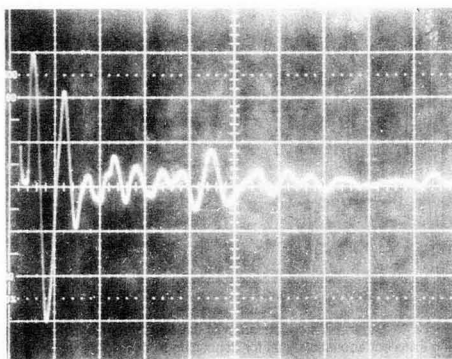


**Figure 2.** Waveform analyzer screen display of transient acoustic signal obtained from a single laser pulse at 15 mJ with  $\text{Cr}(\text{CO})_6$  as the reactant (50  $\mu\text{s}/\text{div}$ , 20 mV/div).

Multiphoton dissociation efficiency depends critically on laser energy. At low laser energy, dissociation occurs mainly in the gas phase in a stepwise fashion, producing only chromium atoms and causing the brown powdery deposit (11). Since the UV laser beam was not uniform, the center part, which had the highest intensity, will eventually produce multiphoton dissociation to form a green film. The outer edge of the beam, which had a lower intensity, will continue to produce a powdery deposit. Although no detailed determination of its composition was performed, the green film can be attributed to  $\text{Cr}_2\text{O}_3$  due to its color. The formation of  $\text{Cr}_2\text{O}_3$  instead of Cr metal film is due to the fact that the surface and the previously deposited photofragments stabilize the partially photolyzed carbonyls, preventing the removal of all the CO ligands from the adsorbed species (4). Our observations parallel those observed for cw 257-nm radiation (4). The low level of oxygen present in the buffer gas can be another reason for oxide formation. When a gold-coated quartz plate was used as the substrate at relatively low laser energy (5–10 mJ), a green film was also formed. As the laser energy increased ( $>15$  mJ), a black electrically conductive film was formed. That is surrounded by a small greenish zone. The black film is characteristic of further pyrolysis and annealing of the oxide film (4). This result indicates that different surface materials used as substrates will also substantially affect the composition of the film.

On the other hand, when  $\text{Mo}(\text{CO})_6$  was used as the reagent gas, quartz plate, gold surface and molybdenum plate all showed similar deposited films. At low laser energy, a non-adhesive black powdery film was formed. When the laser energy increased, a black film was formed with high electrical conductivity. This film cannot be peeled off by Q-tips or Scotch tape. The major composition appeared to be molybdenum. Under microscopic examination, very fine particles ( $<5 \mu\text{m}$ ) were revealed. These had a different morphology from molybdenum metal originally present on the molybdenum plate used as the substrate. This indicated that even when the substrate contained the same atomic composition as the deposited film, the morphology can still be different between the substrate and the film.

**Transient Acoustic Signal.** Figure 2 shows a typical acoustic signal that accompanies photodissociation by a single laser pulse. The height of the first peak in the acoustic waveform was used throughout the entire investigation. The subsequent peaks in this waveform were due to reflections within the nonresonant cell and photoacoustic (photothermal) response. Three processes contributed to this acoustic

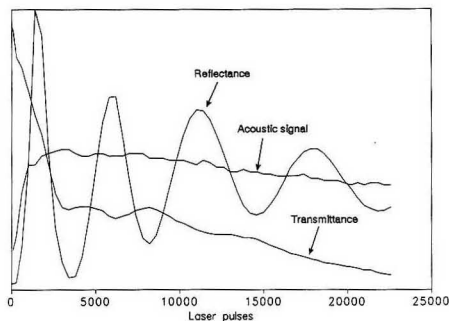


**Figure 3.** Laser pulse dependence of the transmittance, reflectance, and transient acoustic signal for deposition from  $\text{Cr}(\text{CO})_6$  dissociation at a laser energy of 15 mJ/pulse.

waveform. The background acoustic signal due to the absorption of the UV light from the windows, substrate, and the buffer gas was minimal, with contributions no more than 2% of the total acoustic signal. The second process was due to the gas-phase hexacarbonyl photodissociation (11), which contributed to most of the acoustic signal at the initial moment of the experiment. If the carbonyl was totally dissociated through a multiphoton absorption process, seven molar fragments will be produced from each mole of parent hexacarbonyl. Thus, a relatively large acoustic pulse was produced from this transient pressure or density change. Deposition of incompletely dissociated species still involves the release of varying numbers of moles of CO into the gas phase. This acoustic signal derived from gas-phase photodissociation was constant as long as the laser power and gas pressure remained constant. The major contribution to the acoustic signal after the film began to grow was due to surface-induced photodissociation and pyrolysis dissociation. This phenomenon will be discussed later.

**Reflectance.** Figure 3 shows a typical simultaneous measurement of acoustic signal, transmittance, and reflectance as a function of the number of laser pulses for  $\text{Cr}(\text{CO})_6$  vapor deposition. From the reflectance curve, one can estimate the thickness of the film, since the interference effects depend on the thickness of the film. Roughly, each fringe corresponds to about one-quarter of the probe beam wavelength; therefore, at the end of the experiment, a film with a thickness of  $\sim 1.3 \mu\text{m}$  was formed. The thickness obtained here was much more than the one obtained in static conditions (14) under similar laser energy irradiation and is expected since the reagent is constantly replenished at the surface. On average, the deposition rate was about 0.6 Å/pulse. However due to the low-resolution characteristics of reflectance measurement (i.e., one can only use the maximum or minimum of the fringe to calculate the thickness of the film), no details of the real time deposition rate can be obtained. It is important to note that the initial rapid increase in reflectivity indicates a change in refractive index (altering Brewster's angle) rather than a high deposition rate.

**Transmittance.** In order to compare the results from the transmittance and acoustic measurements, the deposition rate, as evaluated from the slope of the transmittance curve as a function of laser pulses, was plotted in Figure 4 superimposed with the acoustic signal. It shows that the acoustic signal is directly proportional to the deposition rate that was obtained from the transmittance measurement. A rapid increase in deposition rate was observed over the first few hundred laser pulses followed by a relatively stable deposition rate. This increase could be explained by the nucleation effect, which can accelerate the deposition rate. The quartz was initially

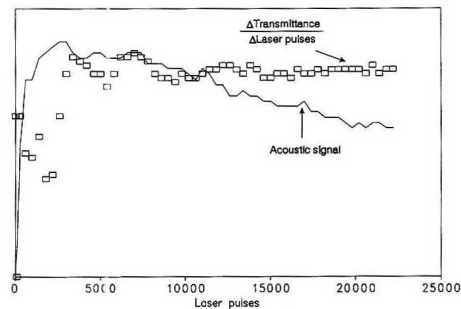


**Figure 4.** Relative deposition rate from  $\text{Cr}(\text{CO})_6$  dissociation as a function of laser pulse (15 mJ/pulse) obtained from the transmittance measurement superimposed with the transient acoustic signal.

transparent to UV light, so gas-phase photolysis deposition is the main mechanism for film formation early on. However, after the surface was preseeded by the deposited material, this nucleation region will absorb the UV light more strongly to accelerate the photolysis. The heating efficiency will continuously increase; therefore, the deposition rate is enhanced. The pyrolytic deposition process will eventually become a dominant mechanism for dissociation because of the strong UV absorption from the film. Until the irradiated surface was covered entirely by the deposit to take on its bulk absorption property, the change in acoustic signal that we observed during the deposition process reflects a changing dissociation rate. This thickness to form a film with characteristics of the bulk material can be estimated from Figure 2 through the reflectance measurement, since the first interference fringe coincided with the transition region of the acoustic profile. This thickness was about 160 nm. In addition, the nucleation process may "catalyze" the deposition process, since the reactant may react much faster on a roughened surface or on surfaces with different chemical compositions. The acoustic signal as the function of laser pulse number certainly reflected this nucleation process. At the initial region, the acoustic signal stayed relatively constant for the first few tens of laser pulses. This region corresponded to the preseeding process. Then the acoustic signal increased substantially due to nucleation and reached its maximum as the nucleation process is completed. Finally, further acoustic signal change was caused by varying surface morphology. Naturally, the buffer gas pressure and the flow rate of the reagent gas will affect the deposition rate (3, 9). We independently confirmed that throughout the many laser pulses in these experiments the acoustic waveform and acoustic profile were constant.

Light transmittance measurement is a useful probe for in situ studies of thin-film deposition rate and thickness determination. However, it cannot be used on nontransparent substrates or for monitoring very thick films. In addition, since the transmittance is strongly affected by the film morphology, density, and purity, accurate calculation of the film thickness may not be possible. On the other hand, the use of transient acoustic signal provides a simple way to monitor the relative deposition rate on any substrate surface, since it directly monitors the surface-induced photodissociation process via the extra number of moles of gas-phase products formed. There is also a substantial difference in sensitivity. An acoustic signal can be obtained on every laser pulse, while transmittance changes are not detectable until after many tens of laser pulses. Finally, we note that in Figure 3 there is a subtle modulation in the transmittance plot which mimics the reflectance plot but in opposite directions. This depicts the effect of interference of light as the thickness changes. The

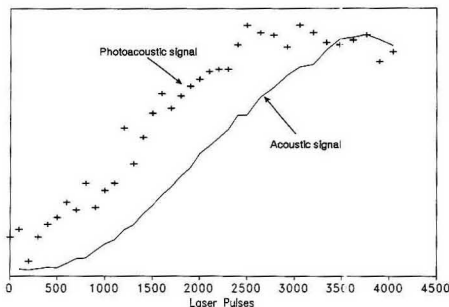


**Figure 5.** Transient acoustic and photoacoustic analysis as a function of laser pulse for deposition from  $\text{Mo}(\text{CO})_6$  dissociation on a quartz surface with a laser energy of 16 mJ/pulse.

determination of film thickness is thus not straightforward.

It should be noticed that when a molybdenum plate was used as the substrate for  $\text{Mo}(\text{CO})_6$  dissociation, a similar acoustic profile (as the function of the laser pulses) was observed. One may expect that the acoustic signal should remain relatively stable since the substrate has a similar composition as the film; i.e. no nucleation process is required. However, when the films with different thicknesses obtained by varying the laser exposure times were examined under the microscope, different morphology of the films compared to the bulk substrate was observed. A much finer grain structure was observed on the film surface. Therefore, the UV absorption efficiency and surface area would still be different between the bulk substrate and the film. In addition, the film may contain some impurities such as C or O (4), which will also affect the laser absorption efficiency. As a result, the nucleation process discussed above still plays a part and affects the deposition rate.

**Photoacoustic Signal.** In order to study the mechanism of the deposition at the initial stages of film formation in more detail, photoacoustic measurement was performed and compared with the transient acoustic measurement. Since the photoacoustic signal was formed by transferring the absorbed energy from the thin film toward the buffer gas through heating, it should be sensitive to the absorption characteristics of the sample surface. Figure 5 shows the photoacoustic signal as a function of the number of laser pulses with simultaneous measurement of the transient acoustic signal. Both traces have similar profiles but do not completely match. In particular, the two signals reached steady-state levels after different numbers of laser pulses. The similarity indicated that the change in deposition rate observed in the transient acoustic measurement was mainly due to an increase in the absorption of UV light by the surface. A large absorption would result in a higher rate of photolysis and pyrolysis. As a result, more gas-phase fragments were produced so that an increase in the acoustic signal was observed.

We found that photoacoustic signal was very sensitive to the surface morphology; i.e. each film may have slightly different surface properties. In addition, the photoacoustic signal is a direct result of heating of the gas above the surface. It not only depends on the absorption property of the film but also depends on a number of other factors such as the heat-transfer efficiency from the surface to the gas phase and heat conduction to the bulk solid. On the other hand, photodissociation depends on light intensity and temperature of the gas (homogeneous dissociation), as well as temperature, morphology, and composition of the surface (heterogeneous dissociation). This explains why the two plots in Figure 5 do not exactly match each other. One may argue that adsorption

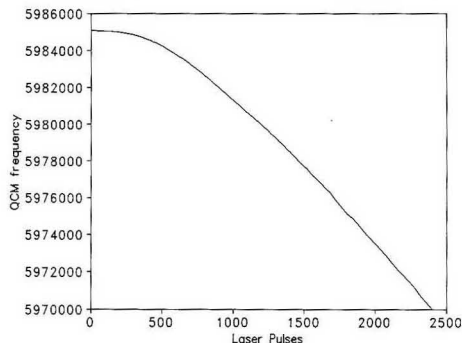


**Figure 6.** QCM frequency as a function of laser pulse for deposition from  $\text{Mo}(\text{CO})_6$  dissociation on gold surface at a laser energy of 12 mJ/pulse.

of hexacarbonyls is enhanced on the deposited film compared to the bare substrate; as a result, more reactants will be available for UV dissociation as the film grows. However, it has been observed from QCM measurements (6, 7) that  $\text{Cr}(\text{CO})_6$  and  $\text{W}(\text{CO})_6$  did not adsorb on either gold or freshly deposited metal films. This rules out the possibility that the deposition rate changes as a result of the adsorption of carbonyls on the surface.

One interesting result was observed for measurements performed on a gold surface. No significant photoacoustic signal change was detected even when the acoustic signal increased, which, as confirmed from the QCM measurement, indicates that the deposition rate has indeed changed. This result is due to efficient heat transfer from the film to the gold surface. Therefore, the absorbed energy was spread over a large area on the gold surface, and heat transfer per unit area to the buffer gas was decreased substantially.

**QCM Measurement.** Figure 6 shows a typical QCM frequency change measurement during the laser-assisted deposition process involving  $\text{Mo}(\text{CO})_6$ . In the absence of carbonyl vapor, the QCM frequency was stable even when the UV laser directly irradiates the electrode surface. This is because at low laser repetition rate, the average temperature change is too small to affect the QCM frequency. Unlike the experiment done with a cw UV laser (6), a nonlinear relationship instead of a linear relationship between the QCM frequency change and the total laser power was obtained. Since the frequency change of the QCM is directly proportional to the mass change on the quartz crystal gold surface, i.e. the amount of material deposited, one can estimate that  $\sim 0.3 \mu\text{g}$  of material is deposited on the QCM after  $\sim 2400$  laser pulses. In order to compare with photodissociation acoustic measurement, the deposition rate (frequency change/pulse) from the QCM measurement was plotted in Figure 7 superimposed with the corresponding acoustic signal. Very good agreement was observed. Again, this indicated that the transient acoustic measurement offers a simple method for monitoring the deposition rate.

However, with the use of  $\text{Cr}(\text{CO})_6$  as the reagent, a slightly different relationship between the deposition rate change obtained from QCM and acoustic signal was observed. This is shown in Figure 8. A steady increase of deposition rate was obtained from QCM measurement but a relatively stable acoustic signal was observed in the first few hundred laser pulses. This gap became larger when lower laser energy was used. The exact reason for this deviation is not certain. This may be due to the fact that the deposition of Cr involves different species (e.g. oxides) at early times. This is supported by the observation that a greenish transparent film was formed

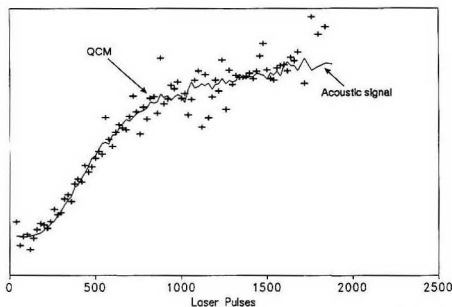


Figure 7. Relative deposition rate for deposition from  $\text{Mo}(\text{CO})_6$  dissociation obtained from QCM and transient acoustic measurements.

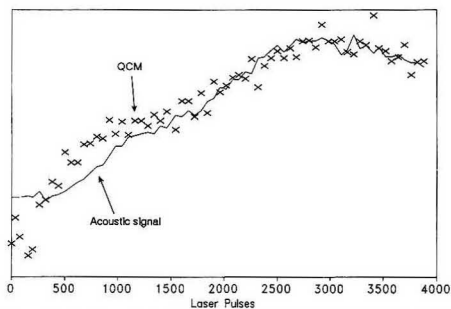


Figure 8. Relative deposition rate for deposition from  $\text{Cr}(\text{CO})_6$  dissociation obtained from QCM and transient acoustic measurements.

first at low laser energy. Reaction stoichiometry affects the acoustic signal much more than the QCM signal. This long latent time has also been observed for  $\text{Cr}(\text{CO})_6$  (5) and  $\text{Cd}(\text{CH}_3)_2$  (15) deposition. QCM provides a reliable means for in situ deposition rate measurement. However, the use of QCM is limited because only certain surfaces can be used and the electrode must be built right onto the surface. The acoustic signal can provide similar information on the relative deposition rate change without the limitation of the substrates. The acoustic signal is also more sensitive so that single-pulse measurements (Figure 2) are feasible. This is in contrast with

QCM measurements (Figures 6 and 7) where even with tens of laser pulses there is still substantial scatter in the data points.

## CONCLUSION

Acoustic monitoring is demonstrated for studying in situ laser-induced chemical vapor thin-film deposition rate. The signal is proportional to the number of moles of gaseous products formed. No specific property for the substrate is required. The transient acoustic signal provides a measure of the extent of dissociation and deposition. Good agreement for the deposition rate measurement in comparison with photoacoustic analysis, reflectance, transmittance, or QCM is observed. The acoustic signal however is much more sensitive, allowing single-pulse measurements to be made. A rapid increase of the deposition rate at the early stage of film formation due to the nucleation process is observed. As the film builds up to manifest bulk property, the deposition rate stabilizes. One can thus distinguish between gas-phase (homogeneous) events (11) and surface-induced heterogeneous events.

## LITERATURE CITED

- (1) Herman, I. P. *Chem. Rev.* **1989**, *89*, 1323-1357.
- (2) Ehrlich, D. J.; Osgood, R. M., Jr.; Deutsch, T. F. *J. Electrochem. Soc.* **1981**, *128*, 2039-2041.
- (3) Ehrlich, D. J.; Osgood, R. M., Jr.; Deutsch, T. F. *J. Vac. Sci. Technol.* **1982**, *21*, 23-32.
- (4) Gluck, N. S.; Wolga, G. J.; Bartosch, C. E.; Ho, W.; Ying, Z. *J. Appl. Phys.* **1987**, *61*, 998-1005.
- (5) Konstantinov, L.; Nowak, R.; Hess, P. *Appl. Phys. A* **1988**, *47*, 171-181.
- (6) Jackson, R. L.; Tyndall, G. W. *J. Appl. Phys.* **1987**, *62*, 315-317.
- (7) Mayer, T. M.; Fisanick, G. J.; Eichelberger, T. S., IV. *J. Appl. Phys.* **1982**, *53*, 8462-8469.
- (8) Dance, V.; Osgood, R. M.; Ehrlich, D. *J. Opt. Lett.* **1981**, *6*, 563-565.
- (9) Braishotte, D.; van den Bergh, H. *Appl. Phys. A* **1988**, *45*, 337-343.
- (10) Comita, P. B.; Kodas, T. T. *J. Appl. Phys.* **1987**, *62*, 2280-2285.
- (11) Cheung, N.; Yeung, E. S. *Chem. Phys. Lett.*, in press.
- (12) Chen, G.; Yeung, E. S. *Anal. Chem.* **1988**, *60*, 2258-2263.
- (13) Zharov, V. P.; Letokhov, V. S. *Laser Photoacoustic Spectroscopy*; Springer series in Optical Sciences; Springer-Verlag: Berlin Heidelberg, 1986; Vol. 37.
- (14) Flynn, D. K.; Steinfeld, J. I. *J. Appl. Phys.* **1986**, *59*, 3914-3917.
- (15) Rytz-Froidevaux, Y.; Salathé, R. P.; Gilgen, H. H.; Weber, H. P. *Appl. Phys. A* **1982**, *27*, 133-138.

RECEIVED for review April 12, 1991. Accepted July 25, 1991. The Ames Laboratory is operated by Iowa State University for the U.S. Department of Energy under Contract W-7405-Eng-82. This work was supported by the Director of Energy Research, Office of Basic Energy Sciences, Division of Chemical Sciences.



# Fundamentals of Sinusoidal Flow Sequential Injection Spectrophotometry

Thomas Gübeli<sup>1</sup>

Alitea U.S.A., P.O. Box 26, Medina, Washington 98039

Gary D. Christian and Jaromir Ruzicka\*

Department of Chemistry, BG-10, University of Washington, Seattle, Washington 98195

**A rational design of the sequential injection analyzer is based on description of the mutual penetration of sample and reagent zones, which are sequentially stacked into a tubular conduit and then injected into a reactor and transported toward the detector by means of a carrier stream, flowing at a preprogrammed rate. Variables governing zone penetration have been identified by a series of dispersion experiments, for sequential injection of two and three zones, thus outlining the conditions for performing single- and double-reagent-based assays. A parallel is drawn between conventional flow injection and corresponding sequential injection colorimetric determinations of chloride and phosphate, with the aim of suggesting guidelines for the development of spectrophotometric- and fluorescence-based sequential injection methods.**

## INTRODUCTION

A need exists for simplification of the system design of flow injection analyzers for their application in process control. Robustness, reliability, long-term stability, and low frequency of maintenance of process analyzers is required. While manual reconfiguration of the flow channel, high reagent consumption due to continuous flow operation, frequent servicing of peristaltic pumps and frequent recalibration of the system is acceptable in laboratory applications, these are prohibitive in terms of cost and manpower in a process environment. By conceptualizing a novel system, comprising only a single piston pump, single valve and single channel, the sequential injection (SI) technique has been conceived (1). Its principle is, along with sinusoidal flow drive (2), discussed below, since it is believed that this technique will find a wide application by replacing conventional flow injection in both process control as well as in laboratory applications.

While in conventional flow injection (3) the sample zone is injected into a flowing carrier stream and auxiliary reagents are merged with it on the way to the detector, sequential injection is based on a different approach (Figure 1, top). Using a selector (rather than injection) valve, a wash solution, sample zone, and reagent zone(s) are sequentially injected into a channel. In this way a stack of well-defined zones is obtained (Figure 1, bottom), which is then injected through a reactor into a detector. The flow reversal as a result of the injection step creates a composite zone in which sample and reagent zone penetrate each other due to combined axial and radial dispersion. For a kinetic based assay, a selected section of the mutually interdispersed reagent and sample zone may be arrested within the observation field of the detector by stopping the flow. The reaction rate during the stopped flow period can be monitored, and the changing signal reflects the rate of the chemical reaction (1, 4). The benefit of the stopped

flow technique is that it extends the reaction time, saves reagents, and eliminates interferences due to background signals and lag phases.

The measuring cycle of the SI technique (Figure 1) comprises the following operations: (1) aspiration of carrier/wash solution with the selector valve in position 1, while the piston makes a large reverse step, (2) aspiration of sample solution with the selector valve in position 3, while the piston makes a small reverse step, (3) aspiration of reagent solution with the valve in position 4, using a small piston reverse step, (4) a forward piston move with the valve in position 5, with the stroke length adjusted such that preselected section of the interdispersed sample/reagent zone is injected through the reactor into the detector, (5) a stopped flow period of reaction rate monitoring, and (6) forward large piston stroke, which expels all sample and reagent as well as the majority of the carrier/wash solutions from the valve and from the flow channel. When the chemical reaction is fast and when peak height is measured rather than reaction rates, step 5 is omitted. If two reagents are used, the optional port 2 and an appropriate flow programming is used to introduce the second reagent.

It follows from the foregoing that zone sequencing and the mutual dispersion of the zones are the key operations. These have to be carried out in such a manner that a desired degree of penetration of sample and reagent zones will be achieved, within an adequate resident time, while yielding a satisfactory sampling frequency. In analogy with conventional FIA (3), the dispersion of the sample zone has to be adjusted to suit the requirement of the intended measurement. Thus, for pH or conductivity measurement, limited dispersion ( $D \rightarrow 1$ ) is required. For reagent-based chemistries such as colorimetry, fluorescence, or chemiluminescence, sample and reagent zones must mix in a suitable proportion and therefore a medium dispersion ( $D = 2-10$ ) has to be achieved. And for extensive sample dilution a large dispersion ( $D > 10$ ) may be necessary. The dispersion coefficient  $D_p$  has been defined as the ratio of the concentration of the sample material before ( $C_s^0$ ) and after ( $C_s$ ) the dispersion process has taken place,  $C_s$  being the concentration in that element of fluid from which the readout is being taken, i.e.,  $D_p = C_s^0/C_s$ . Similarly, reagent dispersion  $D_r$  has been defined so that  $D_r = C_r^0/C_r$ . These simple relations allow estimation of the concentrations of reacting components in the relevant element of the dispersed sample zone. It is the purpose of this work to provide guidelines for optimization of assay conditions by identifying essential parameters which govern penetration of the sequentially injected zones.

## THEORY

**Zone Overlap.** Zone overlap is the key parameter, the control of which is essential to a successful execution of sequential injection. It follows from the foregoing that, for reagent-based chemistries, a region of mutually interdispersed sample and reagent zones must be identified, within which

<sup>1</sup>Present address: Ivers Lee AG, Kirchbergstrasse 160, 3400 Burgdorf, Switzerland.

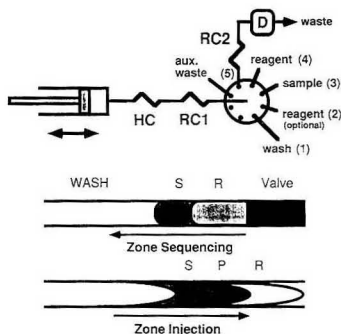


**Figure 1.** Sequential injection system (top) and the structures of sequenced and injected zones (bottom). HC is the holding coil, R1 and R2 are reactor coils, and D is the detector. S, P, and R are the sample, product, and reagent zones. Note that flow reversal occurs during zone injection.

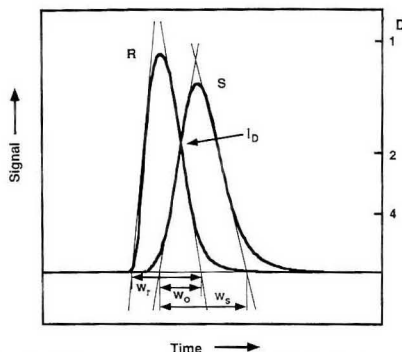


**Figure 2.** Description of zone penetration. S is the "sample" zone, R is the "reagent" zone,  $I_D$  is the isodispersion point, and  $W_r$ ,  $W_o$ , and  $W_s$  are the respective widths of the reagent, overlap, and sample zones. Note that the recording (identical with Figure 6B) shows reagent zone first, since this zone has been stacked closest to the valve (Figure 1, bottom) and, due to the flow reversal, reaches the detector first. Also, the sample zone is more dispersed than the reagent zone for the same reason, and also because it travels through a longer distance than the reagent zone.

$D_s$  is larger than 2, and where at the same time sufficient excess of the reagent is present. For single reagent chemistries, merging of sample and reagent zones (Figure 1) is sufficient; two reagent chemistries will require merging of three sequentially stacked zones, etc. Obviously, a parameter describing the degree of mutual zone penetration has to be established in order to identify the time interval within which a meaningful readout, such as peak height or peak area, can be obtained.

In formal analogy with the definition of resolution as used in chromatography, the concept of zone penetration is introduced here (Figure 2). By defining

$$P = 2W_o/(W_s + W_r) \quad (1)$$

a complete zone overlap is obtained for  $P = 1$ , zero zone overlap would be at  $P = 0$ , and partial zone overlaps will attain values between these two extremes. Further refinements of this definition are discussed later in this work.

Further, it should be noted that in the absence of complete zone overlap, an isodispersion point  $I_D$  is observed where the dispersions of the sample and reagent are identical. This

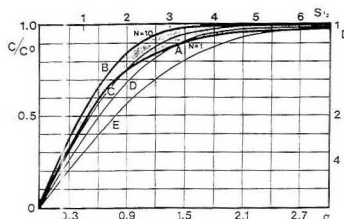


**Figure 3.** Theoretical curves for peak height and dispersion coefficient  $D$  as function of injected sample volume. Curve A is for eq 2, curves B to E are erf ( $f$ , for  $N = 2-10$ ).  $\alpha$  is the injection parameter ( $S_{1/2}/V_r$ ). For details see ref 3, from which the figure has been reproduced with permission.

isodispersion point is independent of concentration. In the element of fluid corresponding to  $I_D$ , the ratio of sample and reagent concentrations is the same as they ratio prior to injection ( $C_s/C = C_s^0/C^0$ ), since they are equally dispersed. Since dispersion describes the physical process only, the chemical reaction will of course affect this ratio further. In the case of a completed reaction and equal (equivalent) input sample and reagent concentrations, a maximum of product concentration will be observed at the isodispersion point, and if the product is detected, the peak maximum will appear at the time  $t$  of  $I_D$ . Since  $C_r^0/C_s^0$  is usually much larger than 1 due to an excess of reagent normally used, the position of the peak maximum will move from the  $I_D$  point toward the center of the sample zone (see, e.g., Figure 7). This shift continues until the reagent gradient causes the value of  $C_r$  to drop to the point where the equivalent sample concentration exceeds it (Figure 7B), and the concentration of the monitored product no longer increases, but decreases. Again, this simplification does not take reaction kinetics into consideration, and therefore, the position of  $I_D$  along the time axis can serve only as a guide for system design and to estimate how input changes of reagent concentration will affect the effective zone overlap and sensitivity of the determination.

**Sample Volume.** Selection of the injected sample volume is the main tool for optimizing readout in conventional flow injection, and therefore this parameter is considered here as well. The injected sample zone can be viewed originally as a rectangular block input function, transformed during the passage through the flow channel, which is visualized as consisting of a number of mixing stages ( $N$ ). For a single mixing stage, (3)

$$C^{max}/C^0 = 1 - \exp(-0.693S_v/S_{1/2}) \quad (2)$$

where  $S_v$  is the injected sample volume and  $S_{1/2}$  is the volume necessary to reach  $D^{max} = 2$ , where  $D^{max}$  is the dispersion in the element of fluid corresponding to the peak maximum. For an increasing number of mixing stages, the skewness of the flow injection response curve decreases and at  $N = 10$  approaches a Gaussian shape. Therefore, for large values of  $N$  eq 2 is replaced by an error function (3), which for  $S_v = S_{1/2}$  leads to

$$S_{1/2} = (V_r/2)(N/2\pi)^{1/2} \quad (3)$$

where  $V_r$  is the reactor volume.

Since values of  $N$  equal to 1-10 describe dispersion within a full range of nearly all conceivable flow injection systems, a series of step response curves for increasing  $N$  (Figure 3) show that for  $S_v < S_{1/2}$ , i.e., for  $D > 2$ , the peak height ( $C/C^0$ ) increases linearly with injected sample volume. More importantly, it follows from eqs 2 and 3 that  $S_{1/2}$  is the parameter which describes dispersion of the zone in any flow injection system, regardless of its geometry and type of flow, since it

is tied to the variance which describes zone broadening via the  $N$  value. Note that

$$\sigma^2 = Nl^2 \quad (4)$$

where  $\sigma^2$  is the variance of the peak width,  $l$  is the length of a mixing step, and  $N$  the number of steps (5). This is why it was decided to make all measurements of the  $P$  value in this work by injecting sample and reagent volumes corresponding to multiples or fractions of  $S_{1/2}$ . In this way, the  $P$  values, positions of  $I_D$  between peak maxima, and overlap of the concentration gradients shown here can serve as a guideline for optimization of all sequential injection systems, even if the reactor volumes and flow rates should differ from the design adopted for this work, because  $S_{1/2}$  values of such other systems will differ accordingly in a similar manner.

## EXPERIMENTAL SECTION

**Reagents.** The concentration of the nonreactive dye (bromothymol blue, BTB), unless otherwise stated, was the same in all experiments reported here, that is, 0.02 g/L in 0.01 M borax buffer (3), using water as a carrier/wash stream.

For chloride determinations, the reagent consisted of 0.626 g of mercury(II) thiocyanate, 30.3 g of iron(III) nitrate, 4.72 g of concentrated nitric acid, and 150 mL of methanol, made up with deionized water to 1 L. Standard chloride solutions in the range 5–50 ppm were prepared by suitable dilution of a 1000 ppm chloride stock solution. The wash/carrier solution consisted of 4.72 g of concentrated nitric acid and 150 mL of methanol diluted to 1 L with deionized water. Measurements were made at 480 nm.

For phosphate determination, reagent 1 consisted of 0.01 or 0.005 M ammonium heptamolybdate in 0.4 M nitric acid. Reagent 2 consisted of a 1.4 or 0.7% aqueous solution of ascorbic acid to which was added 1% (v/v) glycerine to prevent precipitation of reaction products. Standard phosphate solutions in the range 0–30 ppm phosphate were prepared by suitable dilution of a 1000 ppm phosphate stock solution (0.4390 g of  $\text{KH}_2\text{PO}_4/\text{L}$ ). Measurements were at 660 nm.

**Apparatus.** An Alitea U.S.A. prototype syringe-based variable-speed two-piston sinusoidal flow pump was used to propel solutions. This provides a pulseless flow which follows a sinusoidal pattern. For these experiments, the flow was computer controlled and operation was at the top portion of the sinusoidal flow curve. The principle of sinusoidal operation has been previously described (2).

Solutions were directed with an eight-port electrically actuated multiposition valve, dead end flow path, stainless steel, 0.03 in. port diameter,  $1/16$  in. fitting size, 400 psi standard pressure (Valco Instruments, Houston, TX).

The pump and valve were controlled and data collected with an IBM-compatible computer, 80286 processor, 12 MHz, EGA graphics card, in conjunction with a Labpro analog-to-digital converter and control interface (Lab Data Systems, Seattle, WA). A sampling frequency of 10 Hz with 12-bit resolution was used. Software to control the pump and valve and to perform data acquisition was written in-house. A Radiometer strip chart recorder was also used to record signals.

Spectrophotometric measurements were made with an ABI Kratos Spectroflow 783 spectrophotometer, equipped with a 12  $\mu\text{L}$ , 8 mm path length flow cell.

Table I lists the operational parameters for the SI system employed in these studies. The reasons for selecting the listed manifold dimensions have been discussed previously (4). The essential parameters of the programming sequence are given in Table I. It should be emphasized however, that in order to perform sequential injection successfully, it is necessary to turn the valve only when the flow has been stopped (to avoid pressure buildup). This is accomplished by including a 1-s stop period while the valve is tuned. Also, in order to avoid carryover (cf. Figure 4), each sample aspiration sequence is programmed in such a way that a sufficient volume (3 times sampling tube volume)

**Table I. Operational Characteristics of the SI System As Used throughout This Work**

Manifold Dimensions			
R1	100 cm	1.02 mm i.d.	817 $\mu\text{L}$
R2	115 cm	0.5 mm i.d.	226 $\mu\text{L}$
HC	50 cm	1.32 mm i.d.	684 $\mu\text{L}$
			Microline
			Teflon
			Teflon
Sinusoidal Flow Pump Parameters			
max flow rate	5.18 mL/min	cam radius (R)	1.342 cm
stroke vol	3.04 mL	syringe radius (r)	0.60 cm
starting angle	30°	frequency	$9.045 \times 10^{-3}$ Hz
Injected Volumes and Interval Times			
wash	1.92 mL	25-s reverse stroke	
$S_{1/2}$	95 $\mu\text{L}$	1.25-s reverse stroke	
sample aspirated at 114.4° angle			
combined injection and detection			
time		65 s	

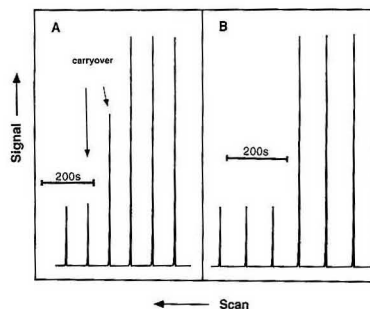


**Figure 4.** Carryover in sequential injection system caused by aspiration of a previous sample situated in the tubing which connects port 3 with a sample container. Sample tubing volume 40  $\mu\text{L}$ , injected sample volume  $S_v = 95 \mu\text{L}$ . Sample composition high 0.04 g/L BTB, low 0.01 g/L BTB. Carryover, caused by sample material remaining in the connector tubing when the discharge cycle is not applied, is 160% in the first and 10% in the second injection following the change from high to low sample concentrations (A). By introducing a discharge cycle, this carryover is completely eliminated (B).

is aspirated by a reversed stroke of the pump and immediately discharged through the auxiliary port. This routine removes all previous sample material, so the next sampling period which is programmed to aspirate the selected sample volume brings uncross-contaminated sample solution into reactor coil 1. Failure to include the discharge cycle may result in carryover (cf. Figure 4).

## RESULTS AND DISCUSSION

**Guidelines for System Design Based on Dispersion Experiments.** *Sample Volume.* The value of  $S_{1/2}$  was obtained by changing the volume of the nonreactive dye (bromothymol blue, BTB) as a tracer injected into a colorless carrier stream and recording a series of peaks by means of a spectrophotometer turned to 620 nm. A series of thus obtained response curves, recorded from the same starting point, is shown in Figure 5A. Indeed the peak height increases with the injected sample volume, in the same way as described for conventional flow injection. As predicted by theory, a plot of  $S_v$  versus  $\log(1 - A^{\text{max}}/A^0)$  yields a straight line (Figure 5B), while for  $S_v$  lower than  $S_{1/2}$  an almost linear relationship between  $S_v$  and peak height is observed. The  $S_{1/2}$  value thus found was 95  $\mu\text{L}$ .

Thus it may be concluded that changing the injected sample volume is an effective way to change the sensitivity of the measurement. While dilution of overly injected sample material is best achieved by reducing the injected sample

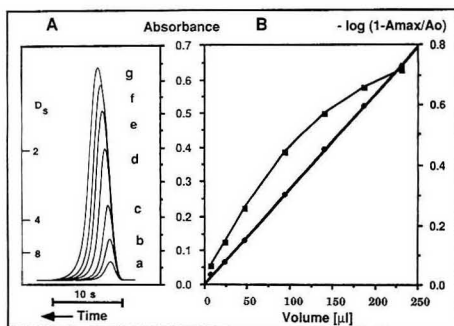


**Figure 5.** Influence of the injected sample volume on peak height and dispersion coefficient  $D_s$ , as obtained by injecting a tracer dye (volumes in  $\mu\text{L}$ : (a) 8.0, (b) 24.0, (c) 47.8, (d) 95.0, (e) 141.4, (f) 186.9, (g) 232.0). The result is the same as in the conventional flow injection technique.

volume, an increase in sensitivity of the measurement will be possible only when sufficient reagent excess is available in the element of fluid situated at the peak maximum.

**Zone Penetration.** Zone penetration was studied as a function of relative volumes of sample and reagent zones. Studies were all made by injecting zones of the same non-reactive dye into a colorless carrier stream in two different experimental runs and by recording separately the injected dye zone as a "sample" and then as a "reagent" peak. In this way, two concentration profiles were recorded, one for the reagent zone (R) and the other for the sample (S) zone, allowing their mutual overlap to be visualized. In all experiments, the reagent zone was less dispersed than the sample zone, since it was stacked as the second one (Figure 1) and therefore being closer to the valve (Figure 1) was subjected to less flow reversal and traveled a shorter distance than the sample zone.

**Increasing zone volumes at equal volume ratios** (Figure 6A,B) causes zone overlap to decrease from nearly a complete one ( $P = 0.796$  for  $R_v = S_v = 0.25S_{1/2}$ ) to a partial one ( $P = 0.498$  for  $S_v = R_v = 2.5S_{1/2}$ ). It follows from this experiment that when the injected volumes of sample and reagent are increased in the same proportion, above one  $S_{1/2}$  value, the increase in peak height is achieved through substantial increase in the consumption of sample, reagent, wash solution, and time. This is further illustrated by the  $D_s$  values shown in Figures 5 and 6, which allow comparison of zone dimensions studied in these experiments and illustrate the reason for the diminishing returns for large-volume injection.

It can thus be concluded that a simultaneous increase in sample and reagent volumes above one  $S_{1/2}$  value is not an effective way to increase peak height and sensitivity of a measurement. These are better achieved by sandwiching the sample zone in between two reagent zones of  $S_{1/2}$  volumes each (see below, zone penetration, Figure 8A).

On the other hand, conditions shown in Figure 6B are suitable for sample dilution by the gradient approach, which is based on selecting a vertical readout within a suitable time interval at the tailing section of the sample zone, past the  $I_D$  point, where gradient dilution can be carried out with a sufficient excess of reagent. These conditions will also be favorable for stopped flow reaction rate measurement.

**Varying of zone volume ratios** allows a wider range of zone overlap to be achieved, from a complete overlap ( $P = 0.806$  for  $S_v = 0.25S_{1/2}$  and  $R_v = S_{1/2}$ ) to only a partial one ( $P = 0.518$  for  $S_v = 2.5S_{1/2}$  and  $R_v = S_{1/2}$ ). Complete overlap, as shown in Figure 7A, results in conditions which are closest to a conventional flow injection technique, as traditionally

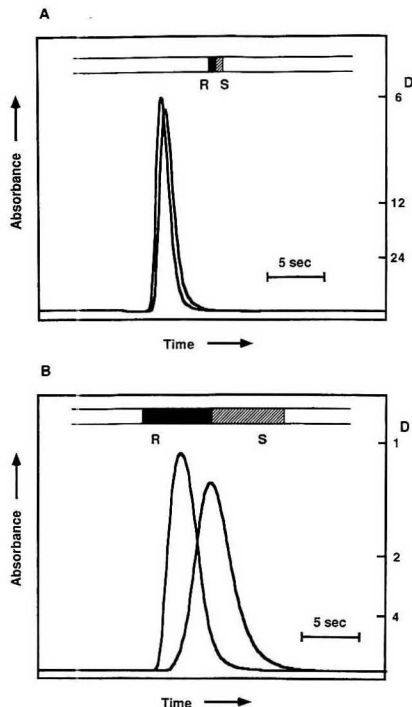


**Figure 6.** (A) Penetration of sample S and reagent R zones for  $R_v = S_v = 0.25S_{1/2}$ ,  $D_D = 6.4$ ,  $P = 0.796$ . (B) Penetration of sample S and reagent F zones for  $R_v = S_v = 2.5S_{1/2}$ ,  $D_D = 1.75$ ,  $P = 0.498$ .

performed by stream confluence: all elements of the dispersed sample zone are mixed with an adequate amount of reagent solution. At these conditions, peak height and peak area measurements will yield comparable results, and the influence of kinetics of chemical reactions will be minimized. In addition, data collected throughout the entire profile will very likely be suitable for chemometric-based single-standard solution techniques (6, 7) which, by ratioing data collected over an entire peak width, also allows interferences to be detected and corrected for.

Partial overlap (Figure 7B), having a low  $P$  value, yields only a limited range of time slices (situated in front of  $I_D$  toward the center of the reagent zone) at which the vertical readout will yield a meaningful result. The part of the response curve past  $I_D$  is starved for reagent and the very end of the zone is devoid of it. The peak maximum will be located (in case of completed chemical reactions) within that element of fluid where sample and reagent components are equivalent, and this equivalence of reagent and analyte will make peak height measurement prone to irreproducibilities caused by flow pulsations or irregularities of the injection process. Yet, the partially overlapped zones structured as shown on Figure 7B offer a wider range of information: not only can analyte readouts be obtained within the time span indicated by the arrow ( $\leftrightarrow$ ) but also sample blank is accessible at the very tail of the sample zone.

Thus it can be concluded by comparison of Figure 7A,B that injecting at least twice as large a reagent zone volume as the sample zone volume, while keeping the volume of the sample zone less than or equal to  $0.5S_{1/2}$ , allows the optimum

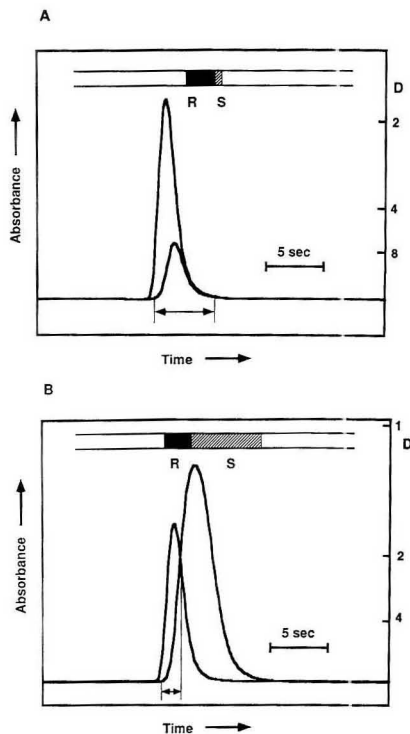


**Figure 7.** Penetration of sample S and reagent R zones for constant reagent volume and increasing sample volume. (A)  $R_v = S_{1/2}$ ,  $S_v = 0.25S_{1/2}$ ,  $I_D$  not identified,  $P = 0.806$ . Note a wide range of time intervals during which a readout can be taken ( $\leftrightarrow$ ), the low  $D$  values of the reagent peak, and the high  $D$  values of the sample peak. (B) Penetration of sample S and reagent R zones for  $R_v = S_{1/2}$ ,  $S_v = 2.5S_{1/2}$ ,  $D_{10} = 2.2$ ,  $P = 0.518$ . Note a narrow range of time intervals during which a readout can be taken ( $\leftrightarrow$ ), and the very low  $D$  values of the sample peak.

conditions for sequential injection single reagent based chemistry to be met.

**Three-Zone Penetration.** A third zone can be introduced into the sequential system by two mechanisms: by introducing this zone into the stack or by stacking two zones, mixing them, and then adding a third zone to the mixture. Obviously, the second mechanism will closely resemble two-zone mixing discussed above, and therefore only the coalescence of three simultaneously stacked zones has been investigated.

All experiments described below were made by injecting two zones of equal volumes of nonreactive dye into a colorless carrier stream in two different experimental runs and by recording separately the absorbance of the injected dye zone as a sample and then as reagent peak. A "spacer", Sp, representing a third zone, was inserted in each of the two runs (Figure 8A,B) as a zone of a colorless carrier stream between the sample and reagent zones. In this way, two concentration profiles were recorded, one for the reagent zone (R) and one for the sample (S) zone, allowing their mutual overlap in the presence of a spacer to be visualized. The spacer remains invisible, but its presence is apparent by an increasing gap as the spacer volume increases. Again, in these experiments the sample zone is progressively more dispersed, since it has been stacked behind the increasingly larger zone of the spacer,

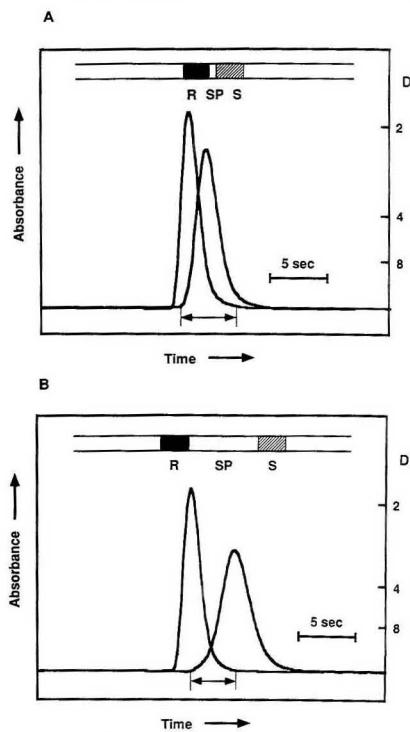


**Figure 8.** Penetration of sample S and reagent R zones for increasing volume of a third (colorless) zone inserted between R and S zones as a spacer (Sp).  $S_v = R_v = S_{1/2}$  in all experiments. (A)  $Sp_v = 0.25S_{1/2}$ ,  $D_{10} = 3.15$ ,  $P = 0.571$ . Note a wide range of time intervals during which a readout can be taken ( $\leftrightarrow$ ), and intermediate  $D$  values of both R and S peaks. (B) Penetration of sample S and reagent R zones for  $Sp_v = 2.5S_{1/2}$ ,  $D_{10} = 15$ ,  $P = 0$ . Note a narrow range of time intervals during which R and S zones penetrate ( $\leftrightarrow$ ) and very high  $D$  values of  $I_D$ . If the spacer peak had been made visible by injecting a dye, its  $D$  value at its maximum would have been seen to be as low as 1.23. If Sp, then, were to be the sample, its concentration, as compared to the high  $D_{10}$  value, would result in a reagent limitation (S and R)—shown in curves B, Figures 10 and 11.

becoming thus subjected to larger flow reversal and traveling a longer distance than the reagent zone (Figure 8A,B). As one would expect, increasing the volume of the spacer zone separates the marginal zones further, causing outside zone overlap to decrease dramatically from a partial one ( $P = 0.571$  for  $Sp_v = 0.25S_{1/2}$ ) to a minimized one ( $P = 0$  for  $Sp_v = 2.5S_{1/2}$ ).

It follows from these experiments that a two-reagent chemistry becomes feasible in the following way. When the sample zone is sequenced in the spacer position (Sp, Figure 8A) and the two complementing reagents are sequenced as R and S zones, while a sample volume of  $0.5S_{1/2}$  is not exceeded, the thus sequentially stacked and injected zones will sufficiently overlap to form a product peak which will yield a meaningful readout. The peak maximum will be close to the  $I_D$  point, provided that the original concentrations of injected reagents ( $C_{r1}$  and  $C_{r2}$ ) are much higher than the concentration of the sample material ( $C_s$ ). Only under these conditions will the sample zone be supplied with sufficient excess of both reagents. Since lack of reagent will affect the peak maximum first, the calibration curve based on peak height measurement will not be linear, while measurement



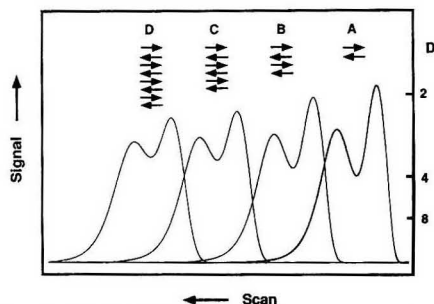


**Figure 9.** Influence of repeated flow reversals on the mutual penetration of sample and reagent zones ( $S_v = R_v = S_{1/2}$ ,  $Sp_v = 1.5S_{1/2}$ ). The top arrow indicates the stacking direction, the additional arrows indicate the number of flow reversals and their direction. The step length had an amplitude of  $1.5S_{1/2}$ .

of peak areas may be influenced to a lesser extent. The reagent deficiency, however, may be corrected by increasing reagent concentrations or by decreasing  $S_v$ .

Thus it can be concluded that two-reagent chemistry can be accommodated in the sequential injection system, provided that the sample volume is kept below the  $S_{1/2}$  value, that the sample zone is surrounded by the reagent zones, and that the concentrations of injected reagents are sufficiently high.

**Flow Reversal.** Flow reversal (8) effectively promotes zone penetration. It is the length of a step ( $l$ , eq 4) which causes zone broadening more effectively than the number of steps ( $N$ ). This can be observed in all the above experiments where all stacked zones have undergone a single flow reversal but experienced different step length, due to insertion of spacers and reagent zones of different volumes. Indeed, comparison of peak heights and peak broadening in Figures 6–8 invariably shows the sample zone to be more dispersed than the reagent zone, and this trend increases with the combined length of the imposed step. In this context, it is useful to consider an increase of the number of reversals at a constant step length and zone sequence composition. For this purpose a three-zone sequence, similar to that shown in Figure 8 ( $S_v = R_v = S_{1/2}$ ,  $Sp_v = 1.5S_{1/2}$ ) was stacked and then injected into the reactor R2. The flow was then reversed to return the mixed zones into R1 and was reversed again to inject the zones through R2 into the detector. During this cycle the composite zone experienced three reversals ( $N = 3$ ). In contrast to previous experiments, the penetration of all three zones was recorded in a single double-humped curve for each cycle (Figure 9). As expected, increasing the number of flow reversals indeed increases mutual zone penetration ( $P = 0.383$  for a single reversal (curve A), while  $P = 0.738$  for seven flow reversals (curve D)).

However, it is the first flow reversal and its length which is most effective in providing mutual zone penetration, and since multiple flow reversals increase overall dispersion—and time to complete a measuring cycle—their use will remain restricted for difficult solution handling tasks, such as mixing of zones of very different viscosities.

**Resolution.** Zone penetration as investigated above in a series of dispersion experiments can be evaluated in several ways. Thus eq 1 can be further refined. First, a simple ratio of zone overlap  $W_s$  and sample  $W_r$  can be used. The thus defined  $P_s = W_o/W_s$  value will describe sample zone penetration only, disregarding the excess of reagent used. Thus, while the  $P$  value of zone overlap shown in Figure 7A is only 0.796 (Table II), the  $P_s$  value for the same experiment will be 1.0 as defined for complete overlap. However, it should be noted that exact and complete overlap of both reagent and

**Table II.** Calculation of Zone Penetration

$S_v = R_v =$ $xS_{1/2}$		$R_v = S_{1/2}$ $S_v = xS_{1/2}$		$S_v = R_v = S_{1/2}$ $Sp_v = xS_{1/2}$	
$x$	$P$	$x$	$P$	$x$	$P$
0.25	0.796	0.25	0.806	0.25	0.571
0.5	0.712	0.5	0.690	0.5	0.497
1.0	0.595	1.0	0.700	1.0	0.319
1.5	0.562	1.5	0.643	1.5	0.228
2.0	0.502	2.0	0.559	2.0	0.023
2.5	0.498	2.5	0.518	2.5	0

sample zone will yield a value of 1 in both cases. Since the purpose of suggesting a  $P$  value is optimization of the system design, including reagent economy, the  $P$  value rather than the  $P_s$  value was used above. Also, in analogy with chromatography, other ways of measuring  $P$  can be based on considering overlapping peak areas, rather than their widths, and also considering peak asymmetry using further approximations. Yet, since  $P$  is to be used in conjunction with  $D$  only as a guideline for system design, the differences these different ways of defining between  $P$  values are not significant in this context.

**Verification of Design Principles by Reagent-Based Assays.** Colorimetric determination of chloride and phosphate were chosen as test chemistries to validate the above postulated guidelines. When flow injection analysis was first introduced, successful implementation of these two assays (3) became a proof of applicability of this then unproven technology to a wide range of reagent-based chemistries. The reason for this choice is that these two chemistries differ considerably: chloride assay is based on a single-reagent fast chemistry, and the measured product is a soluble complex, while phosphate assays requires two reagents (the formation of the product to be measured occurs in two steps), and the product of a relatively slow second step is a colloidal heteropolycomplex. Since these chemistries are also widely used in conventional flow injection configurations, it is believed that their implementation into the sequential injection system will serve as a proof of viability of SI and verification of the guidelines outlined above.

**Single-Reagent Assay.** Colorimetric measurement of iron(III) thiocyanate complexes is the basis for determination of chloride, via reaction of the analyte with a reagent containing a mixture of mercury(II) thiocyanate with iron(III) nitrate in slightly acidic medium. Adaptation of this assay into the sequential injection format turned out to be straightforward. By variation of sample/reagent/spacer configurations and volumes, response curves followed the pattern predicted by the guidelines derived from dispersion experiments. Selected from a wide range of investigated configurations, only two extreme cases are discussed here.

Nearly complete zone overlap ( $S_v = 0.5S_{1/2}$  and  $R_v = S_{1/2}$ ,  $P = 0.690$ ) using an excess of reagent (see Experimental Section) was investigated by injecting a series of standard chloride solutions. These injections, monitored at 480 nm, yielded a typical flow injection response curve, while the resulting calibration graph was a straight line, with a small blank offset typical for chloride reagent chemistry. The results were highly reproducible (better than 1% RSD), and the slope of calibration curve was similar to that obtained by a conventional flow injection technique (Figure 2.1 of ref 3).

Minimized zone overlap was obtained by injecting a spacer plug made of carrier solution ( $R_v = S_v = S_{1/2}$ ,  $Sp = 2S_{1/2}$ ,  $P = 0.023$ ), while reagent and sample concentrations remained the same as in the previous experiment. As predicted, the sensitivity of determination decreased dramatically, since only the trailing edge of the chloride zone was penetrated by the front of the reagent zone (similar to zone overlap shown in

Figure 8B). For reasons discussed in conjunction with Figure 7B, the reproducibility of determination was somewhat lower (2–5% RSD), and the calibration line had a slight tendency to curve upward from linearity at high sample concentrations. In cases when there is a need for extensive sample dilution, as in process control, this approach may find applications. That is, *partial zone overlap is a useful technique allowing assay of highly concentrated samples*, as in Figure 7B.

**Double-Reagent Assay.** Colorimetric measurement of reduced phosphomolybdate complexes (molybdenum blue) is the basis for determination of phosphate, via reduction of the previously formed phosphomolybdate by a second reagent containing a reducing agent. Since the molybdate reagent is incompatible, on storage, with reductants such as ascorbic acid, two separate reagents must be sequentially used. When the phosphate sample was inserted as a central zone, sandwiched between two reagent zones of equal volumes ( $R_v = 0.5S_{1/2}$ ), molybdate zone at rear, ascorbic acid up front, i.e., close to the valve), a sequence typical for a spacer experiment (as shown in Figure 8A) was stacked into reactor 1 and then injected through reactor 2 into a detector, which was tuned to 660 nm. Since in the three-zone configuration the spacer volume and reagent concentrations are the critical parameters, experiments showing their influence are discussed here.

A sequence with a short sample zone ( $S_v = 0.5S_{1/2}$ ) sandwiched between reagent zones of high concentration (0.01 M ammonium heptamolybdate and 1.4% ascorbic acid) gave a response curve and calibration graph which very closely resembled conventional flow injection readouts of comparable sensitivity and linearity (Figure 6.3 of ref 3). The same zone configuration with a longer sample zone ( $S_v = 1.0S_{1/2}$ ) and a lower reagent concentration (0.005 M ammonium heptamolybdate and 0.7% ascorbic acid) resulted in a calibration curve of much lower slope and nonlinearity, due to a reagent limitation at higher analyte concentration. This nonlinearity was also observed in all other zone configurations (e.g., sample zone first, followed by two reagent zones), where insufficient zone penetration, combined with low concentration of injected reagents, led to reagent deficiency in the element of fluid corresponding to the peak maximum. Finally, replicate phosphate determinations by sequential injection at optimized conditions (that is,  $S_v = 0.5S_{1/2}$  or less, sandwiched between two reagent zones of at least  $0.5 S_{1/2}$  and reagent excess) yielded reproducible results (typically 1% RSD).

### CONCLUSION

This study confirms the feasibility of performing single and multireagent chemical assays in a sequential injection system.

Remarkably, all dispersion experiments and two quite different chemistries were performed in the same single-channel flow system, without the need for physical reconfiguration. Thus, unlike conventional flow injection, where transition from chloride assay to phosphate assay requires replumbing of an entire manifold, the single-pump, single-valve, and single-line system is capable of accommodating diverse chemistries and sample concentrations by reconfiguring the zone sequence from a computer keyboard. Since the sinusoidal pump used is a piston pump and since the flow channel and flow cell are filled with wash solution between measurements and during the standby period, the entire system can be closed down and restarted without the need for servicing, such as washing or pump tube adjustment (there are no pump tubes). Additional assets of the sequential injection system combined with the sinusoidal flow pump have been discussed previously (2) and are summarized in Table I of that reference.

There are presently two drawbacks of SI to be mentioned. First, since the aspiration of the wash and sequencing of the zones in reactor 1 takes some time (typically 30 s), the sampling frequency of the SI system is presently half that of a conventional FI system, where filling of the injection valve is a matter of a few seconds. Secondly, SI requires specialized software, since the sequencing, injection, and data collection are entirely computer driven. This, however, is not an obstacle to using the technique.

Still much remains to be explored and optimized. The influence of flow rates and manifold dimensions has not yet been investigated. The presently used configuration is not necessarily optimized, since the channel dimensions may be further decreased.

### LITERATURE CITED

- (1) Ruzicka, J.; Marshall, G. D. *Anal. Chim. Acta* **1990**, *237*, 329.
- (2) Ruzicka, J.; Marshall, G. D.; Christian, G. D. *Anal. Chem.* **1990**, *62*, 1861.
- (3) Ruzicka, J.; Hansen, E. H. *Flow Injection Analysis*, 2nd ed.; Wiley: New York, 1988.
- (4) Ruzicka, J.; Gübeli, T. *Anal. Chem.* **1991**, *63*, 1680.
- (5) Giddings, J. C. *Dynamics of Chromatography*; Marcel Dekker: New York, 1965.
- (6) Sperling, M.; Fang, Z.; Welz, B. *Anal. Chem.* **1991**, *63*, 151.
- (7) Fan, S.; Fang, Z. *Anal. Chim. Acta* **1990**, *241*, 15.
- (8) Clark, G. D.; Zable, J.; Ruzicka, J.; Christian, G. D. *Talanta* **1991**, *38*, 119.

RECEIVED for review March 25, 1991. Accepted August 12, 1991. Gratitude is expressed to the National Institute of General Medical Sciences (Grant No. SSS-6 (b) 1R43 GM 45087-01) for partial financial assistance and to Kurt Scudder for participation in the final stage of this work.

# Determination of the Diffusion Coefficients of Iodine in Porphyrin Thin Films by Utilization of the Battery Effect in Schottky Barrier Devices

W. Andrew Nevin<sup>1</sup>

Department of Electrical and Electronic Engineering, Trent Polytechnic, Burton Street, Nottingham NG1 4BU, England

**A novel method for measuring the diffusion coefficient of a volatile dopant in an organic semiconductor is described, which utilizes the dark battery surface effect found in thin-film Schottky barrier structures containing aluminum as the barrier metal. The method is used to determine the diffusion coefficients of iodine in a series of tetraphenylporphyrin (TPP) films with varying central substituent, Mg, Zn, H<sub>2</sub>, Cu, and Ni. Diffusion coefficients of the order of 10<sup>-15</sup> cm<sup>2</sup>/s are observed, and with the exception of CuTPP, the diffusion coefficient increases exponentially with increasing ring-oxidation potential of the porphyrin. The results indicate that the diffusion is largely governed by charge-transfer interactions between the iodine and porphyrin molecules. In addition, a close relationship is found between the measured diffusion coefficient and the quantum efficiency for charge-carrier photogeneration in the materials.**

## INTRODUCTION

Recently, there has been considerable interest in the doping of organic semiconductors, such as porphyrins and phthalocyanines, with electron-acceptor dopants, in particular the halogens. At high concentration, the acceptor enhances the dark conductivity of the materials up to the metallic range (1), while at low levels, the acceptor has been found to produce large increases in the photovoltaic efficiency of organic solar cells by enhancing the charge-carrier photogeneration (2-4). The effect is thought to be due to the formation of a ground-state donor-acceptor charge-transfer complex between the organic semiconductor and dopant molecules, the extent of transfer increasing with increasing concentration of dopant. It is therefore of fundamental interest to obtain information about the diffusion of the dopants within the organic materials, since this can aid in understanding the nature of the interactions occurring between the dopant and semiconductor molecules. However, measurements of this type are generally difficult with thin films by using normal gravimetric techniques, because of the low diffusion coefficients encountered and the small amounts of dopant incorporated into films.

In this paper, a novel technique is presented which allows measurement of the diffusion coefficient (*D*) of a volatile dopant at low concentration in an organic semiconductor thin film. This utilizes the dark battery surface effect found in Schottky barrier sandwich structures containing an aluminum electrode as the barrier metal. The method has been used to determine, for the first time, the diffusion coefficients of iodine in a series of tetraphenylporphyrins (TPP) with central substituents of Mg, Zn, H<sub>2</sub>, Cu, and Ni. The diffusion coefficient is found to be closely related to the quantum efficiency

for charge-carrier photogeneration in this series of compounds, thus illustrating the usefulness of this type of measurement in analyzing and predicting organic semiconductive and photoconductive behavior.

## THEORY

Diffusion processes in organic solids have been comprehensively reviewed by Rogers (5). In the simple case of "Fickian" diffusion of a dilute component in a second component, the diffusion over the initial stage of sorption or desorption occurs in a semiinfinite medium and often follows the relationship (5)

$$M_t/M_\infty = 4D^{1/2}t^{1/2}/\pi^{1/2}d \quad (1)$$

where *d* is the sample thickness, and *M<sub>t</sub>* and *M<sub>∞</sub>* are the cumulative masses sorbed or desorbed at times *t* = *t* and *t* = ∞, respectively. *M<sub>∞</sub>* is attained when there is no sensible change in mass over a time interval comparable to the interval required to attain that value. *D* can therefore be calculated from the initial slope of a plot of *M<sub>t</sub>/M<sub>∞</sub>* vs *t*<sup>1/2</sup>/*d*, if this is linear. Alternatively, at longer times, when *M<sub>t</sub>/M<sub>∞</sub>* > ca. 0.4, the diffusion can be described by

$$\ln(1 - M_t/M_\infty) = \ln(k_B/\pi^2) - D\pi^2t/d^2 \quad (2)$$

so that *D* can be calculated from the slope of a plot of  $\ln(1 - M_t/M_\infty)$  vs *t/d*<sup>2</sup>. *D* can also be obtained from the time (*t*<sub>1/2</sub>) at which *M<sub>t</sub>/M<sub>∞</sub>* = 0.5, according to

$$t_{1/2}/d^2 = -(1/\pi^2D) \ln[(\pi^2/16) - (1/9)(\pi^2/16)^9] \quad (3)$$

i.e.

$$D = 0.04939/(t_{1/2}/d^2) \quad (4)$$

If the diffusion coefficient is dependent upon the concentration of the diffusing species, for example, as a result of a change in the host material film structure, then the value of *D* obtained from eqs 1-4 is the integral diffusion coefficient over the range of concentrations (*c*) studied in each case (i.e. from *c*<sub>0</sub> to *c*<sub>∞</sub>). It will be shown below that *M<sub>t</sub>/M<sub>∞</sub>* and (*M<sub>∞</sub>* - *M<sub>t</sub>*) can be obtained from analysis of the time dependence of the short-circuit dark current (*J<sub>dk</sub>*) during pumping out of a volatile dopant from an organic semiconductor thin film in a Schottky barrier device.

Previous work on p-type organic Schottky barrier or metal-insulator-semiconductor (MIS) devices containing an aluminum electrode as the barrier contact has shown that in the presence of an atmosphere of electron-acceptor dopant, such as oxygen/water vapor or iodine vapor, a dark battery effect is observed, manifested in the appearance of a high dark current and dark voltage (6). It is thought that this is due to an increase in the surface conductivity of the semiconductor as a result of the adsorption of a high concentration of dopant molecules. Conductive pathways are formed directly between the Al and ohmic contact along the surface of the organic layer,

<sup>1</sup>Present address: Central Research Laboratories, Kanegafuchi Chemical Industry Co. Ltd., 2-80, 1-chome, Yoshida-cho, Hyogo-ku, Kobe 652, Japan.

leading to the occurrence of a battery effect as a result of an electrochemical reaction at the Al electrode. On evacuation of the system, the dark battery effect is rapidly reduced due to the desorption of the surface dopant molecules. In the method described here, this effect is utilized, by exposing the organic layer to excess dopant during its deposition, and subsequently observing the decay of the dark current as the dopant diffuses out of the film under continuous vacuum pumping. The level of dark current is then determined by the concentration of dopant molecules at the surface at any given time, which is, in turn, determined by the rate of diffusion of the dopant from the bulk of the film.

It has been shown previously that the dark conductivity ( $\sigma_d$ ) of an organic semiconductor for low amounts of adsorbed dopant gas or vapor follows the relationship (7)

$$\sigma_d = A \exp(\alpha m) \quad (5)$$

where  $m$  is the amount of gas or vapor adsorbed and  $A$  and  $\alpha$  are constants. At high concentration, this relationship is lost, so that an important feature in the method is to restrict the concentration of adsorbed dopant to low enough values to obey eq 5 but large enough to form weakly conductive pathways across the surface of the organic film to give a significant dark current. This was carried out by continuing the diffusion pumping of the chamber during exposure to the dopant. From eq 5, the surface concentration ( $M$ ) of dopant molecules is then related to the short-circuit dark current according to

$$M \propto \ln J_{dk} \quad (6)$$

Since the concentration at the surface at any time  $t$  will depend upon the diffusion of the dopant molecules from the bulk of the film, it follows from eq 6, that the concentrations of dopant in the film at times  $t = 0, t$  and  $\infty$ , respectively, are given by  $M_0 \propto \ln J_0$ ,  $M_t \propto \ln J_t$ , and  $M_\infty \propto \ln J_\infty$ , where  $J_0$  is the initial short-circuit dark current,  $J_t$  is the dark current at any time  $t$ , and  $J_\infty$  is the value of decayed dark current at a time  $\infty$ , when there is no sensible change in current over a time interval comparable to the time required to reach that value. The amounts of dopant diffused out of the film at times  $t$  and  $\infty$ ,  $M_t$  and  $M_\infty$ , respectively, are then given by

$$M_t = M_0 - M_t' \quad (7)$$

$$M_\infty = M_0 - M_\infty' \quad (8)$$

Hence, it follows that

$$M_t/M_\infty = (\ln J_0 - \ln J_t) / (\ln J_0 - \ln J_\infty) \quad (9)$$

$$M_\infty - M_t = [(\ln J_0 - \ln J_\infty) - (\ln J_0 - \ln J_t)] \quad (10)$$

The diffusion coefficient can then be determined by combining eq 9 with eq 1 or 4, or eq 10 with eq 2.

### EXPERIMENTAL SECTION

The tetraphenylporphyrins were prepared and purified using standard procedures, as described previously (3, 4). A final purification was carried out by sublimation onto glass wool immediately before fabrication of the devices. Iodine crystals were purified by sublimation in air onto a cold glass surface.

The vacuum deposition apparatus in which the devices were fabricated and tested has been described previously (3). The main feature was a rotatable evaporation source, so that devices could be prepared and tested in situ, under high vacuum, without moving at any stage. Electrical output was measured via an electrical feedthrough into the vacuum chamber, using a Keithley Model 616 electrometer. Exposure to iodine vapor was carried out by releasing the vapor from a test tube containing iodine crystals, positioned at ca. 10 cm from the substrate, to give a pressure of  $1 \times 10^{-3}$  Torr in the vacuum chamber, under continuous diffusion pumping (3). The substrates were 2 mm  $\times$  50 mm diameter polished Pyrex disks, cleaned by soaking in 5%

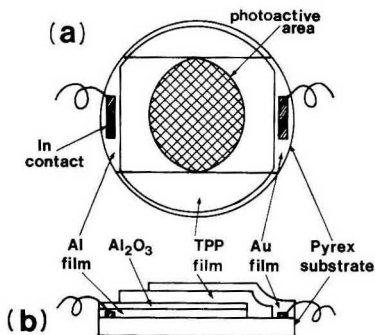


Figure 1. Schematic diagram of the device structure: (a) top view; (b) side view.

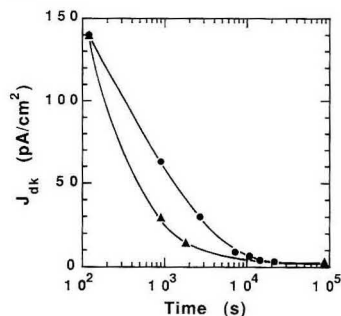


Figure 2. Evolution of the short-circuit dark current ( $J_{dk}$ ) with time after deposition of the Au electrode, for MgTPP (●) and  $H_2$ TPP (▲) cells, normalized to the initial MgTPP value.

Decon-90 solution, followed by heating to red-hot in a roaring gas/air flame for several seconds (8). The devices were MIS sandwich structures, formed by overlapping films of Al,  $Al_2O_3$ , TPP, and Au, as shown in Figure 1, with an active area of ca. 5.6  $cm^2$ .

The procedure for device fabrication and testing was as follows: two tinned Cu wires were first attached to the surface of the substrate with molten indium metal, using a soldering technique. These were connected to the external measuring circuit, to allow measurement of the cell output immediately after fabrication. Deposition of films was carried out at a base pressure of ca.  $10^{-6}$  Torr. A 6-nm film of Al was evaporated over one In contact, and a layer of ca. 3-nm  $Al_2O_3$  was then grown on this by exposure to a controlled mixture of oxygen/water vapor (9). A layer of this type has been found to give additional stability to the fabricated devices (10, 11). Following pumpdown to  $10^{-6}$  Torr, a 130 nm thick porphyrin film was deposited at a rate of 10 nm/min. During its evaporation, the film was exposed to  $I_2$  vapor periodically for a few seconds each time, with a total exposure time of about 20–120 s. A 10 nm thick Au layer was then immediately deposited onto the porphyrin, to cover the second In contact, and the decay of  $J_{dk}$  followed as the  $I_2$  diffused out of the device. Measurements were taken discontinuously in order to minimize any degradation of the Al electrode by the battery effect: since high photovoltaic responses were observed for these devices, any such degradation would appear to be negligible. In this study, the metal electrodes were kept thin enough to be semitransparent, to allow measurement of the photovoltaic properties. However, thicker electrodes could be used, if necessary. All measurements were made at a substrate temperature of ca. 20 °C.

### RESULTS AND DISCUSSION

Figure 2 shows the change of  $J_{dk}$  with time for typical MgTPP and  $H_2$ TPP cells, normalized to the initial value of

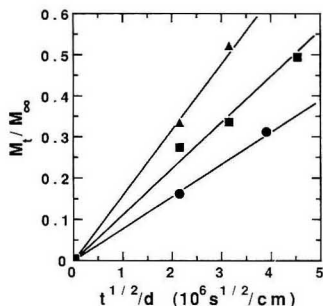


Figure 3. Plots of  $M_t/M_\infty$  vs  $t^{1/2}/d$  for MgTPP (●), ZnTPP (■), and  $H_2$ TPP (▲) cells.

Table I. Diffusion Coefficients ( $D$ ) of Iodine in Tetraphenylporphyrin Thin Films<sup>a</sup>

	MgTPP	CuTPP	ZnTPP	$H_2$ TPP	NiTPP
$D$ ( $10^{-15}$ $cm^2/s$ )	1.1 ( $\pm 42\%$ )	1.5 ( $\pm 6\%$ )	2.3	5.1 ( $\pm 39\%$ )	8.2

<sup>a</sup> Values for MgTPP, CuTPP, and  $H_2$ TPP are averages of six, two, and six devices, respectively.

the MgTPP cell. The current decreases rapidly initially, from a value of the order of  $10^{-10}$  A/cm<sup>2</sup> measured at 2 min after deposition of the Au electrode, toward a saturation level of around  $10^{-12}$  A/cm<sup>2</sup> after 24–48 h under vacuum. Notably, the initial rate of decrease is much larger for the  $H_2$ TPP cell. The ratios  $M_t/M_\infty$  were calculated using eq 9, by taking  $J_0$  as the current measured at 2 min after deposition of the Au electrode, and  $J_\infty$  as the saturated current measured at a time of 24–48 h. For example, for the cells of Figure 2, the values of  $J_0$  and  $J_\infty$  were 140 and 157 pA/cm<sup>2</sup> and 1 and 4 pA/cm<sup>2</sup>, for MgTPP and  $H_2$ TPP, respectively.

Plots of  $M_t/M_\infty$  versus  $t^{1/2}/d$  for MgTPP, ZnTPP, and  $H_2$ TPP devices, measured over the initial period, are shown in Figure 3. Good straight-line plots are obtained in each case, with least-squares fit regression coefficients of 0.999, 0.989, and 0.998 for MgTPP, ZnTPP, and  $H_2$ TPP, respectively. Values of  $D$ , calculated from the slopes using eq 1, are  $1.2 \times 10^{-15}$ ,  $2.3 \times 10^{-15}$ , and  $5.2 \times 10^{-15}$  cm<sup>2</sup>/s, respectively, for these cells. Deviation from linearity occurred at times longer than about 50 min ( $H_2$ TPP) to 4 h (MgTPP), corresponding to  $M_t/M_\infty$  values of ca. 0.5–0.7, in good agreement with the behavior expected for ideal Fickian diffusion (5). A total of six devices for each of MgTPP and  $H_2$ TPP, two of CuTPP, and one for each of ZnTPP and NiTPP were analyzed in this study. Table I lists the average values of  $D$ , calculated from the slopes over the initial time period, together with the total range of values observed for each compound. The diffusion coefficient is found to increase in the order of central substituent Mg < Cu < Zn <  $H_2$  < Ni. Calculation of  $D$  by using eqs 2 and 4 generally gave good agreement with the values listed in Table I, within a variation of about 5–30%.

As far as the author is aware, diffusion coefficients of halogens in porphyrins have not been reported previously. However, the measured values are in good agreement with a value of  $D = 5 \times 10^{-15}$  cm<sup>2</sup>/s for the diffusion of oxygen in lead phthalocyanine single crystals, obtained by extrapolation to 300 K of the results of Yasunaga et al. (12), which were measured at 465–515 K. They are also around the same order as values of  $D = 10^{-13}$ – $10^{-17}$  cm<sup>2</sup>/s measured for  $I_2$  diffusion in conducting polyacetylene films (13).

It has been shown that the stability of a charge-transfer complex is proportional to the energy of the ground-state

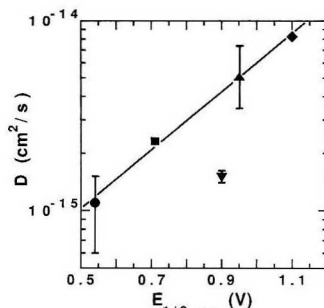


Figure 4. Semilog plot of the measured diffusion coefficient ( $D$ ) of iodine vs the porphyrin first ring-oxidation potential ( $E_{1/2,ox}$ ) for MgTPP (six cells) (●), ZnTPP (one cell) (■), CuTPP (two cells) (▼),  $H_2$ TPP (six cells) (▲), and NiTPP (one cell) (◆). The error bars show the range of values obtained for each compound. The line is the least-squares fit through the data points except CuTPP (regression coefficient = 0.995).

complex ( $W_N$ ) minus the ionization potential ( $I_0$ ) of the donor molecule, according to the relationship (2)

$$\text{stability} \propto \exp[(W_N - I_0)/k_B T] \quad (11)$$

Hence, if the diffusion of iodine in the thin film is controlled primarily by charge-transfer interactions with the porphyrin molecules, the diffusion coefficient would be expected to be an exponential function of the porphyrin ionization potential. In the series of tetraphenylporphyrins studied here,  $I_0$  should be approximately proportional to the first electrochemical oxidation potential of the porphyrin ring. This is plotted (14) versus the logarithm of the measured diffusion coefficients in Figure 4. With the exception of CuTPP, a good linear fit is obtained, indicating that the diffusion is indeed governed largely by charge-transfer interactions. This is also implied by the low values of  $D$ , which are closer to those measured for dopant diffusion in inorganic semiconductors than for the usual diffusion of noninteracting gases and vapors in organic materials (5, 13). From Figure 4, CuTPP shows a value of  $D$  much lower than expected from its oxidation potential. It has also been noted that this compound shows a lower than expected charge-carrier photogeneration efficiency compared to the other porphyrins in the series (15). However, it is presently difficult to explain this seemingly anomalous behavior. Possibly, the lower  $D$  may be due to a relative enhancement of the porphyrin–iodine charge-transfer interaction, as a result of coupling between the unpaired electron in the Cu  $d_{x^2-y^2}$  orbital and that on the oxidized porphyrin ring (14). The lower photogeneration efficiency of CuTPP may be the result of its shorter excited-state lifetimes compared with MgTPP, ZnTPP, and  $H_2$ TPP (15).

Since these devices are also photovoltaically active, it is possible to compare the photovoltaic performance with the diffusion properties. This is of interest, since it has been suggested that a weak charge-transfer complex is important in the charge-carrier photogeneration mechanism in organic photovoltaic cells (2, 15, 16). Figure 5 shows a log–log plot of the diffusion coefficient versus the peak (Soret band) charge-carrier photogeneration quantum efficiency ( $\phi_p$ ), reported previously for devices fabricated under similar conditions (15). Again with the exception of CuTPP, an excellent fit is obtained, according to the relationship  $\phi_p \propto 1/D^{2.2}$ . This close relationship between  $D$  and  $\phi_p$  therefore provides direct evidence for an important role of dopant–semiconductor charge-transfer interactions in the operation of organic photovoltaic devices. In addition, the diffusion coefficient can be seen to be a useful parameter in predicting the design of



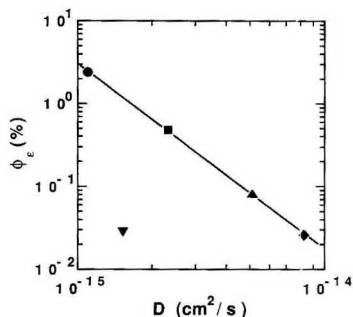


Figure 5. log-log plot of the diffusion coefficient ( $D$ ) of iodine vs the charge-carrier photogeneration quantum efficiency ( $\phi_e$ ) for MgTPP (●), ZnTPP (■), CuTPP (▼),  $\text{H}_2\text{TPP}$  (▲), and NiTPP (◆)  $\text{I}_2$ -doped devices. The line is the least-squares fit through the data points except CuTPP (regression coefficient = 1.00).

organic semiconductive materials which might have high photovoltaic efficiency.

In summary, the use of a novel method, by following the decay of the short-circuit dark current in  $\text{I}_2$ -exposed Schottky barrier MIS devices, has enabled the comparison of the diffusion coefficients of iodine in a series of tetraphenylporphyrin thin films as a function of the porphyrin central substituent. The method should be applicable to other volatile dopant/organic semiconductor systems and appears particularly suitable for the low values of diffusion coefficient found for electron-acceptor dopants in organic semiconducting materials. Although this study has been restricted to the use of an electron-acceptor dopant with a p-type semiconductor, there appears no reason why the method could not also be extended to the measurement of diffusion coefficients of donor gases and vapors in n-type organic semiconductors.

#### ACKNOWLEDGMENT

I am grateful to Max Robinson and Geoff Chamberlain for helpful advice and discussion.

#### LITERATURE CITED

- (1) (a) Meier, H. *Organic Semiconductors*; Verlag Chemie: Weinheim, 1974. (b) Hoffman, B. M.; Ibers, J. A. *Acc. Chem. Res.* **1983**, *16*, 15.
- (2) Chamberlain, G. A. *Sol. Cells* **1983**, *8*, 47.
- (3) Nevin, W. A.; Chamberlain, G. A. *J. Appl. Phys.* **1990**, *66*, 5247.
- (4) Nevin, W. A.; Chamberlain, G. A. *J. Chem. Soc., Faraday Trans. 2* **1989**, *85*, 1729.
- (5) Rogers, C. E. In *Physics and Chemistry of the Organic Solid State*; Fox, D.; Labes, M. M., Weissberger, A., Eds.; Wiley: New York, 1965; Vol. 2, Chapter 6.
- (6) (a) Fan, F.-R.; Faulkner, L. R. *J. Chem. Phys.* **1978**, *69*, 3334. (b) Chamberlain, G. A.; Cooney, P. *J. Chem. Phys. Lett.* **1979**, *66*, 88. (c) Loutfy, R. O.; Sharp, J. H. *J. Chem. Phys.* **1979**, *71*, 1211. (d) Martin, M.; Andre, J.-J.; Simon, J. *Nouv. J. Chim.* **1981**, *5*, 485. (e) Lawrence, M. F.; Dodelet, J. P.; Dao, L. H. *J. Phys. Chem.* **1984**, *88*, 950. (f) Stanbery, B. J.; Gouterman, M.; Burgess, R. M. *J. Phys. Chem.* **1985**, *89*, 4950.
- (7) (a) Misra, T. N.; Rosenberg, B.; Switzer, R. *J. Chem. Phys.* **1968**, *48*, 2096. (b) Aoyagi, Y.; Masuda, K.; Namba, S. *J. Phys. Soc. Jpn.* **1971**, *31*, 524. (c) Rabe, J. G.; Bischoff, G.; Schmidt, W. *Jpn. J. Appl. Phys.* **1989**, *28*, 518. (d) Nakamura, S.; Amatatsu, H.; Ozaki, T.; Yamaguchi, S.; Sawa, G. *Jpn. J. Appl. Phys.* **1987**, *26*, 1878. (e) Nakamura, S.; Amatatsu, H.; Ozaki, T.; Yamaguchi, S.; Sawa, G. *Jpn. J. Appl. Phys.* **1986**, *25*, 1064. (f) Yoshino, K.; Gu, H. B. *Jpn. J. Appl. Phys.* **1989**, *28*, L1032.
- (8) Holland, L. *Vacuum Deposition of Thin Films*; Chapman and Hall: London, 1956.
- (9) Nevin, W. A. Ph.D. Thesis, Trent Polytechnic, Nottingham, 1984.
- (10) Morel, D. L.; Ghosh, A. K.; Feng, T.; Stogryn, E. L.; Purwin, P. E.; Shaw, R. F.; Fishman, C. *J. Appl. Phys. Lett.* **1978**, *32*, 495.
- (11) Chamberlain, G. A.; Cooney, P. J.; Dennison, S. *Nature* **1981**, *289*, 45.
- (12) Yasunaga, H.; Kojima, K.; Yohda, H.; Takeya, K. *J. Phys. Soc. Jpn.* **1974**, *37*, 1024.
- (13) Pekker, S.; Janossy, A. In *Handbook of Conducting Polymers*; Skotheim, T. A., Ed.; Marcel Dekker: New York, 1986; Vol. 1, Chapter 2.
- (14) Davis, D. G. In *The Porphyrins*; Dolphin, D., Ed.; Academic Press: New York, 1978; Vol. 5, Chapter 4.
- (15) Nevin, W. A.; Chamberlain, G. A. *J. Chem. Soc., Faraday Trans. 2* **1989**, *85*, 1747.
- (16) Nevin, W. A.; Chamberlain, G. A. *J. Appl. Phys.* **1991**, *69*, 4324.

RECEIVED for review May 13, 1991. Accepted August 14, 1991. This work was supported by the Science and Engineering Research Council and Shell Research Ltd. through a CASE award.

# Multichannel Amperometric Detection System for Liquid Chromatography and Flow Injection Analysis

Johan C. Hoogvliet,\* Johannes M. Reijn, and Wouter P. van Bennekom

Faculty of Pharmacy, Utrecht University, P.O. Box 80.082, 3508 TB Utrecht, The Netherlands

**A multielectrode amperometric detection system has been developed for use in flow systems. The main purpose of this work was to improve the information content relative to single- and dual-working-electrode detectors, without making any concessions to the attainable detection limits. The system consists of a centrally injected detector with a circular array of 16 working electrodes in a parallel configuration, 1 reference electrode, and 1 auxiliary electrode. A computer-controlled, multichannel potentiostat has been constructed to provide for setting each working electrode at a different potential and measuring the resulting currents independently. Adequate individual input-current offsets and low-pass filters allow measurements at 100 pA full scale. In the prototype arrays, glassy carbon, gold, gold-amalgam, and (modified) carbon paste (CP) have been used as electrode materials. For a 16-electrode CP detector applied in the detection of catecholamines in liquid chromatography, a linearity over a range of  $10^{-5}$ – $10^{-9}$  M and a detection limit for epinephrine of approximately 0.1 pg injected have been achieved. A previously unreported feature of a multichannel amperometric detection system is the use of different electrode materials in one electrode array. The possibilities are demonstrated by the detection of glutathione in flow-injection analysis.**

## INTRODUCTION

Amperometry is widely used for detection of electrochemically oxidizable and reducible substances in liquid chromatography (LC) and flow-injection analysis (FIA). An amperometric detector typically consists of a working electrode (WE), a reference electrode (RE), and an auxiliary electrode (AE). The potential applied to the working electrode is kept constant with respect to the potential of the reference electrode and is—for maximum sensitivity and reproducibility—preferably chosen in the limiting current range of the substance(s) to be detected. The detection potential is generally derived from a hydrodynamic voltammogram. This requires the repeated injection of the sample at a number of detection potentials, which is usually time-consuming.

Several efforts to obtain three-dimensional information (current as a function of both time and potential) have been made. This provides information about the electrochemical characteristics of the eluting substances and the possibility to detect each component in a mixture at an optimum detection potential in a single chromatographic run. It is possible to apply fast-scanning voltammetric detection, instead of amperometric detection (1–4). Serious drawbacks, however, are the significant increase in background (mainly charging current) and the shift of the voltammetric wave/peak toward more extreme potentials if the electrode reactions are not fast. These problems can partly be overcome by application of a more sophisticated technique like square-wave voltammetry (5–9) and coulometric compensation of charging current (10–12) and/or by the use of microelectrodes (9, 13, 14). Another approach is the use of a potential scanning technique with a series configuration dual-electrode detector. The potential

is scanned at the upstream electrode, and the current is monitored amperometrically at the downstream electrode (15, 16). However, in all mentioned cases, the detection limits are 2 or 3 orders of magnitude higher than those obtained by conventional amperometric detection systems.

Another step toward three-dimensional information is the use of more working electrodes set at different potentials. Although the expressions "multichannel" and "multielectrode or multiple-electrode detection" have been used quite frequently in the past, nearly all these contributions involve two working electrodes in a series or parallel configuration (dual-electrode detection).

As far as we know, at present only three publications describe real multichannel electrochemical detection systems (more than two independently controlled working electrodes) for application in flow analysis (17–20). In all designs, arrays of working electrodes in a series configuration have been applied.

Matson et al. (17, 18) described an electrochemical detection system with up to 16 separate Coulometric flow-through cells in series. Each working electrode, having its own reference and auxiliary electrode, is controlled by a separate potentiostat, enabling different potential settings. In this approach, neurotransmitters and associated compounds could be characterized at picogram levels. Matsue et al. (19) described the design of a multichannel electrochemical detection system with a microelectrode array flow cell and a homemade computer-controlled 16-channel potentiostat. By applying a sequence of five potential steps to each of the working electrodes, current responses at 80 different potentials could be obtained in 1 cycle of 0.27 s, as was demonstrated for ferrocene derivatives in a FIA setup (detection limit: 20 pmol injected). The design of a multichannel, computer-controlled detection system with an array of 32 gold working electrodes in a thin-layer flow cell has been reported by DeAbreu (20). Apart from the construction of the flow cell (21), up to now no results with that system have been published in the literature.

Additionally, some designs of a multichannel potentiostat for other electrochemical purposes have been published (22–24). In 1980, Schwabe et al. (22) described a multichannel potentiostat for six working electrodes for corrosion research. Dees and Tobias (23) applied a micromosaic electrode in mass-transfer studies. For that purpose, they used a combination of a conventional potentiostat and a specifically designed 120-channel current follower to monitor independently the currents of 100 electrically isolated segments of the micromosaic electrode. In their design, all segments had to be kept at the same potential. More recently, Harrington et al. (24) published a detailed description of a general purpose multiple-electrode (11 working electrodes) potentiostat. Potential steps and scans can be used with their design with the same regime for all working electrodes.

In this paper, we report on a multichannel amperometric detection system. Its development involves (a) a multielectrode detector cell (parallel configuration), (b) a multichannel potentiostat for up to 16 working electrodes, 1 reference electrode, and 1 auxiliary electrode, and (c) hard- and software for control, data acquisition, and data processing. The system

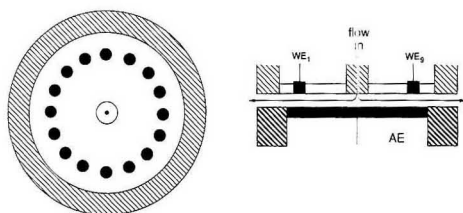


**Figure 1.** Top view (drawn to scale) and cross section of the 16-electrode detector cell.

has been used in liquid chromatography for detection of catechol- and indoleamines and related compounds. Arrays of 4 and 16 equivalent electrodes, set at different potentials, have been used. The detection limit for epinephrine is 100 fg injected. The system has also been used with an array of electrodes which are different in material and/or modification, for the detection of glutathione in a FIA system. This demonstrates a new feature of the multichannel amperometric detection system.

### EXPERIMENTAL SECTION

**Detector Cell and Electrode Arrays.** For the multi-working-electrode version, a modification of a homemade detector cell (PB-2) has been used. Design, construction, and characterization of the electrodes, as well as the hydrodynamics and mass-transfer characteristics of the detector, have been described previously for the one-working-electrode version (25, 26). A minor modification in the design of the multielectrode version has been made: a stainless steel capillary (i.d. 0.25 mm) was mounted in the center of a holder that contains the circular array of working electrodes (Figure 1). The reference electrode was a saturated calomel electrode (SCE), placed downstream. The auxiliary electrode was a glassy carbon (GC) disk of 10-mm diameter, sealed in a glass holder. Silicon was coated on the side of the glassy carbon disk by chemical vapor deposition to ensure a leak-free seal between the electrode material and the glass holder (25). The holder for the working electrodes has been made of poly(trifluorochloroethylene) (Kel-F). Glassy carbon rods of 1-mm diameter (Sigradur-K, Sigrü GmbH, Meitingen, Germany) and gold wire of 1-mm diameter (Drijfhout & Zn. BV, Amsterdam, The Netherlands) were press-fitted in the Kel-F holder at a distance of 2.5 mm from the center (four-electrode arrays). To prevent leaking of electrolyte, a stainless steel ring was pressed around the slightly tapered outer end of the holder. The 16-working-electrode arrays were constructed by drilling 16 holes of 0.8-mm diameter in the holder, symmetrical around the capillary at a distance of 4 mm from the center. The holes were filled with carbon paste (graphite and liquid paraffin 2:1 w/w). Electrical contact was made by copper disks at a depth of 3 mm. Working and auxiliary electrode holders were set at a distance of 50  $\mu$ m by using a three-point poly(vinyl chloride) (PVC) spacer, thus forming a 50- $\mu$ m gap separating the opposing walls of the flow channel (see Figure 1). The cell was placed in a Faraday cage, and all cables were shielded to diminish environmental noise.

**Multichannel Potentiostat.** The computer-controlled, modular potentiostat has been designed to control independently the potential of up to 16 working electrodes, with a common reference and auxiliary electrode. The potentiostat consists of a power supply, an AE/RE board, a decoder board, and an  $i/E$  converter module for each of the 16 channels. The potentiostat is fully computer-controlled. Each  $i/E$  module contains the following: (a) an  $i/E$  converter with an OPA 128 (Analog Devices) as the current follower; the output voltage of the  $i/E$  converter is  $\pm 5$  V full scale; (b) a double-channel DAC ( $2 \times 12$  bits, AD 7547); one channel is used to convert digital signals from the computer into an analog polarization voltage ( $U_{pol}$ ) between  $-3.0$  and  $+2.0$  V vs the reference electrode potential (resolution ca. 1 mV); the other DAC channel is used to control an input current offset (maximum  $\pm 0.2$   $\mu$ A, resolution ca. 50 pA); (c) a digitally addressable array of relays to control the sensitivity at which the currents are measured (1 mA to 1 nA, 7 decades); the sensitivity

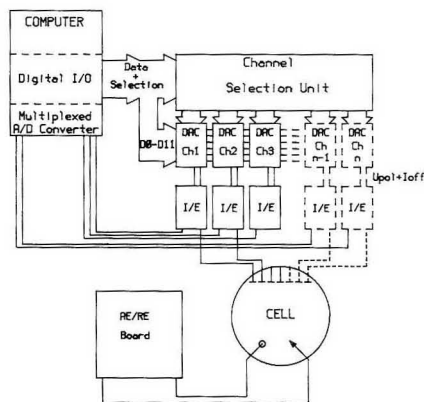


**Figure 2.** Block scheme of the multichannel electrochemical detection system.

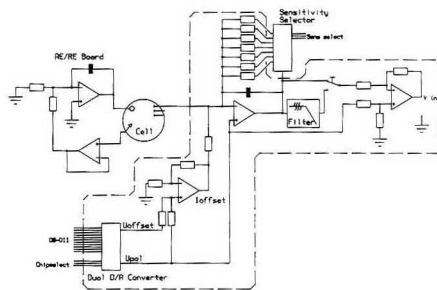


**Figure 3.** Basic circuit of the multichannel potentiostat.

chosen, however, is identical for each channel; (d) an analog low-pass (third-order Bessel) filter with a cut-off frequency of 3.2 Hz; the filter unit can be switched off for application of potential scans and measuring undistorted voltammograms.

The digital input and analog output signals are used through the backplane to interface boards in the personal computer. The basic schematic diagram of the multichannel potentiostat is shown in Figure 2. Figure 3 shows the electronic scheme of an  $i/E$  converter module.

**Computer Hard- and Software.** For data acquisition and control of the multichannel potentiostat, an IBM-AT personal computer was used. The computer was equipped with a Burr-Brown PCI-2000 interface. This interface consists of a carrier (containing 32 1-bit digital I/O ports) and a module, providing for 16-channel multiplexed analog input (12-bit ADC), and a software-selectable gain of 1, 10, 100, or 1000. Digital I/O is used for controlling the sensitivity range, the input current offset, and the potential of the working electrodes. The software-selectable gain of the input module allows for fast autoranging over 3 decades and expansion of the effective sensitivity range to 10 pA full scale. For timing of the data acquisition and for the potential scan-rate control, the programmable interval counter and timer chip of the IBM-AT is used.

Software for control, data acquisition, storage, display, and data processing has been developed in-house and has been written for the main part in Turbo-Pascal V 5.0 (Borland). Several routines have been written in Assembler language. Three different executable programs have been developed: one for electrode pretreatment/conditioning with a sequence of potential steps and/or scans, one for multichannel amperometric detection, and one for data processing and representation.

**Liquid Chromatography and Flow-Injection Analysis.** The LC system consisted of a Bruker LC 21B pump, an injector

with a fixed 20- $\mu$ L sample loop (Rheodyne 7125), and a 100  $\times$  3.0-mm i.d. column with 5- $\mu$ m ChromSphere C18 (Chrompack). The mobile phase was 0.1 M acetate buffer, pH 3.8, with 5% methanol, containing 3 mM heptanesulfonic acid and 0.3 mM EDTA. For elution of both catechol- and indoleamines with their derivatives, a linear methanol gradient was applied between  $t = 5$  min (5% methanol) and  $t = 15$  min (35% methanol). The flow rate was 0.7 mL/min.

The eluent for LC was filtered through a 0.45- $\mu$ m membrane filter (Type SM27, Sartorius) and sonicated. During chromatography, the eluent was degassed with helium.

The FIA measurements were done with a constant-flow plunger pump (Labotron 13A, Gelting, Germany), an injector with fixed 20- $\mu$ L sample loop (Rheodyne 7125), and a single bead string reactor consisting of PTFE tubing (1.8 m  $\times$  1.5-mm i.d.) filled with glass beads (1.0-mm diameter). The carrier was 0.1 M phosphate buffer, pH 7.0. A flow rate of 0.5 mL/min was used.

**Chemicals.** All reagents and solvents were of analytical grade and used as received. All aqueous solutions were prepared with water obtained from a Milli-Q system (Millipore). Solutions of the electroactive substances were made freshly every day. Ascorbic acid (AA), norepinephrine (NE), epinephrine bitartrate (E), dopamine hydrochloride (DA), D-(+)-tryptophan (TRP), 3,4-dihydroxyphenylacetic acid (DOPAC), 4-hydroxy-3-methoxyphenylacetic acid (homovanillic acid, HVA), 5-hydroxytryptamine (5-HT, serotonin), 5-hydroxyindole-3-acetic acid (5-HIAA), 3-methoxytyramine hydrochloride (3-MT), glutathione (reduced form, GSH), 1-heptanesulfonic acid (sodium salt, HSA), and ethylenediaminetetraacetic acid (disodium salt, EDTA) were all from Sigma and were used as received. Graphite (99.999%) was from Le Carbone Lorraine (Gennevilliers, France), and liquid paraffin (spectroscopic quality, Uvasol) was from Merck. Cobalt phthalocyanine was from Aldrich and mercury(II) acetate from Baker.

**Procedures.** The glassy carbon electrode array was polished with 6- $\mu$ m diamond spray on a polishing cloth, and the working electrodes were electrochemically pretreated by potential scans from 0 to +1.5 V vs SCE as described earlier (27). The electrochemical pretreatment was applied by using the pretreatment/conditioning program. The carbon paste electrodes were electrochemically pretreated in the same way as the glassy carbon electrodes. Gold electrodes were conditioned by applying a potential step regime (+0.8/0.0 -0.6/0.0 V vs SCE,  $4 \times 2$  s, 10 cycles) using the pretreatment/conditioning program.

A modified paste was prepared containing 2% (w/w) cobalt phthalocyanine (CoPC) (28, 29). A gold-amalgam electrode was prepared by the deposition of mercury on the gold electrode by electrochemical reduction at -0.5 V vs SCE of a solution of mercury(II) acetate (several 20- $\mu$ L injections of a 1 mM solution in 1 M  $\text{KNO}_3$ ), using the FIA system described above.

## RESULTS AND DISCUSSION

**System Design. Multielectrode Cell.** The centrally injected detector contains hydrodynamically equivalent working electrodes in a parallel configuration. The working electrodes are placed in a circle, equidistant from the inlet capillary (Figure 1). Compared to a single-electrode detector, with the working electrode placed in the center and opposite the capillary, there is some loss in sensitivity due to decreased mass transfer. For the 16-electrode CP detector, it can be calculated that the sensitivity per electrode is approximately one-third of the sensitivity that could have been obtained with one working electrode of the same dimension placed in the center, opposite the capillary, assuming a laminar flow profile (26).

Several working electrode arrays have been constructed. Because arrays of carbon paste electrodes can be constructed relatively easily, initially the 16-electrode versions have been made of this type. Several 4-working-electrode arrays have also been made with glassy carbon or gold as the electrode material. In the construction of the latter electrode arrays, special care must be taken to prevent leakage from electrolyte solution in gaps between electrodes and the holes in the Kel-F holder, in which the electrodes are pressed. Otherwise, background and noise level may be excessive (25).

**Multielectrode Potentiostat.** A multichannel potentiostat is required for setting each working electrode at a different potential and measuring the resulting currents individually. Design and development of the electronics for a modular potentiostat for up to 16 working electrodes and a common reference and auxiliary electrode resulted in a circuitry that differs from that used in conventional (bi)potentiostats. In the generally used circuit to achieve potentiostatic control in a three-electrode system (one WE), the working electrode is connected to the inverting input of a current follower and is virtually grounded. A feedback system, including the reference and auxiliary electrodes, makes the potential of the reference electrode equivalent to the source voltage, which is added to the control amplifier (AE/RE board). Because the working electrode remains at virtual ground, the voltage difference between working and reference electrodes is equal to the source voltage.

The simultaneous control of two working electrodes requires a bipotentiostat. Usually, one electrode is controlled in the way described above for a single-working-electrode system. WE2 is connected to a second current follower, which receives at its noninverting input a potential that is the difference of the source voltages for the two working electrodes. So, WE2 is offset with respect to WE1.

The concept to control more than two working electrodes is as follows. Separate current followers are used for each working electrode. Each of these receives its own source voltage ( $U_{\text{ref}}$ ) at the noninverting input. The AE/RE circuit is essentially the same as used in a conventional potentiostat. However, no source voltage is added to the control amplifier. A potential waveform, affecting all working electrodes in the same way, however, could be applied, in just the same way as is done in conventional circuits. In broad outline, the same setup has been used by Matsue et al. (19) and by Harrington et al. (24).

**Software.** Multichannel electrochemical detection is difficult to perform without computerized instrumentation. Therefore, both the control and data acquisition are fully computerized. To reduce and standardize the amount of data, the number of data sampled per run and per channel is predetermined at 1000. This implies that the sampling frequency is variable and dependent on the selected duration of the run. The time required to obtain a 16-point voltammogram and an on-line screen display of the 16 chromatograms/FIA responses is 30 ms. So, the minimum time for a standard run is ca. 30 s, which is short enough for most FIA applications.

The menu-driven data-acquisition program provides for autoranging over 3 decades. One of the options in the program automatically switches all channels off after overload conditions that exceed a predetermined time interval. All responses are displayed on-line ( $i$  vs  $t$ ) with different colors. The sampled data is stored on a hard disk in a binary data file.

The data-processing and -representation program has been designed to provide for spike rejection, smoothing (digital filter), baseline correction, calibration of the signals, and peak analysis (determination of retention times, peak heights, and peak areas). Several data representation formats are available. The graphical representation includes three-dimensional plots of current vs time and potential, plots of current vs time and channel number, or two-dimensional plots of the currents of one or more selected channels vs time (chromatogram/FIA response) or vs potential (hydrodynamic voltammogram). Numerical representation includes tables with channel numbers, potentials, calibration factors, and—per channel and per peak—the retention times, peak heights, and peak areas. Processed files can be stored on a disk; graphical results can be presented on a plotter or laser printer.

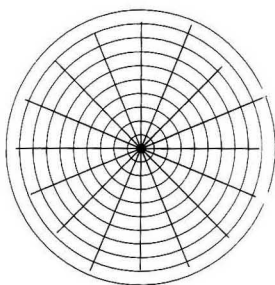


Figure 4. Radial response diagram for the 16-electrode carbon paste array: ca. 400 ng (2 nmol) of epinephrine injected.

**Performance of the Multielectrode System. Equality of Responses.** Ideal behavior of the multielectrode detector would include an equivalent response (signal, noise, and background) of all channels with the working electrodes set at the same potential, no cross-talk between the individual channels, and signal-to-noise ratios comparable with conventional single-electrode amperometric detectors. Equality of the responses is determined by the hydrodynamics and mass-transfer characteristics of the cell, by electrode and detector geometry, by electrode kinetics, and by proper configuration/adjustment of the electronics in the potentiostat. The electrode and detector geometry and the design of the electronic circuitry meet these requirements. A software program has been developed for pretreatment/conditioning of the working electrodes. With this program, a regime of potential steps and/or scans can be applied to all working electrodes in the same way. Its main purpose is to remove as much as possible any inequalities due to differences in electrode kinetics. It can also be used to improve the performance of the electrodes by removing impurities and/or increasing the electron-transfer rates.

The equivalence of the channels has been investigated by comparing the responses of 16 channels—each set at +0.6 V vs SCE—after injection of a standard sample of epinephrine in the LC system. A typical result is plotted in a radial response diagram (Figure 4). The relative standard deviation of the average response was 4.5%. The same level of inaccuracy is obtained by regenerating a fresh carbon paste surface for an individual electrode. Therefore, the observed inhomogeneity of the response pattern in Figure 4 is not the result of differences in geometry or mass transfer. The observed small differences in response can be compensated for by software, as they remain constant as long as the detector is not reassembled. A calibration procedure is included in the data-processing program for that purpose.

Noise and background currents did show larger differences between the individual channels, both for the 16-channel CP and the 4-electrode GC arrays. Probably, there are differences in the quality of the individual electrode surfaces on a microscale that are not expressed in the magnitude of the signal responses. Application of the pretreatment procedure did not diminish these differences.

Cross-talk between individual channels, with the working electrodes at different potentials, has never been observed, neither at a high nor at a low sensitivity range, at flow rates of 0.25 mL/min and higher.

**Detection Limits.** By using the built-in input current offset in each channel, the highest sensitivity at which current could be measured in practice (at  $E < +0.9$  V vs SCE for CP and at  $E < +1.3$  V vs SCE for GC) turned out to be 100 pA full scale. By the application of the digital filter (Savitzky-Golay type) in the data-processing program, only a minor im-

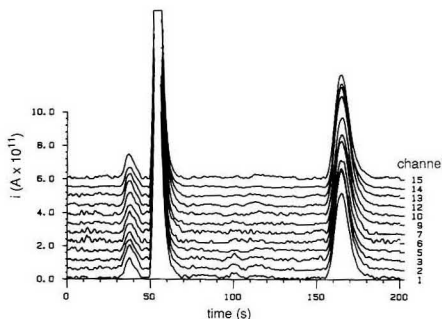


Figure 5. Chromatograms of ca. 4 pg (20 fmol) of epinephrine injected: 16-electrode carbon paste array,  $E = +0.6$  V vs SCE. The first two peaks are injection peaks, the third one is epinephrine.

Table I. Comparison of Detection Limits per Channel for Smoothed Data<sup>a</sup>

channel	$i_p$ , pA	$s$ , pA	det limit, <sup>b</sup> pg
1	52	0.5	0.10
2	60	0.6	0.10
3	57	0.5	0.10
5	62	0.4	0.08
6	51	0.7	0.17
7	57	0.8	0.17
9	55	0.7	0.15
10	58	0.6	0.12
12	60	0.6	0.12
13	57	0.5	0.10
14	57	0.6	0.13
15	64	0.6	0.11
av	57.5	0.6	0.12

<sup>a</sup> Injections of ca. 4 pg (20 fmol) of epinephrine, in duplicate.

<sup>b</sup> Quantity for which  $i_p = 3s$  ( $i_p$  is the peak height,  $s$  is the standard deviation of the noise).

provement in the signal-to-noise ratios could be obtained (factor 1.5). Figure 5 shows a set of 12 digitally filtered (13-point smooth) chromatograms of 4 pg of epinephrine injected (20  $\mu$ L of a 1 nM solution). Four of the 16 channels have not been plotted, because the noise or background was significantly larger than the average value for all channels. The average detection limit for epinephrine detected at an individual working electrode ( $n = 12$ ) was calculated as 0.12 pg or 25 pM (for a signal equal to 3 times the standard deviation of the noise). Some characteristics are shown in Table I.

The low detection limits obtained with the described system are probably due to a combination of well-designed electronic circuits, and the choice of the carbon paste electrode material. Previous (unpublished) work done by us using a circular gold electrode array, constructed with thick-film technology, revealed relatively high background currents, more noise, and a worse reproducibility compared to the carbon paste electrode array.

**Linearity.** The linearity of the 16-channel carbon paste detector has been evaluated from log-log plots of peak height vs concentration. Epinephrine solutions ranging from 10  $\mu$ M to 1 nM were used, and two injections at each concentration were measured. Table II shows the slope, standard error of slope, and correlation coefficient obtained from log-log plots of peak height vs concentration for the 16 channels. The log-log plots were all linear, and the slopes were not deviating very much from unity, indicating linearity of response over 4 decades. Intercepts from lin-lin (linear-linear) plots in the same concentration range showed no statistically significant deviations from zero.



**Table II. Linearity of the 16-Electrode Carbon Paste Detector<sup>a</sup>**

channel	slope <sup>b</sup>	corr coeff
1	0.976 ± 0.003	0.999 8
2	0.972 ± 0.002	0.999 8
3	0.978 ± 0.003	0.999 8
4	1.000 ± 0.003	0.999 7
5	0.968 ± 0.002	0.999 8
6	0.974 ± 0.003	0.999 7
7	0.977 ± 0.002	0.999 8
8	0.988 ± 0.002	0.999 98
9	0.991 ± 0.002	0.999 8
10	0.978 ± 0.002	0.999 998
11	0.975 ± 0.001	0.999 97
12	0.997 ± 0.001	0.999 9998
13	0.986 ± 0.001	0.999 9994
14	0.978 ± 0.001	0.999 998
15	0.985 ± 0.001	0.999 997
16	0.977 ± 0.001	0.999 9994

<sup>a</sup>log-log plots, range 4 pg to 40 ng of epinephrine injected ( $10^{-9}$ – $10^{-6}$  M), in duplicate. <sup>b</sup>The tabulated errors are standard errors of slope.

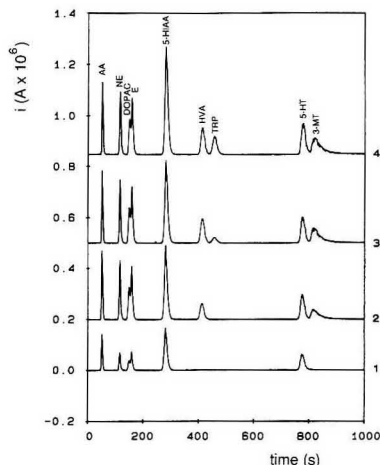


**Figure 6.** Chromatograms of a mixture of 2 nmol of AA, NE, DOPAC, E, 5-HIAA, HVA, TRP, 5-HT, and 3-MT. Detector: 4-electrode glassy carbon array, E1 = 500 mV, E2 = 700 mV, E3 = 900 mV, and E4 = 1100 mV vs SCE. Gradient elution.

**Application in LC.** The 4-electrode GC and the 16-electrode CP arrays have been applied in the amperometric detection of catecholamines, indoleamines, and some precursors and metabolites. An example is shown in Figure 6 for detection with the 4-electrode GC array. In Figure 7a, the resulting responses from 16-electrode CP detection have been plotted in a three-dimensional way. From the latter data, the  $i/E$  relations (equivalent to hydrodynamical voltammograms) can be derived (Figure 7b). The nonideality of the shapes is probably related to the carbon paste electrode material used.

**Application in FIA.** An advantage of the chosen configuration is that electrode arrays can be used consisting of different electrode materials and/or modifications. Because each electrode may respond differently to a particular substance, the information content is further improved relative to the same detector with only one type of electrode material or modification. To explore this possibility, a 4-electrode array was fabricated consisting of a gold (Au), a gold–amalgam

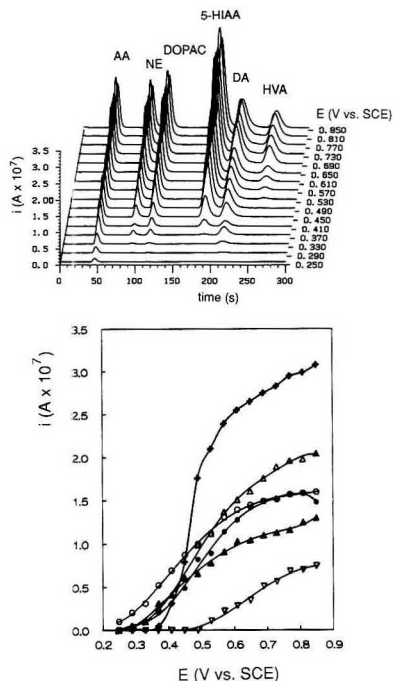


**Figure 7.** (a, top) Three-dimensional chromatogram of a mixture of 2 nmol of AA, NE, DOPAC, DA, 5-HIAA, and HVA. Detector: 16-electrode carbon paste array. Isocratic elution, 5% methanol. (b, bottom)  $i/E$  relations of the six components: AA (O), NE (●), DOPAC (Δ), DA (▲), 5-HIAA (+), and HVA (▽).

(Au–Hg), a carbon paste (CP), and a cobalt phthalocyanine modified carbon paste (CoPC–CP) electrode (Figure 8a). This array was used in the detection of glutathione (GSH), a thiol-containing tripeptide, in a FIA system. As can be seen in Figure 8b, each of the four electrodes responds in a different way to the thiol. Unmodified CP is not suitable for the detection of glutathione, while the modified CP is (28, 29). The small response at the gold electrode is probably related to adsorption and decreases upon repeated injections. The gold–amalgam electrode yields the largest response, which is due to the oxidation of mercury, catalyzed by the thiol group.

## CONCLUSIONS

The described system is superior to earlier reported potential scanning methods in terms of data-acquisition time for the voltammograms and in terms of detection limits. It is superior to single- and dual-working-electrode systems in terms of information content, while it is comparable to these systems in terms of detection limits. Detection limits in the range reported by us have not yet been reported for a true multichannel electrochemical detection system, as far as we know.

The use of a variety of electrode materials and/or modifications can further enhance the information content of multichannel electrochemical detection, relative to a single electrode material/modification. This is a new feature of a multichannel electrochemical detection system not previously demonstrated.

Future work in our laboratory will include the construction of 16-electrode glassy carbon and platinum arrays, the de-

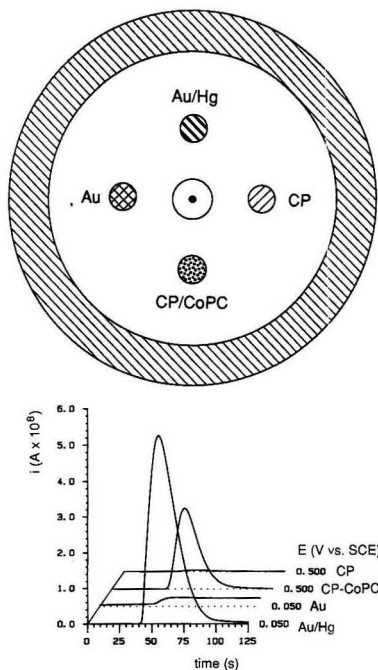


Figure 8. (a, top) Top view of the array of four different electrodes (drawn to scale). (b, bottom) FIA response of 20 nmol of glutathione.

termination of neurotransmitters in biological samples, the application of statistical approaches for the evaluation of the information content in the data (i.e., multivariate resolution of peaks), and the development of multienzyme amperometric biosensors, using different enzymes coated on the working electrodes.

#### ACKNOWLEDGMENT

We acknowledge the contribution of Ronald G. C. van Trigt for the construction of the multichannel potentiostat, of

Willem van der Horst for the fabrication of the electrode arrays, of Rob van Mastriigt and Leo A. van der Hark for development of the software, and of Peter J. H. J. van Os for assistance in the experimental work. We also thank Cees J. van Velzen and Arnold Dirksen for helpful suggestions.

#### LITERATURE CITED

- (1) Janata, J.; Ruzicka, J. *Anal. Chim. Acta* **1982**, *139*, 105-115.
- (2) Caudill, W. R.; Ewing, A. G.; Jones, S.; Wightman, R. M. *Anal. Chem.* **1983**, *55*, 1877-1881.
- (3) Ploegmakers, H. H. J. L.; Mertens, M. J. M.; van Oort, W. J. *Anal. Chim. Acta* **1985**, *174*, 71-82.
- (4) Gunasingham, H.; Fleet, B. In *Electroanalytical Chemistry*; Bard, A. J., Ed.; Marcel Dekker: New York, 1988; Vol. 15.
- (5) Wang, J.; Ouziel, E.; Yarnitzky, C.; Ariel, M. *Anal. Chim. Acta* **1978**, *102*, 99-112.
- (6) Samuelsson, R.; O'Dea, J.; Osteryoung, J. *Anal. Chem.* **1980**, *52*, 2215-2216.
- (7) Scanlon, J. J.; Flaquer, P. A.; Robinson, G. W.; O'Brien, G. E.; Sturrock, P. E. *Anal. Chim. Acta* **1984**, *158*, 169-177.
- (8) Ploegmakers, H. H. J. L.; van Oort, W. J. *Anal. Instrum.* **1987**, *16*, 467-486.
- (9) Kounaves, S. P.; Young, J. B. *Anal. Chem.* **1989**, *61*, 1469-1472.
- (10) Last, T. A. *Anal. Chem.* **1983**, *55*, 1509-1512.
- (11) Last, T. A. *Anal. Chim. Acta* **1983**, *155*, 287-291.
- (12) Trubey, R. K.; Nieman, T. A. *Anal. Chem.* **1986**, *58*, 2549-2550.
- (13) Goto, M.; Shimada, K. *Chromatographia* **1986**, *27*, 631-634.
- (14) White, J. G.; St. Claire, R. L., III; Jorgenson, J. W. *Anal. Chem.* **1988**, *56*, 293-298.
- (15) Lunte, C. E.; Ridgway, T. H.; Heineman, W. R. *Anal. Chem.* **1987**, *59*, 761-766.
- (16) Lunte, C. E.; Wheeler, J. F.; Heineman, W. R. *Anal. Chim. Acta* **1987**, *200*, 101-114.
- (17) Matson, W. R.; Langlais, P.; Volicer, L.; Gamache, P. H.; Bird, E.; Mark, K. A. *Clin. Chem.* **1984**, *30*, 1477-1488.
- (18) Matson, W. R.; Gamache, P. H.; Beal, M. F.; Bird, E. D. *Life Sci.* **1987**, *41*, 905-908.
- (19) Matsue, T.; Aoki, A.; Ando, E.; Uchida, I. *Anal. Chem.* **1990**, *62*, 407-409.
- (20) DeAbreu, M. P. *Diss. Abstr. Int. B* **1989**, *50*, 147.
- (21) DeAbreu, M. P.; Purdy, W. C. *Anal. Chem.* **1987**, *59*, 204-206.
- (22) Schwabe, K.; Oelssner, W.; Suschke, H. D. *Z. Phys. Chem. Leipzig* **1980**, *267*, 113-121.
- (23) Dees, D. W.; Tobias, C. W. *J. Electrochem. Soc.* **1987**, *134*, 369-377.
- (24) Harrington, M. S.; Anderson, L. B.; Robbins, J. A.; Karweik, D. H. *Rev. Sci. Instrum.* **1989**, *60*, 3323-3328.
- (25) Hoogvliet, J. C.; van Bezooen, J. A. G.; Hermans-Lokkerbol, A. C. J.; van der Poel, C. J.; van Bennekom, W. P. *J. Liq. Chromatogr.* **1983**, *6*, 1849-1861.
- (26) Dalhuysen, A. J.; van der Meer, Th. H.; Hoogendoorn, C. J.; Hoogvliet, J. C.; van Bennekom, W. P. *J. Electroanal. Chem.* **1985**, *182*, 295-313.
- (27) Hoogvliet, J. C.; van der Beld, C. M. B.; van der Poel, C. J.; van Bennekom, W. P. *J. Electroanal. Chem.* **1986**, *201*, 11-21.
- (28) Halbert, M. K.; Baldwin, R. P. *J. Chromatogr.* **1985**, *346*, 43-49.
- (29) Halbert, M. K.; Baldwin, R. P. *Anal. Chem.* **1985**, *57*, 591-595.

RECEIVED for review January 29, 1991. Accepted June 27, 1991.

# Development of the H-Point Standard-Additions Method for Ultraviolet-Visible Spectroscopic Kinetic Analysis of Two-Component Systems

Francisco Bosch-Reig, Pilar Campins-Falcó,\* Adela Sevillano-Cabeza, Rosa Herráez-Hernández, and Carmen Molins-Legua

Departamento de Química Analítica, Facultad de Química, Universidad de Valencia, Burjassot (Valencia), Spain

**This work establishes the fundamentals of the H-point standard-additions method (HPSAM) to kinetic data for the simultaneous determination of binary mixtures or the calculation of analyte concentrations, completely free from bias error. Two variants of the method are proposed; one is applied when the reaction of one component is faster than that of the other or the latter does not take place at all; the other is used when the rate constant of the two components are time-dependent. Also it is demonstrated that the shown accuracy of the method allows its application as a diagnostic tool for the reliability of analytical results. The method was applied to the determination of manganese and vanadium by simultaneous oxidation of Pyrogallol Red and also to the determination of creatinine in serum samples and to the simultaneous determination of creatinine and albumin by the Jaffé method.**

## INTRODUCTION

The development of methods for the simultaneous determination of binary occasionally ternary mixtures of closely related species on the basis of differences in their rates of reaction with a common reagent is one of the great successes of kinetic analysis. The evaluation of kinetic data obtained by a kinetic method of analysis based on the reaction of a mixture of substances with a given reagent depends on the ratios between the rate constants of the different reactions involved.

For a binary system consisting of two species X and Y that react with a common reagent R, if the reaction of X is faster than that of Y and the former finishes at a fixed time while the other continues to take place or if the difference between the rates of the two reactions is large enough, component X can be accurately determined in the presence of Y. On the other hand, if the rate of the reaction between Y and R is quite low but conditions can be changed on completion of the reaction of X, then the reaction of Y can be sped up and this component determined as well (1).

The kinetic determination of the more reactive species in a binary mixture is subject to a positive error arising from the slow reaction that takes place in parallel. The magnitude of such an error will depend both on the rates of the reactions involved and on the concentration ratio of the reactants in the mixture.

Some compounds react at a similar rate with a given reagent, so they have to be determined by differential reaction-rate methods.

The literature abounds with differential rate procedures, many of which were reported in the last few years. Most of such methods are aimed at the determination of inorganic species in general, and to transition metal ions and non-metal anions in particular (1).

Logarithmic-extrapolation, single-point, tangent, proportional-equation, and linear graphical methods are some of the

differential kinetic methods most frequently used to determine two-component mixtures from rate measurements (2). Of these, the proportional-equation method appears to be the most flexible for simultaneous determinations; however, it involves the accurate evaluation of rates and proportionality constants and is only applicable in the absence of synergistic effects.

On the other hand, we recently developed a modified equilibrium standard-addition method called the "H-point standard-additions method" (HPSAM) (3, 4) for the determination of unbiased analyte concentrations in the event that the presence of a direct interferent and/or the total Youden blank (TYB) is known. The method relies on the use of multipoint signal data (analytical signal data obtained at two accurately selected wavelengths) to transform otherwise uncorrectable to correctable errors and evaluate the analyte and interferent concentrations. The HPSAM has been applied with analytical spectroscopy to resolve mixtures of two components with extensively or fully overlapped spectra (5). One modification of the HPSAM uses absorbance increments as analytical signals as these only depend on the analyte concentration (6). Such a modified method is of special use when only the analyte concentration is to be calculated or only the overall sample spectrum is available, and in applying the single-standard calibration method.

This work was aimed at establishing the fundamentals for application of the HPSAM to kinetic data for the simultaneous determination of binary mixtures or the calculation of analyte concentrations completely free from bias errors. For this purpose we used two variants of the HPSAM: one is applied when the reaction of one component is faster than that of the other or the latter does not take place at all; the other is used when the rate constants of the two components are time-dependent.

**Theoretical Background. (A) Analysis of Two Species of Which Only One Evolves with Time.** The HPSAM as applied to equilibrium and spectrophotometric data allows the determination of two species X and Y in a mixture, even if their spectra are completely overlapped or only the analyte concentration free of bias error when the spectrum of the sample matrix is known.

The determination of the concentration of X by the HPSAM under these conditions entails selecting two wavelengths  $\lambda_1$  and  $\lambda_2$  lying on each side of the absorption maximum of Y—and at the same distance if the peak is regularly shaped—such that the absorbances of this latter component are the same at both. Then, known amounts of X are successively added to the mixture and the resulting absorbances are measured at the two aforesaid wavelengths. The two straight lines thus obtained intersect at the so-called "H-point" ( $-C_H, A_H$ ), where  $-C_H$  ( $=-C_X$ ) is the unknown concentration of X and  $A_H$  ( $=A_Y$ ) is the analytical signal of Y in the former case and represents the constant bias error of the sample in the latter.

The foundation of the HPSAM for the treatment of kinetic data under the assumption that only one of the species, X,

\* To whom correspondence should be addressed.

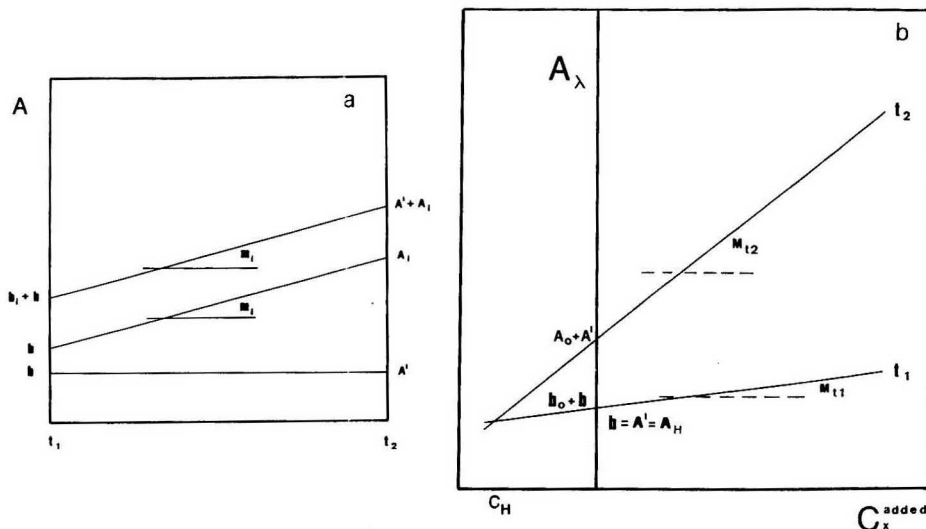


**Figure 1.** (a) Required shape of the  $A-t$  curves for X and Y in case A (see text). (b) Plot of the H-point standard-additions method for case A.  $C_x^{\text{added}}$  is the added concentration of X.

evolves with time, is exposed below. In this case, the variables to be fixed are two times  $t_1$  and  $t_2$  at which the species Y, which does not evolve with time or over the range between these two times, should have the same absorbance, rather than two wavelengths  $\lambda_1$  and  $\lambda_2$  as in the HPSAM as applied to analytical signals obtained at equilibrium (3, 4).

The absorbances of X at a given wavelength  $\lambda$  and two times  $t_1$  and  $t_2$  will be  $b_i$  and  $A_i$  (Figure 1a), while those of Y under the same conditions will be  $b$  and  $A'$ —equal in this case. They will be related through the following equations:

$$(X) \quad A_i = b_i + m_i t_j \quad (t_1 \leq t_j \leq t_2; i = 0, 1, n \dots) \quad (1)$$

$$(Y) \quad A' = b + m t_j \quad (m = 0) \quad (2)$$

where the subscripts  $i$  and  $j$  denote the different solutions for  $n$  additions of the X concentration prepared to apply the HPSAM and for a time comprised in the  $t_1-t_2$  range, respectively. Thus, the overall absorbances of the X-Y mixture at  $t_1$  and  $t_2$  will be  $A_{t_1} = b_i + b$ , and  $A_{t_2} = A_i + A'$ , respectively.

On the other hand, application of the HPSAM at the two aforesaid times will yield

$$A_{t_1} = b_0 + b + M_{t_1} C_i \quad (3)$$

$$A_{t_2} = A'_0 + A' + M_{t_2} C_i \quad (4)$$

which intersect at point H  $(-C_H, A_H) \equiv (-C_X, A_Y)$  (Figure 1b).

At the intercept

$$b_0 + b + M_{t_1} C_H = A'_0 + A' + M_{t_2} C_H \quad (5)$$

Hence

$$C_H = [(A' - b) + (A_0 - b_0)] / (M_{t_1} - M_{t_2}) \quad (6)$$

As species Y is assumed not to evolve over time, then  $A' = b$  and

$$C_H = (A_0 - b_0) / (M_{t_1} - M_{t_2}) \quad (7)$$

which is equivalent to the existing  $C_X (=b_0/M_{t_1} = A_0/M_{t_2})$ . Likewise, substitution of  $C_X$  into eq 3 yields  $A_H = b$ .

As the method of standard additions entails calculating the unknown concentration by extrapolation at a zero ordinate, taking into account that, according to the HPSAM  $A_i = f(t_j)$

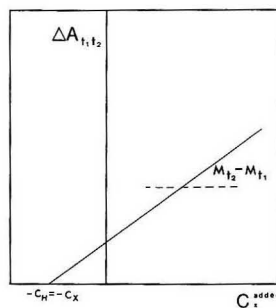


**Figure 2.** Plot of the H-point standard-additions method using absorbance increments for case A.

$= 0$ , then  $b_i = 0$  and  $m_i = m = 0$ , this will be the H-point, at which the slope of the  $A$  vs X concentration plot equals that of species Y.

The overall equation for the absorbance at such a point will thus simplify to

$$A' = b = A_H = A_Y \quad (8)$$

The intercept of the straight lines represented by eqs 3 and 4 will thus directly yield the unknown X concentration ( $C_X$ ) and the analytical signal of species Y ( $A_Y$ ) corresponding to  $t_1$  and  $t_2$  in the original samples, as the two times were chosen in such a way that the latter species had the same absorbance at both. This analytical signal will enable calculation of the concentration of Y from a calibration curve, as this corresponds to the zero point in the calibration curve of the analyte in the presence of the sample according to the basis of the standard-addition method (MOSA).

If the version of the HPSAM involving the use of the absorbance increment as analytical signal is employed by use of  $\Delta A_{t_1-t_2}$  instead  $\Delta A_{\lambda_1-\lambda_2}$  (6), the resulting graph will be similar to that shown in Figure 2 and will allow the analyte concentration,  $C_X$ , to be calculated with no systematic, constant, or

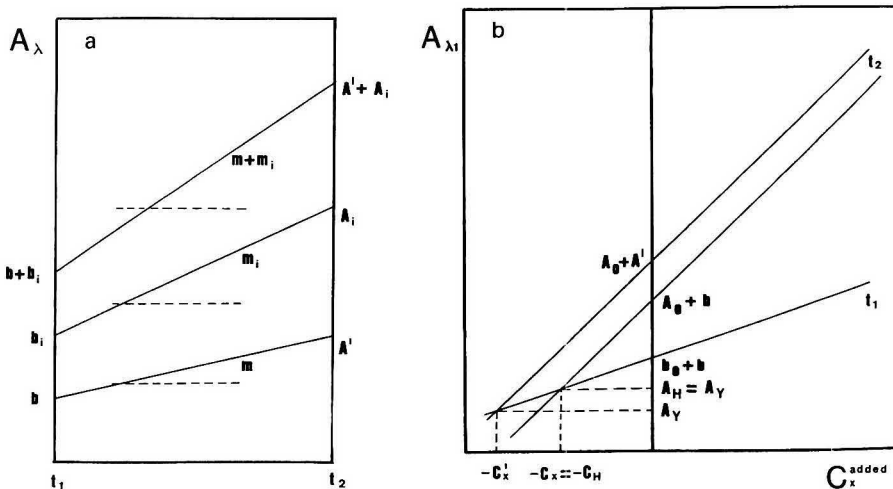


Figure 3. (a) Shape of the  $A-t$  curves for X and Y in case B. (b) Plots of the H-point standard-additions method for case B treated according to case A.

proportional error thanks to the intrinsic features of the HPSAM and the nature of the MOSA. This variant should be of use whenever only the analyte is to be determined or when the  $A-t$  curve rather than the composition of the matrix is known. It should also be useful to apply the single-standard calibration method, which features greater simplicity and rapidity. This version can often be comparable with the classical kinetic method based on the  $\Delta A$  vs  $C_{\text{analyte}}$  plot. This method can also be used to diagnose the occurrence of interferences with a given analytical procedure as, in the absence of errors, the plot of any  $\Delta A_{t_1-t_2}$  against the added analyte concentration will have a common point  $(-C_H, 0)$ .

**(B) Analysis of Two Species with Overlapped Time Evolutions.** When the two species in a mixture, X and Y, evolve with time,  $C_X$  and  $A_i$  can be calculated as shown below by plotting the analytical signal  $\Delta A_{t_1-t_2}$  against the added concentration of X at two wavelengths  $\lambda_1$  and  $\lambda_2$ , provided the absorbances of the Y component at these two wavelengths are the same ( $A_Y$ ), and so are thus the  $\Delta A_{t_1-t_2}$  values. Below are described the HPSAM bases that apply under these conditions, namely the use of two times  $t_1$  and  $t_2$  and two wavelengths  $\lambda_1$  and  $\lambda_2$ , additivity of absorbances and absence of synergistic effects. Thus, if the absorbance is plotted at the two above times and wavelength  $\lambda_1$ , and X is assumed to react faster than Y (Figure 3a), the intercept of the lines described by eqs 3 and 4 will not yield the data pair  $(-C_X, A_i)$ , but rather larger values of these parameters, as can be seen from Figure 3b. By plotting  $\Delta A_{t_1-t_2}$  against  $C_X^{\text{added}}$  at  $\lambda_1$ , one obtains the straight line shown in Figure 4. The intercept of the line can be arranged to

$$\Delta A_0 = (A_0 + A') - (b_0 + b) = (A_0 - b_0) + (A' - b) = \Delta A_X^0 + \Delta A_Y^0 \quad (9)$$

which would correspond to the analytical signal obtained from the solution containing the sample alone. The analytical signal for any other solution would be given by

$$\Delta A^n = \Delta A_X^n + \Delta A_Y^n = \Delta A_X^n + \Delta A_i^0 \quad (10)$$

Thus, the intercept with the x axis ( $-C_X'$ ) will provide a concentration equivalent to the sum of the concentrations of the two species, X and Y, while the intercept with the y axis

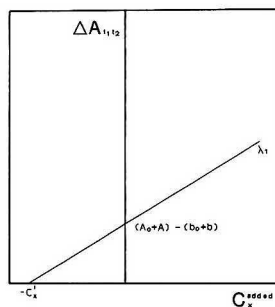


Figure 4. Plot of the H-point standard-additions method using absorbance increments between  $t_1$  and  $t_2$  for case B at  $\lambda_1$ .

will be equivalent to the sum of absorbance increments ( $\Delta A$ ). This plot (Figure 4) provides information complementary to that supplied by Figure 3b.

The application of an analogous procedure at  $\lambda_2$  will yield absorbance values and plots of these against the added analyte concentration similar to those in Figures 3 and 4 and similar nonconclusive results.

The problem can be solved by considering the results obtained at  $\lambda_1$  and  $\lambda_2$ , jointly as these two wavelengths are chosen in such a way that Y has the same absorbance and hence the same  $\Delta A_{t_1-t_2}$  value at both, as can be seen from Figure 5. This figure is similar to Figure 1, with the exception of the analytical variables. Point H in Figure 5 corresponds to the intercept of the straight lines

$$(\Delta A_{t_1-t_2})_{\lambda_1} = \Delta A_X^{01} + \Delta A_Y^0 M_{\lambda_1} C_i \quad (11)$$

$$(\Delta A_{t_1-t_2})_{\lambda_2} = \Delta A_X^{02} + \Delta A_Y^0 M_{\lambda_2} C_i \quad (12)$$

with

$$C_H = (\Delta A_X^{02} - \Delta A_X^{01}) / (M_{\lambda_2} - M_{\lambda_1}) \quad (13)$$

or

$$C_X = \Delta A_X^{02} / M_{\lambda_2} = \Delta A_X^{01} / M_{\lambda_1}$$



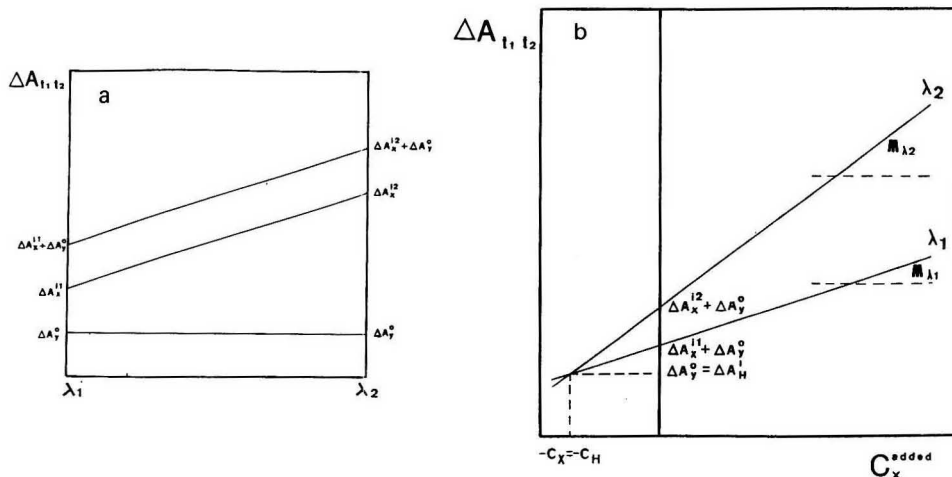


Figure 5. (a) Required shape of the  $\Delta A_{t_1, t_2}$  vs  $\lambda_i$  graphs in case B. (b) Plot of H-point standard-additions method for case B.

Table I. Results for Different Mixtures of Manganese and Vanadium

true concn, mg/L		mean concn found and std dev, mg/L									
$C_V$	$C_{Mn}$	proportional eqs				HPSAM					
		$\bar{C}_V$	$S$	$\bar{C}_{Mn}$	$S$	5 min		10 min			
		$\bar{C}_V$	$S$	$\bar{C}_{Mn}$	$S$	$\bar{C}_V$	$S$	$\bar{C}_{Mn}$	$S$	$\bar{C}_{Mn}$	$S$
0.20	0.55	0.22	0.04	0.57	0.04	0.24	0.05	0.56	0.04	0.56	0.04
0.20	1.10	0.21	0.04	1.12	0.04	0.26	0.06	1.19	0.06	1.18	0.04

Likewise, species Y can be determined from  $\Delta A_{t_1}^0 = \Delta A_H$  by one of two procedures, namely (a) by using  $\Delta A_H$  and a calibration graph for Y [ $\Delta A_Y = f(C_Y)$ ] at either of the chosen wavelengths ( $\lambda_1$  or  $\lambda_2$ ) or (b) by using the plot of  $A_{\lambda_1}$  or  $A_{\lambda_2}$  against the added concentration of X (Figure 3b). As can be seen from the figure, point H can be located at either wavelength by calculating the difference ( $A' - b$ ) and subtracting it from the analytical signals obtained at  $t_2$ ; i.e. by subtracting the calculated value  $\Delta A_Y^0 = \Delta A_H$  we will obtain the  $A_i + b$  values and hence be in a position to apply the H-point method when the absorbance of species Y is constant. Thus, by tracing a parallel to the straight line obtained at  $t_2$ , we shall obtain the actual H-point as the intercept with the straight line at  $t_1$ , the intercepts on the x and y axis will be  $-C_X = C_H$  and  $A' = b = A_H$ , respectively. From a calibration curve for Y at  $t_1$ , one can readily calculate the concentration of this species.

*Some Representative Examples.* Manganese and vanadium can be determined simultaneously by oxidation of Pyrogallol Red (PGR) using an equation system in which the absorbance at a fixed time is assumed to be proportional to the overall concentration of the two elements and their effects on the absorbance of PGR to be additive (7). This simultaneous determination can also be accomplished by using the above-described procedure A, as between 5 and 10 min the oxidation of PGR is due to vanadium exclusively and the oxidation of manganese is finished in less than 5 min. Accordingly, the HPSAM was applied to two samples containing 0.20 mg/L V(V) and 1.10 mg/L and 0.55 mg/L Mn(VII), respectively. The procedure applied was described in detail elsewhere (7). The analyte, V(V), was added at a concentration up to 1.63 mg/L, the absorbance was read after 5 and 10 min, and five replicates were run in every case. The application of the HPSAM allowed us to calculate the concentration of vana-

dium directly from the intercept of the two straight lines obtained by measuring the absorbance of the different solutions at 5 and 10 min.

A calibration graph and the  $A_H$  value allowed the concentration of manganese to be calculated. The results obtained are listed in Table I, which also gives those obtained by using the proportional equations given in ref 7. As can be seen, the two sets of results are quite consistent. The HPSAM will prove to be advantageous when there are bias errors, which it takes due account of, and when only vanadium is to be determined and thus no calibration graph for manganese needs to be run.

Another example of the application of the HPSAM (case A) is the simultaneous determination of creatinine and albumin with alkaline picrate ( $6.6 \times 10^{-3}$  M in picric acid and 0.2 M in NaOH) by measuring the absorbances at 45 and 180 s and a wavelength of 485 nm at 25 °C (8). Creatinine is added up to a concentration of 16.6 mg/L. We assayed a mixture of 8.3 mg/L creatinine and 15.4 g/L albumin; the concentration of the former was directly calculated from the intercept of the straight lines obtained at 45 and 180 s on application of the HPSAM. On the other hand, the albumin concentration was obtained from  $A_H$  and its calibration curve, i.e. from

$$A_{45} = 0.068 + 8.05 \times 10^{-3} C \quad (\text{g/L albumin}) \quad (r = 0.9995)$$

$$A_{180} = 0.075 + 7.98 \times 10^{-3} C \quad (\text{g/L albumin}) \quad (r = 0.9995)$$

The results obtained, namely 8.9 mg/L creatinine and 14.5 g/L albumin, were consistent with the amounts added.

The HPSAM based on the use of absorbance increments as analytical signals should be of use in determining creatinine

Table II. Equations of the MOSA Method in the Reading Interval 45–180 s<sup>a</sup>

vol of serum, mL	no. of runs	creatinine concn, mg/L				
		$\Delta t$ , s				
		180–45	60–15	180–15	120–60	60–10
0.4	1	1.8	1.4	1.6	1.7	1.4
	2	1.6	1.4	1.5	1.5	1.4
	3	1.5	1.4	1.5	1.5	1.5
	4	1.8	1.7	1.7	1.5	1.5
$\bar{C} \pm s$		$1.7 \pm 0.2$	$1.5 \pm 0.2$	$1.6 \pm 0.1$	$1.6 \pm 0.1$	$1.4 \pm 0.1$
0.6	1	2.3	2.3	2.4	2.1	2.4
	2	2.1	2.0	1.8	2.2	1.8
	3	2.1	2.1	1.9	2.2	2.1
$\bar{C} \pm s$		$2.21 \pm 0.08$	$2.0 \pm 0.3$	$2.21 \pm 0.08$	$2.16 \pm 0.05$	$2.1 \pm 0.3$

<sup>a</sup> Conditions: creatinine added 0–8 mg/L, picric acid  $6.6 \times 10^{-3}$  M, sodium hydroxide 0.2 M, and 25 °C.

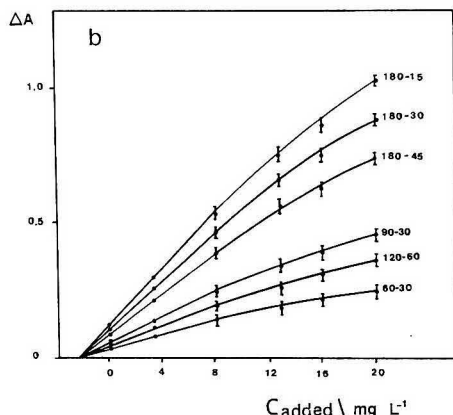
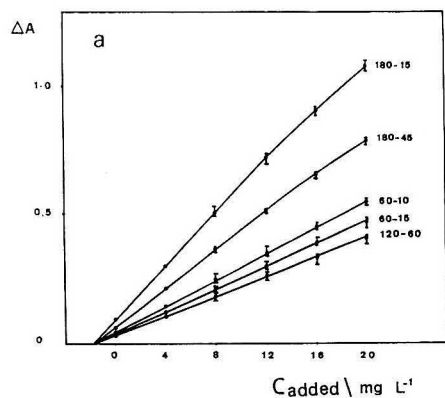


Figure 6.  $\Delta A$  vs added creatinine concentration at different time intervals and 486 nm for (a) serum 1 and (b) serum 2. Conditions: concentration of added creatinine 0–20 mg/L, volume of serum 0.6 mL, picric acid  $6.6 \times 10^{-3}$  M, sodium hydroxide 0.2 M, and 25 °C.

by the Jaffé method; in this case, the HPSAM could be comparable with the classical  $\Delta A$ -C method, but the inherent features of the HPSAM allow one to draw some conclusions on the accuracy of the method on analyzing the results obtained. In this work we used the variant reported elsewhere (8, 9), a picric acid and NaOH concentration of  $6.6 \times 10^{-3}$  and

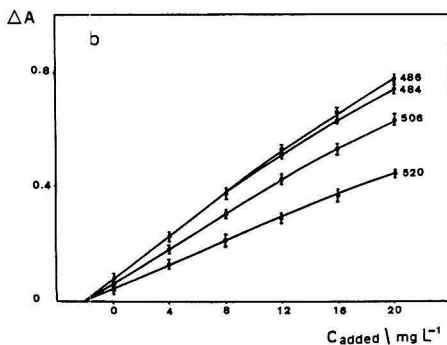
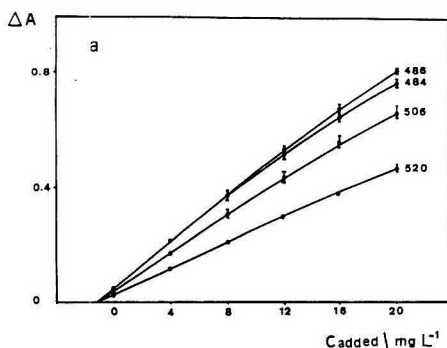


Figure 7.  $\Delta A$  vs added creatinine concentration. Conditions: 0.4 mL (a) and 0.6 mL (b) of serum, concentration of added creatinine 0–20 mg/L, picric acid  $6.6 \times 10^{-3}$  M, sodium hydroxide 0.2 M, and 25 °C.

0.2 M, respectively, a reading interval of 45–180 s, a wavelength of 484 or 486 nm, a temperature of 25 °C, a serum volume of 0.4 or 0.6 mL in the cuvette, an overall volume of 2.5 mL, and calibration by the standard-addition method. We assayed two sera with creatinine contents liable for transfusion and used an HP-8452A diode-array spectrophotometer as the detector.

Application of the HPSAM yielded plots in which the H-point provided the creatinine concentration and the constant systematic error introduced by the sample, which could not be attributed to a specific component as the analytical signal ( $A_H$ ) would correspond to the sum of the contributions from the species making up the mixture. The application of

Table III. Standard-Additions Method: Concentrations of Creatinine for Different Intervals of Time<sup>a</sup>

vol of serum, mL	concn of creatinine, mg/L						concn of creatinine mean values ( $n = 6$ ), mg/L
	$\Delta t$ , s						
	180 - 15	180 - 30	180 - 45	90 - 30	120 - 60	60 - 30	
0.4	1.8	1.76	1.79	1.71	1.74	1.77	1.76 $\pm$ 0.03
0.6	2.4	2.6	2.7	2.6	2.6	2.7	2.6 $\pm$ 0.1

<sup>a</sup> Conditions: concentration of added creatinine 0-8 mg/L, picric acid  $6.6 \times 10^{-3}$  M, sodium hydroxide 0.2 M, and 25 °C.

Table IV. Concentration of Creatinine at Different Wavelengths, in the Interval of Time 45-180 s<sup>a</sup>

vol of serum, mL		concn of creatinine, mg/L				
		484 nm	486 nm	500 nm	506 nm	520 nm
0.4		1.8	1.9	1.8	1.8	1.5
	$C = 1.8 \pm 0.1$ $C_{\text{serum}} = 11.3$					
0.6		2.7	2.6	2.7	2.7	2.4
	$C = 2.6 \pm 0.1$ $C_{\text{serum}} = 10.8$					

<sup>a</sup> Conditions: picric acid  $6.6 \times 10^{-3}$  M, sodium hydroxide 0.2 M, and 25 °C. Volume of serum: 0.4 and 0.6 mL. Concentration of added creatinine: 1.7-8 mg/L.

the HPSAM in its  $\Delta A_{t_1-t_2}-C_{\text{added}}$  variant yields the concentration of creatinine directly from the intercept on the y axis. However, in order to ensure the absence of constant and proportional errors from the calculated concentration, all the possible  $\Delta A_{t_1-t_2}-C_{\text{added}}$  lines for creatinine should intersect at the same point, namely that corresponding to the unknown concentration,  $C_H$ , as this would indicate that the time evolution of the matrix would be a horizontal line. This was the actual result of the determination of the two sera assayed, irrespective of the serum volume used in the reading cuvette (Figure 6). As can be seen from Tables II and III, the creatinine contents found in sera 1 and 2 were independent of the reading time chosen, the most probable value being  $9.4 \pm 0.9$  and  $11.0 \pm 0.5$  mg/L for serum 1 and 2, respectively. In view of these results, one could also calculate the creatinine content from the intercept of the  $\Delta A_{t_1-t_2}-C_{\text{added}}$  lines. The result thus obtained would also be the most probable, as it would be calculated from a larger number of analytical data. The results obtained by this procedure were identical with those given above.

The kinetic spectrophotometric determination of creatinine by the Jaffé method can also be accomplished according to the above-described HPSAM procedure (B) by choosing two wavelengths at which the interferent (the sample matrix in this case) has the same absorbance and hence identical (or similar)  $\Delta A_{t_1-t_2}$  values. The results obtained in the determination of creatinine at the wavelengths of interest (484-486, 500, 506, and 520 nm) are shown in Figure 7 for serum 1 and

listed in Table IV for serum 2. All the lines intersect at a point of zero ordinate, which indicates that, over the wavelength range 484-520 nm, the spectrum corresponding to the sample matrix is horizontal and therefore does not evolve with time, consistent with the HPSAM bases for case B. The creatinine concentrations found by this procedure are similar to those given above.

All this allows one to assume that the determination of creatinine in sera from normal patients will be free from systematic errors provided it is conducted under the conditions described elsewhere (8, 9), since the concentration obtained is independent of the serum volume taken, the time interval considered, and the wavelength set, consistent with the above HPSAM bases.

The demonstrated accuracy of the method is such that it is of analytical utility.

The method has been developed for the kinetic-spectrophotometric analysis but it could also be applicable to other methods of analysis using time as one of the measurement dimensions. HPLC with a diode-array detector and unresolved peaks (both spectroscopic and chromatographic) could be incorporated with the HPSAM. Work in this sense is in progress.

**Registry No.** Manganese, 7439-96-5; vanadium, 7440-62-2; creatinine, 60-27-5.

## LITERATURE CITED

- (1) Mottola, H. A.; Perez-Bendito, D.; Mark, H. B., Jr. *Anal. Chem.* **1988**, *60*, 181R.
- (2) Kopanica, M.; Stara, V. In *Kinetic Methods in Chemical Analysis*; Svehla, G., Ed.; Wilson and Wilson's Comprehensive Analytical Chemistry; Elsevier: Amsterdam, 1983; Vol. XVIII.
- (3) Bosch-Reig, F.; Campins-Falcó, P. *Analyst* **1988**, *113*, 1011.
- (4) Bosch-Reig, F.; Campins-Falcó, P. *Analyst* **1990**, *115*, 111.
- (5) Campins-Falcó, P.; Bosch-Reig, F.; Molina-Benet, A. *Fresenius' J. Anal. Chem.* **1990**, *338*, 16.
- (6) Campins-Falcó, P.; Bosch-Reig, F.; Verdú-Andrés, J. *Talanta*, in press.
- (7) Sevillano-Cabeza, A.; Medina-Escriche, J.; de la Guardia-Cirugeda, M. *Analyst* **1984**, *109*, 1303.
- (8) Llobat-Estellés, M.; Sevillano-Cabeza, A.; Campins-Falcó, P. *Analyst* **1989**, *114*, 597.
- (9) Campins-Falcó, P.; Sevillano-Cabeza, A.; Llobat-Estellés, M. *Analyst* **1989**, *114*, 603.

RECEIVED for review October 10, 1990. Revised manuscript received July 8, 1991. Accepted July 8, 1991. We are grateful to the DGICYT for financial support received for the realization of Project PB 88-0495.

# Simultaneous Determination of Elemental Ratios in Coal by Direct Powder Injection into a Helium Microwave Induced Plasma

Jay M. Gehlhausen<sup>1</sup> and Jon W. Carnahan\*

Department of Chemistry, Northern Illinois University, DeKalb, Illinois 60115

**Milligram amounts of solid, particulate coal are injected directly into a 500-W helium microwave induced plasma. Both discrete and continuous sample injection modes are examined. Upon the introduction of coal to the plasma, molecular emission from C<sub>2</sub>, CN, N<sub>2</sub>, and OH is characterized. Line emission of C, H, Cl, and S is examined for elemental analysis. Ratios of C and H are accurate to within 10% if simultaneous determinations are performed and the coal standards are similar to the samples in composition.**

## INTRODUCTION

Carbon hydrogen, sulfur, and chlorine contents of individual coals ultimately determine their usefulness. Carbon-to-hydrogen ratios (C/H) are associated closely with the volatility and rank of coals (1, 2). Coals of low volatility and high C/H ratios typically burn "cleaner" and produce more energy per unit mass. These coals are classified as high-rank coals. Lower rank, high-volatility, and low C/H ratio coals tend to produce less complete combustion and less energy per unit mass. Because the combustion process converts sulfur in coals to SO<sub>2</sub> and these gaseous emissions are linked to acid rain production, the determination of the sulfur content of coal is critical.

Because sensitive and simultaneous elemental determinations are possible, atomic emission spectrometry has the potential for rapid analysis of the elemental constituents. The ability of the helium microwave induced plasma (He-MIP) to produce intense elemental emission from nonmetals makes this source a possible candidate for direct coal analysis. The development of moderate and higher power He-MIPs facilitate mist introduction for the direct analysis of nonmetal containing solutions (3-5). Therefore, extension to solid samples seems feasible.

A number of techniques have been utilized for the direct analysis of solids by atomic spectrometry. For example, an electrical discharge has been used to thermally dislodge particles from the surface of a sample (6). Subsequently, these particles were directed to an inductively coupled plasma. Ishizuka and Uwamino (7) investigated laser ablation as a method for the direct introduction of solids into an inductively coupled plasma. Mohamed and Fry (8) used a V-groove nebulizer to determine Cu, Mn, and Zn in animal tissue slurries by flame atomic absorption.

A number of advantages exist for the direct introduction of solid particulates for elemental analysis. These advantages include reduced analysis times, minimal contamination problems due to sample preparation, and the absence of sample dilution. Two approaches have been investigated: continuous introduction and direct injection. Guevremont and DeSilva (9) investigated a fluidized-bed device for con-

Table I. Specifications of Equipment

microwave generator	580-W maximum output (Micro-Now Model 420B, Chicago, IL)
TM <sub>010</sub> cavity	described in ref 13
plasma torch	described in ref 15
monochromator	0.35-m scanning monochromator (GCA/McPherson Model EU-700, Acton, MA); for the 200-800-nm experiments, a 1200 groove/mm holographic grating (Schoeffel/McPherson Part No. 8181-3319-0, Acton, MA); for the 800-1300 m/nm experiments, a 600 groove/mm grating blazed at 1000 nm (Schoeffel/McPherson Part No. 8181-3315-0)
polychromator	0.75-m Rowland circle based polychromator (Applied Chromatography Systems Limited Model MPD 850 AG organic analyzer, Luton, Bedfordshire, England)
photomultipliers	Photomultiplier tubes biased at -900 V in the UV-vis (RCA Model IP28, Lancaster, PA) and -1100 V in the NIR spectral regions (Hamamatsu Model R406, Middlesex, NJ)
computer	Kaypro 286 (Microsolutions, DeKalb, IL) equipped with an analog-to-digital converter (MetraByte Corp. Model DAS-8 Taunton, MA)

tinuous sample introduction. Dagnall and co-workers (10) evaluated this approach as well as a "swirl cup" design. Several direct injection designs have been studied. Ng and co-workers (11) used direct powder injection to determine metals in coal fly ash by Ar-ICP-AES. Pfannerstill and co-workers (12) used a dispersion device with an inflatable balloon to create a powder aerosol for Ar-ICP introduction.

This paper presents an evaluation of a 500-W He-MIP for the determination of C, H, Cl, and S directly in coal particulates. This application represents the first report of direct solid sampling with the He-MIP; this capability is the result of the robust nature of the 500-W plasma. Two solid sampling devices were utilized. The first device allows for the continuous introduction of sample. This approach was used to obtain background spectral characteristics. A second device involved discrete sample injection for the determination of coal elemental ratios.

## EXPERIMENTAL SECTION

Details of the plasma, optics, and data acquisition systems are listed in Table I.

**Plasma System.** The resonant cavity was a modified Beekker TM<sub>010</sub> cavity. This design was described by Michlewicz et al. (13) and was similar to the resonant cavity described by Haas et al. (14). The torch was identical with that used by Michlewicz and Carnahan (15). The generator had maximum output of 580 W at 2.45 GHz and was operated with a power output between 450 and 500 W for these experiments.

<sup>1</sup>Present address: Mallinckrodt Speciality Chemicals Co., Mallinckrodt and Second Sts., P.O. Box 5439, St. Louis, MO 63147.

**Table II. Sample Bank and Experimental Argonne Premium Coal Sample Data: Determination of Factors Affecting Response**

designation, seam, and rank <sup>a</sup>	% C	% H	% O	% S <sup>b</sup>	% Cl	C/H <sup>c</sup>	C/H <sup>d</sup> (% $\Delta$ )	% C <sup>e</sup>	% H <sup>e</sup> ( $\Delta$ )
POC-Pocahontas no. 3 low vol bit.	91.0	4.44	2.5	0.66	0.20	20.5	14.2 (-30.7)	89.2	6.2 (+1.8)
UF-Upper Freeport med vol bit.	85.5	4.70	7.5	2.32	0.00	18.2	16.4 (-9.6)	85.0	5.2 (+0.5)
PIT-T-Pittsburgh no. 8 high vol bit.	83.2	5.32	8.8	2.19	0.12	15.6	17.3 (+10.9)	83.7	4.8 (-0.5)
WV-Lewiston Stockton high vol bit.	82.6	5.25	9.8	0.71	0.12	15.7	15.7 (-)	82.6	5.2 (-)
UT-Blind Canyon high vol bit.	80.7	5.76	11.6	0.62	0.03	14.0	16.2 (+16.0)	81.4	5.1 (-0.7)
IL-Illinois no. 6 high vol bit.	77.7	5.00	13.5	4.83	0.06	15.5	16.6 (+6.8)	78.0	4.7 (-0.3)
WY-Wyodak Anderson subbit	75.0	5.35	18.0	0.63	0.03	14.0	9.1 (-35.2)	72.4	8.0 (+2.6)
ND-Beulah Zap lignite	72.9	4.83	20.3	0.80	0.04	15.1	9.6 (-36.3)	70.4	7.3 (+2.5)

<sup>a</sup> Low vol bit. indicates low volatility bituminous coal; med vol bit. indicates medium volatility bituminous; high vol bit. indicates high volatility bituminous; subbit indicates subbituminous; lignite indicates coal of a lower grade. <sup>b</sup> All data, except that for sulfur (% C, % H, % O, and % Cl), are quoted as moisture and ash free (MAF). These are the data for which the oxygen content had been determined. However, these MAF values were not representative of the total sulfur in coal, as the pyritic sulfur was excluded. Therefore, the value for sulfur is the value for dry coal. <sup>c</sup> These carbon to hydrogen mass ratios are based on the coal bank data. <sup>d</sup> These experimental carbon to hydrogen mass ratios were determined by using response factors obtained with the WV coal. The percent errors (% $\Delta$ ) are relative errors calculated by subtracting the sample bank ratio from the experimental ratio and dividing by the sample bank ratio. The resulting values were converted to percentages by multiplying by 100. <sup>e</sup> These experimentally determined % C and % H values are based on the assumption that the sum of the material which is not hydrogen or carbon is known. This information was obtained from the sample data bank. Errors ( $\Delta$ ) are absolute % H errors and were obtained by subtracting the sample bank values from the experimental values.

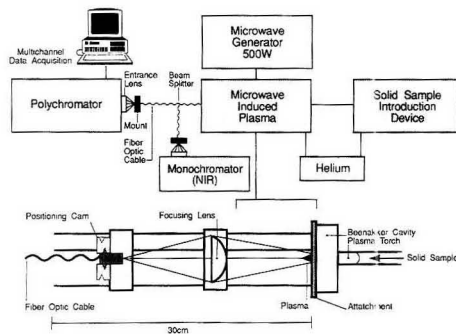


**Figure 1.** System diagram. The inset shows the cavity and optical mount for the focusing lens and fiber optic.

**Spectroscopic Systems.** There were three spectrometer arrangements used for these studies. (i) A 0.35 m focal length spectrometer ( $f/8.6$ ) was used to obtain background spectra, to evaluate emission line suitability, and for initial solid sampling studies. With the appropriate grating and photomultiplier tube, either the ultraviolet-visible (UV-vis) or the near-infrared (NIR) spectral regions could be monitored. Light was focused onto the entrance slit with a 2.5 cm diameter, 20 cm focal length fused-silica lens (Oriol Corp., Stratford, CT). Slit widths were set at 50 and 150  $\mu$ m for the UV-vis and NIR studies, respectively. (ii) A polychromator ( $f/13$ ) allowed for simultaneous elemental determinations. The utilized channels of the polychromator were the 486.1-nm H I, 247.9-nm C I (second order), and 479.5-nm Cl II emission lines. A General Fiber Optics UV silica fiber optic bundle (1.5 mm diameter  $\times$  1 m, Part No. 17-0150-1) was used to direct radiation from the plasma to the spectrometer. A focusing lens was used to focus plasma radiation onto the fiber optic. At the terminus of the fiber optic, focusing onto the entrance slit was accomplished with the "built-in" lens of the polychromator. Figure 1 illustrates this experimental arrangement (with a bifurcated fiber optic and an extra NIR spectrometer). (iii) The polychromator was used in conjunction with the 0.35-m monochromator to monitor sulfur emission. A General Fiber Optics all-silica bifurcated fiber optic bundle (1 m, Part No. 3B-3.2-1.0) was used for this purpose.

**Data Acquisition.** Data were obtained with a Metra Byte DAS-8 system installed in a Kaypro 286 computer. Data collection was controlled by the program Labtech Acquire Version 1.22 (Laboratory Technologies Corp., Wilmington, MA).

**Reagents and Samples.** Helium used for these studies was 99.999% pure from Rockford Welding Supply Co. (Rockford, IL).

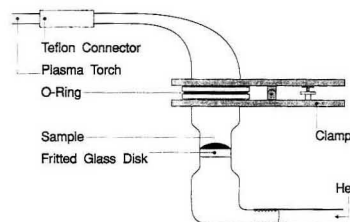


**Figure 2.** Continuous sample introductive device.

A 532 ppm mixture of gaseous dimethyl sulfide in 99.9995% helium (Scott Specialty Gases, Troy, MI) was used for various spectral studies.

**Coal Characteristics.** The eight coal samples were provided by the Argonne Premium Coal Sample Program (APCSP). These coals, listed in Table II, represent a variety of coal types and possess a range of concentrations for the major constituents. The first seven columns list elemental content data compiled at Argonne National Laboratory (16). This information is the moisture and ash-free (MAF) data. Oxygen content was available only with the MAF values. "Dry" data (including ash) were tabulated for sulfur because a large fraction of the sulfur is represented in the ash and, thus, the samples analyzed in this study. Two particle sizes are available for each sample, -100 and -20 mesh. The last three columns of Table II represent experimental data and will be detailed in the Results and Discussion.

## RESULTS AND DISCUSSION

**Spectral Characterizations.** The "continuous" coal sampling device used for spectral characterizations is shown on Figure 2. A powdered coal sample of about 2 g (-100 mesh) was deposited onto the fitted glass disk. Helium was directed through the disk at a rate of 0.8-1.2 L/min and created a fluidized-bed. This procedure allowed coal particles to be carried continuously to the plasma. The rate of coal introduction was on the order of 1 mg/s and decreased somewhat with time. While not useful for quantitative determinations, the device served to obtain useful qualitative spectral information.

Spectra in the 250-600-nm region were obtained by using the "continuous" sampling device with and without coal. These spectra are shown in Figure 3. The introduction of coal caused a large increase in molecular band emission for carbon-containing species such as CN and C<sub>2</sub>. However, molecular background emission near the carbon (247.9 nm),



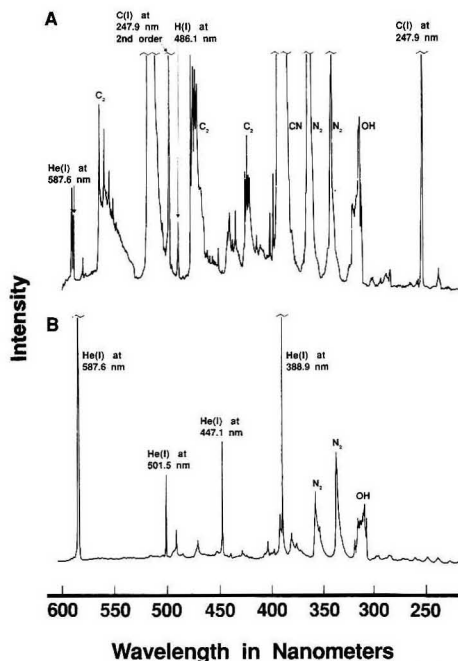


**Figure 3.** Spectra of helium plasma. Lower spectrum = helium plasma with no analyte introduction. Upper spectrum = helium plasma during the introduction of coal from the continuous sampler.

hydrogen (486.1 nm) and chlorine (479.5 nm) atom emission lines was not significant. At the commonly utilized sulfur emission line (545.4 nm), sulfur emission was not discernable. The combination of weak sulfur emission intensity at this wavelength and overlapping  $C_2$  emission caused this behavior. However, molecular band interferences were not seen in the near-infrared spectral region of sulfur emission. Sulfur emission from coal was weak but discernable from the background at the 921.3-nm line. To best illustrate sulfur emission and for wavelength calibration purposes, 6  $\mu\text{g}/\text{min}$  of dimethyl sulfide was introduced as a gas mixture. Emission spectra of these results are presented in Figure 4.

**Direct Powder Injection.** Direction injections of milligram amounts of coal were examined. The injection device is shown in Figure 5. A Teflon stopcock (3 cm long with a 15 mm bore) with a Pyrex housing was used to control the injections. With the stopcock closed, 1-mg samples were loaded into the upper chamber. The sample size represents a compromise between effects of plasma loading and convenience. After replacement of the airtight cap, the chamber was purged of air with a flow of helium (1.4 L/min). Upon rotation of the stopcock to the "open" position, the positive pressure in the upper chamber directed the sample to the plasma torch. A Pyrex stop was used to prevent over-rotation of the stopcock and ensure injection reproducibility. With this device, 30–40 samples could be injected per hour. Studies demonstrated that the bulk of the sample was injected into the plasma if the injector flow rate was maintained greater than approximately 0.5 L/min. A small amount of sample collects between the glass and Teflon of the stopcock, but this material could be removed easily by closing and opening the stopcock three to five times to eliminate loose particulates. Periodically, the valve was disassembled and cleaned. This

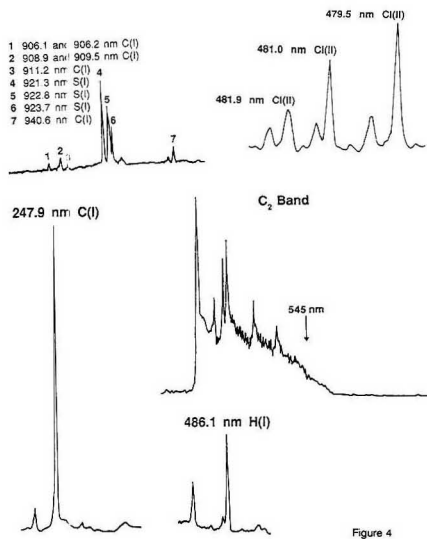


**Figure 4.** Selected spectral regions during the introduction of coal with the continuous sampler. Sulfur introduced as dimethyl sulfide. Regions examined include the 247.9-nm region of C I, 486.1-nm of H I, 479.5 nm of Cl II, 545 nm of S II, and 921.3 nm of S I.

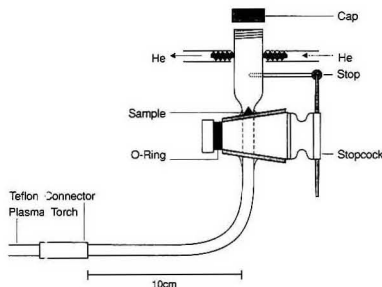


**Figure 5.** Discrete sample injection device.

cleaning step could be performed without destabilizing the plasma.

**Elemental Ratios.** Initial studies with the direct powder injection demonstrated poor sample-to-sample precision. Relative standard deviations, based on integrated carbon emission intensities, were approximately 20%. The dominant source of this imprecision is related to the sampling factor ( $F$ ). This factor represents the fraction of analyte which reaches the plasma and emits radiation.

Elemental atomic emission intensity ratios were investigated as a method to compensate for sampling imprecision. Simultaneous elemental analysis allows sampling variations to be canceled out by the use of elemental ratios. The source of this improvement may be seen in the following discussion. Equation 1 represents the obtained C/H ratio if sequential

$$\frac{C}{H} = \frac{R_C M_1 F_1 I_C}{R_H M_2 F_2 I_H} \quad (1)$$

determinations of C and H are made. C/H represents the experimentally obtained ratio.  $M_i$  and  $F_i$  are the sample mass and sampling factors for samples 1 and 2.  $R_i$  represents the

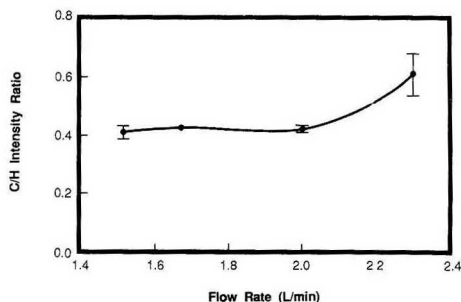


Figure 6. C/H peak intensity ratio as a function of helium flow rate using the discrete sample injection device.

response factor and  $I_i$  is the emission intensity at the C and H channels, respectively. If the statistical behavior is assumed to be random, the error ( $S$ ) in the determined C/H ratio may be estimated by taking the partial derivative of eq 1 with respect to each term. Note that each term following the  $S$  values indicates the source of that error.

$$S_I(C/H) = \left[ \left( \frac{M_1 F_1 I_C}{M_2 F_2 I_H} \right)^2 S^2 \left( \frac{R_C}{R_H} \right) + \left( \frac{R_C M_1 F_1}{R_H M_2 F_2 I_H} \right)^2 S^2(I_C) + \left( \frac{R_C M_1 F_1 I_C}{R_H M_2 F_2 I_H^2} \right)^2 S^2(I_H) + \left( \frac{R_C F_1 I_C}{R_H M_2 F_2 I_H} \right)^2 S^2(M_1) + \left( \frac{R_C M_1 F_1 I_C}{R_H M_2^2 F_2 I_H} \right)^2 S^2(M_2) + \left( \frac{R_C M_1 I_C}{R_H M_2 F_2 I_H} \right)^2 S^2(F_1) + \left( \frac{R_C M_1 F_1 I_C}{R_H M_2 F_2^2 I_H} \right)^2 S^2(F_2) \right]^{1/2} \quad (2)$$

In this determination, measurements of intensities and sample mass are straightforward. However, the sampling factor errors ( $F_i$ ) are dominant. Reasons for this problem reside in the difficulties of reproducibly sampling solid powders. Also, because the response factors ( $R_i$ ) are determined in the presence of this inherent sampling problem, these values exhibit high uncertainties.

In contrast, if carbon and hydrogen are determined simultaneously from the same injection, a dramatic improvement in the precision is expected. Calculation of C/H for this case is as described in eq 3. The  $F_i$  and  $M_i$  terms of eq 1

$$\frac{C}{H} = \frac{R_C I_C}{R_H I_H} \quad (3)$$

cancel because a single injection is used. The error for this case is described in eq 4 and is related only to the spectrometric measurements and the response factors. Provided

$$S_R(C/H) = \left[ \left( \frac{I_C}{I_H} \right)^2 S^2 \left( \frac{R_C}{R_H} \right) + \left( \frac{R_C}{R_H I_H} \right)^2 S^2(I_C) + \left( \frac{R_C I_C}{R_H I_H^2} \right)^2 S^2(I_H) \right]^{1/2} \quad (4)$$

adequate standards are available, the errors in the response factors may be reduced by simultaneous C and H determinations.

**Operating Parameters.** The effect of injection helium flow rate is shown in Figure 6. The IL coal sample was injected at four flow rates between 1.5 and 2.3 L/min. From 1.5 to 2.0 L/min, there is minimal effect on the measured C/H

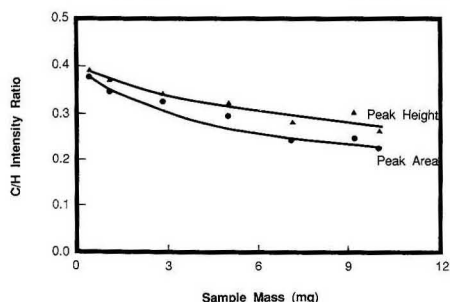


Figure 7. C/H peak intensity ratio as a functions of sample mass.

ratio and the precision is good. However, at 2.4 L/min, there is an increase in the C/H intensity ratio and the standard deviation increases dramatically. The precision at high flows becomes worse due to plasma instability induced by the high-mass flow rate of the sample. Therefore, sample flows were maintained in the range 1.5–2.0 L/min.

The effects of the sample mass on C/H peak height and area ratios are shown in Figure 7. Three important points can be made concerning this plot. First, the C/H intensity ratios decrease slightly with increasing sample mass. Second, the peak height and area ratios follow the same trend. Third, the ratios do not change dramatically within small mass variations. At high sample masses, the plasma is adversely affected by the introduction of solids. The injection of relatively large samples (5–10 mg) caused the plasma to become unstable for 5–10 min. At the other extreme, small samples (less than 0.5 mg) were difficult to quantitatively transfer. The sample size chosen for the remainder of this study was 0.8–1.2 mg. Within this mass range, the samples are manipulated easily, the plasma is not affected adversely, and variations of intensity ratios with respect to sample mass should not be a critical parameter.

**Peak Height and Peak Area Based Calculations.** For the -100- and -20-mesh coals, both peak height and peak areas were examined as a means for quantitation. Although the variances tended to be lower when peak heights were used, the differences tended to be not significantly different. Therefore, peak height was used for the remainder of these studies.

**Choice of Standard and Effects of Composition on C/H Response.** A coal had to be chosen to calibrate the response of the instrument and determine the value of  $R_C/R_H$  defined in eq 3. Table II lists the eight Argonne Premium Coal Samples in order of highest to lowest carbon content. This order is consistent with quality in terms of rank. Low-volatility bituminous POC is of the highest rank of the group (91.0% C) and lignite ND is of the lowest rank (72.9% C). The oxygen contents follow the opposite order; lower oxygen content is indicative of higher rank. Lewiston-Stockton WV coal, a coal of intermediate rank, carbon content, and oxygen content was chosen as the standard.

The eighth column of Table II lists the experimentally determined C/H ratios. These ratios are based on response factors using WV coal as a standard. The number in parentheses indicates the percent error in the C/H ratios. For four of the seven coals (the standard is not included in this set), the errors in the C/H ratios are 16% or less. These four are the medium- and high-volatility bituminous UF, PITT, UT, and II coals with carbon contents in the 77.7–85.5% range and oxygen contents in the 7.5–13.5% range.

To gauge potential effects of these errors on elemental analysis, calculation of carbon and hydrogen contents were

Table III. Comparison of Results with Dried and Untreated Coals

coal	data bank			untreated coal			dried coal		
	% C	% H	C/H	% C	% H (▲)	C/H (%▲)	% C	% H (▲)	C/H (%▲)
UF	85.5	4.70	18.2	85.0	5.2 (+0.5)	16.4 (-9.6)	84.8	5.4 (+0.7)	15.7 (-13.7)
PITT	83.2	5.32	15.6	83.7	4.8 (-0.5)	17.3 (+10.9)	83.1	5.4 (+0.1)	15.4 (-1.3)
WV	82.6	5.25	15.7	82.6	5.2 (-)	15.7 (-)	82.6	5.2 (-)	15.7 (-)
UT	80.7	5.76	14.0	81.4	5.1 (-0.7)	16.2 (+15.7)	80.8	5.7 (-0.1)	14.3 (+2.1)
IL	77.7	5.00	15.5	78.0	4.7 (-0.3)	16.6 (+6.8)	77.4	5.2 (+0.2)	14.7 (-5.2)

made on the basis of a priori knowledge of the non-carbon and hydrogen contents of the coals. As an example, it is known that the non-carbon and hydrogen content of UF coal is 9.8% from the APCSP data bank. On the basis of the MIP-determined C/H mass ratio of 16.4, the remaining 90.2% of the coal can be calculated to be 85.0% C and 5.2% H. Although the percent error of the ratios is relatively large for the UF coal (9.6%), the absolute errors in the carbon and hydrogen contents are small at 0.5%. This trend is similar for all of the aforementioned four coals.

In contrast to the four aforementioned samples, the ratio errors for POC (low-volatility bituminous), WY (subbituminous), and ND (lignite) were in the 30% error range. These errors yielded low C/H ratios in every case. As well, the % C calculation yielded results that were approximately 2.5% low. These trends are explainable if one examines the nature of these three coals compared to the standard WV coal. The WY and ND coals have oxygen contents in the 18–20% range. The low values for the C/H ratios are probably a result of the inability of the plasma to efficiently atomize carbon in the presence of excess oxygen. The carbon-oxygen bond strength is the greatest known at 11.2 eV. Low % C values for the POC coal may be a result of the low volatility of this particular coal. During vaporization-atomization processes in the plasma, it is likely that the more volatile fraction of the coal is selectively sampled. Because the less volatile components in coal tend to be of higher carbon content (aromatic structures, etc.), the sampled fraction may contain a higher hydrogen content than that of the bulk sample (more characteristic of aliphatic type compounds), resulting in low C/H ratios.

These observations indicate that, for like coals, accurate results may be obtained by using a standard coal of known composition. To ensure greatest accuracy, care must be taken that the standard has characteristics similar to those of the samples. Factors that significantly affect results include coal volatility and oxygen content.

**Effects of Coal Mesh Size.** Coals of -100 and -20 mesh were compared in terms of suitability of analysis. Results with the -100-mesh samples from Table II yield a variance of 11% for the five similar coals and 24% if POC, WY, and ND are included. Using -20-mesh samples produced similar results for the five samples with a variance of 13%. However, the variance increased to 32% if the POC, WY, and ND coals are included. This increase is due primarily to an increase in the ND and WY C/H ratio errors from the 35% range to the 55% range. Again, the behavior can be related to the high oxygen content of these coals. It is likely that the larger particle size of the -20-mesh coals accentuates the carbon atomization effects of oxygen, since a smaller fraction of the larger particles are atomized. In this case, the carbon content of the vaporized/atomized fraction is less than in the case with the smaller particulate -100-mesh coals, where a greater fraction of the total sample is atomized.

**Moisture in Coal.** Trapped and surface moisture play significant roles for this study because water contains hydrogen; varying amounts of water associated with the coals will alter the C/H ratios. For this reason, a study was performed to determine the effect of oven drying on C/H.

The percentages of carbon and hydrogen were determined for the five similar coals after drying in a 110 °C oven for 1 h. The data are presented in Table III. In all cases but one, the absolute errors were lower for the oven-dried coal. The average absolute error was reduced by a factor of 2. The variance in the C/H ratio errors were reduced from 11.2 to 7.4%. From these results, it is clear that moisture content is significant and drying is helpful in minimizing errors.

**Chlorine and Sulfur in Coal.** As seen in Figure 4, intense chlorine emission was detectable during the direct injection of coal samples. With the present system, it was not possible to obtain similar spectra for sulfur in coals. While determinations of S and Cl in coals yielded linear increases in atomic emission with increasing mass, the emission signals were small relative to the coal-induced background shifts. It is presently not possible to accurately quantify S and Cl with direct coal injection.

**Conclusions.** Initial results with direct coal injection into the moderate power He-MIP were encouraging. Carbon, hydrogen, and chlorine in coals produced intense atomic emission signals. It was possible to accurately determine C/H mass ratios on the basis of simultaneous spectroscopic determinations. Mandatory was the use of standards similar to the coals being analyzed. Sample oxygen content and volatility appear to play important roles in response. Although accurate direct determinations of sulfur and chlorine were not possible, initial results are promising. Investigations are now directed to enhance the capabilities of the system even more with an emphasis on improving sample decomposition by improving plasma-analyte contact.

**Registry No.** H<sub>2</sub>, 1333-74-0; C, 7440-44-0; Cl<sub>2</sub>, 7782-50-5; S, 7704-34-9; C<sub>2</sub>, 12070-15-4; CN, 2074-87-5; N<sub>2</sub>, 7727-37-9; OH, 3352-57-6.

#### LITERATURE CITED

- (1) *Coal Science*; Hessley, R. K., Reasoner, J. W., Riley, J. T., Eds.; Wiley and Sons: New York, 1986.
- (2) *Coal Structure*; Gorbaty, M. L., Ouchi, K., Eds.; Advances in Chemistry Series 192; American Chemical Society: Washington, DC, 1981.
- (3) McGregor, D. A.; Cull, K. B.; Gehlhausen, J. M.; Viscomi, A. S.; Wu M.; Zhang, L.; Carnahan, J. W. *Anal. Chem.* **1988**, *60*, 1089A.
- (4) Galante, K. D.; Selby, M.; Hietfle, G. M. *Appl. Spectrosc.* **1988**, *42*, 559.
- (5) Perkins, L. D.; Long, G. L. *Appl. Spectrosc.* **1989**, *42*, 559.
- (6) Farnsworth, P. B.; Hietfle, G. M. *Anal. Chem.* **1983**, *55*, 1414.
- (7) Ishizuka, T.; Uwanino, Y. *Spectrochim. Acta* **1982**, *37B*, 1.
- (8) Mohamed, N.; Fry, R. C. *Anal. Chem.* **1981**, *53*, 450.
- (9) Guevremont, R.; De Silva, K. N. *Spectrochim. Acta* **1988**, *41B*, 875.
- (10) Dagnall, R. M.; Smith, D. J.; West, T. S.; Greenfield, S. *Anal. Chim. Acta* **1971**, *54*, 397.
- (11) Ng, K. C.; Zereghli, M.; Caruso, J. A. *Anal. Chem.* **1984**, *56*, 417.
- (12) Pffnerstall, P. E.; Caruso, J. A.; Willeke, K. *Appl. Spectrosc.* **1989**, *43*, 626.
- (13) Michlewicz, K. G.; Uhr, J. J.; Carnahan, J. W. *Spectrochim. Acta* **1985**, *40B*, 493.
- (14) Haas, D. L.; Carnahan, J. W.; Caruso, J. A. *Appl. Spectrosc.* **1983**, *37*, 82.
- (15) Michlewicz, K. G.; Carnahan, J. W. *Anal. Chem.* **1986**, *58*, 3122.
- (16) *Users Handbook for the Argonne Premium Coal Sample Program*; Vorres, K. S., Ed.; Argonne National Laboratory: Argonne, IL, 1989.

RECEIVED for review April 1, 1991. Accepted July 31, 1991. This paper was presented, in part, at the 16th Annual Meeting of the Federation of the Analytical Chemistry and Spectroscopy Societies, Chicago, 1989, Paper No. 610.

# Automated Model Selection for the Simulation of Carbon-13 Nuclear Magnetic Resonance Spectra of Cyclopentanones and Cycloheptanones

Jon W. Ball, Lawrence S. Anker, and Peter C. Jurs\*

Department of Chemistry, The Pennsylvania State University, 152 Davey Laboratory, University Park, Pennsylvania 16802

Linear equations capable of simulating the carbon-13 nuclear magnetic resonance spectra of cyclopentanones and cycloheptanones are developed. The equations relate structural descriptors to  $^{13}\text{C}$  NMR chemical shifts. These descriptors encode the topological, geometrical, and electronic environment surrounding each carbon atom. Due to the conformational flexibility of these compounds, the significance of the geometrical descriptors, in particular, was evaluated. When used together, the models can simulate the chemical shifts of the 36-compound data set with an average spectral error of 1.12 ppm. The models are now included in a spectral simulation database containing 71 predictive equations. This study also involves enhancing the existing model database and the automated model selection procedure used to probe the database. The new model selection scheme determines model suitability based on a similarity measure between a query carbon and all of the carbon atoms used to develop the database models in previous studies. This enhancement dramatically improves the prediction results for an eight-compound external prediction set containing cyclopentanones and cycloheptanones.

## INTRODUCTION

Carbon-13 nuclear magnetic resonance spectroscopy is a valuable analytical tool widely used for the identification of unknown organic compounds. However, limited reference spectra are available to aid the analytical chemist in this process. Therefore, the ability to simulate accurate  $^{13}\text{C}$  NMR spectra has become an extremely useful technique. Two common methods used for  $^{13}\text{C}$  NMR spectra simulation include database retrieval and empirical modeling techniques.

Database retrieval methods require access to a large database containing structurally diverse atoms and their corresponding chemical shifts. In order to predict the chemical shift for an atom using this technique, the most structurally similar atom contained in the database along with its chemical shift must be retrieved. This retrieved shift is then used directly as the simulated shift for the query atom. The accuracy of these predictions is highly dependent on the quality of the database as well as the similarity metric employed.

Empirical modeling techniques involve the development of linear mathematical models relating the chemical shifts to various numerical atom-based structural parameters (descriptors) (*1*). Such models have the form

$$S = b_0 + b_1X_1 + b_2X_2 + \dots + b_dX_d$$

where *S* is the chemical shift of an individual carbon atom, the  $X_i$ 's are the descriptor values, the  $b_i$ 's are the coefficients determined by multiple linear regression analysis, and *d* indicates the number of descriptors used in the model. Unlike database retrieval methods, this approach provides for the interpolation of chemical shift predictions. However, empirical

modeling techniques do not possess the predictive breadth of database retrieval methods. The predictive ability of the models generated with this approach is typically limited to atoms that are structurally similar to those used to generate the models (*2*).

The goal of this research is to develop the capability to simulate  $^{13}\text{C}$  NMR spectra for a wide variety of organic compounds by combining the features of both database retrieval and empirical modeling techniques. The creation of a spectral simulation database containing predictive equations for prior simulation studies was recently reported (*3*). Prior to this study, the database consisted of 66 regression models capable of simulating  $^{13}\text{C}$  NMR spectra of linear and branched alkanes (*4*), cycloalkanes (*5*), cyclohexanols and decalols (*6*), hydroxysteroids (*7*), cyclopentanones and cyclopentanols (*8*), norbornanols (*9*), cyclohexanones and decalones (*10*), piperidines (*11*), polychlorinated biphenyls (*12*), alkyl-substituted benzenes and polyaromatics (*13*), ketosteroids (*3*), and quinolines and isoquinolines (*14*). A complete summary of the current model database is shown in supplemental material Table VII.

In order to use this simulation database effectively, a model selection algorithm must be employed to search the database and retrieve the most appropriate model for each chemical shift prediction. The original model selection routine, MOS (*15*), uses a similarity metric based on six topological descriptors (*16*) which encode the chemical environment of a carbon atom.

Recently, the effectiveness of MOS was investigated using a set of ketosteroid molecules (*3*). The carbon atoms in the ketosteroid molecules are structurally similar to the atoms used to develop models for hydroxysteroids, cyclohexanones, and decalones. As expected, MOS successfully chose appropriate models capable of simulating the chemical shifts for the ketosteroid carbons in most cases. Exceptions occurred when the carbonyl moiety was located on the five-membered ring in the steroid backbone. Poor predictions were obtained in those instances because models capable of simulating  $^{13}\text{C}$  NMR spectra for five-membered rings containing the carbonyl moiety had not yet been developed.

This gap in the database indicated a need for the development of linear models capable of simulating the  $^{13}\text{C}$  NMR chemical shifts for cyclopentanones. In addition, no models have been developed for atoms contained in seven-membered rings. In an attempt to broaden the predictive ability of the database and to investigate the ability of one set of models to predict accurately the chemical shifts of atoms in two different ring systems, models capable of simulating the  $^{13}\text{C}$  NMR spectra for both cyclopentanones and cycloheptanones were generated. The procedure for developing these models will be reviewed along with a detailed analysis of the models' strengths and limitations. In addition, the importance of including geometrical descriptors in these models will be discussed.

As a result of this study, the database was enlarged to 71 models, including five new models developed for cyclo-

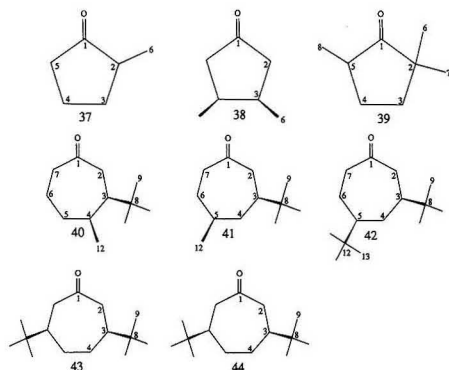


Figure 1. Prediction set compounds with the unique carbons numbered.

pentanones and cycloheptanones. The database was also significantly enhanced to include information on every carbon atom used to generate the 71 models. This enhancement provided the means to perform many new automated model selection experiments. The new approach to model selection will be described and compared to the previously reported model selection and database retrieval techniques.

#### EXPERIMENTAL SECTION

A total of 36 compounds, 13 cyclopentanones and 23 cycloheptanones, with known chemical shifts served as the training set and were used to develop the predictive models. Three cyclopentanones and five cycloheptanones were not included in this training set, and they comprised the eight-compound external prediction set. These 44 compounds are listed in Table I. The structures for compounds 37–44, the prediction set compounds, are shown in Figure 1 with their unique carbon atoms numbered.

The values for the  $^{13}\text{C}$  NMR chemical shifts for all 44 compounds were obtained from three references. Chemical shifts for 16 of the methyl-substituted cyclopentanones were reported by Stothers and Tan (17). These spectra were recorded relative to TMS with a Varian XL-100-15 system operating at 25.2 MHz in the Fourier transform mode. Chemical shifts for 21 methyl-, isopropyl-, and *tert*-butyl-substituted cycloheptanones were compiled from a study by Heathcock and co-workers (18). The  $^{13}\text{C}$  NMR spectra for these compounds were determined with a Nicolet TT-23 spectrometer at 25.14 MHz and a UCB 180 spectrometer at 45.28 MHz. The chemical shift values were reported relative to TMS. The remaining compounds used in this study, seven methyl-substituted cycloheptanones, and their corresponding  $^{13}\text{C}$  NMR chemical shift values were obtained from the work of Christl and Roberts (19). The spectra were recorded at 15.08 MHz with a digital frequency sweep spectrometer. Since these shifts were recorded relative to carbon disulfide, a 192.8 ppm offset was added to each shift in order to convert the shifts to a value relative to TMS.

The ADAPT software system (20–22) was used to enter the structures and their corresponding  $^{13}\text{C}$  NMR chemical shift values into computer disk files. The approximate three-dimensional coordinates were obtained using an interactive molecular mechanics routine (23), and these coordinates were further refined using Allinger's MM2 program (24, 25). All of the software used in this study is written in FORTRAN and is installed on a Sun 4/110 workstation operating at Penn State University.

#### RESULTS AND DISCUSSION

**Need for Cyclopentanone and Cycloheptanone Models in Database.** In order to verify that models capable of simulating the  $^{13}\text{C}$  NMR spectra for cyclopentanones and cycloheptanones would be important in expanding the predictive ability of the existing database, the spectra for the eight

Table I. Compounds Used in the Study

Training Set Compounds	
1	cyclopentanone <sup>a</sup>
2	3-methylcyclopentanone <sup>a</sup>
3	<i>cis</i> -2,3-dimethylcyclopentanone <sup>a</sup>
4	<i>trans</i> -2,3-dimethylcyclopentanone <sup>a</sup>
5	<i>cis</i> -2,4-dimethylcyclopentanone <sup>a</sup>
6	<i>trans</i> -2,4-dimethylcyclopentanone <sup>a</sup>
7	<i>cis</i> -2,5-dimethylcyclopentanone <sup>a</sup>
8	<i>trans</i> -2,5-dimethylcyclopentanone <sup>a</sup>
9	<i>trans</i> -3,4-dimethylcyclopentanone <sup>a</sup>
10	2,4,4-trimethylcyclopentanone <sup>a</sup>
11	2,2,4-trimethylcyclopentanone <sup>a</sup>
12	2,2,4,4-tetramethylcyclopentanone <sup>a</sup>
13	2,2,5,5-tetramethylcyclopentanone <sup>a</sup>
14	cycloheptanone <sup>b</sup>
15	2-methylcycloheptanone <sup>b</sup>
16	3-methylcycloheptanone <sup>b</sup>
17	4-methylcycloheptanone <sup>b</sup>
18	2,2-dimethylcycloheptanone <sup>b</sup>
19	3,3-dimethylcycloheptanone <sup>b</sup>
20	4,4-dimethylcycloheptanone <sup>b</sup>
21	<i>cis</i> -3,5-dimethylcycloheptanone <sup>c</sup>
22	<i>trans</i> -3,5-dimethylcycloheptanone <sup>c</sup>
23	<i>cis</i> -3,6-dimethylcycloheptanone <sup>c</sup>
24	<i>trans</i> -3,6-dimethylcycloheptanone <sup>c</sup>
25	<i>cis</i> -3,4-dimethylcycloheptanone <sup>c</sup>
26	<i>trans</i> -3,4-dimethylcycloheptanone <sup>c</sup>
27	<i>trans</i> -3-methyl-4- <i>tert</i> -butylcycloheptanone <sup>c</sup>
28	<i>trans</i> -3- <i>tert</i> -butyl-4-methylcycloheptanone <sup>c</sup>
29	<i>cis</i> -3-methyl-5- <i>tert</i> -butylcycloheptanone <sup>c</sup>
30	<i>trans</i> -3-methyl-5- <i>tert</i> -butylcycloheptanone <sup>c</sup>
31	<i>trans</i> -3- <i>tert</i> -butyl-5-methylcycloheptanone <sup>c</sup>
32	<i>cis</i> -3,5-di- <i>tert</i> -butylcycloheptanone <sup>c</sup>
33	<i>cis</i> -3-methyl-6- <i>tert</i> -butylcycloheptanone <sup>c</sup>
34	<i>trans</i> -3-methyl-6- <i>tert</i> -butylcycloheptanone <sup>c</sup>
35	<i>cis</i> -3-isopropyl-6-methylcycloheptanone <sup>c</sup>
36	<i>trans</i> -3-isopropyl-6-methylcycloheptanone <sup>c</sup>
Prediction Set Compounds	
37	2-methylcyclopentanone <sup>a</sup>
38	<i>cis</i> -3,4-dimethylcyclopentanone <sup>a</sup>
39	2,2,5-trimethylcyclopentanone <sup>a</sup>
40	<i>cis</i> -3- <i>tert</i> -butyl-4-methylcycloheptanone <sup>c</sup>
41	<i>cis</i> -3- <i>tert</i> -butyl-5-methylcycloheptanone <sup>c</sup>
42	<i>trans</i> -3,5-di- <i>tert</i> -butylcycloheptanone <sup>c</sup>
43	<i>cis</i> -3,6-di- <i>tert</i> -butylcycloheptanone <sup>c</sup>
44	<i>trans</i> -3,6-di- <i>tert</i> -butylcycloheptanone <sup>c</sup>

<sup>a</sup>Shifts taken from ref 17. <sup>b</sup>Shifts taken from ref 19. <sup>c</sup>Shifts taken from ref 18.

prediction set compounds were simulated using models selected by the MOS model selection routine. The MOS routine was recently described (3) and will be only briefly reviewed here. The concept behind this technique is that atoms in structurally similar chemical environments should have chemical shifts that can be predicted with the same model. To measure structural similarity, each regression model is represented by a cluster in a six-dimensional space described by six specially designed topological descriptors, and each query atom is represented by a point in the same space. Model selection is then accomplished by determining to which cluster the query point most likely belongs.

Models selected by MOS were used to predict the shifts of the 61 unique atoms in compounds 37–44. The detailed results are shown in supplemental material Table VIII. Models that were developed with atoms in cyclic ketones were selected for every prediction. Although these were appropriate choices, poor prediction results were obtained. A summary of each compound's standard error of estimate, which is the root-mean-square error adjusted for the correct degrees of freedom, is shown in Table II. The mean standard error of estimate for the prediction of these eight compounds was 5.65 ppm which was considerably above the target of 1.00 ppm.



**Table II. Standard Errors of Estimate (ppm) for the Prediction Set Compounds**

compd	using MOS and limited database (66 models)	using MOS and extended database (71 models)	using most appropriate models
37	5.17	1.94	0.95
38	6.95	2.76	1.32
39	4.04	2.02	0.81
40	4.96	5.44	2.11
41	5.58	5.48	1.33
42	6.23	6.23	2.45
43	6.75	5.99	1.20
44	5.49	5.10	0.78
av	5.65	4.37	1.37

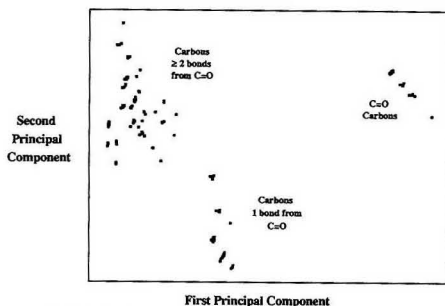
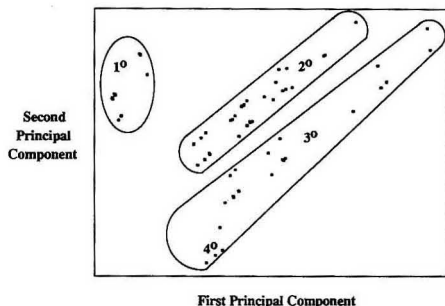
Therefore, a gap existed in the database. The ability to simulate accurately the  $^{13}\text{C}$  NMR spectra for cyclopentanones and cycloheptanones using the existing models was lacking. Thus, models capable of simulating the spectra for both classes of compounds were developed.

**Definition of the Data Set.** In order to develop models capable of simulating shifts for cyclopentanones and cycloheptanones, 36 compounds (compounds 1–36, Table I) along with their corresponding  $^{13}\text{C}$  NMR spectral data were obtained from three references (17–19). These 36 compounds, which included 13 cyclopentanones and 23 cycloheptanones containing methyl, isopropyl, and *tert*-butyl side groups, formed the training set. It is essential to include only the unique carbon atoms contained in the training set when generating regression models. Unique carbon atoms give rise to unique chemical shifts. If a unique carbon atom along with its chemical shift is represented more than once in the training set, the regression models may become skewed or biased. The 36 compound training set contained 253 unique carbon atoms. It is important to note that these 253 atoms did not contain any *tert*-butyl carbons because there were not enough carbons in this environment in the data set to generate a statistically valid model. Therefore, these atoms were excluded from the modeling process.

In addition to the 36 compound training set, the chemical shifts for the prediction set (compounds 37–44, Table I) were obtained from the same three references. These eight compounds contained 61 unique carbon atoms (49 if the *tert*-butyl carbons were excluded). The purpose of the prediction set was to test the external predictive ability of the models generated from the training set.

**Atom Subsetting.** The training set consisting of 253 unique carbon atoms is a large and heterogeneous set of atoms existing in a wide variety of structural environments. It is difficult to generate one model capable of simulating accurate chemical shifts for such a large, diverse set of carbon atoms. Therefore, it is essential to divide the pool of unique carbon atoms into smaller, more manageable and more homogeneous sets of carbon atoms. Two criteria that have been used previously for subsetting are based on an atom's location relative to a functional group (i.e. the number of bonds removed) or an atom's connectivity (primary, secondary, etc.). In this study models developed using the following two subsetting schemes were analyzed.

**Subsetting Scheme 1.** Scheme 1 involves subsetting by location. In previous studies involving the carbonyl moiety, subsetting by location was found to be successful in generating high-quality models with sound predictive ability (3, 10). In these studies, subsets were divided into carbonyl carbons, carbons located one bond from the carbonyl, carbons located two bonds from the carbonyl, etc. Utilizing this method of subsetting, the 253 unique carbon atoms in this study were divided into four subsets: 36 carbonyl carbon atoms, 64

**Figure 2.** Principal components plot for the 253 unique training set carbons.**Figure 3.** Principal components plot for the 153 unique training set carbons located more than one bond from the carbonyl carbon.

carbons located one bond from the carbonyl, 77 carbons located two bonds from the carbonyl, and 76 carbons located three or more bonds from the carbonyl.

**Subsetting Scheme 2.** Scheme 2 employed an entirely new method of subsetting. This scheme combined subsetting by connectivity and location. This unique subsetting scheme was developed through the use of principal component projection plots of six-dimensional E vectors (16). Initially, the six-dimensional E vectors, which encode the topological environment surrounding an atom, were calculated for all 253 unique carbon atoms in the training set. A principal component transformation (26) was performed on the E vectors to obtain the best two-dimensional projection of the data. The result of this transformation is shown as a principal component projection plot in Figure 2. The first two principal components account for 99.2% of the variance present in the original six dimensions. This plot contains three distinct clusters: the cluster in the upper right-hand corner corresponds to the 36 carbonyl carbon atoms; the middle cluster is due to 64 carbons located one bond from the carbonyl; and the cluster in the upper left-hand corner depicts 153 carbons located two or more bonds from the carbonyl. These three clusters represented the initial three atom subsets. A model capable of simulating accurate chemical shifts for the subset containing 153 carbons located two or more bonds from the carbonyl could not be developed. Therefore, it was further divided into smaller, more structurally similar sets of atoms.

Further subsetting was accomplished by performing a principal components transformation on the six-dimensional E vectors for the 153 carbon atoms located two or more bonds from the carbonyl. The resulting principal component projection plot for these 153 atoms is shown in Figure 3. The two principal components in this plot account for 99.6% of

Table III. Model Statistics for Subsetting Scheme 1

atom subset	N	w/out geom descriptors (1)			with geom descriptors (1G)		
		d	R	s, ppm	d	R	s, ppm
C=O	36	6	0.992	0.58	6	0.992	0.58
1 away from C=O	64	10	0.972	1.10	10	0.978	0.98
2 away from C=O	77	11	0.973	2.29	11	0.978	2.06
≥3 away from C=O	76	12	0.981	1.91	12	0.985	1.68
mean std error of est			1.58 ppm			1.33 ppm	

the variance in the original six-dimensional space. This plot again gives rise to three distinct clusters. The cluster on the left contains data points corresponding to 46 primary carbons, the middle cluster depicts 64 secondary carbons, and the cluster on the right corresponds to 39 tertiary and four quaternary carbons. Therefore, the subset containing 153 carbons located two or more bonds from the carbonyl was divided into three smaller subsets.

**Model Development.** Scheme 1 contained four carbon atom subsets, and scheme 2 contained five carbon atom subsets. The carbonyl atom subset and the subset containing atoms located one bond from the carbonyl were present in both subsetting schemes. Therefore, the two subsetting schemes contained a total of seven unique carbon atom subsets.

The models developed with this empirical approach relate chemical shifts to various atom-based structural parameters. One class of these parameters encodes the geometrical environment surrounding each atom. These geometrical descriptors are calculated from the one low-energy conformation determined by molecular mechanics. However, cyclopentanones and cycloheptanones are flexible molecules and can exist in a number of different conformations. Calculations indicate that the most stable conformation of cyclopentanone is the half-chair position, with the maximum puckering occurring at the 3- and 4-positions (17, 27). The most stable conformation for cycloheptanone is similar to the chair conformation in a six-membered ring (28). Although this is the most probable conformation for cycloheptanone, it is likely that it can exist as a conformational mixture (27). Therefore, there is an added degree of error associated with these geometrical descriptors, since cyclopentanones and cycloheptanones exist in more than one conformation at room temperature. Models were developed for all seven subsets using two approaches: excluding and including geometrical descriptors in the models. A total of 14 models were developed in all.

In order to generate each model, a number of procedures, which have been previously described (1), were performed for each subset. Initially, atom-based descriptors were calculated for each atom contained in each atom subset. Next, the atom-based descriptors for each subset were screened in order to assure their statistical significance before being submitted to multiple linear regression analysis. The goal of the descriptor screening step was to reduce the number of descriptors submitted to regression analysis, while simultaneously retaining as much information as possible. Finally, the most orthogonal set of descriptors was submitted to multiple linear regression analysis to yield linear mathematical models that relate the chemical shifts to various atom-based descriptors.

**Model Evaluation.** The goal of the model evaluation step was to choose the most suitable set of models capable of simulating accurate <sup>13</sup>C NMR spectra for cyclopentanones and cycloheptanones. The most suitable set of models is defined as the set which gives rise to the lowest standard errors of estimate and the best library search results for both the training set and prediction set compounds. Four independent

Table IV. Model Statistics for Subsetting Scheme 2

atm subset	N	w/out geom descriptors (2)			with geom descriptors (2G)		
		d	R	s, ppm	d	R	s, ppm
C=O	36	6	0.992	0.58	6	0.992	0.58
1 away from C=O	64	10	0.972	1.10	10	0.978	0.98
1°, ≥2 from C=O	46	7	0.953	1.58	6	0.975	1.14
2°, ≥2 from C=O	64	9	0.978	1.74	10	0.990	1.17
3° and 4°, ≥2 from C=O	43	7	0.953	2.50	7	0.962	2.26
mean std error of est			1.41 ppm			1.12 ppm	

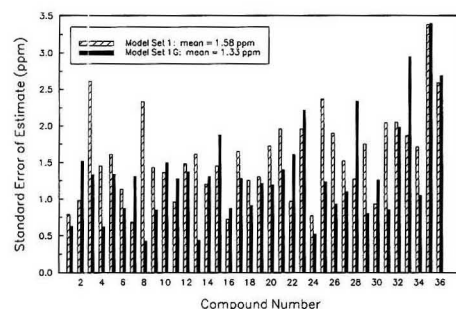


Figure 4. Training set results for atom subsetting scheme 1.

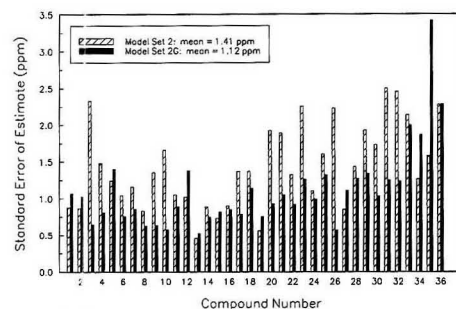


Figure 5. Training set results for atom subsetting scheme 2.

sets of models were evaluated: model set 1 included models developed for the atom subsets in scheme 1 when geometrical descriptors were not used; model set 1G comprised models generated for the atom subsets in scheme 1 when geometrical descriptors were used; model set 2 contained models for the atom subsets in scheme 2 when geometrical descriptors were not used; and model set 2G consisted of models developed for the atom subsets in scheme 2 when geometrical descriptors were used. Table III indicates the statistics for the models contained in model sets 1 and 1G, and Table IV displays the statistics for the models in model sets 2 and 2G. In these tables, N denotes the number of observations in the atom subsets, d indicates the number of descriptors used in the models, R is the multiple correlation coefficient, and s is the standard error of regression.

**Evaluation of the Training Set Results.** The purpose of this model evaluation step was to choose the set of models, 1, 1G, 2, or 2G, which simulates the most accurate spectra for the training set compounds. Tables III and IV show that model set 2G possesses the best statistics. In general, the models in model set 2G have the highest multiple correlation

Table V. Summary of Model Evaluation Results

model set	mean std error, ppm	library searching		
		top match	top 5	
training set	1	1.58	24/36	33/36
	1G	1.33	29/36	35/36
	2	1.41	22/36	33/36
	2G	1.12	32/36	35/36
prediction set	1	2.48	3/8	5/8
	1G	2.62	3/8	6/8
	2	2.21	3/8	6/8
	2G	1.57	5/8	6/8

coefficients,  $R$ , and the lowest standard errors of regression,  $s$ . Using model sets 1, 1G, 2, and 2G independently, the entire  $^{13}\text{C}$  NMR spectrum was simulated for training set compounds 1–36. Figure 4 illustrates the results for model sets 1 and 1G, and Figure 5 displays the results for model sets 2 and 2G. Figures 4 and 5 show that the results improve upon the addition of geometrical descriptors for both subsampling schemes. These figures also indicate that model set 2G, models which include geometrical descriptors, produced the lowest mean standard error of estimate for the 36 training set compounds, 1.12 ppm.

In addition to analyzing the standard errors of estimate, library searching was utilized to further assess the accuracy of the simulated spectra. The five closest spectral matches for each simulated spectrum were retrieved from a library containing 835 reference spectra. The library of reference spectra included the 36 observed spectra for the compounds in the training set. The results for this library search are shown in Table V. Model set 2G yielded the best library search results for the training set.

Although model set 2G produced the best library search results, a top five match could not be found in all instances. The observed spectrum was chosen from the library as the top match to the simulated spectrum for 32/36 compounds. In addition, the observed spectrum was chosen as a top three (shown as top five in Table V) match for 35/36 simulated spectra. A top five match could not be found for compound 32. This is primarily due to the inability of the database models to simulate the shifts for *tert*-butyl groups. This molecule contains four unique atoms in the two *tert*-butyl side groups. Therefore, the simulated spectrum was missing four peaks and could not be matched properly with its observed spectrum. Four of the top five library retrievals for this molecule, however, were cycloheptanones containing a single *tert*-butyl side group, which were reasonable choices.

On the basis of the training set analyses, it appeared that model set 2G was the most suitable in simulating accurate  $^{13}\text{C}$  NMR spectra for cyclopentanones and cycloheptanones. However, the most important diagnostic test in determining the most suitable set of models is their external predictive ability. The models are tested for their accuracy in simulating the shifts for atoms in the prediction set, atoms that were not used in the development of the models.

**Evaluation of the Prediction Set Results.** Using the four sets of models developed from the 36-compound training set, the  $^{13}\text{C}$  NMR spectra for the eight-compound prediction set (structures 37–44) were simulated. The results are displayed in Figures 6 and 7 and compare the standard errors of estimate using models excluding geometrical descriptors versus using models including geometrical descriptors for schemes 1 and 2 respectively. As illustrated by Figures 6 and 7, the predictions improved when models which included geometrical descriptors were utilized. In addition, these figures indicate that model set 2G generated the most accurate predictions: the mean standard error of estimate for compounds 37–44 using model set 2G was 1.57 ppm.

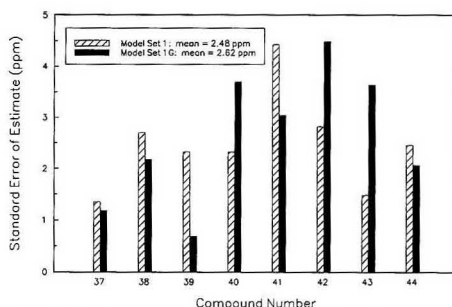


Figure 6. Prediction set results for atom subsampling scheme 1.

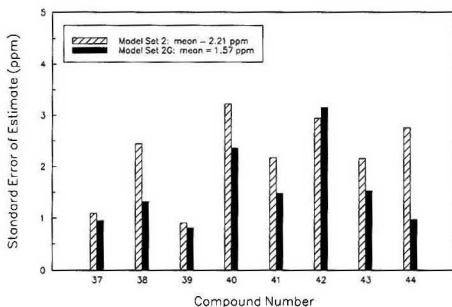


Figure 7. Prediction set results for atom subsampling scheme 2.

In order to evaluate further the accuracy of the simulated spectra for the prediction set using the four sets of models, library searching was performed. For each simulated spectra, the five closest spectral matches were retrieved from a library of 835 reference spectra containing the observed spectra for the eight prediction set compounds. As Table V indicates, the best library searching results were obtained using model set 2G. Model set 2G simulated spectra which retrieved the observed spectra as a top match for five of eight compounds and a top five match for six of eight compounds. The two compounds that did not produce a top five match were compounds 40 and 42. These compounds contained *tert*-butyl carbons whose shifts were not simulated.

**Model Evaluation Summary.** Model set 2G, models developed for scheme 2 using geometrical descriptors, produced superior results for all the evaluation tests. The model evaluation results are summarized in Table V. This set of models yielded the lowest mean standard error of estimate for the training set and prediction set, 1.12 and 1.57 ppm, respectively, and produced the best library searching results for both the training set and prediction set. Hence, these models were found to be the most suitable for simulating the  $^{13}\text{C}$  NMR spectra for cyclopentanones and cycloheptanones and were subsequently added to the existing database containing 66 models, to yield an updated database containing 71 models. A list of the descriptors, coefficients, and additional information regarding these five new regression models are shown in Table IX, supplementary material.

Geometrical descriptors were found to be useful in simulating the  $^{13}\text{C}$  NMR spectra for cyclopentanones and cycloheptanones.  $^{13}\text{C}$  NMR chemical shifts are highly dependent on geometry. For example, in cyclopentanones and cycloheptanones, the chemical shift of a particular atom can vary up to 8 ppm depending on whether it exists in a *cis* or *trans* isomer. Topological and electronic descriptors alone cannot

encode differences in geometry such as axial and equatorial attachments or cis and trans isomerism. However, as indicated by the performance of model set 2G, models including geometrical descriptors are capable of encoding such features and are subsequently capable of simulating  $^{13}\text{C}$  NMR spectra more accurately.

**Spectral Prediction Improvement with Expanded Model Database.** The updated database (71 models) was searched using MOS for the most appropriate models to simulate the  $^{13}\text{C}$  NMR spectra of the prediction set compounds. The results for the prediction of all 61 carbons are displayed in Table X, supplemental material. The results for these predictions are summarized in Table II. Table II shows that the predictions improve slightly when the extended database is searched instead of the limited database. The mean standard error of estimate for the eight predictions is 4.37 ppm using the extended database and 5.65 ppm using the limited database. Even though the new cyclopentanone and cycloheptanone models were present in the extended database, the predictions did not improve significantly. In most cases, the models selected were developed from the cyclohexanones and decalones study rather than from the current one. These models were certainly appropriate, but obviously not the most appropriate, since new models developed for cyclopentanones and cycloheptanones were available in the model database.

Table II also indicates the results that would be obtained for the eight predictions if the most appropriate models were selected. The cyclopentanone and cycloheptanone models were determined to be the most appropriate for all atoms except for the atoms contained in *tert*-butyl groups. As previously mentioned, models were not developed for the *tert*-butyl side group carbons on cyclopentanones and cycloheptanones, because there were not enough of these atoms in the data set to generate statistically sound models. Therefore, the models originally developed for branched alkanes (4) were used to predict the chemical shifts of the *tert*-butyl carbons. Using these most appropriate models, the mean standard error of estimate for the prediction of the eight compounds was 1.37 ppm.

Models are now present in our database which can accurately simulate the  $^{13}\text{C}$  NMR spectra for both cyclopentanones and cycloheptanones; however, the existing model selection routine, MOS, is not able to select these models effectively. One of the primary reasons for these model selection errors was detailed in a recent paper (3) in which similar model selection errors were noticed. In that paper the model selection errors were attributed to *cluster overlap*. In other words, the query atom, when plotted in the six-dimensional space, occupied a point that belonged to more than one model cluster. It is this situation which is probably causing MOS to select a reasonable, yet not the most appropriate, model for the atoms in the prediction set compounds. Therefore, a new model selection algorithm is necessary if this problem is to be averted.

**Atom-Based Approach to Model Selection.** One possible modification to the MOS model selection scheme would be to represent each model as a set of individual points in the six-dimensional descriptor space, rather than as one cluster of points. Each six-dimensional point would correspond to the six environment descriptor values calculated for each atom used to develop a model contained in the database. Then, as proposed in a previous paper (3), the nearest neighbor to the query carbon would be used to determine the most appropriate model. The model selected to predict the chemical shift of the query atom would be the one developed with that nearest-neighbor atom.

There are many advantages to using the atom-based approach to model selection. The primary advantage is that the

Table VI. Standard Errors of Estimate (ppm) for the Prediction Set Compounds

compd	six-descriptor atomic environment		seven-descriptor atomic environment	
	model selection	database retrieval	model selection	database retrieval
37	0.95 (0.95) <sup>a</sup>	1.70 (1.70)	0.95 (0.95)	1.70 (1.70)
38	1.32 (1.32)	3.68 (3.68)	1.32 (1.32)	3.68 (3.68)
39	0.81 (0.81)	1.59 (1.59)	0.81 (0.81)	1.59 (1.59)
40	3.98 (2.36)	3.94 (3.29)	2.71 (2.36)	3.27 (3.29)
41	5.04 (1.48)	4.51 (4.26)	4.11 (1.48)	3.96 (4.26)
42	4.01 (3.15)	7.36 (5.92)	4.01 (3.15)	6.88 (5.92)
43	25.01 (29.33)	9.87 (10.77)	2.38 (1.52)	5.56 (6.84)
44	24.16 (30.80)	8.62 (8.82)	1.87 (0.97)	4.12 (4.87)
av	7.66 (8.78)	5.16 (5.00)	2.27 (1.57)	3.84 (4.02)

<sup>a</sup>The values in parentheses were calculated without the *tert*-butyl carbons included.

new scheme removes the cluster overlap problem. In addition, the new approach will provide increased flexibility in the atomic environment characterizations by allowing the query and model development atoms to be represented by an optimized set of up to 20 descriptors. The new selection scheme also has the possibility for implementing a variety of model selection algorithms to select the most appropriate model, the simplest being to select the model associated with the nearest-neighbor atom. However, it may be of interest to consider the distance to the nearest-neighbor point or the residual of the nearest-neighbor atom in its model as a factor. Another possible algorithm may select the appropriate model to be the one most often represented among the top five or ten nearest neighbor atoms.

The software necessary to implement this atom-based approach to model selection was written and incorporated into the  $^{13}\text{C}$  NMR spectral prediction software system in our laboratory. Additionally, software was developed to predict chemical shifts in a much more automated fashion.

**Comparison of Nearest-Neighbor Model Selection and Database Retrieval Techniques.** The newly developed software was used to select appropriate models and generate chemical shift predictions for all 61 unique carbon atoms contained in the eight prediction set compounds. The first model selection experiment involved the new atom-based approach in which the query and database atoms were represented by the same six descriptors that were used in the MOS scheme and the selection criterion was simply the model associated with the nearest-neighbor atom. In the special case when two or more models were developed with the same database atom (8-11, 13), the model that fit the database atom with the smallest residual was the one selected to predict the query atom. The standard errors (s) for the eight compounds are shown in Table VI. The complete prediction results for each atom are shown in Table XI, supplemental material.

The prediction results improved for six of the eight compounds compared to the MOS results. The appropriate cyclopentanone/cycloheptanone model was selected from the extended model library for each of the 18 cyclopentanone carbons and for 29 of the 31 non-*tert*-butyl cycloheptanone carbons. The only exceptions were the tertiary carbons in compounds 43 and 44. A secondary carbon in compound 31 was selected as the atom with the most similar atomic environment to these two query atoms. Therefore, a model developed for secondary carbons was used to predict the chemical shifts of the two tertiary carbons, resulting in prediction errors in excess of 50 ppm. These errors severely skewed the results, causing the mean standard error to be greater than that obtained by MOS. In addition, since the *tert*-butyl carbons in this study were excluded from the model devel-

opment procedure, no similar carbon environments existed in the database, and the prediction results for these 12 *tert*-butyl cycloheptanone carbons were poor. The models selected were reasonable in that they all resided in cyclic ketone structures; however, none of the models were developed with *tert*-butyl carbons. Table VI also illustrates the negative effect of the *tert*-butyl carbon predictions on the overall  $s$  value for each cycloheptanone structure.

An added benefit to enhancing the database for the new model selection procedures is that database retrieval experiments can also be performed and compared with model selection results. While the database is currently limited in size and scope, most of the carbon atom environments being predicted have very similar matches in the database. For many of the carbons being predicted, the corresponding atom in the *cis*-*trans* isomer was selected as the closest match. For example, the four unique database carbons in compound 9 were selected as the closest match to the four query carbons in compound 38. For this compound, using the chemical shifts directly from the most similar atomic environment led to a standard error of 3.68 ppm, whereas using the models developed with those atoms to predict the query atom chemical shifts led to a standard error of 1.32 ppm. This trend can be observed in Table VI for the other prediction set compounds as well. Therefore, the models which have interpolative ability did better than the database retrieval techniques.

Another advantage of this new model selection procedure is that the atomic environment characterizations are not limited to the six descriptors that are used by MOS. In an attempt to improve the atomic environment descriptions, Randić's atomic ID descriptor (29) was calculated for every atom in the database, in addition to the original six descriptors, and the model selection experiments described above were repeated. The results for the seven-descriptor atomic environment experiments are also shown in Table VI. The complete prediction results are provided in Table XII, supplemental material. No change in the prediction results was observed for the cyclopentanones, and in general, the results for the cycloheptanones did improve both in the model selection and in the database retrieval experiments. Most notably, atom 6 in compound 33, which is a tertiary carbon, was selected as the most similar atomic environment to the tertiary carbons in compounds 43 and 44, which is a more appropriate choice.

The new model selection procedure improved the prediction set results significantly over MOS. The average standard error for the eight compounds was 4.37 ppm using MOS (Table II) and 2.27 ppm using the nearest-neighbor approach with the seven-descriptor atomic environment (Table VI). The new approach selected the models developed for cyclopentanones and cycloheptanones in all cases except for the *tert*-butyl side groups. When the *tert*-butyl side groups were excluded from the predictions, the nearest-neighbor approach was capable of simulating the spectra of the eight prediction set compounds with an average error of 1.57 ppm (Table VI). These results indicate a need for the development of models capable of simulating the  $^{13}\text{C}$  NMR chemical shifts for atoms existing in side chains off cyclic compounds. All previous studies involving cyclic ketone compounds excluded atoms in side chains during the model development phase of the study.

**Future Model Selection Improvements.** The software now exists to perform  $^{13}\text{C}$  NMR spectral predictions in an efficient manner utilizing all of the previously developed models from earlier spectral simulation studies. However, a few enhancements could be made to improve the current model selection capabilities. The most obvious improvement would be to find a better set of descriptors for the atomic environment characterizations of a wide variety of carbon atom

environments. The seven descriptors used in the experiments detailed above were effective, but they were certainly not the best or most effective. The second improvement would be to find a more effective model selection algorithm in that optimized descriptor space. The third and most practical improvement to the model selection procedure would be to develop a prediction confidence value based on model statistics and the distance between the query atom point and nearest-neighbor database point in the  $n$ -dimensional space. This would also indicate if the prediction was an interpolation of an existing model or an extrapolation.

## CONCLUSIONS

High-quality models capable of simulating accurate  $^{13}\text{C}$  NMR spectra for cyclopentanones and cycloheptanones were developed. Since one model was unable to simulate accurately the chemical shifts for all 253 unique carbon atoms in the data set, the atoms were divided into smaller and more homogeneous groups. Two different subsetting schemes were examined: one based on the number of bonds from the carbonyl carbon and one combining the number of bonds from the carbonyl carbon with connectivity information. In addition, the effect of including geometrical descriptors in developing predictive models for conformationally flexible molecules was also evaluated. The five models developed using the second subsetting scheme and including geometrical descriptors was determined to be the most effective set. These models predicted the chemical shifts of the 36-compound training set with an average spectral error of 1.12 ppm. These models were then added to the spectral simulation model database.

The model database was not only enlarged as a result of this study, but it was also improved to include information about the atomic environment of every atom used to develop the models in the database. Additionally, this enhancement provided the necessary information in the database to improve the model selection procedure as well. A model selection procedure is designed to search the database for the most appropriate model to use in the prediction of a query atom's chemical shift. The new method makes this selection on the basis of an atomic environment similarity measurement between the query atom's environment and the environment of every atom used to develop the 71 predictive models contained in the database. This new procedure improved the simulation results for an eight-compound external prediction set, and it has the broad applicability to be useful in the pursuit of the overall goal of this research, which is the development of an automated system capable of simulating the  $^{13}\text{C}$  NMR spectra of organic compounds.

## ACKNOWLEDGMENT

We gratefully acknowledge G. Paul Sutton for his valuable guidance in many aspects of this work and for his efforts in assembling the original spectral simulation database.

**Supplementary Material Available:** Table VII, listing atom subset descriptors and associated models, Table VIII, listing chemical shift prediction results using MOS and the limited model database, Table IX, listing chemical shift models for model set 2G, Table X, listing chemical shift prediction results using MOS and the extended model database, Table XI, listing chemical shift prediction results using the new model selection scheme with a six-descriptor atomic environment, and Table XII, listing chemical shift prediction results using the new model selection scheme with a seven-descriptor atomic environment (22 pages). Photocopies of the supplementary material from this paper or microfiche (105 × 148 mm, 24× reduction, negatives) may be obtained from Microforms & Back Issues Office, American Chemical Society, 1155 16th Street, NW, Washington, DC 20036. Orders must state whether for photocopy or microfiche and give complete title of article, names of authors, journal issue data, and page numbers. Prepayment, check or money order for \$25.00 for photocopy (\$27.00 foreign) or \$10.00 for microfiche (\$11.00 foreign), is re-



quired, and prices are subject to change.

### LITERATURE CITED

- (1) Jurs, P. C.; Sutton, G. P.; Ranc, M. L. *Anal. Chem.* **1989**, *61*, 1115A-1122A.
- (2) Fürst, A.; Pretsch, E. *Anal. Chim. Acta* **1990**, *229*, 17-25.
- (3) Sutton, G. P.; Anker, L. S.; Jurs, P. C. *Anal. Chem.* **1991**, *63*, 443-449.
- (4) Lindeman, L. P.; Adams, J. Q. *Anal. Chem.* **1971**, *43*, 1245-1252.
- (5) Smith, D. H.; Jurs, P. C. *J. Am. Chem. Soc.* **1978**, *100*, 3316-3321.
- (6) Small, G. W.; Jurs, P. C. *Anal. Chem.* **1983**, *55*, 1128-1134.
- (7) Small, G. W.; Jurs, P. C. *Anal. Chem.* **1984**, *56*, 2307-2314.
- (8) Egoif, D. S.; Jurs, P. C. *Anal. Chem.* **1987**, *59*, 1586-1593.
- (9) Egoif, D. S.; Brockett, E. B.; Jurs, P. C. *Anal. Chem.* **1988**, *60*, 2700-2706.
- (10) Sutton, G. P.; Jurs, P. C. *Anal. Chem.* **1989**, *61*, 863-871.
- (11) Ranc, M. L.; Jurs, P. C. *Anal. Chem.* **1989**, *61*, 2489-2496.
- (12) Egoif, D. S.; Jurs, P. C. *Anal. Chem.* **1990**, *62*, 1746-1754.
- (13) Sutton, G. P.; Jurs, P. C. *Anal. Chem.* **1990**, *62*, 1884-1891.
- (14) Ranc, M. L.; Jurs, P. C. *Anal. Chim. Acta* **1991**, *248*, 183-193.
- (15) Small, G. W.; Jurs, P. C. *Anal. Chem.* **1984**, *56*, 2314-2319.
- (16) Small, G. W.; Jurs, P. C. *Anal. Chem.* **1984**, *56*, 1314-1323.
- (17) Stothers, J. B.; Tan, C. T. *Can. J. Chem.* **1974**, *52*, 308-314.
- (18) Heathcock, C. H.; Germroth, T. C.; Graham, S. L. *J. Org. Chem.* **1979**, *44*, 4481-4487.
- (19) Christl, M.; Roberts, J. D. *J. Org. Chem.* **1972**, *37*, 3443-3452.
- (20) Brugger, W. E.; Jurs, P. C. *Anal. Chem.* **1975**, *47*, 781-783.
- (21) Stuper, A. J.; Jurs, P. C. *J. Chem. Inf. Comput. Sci.* **1976**, *16*, 99-105.
- (22) Rohrbaugh, R. H.; Jurs, P. C. *UDRAW. Quantum Chemistry Exchange, Program 300*; Indiana University: Bloomington, IN, 1986.
- (23) Stuper, A. J.; Brugger, W. E.; Jurs, P. C. *Computer Assisted Studies of Chemical Structure and Biological Function*; Wiley-Interscience: New York, 1979; pp 83-90.
- (24) Burkert, U.; Allinger, N. L. *Molecular Mechanics*; ACS Monograph 177; American Chemical Society: Washington, DC, 1982.
- (25) Clark, T. A. *Handbook of Computational Chemistry: A Practical Guide to Chemical Structure and Energy Calculations*; Wiley: New York, 1985; Chapters 1 and 2.
- (26) Tou, J. T.; Gonzalez, R. C. *Pattern Recognition Principles*; Addison-Wesley: Reading, MA, 1974; pp 271-283.
- (27) Eiel, E. L.; Allinger, N. L.; Anyal, S. J.; Morrison, G. A. *Conformational Analysis*; Wiley-Interscience: New York, 1965; pp 201-211.
- (28) St-Jacques, M.; Vaziri, C.; Frenette, D. A.; Goursot, A.; Fliszã, S. J. *Am. Chem. Soc.* **1976**, *98*, 5759-5765.
- (29) Randić, M. *J. Chem. Inf. Comput. Sci.* **1984**, *24*, 164-175.

RECEIVED for review July 1, 1991. Accepted August 8, 1991. This work was supported by the National Science Foundation (Grant CHE-8815785) and by the Department of Defense (Grant DAAL03-89-G-0069). The Sun 4/110 Workstation was purchased with partial financial support of the National Science Foundation. Portions of this paper were presented at the 201st National Meeting of the American Chemical Society, Atlanta, GA, April 1991.

## Scanning Electrochemical Microscopy. 11. Improvement of Image Resolution by Digital Processing Techniques

Chongmok Lee,<sup>1</sup> David O. Wipf, and Allen J. Bard\*

Department of Chemistry and Biochemistry, The University of Texas at Austin, Austin, Texas 78712

Keith Bartels and Alan C. Bovik

Department of Electrical and Computer Engineering, The University of Texas at Austin, Austin, Texas 78712

**Images obtained by scanning electrochemical microscopy (SECM) were improved (deblurred) by use of digital image processing techniques, i.e., a linear combination of Laplacian and Gaussian filtering. Image improvement of repetitive structure (minigrid; interdigitated arrays) and an irregular structure (the bottom surface of a *Ligustrum sinense* leaf) is described.**

### INTRODUCTION

In the last decade, microscopes other than conventional microscopes (e.g., light or electron microscopes that are based on the use of electromagnetic radiation) have been devised by scanning a small tip on or near the surface of interest. For example, the scanning tunneling microscope (STM) (1) has led to several variants, such as the atomic force microscope (AFM) (2) and the ion-conductance microscope (3).

In scanning electrochemical microscopy (SECM), a microvoltammetric tip electrode (with a microdisk geometry and a tip radius of 0.1-12.5  $\mu\text{m}$ ) is rastered in close proximity to the substrate to be imaged in a solution containing an electroactive species (4-6). Previous reports from this laboratory described imaging of surfaces by employing the feedback

mode, where the steady-state tip current,  $i_T$ , controlled by an electrochemical reaction at the tip electrode, is a function of the solution composition, tip-substrate distance,  $d$ , and the nature of the substrate itself. The measurement of  $i_T$  can thus provide information about the topography of the sample surface as well as its electrical and chemical properties; electrodes (e.g., minigrids and interdigitated electrode arrays) (6-8), polymer and oxide films on electrode (7, 9), and biological materials (10) have been imaged. Thus SECM allows, at least in favorable circumstances, analysis of surface features with high spatial resolution. Other groups have used a microdisk electrode to monitor a substance generated at the substrate (11, 12) or a hemispherical microelectrode to measure the local flux of electroactive ions across a porous membrane (13).

Resolution in SECM depends upon the perturbation of the tip current by substrate features and is controlled by the size and shape of the tip electrode and the ability to bring it into close proximity with the substrate surface ( $d < 4a$ , where  $a$  is the radius of a tip) (14). Submicron resolution in SECM has been demonstrated using a tip electrode with a diameter of 0.2  $\mu\text{m}$  (8). This paper deals with the improvement of resolution in SECM by the application of image processing techniques. Such techniques have been applied in a number of areas since its early use in restoring the transmitted moon images in the early 1960s (15, 16). This study demonstrates that the resolution of the SECM images can be substantially

<sup>1</sup> Current address: Division of Chemistry and Chemical Engineering, California Institute of Technology, Pasadena, CA 91125.

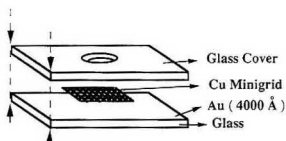


Figure 1. Schematic diagram of the preparation of the inverse indium tin oxide (ITO) grid structure.

improved using this technique. Improvement of the image is shown qualitatively by comparing the raw image with that of the image after processing or that using a smaller tip electrode.

### EXPERIMENTAL SECTION

**Apparatus and Materials.** Instrumental details and operational procedures for the SECM were described previously (6). Milli-Q reagent water (Millipore) was used to prepare aqueous solutions of  $K_3Fe(CN)_6$ ,  $Ru(NH_3)_6Cl_3$ ,  $K_2SO_4$ ,  $KCl$ ,  $H_2SO_4$ , and phosphate-citrate (McIlvaine) buffers. All chemicals were of reagent grade and were used as received. A carbon-microdisk electrode tip (radius 5.5  $\mu m$ ) and a platinum-microdisk electrode tip (radius 1  $\mu m$ ) were fabricated as described (4). Image-processing calculations were performed on a Sun 3/260 work station and an IBM PC compatible 386 computer.

**Preparation of Substrates.** A schematic diagram of the method of preparation of the inverse indium tin oxide (ITO) grid structure is illustrated in Figure 1. A piece (1 cm  $\times$  1 cm) of Cu minigrad screen (25  $\mu m$  periodicity; Ted Pella, Inc., Redding, CA) was placed on a Au film (ca. 400 nm thick) that was sputtered on a glass slide. A second glass slide, with a circular hole (2-mm diameter), was clamped over the Cu minigrad screen. The ITO structure was formed by sputtering about a 20-nm-thick layer of ITO over the screen. This leaves a structure consisting of ITO mounds separated by a less conductive inverse replica of the minigrad. The previously obtained SECM image of the lower surface of a *Ligustrum sinense* leaf (10) was used as another sample to test our program. Pb/Cu sandwich electrodes were constructed by interleaving sheets of 50- $\mu m$ -thick Pb and 18- $\mu m$ -thick Cu foil. The interleaved sheets were compressed and potted in EPON 828 epoxy (Shell Chemical Co., Houston, TX). The epoxy/foil assembly was ground and polished to expose the foil edges. Before use, the Pb/Cu sandwich electrode was polished with 0.05- $\mu m$  alumina. All the Pb and Cu foil sheets were in electrical contact. The interdigitated electrode array (IDA) electrode was a generous gift from Melani Sullivan, University of North Carolina at Chapel Hill. The IDA consists of 3- $\mu m$ -wide platinum bands spaced by 5- $\mu m$  widths of silicon dioxide insulator.

### THEORY

Image-processing techniques (15, 16) are widely used in scanning tunneling microscopy. Generally, these involve treatment of the image by low- or high-pass filters, or Fourier transformation followed by attenuation of certain frequencies and inverse transformation. Since image formation in SECM depends upon electrochemical processes at features, the process which causes blurring is a diffusional one. Thus the approach taken here was to restore (deblur) the image by considering the diffusion process, i.e., using an analogue of Fick's law, eq 1, where  $g(x,y,t)$  is the two-dimensional image,

$$\nabla^2 g(x,y,t) = \frac{\partial}{\partial t} g(x,y,t) \quad (1)$$

$t$  is a function of time, and  $\nabla$  is the Laplacian operator.  $g(x,y,\tau)$ , where  $\tau > 0$ , is the experimentally obtained image and  $g(x,y,0)$  is the desired deblurred image. The tip current, in the usual SECM experiment is a steady-state current. However, time must be considered as a parameter, since it is related to the tip-substrate distance,  $d$ , through the diffusion equation ( $t \approx d^2/2D$ ). In other words, the blurring of the steady-state image represents how far (over a time  $t$ ) mediator diffuses

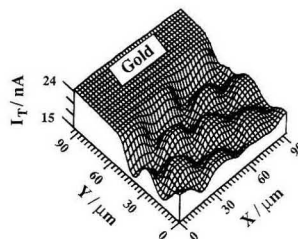


Figure 2. SECM scan of the boundary between Au layer (left) and inverse grid structure (right). The potential of the tip electrode,  $E_T$ , was held at  $-0.38$  V vs SCE in an aqueous solution containing 15 mM  $Ru(NH_3)_6Cl_3$  and 50 mM  $K_2SO_4$  with a C-microdisk tip electrode (radius 5.5  $\mu m$ ).  $i_{T,ss} \approx 15$  nA.

from a feature on the substrate. If we expand  $g(x,y,t)$  at  $t = \tau$  using a Taylor series and truncate the second and higher order terms, we obtain

$$g(x,y,t) = g(x,y,\tau) + (t - \tau) \left[ \frac{\partial}{\partial t} g(x,y,t) \right]_{t=\tau} \quad (2)$$

Substituting eq 1 into eq 2 and letting  $t = 0$ , yields

$$g(x,y,0) \approx g(x,y,\tau) - \tau \nabla^2 g(x,y,\tau) \quad (3)$$

Equation 3 implies that an approximation to the deblurred image can be found by subtracting a constant multiple of the Laplacian of the obtained image from that image. This technique is commonly known as *unsharp masking* (16).

However, SECM images contain high-frequency noise and the parabolic frequency response of the Laplacian operator enhances this noise. The noise from the Laplacian operator can be reduced by low-pass filtering of the output with a Gaussian filter. The Gaussian filter is chosen because of its optimal balance between spatial and spectral localization. The linear combination of Laplacian and Gaussian filtering, which is a band-pass filter, is the Laplacian of Gaussian (LOG) filter often used in edge detection algorithms (17). The LOG filter,  $l(x,y)$ , has the form

$$l(x,y) = \frac{-1}{\pi \sigma^4} \left( 1 - \frac{x^2 + y^2}{2\sigma^2} \right) \exp \left[ \frac{-(x^2 + y^2)}{2\sigma^2} \right] \quad (4)$$

Therefore, our restoration equation becomes

$$g(x,y,0) = g(x,y,\tau) - \tau l(x,y) * g(x,y,\tau) \quad (5)$$

where  $*$  represents the convolution operation. This is implemented by the algorithm

$$\hat{g}(i,j) = g(i,j) - \tau \sum_a \sum_b g(i-a, j-b) l(a,b) \quad (6)$$

where  $(i,j)$  are discrete image coordinates,  $g(i,j)$  is the recorded image,  $\hat{g}(i,j)$  is the restored (deblurred) image,  $l(a,b)$  is the LOG operator, eq 4, and  $a$  and  $b$  are taken from  $(-n+1)/2$  to  $(n-1)/2$ ; the parameters  $n \approx 8\sigma$  and  $\tau$  are adjustable. In this work  $\tau$  was taken as 5.0 or 10.0 and  $\sigma$  as 1.0, so that  $n = 9$ ;  $l(a,b)$  was thus a  $9 \times 9$  matrix indexed  $(-4, -3, \dots, 3, 4)$ . Further details of this approach and choice of parameters, and a comparison of restoration by inverse filtering are described elsewhere (18). By empirically choosing values for  $\tau$  and  $\sigma$  we have improved the SECM images of either repetitive (e.g., minigrad structures or an IDA electrode) or irregular structures (e.g., the bottom surface of a *L. sinense* leaf or a Pb/Cu sandwich electrode).

### RESULTS AND DISCUSSION

**Inverse ITO Minigrad.** The conductive nature of the sample surface was probed by SECM  $x$ - $y$  scans above the

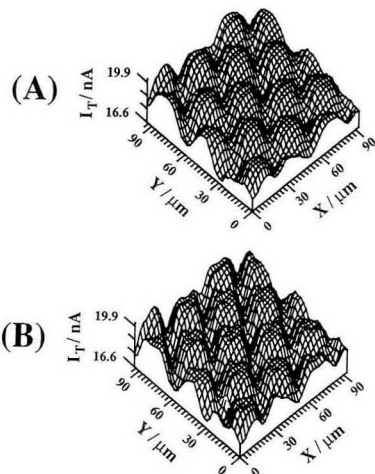


**Figure 3.** (A) Three-dimensional view of SECM scan of the inverse grid structure. Experimental conditions were the same as in Figure 2. (B) Three-dimensional view of (A) after application of the restoration algorithm (eq 6).

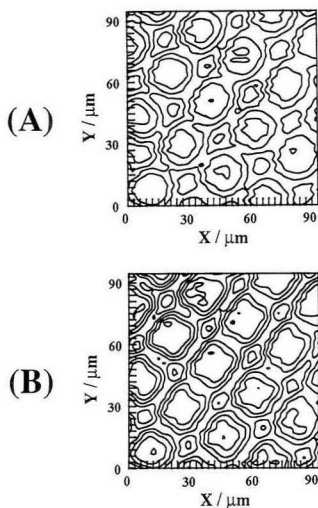


**Figure 4.**  $i_T$  contour map of Figure 3: (A) raw experimental result; (B) after application of the restoration algorithm (eq 6).

region at the boundary between the Au film and the ITO grid structures (Figure 2). The aqueous solution in which this sample was immersed contained 15 mM  $\text{Ru}(\text{NH}_3)_6\text{Cl}_3$  and 50 mM  $\text{K}_2\text{SO}_4$ . The microdisk tip electrode (C; radius 5.5  $\mu\text{m}$ ) was held at  $-0.38$  V vs SCE where the reduction of  $\text{Ru}(\text{NH}_3)_6^{3+}$  to  $\text{Ru}(\text{NH}_3)_6^{2+}$  occurs. As the SECM response depends upon surface conductivity, a positive feedback was observed ( $i_T > i_{T,\infty}$ , where  $i_{T,\infty}$  is the tip current when the tip is held far from the substrate;  $i_{T,\infty}$  was ca. 15 nA in Figure 2) when the tip was over the Au layer because of regeneration of  $\text{Ru}(\text{NH}_3)_6^{3+}$  at the substrate. A similar amount of positive feedback current was also observed above the region where the holes of the Cu minigrd were located, in which 20-nm-thick ITO mounds over

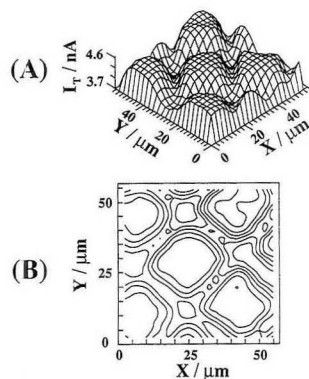


**Figure 5.** SECM scan of the inverse grid structure with a Pt-microdisk tip electrode (radius 1  $\mu\text{m}$ ). The solution and  $E_T$  were the same as in Figure 2: (A) three-dimensional view; (B)  $i_T$  contour map.

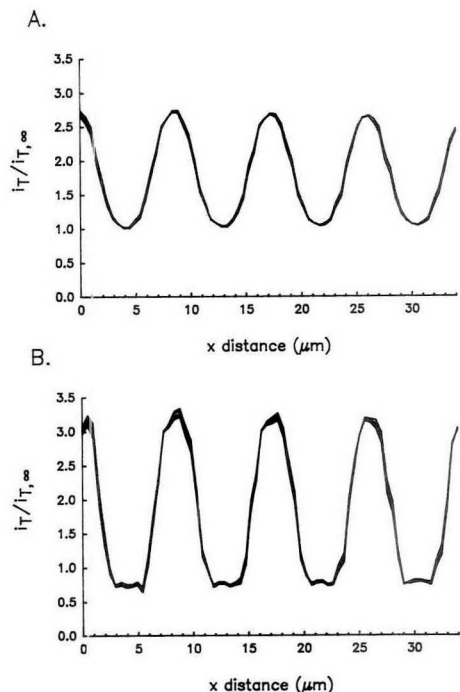


**Figure 6.** Cross-sectional view of the SECM line scan over the  $3 \times 5 \mu\text{m}$  IDA electrode. Tip is a 1- $\mu\text{m}$ -radius Pt disk held at a potential of  $-0.32$  V vs Ag/AgCl. Mediator solution is 2.0 mM  $\text{Ru}(\text{NH}_3)_6^{3+}$  in pH 4.0 buffer: (A) unfiltered scan at a tip-substrate separation,  $d$ , of 0.4  $\mu\text{m}$ ; (B) LOG filtered data from (A) for  $\tau = 5$ ,  $\sigma = 1$ .

the Au film were produced. A much smaller positive feedback current was observed above the region where the lines of Cu minigrd were located (Figure 2). The reason for the decreased rate of oxidation of Ru(II) in the region shadowed by the Cu minigrd is not clear but is an example of differential surface reactivity imaging caused by differences in heterogeneous

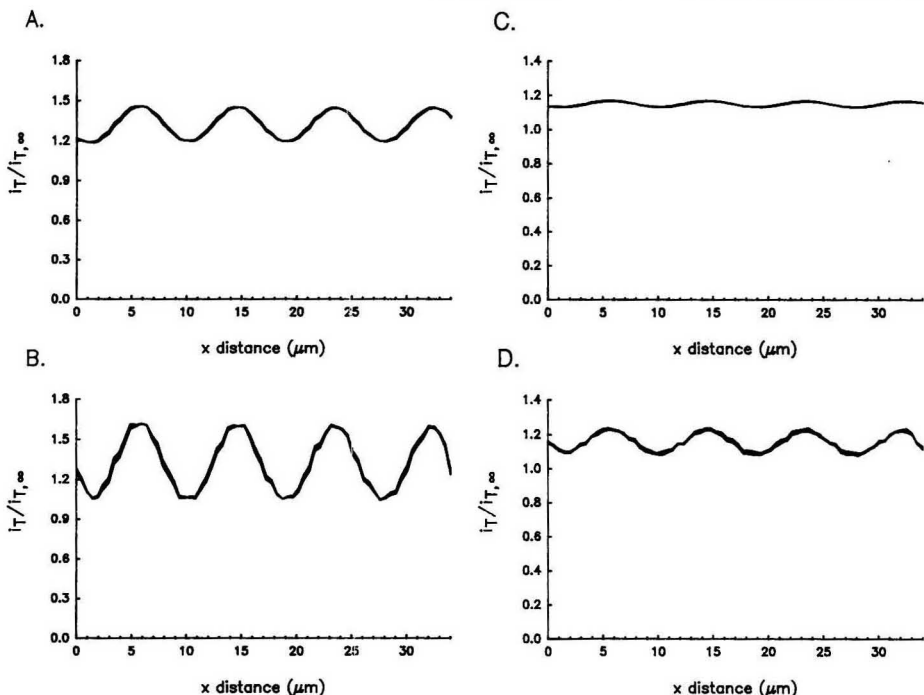


**Figure 7.** Cross-sectional view of SECM line scan over the  $3 \times 5 \mu\text{m}$  IDA electrode. Conditions are the same as in Figure 6: (A) unfiltered scan at  $d = 1.4 \mu\text{m}$ ; (B) restored image from (A) for  $\tau = 10$ ,  $\sigma = 1$ ; (C) unfiltered scan at  $d = 3.3 \mu\text{m}$ , (D) LOG filtered data from (C) for  $\tau = 25$ ,  $\sigma = 1$ .

electron-transfer rates (7, 19, 20). Overall, the SECM scan of this sample is the inverse of that of a Au minigrad shown earlier (6). Note that this SECM scan shows a surface conductivity map of the sample rather than the actual surface topography.

To show the effect of image processing, the raw image of the grid structure (Figure 3A) is compared to one processed via the restoration algorithm (eq 6) (Figure 3B). The three-dimensional views of the SECM images were converted to the current contour maps (Figure 4), where improvement of edge detection is clear. For comparison of the improvement of the SECM resolution by this image-processing technique with that obtained by the use of a smaller tip electrode, an SECM scan of the same substrate with a Pt-microdisk tip electrode (radius  $1 \mu\text{m}$ ) is shown in Figure 5. Although the resolution of Figure 4B is not as good as that in Figure 5B, the original SECM image (Figure 4A) is improved to be equivalent to one obtained with a tip 3–4 times smaller using the image-processing technique.

**Platinum IDA Electrode.** The substrate here is an interdigitated array (IDA) of electrodes with  $3\text{-}\mu\text{m}$ -wide Pt bands separated by a  $5\text{-}\mu\text{m}$ -wide  $\text{SiO}_2$  insulator. The thickness of the Pt bands is about  $0.15 \mu\text{m}$ . A cross-sectional view of a SECM scan over the IDA is shown in Figure 6A. The image was produced with a Pt tip electrode in a solution of  $2.0 \text{ mM Ru}(\text{NH}_3)_6^{3+}$  in pH 4.0 buffer at a tip-substrate separation of  $0.4 \mu\text{m}$ . Although the IDA periodicity of  $3 \times 5 \mu\text{m}$  is clearly seen, the band structure remains incompletely resolved. After application of the LOG-based filter technique (eq 6), ( $\tau = 5$ ,  $\sigma = 1$ ) to the image in Figure 6A, an improvement in the resolution is observed. Note, however, that the sides of the

band structure are still sloped. This demonstrates that the ultimate resolution achievable is limited by the size of the imaging tip itself. In this case, the tip is  $2 \mu\text{m}$  in diameter and, thus, gives about a  $2\text{-}\mu\text{m}$  resolution on the image.

The ability of the restoration algorithm (eq 6) to resolve more diffusively blurred images was tested by scanning over the IDA electrode with greater tip-substrate distance,  $d$ . Figure 7A shows a cross-sectional image taken at  $d = 1.4 \mu\text{m}$ ; because of the greater separation, the diffusional blurring is large. The nominal periodicity of the IDA is preserved in the image, but the structure is unresolved. Application of eq 6 ( $\tau = 10$ ,  $\sigma = 1$ ) improves the resolution slightly but at the cost of decreased signal to noise ratio. Here, the restoration algorithm was unable to remove adequately the diffusional blurring without a simultaneous increase in spurious noise.

**Copper/Lead Sandwich Composite.** The SECM was used to image a substrate constructed of  $50\text{-}\mu\text{m}$ -thick Pb foil sheets interleaved with  $18\text{-}\mu\text{m}$ -thick Cu foil. Upon immersion of the sandwich structure in a solution of  $2.6 \text{ mM Ru}(\text{NH}_3)_6^{3+}$  and  $0.5 \text{ M H}_2\text{SO}_4$ , the exposed Pb edge was passivated (presumably by formation of  $\text{PbSO}_4$ ) while the  $\text{Ru}(\text{NH}_3)_6^{3+}$  was reduced to  $\text{Ru}(\text{NH}_3)_6^{2+}$ . An image of the surface was made with a  $1\text{-}\mu\text{m}$ -radius Pt tip held at an oxidizing potential to regenerate  $\text{Ru}(\text{NH}_3)_6^{3+}$ . The gray-scale image of the surface (Figure 8A) clearly shows a band structure corresponding to the foil edges. Note that this image was preprocessed to remove the scan line-to-scan line variation in the baseline value. A positive feedback signal is observed at the active Cu regions, while the passive Pb produces negative feedback. An improvement in the SECM image is obtained by use of the restoration algorithm (eq 6) ( $\tau = 5$ ,  $\sigma = 1$ ) on the image in

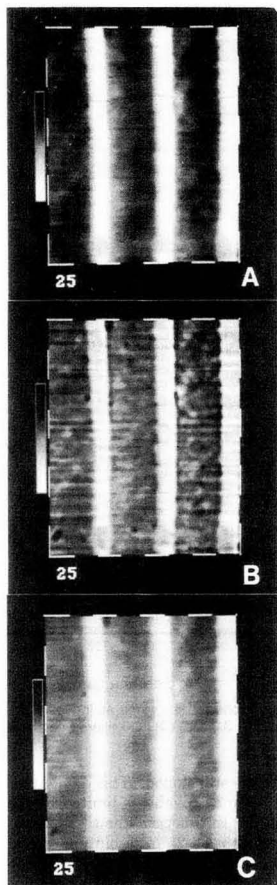


**Figure 8.** Gray-scaled SECM scan of a  $200 \times 200 \mu\text{m}$  section of the Cu/Pb sandwich structure in a 2.6 mM solution of  $\text{Ru}(\text{NH}_2)_6^{3+}$  in 0.5 M  $\text{H}_2\text{SO}_4$  at a  $1\text{-}\mu\text{m}$ -radius Pt-disk electrode. Tip potential,  $E_T$ , was held at  $+0.3$  V vs Ag/AgCl. The substrate was not potentiostated and was poised at a potential of about  $-0.25$  V: (A) unfiltered data, current range = 2.45–3.0 nA; (B) restored image ( $r = 5$ ,  $\sigma = 1$ ), current range = 2.2–3.2 nA; (C) unfiltered data at the same contrast level as the restored data, current range = 2.2–3.2 nA.

Figure 8A, yielding Figure 8B. As in Figure 2, a significant improvement in edge resolution is seen, as well as improvement in the resolution of other features such as the pitlike structures observed at various places in the  $\text{PbSO}_4$  layer. Moreover, a depression running parallel to the Cu/Pb boundary can now be observed. This depression could be due to the thin insulating layer of epoxy joining the two materials. However, an artifact due to the filtering process is not yet ruled out.

**Bottom Surface of a *L. sinense* leaf.** To check the generality of this technique, we used it on the SECM image of the irregular structure on an insulating substrate, the bottom surface of a *L. sinense* leaf (10). Figure 9A is the SECM image obtained with a Pt-microdisk (radius  $1 \mu\text{m}$ ) electrode, where the variation of  $i_T$  was converted to produce a gray-scale presentation; dark color, maximum current; light color, minimum current. The better resolution in Figure 9B

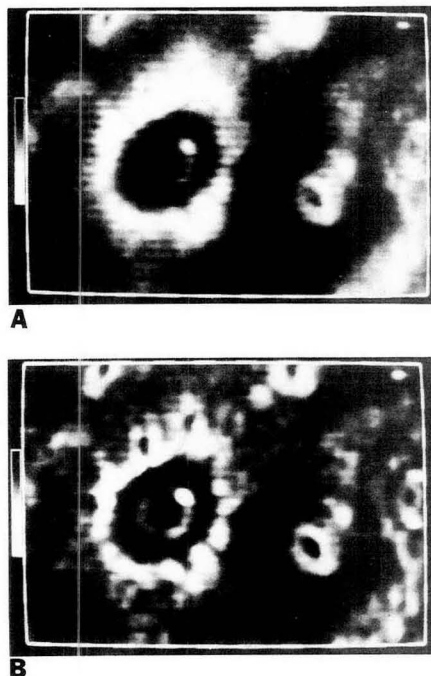


**Figure 9.** Gray-scaled image of the bottom surface of a *L. sinense* leaf in a 20 mM  $\text{K}_3\text{Fe}(\text{CN})_6$  and 0.1 M KCl solution scanned with a  $1\text{-}\mu\text{m}$ -radius Pt tip: scan area,  $188 \times 142 \mu\text{m}$ ;  $0.73 \text{ nA} < i_T < 2.75 \text{ nA}$ . Here the dark shades represent maximum  $i_T$  and larger  $d$ , and light shades, minimum  $i_T$  and smaller  $d$ : (A) raw experimental data; (B) restored image.

was obtained by use of eq 6, where a large craterlike feature at middle-left showed finer structure and some stomata at the upper-right and middle-right edges showed their structures more clearly.

## CONCLUSIONS

The application of image-processing techniques involving a combination of Laplacian and Gaussian filtering improves the resolution of experimentally obtained SECM images for conductive or insulating structures of various types. A combination of this filtering technique and smaller tip electrodes should bring the resolution of SECM to the  $100\text{-}\text{\AA}$  level. However, our best resolution at this time was obtained with tips with a  $0.1\text{-}\mu\text{m}$  radius (8). For higher resolution, smaller metal tips surrounded by insulators, such as those described for use in STM for samples immersed in liquids (21, 22) might be useful in SECM. Such very high resolution SECM will require more precise micropositioning devices and greater attention to the minimization of thermal drift and vibrations. Moreover, the application of small tips will involve very close ( $\sim$ tip radius,  $a$ ) spacings between tip and substrate, which implies that a constant current feedback mode, such as that frequently employed in STM, will be more appropriate. This becomes especially challenging for imaging of surfaces showing both insulating and conductive regions. These aspects of SECM are currently under investigation in this laboratory.

## ACKNOWLEDGMENT

We appreciate the assistance of D. Mandler in the preparation of the ITO sample substrates.



## LITERATURE CITED

- (1) Binnig, G.; Rohrer, H. *Helv. Phys. Acta* **1982**, *55*, 726.
- (2) Binnig, G.; Quate, C.; Gerber, C. *Phys. Rev. Lett.* **1986**, *56*, 930.
- (3) Hansma, P. K.; Drake, B.; Marti, O.; Gould, S. N. C.; Prater, C. B. *Science* **1989**, *243*, 641 and references therein to other types of scanning microscopes.
- (4) Bard, A. J.; Fan, F.-R. F.; Kwak, J.; Lev, O. *Anal. Chem.* **1989**, *61*, 132.
- (5) Bard, A. J.; Denuault, G.; Lee, C.; Mandler, D.; Wipf, D. O. *Acc. Chem. Res.* **1990**, *23*, 357.
- (6) Kwak, J.; Bard, A. J. *Anal. Chem.* **1989**, *61*, 1794.
- (7) Lee, C.; Bard, A. J. *Anal. Chem.* **1990**, *62*, 1906.
- (8) Lee, C.; Miller, C. J.; Bard, A. J. *Anal. Chem.* **1991**, *63*, 78.
- (9) Kwak, J.; Lee, C.; Bard, A. J. *J. Electrochem. Soc.* **1990**, *137*, 1481.
- (10) Lee, C.; Kwak, J.; Bard, A. J. *Proc. Natl. Acad. Sci. U.S.A.* **1990**, *87*, 1740.
- (11) Engstrom, R. C.; Meaney, T.; Tople, R.; Wightman, R. M. *Anal. Chem.* **1987**, *59*, 2005.
- (12) Engstrom, R. C.; Weber, M.; Wunder, D. J.; Burgess, R.; Winquist, S. *Anal. Chem.* **1986**, *58*, 844.
- (13) Scott, E. R.; White, H. S.; Phipps, J. B. *J. Membr. Sci.* **1991**, *58*, 71.
- (14) Kwak, J.; Bard, A. J. *Anal. Chem.* **1989**, *61*, 1221.
- (15) Andrews, H. C.; Hunt, B. R. *Digital Image Restoration*; Prentice-Hall: Englewood Cliffs, NJ, 1977.
- (16) Rosenfeld, A.; Kak, A. C. *Digital Picture Processing*, 2nd Ed.; Academic Press: New York, 1982; Vol. 1.
- (17) Marr, D. *Vision*; W. H. Freeman and Co.: New York, 1982.
- (18) Bartels, K.; Bovik, A. C.; Lee, C.; Bard, A. J. Proceedings of the SPIE/SPSE Symposium on Electronic Imaging Science and Technology, San Jose, California, Feb 24 to March 1, 1991.
- (19) Wipf, D. O.; Bard, A. J. *J. Electrochem. Soc.* **1991**, *138*, 469.
- (20) Wipf, D. O.; Bard, A. J. *J. Electrochem. Soc.* **1991**, *138*, L4.
- (21) Gewirth, A. A.; Craston, D. H.; Bard, A. J. *J. Electroanal. Chem. Interfacial. Electrochem.* **1989**, *61*, 1630.
- (22) Penner, R. M.; Heben, M. J.; Lewis, N. S. *Anal. Chem.* **1989**, *61*, 1630.

RECEIVED for review May 20, 1991. Accepted August 12, 1991. We gratefully acknowledge the support of the study by the National Science Foundation (Grant CHE8901450) and the Texas Advanced Research Program.

## Quantitative Surface Analysis of Organic Polymer Blends Using a Time-of-Flight Static Secondary Ion Mass Spectrometer

Patrick M. Thompson

Surface Science Section, Research Laboratories, Eastman Kodak Company, Rochester, New York 14650-2132

The surface composition of organic polymer blends can be determined using X-ray photoelectron spectroscopy (XPS) provided that each component in the blend has a unique element or functional group present. However, for blends not amenable to XPS, a relatively new technique with greater molecular specificity called static secondary ion mass spectrometry (SSIMS) holds the potential for determining the degree of surface segregation. Although SSIMS is generally considered to be a semiquantitative technique at best, arguments will be presented along with results showing that energy-focusing time-of-flight (TOF) mass spectrometers can overcome some of the possible instrumental artifacts associated with polymer surface analysis done by quadrupole SSIMS and that the SIMS matrix effect is not necessarily a major problem when organic polymer blends are analyzed. In this study, the surface compositions of an immiscible and a miscible polycarbonate/polystyrene blend were determined by TOF SIMS and XPS and these results were compared. The results for these two blends suggest that the accuracy for both TOF SSIMS and XPS can be within  $\pm 0.1$  monomer fraction, while the typical precision of the TOF SSIMS results were primarily determined by counting statistics and were generally better than those from XPS.

### INTRODUCTION

The application of static secondary ion mass spectrometry (SSIMS) toward the qualitative analysis of inorganic and organic surfaces has been well documented (1-6). Success has been achieved with SSIMS as a semiquantitative or quantitative technique for organic surface analysis when calibrated by an independent technique such as X-ray photoelectron spectroscopy (7, 8).

Briggs et al. have shown that SSIMS alone can do semiquantitative if not quantitative surface analysis on random

copolymers of ethyl methacrylate/hydroxyethyl methacrylate, thus showing the potential for its use on other random copolymers (9). In random copolymers the surface composition should be similar to that of the bulk, therefore only a set of known bulk composition standards would be required to calibrate the SSIMS results.

In a study reported by Bhatia et al., XPS was used to calibrate static SIMS measurements made on a miscible blend of polystyrene and poly(vinyl methyl ether) (10). In that paper a sensitivity factor was calculated using XPS results which related the molar concentration of constituents to appropriate ion intensity ratios. This sensitivity factor was assumed to be independent of blend composition. These results suggested that matrix effects may be negligible in certain cases of miscible polymer blends.

In this paper a quantitative analysis scheme is proposed which uses the advantages of an energy-focusing time-of-flight mass spectrometer for determining the surface composition of miscible and immiscible organic polymer blends without necessarily requiring calibration by other surface-sensitive techniques. Similarly to Bhatia et al., this analysis scheme assumes that matrix effects are independent of the blend composition (10). In this paper some consideration is given to how matrix effects can effect the observed results depending on the type of instrument used and why they may be relatively independent of organic polymer blend composition.

Most methods proposed for SSIMS semiquantification and quantification involve comparisons of intensities of appropriately selected mass peaks, usually through a procedure involving their relative peak intensities (RPIs). In the simplest case, such as a two-component polymer blend, a RPI could be obtained between two different mass peaks, each primarily composed of a fragment ion or ions of the same nominal mass that uniquely represent one of the two polymers. By production of a series of blend compositions, a plot of the bulk composition versus RPI could be made. This plot would have

limited utility however, because the bulk composition seldom reflects the surface composition in organic polymer blends. In addition, major changes in the degree of surface segregation can be made by changing the polymer-processing conditions (i.e., different solvents, drying conditions, curing conditions, molecular weights of the polymer components, etc.).

To improve the quantification, an established method of surface analysis, such as X-ray photoelectron spectroscopy (XPS), could be used to independently determine the surface composition of the blend. It has been demonstrated that the surface sensitivity of glancing-angle XPS is close to that of SSIMS (top 2 nm of surface) (7, 11). By plotting appropriate RPIs versus the surface compositions determined by glancing-angle XPS, one obtains a standard curve that can be used to establish the surface composition for this polymer blend system that should be independent of any processing conditions.

Unfortunately, XPS has certain limitations, such as the requirement for each component in the blend to have a unique element or functional group present. For example, XPS can easily distinguish between a blend composed of a simple polyester and polyurethane based on the atomic percent of oxygen and nitrogen at the surface or the relative amounts of ester carbon functionality and urethane carbon functionality at the surface. With this hypothetical polymer blend, these XPS results could be compared for internal consistency. However, when the blend is composed of two similar polymers such as poly(methyl methacrylate) and poly(ethyl acrylate), there are no XPS-distinct elements or functionalities present to separate the two components and, thus, the XPS technique would fail. SSIMS, however, does have the specificity to separate these two polymers based upon the unique secondary ions emitted. In this type of case the SSIMS results would have to "stand alone" in order to establish the surface composition of the blend.

Stand-alone quantitative SSIMS analysis of inorganic and organic surfaces is difficult for many reasons; however, only the three most important will be discussed here. The first involves the well-known and often strong matrix effect, where the secondary ion yield for the same secondary ion can vary over several orders of magnitude depending upon the chemical bonding and type of environment with which the presecondary ion was associated. Unfortunately, methods developed to minimize this matrix effect in dynamic SIMS analyses (i.e. the production of similar composition standards, by generating an internal standard through ion-implantation technology, etc.) do not usually apply in the case of SSIMS. This matrix effect can also change the secondary ion energy distribution for a given ion (12, 13); with potentially important consequences to be discussed later. Atomic secondary ion energy distributions are generally broad with the maximum in the distributions typically between 5 and 15 eV, but it can be anywhere from near 0 out to ~50 eV. The high-energy tail of this energy distribution can extend out to the energy of the primary ion beam. In general, atomic secondary ions have broader energy distributions than molecular secondary ions. Molecular secondary ions have the maximum in their energy distributions that are typically between 0 and 10 eV, a width of a few electronvolts, and a shorter high-energy tail than atomic ions.

Unfortunately, very little can be done at this time to minimize the matrix effects in SIMS unless some type of positionization scheme is employed. (At this time, most positionization methods are not suitable for obtaining quantitative information on organic systems because they induce further fragmentation.)

A second problem involves instrument specific artifacts. For example, in a quadrupole-based SSIMS (QSSIMS) instru-

ment, which is probably the most common type, the relative intensities obtained for the various mass peaks in a spectrum are dependent on how the instrument is "tuned up" for each sample analyzed. This mainly results from the ion-energy requirements of the quadrupole mass filter, which can only effectively mass separate secondary ions with fairly low energies (<15 eV). Therefore, because of the inherently broad secondary ion energy distributions, some type of secondary ion optical column incorporating an electrostatic energy analyzer or "prefilter" (i.e., parallel plates, hemispherical or spherical sector analyzers, cylindrical mirror analyzer, etc.) must be utilized in order to transfer the correct energy secondary ions from the sample into the entrance of the quadrupole mass filter. In QSSIMS instruments, these ion optics have fairly well defined transmission characteristics, with the incorporated prefilter functioning as an "energy window" with a typical ion pass energy centered between 5 and 15 eV and a typical width in the range 2-5 eV. The "band-pass" of a prefilter is the energy range over which secondary ions will be transmitted through the prefilter and is equal to the pass energy  $\pm$  (width/2).

There are at least two common methods employed to "tuneup" a QSSIMS instrument. The first involves tuning-up on a single  $m/z$  peak. In this method the maximum in the secondary ion energy distribution for a selected secondary ion is "moved" onto the pass energy of the prefilter by electrically biasing the sample. This should maximize transmission through the ion optics and, ultimately, maximize the detected signal for that ion.

The second method uses the quadrupole in the rf-only mode, which allows all ions to pass through the QMS instrument without mass filtering. This gives a total ion signal which is maximized in an analogous manner as the single-ion optimization described above.

In general, any method of tuneup used requires some retuning of the lenses in the ion optics, and there is no guarantee that the maximized signal is the global maximum for all of the potential instrument variables.

When the QSSIMS instrument is tuned, the signals from the other secondaries are usually not at a maximum because of their different secondary ion energy distributions. Even small energy shifts in the energy distribution can move portions of the secondary-ion energy distributions in or out of the band-pass of the prefilter. Thus, as the composition of the binary blend changes, the actual matrix effect may not be large, but it may have a significant effect on the RPIs obtained. Even if the RPIs are reproducible for each sample analyzed in a QSSIMS, this RPI may not be equal to the RPI obtained if the measured ion intensities better represented their total secondary ion energy distributions, and not just the portions allowed through the prefilter. The analytical method to be described in this paper requires having RPIs which are reproducible and represent the total secondary ion energy distributions or have secondary ion energy distributions which are not affected by the sample matrix for the chosen ions.

How usable the RPIs obtained on a QSSIMS instrument are depends on how insensitive the secondary ion energy distributions are to the matrix, the widths of the secondary ion energy distributions of the chosen ions, and the width of the energy window of the prefilter. Small matrix effects, narrow secondary ion energy distributions, and a wide energy window will produce more usable RPIs.

The final problem to be considered is sample charging. Many samples that are analyzed are not conductive. Without some type of "charge compensation", the ion signal obtained from insulators on a QSSIMS instrument is very low, due to the secondary ion energy distribution being shifted far outside

of the band-pass of the prefilter. The most common method employed to minimize the effects of charging is the use of an electron flood gun. The flood gun is used to focus electrons having a few hundred electronvolts of energy onto or near the sample in order to reduce the primary ion beam induced positive charge.

For "tuning-up" on nonconductive samples, an iterative technique is used, where the current, location, and perhaps electron energy of the flood gun is adjusted while the primary ion beam location and current is held constant in order to maximize the desired secondary ion signal. Maximizing the secondary ion signal results from moving the maximum in the secondary ion energy distribution of the chosen secondary ion or, if the QMS is used in the rf-only mode, the maximum of the convoluted secondary ion energy distributions back onto the pass energy of the prefilter. Ideally, this charge compensation would lead to a uniform and stable potential on the surface of the sample. However, differential sample charging, where different areas of the sampled area have slightly different levels of charge, and any drift in the ion-gun and electron-gun supplies could change the intensity of the detected signal or move the secondary ion energy distributions relative to the energy window of the prefilter.

Considering the above, it can be seen why a standard QSSIMS instrument is not necessarily a good candidate for potential quantitative surface studies. Some QSSIMS systems now have the ability to scan the sample potential while doing data acquisition. This scanning of the sample potential helps to minimize the possible changes in RPIs discussed earlier. This procedure does not necessarily correct the problem entirely, however, because the secondary ion transmission may not be constant over the energy range scanned and there will usually be loss of ion intensity as the ion energy exceeds some value primarily determined by the characteristics of the secondary ion transfer optics.

A potentially better choice of instrument for quantitative studies on insulators would be a double-focusing mass-spectrometer-based system because it can accept a larger spread ( $\sim 100$  eV) of ion energies than a quadrupole. Thus, minimizing any problems associated with changes in the secondary ion energy distributions. When operating with a large energy window, the double-focusing instrument will suffer some loss in its mass resolution, but it would still be better than a QSSIMS system. However, charge compensation of insulating samples is still a problem because the samples are normally held at a constant high voltage of several kiloelectronvolts during the entire analysis. This requires the electron gun used for charge compensation to be biased at an appropriate potential in order to have the correct quantity and energy of charge-compensating electrons at the proper location on the sample surface.

Another instrument that can accept a large range of ion energies while allowing for sufficient charge compensation is the energy-focusing time-of-flight (TOF) mass spectrometer. There are two principal types of energy-focusing instruments: the reflectron (14) and the Poschenrieder (15) design. Both instruments can accept ions with energies up to a few hundred electronvolts, with the Poschenrieder type excepting a slightly larger energy spread than the reflectron instrument. This virtually minimizes the problems associated with shifting secondary ion energy distributions because typically more than 95% of the molecular secondary ion emitted have energies less than 100 eV. The problems associated with charge compensation are minimized through the use of a pulsed low-energy electron flood gun in a method pioneered by Benninghoven's group (16), where a self-compensating sample charge is maintained during the analysis. Even if the remaining local charge on the sample is nonzero, because of incomplete charge

compensation or differential charging, the detected signal is virtually unchanged because of the energy acceptance of these TOF analyzers.

Now, what can be easily done to minimize the matrix effect? Perhaps not much at this time. However, there is a large class of very important materials for which the matrix effects appear to be small. This class is composed of organic polymer blends. These can be broken down into at least two general cases for quantitative TOF SSIMS analyses.

The first case, and probably most common, would be a blend of two immiscible polymers where phase separation would occur with separate phase domains of 0.1–10- $\mu\text{m}$  diameter in the bulk material. The surface of the immiscible blend could be composed entirely of one of the two components; therefore, no matrix effect should be observed. It is possible that there could be changes in the secondary ion yield of some fragments if the emission processes are sensitive to the surface orientation of the polymer resulting from different crystallinity or hydrogen bonding, etc. However, it may be possible to choose appropriate secondary ions that are insensitive to these secondary effects.

Immiscible blends could also have the surface composed of separate domains of each component with an unknown size distribution. If the domain areas are large, compared to the boundary areas, there may be an insignificant contribution from matrix effects. A case will be made shortly where the expected matrix effect at the boundary areas may be negligible also.

The second general case is that of a miscible polymer blend. In a thermodynamically equilibrated miscible polymer blend the material with the lowest surface energy will be the major component at an uncontaminated surface. The amount of the other blend constituents at the surface, to a first approximation, would depend on the balance between the lowest surface energy component and the entropy of mixing. The thickness of these segregated layers varies from case to case. Angle-resolved XPS has shown that the change from surface to bulk composition occurs within the upper 10 nm of the surface in many cases. In other cases the change is more gradual. In real samples, produced under nonequilibrium conditions, the actual surface compositions seldom reflect the equilibrium case.

In miscible polymer blends, matrix effects would be expected to be more important because of the interactions between groups on the different neighboring chains. It is suggested that the matrix effect in miscible polymer blends may be small because of the "general" elemental and chemical similarities in organic polymers. To introduce this idea, some of the major properties affecting secondary ion desorption yields in organic and inorganic systems will be compared in a brief discussion.

From polymer to polymer, the energy required to break one bond (typically 3–5 eV), but more usually two bonds (6–10 eV), desorb ( $\sim 1$  eV), and ionize (6–13 eV typical) the same organic fragment will likely vary. Any variations in this energy result primarily from the electronic environment at or near the bond to be broken. As an example, the energy required to produce the same  $m/z = 55$  fragment ion  $\text{CH}_2=\text{CH}-\text{C}\equiv\text{O}^+$  from poly(ethyl acrylate) would likely be different than that from Nylon-6 (17). However, the amount of this energy for each case should be nearly independent of the neighboring polymer chains.

Making a case for negligible matrix effects resulting from near-neighbor interactions with the other components in a blend is not a clear-cut matter. The large changes observed in the secondary ion yield for an atomic or molecular ion in inorganic systems is mainly from the different bond energies, coordination number, crystal field potentials, and other types

of short- and long-range interactions that are part of, or result from, the preions environment. In organic polymers the chemical functionalities, composed mainly of C, H, O, N, and occasionally S, have a smaller range of bond energies and ionization energies when compared to the much wider range for these properties in inorganic materials. In addition, the short-range and long-range interactions are generally smaller than those observed in inorganic systems. Therefore, the only obvious perturbation resulting from the different interchain neighbors should be a small change in the energy required for desorption, which is already small compared to the energy required for the intrachain breaking of one or two bonds and the ionization step. As mentioned before, there should be no relative changes in secondary ion intensities from this change in desorption energy if an energy-focusing TOF instrument is used.

If the surface is composed of a "true" blend of miscible polymers, as opposed to very small domains, then the ability of the surface to form a crystalline structure should be minimized and the majority of the area sampled should be amorphous. How important these secondary effects are in determining changes in secondary ion yields is unknown at this time.

The small ( $m/z < 500$ ) fragments useful for quantitative analysis should experience minimal entanglement interactions, or at least these interactions may be similar in the blends and pure polymers. It is generally believed that physical entanglements in polymer systems do not become important until the molecular weight of the polymer is near  $m/z$  10 000.

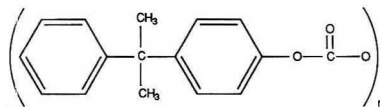
If the above considerations are valid, then an attempt to quantify the surface composition of binary polymer blends using TOF SSIMS can be made. A set composed of an immiscible and a miscible polymer blend series was chosen for this work in order to test the argued suitability of a TOF SIMS instrument and the validity of the assumptions made concerning possible matrix effects. The immiscible binary polymer blend was composed of bis(phenol)-A polycarbonate (BPAPC) and polystyrene (PS), while the miscible blend was composed of tetramethylbis(phenol)-A polycarbonate (TMPC) and PS. BPAPC and TMPC are immiscible over the entire concentration range. The structures of these polymers are shown in Figure 1. These three polymers have similar surface energies; therefore, any obvious prediction as to which material will segregate to a surface is difficult. In addition, the carbonate functionality allows for the independent determination of the surface compositions using XPS.

#### EXPERIMENTAL SECTION

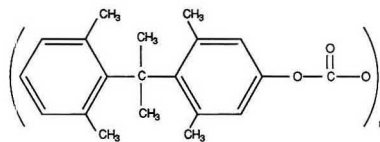
**Instrumentation.** The TOF SSIMS spectra were obtained on a VG-Scientific (Formerly VG-Ionex) time-of-flight instrument of the Poschenrieder design. Most of the characteristics of this instrument have been described elsewhere (18); therefore, only the details necessary for this paper will be discussed.

The mass-filtered Ga liquid-metal primary ion gun was operated at 30 keV and supplied a continuous  $^{69}\text{Ga}^+$  ion current of 2 nA. This gun was pulsed at a frequency of 10 kHz with a square-wave-equivalent pulse width of 5.6 ns for a total of  $9.6 \times 10^6$  pulses during the acquisition of each spectrum. The sampled area was  $\sim 0.09 \text{ mm}^2$ , which gives a total-ion dose of  $\sim 9 \times 10^{11}$  ions/cm<sup>2</sup> for each spectrum acquisition, well within the accepted value of  $< 10^{12}$  ions/cm<sup>2</sup> for static SIMS conditions. The polymer samples were always mounted in the same standard VG TOF SIMS sample stub for each acquisition. These stubs have a spring-loaded plate which forces the sample up against the back of a flat grid arrangement which helps define the proper extraction conditions. Near the center of this grid arrangement are four  $\sim 1 \text{ mm} \times 1 \text{ mm}$  grid openings. It was important to use the same area within the same grid opening for each acquisition because different absolute signal intensities are obtained if areas are sampled which are located under different grid openings or if different sample stubs are used. This apparently results from

a) Bisphenol-A Polycarbonate (BPAPC)  $MW_{\text{repeat}} = 254$



b) Tetramethyl Bisphenol-A Polycarbonate (TMPC)  $MW_{\text{repeat}} = 310$



c) Polystyrene (PS)  $MW_{\text{repeat}} = 104$

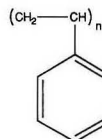


Figure 1. Chemical structures of the three polymers used in this investigation.

slight differences in the extraction field over the front of the sample stub.

The pulsed electron gun is similar to that used by Briggs et al. (19). Two modifications have been made to the as-supplied system. The VG Model No. 401 flood gun supply has been modified to produce  $\sim 18\text{-eV}$  (with respect to ground) electrons instead of the original  $\sim 14\text{ eV}$ . This increased the available current at the sample by  $\sim 50\%$  at most levels of filament emission current. The Kodak VG TOF SIMS also has a quadrupole SIMS system attached to the main analysis chamber. It was found that when the first electrode of the secondary ion transfer optics (VG Model No. HTO 2001) was biased  $\sim 20\text{ V}$ , that the continuous electron current striking the sample stub could be increased by  $\sim 7$  times over the unmodified system. With the above changes the continuous electron current striking the sample stub was increased by  $\sim 10$  times. During the static SIMS acquisition the sample stub is not dropped to ground, but rather an  $\sim 125\text{ V}$  dc potential is placed on the stub in order to draw more electrons to the sample surface. When positive-ion SIMS spectra are being taken and the sample stub potential is being pulsed at an  $\sim 1\text{-kHz}$  rate, the sample stub reaches this  $\sim 125\text{ V}$  level. However, when negative-ion SIMS spectra are being acquired at the same frequency of sample stub pulsing, the sample stub only reaches a potential near  $\sim 125\text{ V}$ . This is probably due to an resistance-capacitance (RC) time constant that does not allow for the full  $\sim 125\text{-V}$  value to be obtained during the short charge compensation period. With this slightly modified system  $\sim 70$  nA (at  $0.5\text{-mA}$  emission current on the VG 401 unit) of  $\sim 150\text{-eV}$  electrons is supplied to a  $\sim 7\text{-mm}^2$  area of the sample surface. This current is being measured as a continuous current; however, the electron gun is being pulsed at  $\sim 1\text{ kHz}$  ( $1/10$ th the ion gun pulse frequency) at a pulse width on the order of tens of microseconds. Thus, a sufficient quantity of electrons should be in the proximity of the area sampled by the primary ion beam to maintain the sample potential within the acceptance energies of the TOF mass spectrometer.

The mass spectra were acquired over a mass range of  $m/z$  1.5–1000. Mass resolution at the instrumental conditions used

was  $M/\Delta M \sim 500$  fwhm at  $m/z = 100$ . Base pressure of the instrument is  $<10^{-10}$  Torr. Pressure during the analyses was  $<5 \times 10^{-10}$  Torr.

The high-resolution C 1s XPS spectra were acquired using a HP 5950A X-ray photoelectron spectrometer equipped with a monochromatized 1486 eV Al K $\alpha$  X-ray source. The monochromatic source minimizes sample damage due to excessive X-ray irradiation. Details of this instrument have been published elsewhere (20). Where appropriate, 18 and 38° electron take-off angles (ETOA) were used in acquiring the XPS spectra for the blends. The maximum sampling depth at the 18 and 38° ETOA sampling depths are  $\sim 2$  nm and  $\sim 5$  nm, respectively. All measurements were made using a Surface Science Laboratory Model 259 angular-rotation probe, Surface Science Laboratories, Mountain View, CA. The electron acceptance solid angle of the electron lens was reduced from 3.5 to 2.8° by altering the magnification of the lens from  $-5.0$  to  $-2.3$ . A low-energy ( $<10$  eV) electron flood gun was used to minimize sample charging. The maximum temperature measured on the sample probe during these analyses was 40 °C. This temperature was well below the glass-transition temperatures for these blends. The base pressure in the instrument is  $\sim 10^{-9}$  Torr. Pressures during the spectral acquisitions were  $<5 \times 10^{-8}$  Torr. The neutral hydrocarbon peak was assigned a value of 284.6 eV. A background-corrected Gaussian peak-fit routine, written by Surface Science Labs, Mountain View, CA, was used to deconvolute the XPS spectra.

Differential scanning calorimetry (DSC) results were obtained on a DSC 7 instrument, manufactured by The Perkin-Elmer Corp., Norwalk, CT. The sample heating rate was 10 °C/min.

Contact-angle measurements were made, using water and diiodomethane, on the dried films with a Ramie'-Hart Goniometer, Ramie'-Hart Inc., Mountain Lakes, NJ. Surface energies were calculated using the Good-Girafalco-Fowkes-Young equation (21).

For the BPAPC/PS blends, the XPS and SSIMS analyses were done on the polymer surface at the polymer/air interface. Unfortunately, the TMPC/PS blends were found to have varying levels of a polydimethylsiloxane (PDMS) type material at the polymer/air interface even after numerous attempts to purify the starting materials and to control the coating process. The surface composition, as determined by XPS, of a polymer/air interface of the TMPC/PS blends did not exhibit a uniform trend, presumably because of the presence of PDMS. However, the polymer blend/polyethylene interface did not have PDMS at the surface and therefore, the XPS and SSIMS results in this paper are for the TMPC/PS surface that was in contact with the polyethylene during the drying process.

**Sample Preparation.** The polystyrene ( $M_w \sim 250,000$ ) was purchased from Pressure Chemical Co., Pittsburgh, PA. Non-UV stabilized bis(phenol)-A polycarbonate (Makralon 5700,  $M_w \sim 45,000$ ) was obtained from Mobay Chemical Co., Germany. Tetramethylbis(phenol)-A polycarbonate ( $M_w \sim 65,000$ ) was obtained from General Electric Co., Schenectady, NY.

The two series of blend compositions obtained were produced on the basis of weight percents, blended in 10 wt % increments, of the two polymers. The films were made by dissolving appropriate amounts of the two polymers in methylene chloride, then, using a 7-mil blade, a knife coating was made on a clean (determined using XPS and SSIMS) polyethylene sheet. These coatings were then dried at 70 °C for 0.5 h. The final coatings were approximately 15  $\mu$ m thick.

The intent of this study was to test the feasibility of doing quantitative SSIMS analyses of organic polymer blends; therefore, no attempt was made to anneal the coatings above their respective  $T_g$  in order to reach their thermodynamically stable surface composition.

## RESULTS AND DISCUSSION

The following method was used to determine the fraction of BPAPC and TMPC at the surface of each sample from the XPS results. The binding energy and peak width of the carbonate carbon in BPAPC and TMPC were experimentally identical (290.3 eV, 1.3 eV fwhm). The carbon  $\pi$ - $\pi^*$  shake-up peak had a width of 2.1 eV fwhm for all three polymers; however, the binding energy of the shake-up peak varied and was at 291.6, 291.3, and 291.1 eV for BPAPC, TMPC, and PS,

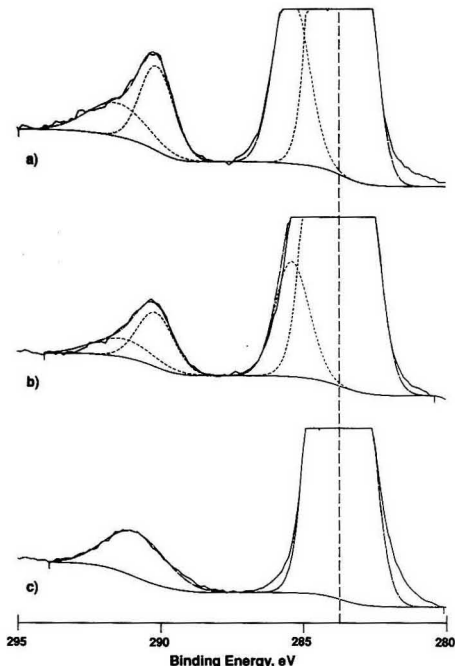


**Figure 2.** High-resolution carbon 1s XPS spectra of the (a) BPAPC, (b) TMPC, and (c) PS showing the deconvoluted peaks and locations of the neutral carbon ( $-\text{CH}_2-$ ) at 284.6 eV, the methoxy carbon (CO) at 286.1 eV, the carbonate carbon  $[-\text{O}(\text{C}=\text{O})\text{O}-]$  at 290.3 eV, and the  $\pi$ - $\pi^*$  shake-up (due to delocalization of the  $\pi$ -electrons in the aromatic rings) at 291.3 eV.

respectively. The deconvoluted high-resolution C 1s spectra for the pure BPAPC, TMPC, and PS are shown in Figure 2 (only the carbonate and shake-up peaks are shown for clarity). These spectra were normalized to the neutral carbon peak at 284.6 eV. The binding energy and peak width obtained for the carbonate carbon was constrained during the fitting procedure for the blends. In accordance with the molecular structures of these polycarbonates, the area ratio between the carbonate carbon and methoxy carbon was also constrained to a value of two. The position and width of the shake-up peak in the blends changed in a manner consistent with those of the pure components. For each sample, a ratio was then obtained between the best-fit carbonate peak area (corrected for number of scans) for the blend and the best fit carbonate peak area of the appropriate pure components. This ratio, within experimental fitting error ( $\sim \pm 10\%$ ), is equal to the "average" monomer fraction of the polycarbonate within the XPS sampling depth for each sample.

Calculating the mole fraction of the BPAPC and TMPC at the surface of the blends from the SSIMS results is more difficult than that from the XPS results. The major assumption made in order to facilitate the calculations was, as explained earlier, that the matrix effects are negligible and, therefore, the secondary ion yield of the fragment ions do not change for either component in the blends. For an  $n$  component blend, a minimum of  $n$  mass fragments or peaks would be required to determine the relative amounts of each component using  $n - 1$  RPIs. The  $n$  mass peaks are chosen on the basis of the relative contribution of each component to the total peak intensity. If the intensity contribution to each



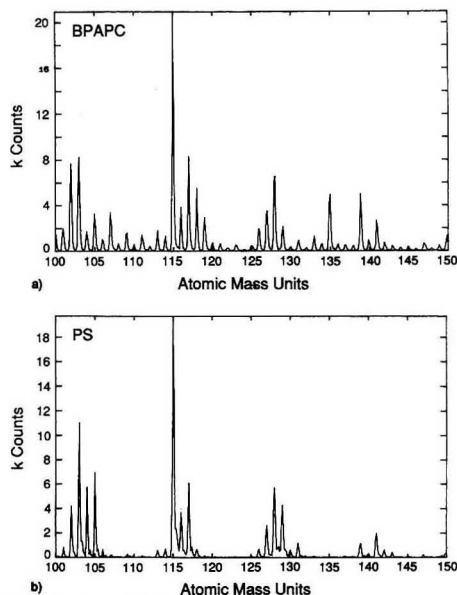


Figure 3. Static SIMS spectra of the 100–150 amu range of (a) BPAPC and (b) PS.

fragment ion is directly related to the amount of that component (actually the polymer repeat unit) at the surface, then linear additions of the appropriate percentages of peak intensities (integrated counts) from the pure components at each mass can be used to calculate a "total" intensity at each  $m/z$  value chosen. These theoretical intensities are then used to calculate the theoretical RPIs. Ideally, if the above assumptions held, RPIs would not have to be used, but rather, individual  $m/z$  intensities could be used. However, the utilization of a ratio helps minimize any problems associated with instrumental drift, signal attenuation from any nonuniform surface contamination that may build up after the samples are prepared, etc.

A mass peak is considered a potentially good candidate for this analytical scheme if it has a large contribution from only one component and minor contributions from the remaining components. It should also have negligible contributions from any fragment ions arising from contaminating species that may be on the surface. Therefore, it is best if the mass peaks chosen are greater than  $m/z$  100 in order to minimize the contributions from any simple aliphatic surface contaminants present. Another criterion that should be met, if possible, is to have a sufficient number of counts in each peak so that any statistical counting errors are not significant. Picking peaks that are relatively close together may further reduce any effects from differential surface charging or transmission and detection inefficiencies for widely different mass ions. (Theoretically, these effects are negligible for this type of instrument for  $m/z < 5000$ .)

Figures 3 and 4 show the positive-ion mass spectra of the  $m/z$  100–150 region of pure BPAPC and PS and the  $m/z$  150–200 region of pure TMPC and PS, respectively. The intensities of the PS peaks used in the following analyses were, within experimental error, identical at both interfaces. Therefore, only the portion of the PS spectrum from the PS/polyethylene interface is shown.

Positive-ion mass spectra were used in this study because

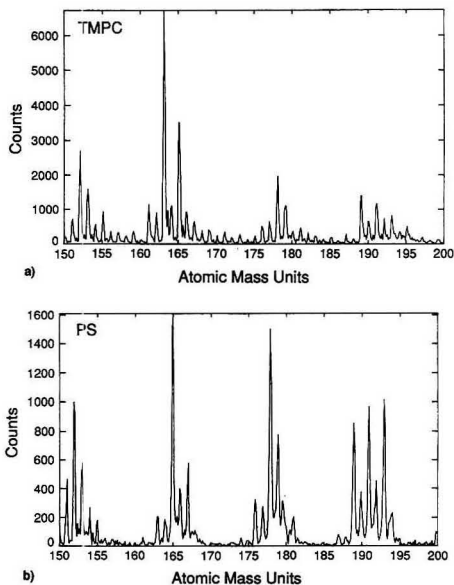


Figure 4. Static SIMS spectra of the 150–200 amu range of (a) TMPC and (b) PS.

the PS does not have an electronegative heteroatom to stabilize the negative charge of the larger ( $m/z > 100$ ) negative ions and the lower mass fragment ions of PS are not very unique. However, it has been shown that for many polymers containing electronegative heteroatoms, such as the polycarbonates used here, the negative-ion spectra often show more polymer-specific fragments (22, 23). It is generally more difficult to obtain reproducible negative-ion spectra because the negative extraction potentials remove the secondary electrons along with the negative secondary ions. Therefore, the flux of charge-compensating electrons required for obtaining negative-ion spectra must be higher than when acquiring positive-ion spectra. If the absolute intensities and RPIs of the peaks chosen in the negative-ion spectra of the pure components are not reproducible, then the analysis scheme described in this paper would not be applicable. The same obviously holds true for the positive-ion spectra.

For the BPAPC/PS blend the peaks chosen for the analyses were  $m/z$  115 and 135. The 115 fragment has relatively equal intensity in both the BPAPC and PS spectra. While the 135 fragment is primarily from the BPAPC, suitable mass peaks for the TMPC/PS blends are 163 and 165, where the 163 peak represents primarily TMPC and the 165 peak has contribution from TMPC and PS. Suggested structures of the PS and BPAPC fragments are shown in Figure 5 (17). The TMPC assignments were an extension of the BPAPC assignments.

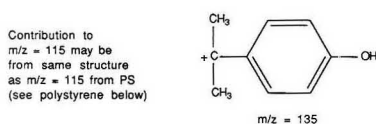
Unfortunately, the PS spectrum is very similar to the BPAPC and TMPC spectra and, therefore, the choices for useful mass spectral peaks were unusually limited. It would be desirable to pick several combinations of RPIs for any one blend in order to have an internal comparison as to the suitability of the chosen ratios. For example, if most of the mass combinations yield similar surface compositions, then any combinations that differ greatly may be due to contributions to a few of the peak intensities from other materials at the surface, such as from ambient contamination. It is also possible that the production of some ions may be more sus-

**Table I. Summary of Physical Data and Results for BPAPC/PS Polymer Blends**

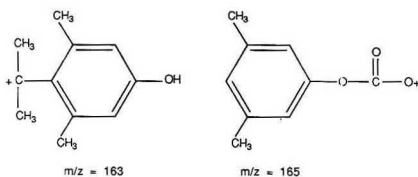
surface energy, ergs/cm <sup>2</sup>		BPAPC = 45.1 ± 1.3	PS = 45.0 ± 1.1		PE = 41.0 ± 1.4	
bulk wt % <sup>a</sup>	bulk monomer fraction	T <sub>g</sub> °C BPAPC/PS	XPS <sup>b</sup>		SSIMS RPI ± σ (3 replicates)	SSIMS surface monomer fraction
			18°	38°		
100	1.00	156/na <sup>c</sup>	1.00	1.00	0.33 ± 0.01	1.02
90	0.79	<i>d</i>	0.90	0.89	0.31 ± 0.01	0.96
80	0.62	<i>d</i>	0.75	0.76	0.27 ± 0.02	0.82
70	0.49	156/102	0.65	0.76	0.14 ± 0.08	0.43
60	0.38	157/104	0.23	0.47	0.05 ± 0.01	0.14
50	0.29	155/104	0.00	0.25	0.02 ± 0.02	0.04
40	0.21	156/103	0.00	0.17	0.01 ± 0.01	0.01
30	0.15	156/103	0.00	0.10	0.02 ± 0.01	0.03
20	0.09	157/103	0.00	0.00	0.02 ± 0.01	0.03
10	0.04	<i>d</i>	0.00	0.00	0.02 ± 0.01	0.04
0	0.00	na/103	0.00	0.00	0.01 ± 0.00	0.00

<sup>a</sup> Weight percents and monomer fractions are based on BPAPC in BPAPC/PS blend. <sup>b</sup> Absolute errors on the XPS values are between 0.05 and 0.1 monomer fraction. <sup>c</sup> na = not applicable. <sup>d</sup> No measurement was made.

a) Fragment ions from bisphenol-A polycarbonate (BPAPC)



b) Fragment ions from tetramethyl bisphenol-A polycarbonate (TMPC)



c) Fragment ions from polystyrene (PS)

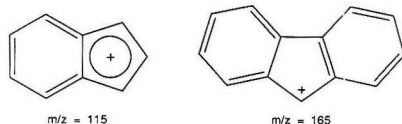


**Figure 5.** Suggested structures of the secondary ion fragments chosen from the (a) BPAPC, (b) TMPC, and (c) PS mass spectra.

ceptible to possible matrix effects than others and this comparison would help to identify matrix-sensitive RPIs.

Because this proposed analysis scheme requires the use of theoretical RPIs calculated from the experimentally measured intensities of the pure components, it should be obvious that the most important spectra are those of the pure components. Therefore, great care should be taken to obtain these spectra under identical experimental conditions and to statistically confirm their suitability.

The average (three different sampled areas from the same sample) experimentally determined integrated peak intensities, and their standard deviation, for  $m/z$  115 and 135 for the pure BPAPC and PS are 38713 ± 231 and 12701 ± 150 counts and 39856 ± 241 and 389 ± 35 counts, respectively. Integrated peaks intensities for  $m/z$  163 and 165 for the pure TMPC and PS are 15531 ± 53 and 8940 ± 121 counts and 627 ± 41 and 4666 ± 88 counts, respectively. The largest and

smallest relative standard deviations (rsd) for these two blends would be for the BPAPC blend, with the pure PS RPI having an rsd of ~0.1 and pure BPAPC RPI having an rsd of ~0.01. The rsd of these average intensities are generally only slightly larger than would be expected from the statistical counting error [(counts)<sup>1/2</sup>/counts]. Therefore, the repeatability of the intensities is considered to be adequate for this work.

Parts a and b of Figure 6 are plots of the calculated theoretical RPIs versus the mole fraction of BPAPC and TMPC. For graphical simplification, the error bars for each data point were omitted. The simplest appropriate least-squares fits obtained for the two curves are

$$y = 3.2x - 0.031 \quad r^2 = 0.998, \text{ for BPAPC/PS} \quad (1)$$

$$y = 0.25x^2 + 0.14x - 0.011 \quad r^2 = 0.999, \text{ for TMPC/PS} \quad (2)$$

where  $x$  and  $y$  are the RPI and monomer fraction of the BPAPC or TMPC, respectively.

Table I contains the bulk monomer fraction of the BPAPC in the BPAPC/PS blends calculated from their known monomer molecular weights and wt %, the glass-transition temperatures of the blends from the DSC results, surface energies for the pure materials, the surface compositions of the analyzed samples calculated from the XPS data, the average experimental RPIs (including the standard deviation and number of replicates), and the surface compositions calculated from the average experimental RPIs using eqs 1 and 2, as appropriate. Table II contains the corresponding information for the TMPC/PS blends.

Parts a and b of Figure 7 are plots of the surface monomer fraction of BPAPC and TMPC, respectively, as a function of their bulk monomer fraction as determined by XPS and SSIMS.

**I. Immiscible BPAPC/PS Blends.** As would be expected for an immiscible polymer blend, the DSC results show two separate  $T_g$  values (Table I) in all of the BPAPC/PS blends analyzed.

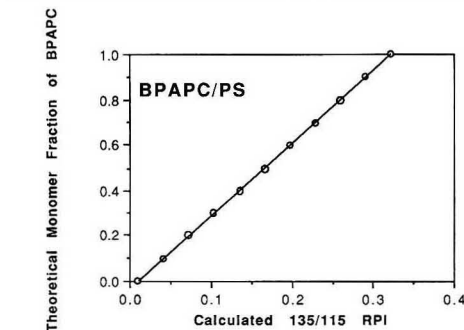
From Figure 7a several trends are readily noticeable. The SSIMS results show an inflection point at ~0.5 bulk monomer fraction of BPAPC (~0.4 surface fraction) with a quick change in surface composition from mostly BPAPC at higher fractions of BPAPC to virtually pure PS at the lower BPAPC fractions. This change at ~0.5 bulk monomer fraction appears to be explainable on the basis of the immiscibility of the two components and their comparable surface energies (refer to Table I).

It is interesting to compare the rsd of the RPIs for these blends. The 0.49 monomer fraction sample had the largest

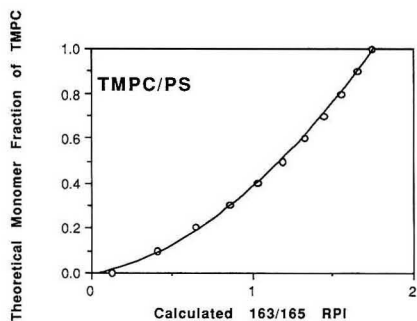
Table II. Summary of Physical Data and Results for TMPC/PS Polymer Blends

surface energy, ergs/cm <sup>2</sup>		TMPC = 44.4 ± 0.8	PS = 45.0 ± 1.1	PE = 41.0 ± 1.4		
bulk wt % <sup>a</sup>	bulk monomer fraction	T <sub>g</sub> , °C TMPC/PS	XPS <sup>b</sup>		SSIMS RPI ± σ (3 replicates)	SSIMS surface monomer fraction
			18°	38°		
100	1.00	196	c	1.00	1.74 ± 0.03	0.99
90	0.75	179	0.95	0.99	1.70 ± 0.03	0.95
80	0.57	c	0.83	0.79	1.45 ± 0.03	0.72
70	0.44	160	c	c	1.25 ± 0.04	0.55
60	0.34	c	c	0.73	1.20 ± 0.03	0.52
50	0.25	142	0.51	0.57	1.00 ± 0.04	0.38
40	0.18	c	c	c	0.91 ± 0.04	0.32
30	0.13	124	c	0.38	0.77 ± 0.05	0.25
20	0.08	c	c	c	0.60 ± 0.05	0.16
10	0.04	110	c	0.10	0.50 ± 0.05	0.12
0	0.00	103	c	0.00	0.13 ± 0.01	0.01

<sup>a</sup>Weight percents and monomer fractions are based on TMPC in TMPC/PS blend. <sup>b</sup>Absolute errors on the XPS values are between 0.05 and 0.1 monomer fraction. <sup>c</sup>NO measurement was made.



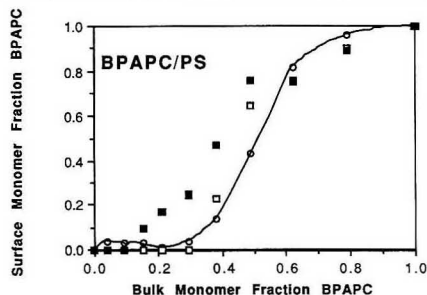
a)



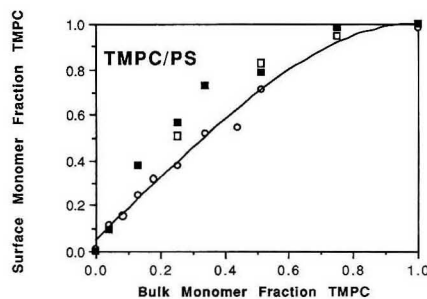
b)

Figure 6. Theoretical monomer fractions of (a) BPAPC and (b) TMPC in the blends as a function of calculated 135/115 and 163/165 peak intensity ratios, respectively.

"replicate" variability with much smaller variability at the higher and lower fractions. This is probably due to large differences in the degree of surface segregation of BPAPC over the surface of the 0.49 monomer fraction sample. This suggests that the surface segregation of two immiscible polymers with similar surface energies can strongly depend on localized differences in processing conditions. If the BPAPC and PS are immiscible then there should be separate domains of each material at the surface; particularly for the samples with



a)



b)

Figure 7. Comparison of the surface monomer fractions of (a) BPAPC and (b) TMPC to their respective bulk monomer fractions in the two blends as determined by SSIMS (O) and XPS at a 18° (□) and 38° (■) ETOA.

BPAPC monomer fractions near 0.5. The size of these domains for the 0.49 BPAPC monomer fraction sample should be comparable to the  $\sim 300 \times 300 \mu\text{m}$  sample area used for the SSIMS analyses. The XPS analysis area was  $\sim 1 \text{ mm} \times 6 \text{ mm}$ ; therefore, the XPS results would reflect more of an "average" surface composition.

The low signal intensity and lack of sufficient "contrast" of the intensity contributions of BPAPC and PS to the  $m/z$  135 peak precluded any ion imaging of surface domains using positive-ion SSIMS. However, BPAPC contains oxygen while



Figure 8. 256 × 256 pixel O<sup>-</sup> SSIMS image of the 0.49-monomer fraction BPAPC/PS sample showing BPAPC (light areas) and PS (dark areas) surface domains. Field of view is ~750 μm.

PS does not. This allowed for O<sup>-</sup> imaging of the separate surface domains of the 0.49 monomer fraction sample by SSIMS. For a flat sample like this, a higher local concentration of oxygen from BPAPC will show up as a brighter area in the image. Figure 8 shows one of the 256 × 256 pixel O<sup>-</sup> images obtained (field of view is ~750 μm total ion dose < 10<sup>12</sup> ions/cm<sup>2</sup>). Many of the imaged domains had "lengths" greater than 1 mm and "widths" ranging from 0.1 to 0.5 mm. The ~750-μm field of view images always showed some BPAPC present at the surface. There was no obvious trend in the direction of the BPAPC (bright areas) and PS (dark areas) domains when different areas were compared. The ~300-μm field of view images ranged from nearly black to nearly white with boundaries between light and dark areas ranging from sharp to diffuse; indicating that the areas being sampled ranged from ~0 to ~100% BPAPC.

The SSIMS results appear to be in excellent agreement with the XPS results when the various forms of error and the different sampling depths are considered. The data at the 18° ETOA produced the closest agreement with the SSIMS results, providing surface compositions with slightly less BPAPC at bulk BPAPC fractions greater than 0.5 and larger surface fractions of BPAPC at bulk BPAPC values under 0.5. This is in agreement with comparable surface sensitivities for SSIMS and glancing-angle XPS.

There is some suggestion from the XPS and SSIMS results that the gradient, in going from the surface composition to the bulk composition, is less steep (distance from surface to bulk compositions is >5 nm) at higher values of the bulk BPAPC fraction, while the change from surface to bulk composition is occurring rapidly (<5 nm) at low bulk fractions of BPAPC.

**II. Miscible TMPC/PS Blends.** The DSC data (Table II) shows a smooth transition between the  $T_g$  of PS and TMPC, as would be expected from miscible polymers. Both the XPS and SSIMS results (Figure 7b) show a smooth

transition from pure TMPC to pure PS at the surface, with a higher-than-bulk concentration of TMPC at the surface for all of the blends. Although the errors associated with the surface energy measurements do not allow for a definitive comparison between the measured surface energies, the measured surface energy value for TMPC is lower than that of PS. If the TMPC surface energy is actually lower than that of PS, then this could explain the observed segregation of the TMPC to the polyethylene surface.

The agreement between the XPS and SSIMS results are very good if the known errors are considered. Only three XPS spectra were recorded using the 18° ETOA, with very similar results to the corresponding 38° ETOA, suggesting that the charge from surface to bulk concentrations starts to occur deeper (>5 nm) than the XPS sampling depth. However, there is the suggestion of a trend in the XPS results showing a higher concentration of TMPC at the surface, particularly at the lower TMPC fractions, when compared to those obtained from SSIMS. On the basis of the XPS results and the sampling depths of the two techniques, it would be expected that the XPS and SSIMS results should overlap. There are at least two obvious possibilities for this. Perhaps the peak intensities for pure PS may be incorrect, because the unknown errors that could bias the calculated values below those calculated from the XPS results. In addition, there may be some bias generated from added contributions to these peak intensities from surface contamination that increases as the surface concentration of PS increases. Another possibility is that matrix effects, such as surface orientation, polymer interactions, etc., are responsible for the observed bias, and therefore the validity of the negligible matrix effect assumption may be questioned. Of course the "validity" of this assumption would depend on the desired accuracy for any given study of polymer-blend surface compositions.

## CONCLUSION

The results of this comparative XPS and SSIMS study suggest that SSIMS may hold the potential for becoming a "stand-alone" technique for the quantitative surface analysis of organic polymer blends.

With an energy-focusing TOF mass spectrometer nearly the entire secondary ion energy spread can be accepted during the secondary ion extraction step while compensation of sample charging is accomplished when the extraction potential is removed.

From these preliminary findings, it appears that the matrix effects in organic polymer blends may be negligible due to the similar requirements for the production of organic fragment ions. However, these results, particularly those for the miscible blend, suggest that additional studies are required to accurately predict the extent to which matrix effects may or may not be negligible. Perhaps, by the study of an appropriate series of miscible polymer systems, correlations can be made between the "lack of fit" of the XPS and SSIMS results with "known" polymer interaction parameters in order to better understand matrix effects in these types of systems. This understanding may allow for a correction of the SSIMS data to agree with the XPS results and, ultimately, to obtain accurate SSIMS results for systems that XPS is incapable of studying. One such parameter may be the Flory-Huggins interaction parameter,  $\chi$ , which describes the free energy of mixing in polymer blends. Polymer chemists have found this interaction parameter to be very useful in quantifying and predicting miscibility in polymer blends.

## ACKNOWLEDGMENT

I thank Hsinjin Yang (Eastman Kodak Co.) for suggesting the use of the BPAPC/PS and TMPC/PS systems, for obtaining and purifying the polymers used in this study, for the

DSC results, and for the many discussions concerning polymer blends. I also thank David Weiss (Eastman Kodak Co.) for producing the coatings and for the numerous discussions. In addition, I thank Kim Goppert-Berarducci (Eastman Kodak Co.) for measuring the surface energies of these polymers and the discussions concerning contact-angle measurements.

Registry No. PS (homopolymer), 9003-53-6; BPAPC (SRU), 24936-68-3; BPAPC (copolymer), 25037-45-0; TMPC (SRU), 38797-88-5; TMPC (copolymer), 136132-65-5.

#### LITERATURE CITED

- (1) Bletsos, I. V.; Hercules, D. M.; Fowler, D.; van Leyen, D.; Benninghoven, A. *Anal. Chem.* **1990**, *62*, 1275-1284.
- (2) Briggs, D. *Br. Polym. J.* **1989**, *21*, 3-15.
- (3) Hook, K. J.; Gardella, J. A. *J. Vac. Sci. Technol. A* **1989**, *7*, 1795-1800.
- (4) Lub, J.; van Leyen, D.; Benninghoven, A. *Polym. Commun.* **1989**, *30*, 74-77.
- (5) van Velzen, P. N. T.; Wierenga, P. E.; Schaake, R. C. F.; van Leyen, D.; Benninghoven, A. *Tribol. Trans.* **1988**, *31*, 489-496.
- (6) Zhao, C. L.; Dobler, F.; Pith, T.; Holl, Y.; Lamba, M. J. *Colloid Interface Sci.* **1989**, *128*, 437-449.
- (7) Hearn, M. J.; Ratner, B. D.; Briggs, D. *Macromolecules* **1988**, *21*, 2950-2959.
- (8) Hearn, M. J.; Briggs, D.; Yoon, S. C.; Ratner, B. D. *Surf. Interface Anal.* **1987**, *10*, 384-391.
- (9) Briggs, D.; Ratner, B. D. *Polym. Commun.* **1988**, *29*, 6-8.

- (10) Bhatia, Q. S.; Burrell, M. C. *Surf. Interface Anal.* **1990**, *15*, 388-391.
- (11) Briggs, D.; Munro, H. S. *Polym. Commun.* **1987**, *28* (Part 10), 307.
- (12) Hennequin, J. F. *J. Phys.* **1968**, *29*, 655.
- (13) Kelner, L.; Patel, T. C. *Secondary Ion Mass Spectrometry, SIMS V*; Benninghoven, A., Colton, R. J., Simons, D. S., Werner, H. W., Eds.; Springer-Verlag, Berlin, 1986; pp 494-496.
- (14) Mamyrin, B. A.; Kartsev, V. I.; Schmitt, D. V.; Zagulin, V. A. *Sov. Phys -JETP (Engl. Transl.)* **1973**, *37*, 45.
- (15) Poschenrieder, W. P. *Int. J. Mass Spectrom. Ion Phys.* **1972**, *9*, 357.
- (16) Hagenhoff, B.; van Leyen, D.; Niehuis, E.; Benninghoven, A. *Secondary Ion Mass Spectrometry, SIMS VI*; Benninghoven, A., Huber, A. M., Werner, H. W., Eds.; John Wiley & Sons: New York, 1988; pp 235-238.
- (17) Briggs, D.; Brown, A.; Vickerman, J. C. *Handbook of Static Secondary Ion Mass Spectrometry (SIMS)*; John Wiley & Sons: Chichester, U. K., 1989.
- (18) Waugh, A. R.; Kingham, D. R.; Hearn, M. J.; Briggs, D. *Secondary Ion Mass Spectrometry, SIMS VI*; Benninghoven, A., Huber, A. M., Werner, H. W., Eds.; John Wiley & Sons: New York, 1988; pp 231-234.
- (19) Briggs, D.; Hearn, M. J.; Fletcher, I. W.; Waugh, A. R.; McIntosh, B. J. *Surf. Interface Anal.* **1990**, *15*, 62-65.
- (20) Fadley, C. S. *Prog. Solid State Chem.* **1976**, *2*, 265-343.
- (21) Dann, J. R. *J. Colloid Interface Sci.* **1970**, *32*, 302.
- (22) Brown, A.; Vickerman, J. C. *Surf. Interface Anal.* **1986**, *8*, 75-81.
- (23) Briggs, D. *Org. Mass Spectrom.* **1987**, *22*, 91-97.

RECEIVED for review January 28, 1991. Accepted August 9, 1991.

## Determination of the Concentration and Stable Isotopic Composition of Nonexchangeable Hydrogen in Organic Matter

Arndt Schimmelmann

University of California at San Diego, Scripps Institution of Oceanography, La Jolla, California 92093-0215

The hydrogen stable isotope ratio of organic matter containing hydrogen that is not solely conservative, nonexchangeable, carbon-bound hydrogen depends on sample preparation, because organic hydrogen bound to oxygen and nitrogen may exchange isotopically with ambient-water hydrogen. The method described here permits the determination of the concentration and stable isotopic composition of the nonexchangeable hydrogen in complex organic matter, such as geochemicals and biological and archaeological organic materials. Allquots of organic substrates were independently equilibrated with water vapors of different hydrogen isotopic compositions, followed by determinations of the bulk D/H ratios. Mass-balance calculations permit eliminating or minimizing the interference of exchangeable hydrogen. The precision of the calculated stable isotope ratio of nonexchangeable hydrogen can be better than  $\pm 3$  per mil, depending on the precision of the measured values for bulk hydrogen. The accuracy of D/H ratios of nonexchangeable hydrogen was improved over that of previously available methods, as shown for cellulose/cellulose nitrate.

#### INTRODUCTION

Stable hydrogen isotope ratios of modern and fossil organic matter bear potentially valuable geochemical, environmental, dietary, and climatic information (1-4). The problem of uncontrolled isotopic exchange between organic hydrogen bound to oxygen (O-H) and nitrogen (N-H) with ambient-water

hydrogen limits the usefulness of measuring total D/H ratios in most organic compounds. Notable exceptions are hydrocarbons and lipids, nitrated cellulose, and chemical derivatives of chitin (5-9), all of which ideally contain only isotopically conservative, nonexchangeable, carbon-bound hydrogen (C-H).

A method is described for the determination of the concentration and stable isotopic composition of the nonexchangeable hydrogen in organic matter, based on controlled isotopic equilibrations of O-H and N-H with isotopically distinct water vapors. Standard techniques are then employed for the determination of the stable isotope ratios of the resulting bulk hydrogen (10, 11).

After isotopic equilibration of an organic substance with water hydrogen, the deuterium in total organic hydrogen is the sum of the deuterium in the nonexchangeable and the exchangeable hydrogen pools, or

$$\delta_T = (1 - f_e)\delta_n + f_e(\delta_w + \epsilon) \quad (1)$$

$$\delta_T = \delta_n - f_e\delta_n + f_e\epsilon + f_e\delta_w \quad (2)$$

where  $\delta_T$  is isotopic composition of total organic hydrogen,  $f_e$  = fraction of total hydrogen which is exchangeable,  $\delta_n$  = isotopic composition of nonexchangeable hydrogen,  $\delta_w$  = isotopic composition of water, and  $\epsilon$  = isotope fractionation effect between exchangeable organic hydrogen and water hydrogen, in per mil. Equation 2 is of the form  $y = a + bx$ , where  $y$  is analogous to  $\delta_T$ ,  $a$  to  $(\delta_n - f_e\delta_n + f_e\epsilon)$ ,  $b$  to  $f_e$ , and  $x$  to  $\delta_w$ . A calculation of  $\delta_n$  is possible based on the basis of two isotopic equilibration experiments, with knowledge of (1) the  $\delta_w$  values of two different water vapors used for equili-



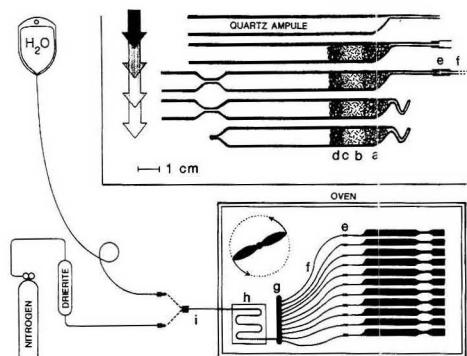


**Figure 1.** Apparatus for the isotopic equilibration of exchangeable organic hydrogen with water vapor. Quartz or Vycor ampules are filled with (a) quartz wool, (b) copper(II) oxide and silver foil, (c) organic substrate, and (d) copper wool or foil and are additionally furnished with a segment of Teflon shrink tubing (e). The arrangement within the oven consists of several filled ampules that are connected via shrink tubing (e), Teflon capillary tubing (f), Teflon manifold (g), stainless steel capillary (h) coiled within an aluminum heating block, and a Teflon capillary (i) to a port outside of the oven. The port receives either dry nitrogen gas or deionized water.

bration, (2) the resulting  $\delta_T$  values of the equilibrated organic substrates, and (3) the isotope fractionation effect  $\epsilon$  for exchangeable hydrogen present in the substrate. Isotope effects  $\epsilon$  are temperature-dependent and can be determined experimentally (shown below for cellulose) or can be calculated for different types of bonds (12–17). Chemically complex substrates with no precise stoichiometry do not permit a precise calculation of  $\epsilon$ . Each molecule of kerogen, for example, would have a unique set of hydroxyl, carboxyl, amino, etc. groups with exchangeable hydrogen. A value  $\epsilon$  for all exchangeable hydrogen can be estimated in the form of a "mean fractionation effect", by first calculating the various fractionation factors for individual functional groups and then using an overall weighted average according to the relative abundances of the functional groups in the substrate.

The presented method is applicable to organic compounds that are chemically stable in water vapor at a chosen equilibration temperature, regardless of the ratio of C–H versus O–H and N–H. Caution should be exercised with compounds containing high concentrations of sulfur, because sulfur has been shown to decrease the hydrogen recovered after the combustion and may thus introduce isotopic artifacts (18).

## EXPERIMENTAL SECTION

**Apparatus.** Samples (3–12 mg) are loaded together with quartz wool, approximately 1 g of copper(II) oxide wire, a few square millimeters of 0.025 mm thick silver foil, and approximately 300 mg of copper foil or wool in a Vycor or quartz ampule (o.d. 9 mm) that has an open tip (o.d. approximately 2 mm, length 6 cm) at one end (Figure 1). The organic sample can be wrapped in quartz wool or another gas-permeable, inert material to avoid contact with CuO, if necessary. All inorganic materials, except Cu foil, are precombusted at 550 °C. The tip of the ampule is fitted with a 1 cm long segment of Teflon shrink tubing (o.d. 3 mm; Cole-Parmer; shrunk 5 mm onto tip), and the ampule receives a constriction at the other end. The shrink tubing is then connected to Teflon capillary tubing within an oven. Several ampules are connected to a Teflon manifold. The temperature-controlled oven with fan-forced air convection holds an aluminum heating block kept at a temperature of 150–200 °C, with a stainless steel capillary (i.d. 0.8 mm) coiled within. The Teflon manifold connects via stainless steel and Teflon capillaries to a port outside of the oven. The port can be linked either to a supply line of dry nitrogen gas or to a Teflon capillary leading to a raised reservoir

of deionized water (with known isotopic composition; head space and evaporative isotope fractionation are avoided by employing an air-free, collapsible, medical-type infusion container).

**Reagents.** Distilled deuterium-depleted water (from Athabasca Glacier, Canada) and various additions of D<sub>2</sub>O to distilled San Diego tap water yielded five waters for the exchange experiments, with  $\delta D$  values of –157, –87, +112, +286, and +704 per mil. Cellulose and the corresponding cellulose nitrate were prepared according to standard techniques by Sternberg (19). Purified cotton was obtained from medical supplies. Humic acid and protokerogen from Recent marine sediment from the Santa Barbara Basin (20) and kerogen from the Miocene Monterey Formation were exhaustively demineralized (21, 22). Chitin from a lobster (*Homarus americanus*) was prepared via decalcification and deproteinization of the carapace (23). Reagent grade oxalic acid diammonium salt was obtained from Sigma.

**Procedure.** Figure 1 describes the preparation of ampules containing organic samples. The connected ampules are continuously flushed with dry N<sub>2</sub>, while the oven temperature is raised to the desired degree, in this study between 104 and 156 °C. After switching from nitrogen to distilled water, the steam pressure and overall flow rate are regulated by adjusting the height at which the water reservoir bag is positioned above the heating block (=vaporizer) level. Average water consumption over 20 h of operation was approximately 10 mL at 0.1 bar water vapor pressure. At the end of the equilibration period, the samples are again flushed with dry N<sub>2</sub> for at least 3 h while the oven is allowed to cool during the last 2 h. While a positive pressure is still maintained with dry N<sub>2</sub>, the samples are then sequentially sealed off with a torch, close to the Teflon connections. The 9 mm o.d. openings are temporarily sealed with paraffin to exclude moist air. Angular break seals are formed at the sealed tips (Figure 1), using a fine torch. After removal of the paraffin, the samples are immediately evacuated on a vacuum line and finally sealed under vacuum. The subsequent processing of the samples and the conversion of water to H<sub>2</sub> follow routine methods (10, 11). Engel and Maynard's (24) observation regarding the possibility of carbon isotope fractionation within combusted ampules after cooling is likely to be valid for hydrogen as well, via formation of hydrated sulfates (18) and hydrated copper carbonates (24). All samples need to be processed on a vacuum line within a few hours following combustion. Gas yields are measured manometrically.

Isotopic results are expressed in  $\delta D_{\text{SMOW}}$  notation in per mil referring to standard mean ocean water (SMOW) isotope standard:

$$\delta D_{\text{SMOW}} \text{ (per mil)} = \left( \frac{D/H_{\text{sample}}}{D/H_{\text{SMOW}}} - 1 \right) \times 10^3$$

The mass spectrometric precision of the measurements is  $\pm 2$  per mil for  $\delta D_{\text{SMOW}}$  values.

## RESULTS AND DISCUSSION

The isotopic responses of various organic compounds to equilibrations with five isotopically different water vapors at 114 °C and 20 h are shown in Figure 2. The slope of a linear regression line connecting data from a given compound reflects a measure of the substance's overall hydrogen isotopic exchangeability [in percent of total hydrogen; this study uses functional GM linear regressions which take into account that both variates are subject to error of measurement (25)]. For example, a slope of 45° would indicate that all hydrogen in a sample is exchangeable. A slope of zero would identify the y intercept as the  $\delta D$  value of the conservative D/H ratio of a compound with no exchangeable hydrogen.

**Case Study of Cellulose versus Cellulose Nitrate.** The slope of the cellulose regression line in Figure 2 translates into an exchangeability of 26.7% at 114 °C, or  $f_e = 0.267$  in eqs 1 and 2 (linear regression coefficient  $R = 0.999$ ,  $n = 8$ ). In theory, 30% of the hydrogen in the biopolymer [C<sub>6</sub>H<sub>7</sub>O<sub>2</sub>(OH)<sub>3</sub>]<sub>n</sub> is O–H and thus potentially exchangeable, but in practice, cellulose is a fibrous, closely knit agglomerate of biopolymers in which not all O–H are physically accessible (26). This cellulose can be compared with its nitrated counterpart,

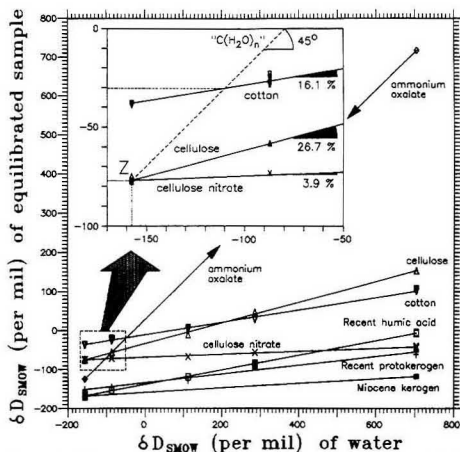


**Figure 2.**  $\delta D_{\text{SNOW}}$  values of isotopically equilibrated organic materials versus  $\delta D_{\text{SNOW}}$  values of the waters used for the equilibration at 114 °C over 20 h.

cellulose nitrate, in Figure 2. Even exhaustively nitrated cellulose still contains some hydroxyl hydrogen (27), resulting here in a 3.9% exchangeability, or  $f_e = 0.039$  ( $R = 0.991$ ,  $n = 7$ ).

The algebraically calculated intersection  $Z$  (Figure 2) of the regression lines for cellulose and cellulose nitrate falls on  $-157$  per mil on the  $x$  axis ( $\delta D$  of water,  $\delta_{WZ}$ ) and  $-77$  per mil on the  $y$  axis ( $\delta D$  of equilibrated substrate,  $\delta_{TZ}$ ). Using eq 2, we can fill in the known  $\delta_T$ ,  $f_e$ , and  $\delta_W$  values for both cellulose and cellulose nitrate, yielding two equations with two unknowns ( $\delta_n$ ,  $\epsilon$ ) and permitting the calculation of  $\delta_n = -77$  per mil and  $\epsilon = 80$  per mil. As expected for higher temperatures, the  $\epsilon$  value falls in the lower range of hydrogen isotopic fractionation for organic O-H bonds [for example, ethanol 110 per mil, benzyl alcohol 100 per mil, phenol 70 per mil; all calculated for 25 °C (12)].

The  $x$  and  $y$  coordinates of the intersection  $Z$  of the regression lines describe unique equilibration conditions when water of  $-157$  per mil is used: The isotopic composition of the exchangeable hydrogen, after equilibration with water of  $-157$  per mil, is identical with the isotopic composition of the nonexchangeable hydrogen ( $-77$  per mil). The isotope fractionation effect  $\epsilon$  between water hydrogen and cellulose hydroxyl hydrogen accounts for  $157 - 77 = 80$  per mil. By rearranging eq 2 to

$$\delta_{TZ} = \delta_n + f_e(\epsilon + \delta_{WZ} - \delta_n) \quad (3)$$

we see that the expression in the bracket is always zero ( $80 - 157 + 77 = 0$  in the numerical example). It follows that  $\delta_{TZ}$  is dependent only on  $\delta_n$ . Therefore,  $f_e$  can be chosen freely between 1 and 0 (for non-nitrated cellulose and completely nitrated cellulose, respectively) without effect on the locus of  $Z$ . In other words, we can substitute any number of hydroxyl groups (equilibrated to  $-77$  per mil) with nitrate groups without changing the overall isotopic composition of  $-77$  per mil. The extent of nitration determines the slope of the cellulose nitrate line, but it does not influence the location of the intersection  $Z$  of the cellulose and cellulose nitrate lines. Moreover, all celluloses, regardless of their C-H isotopic compositions  $\delta_n$ , have their  $Z$  intersections of respective lines of their non-nitrated and nitrated forms falling on a 45° line marked " $C(H_2O)_n$ " in Figure 2. Note that " $C(H_2O)_n$ ", following the formula  $y = x + a$ , or  $\delta_T = \delta_W + \epsilon$ , is valid for a specific

temperature only, here 114 °C, because  $\epsilon$  is responsible for the position of the line along the  $x$  axis.

A " $C(H_2O)_n$ " line is valid for all celluloses, and possibly for all carbohydrates as well, as long as they express the same  $\epsilon$  value, for a given equilibration temperature. For example, with knowledge of  $\epsilon$  the determination of the isotopic composition of C-H of an organic compound is possible by opting for one of the following strategies: If the relative amount of exchangeable hydrogen and the slope of the equilibration line are well-known, it may be sufficient to equilibrate one aliquot of a sample, determine its overall  $\delta D$  value, and construct the intersection of two lines as in the cellulose example. Higher precision could be achieved by multiple equilibrations with various water vapors in combination with regression analyses. If the isotopic exchangeability of a compound is not known, one needs at least two D/H exchange reactions to construct such a line. For cotton, which represents almost pure carbohydrate, the  $y$  coordinate of the intersection with " $C(H_2O)_n$ " in Figure 2 suggests a  $\delta D$  value of C-H of  $-31$  per mil (exchangeability 16.1%;  $R = 0.997$ ,  $n = 17$ ). In terms of accuracy of D/H ratios of C-H in cellulose, the equilibration method outperforms the use of nonequilibrated nitrated cellulose, because the isotopic influence of even small amounts of remaining exchangeable hydrogen in nitrated cellulose is taken into account.

**Implications for Non-Carbohydrate Substrates.** A suitable line parallel to the " $C(H_2O)_n$ " line is valid for all organic compounds with the same  $\epsilon$  value, for a given equilibration temperature. The " $C(H_2O)_n$ " line would need to be shifted along the  $x$  axis to account for differences in the isotope fractionation effect  $\epsilon$ . The displacement can either be determined experimentally by chemical replacement of exchangeable hydrogen with inert groups (e.g., nitration, if chemically possible), or can be calculated on the basis of the knowledge of stretching and bending force constants (12-17). For example, Bigeleisen and Ishida's simple first-order calculation of isotope effects, particularly applicable to deuterium substitution, reflects the relative importance of bending and stretching forces to the isotope effect as a function of temperature (14). Unlike all other theoretical methods, Polyakov (17) uses  $\alpha$  and  $\beta$  factors in an innovative approach based on Galimov's (28) theory of thermodynamically controlled intramolecular isotope ordering. One may also choose compounds for comparison that contain only one kind of hydrogen bond, such as N-H, for example in ammonium oxalate ( $(NH_4)_2(COO)_2$  (Figure 2). In crystalline ammonium oxalate, 98.1% of the hydrogen was found to be exchangeable. A graphical evaluation, similar to the one discussed for cellulose O-H, yields a N-H fractionation of 17 per mil, at 114 °C. For comparison, Bigeleisen's (12) calculated values for N-H at 25 °C vary between  $-4.5$  (ammonia) and  $+110$  per mil (aniline).

Chemically complex kerogen, humic compounds, bulk organic tissues, etc. do not permit chemical replacement of O-H and N-H and would require the use of a calculated O-H and N-H mean isotope effect. The calculation could be aided by  $^1H$  NMR and IR data on the distribution and abundance of different types of functional groups bearing exchangeable hydrogen. Figure 2 does not attempt the determination of  $\delta_n$  for complex compounds, but it documents different degrees of exchangeability. The decline of exchangeability from Recent humic acid (18.8%;  $R = 0.999$ ,  $n = 7$ ) over Recent protokerogen (11.4%;  $R = 0.979$ ,  $n = 6$ ) to Miocene kerogen (6.3%;  $n = 2$ ; see also Table I) is consistent with decreased abundances of functional O-H and N-H containing groups in that order (29).

**Effect of Temperature on Isotopic Equilibration.** Table I illustrates the effect of temperature on the observed hydrogen exchangeability in various organic compounds.

**Table I. Hydrogen Isotopic Exchangeability (in Percent of Total Hydrogen) in Various Organic Compounds That Were Equilibrated for 20 h at 104, 114, 140, 143, and 156 °C<sup>a</sup>**

compd	exchangeability, %				
	104 °C	114 °C	140 °C	143 °C	156 °C
cellulose	23.1 (2)	26.7 (8)	nd	nd	26.8 (2)
chitin	nd	15.8 (2)	16.4 (2)	nd	17.2 (2)
cotton	15.7 (3)	16.1 (17)	nd	19.2 (6)	nd
humic acid	nd	18.8 (7)	20.7 (2)	nd	nd
kerogen	nd	6.3 (2)	8.4 (2)	nd	9.1 (2)

<sup>a</sup>The number of  $\delta D$  values used for calculation is given in parentheses; nd = not determined.

Isotopic equilibrations were performed over 20 h at 104, 114, and 143 °C in water vapors with  $\delta D$  values of -157, -87, and +704 per mil. At higher temperatures, exchangeability is larger, because isotopic exchange is kinetically controlled by diffusion of hydrogen species through the substrate. The exchange rate may widely vary depending on chemical composition and structure. Future studies of specific classes of compounds (e.g., crystalline or amorphous substrates, biopolymers, geopolymers, etc.) would be required to establish a temperature dependence and time regime for isotopic equilibration that achieves reproducible exchangeability while not compromising the chemical stability.

For the isotopic equilibration of temperature-sensitive substrates the oven temperature could be set below 100 °C if a regulated vacuum oven is used that can avoid having a liquid water phase in contact with the samples. One should bear in mind that even temperatures of a few degrees above boiling point, below critical temperature, may permit the existence of liquid water in porous samples, due to reduced vapor pressure within narrow pore spaces. Soluble constituents in the sample have a similar effect by forming solutions with lower vapor pressure. Any hydrous liquid phase in contact with a sample would be enriched in deuterium and would thus cause increased D/H ratios compared to properly equilibrated samples.

### CONCLUSIONS

The determination of the D/H ratio of nonexchangeable hydrogen in organic substrates via controlled isotopic equilibration of the exchangeable hydrogen pool is applicable to a large variety of materials. The equilibration method is the only approach feasible for those oxygen- and nitrogen-containing compounds that do not permit a chemical replacement of all their hydroxyl, amino, etc. groups by nitrate or other inert groups. Paleodietary, paleoclimatic, and paleoenvironmental stable isotope studies can utilize the hydrogen isotopic composition of chemically complex substrates, for example collagen from bone, amino acids, lignin, and various solid fossil fuels and biogeochemical isolates. Further use of the isotopic equilibration method might be extended to inorganic sub-

strates, for example phyllosilicates and zeolites.

### ACKNOWLEDGMENT

I sincerely thank John Hayes, Max Coleman, and Michael J. DeNiro for their helpful criticism. Leonel Sternberg provided cellulose and cellulose nitrate samples. I am grateful to Dave Winter (UCLA) and to the Stable Isotope Laboratory at the Southern Methodist University (Dallas) for their support and their mastery over stable isotope ratio mass spectrometry.

### LITERATURE CITED

- Buchardt, B.; Fritz, Peter, *Handbook of Environmental Isotope Geochemistry*; Elsevier: Amsterdam, 1980; Vol. 1, Chapter 12.
- Estep, Marilyn, F.; Dabrowski, Halina. *Science* **1980**, *209*, 1537-1538.
- Smith, J. W.; Rigby, D.; Schmidt, P. W.; Clark, D. A. *Nature* **1983**, *302*, 322-323.
- Schliowski, Manfred; Hayes, John M.; Kaplan, Isaac R. *Earth's Earliest Biosphere*; Princeton University Press: Princeton, NJ, 1983; pp 149-186.
- Epstein, Samuel; Yapp, C. J.; Hall J. *Earth Planet. Sci. Lett.* **1976**, *30*, 241-251.
- Schoell, Martin. *Org. Geochem.* **1984**, *6*, 645-663.
- Schimmelmann, Arndt; DeNiro, Michael J. *Geochim. Cosmochim. Acta* **1986**, *50*, 1485-1496.
- Miller, Randall F.; Fritz, Peter; Morgan, Alan V. *Palaeoogeogr., Palaeo-climatol., Palaeoecol.* **1988**, *66*, 277-288.
- Sternberg, Leonel. *Nature* **1988**, *333*, 59-61.
- Stump, R. K.; Frazer, J. W. *Nucl. Sci. Abstr.* **1973**, *28*, 746.
- Northfelt, Donald W.; DeNiro, Michael J.; Epstein, Samuel. *Geochim. Cosmochim. Acta* **1981**, *45*, 1895-1898.
- Bigeleisen, Jacob. *Science* **1965**, *147*, 463-471.
- Stern, M. J.; Wolfsberg, M. J. *Chem. Phys.* **1966**, *45*, 4105-4124.
- Bigeleisen, Jacob; Ishida, Takanobu. *J. Am. Chem. Soc.* **1973**, *95*, 6155.
- Bigeleisen, Jacob; Ishida, Takanobu. *J. Chem. Phys.* **1975**, *62*, 80-89.
- Bigeleisen, Jacob; Ishida, Takanobu. *J. Chem. Phys.* **1975**, *63*, 1702.
- Polyakov, V. B. *Geochim. Int.* **1988**, *25*, 117-121.
- Krishnamurthy, R. V.; DeNiro, Michael J. *Anal. Chem.* **1982**, *54*, 153-154.
- Sternberg, Leonel. *Plant Fibers; Modern Methods of Plant Analysis, New Series*; Springer: Berlin, 1989; Vol. 10, pp 89-99.
- Schimmelmann, Arndt; Lange, Carina B.; Berger, Wolf H. *Limnol. Oceanogr.* **1990**, *35*, 165-173.
- Wedeking, K. W.; Hayes, John M.; Matzigkeit, Udo. *Earth's Earliest Biosphere*; Princeton University Press: Princeton, NJ, 1983; pp 428-441.
- Idiz, Erdem, F. Ph.D. Dissertation, University California Los Angeles, 1987.
- Schimmelmann, Arndt; DeNiro, Michael J. *Chitin in Nature and Technology*; Plenum Publishing Corp.: New York, 1986; pp 357-364.
- Engel, M. H.; Maynard, R. J. *Anal. Chem.* **1989**, *61*, 1996-1998.
- Ricker, W. E. *J. Fish. Res. Board Can.* **1973**, *30*, 408-434.
- Young, Raymond, A.; Rowell, Roger M. *Cellulose: Structure, Modification, and Hydrolysis*; Wiley: New York, 1986; 379 pp.
- DeNiro, Michael J. *Earth Planet. Sci. Lett.* **1981**, *54*, 177-185.
- Galimov, Erik Mikhailovich. *The Biological Fractionation of Isotopes*; Academic Press: Orlando, FL, 1985.
- Tissot, Bernard, P.; Welte, Dietrich, H. *Petroleum Formation and Occurrence*, 2nd ed.; Springer: Berlin, 1984; 699 pp.

RECEIVED for review February 11, 1991. Accepted July 8, 1991. This work was supported by the Universitywide Energy Research Group Account No. 6-506290 to M. Kastner. Additional support was provided by Scripps Industrial Associates and by a Biomedical Research Support Grant to A.S.

# Theoretical Analysis of Probe Dynamics in Flow Injection/Membrane Introduction Mass Spectrometry

Gow-Jen Tsai, Glen D. Austin, Mei J. Syu, and George T. Tsao

Laboratory of Renewable Resources Engineering, Purdue University, West Lafayette, Indiana 47907

Mark J. Hayward, Tapio Kotiaho,<sup>1</sup> and R. Graham Cooks\*

Department of Chemistry, Purdue University, West Lafayette, Indiana 47907

The dynamic response of the membrane probe in flow injection/membrane introduction mass spectrometry has been studied theoretically. A mathematical model is formulated to obtain analyte concentration profiles in the flow chamber and inside the membrane and to calculate the analyte flux across the membrane. For ideal input perturbations such as block and step inputs, analytical solutions are provided; for nonlinear input perturbations an efficient and robust computational procedure for obtaining numerical solutions is presented to account for mixing of the analyte sample in the flow conduit before entering the flow chamber. The effect of some system parameters and operational variables on the dynamic behavior of the probe is investigated. This information should help in the design of new membrane probes and in the selection of new membranes.

## INTRODUCTION

Membrane introduction mass spectrometry (MIMS) has received considerable attention recently for identification and quantification of organic compounds in aqueous media (1-6). The technique is based on the preferential pervaporation of analytes as opposed to the solvent across the membrane. When the membrane probe is inserted directly into the mass spectrometer ion source, better performance is achieved in terms of response time and sensitivity compared to membranes that are located at a greater distance (7-11). For process monitoring and control, rapid and continuous measurements of the concentrations of target compounds in the analyte solution are essential. The use of MIMS with flow injection analysis (FIA) sampling is appropriate to achieve this requirement. This technique has been demonstrated successfully for on-line monitoring and control of fermentation processes for the production of optically active isomers of 2,3-butanediol (12-15).

The membrane probe has two main parts; a flow chamber and the membrane (Figure 1). The flow chamber allows direct contact of the analyte with the membrane, while the membrane itself allows pervaporation, a process which includes adsorption of analyte onto the membrane surface, diffusion through its body, and release from the inner surface into vacuum. The major concerns in the selection of polymeric materials for the membrane probe are achievement of the maximum flux across the membrane and the time required to complete the analysis of one sample. The first determines the response sensitivity and the second determines the sampling frequency. The desired membrane will be the one that gives a high sampling frequency with high sensitivity to all the analytes, while simultaneously rejecting solvent.

This work presents a theoretical analysis of the dynamics of the operation of the membrane probe in the FIA/MIMS system. Although theoretical analyses of membrane transport and flow injection sampling has been intensively studied in the past (16-19), these topics have been dealt with separately and the combination of both phenomena in the FIA/MIMS system has not yet been analyzed. Therefore, this paper provides analytical tools to fill this gap and so provide a better understanding of the time-dependent phenomena associated with use of this type of probe.

A mathematical model has been formulated and solved analytically for block and step inputs (defined in Figure 1) and numerically for any arbitrary inputs. The method of Laplace transforms was employed to obtain the analytical solution, and the orthogonal collocation (20) and Gear's stiff method (21) were used to obtain the numerical solutions. The effect of each system parameter on the dynamic responses is investigated and discussed.

## THEORETICAL CONSIDERATIONS

Figure 1 shows a simplified schematic diagram of the membrane probe. The analyte solution is pumped through the flow chamber, in which the analyte is dissolved, and analyte diffuses through the membrane. Obviously, the concentration of analyte in the flow chamber largely affects its mass flux across the membrane, especially when the sample volume is comparable to the volume of the chamber and mixing in the chamber is negligible. Therefore, we also consider the variation of analyte concentration in the flow chamber in obtaining results from the model. The model shown below is the simplest one, which assumes that the fluid inside the chamber is well mixed and the analyte transport across the membrane is one-dimensional. Also, the film model is employed to account for mass transfer between the fluid phase and the membrane phase. If we further assume that the effective diffusivity ( $D$ ) in the membrane and the partition coefficient ( $H$ ) between solution and the membrane surface are constant over time, then the governing equations can be expressed as follows:

$$\frac{dC}{dt} = v(C_i - C) - K_s a_s \left( C - \frac{C_m}{H} \Big|_{x=0} \right) \quad (1)$$

$$\frac{\partial C_m}{\partial t} = D \frac{\partial^2 C_m}{\partial x^2} \quad (2)$$

with initial and boundary conditions

$$t = 0 \quad C = 0 \quad C_m = 0 \quad (3)$$

$$x = 0 \quad -D \frac{\partial C_m}{\partial t} = K_s \left( C - \frac{C_m}{H} \Big|_{x=0} \right) \quad (4)$$

$$x = L \quad C_m = 0 \quad (5)$$

where  $C$  = concentration of analyte in the chamber,  $C_m$  = concentration of analyte inside the membrane,  $C_i$  = concen-

\*Corresponding author.

<sup>1</sup> On leave from the Technical Research Center of Finland, Chemical Laboratory, Biologinkuja 7, 02150 Espoo, Finland.

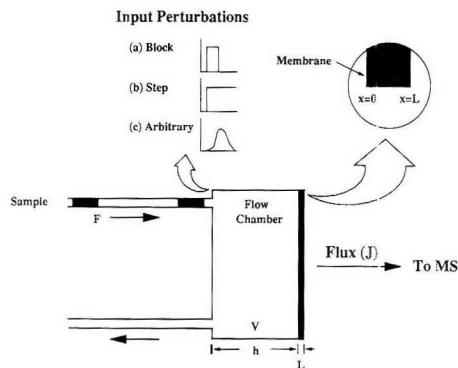


Figure 1. Schematic diagram of a membrane probe.

tration of analyte in the inlet,  $H$  = partition coefficient,  $C_m/C$ ,  $K_s$  = interphase mass-transfer coefficient, cm/s,  $a_s$  = ratio of total membrane surface to chamber volume,  $\text{cm}^{-1}$ ,  $D$  = effective diffusivity of sample solute in the membrane,  $\text{cm}^2/\text{s}$ ,  $t$  = response time, s,  $x$  = spatial coordinate, cm,  $L$  = thickness of membrane, cm,  $v$  = ratio of inlet liquid flow rate to chamber volume,  $\text{s}^{-1}$ . Note that eq 5 holds only when the downstream side of the membrane is under vacuum, which is true for the system in which we are interested.

The sample concentration in the inlet can be any arbitrary input perturbation, i.e.

$$C_i(t) = C_{i0} f(t) \quad (6)$$

in which  $f(t)$  is the normalized input perturbation. The function  $f(t)$ , which accounts for mixing of sample solution between the sample injection port and the flow chamber, is experimentally measurable. For ideal input perturbations such as the step or the block function, eq 6 becomes

$$C_i(t) = C_{i0}[u_a(t) - u_b(t)] \quad (7)$$

in which  $u_a$  and  $u_b$  are unit step functions starting from  $t = a$  and  $t = b$ , respectively. When  $b$  approaches infinity, the input perturbation becomes a step change.

Equations 1 and 2 give concentration profiles of analyte in the flow chamber and at each position of the membrane. However, the quantity in which we are interested is the total analyte flux at the downstream side of the membrane, i.e.

$$J_{|x=L} = -DA \left. \frac{\partial C_m}{\partial x} \right|_{x=L} \quad (8)$$

in which  $A$  is the membrane surface area. Note that  $J_{|x=L}$  also represents the total flux of analyte entering the ion chamber. Since the response of the mass spectrometer (ion current) is proportional to the mass flux inside the ion chamber, the dimensionless flux shown in eq 9 will be the same as that

$$J_R = \frac{J_{|x=L}}{J_{ss} \text{ (step change)}} \quad (9)$$

obtained from the mass spectrometer; i.e. this is the ratio of the flux for any arbitrary input to the steady-state flux ( $J_{ss}$ ) for the step input perturbation.

The governing equations can be solved analytically when the input perturbation is a block or step input; however, they can only be solved numerically when the input perturbation is any arbitrary nonlinear function. Both cases are detailed below.

**Analytical Solution.** Equations 1-5 and 7 are solved analytically by the method of Laplace transforms. First, these equations are transformed from the time domain,  $t$ , into the

Laplace domain,  $S$ , through the following transformation:

$$C(S) = \int_0^{\infty} e^{-St} C(t) dt \quad (10)$$

$$C_m(x,S) = \int_0^{\infty} e^{-St} C_m(x,t) dt \quad (11)$$

The transformed equations are then solved simultaneously to obtain the following Laplace domain solution:

$$C(S) = \frac{\frac{vC_{i0}}{S}(e^{-aS} - e^{-bS}) \left( \frac{K_s/H}{\sqrt{DS}} \tanh \sqrt{\frac{S}{D}} L + 1 \right)}{\left( \frac{K_s/H}{\sqrt{DS}} \tanh \sqrt{\frac{S}{D}} L + 1 \right) (S + v) + K_s a_s} \quad (12)$$

$$C_m(x,S) = \frac{\frac{vC_{i0}}{S}(e^{-aS} - e^{-bS}) \frac{K_s}{\sqrt{DS}} \sinh \sqrt{\frac{S}{D}} L}{\left( \frac{K_s/H}{\sqrt{DS}} \tanh \sqrt{\frac{S}{D}} L + 1 \right) (S + v) + K_s a_s} \times \left[ \frac{\cosh \sqrt{\frac{S}{D}} x}{\cosh \sqrt{\frac{S}{D}} L} - \frac{\sinh \sqrt{\frac{S}{D}} x}{\sinh \sqrt{\frac{S}{D}} L} \right] \quad (13)$$

Then, the time domain solution is obtained by inverting eqs 12 and 13 using the inversion theorem for Laplace transform and Cauchy's residue theorem. Since eqs 12 and 13 are analytic in the  $S$  domain except the poles at  $S = 0$  and  $S_n = -(D/L^2)\lambda_n^2$  ( $n = 1, 2, \dots, \infty$ ), the analytical solution is simply the summation of the residues evaluated at these poles. Note that  $\lambda_n$  is the eigenvalue at pole  $S_n$ , which was obtained from the following characteristic equation:

$$\lambda_n \cot \lambda_n - 1 = - \frac{(S_n + v) \left( \frac{K_s L}{DH} + 1 \right) + K_s a_s}{S_n + v + K_s a_s} \quad (14)$$

Notice that eq 14 was derived by letting the denominator of eq 12 or 13 equal zero. After complicated mathematical manipulations, the time domain solution is obtained as follows:

$$0 \leq t < a \quad C(t) = C_m(x,t) = 0 \quad (15)$$

$$a \leq t < b \quad C(t) = C_{ss} + \sum_{n=1}^{\infty} A_n(\lambda_n) e^{S_n(t-a)} \quad (16)$$

$$C_m(x,t) = C_{ss}^m(x) + \sum_{n=1}^{\infty} A_n^m(\lambda_n) \left[ \frac{\cos\left(\lambda_n \frac{x}{L}\right) - \sin\left(\lambda_n \frac{x}{L}\right)}{\cos(\lambda_n) - \sin(\lambda_n)} \right] e^{S_n(t-a)} \quad (17)$$

$$t \geq b \quad C(t) = \sum_{n=1}^{\infty} A_n(\lambda_n) (e^{S_n(t-a)} - e^{S_n(t-b)}) \quad (18)$$

$$C_m(x,t) = \sum_{n=1}^{\infty} A_n^m(\lambda_n) \left[ \frac{\cos\left(\lambda_n \frac{x}{L}\right) - \sin\left(\lambda_n \frac{x}{L}\right)}{\cos(\lambda_n) - \sin(\lambda_n)} \right] \times (e^{S_n(t-a)} - e^{S_n(t-b)}) \quad (19)$$



where

$$A_n(\lambda_n) = \left[ vC_{io}(e^{-a\lambda_n} - e^{-b\lambda_n}) \left( \frac{K_s L}{HD\lambda_n} \tan \lambda_n + 1 \right) \right] / \left[ vS_n \left( \frac{K_s L}{HD\lambda_n} \tan \lambda_n + 1 \right) + \frac{K_s}{2HD \cos^2 \lambda_n} (S_n + v) \left[ 1 - \frac{\sin(2\lambda_n)}{2\lambda_n} \right] \right] \quad (20)$$

$$A_n^m(\lambda_n) = \left[ vC_{io}(e^{-a\lambda_n} - e^{-b\lambda_n}) \frac{K_s L}{D\lambda_n} \sin \lambda_n \right] / \left[ vS_n \left( \frac{K_s L}{HD\lambda_n} \tan \lambda_n + 1 \right) + \frac{K_s}{2HD \cos^2 \lambda_n} (S_n + v) \left[ 1 - \frac{\sin(2\lambda_n)}{2\lambda_n} \right] \right] \quad (21)$$

$$C_{ss} = \frac{vC_{io}(K_s/H)(L/D) + 1}{v[(K_s/H)(L/D) + 1] + K_s a_s} \quad (22)$$

$$C_{ss}^m(x) = \frac{vC_{io}K_s(L/D)}{v[(K_s/H)(L/D) + 1] + K_s a_s} \left( 1 - \frac{x}{L} \right) \quad (23)$$

In the case of a block input perturbation, the total analyte flux at  $x = L$  can be derived as follows:

$$J|_{x=L} = -DA \left. \frac{\partial C_m}{\partial x} \right|_{x=L} = \sum_{n=1}^{\infty} A_n^m(\lambda_n) \left( \frac{DA\lambda_n}{L} \right) [\tan(\lambda_n) + \cot(\lambda_n)] (e^{S_0(t-a)} - e^{S_0(t-b)}) \quad (24)$$

Since  $A_n^m(\lambda_n)$  is linearly related to  $C_{io}$  (eq 21), it is obvious that the total flux at any time should be linearly dependent on  $C_{io}$ . Therefore, the peak height should be linearly related to  $C_{io}$ . This conclusion is also true even for any arbitrary inputs. This can be easily shown by nondimensionalizing the governing equations (eqs 1 and 2) to factor out  $C_{io}$ . After carrying out the same analysis procedure, the factor  $C_{io}$  is brought back to the results again. Since  $C_{io}$  can be always factored out of the equations, the flux is, therefore, always linearly dependent on the initial analyte concentration in the inlet. Notice that  $C_{ss}$  and  $C_{ss}^m(x)$  are steady-state solutions of  $C(t)$  and  $C_m(x,t)$ , respectively, when the step input perturbation is employed. The steady-state solutions are the residues evaluated from the pole at  $S = 0$ . Here, the total analyte flux at  $x = L$  was obtained as

$$J_{ss} = \frac{vC_{io}K_s A}{v[(K_s/H)(L/D) + 1] + K_s a_s} \quad (25)$$

It shows that the steady-state flux depends on all the system parameters. When the diffusion process is the rate-determining step, eq 25 is reduced to the following equation directly derived from Fick's diffusion law under steady-state conditions:

$$J_{ss}|_{x=L} = A \left( \frac{DH}{L} \right) C_{io} = A \frac{P}{L} C_{io} \quad (26)$$

in which  $P (=DH)$  is the permeability of the analyte across the membrane.

**Numerical Solution.** Equations 1-6 can be solved numerically if the input perturbation is any nonlinear function.

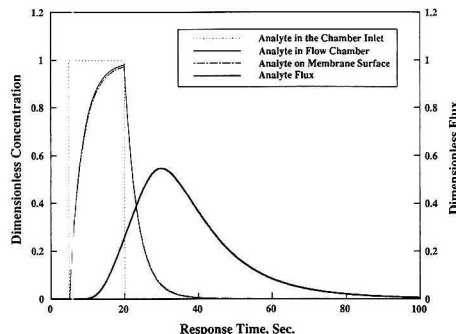


**Figure 2.** Typical dynamic responses for a block input with  $K_s = 5 \times 10^{-2}$  cm/s,  $H = 1.0$ ,  $L = 0.025$  cm,  $h = 0.2$  cm, membrane diameter = 0.6 cm,  $D = 5.0 \times 10^{-6}$  cm<sup>2</sup>/s, and  $F = 1.0$  cm<sup>3</sup>/min.

In this case, a powerful and robust numerical procedure was employed to solve these equations. First, eq 2 was transformed into  $N$  ordinary differential equations (ODE) by the orthogonal collocation method, which has been shown to be a very efficient and accurate numerical approach in solving the diffusion equation (20). Then, the transformed equations were combined with eq 1 to form an ODE system that was solved by Gear's stiff method (21). This approach is efficient even under stiff conditions.

## RESULTS AND DISCUSSION

**Computer Simulation.** Two FORTRAN programs have been developed on the SUN 4/280 and IBM PS/2 30286 computers. One program is used to obtain the analytical solution for block and step inputs, and the other is used to obtain the numerical solution for any type of input. Both programs are efficient and robust even on the low-end IBM PS/2 30286 machine. The programs provide the following data: analyte concentrations in the flow chamber and on the upstream membrane surface, the analyte concentration profile inside the membrane at the specified response time, and the analyte flux on the downstream membrane surface. For the analytical solution, the use of the first 200 eigenvalues in the calculation are sufficient to provide accurate solutions in most cases. For the numerical solution, the order of approximation ( $N$ ) in the orthogonal collocation method was set to 7 and that also provides accurate solutions. The results shown below are based on these two choices.

**Input Perturbation.** The input perturbation gives the analyte concentration profile at the inlet to the flow chamber, which directly affects the dynamic responses of the probe. When mixing between the sample injection port and the entrance of the flow chamber is negligible, the input perturbation resembles either the block function (dotted line in Figure 2) or the step function (dotted line of Figure 3) input selected. However, when mixing is important, the input perturbation gives a dispersed profile at the membrane surface. It should be pointed out that the block and step inputs are ideal; however, they provide a basis for understanding the dynamic behavior of the probe. The dispersed input is close to the real situation, represented by the experimental data shown in Figure 4, which are actual measurements taken by UV absorbance on an aniline sample using the membrane introduction mass spectrometry system developed in our laboratory (22).

Typical responses for three different input perturbations are shown in Figures 2-4, respectively. These figures clearly show that the addition of mass-transfer resistances, such as interphase mass transfer and diffusion across the membrane,

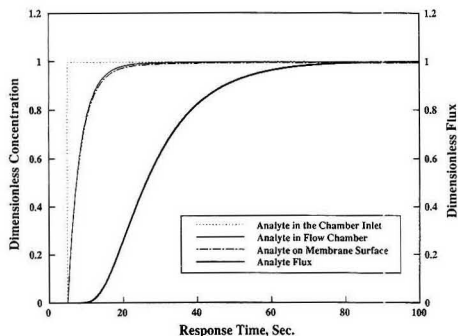


**Figure 3.** Typical dynamic responses for a step input with conditions the same as in Figure 2.

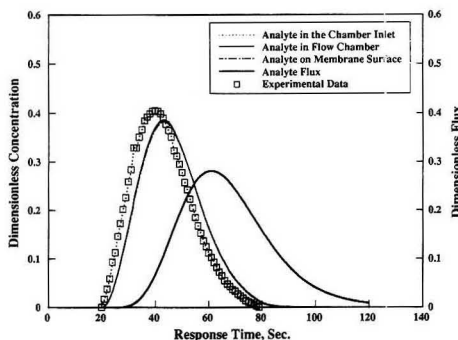


**Figure 4.** Typical dynamic responses for a dispersed input with conditions the same as in Figure 2 except that  $D = 5.0 \times 10^{-6} \text{ cm}^2/\text{s}$ . The probe configuration and the system employed in the study was detailed in ref 11. The data were obtained by using an ISCO absorbance detector (Model 228; 254 nm) connected to the chamber inlet. Aniline was used as a model compound in this study.

delays the response of analyte (flux) that can be detected by the mass spectrometer. Note that the mass-transfer resistance includes contributions from both diffusion across the membrane and interphase mass transfer, i.e., transfer from solution to the membrane surface. Comparing Figure 2 with Figure 3, we can easily deduce that the use of a block input is superior to the step input in terms of the time required for analysis of one sample; however, it is inferior to the step input in the aspect of response sensitivity, i.e., the magnitude of the response.

Figure 4 shows the effect of dispersed input on the analyte flux detected by the mass spectrometer. In this case, the input perturbation gives a highly dispersed peak even though the sample coming from the injection port was a block input that lasted for 15 s. This unexpected result is simply due to the high dispersion of the analyte sample in the flow conduit between the sample injection port and the flow chamber. The dispersion of sample in the flow conduit results in the prolongation of response time and the decrease of analyte flux across the membrane as compared to the block input. Therefore, the probe system performance is reduced if the dispersion in the flow conduit is high and this is a significant factor which could easily be overlooked.

When a block input or any arbitrary input is employed, it can be easily shown that the peak height is proportional to the analyte concentration in the sample when the experimental conditions are kept the same, provided the assumption of

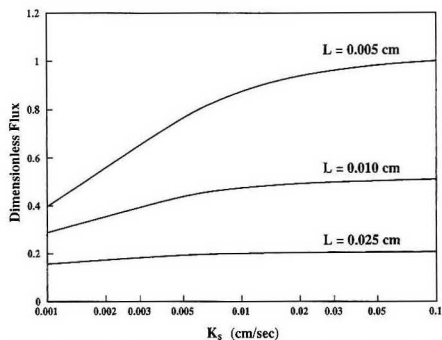


**Figure 5.** Effect of interphase mass-transfer coefficient (adsorption at membrane surface) on the analyte flux across the membrane with  $H = 1.0$ ,  $h = 0.2 \text{ cm}$ ,  $D = 8.0 \times 10^{-6} \text{ cm}^2/\text{s}$ , and membrane diameter = 0.6 cm. The dimensionless flux is based on the flux in the case of  $L = 0.005 \text{ cm}$  and  $K_s = 0.1 \text{ cm/s}$ .

constant partition coefficient holds. This proves the applicability of using the impulse method for chemical analysis in the FIA/MIMS system.

**Liquid/Membrane Interphase Mass Transfer.** Figures 2–4 also show that the interphase mass-transfer resistance is significantly smaller than the resistance resulting from diffusion across the membrane under the probe configuration we simulated. Unless the membrane surface area and the membrane thickness (Figure 5) are much smaller than those chosen in this probe configuration, the interphase mass-transfer resistance will not contribute significantly to the probe dynamics.

The effect of interphase mass-transfer coefficient on the analyte flux across the membrane is shown in Figure 5. The results are based on the step input under the steady-state conditions (eq 25). It can be seen that interphase mass transfer only becomes important when the membrane thickness is much reduced. This is because the reduction of membrane thickness decreases the mass-transfer resistance from the diffusion process. Therefore, for thin membranes the resistance from the interphase mass transfer becomes comparable to the resistance from diffusion and may affect the probe performance significantly.

It is well-known that a major effect of inlet liquid flow rate is on analyte flux across the depletion zone, i.e. the stagnant liquid film between the bulk liquid and the membrane surface. In other words, an increase in the flow rate reduces the thickness of the stagnant liquid film, resulting in an increase of mass-transfer coefficient as well as increasing analyte flux across the membrane. The same conclusion was also reported by LaPack et al. (19), using a hollow-fiber membrane and varying the inlet liquid flow rate.

**Diffusion in Membrane.** Typical results with different effective diffusivities are shown in Figure 6 with the input perturbation the same as Figure 4. They clearly show that effective diffusivity is one of the major factors that determine both the maximum analyte flux and the response time. The smaller the effective diffusivity, the longer the response time and the smaller the maximum analyte flux. The effective diffusivity can be enhanced by increasing the probe operation temperature (17) or modifying the membrane.

**Partition Coefficient.** The partition coefficient is the ratio of analyte concentration in the bulk fluid to that inside the membrane at equilibrium. It largely affects the magnitude of analyte flux across the membrane, as shown in eq 25 or 26 in the steady-state cases. Figure 7 shows results of simulations in which the partition coefficients range from 0.5 to 2.0 with

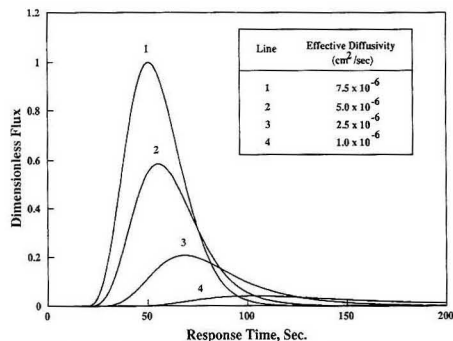


**Figure 6.** Effect of effective diffusivity on the analyte flux across the membrane with other conditions the same as in Figure 4. The dimensionless flux is based on the flux at the peak tip of line 1.

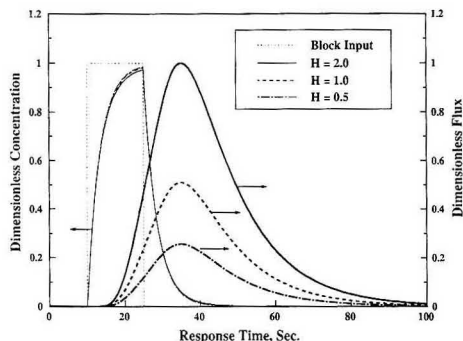


**Figure 7.** Effect of partition coefficient on the probe dynamics with other conditions the same as in Figure 2. The dimensionless flux is based on the flux at the peak tip of the case  $H = 2.0$ .

other conditions the same as Figure 2. The variation of analyte flux profiles among these cases also demonstrates that a high partition coefficient gives a high analyte flux under the dynamic conditions. Notice that the dimensionless fluxes are based on the maximum flux for the case  $H = 2.0$ .

The partition coefficient is a system parameter that directly relates to the chemical interaction between membrane and analyte. Therefore, modification of the membrane to give better compatibility between membrane and analyte, will certainly increase the partition coefficient and response sensitivity. This prediction is yet to be tested in practice.

**Chamber Volume and Liquid Flow Rate.** Figure 8 shows the effect of chamber volume on the response of the probe for a block input that lasts for 15 s. It is obvious that the larger the flow chamber, the worse the probe efficiency in terms of response sensitivity and sampling frequency. Therefore, minimization of the chamber volume is essential to increase probe efficiency. The considerations which underlie this result parallel those that are obtained for chromatography detectors.

The effect of liquid flow rate on the probe dynamics can be discussed from two different aspects: (1) the dispersion between the sampling port and the chamber inlet and (2) interphase mass transfer and diffusion across the membrane. It has been well documented that an increase in flow rate changes the liquid flow in the conduit from laminar flow to turbulent flow. This results in increased dispersion of the liquid sample before entering the flow chamber, and thus increases the response time and decreases the response sen-

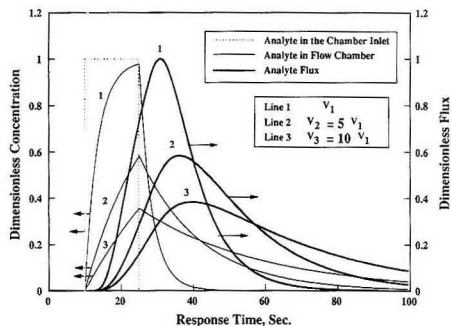


**Figure 8.** Effect of chamber volume on the probe dynamics with other conditions the same as in Figure 2. The dimensionless flux is based on the flux at the peak tip of line 1.

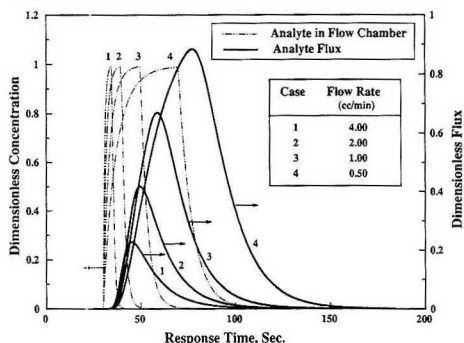


**Figure 9.** Effect of flow rate on the probe dynamics with other conditions the same as in Figure 2.

sitivity (16). Therefore, there is no advantage to be gained from this factor in FIA analysis by increasing the liquid flow rate. In our system, the liquid flow rate is typically 1.0 mL/min, and the conduit diameter is only 0.5 mm. Therefore, laminar flow for these conditions is assured judging from the Reynolds number.

Figure 9 shows the effect of liquid flow rate on the probe dynamics. In this study, a block input is chosen to concentrate the effect of liquid flow rate on the second aspect mentioned above. As shown in the figure, the increase in the inlet flow rate shortens the residence time of analyte in the flow chamber (dash-dotted lines), which results in a decrease of response sensitivity and response time.

Combining the conclusions from both aspects, we deduce that the increase of flow rate decreases the response sensitivity and the response time, as compared to the case of block input. The need to balance these two factors makes the selection of a suitable flow rate for the particular system important. Note that the above conclusions are valid only when the same volume of analyte sample is employed in each case. When large (essentially unlimited) sample volumes are available, as can be the case in many process monitoring experiments, high flow rates are desirable since they avoid the creation of a depletion zone near the membrane surface and allow maximum responses to be achieved. Quantification using external standard solutions may be best achieved at intermediate flow rates which represent a compromise between response time and magnitude of response.

**Sample Size and Membrane Thickness.** Figure 10 shows the effect of sample size on the dynamics of the membrane

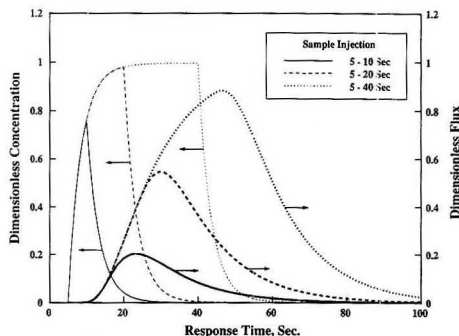


Figure 10. Effect of sample size on the probe dynamics with other conditions the same as in Figure 2.

Table I. Effect of Some System Parameters and Operational Variables on the Peak Height and Response Time\*

param/variable	max flux (peak height)	response time
membrane thickness	+++	+++
diffusion coeff	+++	+++
partition coeff	+++	+
sample size	++	++
sample concn	+++	+
mixing in the flow chamber	++	++
dispersion in the flow conduit	++	++
chamber vol	++	++
flow rate	++	++
interphase mass transfer	++	++

\* Key: (+++) highly interrelated; (++) interrelated; (+) weakly interrelated.

probe with the introduction of sample as a block input to the probe chamber. When the sample size is increased, the analyte duration in the flow chamber is prolonged. This results in an increase of analyte flux across the membrane; however, it also increases the time needed to analyze one sample.

The membrane thickness affects the probe performance significantly (Figure 5). Reduction of membrane thickness decreases the transport resistance of analyte molecules across the membrane and, hence, increases the analyte flux and response sensitivity.

**Probe Design.** As mentioned above, a well-designed membrane probe for the FIA/MIMS system should possess high analyte sensitivity and sampling frequency. The sensitivity analysis shown above provides information on the relative importance of each system parameter or operational variable on the probe performance. Table I summarizes this

analysis, which should help in designing suitable probes for particular uses. It should be pointed out that the analysis is based on the assumption of constant partition coefficient and is valid only when the concentration of analyte is low. Although the analysis is only for a single analyte, it is also valid for multiple analytes in one sample as long as the assumption of constant partition coefficient for each analyte holds true and interference among analytes is negligible.

## CONCLUSIONS

The dynamics of the membrane probe in the FIA/MIMS system have been simulated. An analysis of the simulation provides insights into the complexity of the probe dynamics and provides essential knowledge needed for design of a membrane probe. The results show that membrane thickness, partition coefficient, and effective diffusivity play the most important roles in the probe performance.

## LITERATURE CITED

- Savickas, P. J.; LaPack, M. A.; Tou, J. C. *Anal. Chem.* **1989**, *61*, 2332.
- Dheandhanoo, S.; Dulek, J. *Rapid Commun. Mass Spectrom.* **1989**, *3*, 175.
- Sturaro, A.; Doretto, L.; Parvoli, G.; Cecchinato, F.; Frison, G.; Traldi, P. *Biomed. Environ. Mass Spectrom.* **1989**, *18*, 707.
- Wenhu, D.; Kuangnan, C.; Jianli, L.; Zhenying, D. *Mass Spectrosc. (Tokyo)* **1987**, *35*, 122.
- Lister, A. K.; Wood, K. V.; Noon, K.; Cooks, R. G. *Biomed. Environ. Mass Spectrom.* **1989**, *18*, 1063.
- Heinzle, E.; Reuss, M. *Mass Spectrometry in Biotechnological Process Analysis and Control*; Plenum Press: New York, 1987.
- Harland, R. J.; Nicholson, P. J. D.; Gillings, E. *Water Res.* **1987**, *21*, 107.
- Brodbeck, J. S.; Cooks, R. G.; Tou, J. C.; Kallos, G. S.; Dryzga, M. D. *Anal. Chem.* **1987**, *59*, 454.
- Schmidt, W. J.; Meyer, H. D.; Shügerl, K.; Kuhlman, W.; Bellgardt, K.-H. *Anal. Chim. Acta* **1984**, *163*, 101.
- Bier, M. E.; Cooks, R. G. *Anal. Chem.* **1987**, *59*, 597.
- Bier, M. E.; Kotiaho, K.; Cooks, R. G. *Anal. Chim. Acta* **1990**, *231*, 175.
- Hayward, M. J.; Lister, A. K.; Kotiaho, T.; Cooks, R. G.; Austin, G. D.; Narayan, R.; Tsao, G. T. *Anal. Chem.* **1990**, *62*, 1798.
- Hayward, M. J.; Lister, A. K.; Kotiaho, T.; Cooks, R. G.; Austin, G. D.; Narayan, R.; Tsao, G. T. *Biotechnol. Tech.* **1989**, *3* (6), 361.
- Hayward, M. J.; Riederer, D. E.; Kotiaho, T.; Cooks, R. G.; Austin, G. D.; Syu, M.; Tsao, G. T. *Process Control Qual.* **1991**, *1*, 105.
- Austin, G. D.; Tsao, G. T.; Hayward, M. J.; Kotiaho, T.; Lister, A. K.; Cooks, R. G. *Process Control Qual.* **1991**, *1*, 117.
- Ruzicka, J.; Hansen, E. H. *Flow Injection Analysis*, 2nd ed.; John Wiley & Sons: New York, 1988.
- Hwang, S.-T.; Kammermeyer, K. *Membranes in Separation*; (Techniques of Chemistry); Wiley: New York, 1975; Vol. VII.
- Tou, J. C.; Rulf, D. C.; DeLassus, P. T. *Anal. Chem.* **1990**, *62*, 592.
- LaPack, M. A.; Tou, J. C.; Enke, C. G. *Anal. Chem.* **1990**, *62*, 1265.
- Finlayson, B. A. *Nonlinear Analysis in Chemical Engineering*; McGraw-Hill: New York, 1990.
- Gear, C. W. *Numerical Initial-Value Problems in Ordinary Differential Equations*; Prentice-Hall: NJ, 1972.
- Hayward, M. J. PhD Thesis, Purdue University, 1990.

RECEIVED for review February 14, 1991. Accepted July 24, 1991. This work was supported by the National Science Foundation (Grant EE-8712867A2-BCS). The support provided by the Emil Aaltonen Foundation and Suomen Kulttuurirahasto (to T.K.) is also acknowledged.

# Supercritical Fluid Chromatography and Time-of-Flight Secondary Ion Mass Spectrometry of Poly(dimethylsiloxane) Oligomers in the Mass Range 1000-10 000 Da

Birgit Hagenhoff, Alfred Benninghoven,\* Herbert Barthel,<sup>1</sup> and Wolfgang Zoller<sup>1</sup>

Physikalisches Institut der Universität Münster, Wilhelm-Klemm-Strasse 10, D-4400 Münster, FRG

Both supercritical fluid chromatography (SFC) and time-of-flight secondary ion mass spectrometry (TOF-SIMS) provide well-resolved signal intensities of low molecular weight poly-(dimethylsiloxane) (PDMS) oligomers. To determine the achievable accuracy of these independent analytical methods, a direct comparison was performed on PDMS oligomers in the mass range from 1000 to 10 000 Da. Results obtained by SFC and TOF-SIMS fit well up to mass 3000 Da whereas remarkable differences occur for higher masses due to mass discrimination effects. These have been found to be more pronounced for SFC than for TOF-SIMS.

## 1. INTRODUCTION

In the last 4 decades siloxanes have found important industrial applications. Methylsiloxanes, in particular poly-(dimethylsiloxanes) (PDMS), cover a major part of organo-silicon compounds. Low molecular PDMS are well-known as silicone oils and provide the main intermediates for most silicone additives and silicone rubbers.

For industrial use methods of characterization of PDMS are most commonly based on rheological data (1, 2). Gel permeation chromatography (GPC) (3) and <sup>29</sup>Si NMR spectroscopy provide additional information about the average molecular weight.

Due to the condensation process, low molecular weight PDMS, however, consist of both cyclic and linear siloxanes that are poorly resolvable by GPC and <sup>29</sup>Si NMR methods. Therefore certain classes of high molecular weight substances have additionally been analyzed by high-temperature gas chromatographic (GC) methods (4). These methods, however, are only capable of analyzing substances with boiling points ranging from 650 to 750 °C corresponding to e.g. PDMS oligomers of masses between 1000 and 1200 Da.

Supercritical fluid chromatography (SFC) (5) and time-of-flight secondary ion mass spectrometry (TOF-SIMS) (6) have proved to be valuable methods for the analysis of oligomeric species. Both offer comparably good resolutions of individual oligomeric species of PDMS (7-9). Therefore the detection of resolved individual PDMS species and even a distinction between cyclic and linear low-mass PDMS oligomers is available. So far, however, little has been known about the accuracy of average molecular weight determinations performed by SFC. In the case of TOF-SIMS, comparisons have only been carried out for poly(styrenes) and perfluorinated polyethers (comparison with GPC (8, 10)). In this report, we describe a comparison of SFC and TOF-SIMS of PDMS in order to determine the achievable accuracy of both methods. Standards of individual oligomeric species covering the mass range from 1000 up to 10 000 Da are not available. We therefore compared three low molecular weight PDMS samples with different molecular weight distributions.

<sup>1</sup> Wacker Chemie GmbH, D-8263 Burghausen, FRG.

Table I. Kinematic PDMS Sample Viscosities (at 25 °C) and Number Average Molecular Weights from <sup>29</sup>Si NMR Data

sample	viscosity, mm <sup>2</sup> /s (cSt)	molecular weight M <sub>n</sub> , Da
1	20.7	1724
2	25.1	2216
3	41.3	3449

Table II. Parameters of Operation of the SFC Instrument

instrumentation	Lee Scientific Model 501 SFC
detn	FID at 350 °C, makeup gas N <sub>2</sub> at 30 mL/min
column	10 m × 50 μm i.d. × 0.25 μm SB methyl 100
restrictor	frit restrictor
injection	2 μL of 20% PDMS in <i>n</i> -hexane, flow splitting, split capillary 15 μm i.d. 18 cm, autosampler
carrier	CO <sub>2</sub> pressure programmed (see Table III)
temp	100 °C, hold 20 min, rate 1.5°/min to 250 °C

Table III. CO<sub>2</sub> Pressure Program

init	99.00 bar	
hold	8.00 min	
ramp	5.50 bar/min	110 bar
ramp	5.00 bar/min	185.00 bar
ramp	1.80 bar/min	194.00 bar
ramp	1.40 bar/min	201.00 bar
ramp	1.60 bar/min	217.00 bar
ramp	1.80 bar/min	235.00 bar
ramp	2.00 bar/min	255.00 bar
ramp	2.40 bar/min	279.00 bar
ramp	3.20 bar/min	295.00 bar
ramp	3.50 bar/min	312.50 bar
ramp	3.90 bar/min	332.00 bar
ramp	4.50 bar/min	354.50 bar
ramp	5.00 bar/min	369.50 bar
hold	30.00 min	

In addition to the average molecular weight, the polydispersity of the distribution, in particular the amount of higher mass oligomers, is a point of major interest. Thus special attention has been paid to the inherent mass discrimination effects of these methods.

## 2. EXPERIMENTAL SECTION

**2.1. Sample Preparation.** Three samples of  $\alpha,\omega$ -bis(trimethylsiloxy)poly(dimethylsiloxanes) (PDMS) were prepared from three different industrial grade silicone oils (Wacker Silicone Fluid AK, Wacker Chemistry, Munc, West Germany) by vacuum distillation. The samples were characterized by viscosimetry and <sup>29</sup>Si NMR spectroscopy. Data are presented in Table I.

**2.2. Instrumentation and Methods.** **2.2.1. SFC.** A commercially available instrument (Lee Scientific) was used for the SFC investigations. Typical parameters of operation are listed in Tables II and III.

**2.2.2. TOF-SIMS.** The TOF-SIMS measurements were performed with an instrument built at the University of Münster in 1982 (TOF I (11)). It consists of a pulsed primary ion source, a Poschenrieder-type multiple (energy and angle) focusing time-of-flight analyzer, and a single-ion counting registration



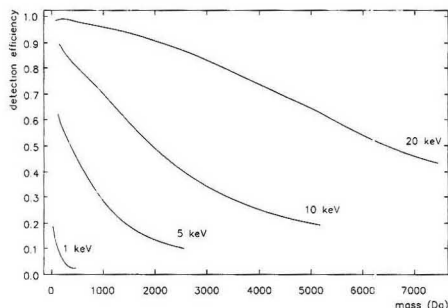


**Figure 1.** Detection efficiency  $D$  as a function of secondary ion mass for different postacceleration voltages (12).

system. The primary ion source generates short mass-separated ion packets (10 ns, 12-keV  $\text{Ar}^+$ ) hitting the sample in an area of about  $1 \text{ mm}^2$  (typical primary ion current density  $100 \text{ pA/cm}^2$ ). Secondary ions generated at the sample surface are accelerated to 3 keV before entering the flight path. They are detected by a channel plate, scintillator, photomultiplier combination. Since the ion-electron conversion at the channel plate as the first step of ion detection is a velocity-dependent process (kinetic ion induced electron emission), the detection efficiency decreases with increasing mass. In order to obtain sufficiently high secondary ion velocities, secondary ions can be postaccelerated up to an energy of 20 keV. Figure 1 shows the detection efficiency as a function of secondary ion masses for different postacceleration voltages (12). The data were obtained for Cr-cluster ions. Recent investigations have shown (13) that these data also represent the detector-dependent mass discrimination effects for PDMS oligomers. A computer program based upon the curves for 10 and 20 keV can be used to correct secondary ion intensities for mass discrimination effects.

For the TOF-SIMS investigations,  $0.5 \mu\text{L}$  of a  $1 \text{ mg/mL}$  solution in toluene was deposited onto about  $80 \text{ mm}^2$  of an etched silver substrate (monolayer preparation) and subsequently dried in the airlock of the TOF-SIMS instrument. Typical spectra acquisition times are 100 s, which leads to total ion doses in the range of  $10^{11}$  ions (static conditions).

**2.2.3. Determination of Average Molecular Weights.** For the calculation of the number and weight average molecular weights  $M_n$  and  $M_w$ , respectively, peak areas of the linear PDMS oligomers were used.

**SFC.** The calculation of average molecular weights from SFC peak areas has to take into account the mass-dependent signal generation of the FID detector:

$$M_n = \sum I_i / \sum (I_i / M_i) \quad M_w = \sum I_i M_i / \sum I_i$$

with  $I_i$  = peak area at a retention time of a PDMS species with mass  $M_i$ .

**TOF-SIMS.** For TOF-SIMS average molecular weights were determined as follows.

1. Determination of all peak areas ( $(M_i + \text{Ag})^+$ , see 3.2) with background subtraction. Metastable decay of secondary ions in the acceleration gap leads to an exponentially decreasing background in SIMS spectra of organic materials. Therefore background integral values were taken in the direct neighborhood of the respective peak.

2. Computer-based correction of peak areas for loss in detection efficiency (see 2.2.2).

3. Determination of number ( $M_n$ ) and weight ( $M_w$ ) average molecular weights according to the equations

$$M_n = \sum I_i M_i / \sum I_i \quad M_w = \sum I_i M_i^2 / \sum I_i M_i$$

with  $I_i$  = corrected peak area for mass  $M_i$ .

The repeatability is in the order of 1% for both methods.

### 3. RESULTS AND DISCUSSION

**3.1. SFC.** A typical SFC chromatogram of PDMS sample 2 is given in Figure 2. The chromatogram shows two series

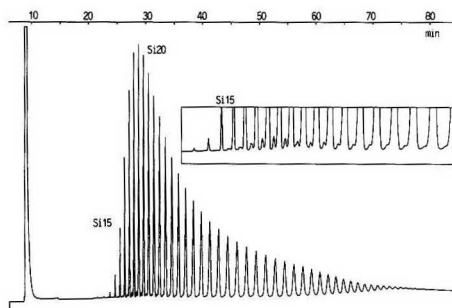


**Figure 2.** SFC chromatogram of PDMS sample 2.

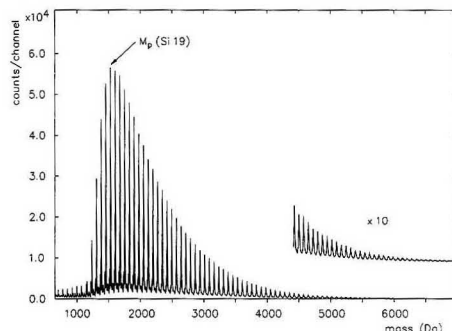


**Figure 3.** TOF-SIMS spectrum (positive secondary ions) of PDMS sample 2.

of consecutive repeating peaks. The main peaks are due to linear PDMS end-capped by trimethylsilyloxy groups. The distribution of peak intensities ranges from oligomers containing 13 up to 57 silicon atoms with a maximum peak area at an oligomer with 21 silicon atoms.

A second series of peaks occurs with lower intensities. A comparison with GC-MS and Si NMR spectroscopy as well as investigations on standards of pure PDMS cycles have shown that these homologies must be assigned to cyclic oligomers of PDMS. Cyclic and linear oligomers were separated up to a chain length of 30 silicon atoms per oligomer molecule. The amount of cyclic PDMS resolved was calculated by SFC (internal standard method) as 0.48% (sample 1), 0.48% (sample 2), and 0.17% (sample 3).

**3.2. TOF-SIMS.** Figure 3 shows the corresponding TOF-SIMS spectrum of PDMS sample 2. As in the case of SFC two different series of peaks can be distinguished. The most abundant peaks are due to intact linear PDMS oligomers cationized by the attachment of  $\text{Ag}^+$  from the substrate. Cyclic oligomers (also  $\text{Ag}^+$  cationized) are responsible for the second weaker series. The series are clearly separated up to a mass of about 3300 Da, which corresponds to oligomers containing 45 silicon atoms. The portion of cyclic oligomer peak areas referring to the summarized peak areas is in the order of 15%. The distribution of linear oligomers ranges from molecules containing 14 up to 91 silicon atoms. The maximum peak area is found for the oligomer containing 20 silicon atoms. Further peaks of very low intensities are due to fragmentation ( $(\text{M} - \text{CH}_3)^+$ ,  $\text{M}^+$ , or  $(\text{M} + \text{H})^+$ ).

**3.3. Comparison of SFC and TOF-SIMS.** A comparison of the results from the SFC chromatograms and the TOF-SIMS spectra is given in Table IV. The masses  $M_p$  of peaks with maximum intensities agree for sample 1 and differ no

Table IV. Comparison of SFC and TOF-SIMS Data<sup>a</sup>

	sample 1		sample 2		sample 3	
	SFC	TOF-SIMS	SFC	TOF-SIMS	SFC	TOF-SIMS
$M_n$	1542	1650	1923	2080	2278	2748
$M_w$	1674	1814	2095	2324	2433	3191
$M_w/M_n$	1.09	1.10	1.09	1.13	1.07	1.16
$M_{min}$	830	978	978	1052	1126	978
$M_p$	1274	1274	1571	1497	1942	1869
$M_{max}$	3648	5056	4093	6541	4389	8103

<sup>a</sup>  $M_n$ : number average molecular weight (Da);  $M_w$ : weight average molecular weight (Da);  $M_{min}$ : mass of oligomer peak with lowest mass (>0.1%) (Da);  $M_p$ : mass of oligomer peak with 100% (Da);  $M_{max}$ : mass of oligomer peak with highest mass (>0.1%) (Da).

more than the mass of one dimethylsiloxy group (74 Da) within samples 2 and 3. Figure 4 shows a comparison of relative peak area distributions for SFC and TOF-SIMS. The curves fit well for sample 1. But SFC and TOF-SIMS data of PDMS samples 2 and 3 show remarkable differences for the distributions of the peak areas. In the range from 2000 to 3000 Da, SFC provides higher relative intensities than TOF-SIMS. Above 3000 Da SFC relative intensities decrease sharply and show lower values than those of TOF-SIMS. Especially the curve shapes are different.

Two factors may contribute to these observed differences of peak area distributions produced by an identical molecular weight distribution: (a) mass dependence of the detection systems and (b) effects inherent in the different separation processes. The process of signal detection of SFC instruments is based on a flame ionization detector (FID). Therefore the signal intensity of molecules to be detected should increase proportionally with the mass of the oligomers (14). A rough correction of SFC peak intensities  $I(i)$  is possible by calculating the mass independent SFC peak area  $I_{corr}$ :

$$I_{corr}(i) = I(i)/N(i)$$

with  $N(i)$  = number of Si atoms in the PDMS chain. As shown in Figure 4 this simple correction fairly well explains the observed differences of curve shapes between SFC and TOF-SIMS up to a mass range of about 3000 Da. The correction corresponds to the formula used for the calculation of  $M_n$  and  $M_w$  out of SFC data in Table IV since  $N(i)$  is proportional to the mass of the oligomer  $M_i$ .

The mass discrimination effect of the TOF-SIMS detection system has already been described in section 2.2.2.

So far little has been published about mass discrimination in SFC. Capillary SFC with combined temperature/pressure programs may enlarge the application area to higher molecular weights (15). Even with this technique there is a significant decrease of relative signal intensities in SFC for PDMS with molecular weights greater than 3000 Da. The interpretation by a particular mass discrimination of SFC is confirmed by the distribution of corrected SFC peak areas (Figure 4). At masses of about 3000 Da a sharp decrease of relative SFC intensities is observed compared to TOF-SIMS and therefore leads to lower average molecular weights.

Although TOF-SIMS results are corrected for loss in detection efficiency, no signals could be detected above 10 000 Da. Calculations, however, show (12, 13) that secondary ion velocities are still high enough for a detection. Therefore the process of ion formation itself has to be considered. In TOF-SIMS analysis the total number of detectable ions  $N_d(X)$  of a species X is defined as

$$N_d(X) = N(M) \times P(M \rightarrow X) \times T(X) \times D(X)$$

where  $N(M)$  is the number of analyte molecules in the analyzed area,  $T(X)$  is the geometrical transmission of the instrument for X,  $D(X)$  is the detection efficiency for X, and  $P(M \rightarrow X)$  is the probability that the molecule M sputtered

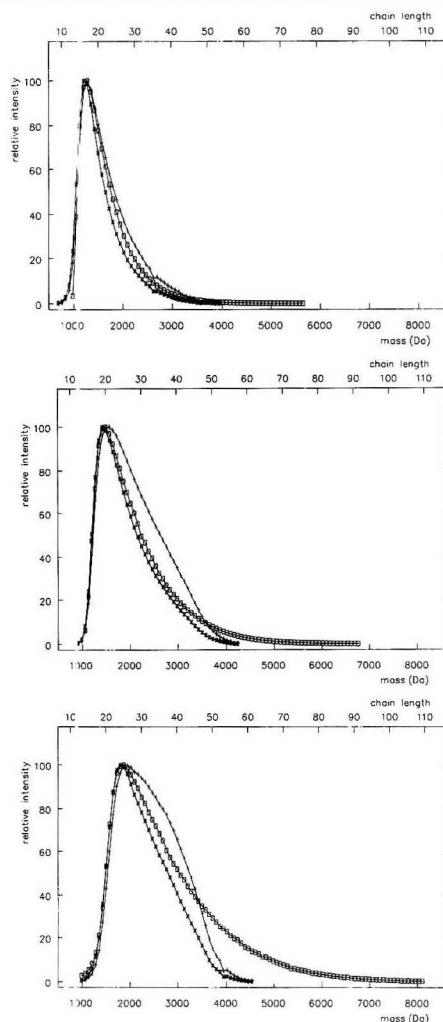


Figure 4. Comparison of the distributions of the relative peak areas in SFC and TOF-SIMS of the PDMS samples 1 (a, top), 2 (b, middle), and 3 (c, bottom): (○) TOF-SIMS, (●) SFC, (—) SFC corrected.

from the surface is emitted as a certain secondary ion species X (transformation probability). Since  $T(X)$  is constant for

the whole mass range and  $D(X)$  is known (see 2.2.2), the influence of  $P(M \rightarrow X)$  has to be considered.  $P(M \rightarrow X)$  has been found to be a function of mass and substance. For poly(styrene) oligomers it decreases from  $3 \times 10^{-4}$  at 2000 Da to  $2 \times 10^{-6}$  at 7000 Da. Extrapolation up to 12000 Da leads to transformation probabilities in the range of  $1 \times 10^{-7}$  (8). Further investigations must show whether this effect is due to a hindered desorption (e.g. cross-linking effects) or results from reduced cationization efficiencies. Taking into account that the number of molecules which can be deposited in the analyzed area decreases with increasing chain length and that a minimum number of 300 molecular ions per peak is necessary for an unambiguous peak identification, the detection limit for intact oligomers under these experimental conditions is in the range of 10000 Da. Better results have been obtained for fluorine containing polymers, e.g. perfluorinated polyethers (16). Fragmentation is only a subordinated process and the decrease of the transformation probability with increasing mass is the same for fragments and oligomers (17). An influence of fragmentation on the shape of the molecular weight distribution curves can therefore be neglected.

Compared to the SFC results the portion of cyclic oligomers detected by TOF-SIMS is significantly higher. Therefore different transformation probabilities for linear and cyclic oligomers have to be assumed. Future investigations on isolated individual linear and cyclic oligomers will offer further quantification of this effect.

To obtain an estimation on the accuracy of both the SFC and the TOF-SIMS data additional measurements using  $^{29}\text{Si}$  NMR spectroscopy have been performed.  $^{29}\text{Si}$  NMR spectroscopy provides the number average molecular weight by counting the integral of dimethylsilyloxy moieties in relation to the end-capping trimethylsilyloxy moieties. This value will include high-mass oligomers despite their discrimination by SFC and TOF-SIMS but also cyclic low-mass PDMS. The content of cyclic compounds has been determined to be less than 0.5% of the total PDMS, as mentioned above (see section 3.1). Therefore  $^{29}\text{Si}$  NMR spectroscopy in our report will provide the number average molecular weights of the linear PDMS within a reasonable error.  $^{29}\text{Si}$  NMR spectroscopy (see Table I) results in higher number average molecular weights compared to those calculated from SFC or even TOF-SIMS (see Table IV). The observed difference is particularly remarkable for the highest molecular weight PDMS (sample 3).

TOF-SIMS and SFC maximum peak intensities are related to masses that differ only for one dimethylsilyloxy unit (74 Da) within one sample. It may hence be concluded that there is a remarkably good agreement of both the SFC and TOF-SIMS method concerning the molecular weight distributions of low-mass PDMS. Deviations from the  $^{29}\text{Si}$  NMR results may therefore be due to higher molecular weight oligomers. Thus we see a mass discrimination affecting both methods, SFC and TOF-SIMS. Concerning the mass range above 3000 Da, this discrimination is stronger in SFC than in TOF-SIMS.

#### 4. CONCLUSION

In the mass range between 1000 and 3000 Da, both SFC and TOF-SIMS give similar results concerning average molecular weights and resolution of individual PDMS species. Between 3000 and 4500 Da, SFC is more influenced by mass discrimination effects than TOF-SIMS so that the last one

gives higher average molecular weights which are in better accordance with data obtained by NMR spectroscopy. Above 4500 Da no intact oligomers could be detected by SFC whereas TOF-SIMS yields signals up to 10000 Da. Further investigations will focus on expanding the mass range accessible to TOF-SIMS above this mass limit by (a) improvement of sample preparation and bombardment conditions in order to enlarge the transformation probability and (b) assessment of larger fragments which do or do not contain oligomer end groups. From ratios of such fragments the average molecular weight can be derived (18).

In contrast to NMR spectroscopy both methods SFC and TOF-SIMS give information on number as well as weight average molecular weights of PDMS oligomers, and therefore the polydispersity of a molecular weight distribution can be assessed.

By SFC individual cyclic and linear PDMS species in the mass range 100-1500 Da can be determined. Up to a mass range of 3000 Da, SFC is useful for quality control and routine analysis without a remarkable mass discrimination.

However, the applicability to other polymer classes, the small amount of sample material necessary for an analysis, the short times of measurements, and the ease of operation makes especially TOF-SIMS a unique analytical tool in the mass range up to 10000 Da.

#### ACKNOWLEDGMENT

We wish to thank Jürgen Burkhardt (Wacker Chemie GmbH, 8263 Burghausen, FRG) for providing the PDMS samples and G. Sicking (Verbundzentrum für Oberflächen- und Mikrobereichsanalyse, V.O.M., Münster) for initiating the collaboration.

#### LITERATURE CITED

- Barry, A. J. *J. Appl. Phys.* **1946**, *17*, 1020.
- Warrick, E. L.; Piccoli, W. A.; Stark, F. O. *J. Am. Chem. Soc.* **1955**, *77*, 5017.
- Yan, W. W.; Kirkland, J. J.; Bly, D. D. *Modern Size Exclusion Liquid Chromatography*; John Wiley: New York, 1979.
- Lipsky, S. R.; Duffy, M. L. *HRC & CC* **1986**, *9*, 725.
- Novotny, M.; Springston, S. R.; Peaden, P. A.; Fieldsted, J. L.; Lee, M. L. *Anal. Chem.* **1981**, *53*, 407A.
- Benninghoven, A.; Rüdener, F. G.; Werner, H. W. *Secondary Ion Mass Spectrometry*; John Wiley: New York, 1987.
- Leyendecker, D.; Leyendecker, D.; Höfler, F. *GIT Fachz. Lab.* **1989**, *5*, 465.
- van Leyen, D.; Hagenhoff, B.; Niehuis, E.; Benninghoven, A.; Bletsos, I. V.; Hercules, D. M. *J. Vac. Sci. Technol.* **1989**, *A7*, 1790.
- Bletsos, I. V.; Hercules, D. M.; van Leyen, D.; Benninghoven, A. *Macromolecules* **1987**, *20*, 407.
- Bletsos, I. V.; Hercules, D. M.; Fowler, D.; van Leyen, D.; Benninghoven, A. *Anal. Chem.* **1990**, *62*, 1275.
- Steffens, P.; Niehuis, E.; Friese, T.; Greifendorf, D.; Benninghoven, A. *J. Vac. Sci. Technol.* **1985**, *A3*, 1322.
- Niehuis, E. *Thesis*, Münster, 1988.
- Deimel, M. *Diploma work*, Münster, 1989.
- Leibnitz, E.; Struppe, H. *Handbuch der Gaschromatographie*; Akademische Verlagsgesellschaft: Leipzig, 1984.
- Knowles, D. E.; Nixon, L.; Champell, E. R.; Lator, D. W.; Richter, B. E. *Fresenius Z. Anal. Chem.* **1989**, *330*, 225. Symposium on Supercritical Fluid Chromatography, 29th Rocky Mountain Conference, Denver, CO, Aug 2-6, 1987.
- Feld, H.; Leute, A.; Rading, D.; Benninghoven, A. Submitted for publication in *Org. Mass Spectrom.*
- Hagenhoff, B.; van Leyen, D.; Feld, H.; Benninghoven, A. *Ion Formation from Organic Solids (IFOS V)*; John Wiley: Chichester, U.K. 1990.
- Fowler, D. E.; Johnson, R. D.; van Leyen, D.; Benninghoven, A. *Anal. Chem.* **1990**, *62*, 2088.

RECEIVED for review April 25, 1991. Accepted July 24, 1991.

# Matrix-Assisted UV-Laser Desorption/Ionization Mass Spectrometric Analysis of Monoclonal Antibodies for the Determination of Carbohydrate, Conjugated Chelator, and Conjugated Drug Content

Marshall M. Siegel,\* Irwin J. Hollander, Philip R. Hamann, John P. James, and Lois Hinman

American Cyanamid Company, Medical Research Division, Lederle Laboratories, Pearl River, New York 10965

Bryan J. Smith, Andrew P. H. Farnsworth, Alison Phipps, and David J. King

Celltech, Ltd., Slough SL1 4EN Berkshire, U.K.

Michael Karas, Arndt Ingendoh, and Franz Hillenkamp

Institute of Medical Physics, University of Münster, D-4400 Münster, FRG

The chemically averaged molecular weights of a variety of native and conjugated monoclonal antibodies, ~150 000, were measured by matrix-assisted UV-laser desorption/ionization mass spectrometry. The average mass of the carbohydrate present in a monoclonal antibody was estimated from the difference between the measured mass of the monoclonal antibody and the mass of the protein present in the monoclonal antibody computed from the amino acid translation of the DNA sequence. The loading of chelators and anticancer drugs conjugated to a monoclonal antibody was quantitated from the difference in the measured masses for the conjugated and untreated monoclonal antibody relative to the expected mass change upon conjugation of 1 mol of chelator or drug. The loading results obtained by mass spectrometry were consistent in most cases with measurements obtained by radioactivity trace assay or UV spectrometry. Similar matrix-assisted UV-laser desorption/ionization mass spectrometric studies were also made after reducing untreated and conjugated monoclonal antibodies with dithiothreitol to determine the distribution of carbohydrate and chelator between the light and heavy chains of the molecules. Matrix-assisted UV-laser desorption/ionization mass spectra were used to compute loading values for covalently bound drugs and proteins, while the loading values obtained by use of gel-filtration HPLC and UV spectrometry cannot distinguish between covalently and noncovalently bound drugs and proteins.

## INTRODUCTION

Matrix-assisted UV-laser desorption/ionization mass spectrometry (LDI-MS) has recently been demonstrated to be a powerful technique for producing abundant molecular ions of molecules with molecular weights of up to 300 000 with nearly no fragmentation (1-15). In this technique, analyte molecules are embedded in a large molar excess of a matrix substance, isolating the analyte molecules from one another thereby reducing their intermolecular forces. Energy from a laser beam is absorbed by the matrix, resulting in the disintegration of the condensed phase. Photochemical processes with the matrix are thought to enhance or even induce analyte ionization (1). The analytes of interest in this paper are IgG monoclonal antibodies and their derivatives, which have molecular weights of about 150 000. Monoclonal antibodies are homogeneous preparations of antibodies produced in large quantities by hybridoma technology (16). They are glycoproteins made from two identical light chains (LC, MW

~24 000 each) and two identical heavy chains (HC, MW ~50 000 each) that form a Y-shaped molecule held together by disulfide bonds. The heavy chains typically contain carbohydrates while the light chains generally do not (17). Traditionally, biochemical techniques have been used to generate knowledge of the structure and function of antibodies. In this paper, we will demonstrate how modern mass spectrometric methods coupled with chemical methods can be used to derive useful structural information of monoclonal antibodies and their derivatives.

We have used the technique of matrix-assisted UV-laser desorption/ionization mass spectrometry and have generated the mass spectra of a variety of purified monoclonal antibodies. The monoclonal antibodies were also analyzed after being treated with dithiothreitol (DTT) to reduce the disulfide bonds, thereby generating reduced light chain monomers and reduced heavy chain monomers. The average mass of the carbohydrate present in a monoclonal antibody, a reduced light chain or a reduced heavy chain, can be computed from the respective differences between the measured masses by using LDI-MS and the predicted masses of the amino acid sequence derived from the DNA structure. In this way, the general location of the carbohydrate in the monoclonal antibody (MoAb) can be identified.

A pharmaceutical use of monoclonal antibodies actively being developed worldwide is for the targeting of imaging reagents and anticancer drugs to the sites of tumors (18, 19). The imaging reagents may be radioactive metal ions that bind to chelating agents. These small chelator or drug molecules, typically having molecular weights between 300 and 1500, are chemically conjugated to either the lysines or the carbohydrates present in the monoclonal antibody. The average number of moles of chelator or drug conjugated to a monoclonal antibody is referred to as the loading value of that chelator or drug on the conjugate. Presently, radioactivity trace assay (20-22) or UV spectrometry (23-25) is principally used to quantitate the loading of the imaging reagents or anticancer drugs to monoclonal antibodies. A number of assumptions and experimental difficulties are associated with both techniques that may result in inaccurate loading values. An assumption made in the radioactivity trace assay is that the binding constants for pure and contaminated radioactive metal ions are identical for both the free and conjugated chelators. Deficiencies with UV spectrometry are that chelators and drugs conjugated to monoclonal antibodies cannot be quantitated accurately when their absorptivities are low or occur in the protein absorption region and that the absorptivity of the UV chromophore may change upon conjua-

tion. In addition, both radioactivity trace assay and UV spectrometry methods cannot distinguish between covalently and noncovalently bound compounds. To overcome these difficulties, matrix-assisted UV-laser desorption/ionization mass spectrometry was investigated as an alternative method for obtaining the loading data for the small molecules conjugated to monoclonal antibodies. Normally, under the experimental conditions used, only covalently bound conjugated molecules are detected in the LDI-MS spectra. Noncovalently bound molecules dissociate from the monoclonal antibody because the energy needed for desorption and ionization is greater than the dissociation energy for such systems. Also, LDI-MS should be routine, accurate, and free from all the limitations described above for radioactivity trace assay and UV spectrometry. The LDI-MS loading value is the average number of conjugated molecules per monoclonal antibody molecule and is determined from the mass difference between the conjugated and untreated monoclonal antibodies when divided by the expected mass change upon conjugation with 1 mol of chelator or anticancer drug. Any other changes in the mass of the monoclonal antibody due to chemical treatments during conjugation must also be considered when the loading values are calculated. To obtain the data needed for computing the LDI-MS loading values, matrix-assisted UV-laser desorption/ionization mass spectra were generated from a variety of monoclonal antibodies either when unmodified or when chemically conjugated to low molecular weight chelators and anticancer drugs. The LDI-MS loading values were computed from the peak centroids and the distribution in the number of small molecules conjugated to the monoclonal antibodies determined from the widths of the peak contours. The LDI-MS loading values were also compared to the respective loading values obtained by either radioactivity trace assay or UV spectrometry.

#### EXPERIMENTAL SECTION

The mass spectrometer used for analyzing the monoclonal antibodies was a reflector-type time-of-flight microprobe instrument (LAMMA 1000) equipped with a Q-switched (7 ns) frequency-quadrupled Nd-YAG laser (Quantel YG 660S), which operated at a wavelength of 266 nm. The laser was focused at the sample surface to spot size diameters of 10–50  $\mu\text{m}$  with irradiances between  $10^{14}$  and  $10^{17}$  W/cm<sup>2</sup>. The ions generated were accelerated to a potential of 3 kV in the ion source and postaccelerated to a potential of 20 kV for detection with a secondary ion multiplier (EMI 9643). To detect all ions from 1 to 250 000 Da in a single spectrum, a window of arrival times from 3  $\mu\text{s}$  to 1.5 ms must be recorded. Registration of the analog signal was performed with a PC-board (PC-SOPE T12840, IMTEC Inc., FRG) or a transient recorder (LeCroy 9400) with 40 or 50 ns/channel resolution, which corresponds to about 15 Da/channel at a mass of 150 000 Da. The spectra acquired consisted of the sum of 20–30 single acquisitions. The centroids of the peaks appearing in the spectra were computed from all the data above the spectral noise level for each peak. The whole process of sample preparation, data acquisition and analysis, typically takes from 10 to 15 min. All the spectra illustrated in this publication are the acquired raw data. No manipulations of the data such as smoothing or background subtraction were performed. The molecular weights reported for all the measured high-mass compounds are the isotopically averaged chemical masses because the mass resolution, defined as  $m/\delta m$ , where  $m$  is the mass of the ion and  $\delta m$  is the full width of the peak envelope at half maximum height (FWHM), was limited to only 50–100 for the time-of-flight mass spectrometer in the high-mass range of interest.

The time ( $t$ ) axis for the spectra produced on the time-of-flight mass spectrometer was calibrated as a function of mass ( $m$ ) using the signals of two or more ions of known mass according to the relation

$$t = A + B(m)^{1/2} \quad (1)$$

When more than two calibration peaks were used, A and B were determined by a least-squares fit procedure. The protonated ions

of the singly and doubly charged parent molecule of horse heart cytochrome *c* (MW 12 360) and its singly charged dimer as well as in some cases the parent molecular ion of the aglycosyl chimeric B72.3 (c B72.3) monoclonal antibody (MW 143 919) were used as calibration peaks. The mass of cytochrome *c* was computed from the published sequence, and the mass of the aglycosyl chimeric B72.3 monoclonal antibody was computed from the protein structure derived from its DNA sequence (26). Typical values for A and B are  $-0.35 \mu\text{s}$  and  $3.075 \mu\text{s Da}^{-1/2}$ , respectively. Under matrix-assisted UV-LDI-MS experimental conditions, proteins tend to produce molecular ions as well as matrix adducts of the molecular ions (12, 13). For mass calibrations using proteins of known mass to yield correct results for unknown samples, one must assume that the probability for binding of matrix related ions to the protein increases in proportion to the mass of the protein. This will result in a constant fractional mass increase  $m'/m$  (where  $m'$  is the mass of the protein plus the sum of all adducts and  $m$  is the mass of the pure protein), which is independent of the specific protein structure. Control experiments with several different proteins of known mass support this assumption to a first-order approximation. Earlier calibration measurements utilized the low-mass ions Na<sup>+</sup> and K<sup>+</sup> and several nicotinic acid matrix ions. Calibration with cations or matrix ions will lead to protein masses that are systematically too high because the flight time of these ions will be determined by the mass of the protein plus that of the matrix adduct. Under the assumption of constant fractional mass increase due to adduct formation, as described above, it can be rigorously shown that the earlier mass calibrations can be corrected for adduct formation by leaving unchanged the factor A of eq 1 and using the new factor  $B' = B(m/m')^{1/2}$ . Therefore, all the unknown masses measured with the earlier calibrations are then multiplied by the same factor to obtain the corrected mass. Hence, all mass data reported in this paper are based upon a calibration using protein signals. Investigations of a number of proteins of known mass, including the determination of the mass for aglycosyl chimeric B72.3 monoclonal antibody, revealed that a precision and accuracy of typically  $\pm 0.1\%$ , viz., about  $\pm 150$  Da for a monoclonal antibody of mass  $\sim 150$  000 Da, is achieved under these conditions. This value is determined by the limited mass resolution of only 50–100 for the instrumentation used, resulting in limited precision for the peak centroid, particularly in the high-mass range, as well as the assumed condition of constant fractional mass increase due to adduct formation. The mass accuracy achieved is quite favorable for the absolute mass determination of large molecules but still needs to be improved in cases where the mass difference between two large molecules is relatively small, such as occurs occasionally in the measurements for the carbohydrate content of monoclonal antibodies or the determination of the loading values in conjugation studies.

Nearly all the monoclonal antibody samples were prepared in a nicotinic acid matrix in the following manner for analysis by UV-LDI-MS. Subsamples of the monoclonal antibodies were dissolved in ultrapure water to a concentration of 0.10–0.75 mg/mL. Aliquots of the samples (0.5–1.0  $\mu\text{L}$ ) were mixed with equal volumes of 0.05 M nicotinic acid (Serva Biochemicals, USP XX grade), deposited on silver substrates and air-dried for subsequent LDI-MS analysis. Nicotinic acid has been used as a matrix in nearly all the experiments because signal quality was highly superior to any other matrix in the mass range above 100 000 Da. Whereas a high tolerance toward low molecular weight contaminants was reported for sinapinic acid, where admixtures of 1 M NaCl or urea did not have any effects on the spectral quality (13), samples analyzed with nicotinic acid have to be exhaustively purified to remove all salt and buffer contamination. In adulteration experiments where known quantities of salts, up to concentrations in the millimolar range, were added to purified monoclonal antibodies in nicotinic acid matrix, the resulting peaks in the spectra were very broad with lower signal-to-noise ratios relative to the pure monoclonal antibody. Sample purity in the LDI-MS experiment was judged acceptable if the Na<sup>+</sup> and/or K<sup>+</sup> ion signals in the low-mass range were very small or absent.

The monoclonal antibodies analyzed by LDI-MS and their corresponding sources, indicated in parentheses, were as follows: B72.3, chimeric B72.3, aglycosyl chimeric B72.3, CTM01, MOPC21, MAC68 (Celltech Ltd., Berkshire, UK); LYM1, LYM2



(Technicon International, Santa Ana, CA). The purified monoclonal antibodies were exhaustively dialyzed against 10 mM ammonium acetate buffer (pH 7) using an ~8000-Da cutoff membrane to remove salts and low molecular weight contaminants in order to prevent peak broadening. The monoclonal antibody samples showed no detectable light chain by analytical biochemical methods. For dissociation studies, DTT was added into dialyzed monoclonal antibody solutions (1–3 mg/mL) to a concentration of 1 or 10 mg/mL. The mixture was incubated for ~2 h at 37 °C to reduce the disulfide bonds, thereby producing reduced light and heavy chains of the monoclonal antibodies. The pure and reduced monoclonal antibody samples were then lyophilized and stored at -20 °C. Because of the normal variability in the carbohydrate content of monoclonal antibodies from batch to batch, the conjugated monoclonal antibodies were prepared, when feasible, from the same batches of purified monoclonal antibodies used as controls in the LDI-MS experiments.

The chimeric B72.3 monoclonal antibodies conjugated with chelating agents at lysine residues which were studied by matrix-assisted UV-LDI-MS are illustrated as structures 1–4 in Table I. The conjugated chelating agents were derivatives of DTPA (diethylenetriaminepentaacetic acid) in 1, macrocycle 12N4 (1,4,7,11-tetraazacyclododecane tetraacetic acid) in 2, macrocycle 12N4 with maleimide (a maleimide derivative of 1,4,7,11-tetraazacyclododecane tetraacetic acid) in 3, and macrocycle 12N4P4 (1,4,7,11-tetraazacyclododecane tetraphosphonic acid) in 4. The DTPA conjugate, 1, was prepared according to the method reported in ref 20. For conjugates prepared by using macrocycles 12N4 and 12N4P4, 2 and 4, the chelating agents were attached directly to the  $\epsilon$ -NH<sub>2</sub> group of lysines in the antibody by reaction of them with *p*-nitrophenol ester derivatives of the chelator-linker molecules, used at a predetermined molar excess. Conjugates prepared with macrocycle 12N4 with maleimide, 3, required the antibody to be chemically modified by 2-iminothiolane, to generate thiol groups that were then reacted with maleimide derivatives of 3. The conjugates were purified by gel-filtration (Sephadex G25 [PD10] in 0.1 M potassium acetate, pH 6). Samples of these conjugates were prepared for LDI-MS studies by desalting on a PD10 column, eluting with water, and lyophilizing. The LDI-MS loading results were compared with those obtained by radioactivity trace assay studies (20–22) for compounds 1, 2, and 4 and by titration assay for compound 3. The radioactivity trace assay was performed according to the method of ref 21. Briefly, an aliquot of the reaction mixture of conjugated and unreacted chelating agent was labeled with ~10  $\mu$ Ci of <sup>111</sup>In<sup>3+</sup>. The mixture was then analyzed by gel-filtration HPLC (Zorbax GF250 column in 0.2 M sodium phosphate buffer, pH 7) and the number of chelators per antibody determined from the labeling efficiency of the antibody conjugate and the molar excess of chelating agent employed in the original reaction. The estimated error in the loading values based upon this radioactivity trace assay was approximately 10%. The titration assay, performed for conjugated chelator 3, involved the determination of the difference in the numbers of available thiol groups before and after the reaction of the maleimide derivative of macrocycle 12N4 with the monoclonal antibody modified with 2-iminothiolane. The titration of the free thiol group utilized 4,4'-dithiodipyridine (Ellman's reagent) (27). The estimated errors in the titration assay for the loading values of 3 were approximately 20%.

The monoclonal antibodies conjugated with anticancer drugs that were studied by matrix-assisted UV-LDI-MS are illustrated as structures 5–10 in Table I. The conjugated anticancer drugs were derivatives of mitoxantrone in 5, calicheamicins in 6–9, and methotrexate in 10. The anticancer drugs that were conjugated to the carbohydrate of the monoclonal antibodies were prepared as hydrazide derivatives. The carbohydrate was prepared for conjugation by oxidizing the sugar *cis*-diols with periodic acid to the corresponding aldehydes to which the hydrazide derivative of the drug was reacted. To block any unreacted aldehyde, the conjugated monoclonal was exhaustively reacted with acetylhydrazide. For conjugating an anticancer drug to a lysine group present in the monoclonal antibody, the drug was prepared as an *N*-hydroxysuccinimide derivative and reacted directly with the monoclonal antibody. The purified and conjugated monoclonals were dialyzed, lyophilized, and prepared for LDI-MS analysis as described above. The LDI-MS drug loading values

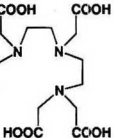
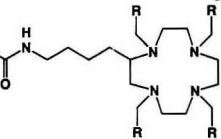
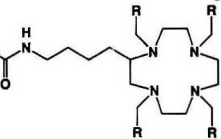
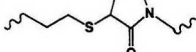
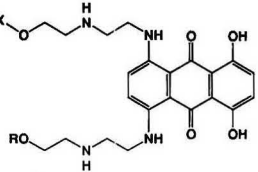
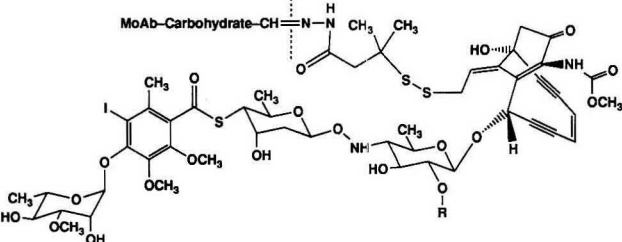
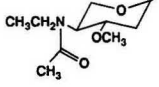
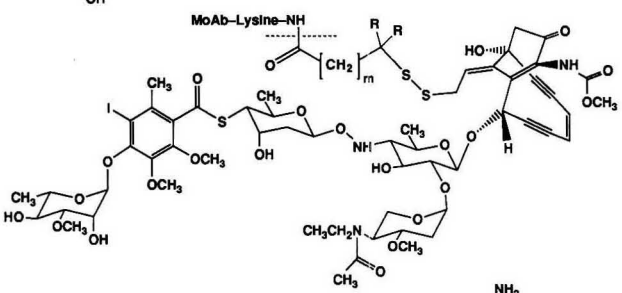
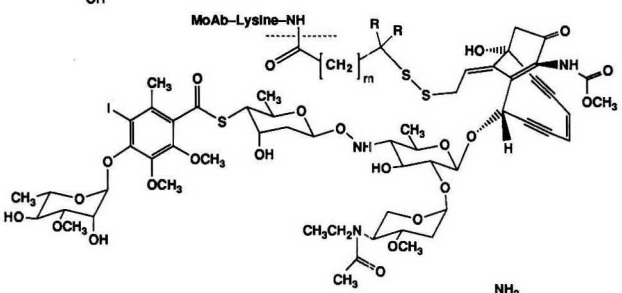
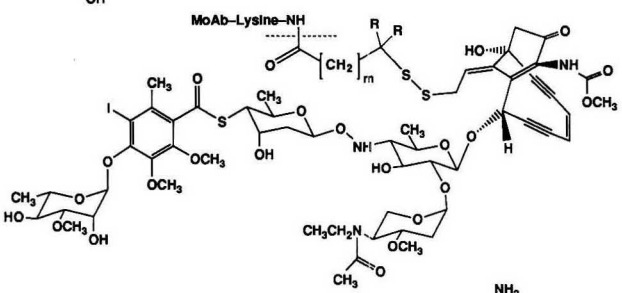
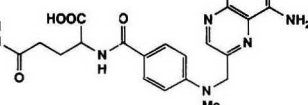
were computed as defined above at the end of the Introduction. In the case of a drug conjugated to carbohydrate, the net change in mass per drug molecule was decreased by an additional 74 Da to account for the displacement of one acetylhydrazide group for each drug molecule bound to the monoclonal antibody. The LDI-MS loading values were compared to the loading values obtained by UV spectrometry for the respective conjugated monoclonal antibodies. The estimated errors in the UV loading values for mitoxantrone and methotrexate derivatives, intensely colored materials, are relatively small, ranging from 2% to 5%, while those for the calicheamicin derivatives, very poor UV absorbing materials, range from 5% to 15%.

## RESULTS AND DISCUSSION

**Matrix-Assisted UV-LDI-MS Results for Characterizing Pure and Reduced Monoclonal Antibodies.** Figures 1A and 2A illustrate typical matrix-assisted UV-laser desorption/ionization mass spectra of a purified monoclonal antibody and that of a DTT-reduced monoclonal antibody, respectively. The intense peaks observed in the pure monoclonal antibody spectra correspond to M<sup>1+</sup>, M<sup>2+</sup>, M<sup>3+</sup>, and LC<sup>1+</sup>. The weak peaks observed were 2M<sup>1+</sup>, 2M<sup>2+</sup>, LC<sup>2+</sup>, and 3M<sup>2+</sup>. Since aggregate was absent from the samples, the weak dimer peaks most probably originated from the association of the high levels of monomer present in the aqueous solution. These signals are typically found in LDI mass spectra and facilitate correct mass assignments. The presence of the LC peak was unexpected since no LC was observed in the sample by traditional bioanalytical methods and because fragmentation even of disulfide bonds has never been unequivocally observed before under matrix-assisted UV-LDI-MS conditions. The strong peaks observed in the spectra of the monoclonal antibodies when treated with DTT were LC<sup>1+</sup> and LC<sup>2+</sup>. The weak peaks observed were (M - LC)<sup>1+</sup>, (M - 2LC)<sup>1+</sup>, (HC + LC)<sup>1+</sup>, (HC + LC)<sup>2+</sup>, 2LC<sup>1+</sup>, HC<sup>1+</sup>, and HC<sup>2+</sup>. Under the DTT treatment conditions, the monoclonal antibodies appeared to be reduced to different degrees and in no case did the monoclonal antibodies seem to be completely reduced. This was apparently due to reoxidation of reduced samples. Freshly reduced samples treated with *N*-ethyl maleimide to block free sulfhydryl groups were prepared and analyzed by LDI-MS. LC and HC peaks were mainly produced, both slightly broader than those observed in the untreated samples. Presumably all interchain disulfides had been reduced and blocked, but not all intrachain disulfides, resulting in mass heterogeneity and peak broadening. The appearance of the 2LC<sup>1+</sup> peak is dependent on the analytical concentration in the aqueous phase and is, therefore, most probably caused by cluster formation already in solution. The 2LC<sup>1+</sup> peak appeared as a weaker shoulder on the low-mass side of the weak HC<sup>1+</sup> peak, thereby reducing the mass accuracy for each of the ions. A feature in the spectra of the DTT-reduced monoclonal antibodies generally observed is that the intensity of the LC<sup>1+</sup> peak is significantly more intense than that of the HC<sup>1+</sup> peak in spite of the fact that both components were of equal molar concentrations and by taking into account the decreasing detector sensitivity with increasing molecular mass. This is not due to the carbohydrate presence or heterogeneity on the heavy chain since the same results were observed with aglycosyl chimeric B72.3 monoclonal antibody, where no carbohydrate is present on the heavy chain. The disparity in the relative intensities of the LC and HC peaks in the LDI mass spectra for a variety of dissociated monoclonal antibodies was also observed in recently acquired electrospray ionization mass spectra for related studies (28) further supporting the assumption that physicochemical reasons, e.g., ionization efficiency, account for these phenomena.

To calculate the best estimate of the parent molecular mass, all peaks in the spectrum above the noise level were mass-calibrated. The masses of those peaks that could unambigu-

Table I. Structures of Monoclonal Antibody (MoAb) Chelator and Drug Conjugates

Monoclonal Antibody	Chelator or Drug	Name of Conjugate
MoAb-Lysine-NH		1 DTPA Conjugate
MoAb-Lysine-NH		2 Macrocycle 12N4 Conjugate Y = O, R = -COOH, X = -CH <sub>2</sub> -
MoAb-Lysine-NH		3 Macrocycle 12N4-Maleimide Conjugate Y = NH, R = -COOH, X = 
MoAb-Carbohydrate-CH=N-N		5 Mitoxantrone Dihydrazone Conjugate X = -CH <sub>2</sub> CH <sub>2</sub> (CO)-, R = NH <sub>2</sub> NHCOCH <sub>2</sub> CH <sub>2</sub> -
MoAb-Carbohydrate-CH=N-N		6 Calicheamicin N-Acetyl $\gamma_1^1$ Dimethyl Propionyl Hydrazone Conjugate R = 
MoAb-Lysine-NH		7 Calicheamicin $\alpha_3$ Dimethyl Propionyl Hydrazone Conjugate R = -H
MoAb-Lysine-NH		8 Calicheamicin N-Acetyl $\gamma_1^1$ Proplonyl Conjugate R = -H, m = 1
MoAb-Lysine-NH		9 Calicheamicin N-Acetyl $\gamma_1^1$ Dimethyl Butyryl Conjugate R = -CH <sub>3</sub> , m = 2
MoAb-Carbohydrate-CH=N-N		10 Methotrexate Hydrazone Conjugate

**Table II. Masses of Monoclonal Antibodies and Their Respective Light and Heavy Chains Measured by Matrix-Assisted UV-Laser Desorption/Ionization Mass Spectrometry and Peptide Translation of the DNA Sequence**

MoAb	exp	molecular mass <sup>a</sup>	FWHM of molecular mass	reduced LC mass <sup>b</sup>	reduced HC mass <sup>b</sup>	reduced bound LC + HC mass <sup>b</sup>
aglycosyl c B72.3	LDI <sup>c</sup>	144 070 ± 50	2350	23 550 ± 20 (23 430 ± 10 <sup>d</sup> )	48 520 (48 430 <sup>e</sup> )	NO <sup>h</sup>
c B72.3	DNA <sup>f</sup>	143 919		23 433	48 543	71 974
	LDI	147 400 ± 30	2080	23 480 ± 10	50 090 ± 10	74 060 ± 210
B72.3	DNA <sup>f</sup>	143 891		23 433	48 529	71 960
	LDI	147 470 ± 190 (147 320 ± 50 <sup>g</sup> )	2480	23 630 ± 80	49 900 ± 20	73 680 ± 10
LYM1	DNA <sup>h</sup>	143 757		23 603	48 311	71 912
	LDI	147 820 ± 100	3750	23 510 ± 10	50 290 ± 20	73 900 ± 10
MOPC21	DNA <sup>f</sup>	145 022		23 450	49 061	72 509
	LDI	147 430 ± 90 (148 430 ± 30 <sup>g</sup> )	2400	23 510 ± 20	50 060	NO
CTM01	DNA <sup>g</sup>	143 952		23 639	48 355	71 992
	LDI	149 610 ± 50 (149 470 ± 40 <sup>g</sup> )	2540	24 170 ± 10	50 460 ± 60	74 770 ± 10
LYM2	LDI	150 490 ± 70 (150 420 ± 25 <sup>g</sup> )	2690	23 730 ± 20	51 390 ± 70	75 180 ± 40
MAC68	LDI	150 070 ± 20 (149 980 ± 20 <sup>g</sup> )	2800	24 140 ± 10	50 800 ± 20	75 010 ± 10

<sup>a</sup>LDI values were computed from the average value of  $z \cdot M^{z+}$ ,  $z = 1, \dots, 4$ , where  $z$  is the charge number and  $M^{z+}$  is the mass-to-charge ratio of the (multiply charged) molecular ion, observed in the analysis of the pure monoclonal antibodies. <sup>b</sup>LDI values were computed from the average mass of the respective ions observed in the analysis of the dithiothreitol (DTT) reduced monoclonal antibodies. The results from two DTT concentrations were averaged. <sup>c</sup>First analysis of monoclonal antibody used as LDI mass reference standard with molecular mass assigned to the DNA value. These data are from the second analysis of monoclonal antibody (spectrometer not optimized). <sup>d</sup>Periodic acid oxidized and acetylchrydine blocked carbohydrate. <sup>e</sup>DTT reduced and sulhydryl blocked with *N*-ethyl maleimide. <sup>f</sup>Jones, T. R.; Muzithras, V. P.; Gluzman, Y. Personal communication, Jan 1990, American Cyanamid Co. <sup>g</sup>[For refs g-j: Paper = Whittle, N.; Adair, J.; Lloyd, C.; Jenkins, L.; Devine, J.; Schlom, J.; Raubitschek, A.; Colcher, D.; Bodmer, M. *Protein Eng.* 1987, 1, 499-505. Book = Kabat, E. A.; Wu, T. T.; Reid-Miller, M.; Pery, H. M.; Gottesman, K. S. *Sequences of Proteins of Immunological Interest*, 4th ed., U. S. Department of Health and Human Services; National Institutes of Health: Bethesda, MD, 1987.] MOPC21: LC, Book p 109 column 105, p 282 column 20; HC, Book pp 235, 296, 303, 310, 317 column 72. <sup>h</sup>B72.3: LC, Paper Figure 1b, Book p 288 column 11; HC, Paper Figure 1a, Book pp 296, 303, 310, 317 column 70. <sup>i</sup>c B72.3: LC, Paper Figure 1b, Book p 282 column 1; HC, Paper Figures 1a, Book pp 295, 302, 309, 316 column 46 with the following amino acid assignment changes: A349 S, P350 S, T359 A. <sup>j</sup>Aglycosyl c B72.3: LC same as for c B72.3; HC same as c B72.3 with the following amino acid change: N314 Q. <sup>k</sup>Not observed.

**Table III. Masses of Carbohydrates Present in Monoclonal Antibodies Computed from Matrix-Assisted UV-Laser Desorption/Ionization Mass Spectrometry Data and the Protein Translation of the DNA Sequence**

MoAb (pred carbohydrate mass <sup>b</sup> )	(LDI - DNA) molecular mass	2(LDI - DNA) reduced LC mass	2(LDI - DNA) reduced HC mass	2(LDI - DNA) reduced bound LC + HC mass	av carbohydrate mass <sup>c</sup>
aglycosyl c B72.3 <sup>e</sup> (MW 0, no carbohydrate)	150	230	-40	NO <sup>g</sup>	
c B72.3 (MW 3616 <sup>d</sup> )	3510	120	3130	4200	3620 ± 540
B72.3	3710	40	3170	3540	3470 ± 280
LYM1	2900	120	2450	2790	2680 ± 200
MOPC21	3480	-260	3410	NO	3450 ± 50

<sup>a</sup>Based upon the average mass of the calculated carbohydrates for the LDI measured masses of the molecular ion (column 2), reduced heavy chain (column 4), and the sum of the reduced bound light and heavy chains (column 5). <sup>b</sup>A fully sialylated carbohydrate structure for antibodies accounts for a mass of 5104 Da/antibody. <sup>c</sup>First analysis of monoclonal antibody used as LDI mass reference standard. Data from second analysis of sample (instrument not optimized). <sup>d</sup>Determined by Raubitschek (32) from a carbohydrate analysis. <sup>e</sup>Not observed.

ously be identified as integer multiples of the parent molecular mass (oligomers of parent molecules), fractions thereof (multiply charged parent molecules), and combinations of the two (multiply charged oligomers) were multiplied by the appropriate factor and averaged to yield an average mass and a standard deviation. Table II summarizes the LDI-MS and DNA data for the measured and calculated masses, respectively, for the M, LC, HC, and LC + HC components. The masses for the LC's compare favorably with those previously observed in liquid secondary ion mass spectra (29). Table III summarizes the mass differences between the LDI-MS and DNA values for the respective components. These mass differences are attributed to the average mass of carbohydrate present in the respective monoclonal antibodies. These data indicate that the carbohydrate is principally present on the HC and absent from the LC. The average mass of the car-

bohydrate ranges from 2600 to 3600 Da. The carbohydrate present in these monoclonal antibodies is of lower mass than the general carbohydrate structure for antibodies (where all structures are assumed to be fully sialylated) which has a mass of 5104 Da (30). This is expected from the observed distributions of carbohydrates in antibodies and may account for some of the chemical and biological properties of these monoclonal antibodies (31).

Raubitschek (32) measured the saccharides present in the chimeric B72.3 monoclonal antibody and found it to contain principally two fucose units, eight *N*-acetylglucosamine units, two galactose units, and six mannose units. The mass of the carbohydrate formed from these saccharides corresponds to 3616 Da. This mass correlates reasonably well with the measured value by LDI-MS of 3620 ± 540 Da. These results demonstrate that matrix-assisted LDI-MS can be used to

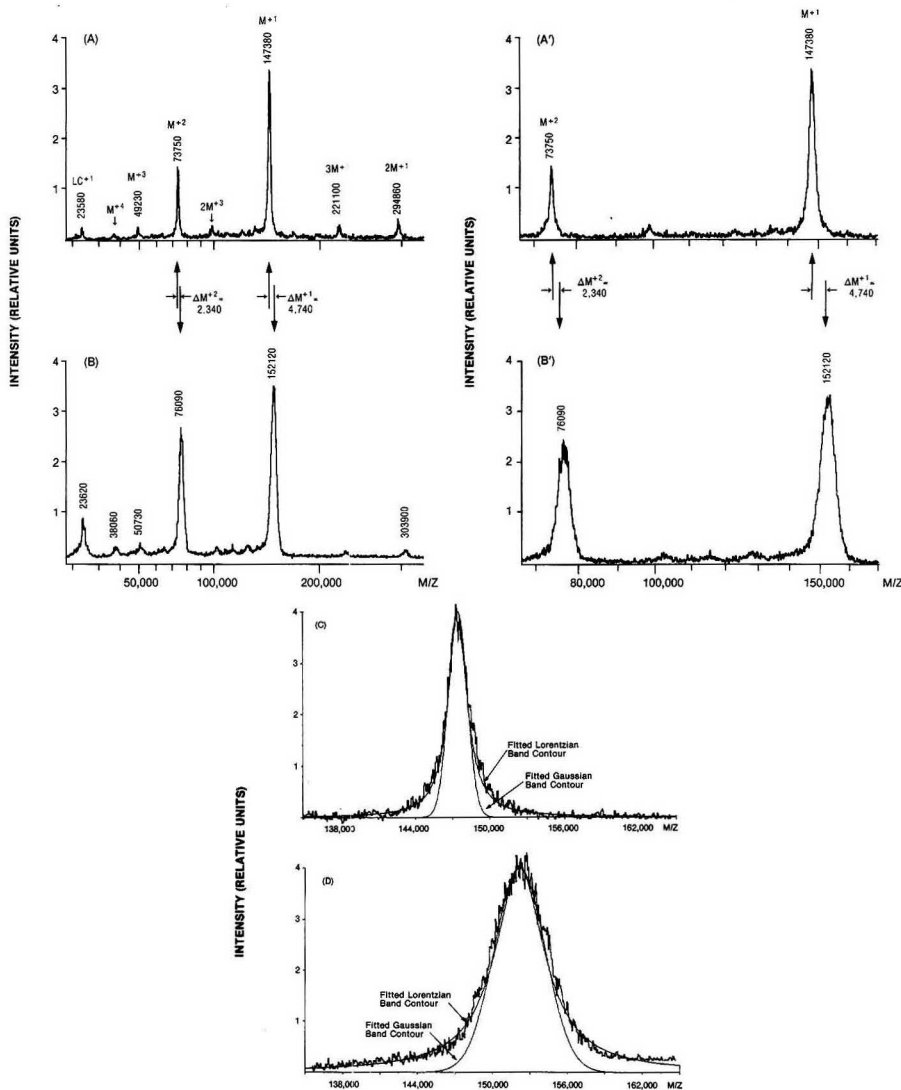


**Figure 1.** (A) Matrix-assisted UV-laser desorption/ionization mass spectrum of chimeric B72.3 monoclonal antibody. (B) Matrix-assisted UV-laser desorption/ionization mass spectrum of chimeric B72.3 monoclonal antibody conjugated with macrocycle 12N4-maleimide chelator, **3**, with an LDI-MS loading value of 6.5. The mass regions 70 000–170 000 Da are exploded in the primed figures (A' and B'). Note the mass shifts between the conjugated and untreated monoclonal antibodies for the corresponding singly and doubly charged molecular ion peaks ( $\Delta M$ ) and the larger peak widths for the conjugated monoclonal antibody versus the untreated sample. (C) Fit of the molecular ion LDI-MS peak of chimeric B72.3 monoclonal antibody to Lorentzian and Gaussian peak shapes. (D) Fit of the molecular ion LDI-MS peak of macrocycle 12N4-maleimide chelator conjugated with chimeric B72.3 monoclonal antibody, **3**, with an LDI-MS loading value of 6.5, to Lorentzian and Gaussian peak shapes.

estimate in a very simple set of mass spectrometric measurements the mass of the carbohydrate present in a monoclonal antibody when the DNA sequence of that antibody is known.

**Matrix-Assisted UV-LDI-MS Results for Characterizing Chelators Conjugated to Monoclonal Antibodies.** Figure 1B illustrates a typical matrix-assisted UV-laser desorption/ionization mass spectrum of a monoclonal antibody

conjugated to a chelator. The intense peaks observed correspond to  $M^{1+}$ ,  $M^{2+}$ , and  $M^{3+}$ . The weak peaks observed were  $LC^{1+}$ ,  $M^{4+}$ ,  $2M^{1+}$ , and  $2M^{3+}$ . Also illustrated in Figure 1B, with an exploded view in Figure 1B', are the mass shifts for the  $M^{1+}$  and  $M^{2+}$  peaks between a typical conjugated and untreated monoclonal antibody. Figures 1C and 1D illustrate the fit of the molecular ion peaks for unreacted and conjugated monoclonal antibodies, respectively, to a Lorentzian band

Table IV. Masses and Loadings of Monoclonal Antibodies Conjugated to Chelating Agents

structure	MoAb	conj chelator	mass change on conjugation	LDI-MS			loading value		
				conj MoAb mass <sup>a</sup>	FWHM conj MoAb mass <sup>a</sup>	pure MoAb mass <sup>a</sup>	mass shift: conj-pure mass <sup>a</sup>	LDI-MS	radioactivity
1	c B72.3	DTPA <sup>b</sup>	375.3	148 530 ± 60	2690	147 430 ± 50 <sup>c</sup>	1100 ± 80	2.9 ± 0.2	1.8
1	c B72.3	DTPA <sup>b</sup>	375.3	149 680 ± 80	3580	147 430 ± 50 <sup>c</sup>	2250 ± 90	6.0 ± 0.2	4.0
2	c B72.3	12N4 <sup>b</sup>	557.6	148 560 ± 30	2390	147 430 ± 50 <sup>c</sup>	1130 ± 60	2.0 ± 0.1	1.9
2	c B72.3	12N4 <sup>b</sup>	557.6	149 430 ± 60	2780	147 430 ± 50 <sup>c</sup>	2000 ± 80	3.6 ± 0.1	2.7
2	c B72.3	12N4 <sup>b</sup>	557.6	149 620 ± 40	4040	147 400 ± 30 <sup>d</sup>	2220 ± 50	4.0 ± 0.1	3.5
2	c B72.3	12N4 <sup>b</sup>	557.6	150 420 ± 40	2780	147 430 ± 50 <sup>c</sup>	2990 ± 60	5.4 ± 0.1	2.7
2	c B72.3	12N4 <sup>b</sup>	557.6	151 630 ± 200	4770	147 430 ± 50 <sup>c</sup>	4200 ± 200	7.5 ± 0.4	1.0
3	c B72.3	12N4-maleimide <sup>b</sup>	727.8	152 180 ± 50	4770	147 430 ± 50 <sup>c</sup>	4750 ± 70	6.5 ± 0.1	(4.7) <sup>e</sup>
3	c B72.3	12N4-maleimide <sup>b</sup>	727.8	152 760 ± 60	3990	147 430 ± 50 <sup>c</sup>	5330 ± 80	7.3 ± 0.1	(4.7) <sup>e</sup>
4	c B72.3	12N4P4 <sup>b</sup>	693.6	149 530 ± 40	3580	147 430 ± 50 <sup>c</sup>	2100 ± 60	3.0 ± 0.1	4.9

<sup>a</sup>LDI-MS values were computed from the average value of  $z^*M^{z+}$ ,  $z = 1, \dots, 4$ , where  $z$  is the charge number and  $M^{z+}$  is the mass-to-charge ratio of the (multiply charged) molecular ion, observed in the analysis of the pure or conjugated monoclonal antibodies. <sup>b</sup>Lysine conjugate. <sup>c</sup>FWHM 1790 Da. <sup>d</sup>FWHM 2480 Da. <sup>e</sup>Titration assay.

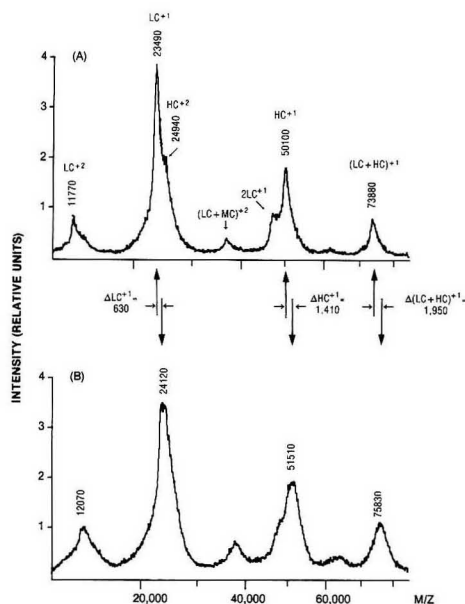


Figure 2. (A) Matrix-assisted UV-laser desorption/ionization mass spectrum of chimeric B72.3 monoclonal antibody treated with dithiothreitol. (B) Matrix-assisted UV-laser desorption/ionization mass spectrum of chimeric B72.3 monoclonal antibody conjugated with macrocyclic 12N4-maleimide chelator, 3, treated with dithiothreitol with an LDI-MS loading value of 6.5. Note the mass shifts between the conjugated-reduced and reduced monoclonal antibodies for the corresponding light chain ( $\Delta LC$ ), heavy chain ( $\Delta HC$ ), and bound LC + HC peaks ( $\Delta(LC + HC)$ ).

contour and not a Gaussian band contour. These results suggest that added signal intensity on the low- and high-mass sides of the peak centroids transformed the expected Gaussian peak shape into the observed Lorentzian peak shape. The added intensity on the low-mass side of the peak centroid may be due to metastable ions and the loss of small mass fragments from the molecular ion, and on the high-mass side, due to salt and matrix adduct formation (33). Table IV summarizes the measured masses and peak widths for a number of chelators conjugated to chimeric B72.3 monoclonal antibody and com-

pare the LDI-MS loading values with ones obtained by radioactivity trace assay measurements. The LDI-MS loading values follow the trends observed in the radioactivity trace assay loading values but tend to be higher. The peak widths at half maximum height are larger for the conjugated monoclonals versus the untreated monoclonal antibodies and are indicative of the distribution of the chelators conjugated to the monoclonal antibodies. A clear trend is observed, that as the loading increases the peak widths at half maximum height of the conjugated molecular ions increase, indicating the broadening of the chelator distribution as loading increases.

The chelator loading values measured by the radioactivity trace assay were, in nine out of ten cases, lower than the corresponding LDI-MS values. Two factors might contribute to this. Firstly, the reaction of radioactive metal with the chelator may become partially hindered once the chelator is bound to the surface of the protein. The LDI-MS-derived loading values could then be higher because total conjugated chelator is measured whether or not it is available for chelation with a radioactive metal ion. Secondly, if during the conjugation reaction of chelator with monoclonal antibody the chelator was contaminated with nonradioactive metal, a step in which the reference chelating agent was not processed, the radioactivity trace assay loading values will be lower than the LDI-MS loading values since possible sites for radioactive metal ions were already occupied with nonradioactive metal ions.

The conjugated chelators, listed in Table IV, were treated with DTT to dissociate the chimeric B72.3 monoclonal antibody into reduced light and heavy chains. Figure 2B illustrates a typical LDI mass spectrum of a monoclonal antibody conjugated with a chelator reduced with DTT. Also illustrated in Figure 2B are the mass shifts between a conjugated and untreated monoclonal antibody for the LC, HC, and bound LC + HC peaks. The masses of the conjugated light and heavy chains were individually measured to determine the distribution of the chelator between the two chains. (See Table V, subentries labeled LC and HC.) The average distributions of the chelators 12N4-maleimide, 12N4, and 12N4P4 between the light chains/heavy chains were 30%/70%,  $50 \pm 10\%/50 \pm 10\%$ , and 54%/46%, respectively. Since chimeric B72.3 monoclonal antibody has 12 lysines on the light chain and 33 lysines on the heavy chain, the predicted distribution for the chelator should be 27% on the light chains and 73% on the heavy chains. A molecular model of chimeric B72.3 was constructed and suggested that of the exposed lysines about 33% were present on the light chain and 66%



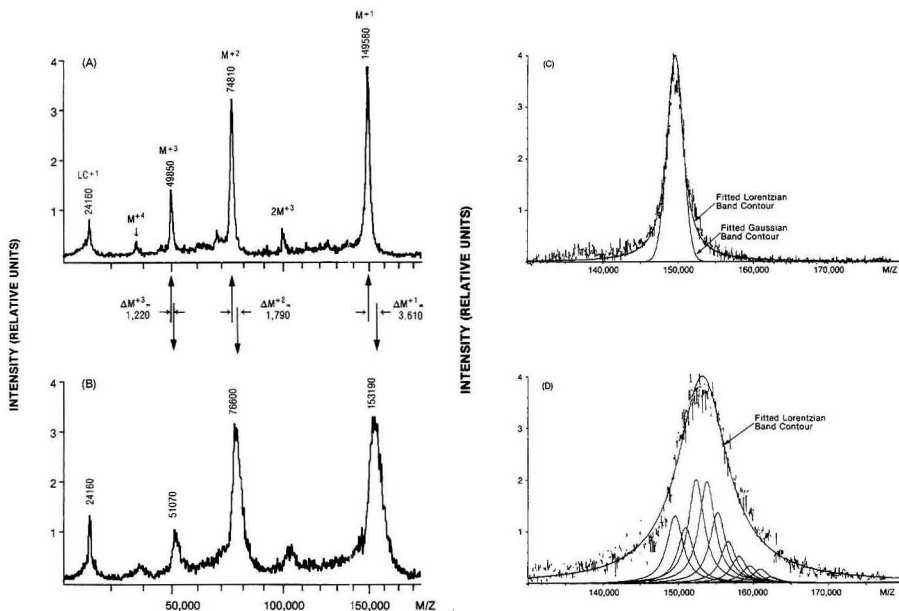


**Figure 3.** (A) Matrix-assisted UV-laser desorption/ionization mass spectrum of CTM01 monoclonal antibody. (B) Matrix-assisted UV-laser desorption/ionization mass spectrum of anticancer drug calicheamicin *N*-acetyl  $\gamma_1$  propionyl ("aggregate") conjugated with CTM01 monoclonal antibody, **8**, with an LDI-MS loading value of 2.6. Note the mass shifts ( $\Delta M$ ) between the corresponding singly, doubly, and triply charged molecular ion peaks of the conjugated and untreated monoclonal antibodies and the larger peak widths for the conjugated monoclonal antibody versus the untreated sample. (C) Fit of the molecular ion LDI-MS peak of CTM01 monoclonal antibody to Lorentzian and Gaussian peak shapes. (D) Fit of the molecular ion LDI-MS peak of calicheamicin *N*-acetyl  $\gamma_1$  propionyl ("aggregate") conjugated with CTM01 monoclonal antibody, **8**, with an LDI-MS loading value of 2.6, to a Lorentzian peak shape and deconvoluted with peak shapes corresponding to CTM01 monoclonal antibody loaded with from zero to nine drug molecules.

on the heavy chains. Given the small numbers of samples analyzed and the experimental errors observed, the measured distributions of chelators are not inconsistent with a mechanism of random attachment to lysine sidechains. Sampling of additional preparations will be required to assess this further, to reveal any small differences in distribution that might be due to steric effects, for example. Also observed in the spectra of the DTT-treated conjugated and untreated samples were peaks corresponding to bound LC + HC chains. The mass shifts between the conjugated and untreated samples were measured, and the loading values correlated reasonably well with the loading values for the whole monoclonal antibody, serving thereby as an internal check on the LDI-MS loading values. (See Table V, subentries labeled LC + HC.)

**Matrix-Assisted UV-LDI-MS Results for Characterizing Anticancer Drugs Conjugated to Monoclonal Antibodies.** Figure 3B illustrates a typical matrix-assisted UV-laser desorption/ionization mass spectrum of an anticancer drug conjugated to a monoclonal antibody. (The spectrum of the corresponding unmodified monoclonal antibody, Figure 3A, is illustrated to show the mass shifts of the singly and doubly charged molecular ions of the monoclonal antibody upon conjugation.) The intense peaks observed in the spectra of anticancer drugs conjugated to monoclonal antibodies were  $M^{1+}$ ,  $M^{2+}$ ,  $M^{3+}$ , and  $LC^{1+}$ . The weak peaks observed were  $M^{4+}$ ,  $2M^{1+}$ ,  $2M^{3+}$ , and  $LC^{2+}$ . The masses of the untreated and conjugated monoclonal antibodies were computed from the average values of the measured masses for the molecular ion and the multiply charged molecular ions when multiplied by the appropriate charge numbers. Table VI summarizes the LDI-MS measured molecular masses for

a number of monoclonal antibodies conjugated to anticancer drugs and the drug loadings computed from the LDI-MS and UV data. Also included in Table VI are the full peak widths at half maximum height for the conjugated monoclonal antibodies that systematically increase as anticancer drug loading increases. These results are consistent with a broadening in the distribution of conjugated molecules to the monoclonal antibodies with increasing drug loading. The molecular ion peak for unreacted and conjugated monoclonal antibodies fit the Lorentzian peak shape, rather than a Gaussian peak shape, as illustrated in Figure 3C,D, respectively. In addition, the conjugated monoclonal antibody peak shape, Figure 3D, was deconvoluted by using the Lorentzian peak shape parameters for the unreacted monoclonal antibody by a weight multivariable minimization procedure to illustrate the individual contributions to the peak shape of the monoclonal antibody conjugated with from zero to nine anticancer drug molecules. No bimodal distributions have been detected; however, the LDI-MS technique would be capable of detecting them, which would not be possible with the HPLC, UV or any other method now in use. These kinds of bimodal distributions could arise from the use of monoclonal antibody batches with heterogeneities that are generally unlikely but possible.

In order to accurately determine the LDI-MS drug loading values, a control (reference) sample should be prepared and chemically treated in the same manner as was the conjugated monoclonal antibody excluding, of course, the reaction of the drug with the monoclonal antibody. The control sample for anticancer drugs conjugated to the carbohydrate should be the purified monoclonal antibody, which was reacted with periodic acid followed by an exhaustive reaction with acet-

Table V. Masses and Loadings of Monoclonal Antibody Fragments Conjugated to Chelating Agents

structure	MoAb	conj chelator	mass change on conjugation	measd frag type	LDI-MS			LDI-MS loading values		
					conj frag mass	pure frag mass	mass shift: conj-frag mass	measd frag <sup>d</sup>	pred MoAb	obsd MoAb
1	c B72.3	DTPA <sup>a</sup>	375.3	LC	23 660	23 510	150	0.40 (43%)	1.9 <sup>b</sup>	6.0 ± 0.2
				HC	50 300	50 100	200	0.53 (57%)		
2	c B72.3	12N4 <sup>a</sup>	557.6	LC	23 720	23 510	210	0.38 (42%)	1.8 <sup>b</sup>	2.0 ± 0.1
				HC	50 400	50 100	300	0.54 (58%)		
2	c B72.3	12N4 <sup>a</sup>	557.6	LC	24 320	23 490	830	1.5 (64%)	4.6 <sup>b</sup>	4.0 ± 0.1
				HC	50 530	50 090	440	0.8 (36%)		
2	c B72.3	12N4 <sup>a</sup>	557.6	LC + HC	74 860	74 060	790	1.4	2.8 <sup>c</sup>	
				LC	24 140	23 510	630	1.14 (58%)	4.0 <sup>b</sup>	5.4 ± 0.1
2	c B72.3	12N4 <sup>a</sup>	557.6	HC	50 570	50 100	470	0.84 (42%)		
				LC + HC	74 730	73 860	850	1.5	3.1 <sup>c</sup>	
2	c B72.3	12N4 <sup>a</sup>	557.6	LC	24 150	23 510	640	1.15 (58%)	4.0 <sup>b</sup>	7.5 ± 0.4
				HC	50 570	50 100	470	0.85 (42%)		
3	c B72.3	12N4-maleimide <sup>a</sup>	727.8	LC	24 130	23 510	630	0.86 (29%)	5.9 <sup>b</sup>	6.5 ± 0.1
				HC	51 600	50 100	1500	2.07 (71%)		
3	c B72.3	12N4-maleimide <sup>a</sup>	727.8	LC + HC	75 830	73 880	1950	2.7	5.4 <sup>c</sup>	
				LC	24 330	23 510	820	1.13 (31%)	7.3 <sup>b</sup>	7.3 ± 0.1
3	c B72.3	12N4-maleimide <sup>a</sup>	727.8	HC	50 300	50 100	200	2.53 (69%)		
				LC + HC	76 290	73 880	2410	3.1	6.2 <sup>c</sup>	
4	c B72.3	12N4P4 <sup>a</sup>	693.6	LC	24 130	23 510	620	0.90 (54%)	3.4 <sup>b</sup>	3.0 ± 0.1
				HC	50 650	50 100	550	0.79 (46%)		
				LC + HC	74 760	73 880	880	1.3	2.5 <sup>c</sup>	

<sup>a</sup>Lysine conjugate. <sup>b</sup>Computed MoAb loading = [2(reduced LC + reduced HC)]. <sup>c</sup>Computed MoAb loading = [2(reduced bound LC + HC)]. <sup>d</sup>The percentages refer to the relative amounts of chelator on the related LC and HC pairs.

hydrazide. The increase in mass due to acetylhydrazide reaction with aldehyde should be compensated, in some part, by losses in mass due to oxidative cleavage of sialic acids, galactoses, and mannoses. Peptide residues may also undergo small mass changes but peptide bond cleavages resulting in significant mass loss do not occur under such mild conditions. When monoclonal antibodies B72.3, CTM01, LYM2, and MAC68 were oxidized and blocked in this way, very small mass changes versus the untreated sample were measured (<150 Da), which was within the experimental mass error. (See Table II, entries in parentheses, under "molecular mass" values.) Therefore, the measured masses for these untreated monoclonal antibodies were used, except in the first two entries of Table VI, where calculations using both untreated and chemically treated monoclonal antibody reference compounds were performed. No significant differences in the loading values were observed. (An unusual exception to small mass changes upon oxidation and blocking was the mass change of +1000 Da observed for monoclonal antibody MOPC21.)

The LDI-MS anticancer drug loading values computed for the mitoxantrone derivatives were reasonably consistent with those measured by UV. (See Table VI, first six entries.) On the other hand, the LDI-MS loading values for the calicheamicin derivatives were much lower than the UV values and do not correlate well with them. (See Table VI, entries seven through twelve.) These low LDI-MS loading values are independent of the matrices used (nicotinic acid, 3-nitrobenzyl alcohol, and 2,5-dihydroxybenzoic acid) and the chemical method of conjugation, i.e., whether the calicheamicin derivatives are conjugated to lysines or to the carbohydrate. Although it can be argued that the LDI-MS loading values are low because only covalently bound drug was measured and the UV loading values are high because noncovalently bound drug was also measured, this is unlikely. The higher UV loading values appear to be consistent with the observed activity of the conjugated drug when administered in *in vitro* cytotoxicity assays and in *in vivo* animal testing (34, 35). After carrying out the standard dialysis, lyophilization, and storage procedures on the monoclonal antibody conjugates, the samples were reconstituted in water and also in nicotinic acid

solutions. These samples were found to be soluble, very stable, immunoreactive, and monomeric. Nearly all drug was still conjugated to the monoclonal antibody. Therefore, the conjugates were unchanged until inserted into the laser desorption/ionization mass spectrometer. Two possibilities associated with the laser desorption/ionization experiment may explain these low loading values for the calicheamicin derivatives. Either the drug conjugate degraded while in contact with the silver substrate sample holder or upon exposure to the UV irradiation as was described earlier (see first paragraph of Results and Discussion) where it was proposed that cleavage of disulfide bonds during the LDI-MS experiments of pure monoclonal antibodies may account for the measurable amounts of light chain observed. The disulfide bonds found in the conjugated calicheamicin derivatives are more labile than those found in monoclonal antibodies such that the silver metal or UV radiation may easily trigger the cyclization reaction of the enediyne group in the calicheamicin derivatives, thereby aromatizing and releasing the molecule from the monoclonal antibody (36). Calicheamicin compounds readily fragment in matrix-assisted UV-LDI-MS experiments as was also observed in fast atom bombardment MS experiments (36). In the low-mass region of the LDI mass spectra (100–1300 Da) of calicheamicin conjugates, a number of fragment ions are observed but in no case have all of them been unambiguously assigned to the calicheamicin derivatives. These ions could, however, be a result of yet unidentified fragmentation processes of low ionization yield, in part, perhaps, due to the high absorptivity of the drug at the wavelength studied. Biochemical and instrumental procedures are presently being evaluated in order to stabilize the drug during LDI-MS analysis.

In order to investigate the role of the sample substrate in the LDI-MS analysis, sample holders besides silver were made from gold and quartz and used to evaluate conjugated monoclonal antibody structures 7 and 9. The results were inconclusive as to the best material for the substrate. The loading results for conjugate 9 are listed in Table VI (third from last structural entry) suggesting that the highest loading values obtained were in the order gold > quartz > silver.

Table VI. Masses and Loading of Monoclonal Antibodies Conjugated to Anticancer Drugs

structure	MoAb	conj drug	mass change on conjugation	LDI-MS				loading value	
				conj MoAb mass <sup>a</sup>	FWHM		mass shift: conj-pure mass <sup>a</sup>	LDI-MS	UV
					conj MoAb mass	pure MoAb mass <sup>a,c</sup>			
related to 5	B72.3	mitoxantrone analogue <sup>b</sup> (MW 502.5)	428.5	148 950 ± 230	4820	147 470 ± 190	1480 ± 300	3.5 ± 0.7	2.3
related to 5	B72.3	mitoxantrone analogue <sup>b</sup> (MW 502.5)	428.5	148 950 ± 230	4820	147 320 ± 50 <sup>e</sup>	1630 ± 240	3.8 ± 0.6	2.3
related to 5	B72.3	mitoxantrone analogue <sup>b</sup> (MW 502.5)	428.5	149 090 ± 330	4770	147 470 ± 190	1620 ± 380	3.8 ± 0.9	3.7
related to 5	LYM1	mitoxantrone analogue <sup>b</sup> (MW 502.5)	428.5	149 090 ± 330	4770	147 320 ± 50 <sup>e</sup>	1780 ± 330	4.1 ± 0.8	3.7
related to 5	CTM01	mitoxantrone analogue <sup>b</sup> (MW 502.5)	428.5	149 920 ± 330	4590	147 820 ± 100	2110 ± 340	4.9 ± 0.8	4.1
5	LYM1	mitoxantrone dihydrazide <sup>b</sup> (MW 672.7)	598.6	151 420 ± 160	4800	149 610 ± 50	1810 ± 170	4.2 ± 0.4	3.7
5	CTM01	mitoxantrone dihydrazide <sup>b</sup> (MW 672.7)	598.6	149 260 ± 350	4090	147 750 ± 190	1510 ± 400	2.5 ± 0.7	3.8
5	CTM01	mitoxantrone dihydrazide <sup>b</sup> (MW 672.7)	598.6	150 820 ± 250	4320	149 640 ± 130	1170 ± 280	2.0 ± 0.5	4.4
6	CTM01	calicheamicin <i>N</i> -acetyl $\gamma_1^I$ dimethyl propionyl hydrazide <sup>b</sup> (MW 1478.5)	1404.5	150 090 ± 230	4090	149 560 ± 30	530 ± 230	0.4 ± 0.2	2.1
7	CTM01	calicheamicin $\alpha_3$ dimethyl propionyl hydrazide <sup>b</sup> (MW 1279.2)	1205.2	150 800 ± 170	3110	149 560 ± 30	1240 ± 170	1.0 ± 0.1	2.1
related to 6	CTM01	calicheamicin $\gamma_1^I$ analogue <sup>b</sup> (MW 1509.6)	1435.6	149 960 ± 320	3800	149 560 ± 30	400 ± 320	0.3 ± 0.2	1.8
8	CTM01	calicheamicin <i>N</i> -acetyl $\gamma_1^I$ propionic acid <sup>d</sup> ("monomer") (MW 1436.4)	1418.4	149 720 ± 10	4480	149 560 ± 30	170 ± 30	0.12 ± 0.02	3.0
8	CTM01	calicheamicin <i>N</i> -acetyl $\gamma_1^I$ propionic acid <sup>d</sup> ("aggregate") (MW 1436.4)	1418.4	153 200 ± 10	8010	149 560 ± 30	3640 ± 30	2.57 ± 0.02	6.5
9	CTM01	calicheamicin <i>N</i> -acetyl $\gamma_1^I$ dimethyl butyric acid <sup>d</sup> (MW 1478.4)	1460.4	150 600 ± 20/ 150 150 ± 10 <sup>e</sup>	4100 4200	149 560 ± 30	1040 ± 40 590 ± 30	0.71 ± 0.03 0.40 ± 0.02	2.0 2.0
10	LYM1	methotrexate hydrazide <sup>b</sup> (MW 482.5)	408.5	149 820 ± 40 <sup>e</sup> 149 510 ± 90	4100 4000	149 560 ± 30	260 ± 50 1720 ± 210	0.18 ± 0.03 4.2 ± 0.5	2.0 4.9
10	B72.3	methotrexate hydrazide <sup>b</sup> (MW 482.5)	408.5	147 100 ± 240	4370	147 340 ± 80	-230 ± 250	-0.6 ± 0.6	5.1

<sup>a</sup>LDI-MS values were computed from the average value of  $z^*M^{z*}$ ,  $z = 1, \dots, 4$ , where  $z$  is the charge number and  $M^{z*}$  is the mass-to-charge ratio of the (multiple charged) molecular ion, observed in the analysis of the pure or conjugated monoclonal antibodies. <sup>b</sup>Carbohydrate conjugated. <sup>c</sup>Carbohydrate periodic acid oxidized and blocked with acetylhydrazide. <sup>d</sup>Lysine conjugate. <sup>e</sup>See Table II for FWHM values. <sup>f</sup>With gold substrate. <sup>g</sup>With quartz substrate. <sup>h</sup>With silver substrate.

Nevertheless, the highest LDI-MS loading value was still lower than that obtained by UV spectrometry, suggesting that additional factors are affecting the LDI-MS analysis of these conjugates.

Matrix-assisted UV-LDI-MS was used to differentiate between covalent and noncovalent association of proteins. Two species of conjugates of calicheamicin *N*-acetyl  $\gamma_1^I$  propionyl conjugated to monoclonal antibody CTM01, 8, were separated by gel-filtration HPLC and collected. They are referred to as the "monomer" and "aggregate" forms. The apparent molecular weight of the "aggregate" (based upon the gel-filtration HPLC retention time) indicated that two or three drug-loaded monoclonal antibody molecules were bound together. The UV and LDI-MS loading values were determined and found to be lower for the monomer and higher for the aggregate form; however the absolute loading values were significantly lower for the LDI-MS values than for the UV values. (See Table VI, entries ten and eleven). The significant feature of the LDI-MS spectra for these samples is that both samples produced only monomeric molecular ions. Thus, the LDI-MS spectra indicate that the aggregate is *not* made-up of drug-loaded monoclonal antibodies covalently bound together but rather is held together by weaker chemical and physical forces. Concentration and gel-electrophoresis studies subsequently performed were consistent with these LDI-MS results.

The strongest case for using LDI-MS to readily differentiate between covalently and noncovalently bound drug to monoclonal antibodies is illustrated in the following example. Methotrexate conjugated to monoclonal antibody LYM1, 10, was initially found to have a UV loading value of 9.5. However, the corresponding LDI-MS loading value was only 4.2. (See Table VI, next to last entry.) Since it was suspected that the high UV loading value was due to noncovalently bound drug, the sample was extensively dialyzed versus buffers. This slightly reduced the UV loading value to 9.1. When harsh denaturing treatments were applied followed by dialysis, to rigorously remove noncovalently bound drug, a UV loading value of 4.9 was measured, consistent with the reported LDI-MS loading value. These data illustrate that the UV loading values can include both covalently and noncovalently bound drug while the LDI-MS loading values are consistent with only covalently bound drug. A sample of methotrexate conjugated to monoclonal antibody B72.3, 10, produced an unexpected negative LDI-MS loading value. (See Table VI, last entry.) This result is considered an anomaly. The UV drug loading value was high enough to suggest strongly that covalent attachment of methotrexate to the monoclonal antibody occurred. Most likely, losses in mass of the monoclonal antibody occurred during conjugation and/or the sample degraded during preparation and storage. Other types of methotrexate conjugates have produced consistent LDI-MS

and UV loading values.

### CONCLUSIONS

Matrix-assisted UV-LDI-MS has been used in a routine fashion to acquire molecular weight data on a variety of untreated monoclonal antibodies and monoclonal antibodies conjugated with chelators and anticancer drugs. From the relative differences in mass between the conjugated and untreated monoclonal antibodies, the loading of chelators and anticancer drugs on the monoclonal antibodies were readily computed. Likewise, from the differences in mass between the pure monoclonal antibodies and the aglycosylated structures of the monoclonal antibodies derived from the DNA sequence for the antibody, the mass of the carbohydrate present in the monoclonal was estimated. The LDI-MS method is well-suited for obtaining accurate estimates of glycoprotein carbohydrate content, as shown by the estimation of chimeric B72.3 carbohydrate content. The method is also suitable for estimation of loading of chelator on antibody-chelator conjugate preparations. The variance between LDI-MS-derived and alternative assay-derived estimations is probably due to a combination of variations in both assay methods. Lability in the molecule, as seen with antibody-drug conjugates, may exacerbate this and lead to greater assay differences. Despite these variances, the LDI-MS method for obtaining loading values is useful as a means for rapid, non-radioactive estimation of covalently bound chelators and drugs conjugated to antibodies. Likewise, this method should be useful for obtaining meaningful loading values for any ionizable high mass molecule provided of course that the mass shift between the conjugated and unconjugated molecules is greater than the experimental errors in the mass measurements, viz., greater than ~0.1% relative mass error with the present technology.

The following trends were observed in the LDI-MS studies of the conjugated monoclonal antibody samples. As the loading of conjugated chelator or anticancer drug increased, the distribution of the drug in the monoclonal antibody increased, as measured by the increase in the mass spectral peak widths at half maximum height. The peak shapes appeared to be Lorentzian rather than Gaussian. The loading values obtained by radioactivity trace analysis were consistently slightly lower than the corresponding LDI-MS loading values for conjugated chelators. For anticancer drugs, on the other hand, the loading values obtained by UV and LDI-MS correlated well with conjugated mitoxantrone compounds, while for conjugated calicheamicin compounds, the UV loading values tended to be higher than the corresponding LDI-MS values. The suggested overall conclusion for the conjugation studies is that the LDI-MS loading values are reliable for conjugated stable molecules (such as the chelators, mitoxantrone, and methotrexate) but not as reliable for conjugated labile molecules (such as calicheamicin). Presently, we are developing methodologies for obtaining more reliable LDI-MS data with conjugated labile molecules.

The coupling of chemical methods with LDI-MS will be necessary for obtaining useful detailed structural information of high-mass molecules. DTT-treated samples of monoclonal antibodies, namely, mixtures of light and heavy chains, can also be routinely analyzed via matrix-assisted UV-LDI-MS. This information provides subtle structural details of the monoclonal antibody. Results obtained in these studies determine the distribution of chelator between the light and heavy chains and confirm that the majority of the carbohydrate present in the monoclonal antibodies studied were bound to the heavy chain. If reoxidation (reformation of disulfide bonds) of the DTT-treated monoclonal antibodies generates detectable aggregates in the LDI mass spectra, treatment with *N*-ethyl maleimide may be advisable. Alternatively, storage

of DTT-treated samples in oxygen-free environments, e.g., under an argon atmosphere, should minimize reoxidation processes that cause aggregation without the problems of peak broadening due to *N*-ethyl maleimide treatment.

At present, matrix-assisted LDI-MS is the method of choice for mass determinations of large molecules, viz., those with molecular weights in excess of about 65 000. A feature that makes LDI-MS so successful is that molecular ions are directly produced rather than highly multiply charged molecular ions as in electrospray ionization mass spectrometry (ESI-MS). This is significant for high-mass molecules, which generally are not pure single components but rather heterogeneous mixtures. For example, in monoclonal antibodies the protein content is homogeneous (except for any aggregate and products of posttranslational modification, such as deamidation) but the carbohydrates are heterogeneous. In LDI-MS, the singly charged molecular ion peak of the monoclonal antibodies is broadened by the carbohydrate heterogeneity and is well resolved from the doubly charged molecular ion peak. The centroids of these peaks can be easily computed to obtain the average mass of the molecules. Likewise, when the monoclonal antibodies are conjugated with chelators or anticancer drugs, the distribution of the conjugate on the monoclonal antibody imposes a second-order heterogeneity on the chemical system. In spite of this additional broadening of the molecular ion peaks, the observed peaks can be resolved and accurately centroided. In the case of ESI-MS, the heterogeneity of the chemical system has imposed upon it an additional heterogeneity of multiple charges. This multiple charged chemically heterogeneous system generates a very broad, unresolvable envelope of ions from which it is impossible to compute the loading values for the conjugated monoclonal antibodies. To overcome this problem in ESI-MS, the molecule must be degraded or dissociated into lower molecular weight fragments for indirect loading measurements (28).

The application of LDI-MS to the study of small molecules covalently conjugated to much larger ones has now been initiated. There are experimental situations, described above, that require refinement. Despite this, many of the LDI-MS studies correlated well with nonmass spectrometric methods and produced meaningful results. LDI-MS should therefore be used as an additional alternative method to analytical techniques in general use for determining the loadings of substances conjugated to large molecules. Even more accurate quantitative loading results and chemical details will be obtained with the anticipated future improvement in matrix-assisted LDI-MS instrumentation and techniques. Improved resolution will permit the direct measurement of the distributions of carbohydrates and conjugates in the molecular ions. Improved matrices (1, 11, 37-40) and the availability of a variety of UV (12) and IR (40, 41) laser frequencies and irradiances should make the matrix-assisted LDI-MS technique even more successful in generating molecular ions from intractable samples.

### ACKNOWLEDGMENT

We greatly appreciate the work of Rolf Paul, Martin Sasser, and Dennis Dean (American Cyanamid Co.) in preparing the anticancer drugs, the assistance of Dee Athwal (Celltech, Ltd.) in molecular modeling of the B72.3 monoclonal antibody, and the technical and editorial comments of David Sammons (University of Arizona) and Janis Upeslacis (American Cyanamid Co.) in preparing this manuscript.

### LITERATURE CITED

- (1) Karas, M.; Bachmann, D.; Bahr, U.; Hillenkamp, F. *Int. J. Mass Spectrom. Ion Processes* **1987**, *78*, 53-68.
- (2) Karas, M.; Hillenkamp, F. *Anal. Chem.* **1988**, *60*, 2299-2301.
- (3) Karas, M.; Bahr, U.; Ingendoh, A.; Hillenkamp, F. *Angew. Chem., Int. Ed. Engl.* **1989**, *28*, 760-761.

- (4) Karas, M.; Ingendoh, A.; Bahr, U.; Hillenkamp, F. *Biomol. Environ. Mass Spectrom.* **1989**, *18*, 841-843.
- (5) Karas, M.; Bahr, U.; Hillenkamp, F. *Int. J. Mass Spectrom. Ion Processes* **1989**, *92*, 231-242.
- (6) Hillenkamp, F.; Karas, M.; Ingendoh, A.; Stahl, E. In *Biological Mass Spectrometry*; Burlingame, A. L., McCloskey, J. A., Eds.; Elsevier Science Publishers B. V.: Amsterdam, 1990; pp 49-60.
- (7) Karas, M. *Phys. Bl.* **1990**, *46*, 149-154.
- (8) Karas, M.; Bahr, U.; Ingendoh, A.; Nordhoff, E.; Stahl, E.; Strupat, K.; Hillenkamp, F. *Anal. Chim. Acta* **1990**, *241*, 175-186.
- (9) Hillenkamp, F.; Karas, M. In *Methods in Enzymology: Mass Spectrometry*, McCloskey, J. A., Ed.; Academic Press: New York, 1990; Vol. 193, pp 280-295.
- (10) Beavis, R. C.; Chait, B. T. *Rapid Commun. Mass Spectrom.* **1989**, *3*, 233-237.
- (11) Beavis, R. C.; Chait, B. T. *Rapid Commun. Mass Spectrom.* **1989**, *3*, 432-435.
- (12) Beavis, R. C.; Chait, B. T. *Rapid Commun. Mass Spectrom.* **1989**, *3*, 436-439.
- (13) Beavis, R. C.; Chait, B. T. *Anal. Chem.* **1990**, *62*, 1836-1840.
- (14) Beavis, R. C.; Chait, B. T. *Proc. Natl. Acad. Sci. U.S.A.* **1990**, *87*, 6873-6877.
- (15) Vertes, A.; Balazs, L.; Gijbels, R. *Rapid Commun. Mass Spectrom.* **1990**, *4*, 263-266.
- (16) Köhler, G.; Milstein, C. *Nature (London)* **1975**, *256*, 495-497.
- (17) Kohata, A. *Glycobiology* **1990**, *1*, 5-8.
- (18) Collier, R. J.; Kaplan, D. A. *Sci. Am.* **1984**, *251*, 56-64.
- (19) Koppel, G. A. *Biorconjugate Chem.* **1990**, *1*, 13-23.
- (20) Hnatowich, D. J.; Childs, R. L.; Lantaigne, D.; Najafi, A. *J. Immunol. Methods* **1983**, *65*, 147-157.
- (21) Meares, C. F.; McCall, M. J.; Reardon, D. T.; Goodwin, D. A.; Diamanti, C. I.; McTigue, M. *Anal. Biochem.* **1984**, *142*, 68-78.
- (22) Palk, C. H.; Hong, J. J.; Ebbert, M. A.; Heald, S. C.; Reba, R. C.; Eckelmann, W. C. *J. Nucl. Med.* **1985**, *26*, 482-487.
- (23) Kanellos, J.; Pietersz, G. A.; McKenzie, I. F. C. *J. Natl. Cancer Inst.* **1985**, *75*, 319-332.
- (24) Shen, W. C.; Balou, B.; Rlyser, H. J.-P.; Hakala, T. R. *Cancer Res.* **1986**, *46*, 3912-3916.
- (25) Pietersz, G. A.; Cunningham, Z.; McKenzie, I. F. C. *Immunol. Cell Biol.* **1988**, *66* (Part 1) 43-49.
- (26) Rhind, S. K.; King, D. J.; Boden, J.; Pedley, R. B.; Searls, F. A.; Berger, R. H. J.; Bagshawe, K. D.; Abrams, D.; Yarranton, G.; Bodmer, M.; Secher, D. S.; Adair, J. *Antibody, Immunoconjugates, Radiopharm.* **1990**, *3*, 55; A57-72.
- (27) Ellman, G. L. *Arch. Biochem. Biophys.* **1958**, *74*, 443.
- (28) Siegel, M. M.; Hollander, I. J.; Smith, B. J.; Farnsworth, A. P. H.; Phipps, A.; King, D. J.; Karas, M.; Ingendoh, A.; Hillenkamp, F.; Konishi, Y. *Annu. Conf. Mass Spectrom. Allied Topics*, **39th** **1991**, PT 174, 883-884.
- (29) Siegel, M. M.; Tsao, R.; Doelling, V. W.; Hollander, I. J. *Anal. Chem.* **1990**, *62*, 1536-1542.
- (30) Turner, M. W. In *Structure and Function of Antibodies*; Glynn, L. E., Steward, M. W., Eds.; John Wiley: New York, 1981, Chapter 1, pp 1-57.
- (31) Nose, M.; Wigzell, H. *Proc. Natl. Acad. Sci. U.S.A.* **1983**, *80*, 6632-6636.
- (32) Raubitschek, A. Personal communication, Nov 22, 1989, NIH, Bethesda, MD.
- (33) Spengler, B.; Kirsch, D.; Kaufmann, R. *Rapid Commun. Mass Spectrom.* **1991**, *5*, 198-202.
- (34) Hinman, L. M.; Wallace, R. E.; Hamann, P. R.; Durr, F. E.; Upeslacs, J. *Antibody, Immunoconjugates, Radiopharm.* **1990**, *3*, 59; Abstr 84.
- (35) Wallace, R. E.; Hinman, L. M.; Hamann, P. R.; Lee, M.; Upeslacs, J.; Durr, F. E. *J. Cancer Res. Clin. Oncol.* **1990**, *116* (Suppl. Part 1), 323.
- (36) Lee, M. D.; Dunne, T. S.; Chang, C. C.; Ellestad, G.; Siegel, M. M.; Morton, G. O.; McGahren, W. J.; Borders, D. B. *J. Am. Chem. Soc.* **1987**, *109*, 3466-3468.
- (37) Tanaka, K.; Waki, H.; Ido, Y.; Akita, S.; Yoshida, Y.; Yoshida, T. *Rapid Commun. Mass Spectrom.* **1988**, *2*, 151-153.
- (38) Nelson, R. W.; Thomas, R. W.; Williams, P. *Rapid Commun. Mass Spectrom.* **1990**, *4*, 348-351.
- (39) Zhao, S.; Somayajula, K. V.; Sharkey, A. G.; Hercules, D. M.; Hillenkamp, F.; Karas, M.; Ingendoh, A. *Anal. Chem.* **1991**, *63*, 450-453.
- (40) Overberg, A.; Karas, M.; Bahr, U.; Kaufmann, R.; Hillenkamp, F. *Rapid Commun. Mass Spectrom.* **1990**, *4*, 293-296.
- (41) Overberg, A.; Karas, M.; Hillenkamp, F. *Rapid Commun. Mass Spectrom.* **1991**, *5*, 128-131.

RECEIVED for review May 3, 1991. Accepted August 5, 1991.

## Direct Introduction of Large-Volume Urine Samples into an On-Line Immunoaffinity Sample Pretreatment-Capillary Gas Chromatography System

A. Farjam, J. J. Vreuls, W. J. G. M. Cuppen, U. A. Th. Brinkman,\* and G. J. de Jong<sup>1</sup>

Department of Analytical Chemistry, Free University, De Boelelaan 1083, 1081 HV Amsterdam, The Netherlands

An immunoaffinity precolumn containing immobilized antibodies raised against the synthetic steroid hormone  $\beta$ -19-nortestosterone, has been used for the automated sample pretreatment of urine samples containing  $\beta$ -19-nortestosterone or the related steroids norethindrone and norgestrel. The sample pretreatment system was coupled on-line to a capillary GC. The on-line connection between the immunoaffinity precolumn and the capillary GC was realized with an interface that consisted of a 10 mm  $\times$  2 mm i.d. reversed-phase precolumn and a diphenyltetramethylsilylazane-deactivated GC retention gap. After preconcentration on the immunoaffinity precolumn the analytes were eluted and reconcentrated on the reversed-phase precolumn. Subsequently, this precolumn was desorbed with 75  $\mu$ L of ethyl acetate, which was directly introduced into the retention gap by using partially concurrent solvent evaporation. The system allows the automated pretreatment and GC analysis of 5-25-mL urine samples for the ppt-level determination of 19-norsteroids. The general applicability and potential of on-line immunoaffinity-capillary GC systems are discussed.

<sup>1</sup> Present address: Duphar BV, Analytical Development Department, P.O. Box 900, 1380 DA Weesp, The Netherlands.

### INTRODUCTION

Sample pretreatment is often the most time-consuming part in the quantitative chromatographic analysis of complex samples. In order to automate this step, precolumns have been used as an efficient tool for many years. In applications where utmost selectivity is needed, as for example in trace-level analysis of biological samples, precolumns containing immobilized antibodies, so-called immuno precolumns, are gaining importance (1-16). We recently showed that sample pretreatment procedures with such immuno precolumns can be fully automated in combination with liquid chromatography (LC) by means of LC-LC column-switching techniques (12, 14-16). In these systems an antibody is raised against the analytes of interest, covalently immobilized to a stationary phase, and the antibody-containing phase is packed into a precolumn that is inserted in the automated column-switching device. The whole analysis can be run unattended and typically takes about 40-50 min.

In this study we investigate the possibility to couple an immunoaffinity sample pretreatment system on-line to a capillary gas chromatograph (GC). This approach can be of great interest in GC analysis: the possibility to automatically process large volumes of, e.g., biological or environmental samples and introduce them directly into the GC will greatly reduce the



cost of the sample pretreatment. In addition to selectivity, sensitivity will also be increased by this specific antibody-antigen interaction because it allows the injection of relatively large volumes, of aqueous samples, on a capillary GC column.

For a coupled immunoaffinity-GC method, the same desorption technique can be used as with the coupled immunoaffinity-LC systems. However, the aqueous methanol eluate of the immuno precolumn cannot be introduced directly into the GC system, due to its large volume of 1–2 mL and its water content. This problem can be solved by using a small reversed-phase (RP) LC column as an interface between the immunoaffinity system and the GC system. The analytes are, after desorption from the immunoaffinity precolumn, first diluted on-line with water and subsequently refocused on the RP interface column. Next the analytes are desorbed from the RP interface column with a small volume of ethyl acetate and introduced into a diphenyltetramethylsilazane-deactivated GC retention gap according to the partially concurrent solvent evaporation technique (17). With this technique, the oven temperature during introduction of the zone eluting from the interfacing RP precolumn is below the boiling point of ethyl acetate. This solvent is subsequently introduced into a suitably deactivated retention gap at a rate somewhat higher than the evaporation rate forming a solvent film on the surface. The evaporation of the solvent will start at the rear of the front at a rate that depends on the introduction temperature and the carrier gas flow rate. The relatively nonpolar analytes spread out over the retention gap, but they are re-concentrated at the beginning of the separation column.

The development of such a system and its performance with standard and spiked urine samples is reported in this paper by using 19-norsteroids as model compounds.

#### EXPERIMENTAL SECTION

**Materials.** CNBr-activated Sepharose 4B was obtained from Pharmacia (Woerden, The Netherlands). HPLC grade acetonitrile and HPLC grade methanol were obtained from Baker (Deventer, The Netherlands) and Merck (Darmstadt, FRG). HPLC grade water was prepared from demineralized water by using a Milli-Q (Millipore, Bedford, MA) water purification system with subsequent filtration over an LC column filled with 40- $\mu$ m Baker C<sub>18</sub> material. The eluents were degassed under vacuum in an ultrasonic bath.  $\beta$ -19-Nortestosterone ( $\beta$ -19-NT), norethindrone (NE), and norgestrel (NG) were obtained from Sigma (St. Louis, MO). Stock solutions of the steroids were prepared in methanol (1 mg/mL) and stored at 4 °C until use. Ethyl acetate was from Baker, it was purified by distillation over a 100  $\times$  5 cm i.d. Hempel column filled with Raschig rings before use. All other chemicals were of normal analytical grade quality.

**Apparatus.** The setup of the on-line immunoaffinity-GC system is schematically shown in Figure 1. Pump 1 was a Kratos (Ramsey, NJ) Model Spectroflow 400 pump. The flow rate of this pump was controlled by a Kontron (Zuerich, Switzerland) Model 200 programmer via a homemade interface. Pump 2 was an Altex (Berkeley, CA) Model 100 pump, equipped with a homemade membrane pulse damper, set at a fixed flow rate of 5.0 mL/min and switched on and off by the programmer. Pump 3 was a Carlo Erba (Milan, Italy) Phoenix 20 pump set at a flow rate of 25  $\mu$ L/min. The switching valves were from a Kontron MCS 670 Tracer valve switching unit and were controlled by the programmer. A Kipp & Zonen (Delft, The Netherlands) BD 40 recorder was used. The 10 mm  $\times$  2 mm i.d. RP interface column was packed with a 40- $\mu$ m Baker C<sub>18</sub> stationary phase. The immunoaffinity precolumn was a homemade 10 mm  $\times$  10 mm i.d. stainless steel precolumn equipped with 5- $\mu$ m stainless steel screens and with PTFE rings at the column inlet and outlet. A 1/16-in. stainless-steel capillary with an i.d. of 0.5 mm, coiled with a helix of 5 cm, was used as a mixing coil. The Carlo Erba Model 5300 Mega GC, which was equipped with a flame ionization detector (FID), was connected to valve 4 with a 30 cm  $\times$  75  $\mu$ m i.d. fused silica capillary. The GC contained a diphenyltetramethylsilazane (DPTMS) deactivated 5.0 m  $\times$  0.53 mm i.d. retention gap from Carlo Erba that was connected to a 25 m  $\times$

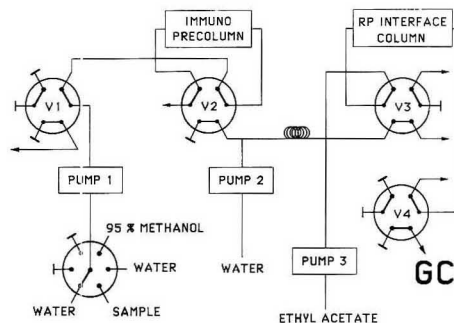


**Figure 1.** Setup of the on-line immunoaffinity-GC system. Valves V1–V4 are all shown in position A (compare Table I). The various parts of the system are described in the Experimental Section.

0.32 mm i.d. DB 5 J&W (Folsom, CA) column with a press-fit connection from ICT (Frankfurt, FRG). The injections into the retention gap were made at a temperature of 85 °C with pump 3 during 3 min; this corresponds with an injection volume of 75  $\mu$ L. After the start of the injection (6.5 min), which corresponds with the tail of the solvent peak passing the FID, the temperature gradient was started with 15 °C/min to 265 °C. After 6 min at 265 °C, the temperature was programmed with 4 °C/min to the final temperature of 295 °C. The carrier gas was helium at 70-kPa inlet pressure.

Initially, the characterization and optimization of the immunoaffinity precolumn was performed with the help of an immunoaffinity-LC system. The setup of this system was similar to the setup of the immunoaffinity-GC system, except that the LC column and the RP interface column were directly connected to valve 3, so that analytes could be desorbed from the RP interface column onto the analytical LC column in the back-flush mode with the LC mobile phase. The analytical column was an upward-slurry (acetone using acetonitrile-water using (70:30, v/v) after wash) packed 100 mm  $\times$  3 mm i.d. glass column filled with 5- $\mu$ m Lichrosorb RP-18 from Merck (Darmstadt, FRG) and was protected with a 10 mm  $\times$  2 mm i.d. guard column packed with the same material. The mobile phase of the LC analytical column was acetonitrile-water (35:65, v/v). The Kratos (Ramsey, NJ) Model Spectroflow 757 UV detector, equipped with a 10- $\mu$ L flow cell, was set at 247 nm.

**Procedures.** The production and purification of the anti- $\beta$ -19-NT antiserum has been described in a previous study (12).

Immobilization of the anti- $\beta$ -19-NT antibody on CNBr-activated Sepharose 4B and packing of the immunoaffinity precolumn were performed as described before (12). IgG/ml gel (7 mg) was used for immobilization. The immunosorbent was stored in 0.1 M phosphate buffer (pH 7.2) containing 0.02% sodium azide. The packed immunoaffinity precolumns were stored in methanol-water (95:5, v/v) at room temperature, if not in use. This solvent was chosen because the immunoaffinity precolumns were relatively stable in this solvent.

The final on-line immunoaffinity-GC analyses were performed with the setup described in Figure 1 according to the schedule of Table I. The first step involves flushing of the immunoaffinity precolumn with 15 mL of water in order to displace the methanol-water (95:5, v/v) that is still present in the column from the previous run. Next, the sample is loaded on the immunoaffinity precolumn, followed by a 15 mL water flush that displaces residual sample and removes weakly bound impurities. Simultaneously, the RP interface column, which still contains ethyl acetate from the previous run, is preconditioned with water via pump 2. Subsequently, the immunoaffinity precolumn and the RP interface column are switched in series and the immunoaffinity precolumn is desorbed with 2 mL of methanol-water (95:5, v/v) in the back-flush mode. The methanol-water mixture is diluted with water via pump 2 in order to reduce the methanol content to about 8%, in order to allow reconcentration of the analytes on the RP interface column. After transfer of the analytes, the RP interface

Table I. Schedule of the On-Line Immunoaffinity-GC Analysis Using the Setup According to Figure 1

step	event	valve position <sup>a</sup>			
		valve 1	valve 2	valve 3	valve 4
1	flushing immunoaffinity precolumn with water (3 min, 15 mL)	A	A	A	A
2	flushing stainless steel tubing with sample	B	A	A	A
3	flushing immunoaffinity precolumn with sample (10–200 mL, flow of 5 mL/min)	A	A	A	A
4	flushing stainless steel tubing with water and RP interface column with water via pump 2 (5 min, 25 mL)	B	A	B	A
5	flushing immunoaffinity precolumn with water (3 min, 15 mL)	A	A	B	A
6	flushing stainless steel tubing with methanol-water (95:5, v/v)	B	A	B	A
7	desorption of the immunoaffinity precolumn with methanol-water (95:5, v/v) (4 min, 2 mL) with subsequent dilution with water (4 min, 20 mL) and reconcentration on the RP interface column	A	B	B	A
8	flush content of mixing coil to RP interface column with water and back-flushing immunoaffinity precolumn with methanol-water (0.5 min, 2.5 mL)	A	A	B	A
9	displacing water from the RP interface column with pump 3 (1.05 min, 26.25 $\mu$ L)	A	A	A	A
10	desorbing RP interface column with ethyl acetate and on-column injection into the retention gap (3.0 min, 75 $\mu$ L)	A	A	A	B
11	flushing RP interface column with additional ethyl acetate (10.0 min, 250 $\mu$ L); start GC temperature gradient	A	A	A	A

<sup>a</sup>Position A corresponds to the valve positions shown in Figure 1.

column is flushed with ethyl acetate. The first 26.25  $\mu$ L of this flush, which contains the water that has been displaced from the RP interface column, is sent to waste. The next 75  $\mu$ L, which contains the analytes of interest, is injected into the retention gap of the GC system. Finally, the RP interface column is flushed with an additional 250  $\mu$ L of ethyl acetate in order to remove strongly bound impurities. The GC temperature program is started 6.5 min after starting the introduction of ethyl acetate into the retention gap.

The on-line immunoaffinity-LC analyses were performed with the modified setup (cf. Apparatus section). The analyses were run according to the schedule in Table I, except that steps 9–11 were replaced by a single step, in which the RP interface column was switched on-line with the LC column (valves 1–3 all in position A).

The preconcentration of samples directly on the RP interface column with subsequent on-line GC analysis was performed with the setup of Figure 1, modified such that switching valve V1 was directly connected to V3, thus bypassing V2, the immunoaffinity precolumn, and pump 2. After preconcentration, the precolumn was flushed with 5 mL of HPLC grade water and subsequently processed according to the schedule of Table I (steps 7–11).

The urine samples used were collected from three healthy males, pooled, divided into 100-mL fractions and stored at -20 °C. The samples were thawed 1 h before use.

## RESULTS AND DISCUSSION

An antibody raised against the synthetic steroid  $\beta$ -19-nortestosterone is used in this study as a model system. The antibody shows a group selectivity such that it recognizes molecules bearing the same structure as  $\beta$ -19-NT in the A and B ring of the steroid skeleton. Two such compounds, the synthetic steroids norethindrone and norgestrel, are of analytical interest, because they are used in oral contraceptives. Hence, the optimization and characterization of the present method is performed with  $\beta$ -19-NT, NE, and NG as the analytes.

**Immunoaffinity Sample Pretreatment.** The immunoaffinity sample pretreatment consists of the following steps: sorption of the analytes on the immunoaffinity precolumn, desorption, dilution, and finally, reconcentration of the analytes on the RP interface column. Since it has been shown in previous studies that the sorption of  $\beta$ -19-NT on the present immuno precolumn is almost quantitative (>97%), in the first instance this step was not further optimized (12).

In principle, a number of different desorption techniques can be used such as selective methods by using cross-reacting agents (4, 12) or nonselective methods by using, e.g., pH changes, chaotropic agents, and organic solvents (13, 15).

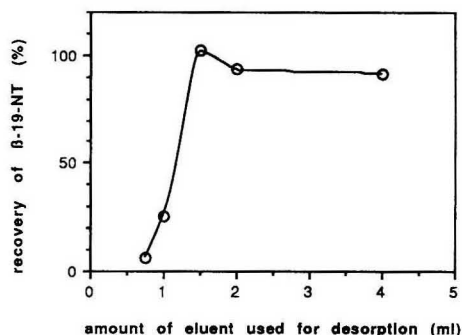
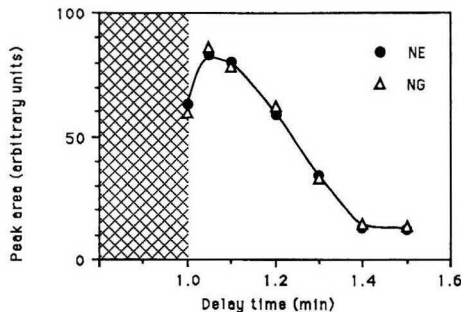


Figure 2. Recovery of  $\beta$ -19-NT as a function of the amount of methanol-water (95:5, v/v) used for desorption. A 10-mL aliquot of a standard solution containing 2  $\mu$ g/L of  $\beta$ -19-NT was loaded on the immunoaffinity precolumn and processed according to the immunoaffinity-LC procedure. The dilution was kept constant in all experiments by setting the flow rate of pump 1 (methanol-water [95:5, v/v] for desorption of immunoaffinity precolumn) at 0.5 mL/min, and the flow rate of pump 2 (water for the on-line dilute) at 5 mL/min. The amount of eluent used for desorption was varied by setting the duration of step 7 (schedule A) to 1.5, 2, 3, 4, and 8 min. The recovery was calculated by comparing the peak area obtained with that of a loop injection.

Recently, it has been demonstrated that several types of immuno precolumns can efficiently be desorbed with aqueous solutions containing high amounts (50–100%) of an organic modifier (15, 16, 18, 19). It is generally accepted that, under these conditions, all antibodies will be denatured and, thus, release the bound analytes of interest. Methanol-water (95:5, v/v) was chosen as the desorbing solvent in the present study. After desorption the eluate of the immunoaffinity precolumn was diluted on-line with a 10-fold excess of water by adjusting the flow rates of pumps 1 and 2 (cf. Figure 1) to 0.5 and 5 mL/min, respectively. Dilution was necessary to allow the subsequent on-line reconcentration of the analytes on the RP interface column. Figure 2 shows the recovery of  $\beta$ -19-NT as a function of the amount of methanol-water (95:5, v/v), which was used to desorb the immunoaffinity precolumn. In all experiments 10 mL of a standard solution containing 2  $\mu$ g/L of  $\beta$ -19-NT was loaded on the immunoaffinity precolumn and processed according to the on-line immunoaffinity-LC procedure (see Experimental Section). The curve in Figure 2



**Figure 3.** Recovery of NE and NG as a function of the delay time between the start of the desorption of the analytes from the RP interface column and the introduction of the eluate into the retention gap (step 9 in Table I). For conditions, see text. The shaded area corresponds to introduction of water into the retention gap.

shows an essentially quantitative recovery if at least ca. 1.5 mL of methanol-water (95:5, v/v) is used for desorption (with subsequent dilution and preconcentration on the RP interface column). We used 2 mL of desorbing solution in all further experiments. Larger volumes of methanol-water (95:5, v/v) should not be used because this will cause breakthrough of the analytes on the RP interface column.

The final procedure of the sample pretreatment is given by steps 1-7 of the schedule in Table I.

**Transfer of Analytes from the RP Interface Column to the GC.** In a previous study on on-line LC-GC (17), it was shown that ethyl acetate is a suitable solvent for the on-line transfer of various types of trapped analytes from a styrene-divinylbenzene precolumn into the retention gap of a capillary GC. Because in the sample pretreatment procedure described above another hydrophobic material, viz, 40- $\mu\text{m}$   $\text{C}_{18}$  bonded silica, was used in the RP interface column, the efficiency of the ethyl acetate desorption with this column material had to be evaluated first. In both cases the elution power of ethyl acetate was such that no retention at all was observed for the analytes. To this end standard samples were directly preconcentrated on the RP interface column (see Experimental Section). After preconcentration, the RP interface column was desorbed with 75  $\mu\text{L}$  of ethyl acetate, a volume shown to be sufficient for desorption of the analytes from the polymeric precolumn (17). The same volume was now found to be sufficient for desorption of the steroids from the column containing the  $\text{C}_{18}$  bonded silica. Since the initial GC temperature and the type of retention gap were the same as in the earlier paper, also the same speed of 25  $\mu\text{L}/\text{min}$  was chosen for desorption of the RP interface precolumn and, consequently, introduction into the retention gap.

The only parameter still to be optimized was the delay time between the start of the desorption of the analytes from the RP interface column and the introduction of the eluate into the retention gap. This delay time is necessary since the ethyl acetate, which is not miscible with water, has to displace the water present in the void volume of the RP interface column, before it is introduced into the retention gap. Exact timing of the water fraction removal is essential for the good performance of the total system. If the delay time is too short (see shaded area in Figure 3), water will enter the retention gap and deteriorate the deactivation layer. If, on the other hand, the introduction into the retention gap is started too late, the first ethyl acetate fraction, which contains a significant amount of analyte, will be lost. In other words, the correct value for the delay time between the start of the desorption of the RP interface column and the start of solvent

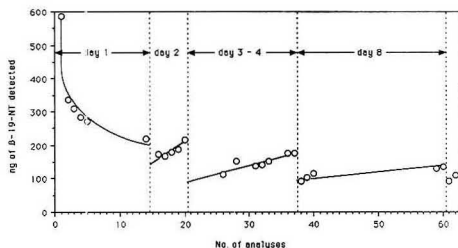


**Figure 4.** Capacity of the anti- $\beta$ -19-NT immunoaffinity precolumn as a function of the number of analyses. For each capacity determination, the immunoaffinity precolumn was overloaded with 10 mL of a standard solution containing 100  $\mu\text{g}/\text{L}$  of  $\beta$ -19-NT; analysis was done according to the immunoaffinity-LC procedure. The amount of  $\beta$ -19-NT was calculated by peak area comparison with a loop injection. The dashed lines indicate storage of the immunoaffinity precolumn at room temperature in methanol-water (95:5, v/v) during one or more nights.

introduction into the retention gap must be determined accurately.

Since precolumns filled with different stationary phases can have different void volumes, the delay time had to be optimized again. The results are shown in Figure 3. In all experiments, 25 mL of a standard solution containing 1  $\mu\text{g}/\text{L}$  of each NE and NG were preconcentrated directly on the RP interface column (cf. Experimental Section). Subsequently, ethyl acetate was pumped over the RP interface column and the displaced water was led to waste during the indicated delay period (step 9 in Table I). Next, the ethyl acetate eluate was injected into the retention gap (step 10). A maximum recovery was found for a delay time of 1.05 min between the start of ethyl acetate desorption and the start of ethyl acetate introduction into the retention gap. Since the flow rate of pump 3 was set at 25  $\mu\text{L}/\text{min}$ , a volume of 26.25  $\mu\text{L}$  has to be pumped to waste before ethyl acetate is introduced. The delay time of 1.05 min was used in all further work.

The reproducibility of the on-line desorption technique was good, with a relative standard deviation of 2.8 and 2.4% ( $n = 4$ ) for the peak areas of NE and NG, respectively, if 25 mL of standard samples containing 1  $\mu\text{g}/\text{L}$  of the individual steroids were preconcentrated and processed as mentioned above. The recovery for all three steroids was over 90%.

**On-Line Immunoaffinity-GC Analysis with Standard Samples.** A calibration plot for 25-mL standard samples spiked with NE and NG was constructed by using the procedure of Table I. The plot was linear ( $r = 0.9997$ ), with recoveries for the total procedure of over 90% for both steroids up to concentrations of 1  $\mu\text{g}/\text{L}$  of each steroid (25 ng of each). For higher concentrations the recovery decreased—reaching, e.g., 40% for each steroid at the 4  $\mu\text{g}/\text{L}$  level—due to the limited capacity of the immunoaffinity precolumn. The 1  $\mu\text{g}/\text{L}$  limit for the linear range corresponds with a total steroid loading of about 50% of the immunoaffinity precolumn capacity.

The breakthrough characteristics of the immunoaffinity precolumn were investigated by loading 25 ng of each NE and NG from sample volumes of 25, 50, 100, and 200 mL. No dependence on the sample volume was found: the recoveries were still over 90% in all experiments. This result indicates that a high sensitivity can be achieved because of the large sample volumes that can be processed with this immunoaffinity precolumn.

The long-term stability of an immuno precolumn, obtained by overloading it each time with 1  $\mu\text{g}$  of  $\beta$ -19-NT, is shown in Figure 4. In the first 10 or so analyses, a rapid decrease of the capacity is observed. Subsequently, it stabilizes at a value of 100-150 ng of  $\beta$ -19-NT. It is not likely that this

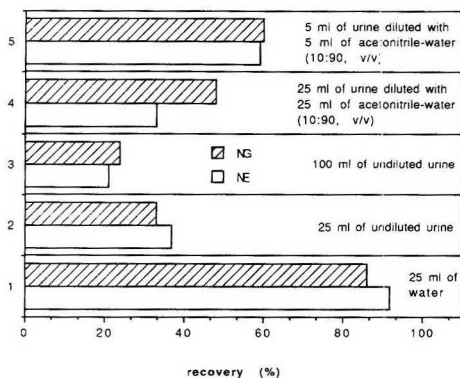


**Figure 5.** Recoveries for NE and NG after loading of 25 ng each of the steroids on the immunoaffinity precolumn from 25 mL of water (1), 25 mL of urine (2), 100 mL of urine (3), 25 mL of urine, diluted with 25 mL of acetonitrile-water (10:90, v/v) (4), and 5 mL of urine diluted with 5 mL of acetonitrile-water (10:90, v/v) (5). The samples were processed according to the immunoaffinity-GC procedure (Experimental Section). Recoveries were calculated by peak height comparison with a preconcentration of a NE and NG standard solution preconcentrated directly on the RP interface column.

decrease is caused by storage of the immunoaffinity precolumn in methanol-water (95:5, v/v) because most of the antibody activity was lost during the first analyses. The exponential decrease has also been found with other immunoaffinity precolumns (10, 14, 15, 17) and most probably is due to both irreversible denaturation and ligand leakage. This capacity decrease will have no significant effect on the recovery, if the amount of analytes loaded is lower than 50% of the capacity of the immunoaffinity precolumn (cf. above). Capacity determinations performed by overloading the immunoaffinity precolumn with a mixture of NE and NG (not shown) showed that both compounds have essentially the same affinity for the anti- $\beta$ -19-NT antibody and that the capacity of the immunoaffinity precolumn for these compounds is about 20% lower than for  $\beta$ -19-NT. This result is consistent with the fact that NE and NG are merely cross-reacting compounds and not the hapten against which the antibody was raised.

It is interesting to note that the immunoaffinity precolumn lost some of its capacity during storage in methanol-water (95:5, v/v), but slowly regained activity when in use. Apparently, the repeated water flushes during the daily operation slowly restore the activity of the antibodies. A similar effect was observed with a monoclonal anti-aflatoxin immuno precolumn (15). In that study an essentially linear relationship between the water-flushing time, employed for regeneration of the immunoaffinity precolumn (corresponding to step 1 in Table I), and the capacity has been observed. Since not the water volume but the contact time was the critical parameter, it was concluded that the regeneration was a slow process with that antibody. We therefore checked whether the capacity of the present immunoaffinity precolumn would also improve upon increasing the time of flushing with water. Since a substantial increase in contact time from 3 to 15 min flushing (15 mL of water in both cases) did not substantially increase the capacity, the shorter—i.e., 3 min—flushing time was preferred for the final procedure. Obviously, the regeneration kinetics are an antibody-specific parameter, which has to be evaluated with every new type of immunoaffinity precolumn.

**Optimization of the Immunoaffinity-GC Analysis with Urine Samples.** Figure 5 compares the recoveries of spiked standard and spiked urine samples that were processed

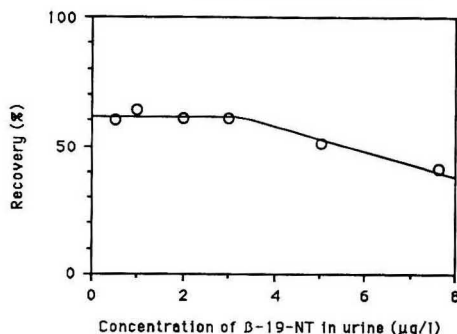


**Figure 6.** Recovery of  $\beta$ -19-NT-spiked urine samples. A 10-mL aliquot of a pooled male urine sample spiked with the indicated amount of  $\beta$ -19-NT and diluted with an equal volume of acetonitrile-water (90:10, v/v) was processed according to the immunoaffinity-GC procedure. Recoveries were calculated by peak height comparison with a preconcentration of a  $\beta$ -19-NT standard solution performed directly on the RP interface column.

according to the final schedule of Table I. Buffering of the urine samples was not necessary because the pH hardly influenced the sorption of the analytes onto an immunoaffinity precolumn. All samples contained 25 ng of each NE and NG, but the loading volume and/or matrix composition was different. Loading the steroids from 25 mL of urine (Figure 2)) showed a 50% lower recovery compared to the 25 mL standard sample (Figure 5(1)). Obviously, competitive and/or other physicochemical interactions by the urine components adversely affect the antibody-antigen interaction. This became also evident if, instead of a 25-mL urine sample which contained 25 ng of each NE and NG, a 100-mL sample containing the same absolute amount of analytes was loaded on the immunoaffinity precolumn and analyzed. The recoveries for NE and NG decreased from 37 to 21% and from 33 to 24%, respectively (cf. Figure 5(2,3)). In contrast to the analysis of aqueous samples, where no breakthrough effects were seen for sample volumes of between 25 and 200 mL, now, with urine samples, breakthrough effects became evident upon sample volume increase. This was unexpected because no significant difference was found for spiked standard and urine samples in earlier immunoaffinity-LC studies with the same antibody (12). However in the present study an immunoaffinity precolumn with a capacity of only 100–150 ng was used as against 250 ng in the previous study. There can be several reasons for this lower capacity. First of all, less antibody, 7 mg instead of 10 mg/g of CNBr-Sephacrose, were used for the immobilization. Secondly, in the present study the antibody was not immobilized directly after isolation, but stored for about 2 years in a lyophilized form at  $-20^\circ\text{C}$  before immobilization was performed. The long storage may well have reduced the antibody activity.

In order to solve the problems, the urine samples were diluted with acetonitrile-water (10:90, v/v), which—in a previous study due to reduction of nonspecific interactions (12)—proved to be superior to dilution with pure water; secondly, the sample volume was reduced. Figure 6 shows an increased recovery for NG if the 25-mL urine sample was diluted with an equal amount of acetonitrile-water (10:90, v/v), compared to the analysis of 25 mL of undiluted urine (cf. Figure 5(2,4)). If in addition to this dilution step the total urine sample volume is reduced to 5 mL, a recovery of about 60% was achieved for NE and NG (cf. Figure 5(5)). Dilution of 5 mL of urine with an equal amount of acetonitrile-water (10:90, v/v) was chosen as the standard procedure for the processing of urine samples.

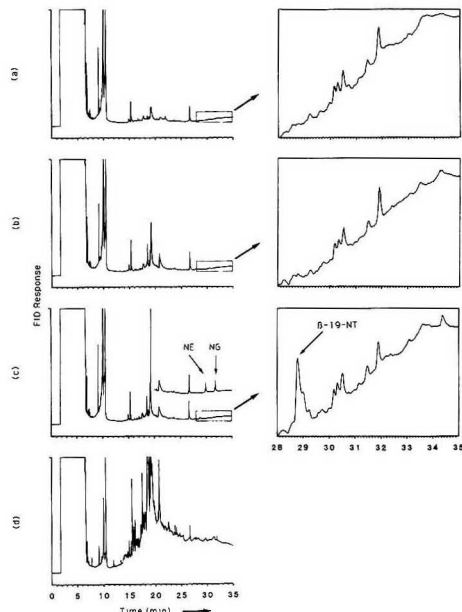


**Figure 7.** (a, b, c) Immunoaffinity-GC-FID chromatograms of (a) HPLC grade water, (b) urine, and (c) urine spiked with  $0.5 \mu\text{g/L}$  of  $\beta$ -19-NT or with  $4 \mu\text{g/L}$  of both NE and NG. Chromatograms a, b, and c were obtained by diluting 5 mL of sample with an equal volume of acetonitrile-water (10:90, v/v) and processing the samples according to the immunoaffinity-GC procedure. (d) GC-FID chromatogram obtained by loading 5 mL of the diluted urine sample directly on the RP interface column. Chromatograms a and b and the  $\beta$ -19-NT chromatogram in c, which have been digitally recorded, are also shown in a closeup where the x axis is stretched by a factor of 5 and the y axis by a factor of 33.3, respectively.

**Analytical Data.** The recovery as a function of the amount of  $\beta$ -19-NT in spiked urine is shown in Figure 6. If 5 mL of urine were analyzed—i.e. 10 mL of diluted urine—a constant recovery of 60% was found up to  $\beta$ -19-NT amounts of 20 ng (corresponding to  $4 \mu\text{g/L}$  in urine). If higher concentrations were analyzed, the recovery slowly decreased. The relatively poor capacity of the immunoaffinity precolumn used in this study was the cause for the short linear detection range.

The high selectivity of the system is revealed in Figure 7. All chromatograms show the analysis of 5 mL of sample diluted with an equal volume of acetonitrile-water. Parts a and b of Figure 7 show the chromatograms of an automated analysis of a 5-mL HPLC grade water sample and a 5-mL blank urine sample, respectively, showing the selectivity of the system, and the number and amount of the impurities introduced by the reagents. The chromatograms are virtually identical in the region in which  $\beta$ -19-NT, NE, and NG elute, i.e. between 28 and 35 min. Figure 7c shows chromatograms for the same urine sample, spiked with either  $0.5 \mu\text{g/L}$   $\beta$ -19-NT or  $4 \text{ ng/L}$  both NE and NG. The peak of  $\beta$ -19-NT together with an impurity that was already present in the stock solution, shows up at a retention time of 29.0 min and an elution temperature of  $295^\circ\text{C}$ . The peaks of NE and NG had retention times of 29.8 and 31.9 min, respectively. The blank urine was also analyzed by omitting the immunoaffinity precolumn and loading the sample directly on the RP interface column (Figure 7d). Comparison with Figure 7b clearly demonstrates the superior selectivity of the immunoaffinity

system: with nonselective preconcentration a large number of interfering peaks show up at the retention times of the analytes. These interferences caused an average baseline shift of about 15 mV, which corresponds with the peak height of about 10 ng of  $\beta$ -19-NT (compare Figure 7c).

The selectivity and, also, the sensitivity of the immunoaffinity sample pretreatment are limited by the peaks that are present in the blank chromatograms. Most of these peaks are introduced into the system with the solvents that are used for sample pretreatment. Methanol and, to a lesser extent, HPLC grade water were the main contributors. This was confirmed by loading either HPLC grade water or water containing 8.6% of methanol (same percentage as used in the dilution step of the total procedure) directly on the RP interface column and analyzing by on-line gas chromatography. These impurities showed up in the chromatograms, although the methanol had been distilled over a  $100 \text{ cm} \times 5 \text{ cm}$  i.d. Hempel column filled with Raschig rings and the water had been purified in a two-step procedure (cf. Experimental Section). However, some interferences did not show the same peak area during all analyses. Frequently, the blank peaks slowly decreased during the day when analyses were run. Since adsorption can occur in, e.g., the precolumns or on the PTFE tubing connecting the solvent reservoirs with the solvent selection valve, memory effects may be considered as a likely explanation. For the analytes of interest, however, no memory effects have been observed.

The detection limit for  $\beta$ -19-NT was about  $0.1 \mu\text{g/L}$  with a repeatability ( $n = 6$ ) of 6%, if a sample volume of 5 mL of urine diluted with an equal amount of acetonitrile-water (10:90, v/v) was loaded on the immuno precolumn.

The repeatability of the total procedure was measured by analyzing repeatedly at 25-mL urine sample spiked with  $1 \mu\text{g/L}$  of each NE and NG. The relative standard deviations ( $n = 4$ ) of the peak areas of NE and NG were 4 and 6%, respectively. The detection limits for these solutes were also about  $0.1 \mu\text{g/L}$ .

The analysis time of the method including the on-line sample pretreatment was 40 min.

## CONCLUSIONS

The on-line coupling of immunoaffinity sample pretreatment and capillary GC is presented here for the first time. The general setup has been exemplified by using an anti- $\beta$ -19-NT immunoaffinity precolumn for the preconcentration of 19-norsteroids. The method allows the direct introduction of rather large volumes of urine into a capillary GC in an automated way. The analytes of interest are preconcentrated on the immunoaffinity precolumn, next they are desorbed and reconcentrated on a reversed-phase interface column and desorbed from this column with ethyl acetate, and finally, the ethyl acetate is introduced into a retention gap according to the partially concurrent solvent evaporation technique. The high selectivity of the immunoaffinity precolumn combined with the separation power of the capillary GC allows the selective analysis of a group of structurally related analytes in a complex matrix. Due to the strong antibody-antigen interaction in the immuno precolumn, many milliliters of urine can be preconcentrated and very low detection limits can consequently be obtained. Actually, the purity of the solvents used for sample treatment, rather than the selective sorption on the immuno precolumn, is the main barrier for a further increase of selectivity and sensitivity.

At present, the main limitation of the method is the effort necessary in order to obtain the proper antibodies for a specific application. First of all they should possess the appropriate selectivity and high affinity for the analytes of interest—as required in the field of conventional antibody-based assays. In addition, after immobilization on a proper support, they



should exhibit sufficient stability. As was found also in other studies (4, 12, 14, 17), the stability of such columns often is surprisingly high; for example several hundreds of analyses have been run on a single anti- $\beta$ -19-NT immuno precolumn (4) while, in this particular case, the immunoaffinity precolumn can be used for at least 70 analytes. Finally, the capacity of the immuno precolumn should be sufficiently high. The relatively low capacity of the immuno precolumn used in the present study resulted in a short linear detection range, and further studies should certainly be directed at an increase of the capacity. The antibody (active site) density in the immunoaffinity precolumn should be increased either by the use of affinity-purified antibodies, by immobilizing the smaller active-site-bearing Fab fraction of the antibody molecule, or by employing a specific immobilization (20) which ensures that the analytes have free access to the antibody.

Finally, it should be evident that, by the mere introduction of a different type of immunoaffinity precolumn and adaption of the GC conditions, many other applications can be run with the presented system.

Registry No.  $\beta$ -19-NT, 434-22-0; NE, 68-22-4; NG, 6533-00-2.

#### LITERATURE CITED

- Ong, H.; Adam, A.; Perreault, S.; Marleau, S.; Bellemare, M.; Du Souich, P. *J. Chromatogr.* **1989**, *497*, 213-221.
- Van Ginkel, L. A.; Van Blitterswijk, H.; Zoonjies, P. W.; Van den Bosch, D.; Stephany, R. W. *J. Chromatogr.* **1988**, *445*, 385-392.
- Ulsvkov, P.; Marcussen, J.; Rajagopal, R.; Prinsen, E.; Rüdelsheim, P.; Van Onckelen, H. *Plant Cell Physiol.* **1987**, *28*, 937-945.
- Haasnoot, W.; Schilt, R.; Hamers, A. R. M.; Huf, F. A.; Farjam, A.; Frei, R. W.; Brinkman, U. A. Th. *J. Chromatogr.* **1989**, *489*, 157-171.
- Nilsson, B. *J. Chromatogr.* **1983**, *276*, 413-417.
- Johansson, B. *J. Chromatogr.* **1986**, *381*, 107-113.
- Hayashi, T.; Sakamoto, S.; Wada, I.; Yoshida, H. *Chromatographia* **1989**, *27*, 574-580.
- Janis, L. J.; Grott, A.; Regnier, F. E.; Smith-Gill, S. J. *J. Chromatogr.* **1989**, *476*, 235-244.
- Rybacek, L.; D'Andrea, M.; Tarnowski, J. *J. Chromatogr.* **1987**, *397*, 355-364.
- Van de Water, C.; Tebbal, D.; Haagsma, N. *J. Chromatogr.* **1989**, *478*, 205-215.
- Reh, E. *J. Chromatogr.* **1989**, *433*, 119-130.
- Farjam, A.; De Jong, G. J.; Frei, R. W.; Brinkman, U. A. Th.; Haasnoot, W.; Hamers, A. R. M.; Schilt, R.; Huf, F. A. *J. Chromatogr.* **1988**, *452*, 419-433.
- Davis, G. C.; Hein, M. B.; Chapman, D. A.; Neely, B. C.; Sharp, C. R.; Durlay, R. C.; Biest, D. K.; Heyde, B. R.; Carnes, M. G. *Plant Growth Substances*; Springer: Berlin, 1985; p 44-51.
- Farjam, A.; Brugman, A. E.; Soldaat, A.; Timmerman, P.; Lingeman, H.; De Jong, G. J.; Frei, R. W.; Brinkman, U. A. Th. *Chromatographia* **1991**, *31*, 469-477.
- Farjam, A.; Van de Merbel, N. C.; Lingeman, H.; Frei, R. W.; Brinkman, U. A. Th. *Int. J. Environ. Anal. Chem.*, in press.
- Farjam, A.; Brugman, A. E.; Lingeman, H.; Brinkman, U. A. Th. *Analyst*, in press.
- Munari, F.; Frisciani, A.; Mapelli, G.; Trestianu, S.; Grob, K., Jr.; Colin, J. M. *HPLC & CC, J. High Resolut. Chromatogr.* **1985**, *8*, 801.
- Van Ginkel, L. A.; Stephany, R. W.; Van Rossum, H. J.; Steinbuch, H. M.; Zomer, G.; Van De Heeft, E.; De Jong, A. P. *J. Chromatogr.* **1989**, *489*, 111-120.
- Sharma, M.; Patey, A. L.; Gilbert, J. *J. Chromatogr.* **1989**, *474*, 457-461.
- Hoffmann, W. L. *J. Immunol. Methods* **1988**, *112*, 113-120.

RECEIVED for review December 26, 1990. Revised manuscript received June 4, 1991. Accepted July 29, 1991.

# Tandem Mass Spectrometry of Very Large Molecules: Serum Albumin Sequence Information from Multiply Charged Ions Formed by Electrospray Ionization

Joseph A. Loo, Charles G. Edmonds, and Richard D. Smith\*

Chemical Sciences Department, Pacific Northwest Laboratory, Richland, Washington 99352

Serum albumin proteins,  $M_r$  ~66 kDa, from 10 different species (bovine, human, rat, horse, sheep, goat, rabbit, dog, porcine, and guinea pig) have been studied by electrospray ionization mass spectrometry (ESI-MS) and tandem MS using a triple-quadrupole instrument. The effectiveness of collisional activation for the multiply charged albumin ions greatly exceeds that for singly charged ions, allowing an extension by a factor of at least 20 to the molecular mass range for obtaining sequence-specific product ions by tandem MS. Efficient dissociation is largely attributed to "preheating" in the interface Coulombic instability and the large number of collisions. Increasing the electric field in the intermediate pressure region, between the nozzle-skimmer elements of the atmospheric pressure/vacuum interface, allows fragmentation of the multiply protonated (to 96+) molecules produced by ESI. The most abundant dissociation product ions assigned have a low charge state (2+ to 5+) and are attributed to "b<sub>n</sub>" mode species from cleavage of the -CO-N- peptide backbone bonds. Particularly abundant dissociation products originate from regions near residues  $n = 20-25$  from the NH<sub>2</sub> terminus for parent ions of moderate charge (~50+). Collisionally activated dissociation (CAD) mass spectra from porcine serum albumin, in contrast to the other albumins, also gave prominent singly charged "y<sub>n</sub>" fragments formed from cleavages near the COOH terminus. Tandem mass spectrometry (MS/MS) of the multiply charged molecular ions, and of fragment species produced by dissociation in the interface (i.e., effective MS/MS/MS), produced similar "b<sub>n</sub>" species and served to confirm spectral assignments. We also show that ESI mass spectra allow a qualitative assessment of protein microheterogeneity and, in some cases, resolution of major contributions. The physical and analytical implications of the results are discussed, including the identification of possible errors in previously published sequences.

## INTRODUCTION

Mass spectrometry continues to mature as an analytical methodology for biomolecules of increasingly greater molecular mass (1-5). In the past several years, new ionization techniques have been developed that have allowed extension to biomolecules with relative molecular mass ( $M_r$ ) in excess of 100 kDa. Matrix-assisted laser desorption (LD) (6-8) coupled to time-of-flight (TOF) mass spectrometers has produced mass spectra for proteins as large as catalase ( $M_r$  236 kDa) (6). Another ionization method utilized for large biomolecules is electrospray ionization (ESI) (9-14), which produces multiply charged molecules from highly charged droplets formed by electrostatic nebulization at near atmospheric pressure. Sufficient charges on analyte molecules are often retained so that conventional quadrupole mass spectrometers of limited mass-to-charge ratio ( $m/z$ ) can be used for the study of proteins, typically as multiply protonated molecules, with  $M_r$  of

at least 133 000 Da (12) and more recently to nearly 200 000 Da (14). No fragmentation of covalent bonds is typically evident in ESI mass spectra since the conditions required to obtain nearly complete desolvation are less severe than necessary for dissociation (15). Fragmentation can be induced in a separate step using collisionally activated dissociation (CAD), generally with tandem mass spectrometry (MS/MS), by applying an additional stage of mass ( $m/z$ ) selection prior to the dissociation step. In contrast to TOF mass analyzers used for laser desorption, quadrupole instruments are well suited to tandem mass spectrometry experiments. Thus, the use of ESI-MS/MS for structural characterization of large peptides and proteins with existing instrumentation appears promising (13, 15-18).

Tandem mass spectrometry has been utilized for many years to obtain structural information from organic molecules (19, 20). MS/MS experiments coupled to fast atom bombardment (FAB) have been fruitful for small peptides to  $M_r$  3000 Da (21-23). Complete amino acid sequence information for larger peptides and proteins is obtainable by FAB-MS/MS after selective enzymatic digestion (24-26). However, CAD of singly charged molecules becomes less efficient with increasing molecular mass (27-29). The decreased efficiency of molecular ion formation, substantial "matrix" background, the modest extent of initial molecular ion internal excitation, and practical limitations on the average number of collisions allowed using conventional sector instruments conspire to prevent application of these methods at higher  $m/z$ . We have previously demonstrated (16) that multiply charged molecular ions from ESI of a 26-residue peptide (mellitin) subjected to CAD conditions yields singly and multiply charged product ions that can be correlated with the known sequence. Multiply charged ions appear to be more susceptible to CAD than their singly charged counterparts at the same collision energy, allowing larger molecules to be addressable by tandem mass spectrometry (13, 15-18). More recently we have extended these methods to ~14 kDa in studies of ribonuclease A (18). Thus, in addition to molecular mass determination (9-14), the polypeptide sequence or related information can potentially be obtained for molecules much larger than the nominal "mass" limit of the quadrupole instrument due to the multiple charging phenomena.

In this report we expand on our initial communication regarding MS/MS of ESI-generated multiply charged molecular ions from serum albumins with  $M_r$  ~66 000 Da (13, 30). We show that the efficient dissociation of these large molecules can be induced and their product ions correlated to the available sequence. In addition to CAD processes in the conventional collision chamber of the triple-quadrupole instrument, effective dissociation in the atmospheric pressure/vacuum interface of the mass spectrometer can also be induced (31), leading to sequence-specific fragmentation. Although only limited primary sequence information is obtained, the potential of tandem MS with electrospray ionization for large biomolecules is demonstrated. More generally,

these studies provide new insights regarding the nature of activation and dissociation processes at the large molecule limit.

### EXPERIMENTAL SECTION

The ESI source and mass spectrometer have been previously described (12, 13, 15-18). Briefly, the analyte solution, in a 100- $\mu\text{m}$ -i.d. fused silica capillary, mixes with a flowing liquid methanol sheath electrode (32) at the tip of the ESI source. A potential of +4 kV is applied to the sheath electrode to produce a fine mist of highly charged droplets. The flow rates of the analyte solution and liquid sheath are independently controlled by separate syringe pumps (Harvard Apparatus, South Natick, MA, and Sage Instruments, Cambridge, MA) at flow rates of 0.2-0.5 and 2.5  $\mu\text{L min}^{-1}$ , respectively. Ions are sampled by a differentially pumped nozzle/skimmer interface of our design, similar to that used on our previously described single-quadrupole instrument (31), to the triple-quadrupole MS (TAGA 6000E, Sciex, Thornhill, Ontario, Canada) with  $m/z$  limit of 1400. A lens element, typically at +650 V, mounted in front of the nozzle/skimmer assembly, improves the ion-sampling efficiency. Desolvation of the droplets is accomplished by a counter-current stream of dry nitrogen gas and through more energetic collisions in the interface region. The collisional heating in the interface region is controlled by varying the voltage difference between the nozzle and skimmer elements ( $\Delta\text{NS}$ ); a typical bias used is +135 to +200 V before dissociation of the analyte molecule occurs. Thus, the activation in this region occurs through a large number of collisions which have increasing energy and decreasing frequency due to the decreasing pressure. The pressure in the atmosphere/vacuum interface (in the stagnant region displaced from the beam axis) and in the mass spectrometer is typically  $\sim 1$  Torr and  $6 \times 10^{-6}$  Torr, respectively.

All serum albumin samples were commercially obtained from Sigma Chemical Co. (St. Louis, MO) and were used without further purification. Their origin, catalog number, and lot number are as follows: bovine (A-7638, 77F9369), human (A-8763, 67F9351), rat (A-6414, 97F93211), porcine (pig) (A-1173, 87F9307), sheep (A-4289, 37F93071), horse (A-5280, 66F9381), rabbit (A-0764, 19F9301), dog (A-9263, 108F9327), goat (A-4164, 37F93081), and guinea pig (A-6539, 38F93001). Crystallized and lyophilized samples from Sigma that are essentially fatty acid free (<0.005%) and/or globulin free ( $\leq 1\%$ ) were analyzed (if available). Only a "Fraction V" (modified Cohn low-temperature ethanol precipitate) sample of dog albumin was available from Sigma. Since our goal was to evaluate the nature and potential of collisional dissociation processes, no attempt was made to minimize sample consumption. Analyte solutions (50-100 pmol  $\mu\text{L}^{-1}$ ) were prepared in distilled water with 5% acetic acid. Multiply charged ions from horse myoglobin were used to calibrate the  $m/z$  scale of the mass spectrometer. The argon collision gas target thickness was approximately  $1 \times 10^{14}$  molecules  $\text{cm}^{-2}$  for tandem MS experiments.

### RESULTS AND DISCUSSION

**Electrospray Ionization Mass Spectra of Serum Albumins.** Albumin is an acidic, stable, 66-kDa monomeric protein that is among the most studied in biochemistry (33). Complete sequences are available for human, bovine, and rat albumin (33), sheep (34, 35) and porcine (36) albumin, and partial amino acid sequences (typically the  $\text{NH}_2$  terminal residues) are known for species such as dog (37), rabbit (38), goat (38), and horse (38, 39). Albumin is well conserved among various species; a homology (amino acid sequence alignment) of 80% between human and bovine, 80% between rat and human, and 63% total conservation among the three species is maintained (33). A total of 18 out of the first 31 residues are identical among albumins from human, horse, bovine, rat, sheep, goat, porcine, rabbit, and hamster species. Table I lists the first 31 "known" residues (from the  $\text{NH}_2$  terminus) for nine of the ten albumins studied.

Serum albumins are readily amenable to ESI-MS analysis for  $M_r$  determination, as demonstrated by our laboratory (12, 13, 30, 40) and a number of other researchers (41-47). Figure 1 (top) shows the ESI mass spectrum for rabbit serum albumin

**Table I. Published  $\text{NH}_2$  Terminal Amino Acid Sequences for Serum Albumins<sup>a</sup>**

Species	Sequence																														
	1	5	10	15	20	25	30																								
Bovine	D	T	H	K	S	E	I	A	H	R	F	K	D	L	G	E	E	H	F	K	G	L	V	L	I	A	F	S	Q	Y	L
Human	D	A	H	K	S	E	V	A	H	R	F	K	D	L	G	E	E	H	F	K	G	L	V	L	I	A	F	S	Q	Y	L
Rat	E	A	H	K	S	E	I	A	H	R	F	K	D	L	G	E	E	H	F	K	G	L	V	L	I	A	F	S	Q	Y	L
Porcine	D	T	Y	K	S	E	I	A	H	R	F	K	D	L	G	E	Q	Y	F	K	G	L	V	L	I	A	F	S	Q	Y	L
Sheep	D	T	H	K	S	E	I	A	H	R	F	N	D	L	G	E	E	H	F	K	G	L	V	L	I	A	F	S	Q	Y	L
Goat	D	T	H	K	S	E	I	A	H	R	F	N	D	L	G	E	E	H	F	K	G	L	V	L	I	A	F	S	Q	Y	L
Horse	D	T	H	K	S	E	I	A	H	R	F	N	D	L	G	E	K	H	F	K	G	L	V	L	V	A	F	S	Q	Y	L
Rabbit	E	A	H	K	S	E	I	A	H	R	F	N	D	V	G	E	Z	H	F	K	G	L	V	L	I	A	F	S	Q	Y	L
Dog	E	A	Y	K	S	E	I	A	H	R	F	N	D	L	G	E	E	H	F	R	G	L	V	L	I	A	F	S	Q	Y	L

<sup>a</sup>Standard one-letter code used for amino acids: A = Ala, R = Arg, N = Asn, D = Asp, C = Cys, E = Glu, Q = Gln, G = Gly, Z = Glx, H = His, I = Ile, L = Leu, K = Lys, M = Met, F = Phe, P = Pro, S = Ser, T = Thr, W = Trp, Y = Tyr, V = Val.

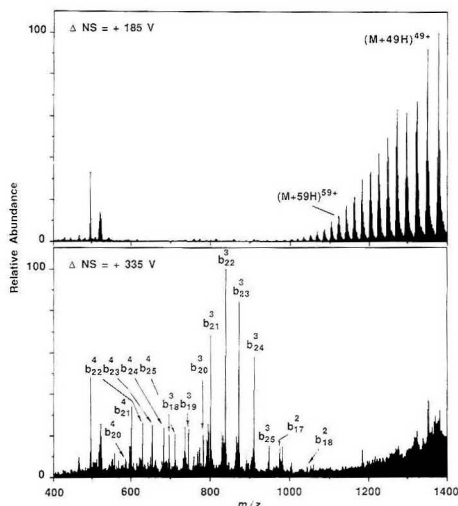


**Figure 1.** Electrospray ionization mass spectra of rabbit serum albumin ( $M_r \sim 66$  100 Da) with nozzle/skimmer potential of (top) +185 V and (bottom) +335 V. See text for sequence ion notation.

with  $\Delta\text{NS} = +185$  V. Experience has shown that this  $\Delta\text{NS}$  voltage difference results in a degree of collisional "heating" in the interface sufficient to result in complete desolvation of electrospray ions (but insufficient for cleavage of covalent bonds) over the  $m/z$  400-1400 range. No ions assigned as fragment species were detected under these conditions. Relative molecular masses with precisions on the order of 0.01% or better can be obtained, as demonstrated by the data in Table II for the 10 different serum albumin species. Although the experimental  $M_r$  precision was similar to that determined for smaller polypeptides and proteins by ESI-MS at our laboratory (13) and others (10, 11, 42, 43), the  $M_r$  measurements for serum albumins were generally high by as much as 0.25% compared to  $M_r$  values based on the complete amino acid sequences (available for five of the species listed in Table II). Molecular weight accuracy by ESI-MS has been found to generally be better than 0.01% for most relatively pure polypeptides up to 30 kDa (10-13, 42, 43). Although the purity of the commercially obtainable serum albumins may

**Table II. Molecular Masses and Peak Widths from Electrospray Ionization Mass Spectra of Serum Albumins**

species	$M_r$ (exptl), Da	$M_r$ (seq), <sup>a</sup> Da	FWHH (50+) <sup>b</sup>
bovine	66 443 ± 5	66 430	4.3
human	66 605 ± 7	66 438	8.2
rat	66 000 ± 6	65 870	5.0
porcine	66 770 ± 5	66 731	4.3
sheep	66 385 ± 6	66 293	5.0
horse	65 667 ± 6		8.7
rabbit	66 148 ± 6		4.0
dog	65 854 ± 7		10.7
goat	66 304 ± 5		(8.9)
	66 578 ± 8		
guinea pig	65 962 ± 8		(15.8)
	66 284 ± 8		
	66 586 ± 7		

<sup>a</sup> Average molecular masses calculated from available complete amino acid (or nucleotide) sequences. <sup>b</sup> Full width in  $m/z$  units at half the peak height for the  $(M + 50H)^{50+}$  multiply charged molecular ion. Values in parentheses indicate that more than one molecular ion component is partially resolved.

be as high as 96% based on the nitrogen content, as Peters (33) points out, microheterogeneity may arise from various contributions, including adducts (fatty acids, bilirubin, glycans, etc.) and structural modifications (cleavages due to traces of proteolytic enzymes in the preparation, amino acid modifications, etc.).

The relative purity of the serum albumins can be qualitatively assessed on the basis of the width of a molecular ion peak and agreement with  $M_r$  based on the amino acid sequence (where available). This requires that spectra be obtained under conditions which result in sufficient activation to remove residual solvent and non-covalently associated molecules. Table II lists the measured widths (in  $m/z$  units) at half the peak maxima for the  $(M + 50H)^{50+}$  species (between  $m/z$  1310 and 1340) for each albumin analyzed. For example, dog serum albumin sample is attributed as having more *major* (i.e., abundant) unresolved components than rat albumin based on the larger peak widths, although all albumin samples showed a significant "tail" to higher  $m/z$ , possibly indicating contamination, or small amounts of residual solution-related adducts, in addition to naturally occurring heterogeneity. Porcine and bovine albumin, which gave the closest agreement with the measured molecular masses, also gave the narrowest peak widths. A few of the albumins, most notably goat and guinea pig albumin, showed additional resolved components, as indicated in Table II. Figure 2 compares a region of the porcine and guinea pig albumin ESI-mass spectra, clearly showing the greater heterogeneity of the latter where at least three major components are evident. Because our  $M_r$  measurements in Table II are based on peak maxima, microheterogeneity could at least partially account for a shift in peak maxima sufficient to explain the difference with  $M_r$  values based on the sequence. Peak widths may not directly correlate to the observed  $M_r$  deviation because of the variable peak shapes between albumin species. Two mass spectra from the same albumin species, but of different origin, may show similar peak widths, yet different experimentally measured  $M_r$  values due to different centroid positions. Using the peak maxima to calculate  $M_r$  emphasizes the major component in the sample, which may not represent the native albumin species. Thus, a properly deconvoluted peak shape (i.e., corrected for instrumental contributions) should provide useful information on the microheterogeneity of such materials. We note, however, that definitive experiments which provide both separation, perhaps based upon capillary electrophoresis (12, 13) of the closely related mixture components, and their separate MS/MS analysis has not yet been demonstrated.

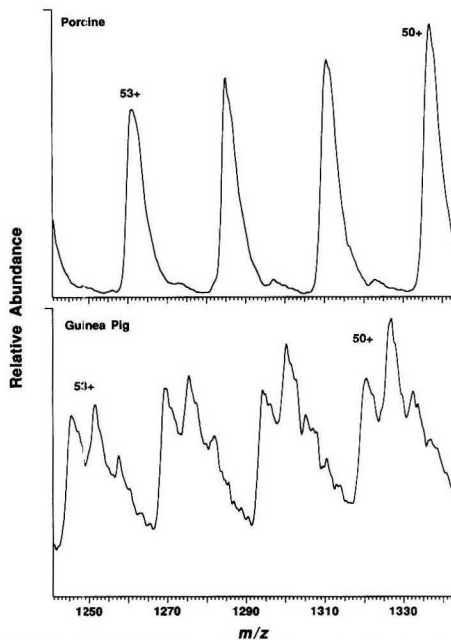


**Figure 2.** Expanded region of the ESI mass spectra of (top) porcine and (bottom) guinea pig serum albumin with  $\Delta NS = +185$  V. A three-point smoothing function was applied to the spectra.

Supportive of our suggestion is recent work by Geisow and co-workers (46) who presented ESI-MS data for a commercial sample of human albumin and recombinant human albumin expressed in yeast. Their ESI mass spectrum of the commercially available albumin showed  $M_r$  and peak widths similar to our data. However, the spectrum for the recombinant form showed much narrower peak widths, approximately 2  $m/z$  units at half the peak maximum at  $\sim m/z$  1545 versus  $\sim 6$   $m/z$  units for the commercial sample, indicating a much "cleaner" sample, and yielding a  $M_r$  value only 3 Da from the calculated sequence value. Hirayama et al. (47) recently determined the published amino acid sequence of bovine serum albumin to be incorrect based on FAB LC-MS and MS/MS results from enzymatic digests. The addition of a tyrosine residue to position 156 corresponds to a corrected  $M_r$  value of 66 430 Da, in relatively close agreement to our result. Thus, published sequences may be incorrect, as discussed in the following sections.

Other information is also supportive of the proposed relationship between microheterogeneity and peak shape. Ideally, the peak widths measured at half height for multiply charged species, in which the isotopic contributions are unresolved, are expected to decrease with increasing molecular weight at constant  $n/z$ , and (equivalently) decrease with increasing charge (12, 48). For example, upon the addition of 1,4-dithiothreitol (DTT) to cleave disulfide bonds (49) and increase the extent of ESI charging (13, 40, 50), peak widths (in  $m/z$  units) for sheep albumin decreased from 5.0 for the 50+ ion to 2.7 for the 80+ ion. The peak width at half-height at  $m/z$  1304.9 for the  $(M + 13H)^{13+}$  ion of horse myoglobin ( $M_r$ , 16950 Da), a relatively pure material, was approximately 3.2  $m/z$  units for the same instrumental resolution. A multiply charged molecular ion in the same  $m/z$  vicinity for a pure 66-kDa protein should have a peak width much less than 3.2. From

the theoretical isotopic distribution of bovine albumin, a peak width of slightly greater than 0.3 for the  $(M + 50H)^{30+}$  ion would ideally be obtained. Experimentally, a peak width of  $\sim 2 m/z$  units would be expected due to limitations on instrumental performance (i.e., resolution). Most of the albumins studied have peak widths greater than 3.2 (Table II), consistent with a contribution due to sample microheterogeneity. Whether peak width measurements can be used to unambiguously determine ion charge state is uncertain at this time, but such a capability will certainly be limited to lower charge states and be impractical in cases where substantial microheterogeneity exists.

It should be pointed out that the peak widths for albumin molecular ions do not decrease appreciably with increasing  $\Delta NS$ . By increasing the collision energy in the interface region, weakly bound adducts and solvent molecules can be "stripped" from the larger analyte species (15, 31, 51). It has recently been demonstrated that sulfuric acid and phosphoric acid generated in the acidified spray solutions from ubiquitous sulfate and phosphate impurities associate strongly with proteins (51). However, it was also shown that these noncovalently bound adducts can be completely removed by activation in the atmosphere/vacuum interface with modest collision energies. Since no change in peak widths was observed upon further increase in  $\Delta NS$ , even to collision energies sufficient for polypeptide backbone dissociation (see next section), this clearly suggests that the large peak widths in our studies are not due to solvent or other noncovalently attached species.

Although the purity and exact chemical composition of the albumin samples are in question, one or a few components with relatively similar composition are likely to (and apparently) predominate. As will be discussed in the following sections, our results indicate that any chemical modifications that might be present in substantial abundance apparently occur in a region other than the first 30 residues from the  $NH_2$  terminus.

**Dissociation Induced in the Interface Region.** As previously shown (13, 15, 18, 30, 31), dissociation of intact proteins can be induced in the atmospheric pressure/vacuum interface at elevated nozzle/skimmer potentials. We have previously presented preliminary dissociation spectra for bovine, human, and rat albumins (13, 30). Additional mass spectra are shown in Figure 1 (bottom) for rabbit albumin and in Figure 3 for dog, sheep, and horse albumins. All such spectra were obtained using  $\Delta NS = +335$  V and otherwise identical instrumental conditions. Nomenclature used for the designated fragment species is based on the modified Roepstorff (52) notation proposed by Biemann (22), in which lower case letters are utilized and subscripts are used to denote the type of fragmentation and residue position, respectively, counting from the  $NH_2$  terminus for  $a_n$ ,  $b_n$ , and  $c_n$  ions and from the COOH terminus for  $x_n$ ,  $y_n$ , and  $z_n$  product ions. A superscript is added to indicate the fragment ion charge state. Lack of a superscript denotes a singly charged fragment.

Nearly all the more abundant product ion peaks detected have been assigned as multiply charged  $b_n$  ions arising from fragmentation within the first 30 residues from the  $NH_2$  terminus. The limitation to the terminal regions is consistent with other CAD data of large polypeptides having intermediate charge states and showing fragmentation generally occurring with decreased efficiency at greater distances from the ends of the molecule (13, 15, 16, 18). However, it is important to realize that these spectra are dominated by dissociation of a range of charge states, defined at lower  $m/z$  by the envelope of molecular ion charge states (i.e., those observed at low  $\Delta NS$ ), and at a higher  $m/z$  due to decreased activation efficiency. For native albumins the relevant range of charge states con-

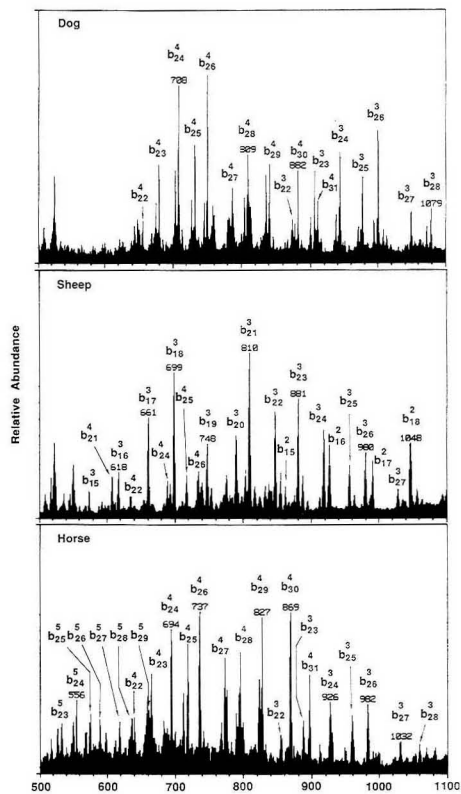


Figure 3. ESI mass spectra of (top) dog, (middle) sheep, and (bottom) horse serum albumins with  $\Delta NS = +335$  V.

tributing typically extends from 60+ to perhaps 40+ for the conditions used. Our sequence assignments are facilitated by other factors, such as the expected (18, 30) low probability of observing products due to bond cleavage from regions enclosed by disulfide bonds (62% of bovine albumin is enclosed by its 17 Cys-Cys bonds) because at least two bonds must be broken, increasing the confidence level of our interpretation. Of particular value is the fact that albumins as a class of proteins exhibit a high level of sequence homology. The assumption that dissociation products occur from similar regions of the molecule for all albumin species is a major factor in the tractability of the interpretation procedure. At least two overlapping product ion charge state distributions were observed for all albumin species, providing additional support for our assignments. For example, dissociation of the Asn<sup>18</sup>-Phe<sup>19</sup>-CO-N- bond (giving the  $b_{18}$  ion) of sheep albumin is represented by products at both  $m/z$  1048 (doubly charged) and 699 (triply charged). Cleavage of the Ala<sup>26</sup>-Phe<sup>27</sup> bond ( $b_{26}$  ion) of horse serum albumin is indicated by product ions at  $m/z$  982 (3+), 737 (4+), and 590 (5+). We attribute this distribution of product charge states to the dissociation of parent ions with a variety of charge states. In addition, parent species of the same total charge may have their charges distributed differently throughout the molecule leading to a similar result. It might be possible to aid the interpretation procedure of such spectra by applying deconvolution algo-



**Table III. Electrospray Ionization  $b_n$  Product Ion  $m/z$  for Dog Serum Albumin**

$n^a$	amino acid	3+		4+	
		calcd	exptl	calcd	exptl
22	L	873.3	873.3	655.2	655.3
23	V	906.3	906.5	680.0	680.1
24	L	944.1	944.0	708.3	708.4
25	V	977.1	977.0	733.1	733.1
26	A	1000.8	1000.7	750.8	750.9
27	F	1049.8	1049.9	787.6	787.5
28	S	1078.9	1079.0	809.4	809.6
29	Q/K	1121.6	1121.7	841.4	841.4
30	Y	1176.0	1176.1	882.2	882.4
31	L/I	1213.7	1213.7	910.5	910.5

<sup>a</sup> Residue position from the  $\text{NH}_2$  terminus.

ithms (53), used to "collapse" distributions of multiply charged molecular ions to a single peak, for product ion spectra composed of several fragment ion charge states.

Subtle differences in the degree of charging for the fragment ions for the albumins were also observed and found consistent with the spectral assignments. We have previously demonstrated a good correlation between the number of basic residues and the maximum positive charge for molecular ions observed in ESI mass spectra for a number of polypeptides and proteins (13, 40). In a 5% acetic acid solution, most, if not all, basic groups might be protonated in solution since all  $\text{pK}_a$  values are above 3. Horse, bovine, and rat albumin each have 7 basic amino acid residues (lysine, arginine, and histidine) within the first 28 residues, in addition to the possible  $\text{NH}_2$  terminal charge site, and we observe multiple charging for product ions up to the 5+ state. On the other hand, the most highly charged fragment is 4+ for dog, sheep, rabbit, porcine, goat, and human albumin, which contain either 5 or 6 basic sites within the initial 28 residues.

Distinctive  $m/z$  patterns were obtained for the albumin species analyzed by collisional dissociation as described above. These permitted detailed verification of reported sequences for residues between position ~18 and ~28 from the  $\text{NH}_2$  terminus, depending upon the serum albumin species. For example, a sample of goat serum albumin yielded ESI mass spectra similar to those of sheep albumin at high  $\Delta\text{NS}$  values. Although one difference in the initial 30 residues between goat and sheep albumin has been indicated by conventional Edman degradation sequence analysis (38), as shown in Table I, the ESI mass spectra indicate otherwise. Asparagine residues at position 18 in the case of sheep albumin, whereas histidine is reputed to be present at this site for goat albumin. Thus, a 23-Da shift should be observed and easily identified in the collision spectra for the two species. Instead, identical product ion spectra were obtained with  $\Delta\text{NS} = +335$  V, indicating Asn at position 18 for goat albumin. Peptide-mapping experiments from tryptic digestion followed by separate HPLC analysis and ESI-MS (data not shown) also revealed similarities in their primary structure for the samples examined.

Unfortunately, the additional tyrosine residue at position 156 and the reversal of residues 94–95 from –GluGln– to –GlnGlu– detected for bovine serum albumin by Hirayama et al. (47) were not observed in our work because only the  $\text{NH}_2$  terminus was probed.

In the case of dog serum albumin, only the first 24 residues are available from the literature (37). Along with known sequence homologies, the experimentally observed product ions allowed prediction of the sequence for residues 25–31, as indicated by Table III. Ions  $b_{22}$  to  $b_{24}$  were assigned from calculations for all possible  $m/z$  values based upon the available amino acid sequence. Remaining products were assigned as sequential  $b_n$  dissociation products starting from

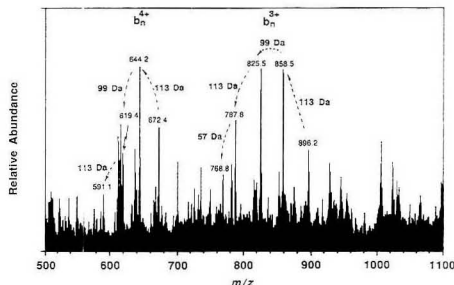


**Figure 4.** Partial ESI mass spectrum of guinea pig serum albumin with  $\Delta\text{NS} = +335$  V.

$b_{24}$ . For example, the ion at  $m/z$  708.3 was assigned as  $b_{24}^4$  with a mass of 2830 Da. The next major ion at higher  $m/z$  is  $m/z$  733.1; its mass for a 4+ ion would be 2929.2 Da, or an increase of 99 Da, corresponding to a valine residue ( $b_{25}^4$ ). An overlapping suite of triply charged ions is also present and was used for confirmation of the assignments. An ion at  $m/z$  977.0 is assigned as the  $b_{25}^3$  product, and so forth to  $b_{31}^3$ . In the case of the sequence for dog albumin, it was not possible with our current instrumentation to distinguish the presence of lysine versus glutamine (0.04-Da difference) at position 29 or leucine versus isoleucine at position 31 from the data.

It should be noted that although major fragmentation generally occurs between residues 18–28 for the serum albumins, allowing for sequence determination in this region, it also allows for a limited verification of the previous 1–17 residues by comparison of the  $M_r$  of the smallest size product ion to the expected value. For example, the smallest  $M_r$  fragment ion observed for dog serum albumin ( $b_{22}$ ) is in good agreement with the  $M_r$  calculated for the first 22 residues. However, this does not provide data for the residue sequence. Nor does it rule out possible substitutions that sum to the same  $M_r$  (e.g., Asp for Leu (+2 Da) and Val for Thr (-2 Da)). MS/MS of the multiply charged product ions could possibly provide this additional information (see following section).

Interpretation of the collision mass spectrum for guinea pig serum albumin was slightly more difficult. To our knowledge, no published sequence information is available. In addition, as indicated in Table II and Figure 2, three resolvable components differing by approximately 300 Da were suggested by the ESI mass spectrum. Also evident was a set of low abundance peaks between  $m/z$  750 and 1100 in the low-voltage  $\Delta\text{NS}$  spectra that correlate to a molecular species of  $M_r$  13.9 kDa (18+ to 13+ charges) and may also contribute to the collisional dissociation spectra. The spacings between the most abundant peaks in the spectrum at high  $\Delta\text{NS}$  (Figure 4), ascribed as a series of triply and quadruply charged product ions, indicate a sequence of amino acids separated in mass by 57, 113, 99, and 113 Da. This suggests a portion of the sequence to be Gly-Leu(Ile)-Val-Leu(Ile) (although evidence for Gly is weaker because of the poor signal-to-noise ratio for the 4+ ion). This is similar to residues 21–24 of most of the other albumin species listed in Table I. Many peaks in the same spectral region remain unassigned because of the complexity of this mixture. Simplification of the mixture by prepreparation and analysis of the individual constituents may provide for a more complete sequence determination.

**Tandem Mass Spectrometry.** Dissociation of selected molecular ion charge states for proteins as large as 66 kDa has been achieved in this study, a factor ~20 larger than feasible for singly charged ions using equivalent methods. Results from collisionally activated dissociation tandem MS of the ( $M + 49\text{H}$ )<sup>49+</sup> ion of sheep albumin is shown in Figure 5. The

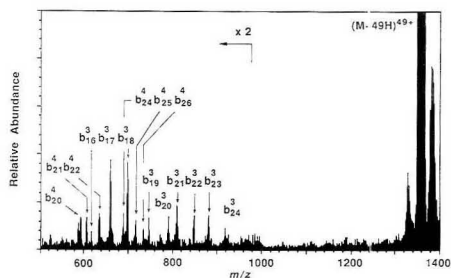


**Figure 5.** Tandem mass spectrum of the  $(M + 49H)^{49+}$  molecular ion of sheep albumin with  $E_{lab} = 6860$  V (argon collision target).

fragment ions identified in the tandem MS experiments were generally of the same  $m/z$  values produced by CAD in the nozzle/skimmer interface (compare with Figure 3). These CAD studies used argon as the neutral target and a laboratory-frame translational energy ( $E_{lab} = q\Delta V$ , where  $q$  is the net ion charge and  $\Delta V$  is the voltage difference between the skimmer and the quadrupole collision cell) of 6.86 keV. The resolution in the first quadrupole was lowered to increase parent ion intensity for subsequent CAD, such that the peak width at half-maximum was 7–8  $m/z$  units compared to 5  $m/z$  units used in Table II.

In addition to the product ions at lower  $m/z$ , all MS/MS studies of albumins gave product ions near the parent species, such as shown in Figure 5, with peaks at approximately  $m/z$  1329 and 1384 for sheep albumin. There are several possible origins for these peaks, three of which are discussed below. Their  $m/z$  values closely correspond to intact molecular ions with 50+ and 48+ charges, respectively. Charge-transfer/charge-stripping reactions, although postulated previously (17, 54), seem unlikely for the experimental conditions. A second possibility is that these peaks might also arise due to fragmentation producing a species of approximately 33.2 kDa, roughly half the intact molecule. Support for this is found in the ESI mass spectrum shown in Figure 6 (bottom) for the collisional dissociation of sheep albumin at  $\Delta NS = +335$  V. Above the broad rising baseline extending to the instrumental  $m/z$  limit are very broadened peaks at  $m/z$  1384, 1329, 1277, and 1230 that correspond to a 33.2-kDa fragment (with 24+ to 27+ charges, respectively). Alternatively, dissociation of a 49+ ion from a 66.4-kDa molecule may also produce a complementary ion pair (i.e., two charged fragments that in sum total the parent ion) of nearly equal size, 33.2 kDa, with 24+ and 25+ charges. One possible dissociation site to explain a 33.2-kDa fragment would be in the vicinity of Glu<sup>291</sup>, in a region near the middle of the primary sequence that is unbound by Cys–Cys bridges (i.e., only a single bond cleavage is necessary to liberate two charged fragments). A third possibility, which we consider most likely, is that these ions arise from dissociation of a noncovalently bound dimer [i.e.,  $(2M + 98H)^{98+}$ , whose  $m/z$  position would be essentially the same as the  $(M + 49H)^{49+}$  ion]. It is well established that multimeric proteins generally separate into their noncovalently bonded species with normal ESI-MS conditions (12, 13), and one could expect a dimer would fragment readily. Such a dimer species may be present in low abundance ( $\leq 5\%$  of the monomer on the basis of Figure 2) due to the relatively high sample concentration. Closer inspection of ESI mass spectra of bovine serum albumin obtained on  $m/z > 1400$  limit quadrupole instruments (43, 47) show peaks at high  $m/z$  in between the major peaks, similar to Figure 2 for porcine albumin, that may be indicative of dimeric species. We have observed dimeric species of smaller peptides, such as bovine

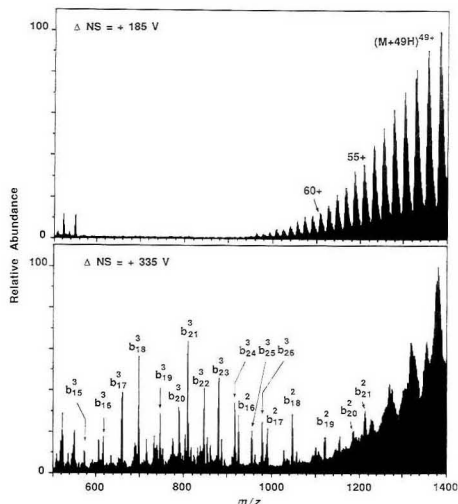


**Figure 6.** ESI mass spectra of sheep serum albumin ( $M_r \sim 66$  400 Da) with nozzle/skimmer potential of (top) +185 V and (bottom) +335 V.

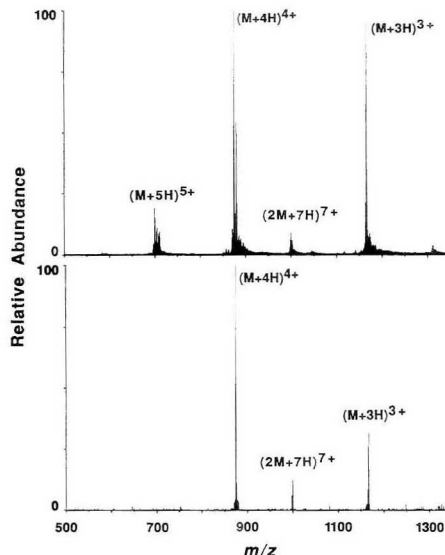


**Figure 7.** (Top) Electro spray ionization mass spectra of bovine insulin B-chain (oxidized) and (bottom) ESI tandem mass spectrum showing dissociation of the  $(2M + 7H)^{7+}$  ion ( $E_{lab} = 525$  eV).

insulin A-chain (oxidized,  $M_r$  2533 Da) and B-chain (oxidized,  $M_r$  3496 Da). MS/MS of the  $(2M + 7H)^{7+}$  of B-chain insulin shown in Figure 7 yields the  $(M + 3H)^{3+}$  and  $(M + 4H)^{4+}$  monomeric ions. Similarly, dissociation of the  $(2M - 7H)^{7-}$  ion from A-chain insulin gives the  $(M - 3H)^{3-}$  and  $(M - 4H)^{4-}$  products. We have also recently interpreted similar earlier results for cytochrome *c* and myoglobin in terms of such dimer dissociation processes (55). While this explanation seems most likely for the albumins, definitive distinction among these

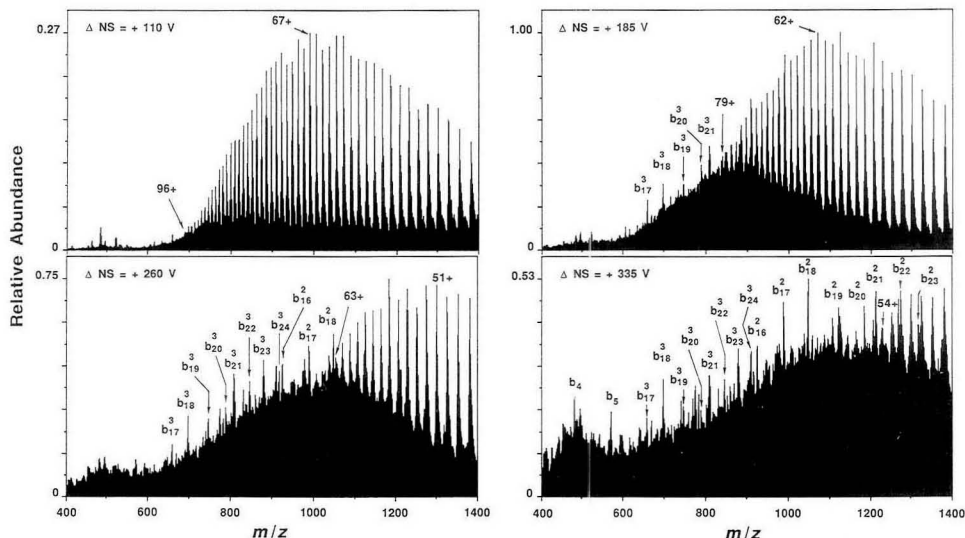


Figure 8. Electrospray ionization mass spectra of disulfide-reduced (with 1,4-dithiothreitol) sheep serum albumin at various nozzle/skimmer potentials.

possibilities has not been achieved.

Relatively few sites are available to produce potentially observable product ions because over 60% of the molecule is enclosed by disulfide bonds. Reduction of the disulfide bonds should allow access to additional dissociation pathways. This issue has been examined in more detail elsewhere (56) using bovine proinsulin, a much smaller molecule. Bovine proinsulin is an 81-residue polypeptide of  $M_r$  8681 Da containing 3 disulfide linkages that effectively encompass over 90% of the molecule in ring structures (i.e., only the first 6 residues from the  $\text{NH}_2$  terminus and the  $\text{COOH}$  terminal asparagine amino acid are "accessible" by tandem mass spectrometry). Dissociation of the  $(M + 8H)^{6+}$  molecular ion from the native form yields fragments only from the 6-residue region of the  $\text{NH}_2$  terminus. CAD of proinsulin in which the Cys-Cys bonds have been reduced results in high yield of singly and multiply charged product ions originating from cleavages in regions formerly enclosed by the disulfide bonds (56).

Figure 8 shows ESI mass spectra of disulfide-reduced sheep albumin with varying  $\Delta\text{NS}$  values. With increasing  $\Delta\text{NS}$ , dissociation of the more highly charged molecular ions is favored, with a corresponding shift in the undissociated molecular ion charge distribution to higher  $m/z$  (lower charge). In addition, a broad baseline "hump" increasingly dominates the spectra with increasing  $\Delta\text{NS}$ . The rising baseline is partly attributed to large numbers of unresolved product ions that originate from the many available dissociation pathways and charge states. It should be noted that the more highly charged molecular ions for the reduced albumin will attain a greater degree of collisional activation at a given  $\Delta\text{NS}$  value, which would be expected to yield additional peaks (at a different  $m/z$ ), and possibly open additional dissociation pathways. However, it is apparent that dissociations adjacent to the  $\text{NH}_2$  terminus still constitute favored processes, as evidenced by the prominent triply charged  $b_3$  products.

Supporting results were obtained by MS/MS of a selected molecular ion species in the CAD triple-quadrupole studies, as shown in Figure 9. These results also show that the location of charge sites is different for the native and reduced forms of albumin. Dissociation of the  $(M + 49H)^{49+}$  molecular

ion of disulfide-reduced sheep albumin produces fragmentation similar to that shown in Figure 5, under identical  $\Delta\text{NS}$  and  $E_{\text{lab}}$  conditions, but without the prominent 4+ charge state products. Product ions extending to slightly farther into the sequence (to residue 26), compared to the MS/MS spectrum for the native state, are evident along with a rising baseline to higher  $m/z$  due to additional fragmentation processes that are unresolved. Clearly, the reduced (and presumably extended) form of albumin opens additional charge sites (40). The  $(M + 49H)^{49+}$  ion for the reduced form might therefore be expected to have fewer charges on the  $\text{NH}_2$  terminal region probed by CAD in these studies, leading to the observed lowering of product charge state. More complete CAD studies with instrumentation giving improved sensitivity should provide additional information on the distribution of charge sites and their effects on dissociation processes.

Although collisional dissociation of multiply charged ions is more efficient with increasing charge state, spectral assignments are more difficult due to the increased number of possible charge states. MS/MS of the  $(M + 68H)^{68+}$  molecular ion (Figure 9B, bottom) produces an ion tentatively assigned as a  $b_{25}^2$  species as the only resolvable product species on top of a broad "hump" distributed near the parent ion, and attributed to additional unresolved CAD products. The MS/MS spectra in Figures 5 and 9 were produced at constant  $E_{\text{lab}}$  and thus constant center-of-mass energy [ $E_{\text{cm}} = E_{\text{lab}}[M_{\text{A}^+}/(M_{\text{albumin}} + M_{\text{A}^+})] \approx 4.1$  eV]. The  $\Delta\text{NS}$  was adjusted such that  $E_{\text{lab}}$  was also relatively constant in the atmosphere/vacuum region, so that the 68+ ions were excited to the same extent as the 49+ molecular ions.

The increased Coulombic effects for more highly charged molecules may also give rise to larger dissociation rates and perhaps alter the relative abundances of dissociation products. A theoretical evaluation of possible Coulombic effects (57) shows that doubling of charge state can lead to dramatic increases in dissociation rates. The effect is greatest for cleavage toward the center of a linear polymer where charge would be evenly distributed between the two fragments. Here the Coulombic interactions effectively lower the barrier to dissociation to the greatest extent. The importance of Cou-

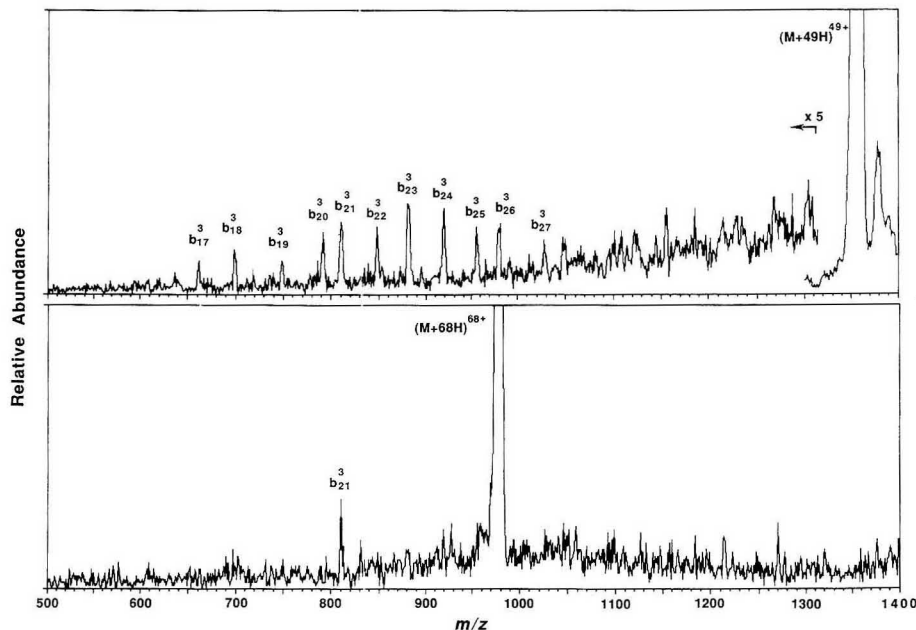


Figure 9. MS/MS spectra of the  $(M + 49H)^{49+}$  (top) and  $(M + 68H)^{68+}$  (bottom) parent ions from disulfide-reduced sheep albumin.

lombic effects depends upon the internal energy of the molecular ions; at high levels of excitation branching ratios are increasingly determined by the preexponential "frequency factor" associated with the dissociation pathway (57). Bunker and Wang (58) have previously shown that for uncharged (or singly charged) molecules, in the absence of Coulombic effects, the frequency factor (which is related to the reduced mass of the products for a simple linear homopolymer) is greatest for cleavage near the chain termini, and at the large molecule limit approaches zero for particular cleavages near the chain center. Our calculations (57) show that consideration of Coulombic forces completely reverses this situation if a sufficiently high charge state is obtained. Of particular relevance, however, is that at levels of charge and excitation qualitatively similar to those of our MS/MS studies, Coulombic effects can range from small to dominant (57). Thus higher charge states may dissociate more rapidly, but more importantly, may dissociate to yield products due to cleavages nearer the molecule's center which are not evident for lower charge state molecular ions. This may explain, at least in part, the fact that products evident for the  $(M + 49H)^{49+}$  MS/MS spectra are not prominent for the  $(M + 68H)^{68+}$  spectra, even though CAD efficiencies are greater.

For the albumin species, most of the fragmentation is centered around residue 20 from the  $NH_2$  terminus, with the various multiple charge distributions providing information on a series of  $\sim 10$  sequential residues. These originate in the molecular region known as subdomain IA (33). The three-dimensional structure for human serum albumin was recently obtained with 4-Å resolution (59, 60). It is tempting to correlate such 3-D structural information with observed gas-phase dissociation processes, but more information and additional experimentation is required before this will be feasible.

It is unclear how higher order protein structure (in solution, and perhaps even gas phase) may also affect the dissociation process. Chait and co-workers (61, 62) and our laboratory (63)

have demonstrated the effects of protein conformations (three-dimensional structure) on the resulting ESI mass spectra. Factors such as disulfide reduction (13, 18, 40) and solvent conditions such as pH (61, 63) and organic solvent content (62, 63) can have dramatic roles in the higher order structure and the observed charge distribution in ESI mass spectra. We have also previously observed possible higher order structural effects on collisional dissociation spectra for ribonuclease A ( $M$ , 13 682 Da) (18) by comparison of MS/MS spectra of the native versus disulfide-reduced forms for the same parent charge state. It is arguable that removal of structural inhibitions, such as the reduction of disulfide bonds, allows the molecule to relax to a more extended conformation. Whether the addition of more positive charges forces the molecule to an even more "stretched" form due to electrostatic charge repulsion will likely depend on both thermodynamic and kinetic constraints.

CAD/MS/CAD/MS. Tandem mass spectrometry can be further extended by CAD of fragment ions produced at an elevated  $\Delta NS$  bias in the atmospheric pressure/vacuum interface. These experiments, effectively MS/MS/MS or  $MS^3$ , can be used to confirm product ion assignments and, in more favorable cases (15, 18), extend the amount of sequence information. This experiment is analogous to MS/MS of small peptides generated by enzymatic digestion of a larger protein for the purpose of complete sequence determination (21-26). CAD/MS/CAD/MS experiments for sheep albumin were performed on the triply charged  $b_{18}$  and  $b_{21}$  fragments with  $\Delta NS = +335$  V (Figure 10). Doubly charged  $b_{16}$ - $b_{19}$ ,  $b_{23}^2$ , and singly charged  $b_2$ - $b_4$  and  $y_2$ - $y_3$  are found for the  $b_{21}^2$  parent ion. CAD of  $b_{18}^3$  yields  $b_{13}^2$ - $b_{17}^2$ ,  $b_{15}^2$ - $b_{17}^2$ , and  $b_3$ - $b_4$ , along with weak signals indicating internal fragmentation designated as  $(b_{13} - DTHK)$  to  $(b_{16} - DTHK)$  (see figure caption for nomenclature). Although only limited additional sequence information was obtained relative to MS/MS of the molecular ions (compare, with Figure 3, middle) due to the currently

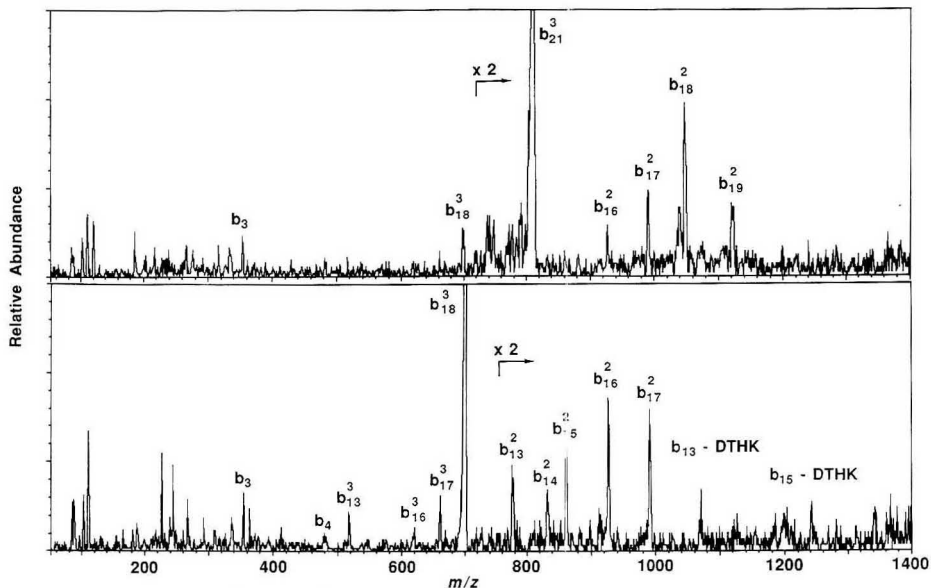


**Figure 10.** MS/MS spectra of the  $b_{21}^3$  (top) and  $b_{18}^3$  (bottom) product ions of sheep albumin with  $\Delta NS = +335$  V and  $E_{\text{lab}} = 429$  eV for CAD. Internal fragmentation due to additional loss of the initial four residues, Asp Thr His Lys is denoted by "b<sub>n</sub>-DTHK", where D = Asp, T = Thr, H = His, and K = Lys.

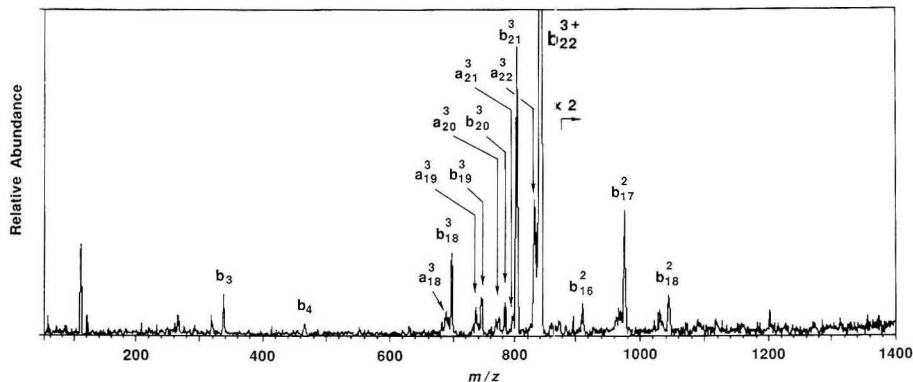


**Figure 11.** ESI-MS/MS spectrum of the  $b_{22}^3$  sequence ion of rabbit albumin with  $\Delta NS = +335$  V and  $E_{\text{lab}} = 420$  eV.

limited sensitivity and resolution, such studies provide information confirming the original product ion assignments and serve to demonstrate the potential of extended MS analysis (i.e., MS<sup>n</sup>, where  $n \geq 3$ ) for more complete structural analysis.

CAD/MS/CAD/MS experiments have also provided support for peptide sequence assignments for rabbit serum albumin. The ESI mass spectrum of rabbit serum albumin at high  $\Delta NS$  (Figure 1, bottom) shows most of the intense peaks between  $m/z$  500 and 1000 are observed at  $m/z$  values lower than predicted based on its amino acid sequence (38). Triply charged ions corresponding to  $b_{18}^3$  and  $b_{19}^3$  of the published sequence were found. However,  $b_{20}^3$ - $b_{26}^3$  and  $b_{20}^4$ - $b_{26}^4$  ions are  $\sim 15$  Da too low, suggesting the possibility that residue 20 is not Lys (incremental mass = 128 Da) but an alternative residue of mass  $\sim 113$  Da such as Ile or Leu (as indicated in

Table IV). Interestingly, position 20 (Lys) is homologous for 7 species reported in this study and for hamster albumin, as reported by Vötsch et al. (38). Our suggestion of an error in the previously suggested sequence is supported by an additional study involving further dissociation of the  $b_{22}^3$  product ion (Figure 11), resulting in doubly charged  $b_{16}$ - $b_{18}$  ions and triply charged  $a_{18}$ - $a_{22}$  and  $b_{18}$ - $b_{21}$  products at  $m/z$  values consistent with Ile/Leu at position 20.

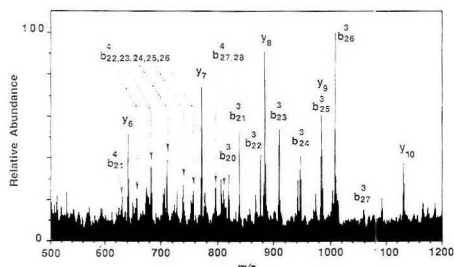
The nucleotide sequence of porcine albumin was recently elucidated to reveal a protein of 583 amino acids (36). An  $M_r$  value from the measured ESI mass spectrum (Table II) is in relatively close agreement with the predicted value (see previous discussion). The interface CAD spectrum ( $\Delta NS = +335$  V) shows the expected 3+ and 4+ NH<sub>2</sub> terminal fragment ions ( $b_{20}$ - $b_{26}$ ) (Figure 12). Further dissociation of the  $b_{26}^3$  product ion ( $m/z$  1009) yielded a weak spectrum showing ions at  $m/z$



**Table IV. Electrospray Ionization  $b_n$  Product Ion  $m/z$  for Rabbit Serum Albumin**

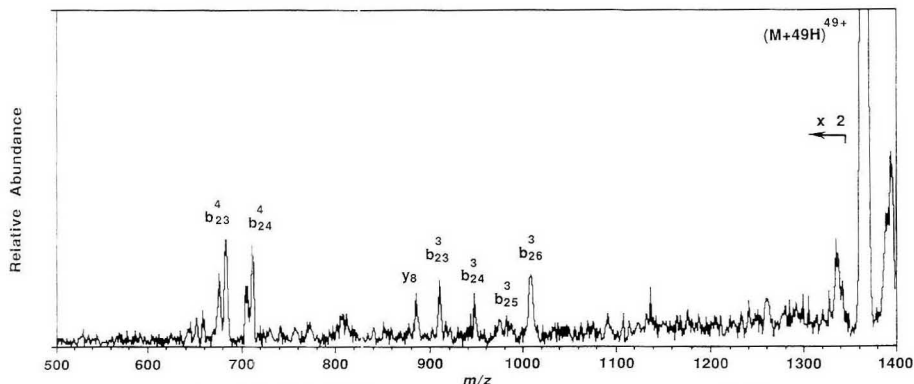
$n^a$	amino acid	3+			4+		
		calcd <sup>b</sup>	calcd <sup>c</sup>	exptl	calcd <sup>b</sup>	calcd <sup>c</sup>	exptl
18	H	696.4	696.4	696.5	522.6	522.6	
19	F	745.5	745.5	745.5	559.4	559.4	
20	K <sup>b</sup> (I/L) <sup>c</sup>	788.2	783.2	783.3	591.4	537.6	587.6
21	G	807.2	802.2	802.3	605.7	601.9	602.0
22	L	844.9	839.9	840.0	634.0	630.2	630.2
23	V	878.0	873.0	873.1	658.7	655.0	654.9
24	L	915.7	910.7	910.8	687.0	683.3	683.3
25	I	953.4	948.4	948.5	715.3	711.6	711.5

<sup>a</sup> Residue position from the NH<sub>2</sub> terminus. <sup>b</sup> According to published sequence (38) with E at position 17. <sup>c</sup> According to best sequence fit of ESI-MS data.

**Figure 12.** ESI-MS collisional dissociation (interface) spectrum for porcine serum albumin with  $\Delta NS = +335V$ .

985 ( $b_{23}^3$ ), 948 ( $b_{24}^3$ ), 910 ( $b_{25}^3$ ), and 217 ( $b_2$ ). However, significant contributions from singly charged COOH terminal products ( $y_5$ - $y_{10}$ ) were also found at high  $\Delta NS$  (Figure 12), and to a lesser extent in the ESI-MS/MS spectrum for the ( $M + 49H$ )<sup>49+</sup> molecular ion (Figure 13). In the CAD/MS/CAD/MS experiment of the  $m/z$  885 ion, no ions were detected above the parent  $m/z$ , consistent with expectations for a singly charged  $y_8$  parent ion. The major product ions that correlate to the published sequence were the  $y_7$  fragment, the complementary charged species ( $b_2$ ), and ions tentatively assigned as internal product ions (i.e., where both NH<sub>2</sub> and COOH terminal residues of the octapeptide have been lost), as shown in Figure 14.

Porcine albumin provided the only example in which  $y_n$  products were identified for the 10 serum albumins examined.

**Figure 13.** Tandem mass spectrum of the ( $M + 49H$ )<sup>49+</sup> molecular ion of porcine serum albumin ( $E_{bb} = 6615 eV$ ).**Table V. Published COOH Terminal Amino Acid Sequences for Serum Albumins**

Species	Sequence <sup>a</sup>
Bovine	-C Q A A D D K E A C F A V E G P K L V I V S T O T A L L A (582)
Human	-C K A A D D K E T C F A E E G K K L V A A S O A A L G L (585)
Rat	-C C K A A D K N C F A T E G P N L V A R S K E A L A (584)
Sheep	-C C A A D D K E G C F V L E G P K L V A S T O A A L A (583)
Porcine	-C C A A P D H E A C F A V E G P K F V I I E I R G I L A (583)

<sup>a</sup> Sequences are aligned by the Cys residues (COOH terminus at right). Invariant amino acid residues are indicated by the boxed regions. Total number of residues are indicated by the value in parentheses. See Table I for one-letter code.

Inspection of  $\sim 27$  amino acid residues from the COOH terminus for the 5 available complete sequences (Table V) reveals very few obvious significant differences with the porcine albumin sequence compared to bovine, rat, human, and sheep. The arginine situated 5 residues from the COOH terminus in the porcine sequence would be a good candidate for positive-charge retention by COOH terminal fragments ( $y_n$ ). However,  $y_n$  products were not significant for rat albumin (30), even though an arginine and lysine are present within the first 8 residues from the COOH terminus. A Pro residue at position 561 of its sequence is present for porcine albumin, but not present for the other species. The proline is located inside a disulfide loop of porcine albumin and may affect the conformation of the polypeptide backbone near the COOH terminus due to the rigid constraints on rotation about the N-C backbone bond by its fairly rigid five-membered ring structure. We have previously noted that fragmentation of multiply charged polypeptides appears to be more facile in the vicinity of proline residues (15, 16, 18, 55, 56) and suggest its possible role in the present case.

## CONCLUSIONS

Prior to the use of highly charged ions produced by ESI, nearly complete primary sequence information could be obtained using tandem MS for molecules of molecular mass up to  $\sim 2500$  Da, and partial sequences to perhaps 5000 Da, with practical limitations depending on the nature of the molecular species. Limitations arise in substantial part from decreases in ionization efficiency for most ionization methods with increasing  $M_r$ , as well as reduced dissociation efficiency (27-29). We have recently reported that for triple-quadrupole MS studies, the most significant constraints to CAD of large

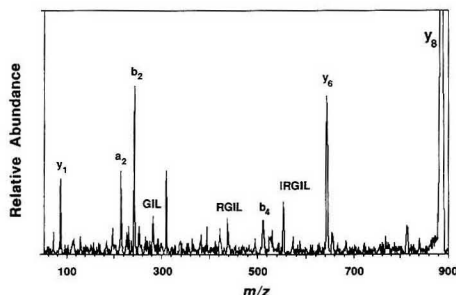


**Figure 14.** CAD/MS/CAD/MS of the  $y_6$  product ion (Ile Glu Ile Arg Gly Ile Leu Ala) of porcine albumin with  $\Delta NS = +360$  and  $E_{lab} = 140$  eV. Internal fragmentation due to loss of residues from both termini of the  $y_6$  ion are denoted by the single-letter codes for the amino acids (e.g., GIL is Gly Ile Leu).

molecules arise due to parent ion charge state (13, 15–18). Ions of low  $m/z$  (higher charge) can be more efficiently activated and dissociated than ions of lower charge state. The dissociation processes must be sufficiently rapid for dissociation during the  $10^{-4}$ -s residence time in the collision quadrupole region.

In this work we have shown that useful structural information is obtainable for multiply charged molecules of at least 66 kDa, a factor of about 20 larger than that reported for singly charged ions. Although the sequence information obtained is presently limited for intact molecules of such size (~10 residues out of ~580 amino acids), the potential of the technique is clearly demonstrated. Currently, for complete primary sequence information of proteins by mass spectrometry, the use of proteolytic enzymes followed by FAB-MS/MS (21–26) or even ESI-MS/MS (64) of the resulting peptides is the method of choice. However, the development of CAD-MS/MS for multiply charged ions is still very much in its infancy.

ESI mass spectra and CAD/MS have been used to differentiate among 66-kDa serum albumin proteins from 10 species. In two cases, assignment of interface CAD and conventional MS/MS spectra have unexpectedly indicated differences near the  $NH_2$  terminus with reported amino acid sequences. However, we note that all albumins analyzed were commercially obtained (Sigma) and may show differences from samples previously sequenced by conventional Edman methods (38). Strong support for our product ion assignments was provided by further dissociation of fragment species produced in the atmospheric pressure/vacuum interface. This capability is a uniquely valuable feature of ESI with tandem mass spectrometry and can potentially be used to probe molecular regions unaccessed by the initial CAD process. However, for the albumins, due to the limited  $m/z$  and sensitivity of our quadrupole instrument, only the initial  $NH_2$  terminal 30 residues and, in the case for porcine albumin, 10 residues from the COOH terminus, could be probed. It is conceivable that ESI-MS/MS may have utility for rapid detection of genetic variants. Over 30 different human serum albumin variants are known, mostly due to single-point mutations in the albumin gene (65). Some have altered residues near the  $NH_2$  terminus or the COOH terminus that may be probed by ESI-MS/MS.

For molecules of such large  $M_n$ , we find that the dominant fragmentation products for moderate charge states (i.e., ~+50) are limited to regions near the ends of the molecule, consistent with the RPKM model used by Bunker and Wang (58) for the large-molecule limit. A recent theoretical study (57) suggests that dissociation from the center region will become

more important as charge state increases. We also note that both the MS/CAD/MS and CAD/MS/CAD/MS spectra also suggest an abundance of lower intensity dissociation processes that cannot be suitably examined at present due to limited sensitivity and spectral "congestion" arising from the range of potential products and charge states. In addition, it is possible that larger fragmentation products from regions more interior of the molecule and possible complementary ions may be produced, yet may fall outside our current  $m/z$  limit of detection.

An exciting possibility of ESI is the future use of more sensitive and higher resolution MS methods which might allow much more extensive sequence information to be obtained. It may be possible that ion-trapping methods, such as ion trap MS (41) and Fourier transform ion cyclotron resonance MS (44, 50) allowing sequential MS<sup>n</sup> analyses may provide much more extensive primary structure determination in only a small fraction of time required by conventional methodologies. MS<sup>4</sup> spectra for multiply charged ions from peptides have recently been accomplished with ESI ion trap MS (41, 66). Interpretation of such collisional dissociation spectra for "unknowns" is currently extremely difficult due to the complexity of the spectra and the uncertainty of product ion charge states. With higher resolution methods (e.g., FTMS), charge-state assignments from either resolved isotopic peaks or unresolved isotopic envelopes is possible (44). Indeed, charge-state assignments from resolved isotopic peaks of up to the 18+ molecular ion charge state for equine myoglobin by ESI-FTMS have been published by McLafferty and co-workers (67). Such methods would largely circumvent the sensitivity and resolution limitations of the present triple-quadrupole methods, suggesting the potential for extension to even greater molecular weights.

#### ACKNOWLEDGMENT

We thank J. A. Burghard, D. G. Camp, and R. R. Ogorzalek Loo for experimental assistance and encouragement.

#### LITERATURE CITED

- (1) *The Analysis of Peptides and Proteins by Mass Spectrometry*; McNeal, C. J., Ed.; John Wiley & Sons: Chichester, U.K., 1988.
- (2) *Mass Spectrometry of Biological Materials*; McEwen, C. N., Larsen, B. S., Eds.; Marcel Dekker: New York, 1990.
- (3) Barber, M.; Bordoli, F. S.; Elliott, G. J.; Sedgwick, R. D.; Tyler, A. N. *Anal. Chem.* **1982**, *54*, 845A–857A.
- (4) Barber, M.; Green, B. N. *Rapid Commun. Mass Spectrom.* **1987**, *1*, 80–85.
- (5) Sundqvist, B.; Macfarlane, R. D. *Mass Spectrom. Rev.* **1985**, *4*, 421–460.
- (6) Karas, M.; Bahr, U.; Ingendoh, A.; Hillenkamp, F. *Angew. Chem., Int. Ed. Engl.* **1989**, *28*, 760–761.
- (7) Karas, M.; Bahr, U.; Hillenkamp, F. *Int. J. Mass Spectrom. Ion Processes* **1989**, *92*, 231–242.
- (8) Beavis, R. C.; Chait, B. T. *Rapid Commun. Mass Spectrom.* **1989**, *3*, 233–237.
- (9) Meng, C. K.; Mann, M.; Fenn, J. B. Z. *Phys. D: At., Mol. Clusters* **1988**, *10*, 361–368.
- (10) Fenn, J. B.; Mann, M.; Meng, C. K.; Wong, S. F.; Whitehouse, C. M. *Science* **1989**, *246*, 64–71.
- (11) Covey, T. R.; Bonner, R. F.; Shushan, B. I.; Henion, J. *Rapid Commun. Mass Spectrom.* **1988**, *2*, 249–256.
- (12) Loo, J. A.; Udseth, H. R.; Smith, R. D. *Anal. Biochem.* **1989**, *179*, 404–412.
- (13) Smith, R. D.; Loo, J. A.; Edmonds, C. G.; Barinaga, C. J.; Udseth, H. R. *Anal. Chem.* **1990**, *62*, 882–899.
- (14) Feng, R.; Bouthillier, F.; Konishi, Y.; Cygler, M. Presented at the 39th ASMS Conference on Mass Spectrometry and Allied Topics, May 1991, Nashville, TN.
- (15) Smith, R. D.; Loo, J. A.; Barinaga, C. J.; Edmonds, C. G.; Udseth, H. R. *J. Am. Soc. Mass Spectrom.* **1990**, *1*, 53–65.
- (16) Barinaga, C. J.; Edmonds, C. G.; Udseth, H. R.; Smith, R. D. *Rapid Commun. Mass Spectrom.* **1989**, *3*, 160–164.
- (17) Smith, R. D.; Barinaga, C. J. *Rapid Commun. Mass Spectrom.* **1990**, *4*, 54–57.
- (18) Loo, J. A.; Edmonds, C. G.; Smith, R. D. *Science* **1990**, *248*, 201–204.
- (19) *Tandem Mass Spectrometry*; McLafferty, F. W., Ed.; John Wiley & Sons: New York, 1983.
- (20) Busch, K. L.; Glish, G. L.; McLuckey, S. A. *Mass Spectrometry/Mass Spectrometry: Techniques and Applications of Tandem Mass Spectrometry*; VCH: New York, 1988.

- (21) Biemann, K.; Scoble, H. A. *Science* **1987**, *237*, 992-998.
- (22) Biemann, K. *Biomol. Environ. Mass Spectrom.* **1988**, *16*, 99-111.
- (23) Carr, S. A.; Green, B. N.; Hemling, M. E.; Roberts, G. D.; Anderregg, R. J.; Vickers, R. Presented at the 35th ASMS Conference on Mass Spectrometry and Allied Topics, May 1987, Denver, CO (conference proceedings pp 830-831).
- (24) Hunt, D. F.; Yates, J. R., III; Shabanowitz, J.; Winston, S.; Hauer, C. R. *Proc. Natl. Acad. Sci. U.S.A.* **1986**, *83*, 6233-6237.
- (25) Johnson, R. S.; Biemann, K. *Biochemistry* **1987**, *26*, 1209-1214.
- (26) Johnson, R. S.; Mathews, W. R.; Biemann, K.; Hopper, S. J. *Biol. Chem.* **1988**, *263*, 9589-9597.
- (27) Gross, M. L.; Tomer, K. B.; Curry, R. L.; Glibin, D. E. In *Mass Spectrometry in the Analysis of Large Molecules*; McNeal, C. J., Ed.; Wiley: Chichester, U.K., 1986; pp 171-190.
- (28) Neumann, G. M.; Derrick, P. J. *Org. Mass Spectrom.* **1984**, *19*, 165-170.
- (29) Neumann, G. M.; Sheil, M. M.; Derrick, P. J. *Z. Naturforsch.* **1984**, *39A*, 584-592.
- (30) Loo, J. A.; Edmonds, C. G.; Udseth, H. R.; Smith, R. D. *Anal. Chim. Acta* **1990**, *241*, 167-173.
- (31) Loo, J. A.; Udseth, H. R.; Smith, R. D. *Rapid Commun. Mass Spectrom.* **1988**, *2*, 207-210.
- (32) Smith, R. D.; Barinaga, C. J.; Udseth, H. R. *Anal. Chem.* **1988**, *60*, 1948-1952.
- (33) Peters, T., Jr. In *Advances in Protein Chemistry*; Anfinsen, C. B., Edsall, J. T., Richards, F. M., Eds.; Academic Press: Orlando, FL, 1985; Vol. 37, pp 161-245.
- (34) Sepulveda, P. M. J. Ph.D. Thesis, University of Texas at Austin, 1972.
- (35) Brown, W. M.; Dziegielewska, K. M.; Foreman, R. C.; Sanders, N. R. *Nucl. Acids Res.* **1989**, *17*, 10495.
- (36) Weinstock, J.; Baldwin, G. S. *Nucl. Acids Res.* **1988**, *16*, 9045.
- (37) Dixon, J. W.; Sarkar, B. J. *Biol. Chem.* **1974**, *249*, 5872-5877.
- (38) Vötsch, W.; Wagner, H. A.; Anderer, F. A. *Comp. Biochem. Physiol.* **1980**, *66B*, 87-91.
- (39) Chincarini, C. C.; Brown, J. R. *Fed. Proc.* **1976**, *35*, 1334.
- (40) Loo, J. A.; Edmonds, C. G.; Udseth, H. R.; Smith, R. D. *Anal. Chem.* **1990**, *62*, 693-698.
- (41) Van Berkel, G. J.; Glish, G. L.; McLuckey, S. A. *Anal. Chem.* **1990**, *62*, 1284-1295.
- (42) Chowdhury, S. K.; Katta, V.; Chait, B. T. *Rapid Commun. Mass Spectrom.* **1990**, *4*, 81-87.
- (43) Feng, R.; Konishi, Y.; Bell, A. W. *J. Am. Chem. Soc. Mass Spectrom.* **1991**, *2*, 387-401.
- (44) Henry, K. D.; McLafferty, F. W. *Org. Mass Spectrom.* **1990**, *25*, 490-492.
- (45) Gallagher, R. T.; Chapman, J. R.; Mann, M. *Rapid Commun. Mass Spectrom.* **1990**, *4*, 369-372.
- (46) Geisow, M. J.; Harris, R.; Dodsworth, N.; Green, B. N.; Hutton, T. In *Techniques in Protein Chemistry II*; Villafranca, J. J., Ed.; Academic Press: San Diego, CA, 1981; pp 567-572.
- (47) Hirayama, K.; Akashi, S.; Furuya, M.; Fukuhara, K. *Biochem. Biophys. Res. Commun.* **1990**, *173*, 639-646.
- (48) Chan, K.; Wintergrass, D.; Straub, K. *Rapid Commun. Mass Spectrom.* **1990**, *4*, 139-143.
- (49) Cleland, W. W. *Biochemistry* **1964**, *3*, 480-482.
- (50) Henry, K. D.; Williams, E. R.; Wang, B. H.; McLafferty, F. W.; Shabanowitz, J.; Hunt, D. F. *Proc. Natl. Acad. Sci. U.S.A.* **1989**, *86*, 9075-9078.
- (51) Chowdhury, S. K.; Katta, V.; Beavis, P. C.; Chait, B. T. *J. Am. Soc. Mass Spectrom.* **1990**, *1*, 382-388.
- (52) Roeppstorff, P.; Fohlman, J. *Biomol. Mass Spectrom.* **1984**, *11*, 601.
- (53) Mann, M.; Meng, C. K.; Fenn, J. B. *Anal. Chem.* **1989**, *61*, 1702-1708.
- (54) Smith, R. D.; Barinaga, C. J.; Udseth, H. R. *J. Phys. Chem.* **1989**, *93*, 5019-5022.
- (55) Smith, R. D.; Loo, J. A.; Ogorzalek Loo, R. R.; Busman, M.; Udseth, H. R. *Mass Spectrom. Rev.* in press.
- (56) Loo, J. A.; Edmonds, C. G.; Udseth, H. R.; Ogorzalek Loo, R. R.; Smith, R. D. In *Experimental Mass Spectrometry*; Russell, D. H., Ed.; Plenum: New York, in press.
- (57) Rockwood, A. L.; Busman, M.; Smith, R. D. *Int. J. Mass Spectrom. Ion Proc.* in press.
- (58) Bunker, D. L.; Wang, F.-M. *J. Am. Chem. Soc.* **1977**, *99*, 7457-7459.
- (59) Carter, D. C.; He, X.-M.; Munson, S. H.; Twigg, P. D.; Gernert, K. M.; Broom, M. B.; Miller, T. Y. *Science* **1989**, *244*, 1195-1198.
- (60) Carter, D. C.; He, X.-M. *Science* **1990**, *249*, 302-303.
- (61) Chowdhury, S. K.; Katta, V.; Chait, B. T. *J. Am. Chem. Soc.* **1990**, *112*, 9012-9013.
- (62) Katta, V.; Chait, B. T. *Rapid Commun. Mass Spectrom.* **1991**, *5*, 214-217.
- (63) Loo, J. A.; Ogorzalek Loo, R. R.; Udseth, H. R.; Edmonds, C. G.; Smith, R. D. *Rapid Commun. Mass Spectrom.* **1991**, *5*, 101-105.
- (64) Covey, T. R.; Huang, E. C.; Henion, J. D. *Anal. Chem.* **1991**, *63*, 1193-1200.
- (65) Watkins, S.; Madison, J.; Davis, E.; Sakamoto, Y.; Gilliano, M.; Minchiotti, L.; Putnam, F. W. *Proc. Natl. Acad. Sci. U.S.A.* **1991**, *88*, 5959-5963.
- (66) Jardine, I.; Hall, M.; Lewis, S.; Zhou, J.; Schwartz, J.; Whitehouse, C. Presented at the 38th ASMS Conference on Mass Spectrometry and Allied Topics, June 1990, Tucson, AZ (conference proceedings pp 16-17).
- (67) Henry, K. D.; Quinn, J. P.; McLafferty, F. W. *J. Am. Chem. Soc.* **1991**, *113*, 5447-5449.

RECEIVED for review May 13, 1991. Accepted August 9, 1991. We are grateful for the support of the U.S. Department of Energy, Office of Health and Environmental Research (Grant DE-AC06-76RLO 1830), the National Science Foundation, Instrumentation and Instrument Development Program (Grant DIR 8908096), and the National Institutes of Health, National Center for Human Genome Research (Grant HG 00327). Pacific Northwest Laboratory is operated by Battelle Memorial Institute.

## Nondependence of Diffusion-Controlled Peak Dispersion on Diffusion Coefficient and Ionic Mobility in Capillary Zone Electrophoresis without Electroosmotic Flow

Ernst Kenndler\* and Christine Scherzer

Institute for Analytical Chemistry, University of Vienna, Währingerstrasse 38, A 1090 Vienna, Austria

The ratio of the ionic mobility,  $u$ , and the diffusion coefficient,  $D$ , in the expression for the plate number,  $N$ , given by  $N = uU/2D$ , ( $U$  being the applied voltage) for capillary zone electrophoresis without electroosmotic flow was substituted by the Einstein relation between these two parameters. As a consequence, the plate number is dependent exclusively on the charge number of the individual analyte, but not on  $u$  and  $D$ . The validity of this conclusion was demonstrated experimentally with anions of different charge number. Further, the plate number was found to depend on the charge of weak acids according to the degree of dissociation, as expected from theory.

## INTRODUCTION

Peak dispersion in capillary zone electrophoresis can be described by a surprisingly simple theory, when only diffusion in the longitudinal direction, the direction of the electrophoretic migration of the ions, is considered. In this case (when dispersion due to the radial temperature profile within the capillary, and peak broadening caused by electroosmotic or hydrodynamic flow, by extracolumn effects and by the difference in electric conductivity between the analyte zone and the buffering electrolyte are neglected), the variance,  $\sigma_z^2$ , of the solute peak, based on length, is dependent on the diffusion coefficient,  $D$ , and the residence time,  $t$ , given by

Einstein:

$$\sigma_z^2 = 2Dt \quad (1)$$

Connecting this expression with the relation of the variance on the migration distance,  $z$  gives

$$\sigma_z^2 = Hz \quad (2)$$

which is also valid for elution chromatography. An expression for the plate height,  $H$ , can be derived for the case, such that the limitations mentioned above are fulfilled (1, 2):

$$H = 2D/uE \quad (3)$$

where  $u$  is the ionic mobility and  $E$  is the electric field strength.

The plate number,  $N = L/H$ , which is decisive for the resolution of two components, is thus

$$N = uU/2D \quad (4)$$

$U$  being the applied voltage along the length,  $L$ , of the separation capillary.

It can be seen from eqs 3 and 4, that the dispersion property of the separation system depends on an external parameter, the voltage (or the electric field strength  $E = U/L$ ), and on parameters  $u$  and  $D$ , being specific for the particular analytes.

However, it must be taken into account that these two parameters are related properties: the ionic mobility describes the transport of ions along the gradient,  $d\Psi/dz$  of the electric field,  $\Psi$ , whereas the diffusion coefficient stands for the transport of particles along the gradient,  $d\mu/dz$ , of the chemical potential,  $\mu$ . Both parameters are connected by a relation given by Einstein (cf. e.g. ref 3):

$$D = \frac{u}{ze_0} kT \quad (5)$$

where  $z$  is the charge number of the ion,  $e_0$  is the electronic charge,  $k$  is the Boltzmann constant, and  $T$  is the absolute temperature. It can be concluded from this equation, that the ratio  $u/D$ , occurring in the expression for the plate number, must have a distinct, constant value. This relation was mentioned by Giddings (4) and is experimentally evaluated here.

In this paper, the plate number, a measure for the peak dispersion, will be discussed with regard to the correlation of mobility and diffusion coefficient, and the conclusions of the theoretical findings will be supported experimentally for free capillary zone electrophoresis without electroosmosis. In subsequent papers, electroosmotic flow will be taken into consideration, too (5), and an appropriate explanation for the peak dispersion in zone electrophoresis with gel-filled capillaries will be given (6).

## EXPERIMENTAL SECTION

**Apparatus.** The measurements were carried out with an instrument (P/ACE system 2000, Beckman, Palo Alto, CA), which was equipped with a UV-absorbance detector (254 nm). The fused-silica capillary used for zone electrophoresis had a total length of 57.4 cm (50.7 cm to the detector cell), and an inner diameter of 75  $\mu$ m (Scientific Glass Engineering, Ringwood, Victoria, Australia). Since the measurements needed to be carried out without electroosmosis, the capillary was coated as described below.

The capillary was thermostated at 25 °C. Electrophoresis was performed at a total voltage of 10 or 5 kV, respectively, leading to currents of less than 25  $\mu$ A in all buffers. Injection was carried out by pressure.

**Reagents.** Chemicals used for the preparation of the buffer solutions were either of analytical grade (*o*-phosphoric acid, sodium hydroxide; E. Merck, Darmstadt, Germany) or purissimum (lactic acid; Merck). The test substances were of synthesis grade (Merck),

**Table I. Ratios of Ionic Mobility,  $u$ , and Diffusion Coefficient,  $D$ , for Anions with Different Charge Numbers<sup>a</sup>**

anion	$D$ , 10 <sup>-6</sup> cm <sup>2</sup> s <sup>-1</sup>	$u$ , 10 <sup>-4</sup> cm <sup>2</sup> V <sup>-1</sup> s <sup>-1</sup>	$(u/D)^{\text{theor}}$ , V <sup>-1</sup>	$(u/D)^{\text{exp}}$ , V <sup>-1</sup>
benzene-1,3-disulfonate	7.17	57.2	77.9	79.8
1-naphthol-3,6-disulfonate	5.95	46.3	77.9	77.8
toluene-4-sulfonate	8.23	33.5	39.0	40.7
naphthalene-2-sulfonate	7.51	31.4	39.0	41.8
pyrocatechol violet <sup>b</sup>	4.83	18.6	39.0	38.5

<sup>a</sup>The ionic mobilities and the diffusion coefficients were measured at 25 °C as described in the Experimental Section.  $(u/D)^{\text{theor}}$ : ratio calculated from eq 6.  $(u/D)^{\text{exp}}$ : ratio obtained from the measured values. <sup>b</sup>Pyrocatechol violet has the charge number 1 under these experimental conditions.

except 2,3-dihydroxybenzoic acid (purum; Fluka, Buchs, Switzerland) and disodium 1-naphthol-3,6-disulfonate (technical grade, Fluka). Pyrocatechol violet was the common metal indicator (Merck). For the coating procedure methylcellulose (Methocel MC, 3000-5000 mPa·s, Fluka) was used. The cross-linking reagents (formaldehyde and formic acid) were of analysis grade (Merck).

Water used as the solvent was distilled twice from a quartz apparatus.

**Procedures.** In order to prevent electroosmosis, the capillary surface was coated with methylcellulose at an elevated temperature using formaldehyde and formic acid as cross-linking agents according to the procedure described by Hjerten (7).

The mobilities of the sulfonic acids were calculated in the usual way from their migration times and distance (50.7 cm), in a buffering electrolyte at pH 5.1 (phosphate, 0.05 mol/L) at 25 °C.

The diffusion coefficients were determined by the stopped-flow method under conditions identical with those of the mobilities: the variances (second moments) of the peaks obtained after interrupting the electromigration for 2 h, 5 min after injection, were compared to the variances from the normal electropherogram. From the resulting increase of the variances due to the additional diffusion for 2 h the diffusion coefficients were calculated.

The  $\text{pK}_a$  values of the benzoic acids were determined by potentiometric titration at 25 °C.

## RESULTS AND DISCUSSION

It can be seen from eq 5 that the diffusion coefficient  $D$  and the ionic mobility  $u$  are related quantities. Thus, the ratio  $u/D$ , which occurs in the equations for the plate height (eq 3) and the plate number (eq 4), respectively, can be expressed by

$$u/D = ze_0/kT = zF/RT \quad (6)$$

where  $F$  is the Faraday constant and  $R$  is the gas constant.

It follows that for a given temperature this ratio depends only on the charge number,  $z$ , of the ion and is independent of the nature of the particle. For a temperature of 25 °C, this ratio can therefore be numerically expressed by

$$u/D = 38.96z \quad (7)$$

when  $u$  is given in  $\text{cm}^2\text{V}^{-1}\text{s}^{-1}$  and  $D$  in  $\text{cm}^2\text{s}^{-1}$ .

The proof of this assumption can be seen from the results given in Table I, where the ratio  $u/D$  is derived from experimental data for five different test substances with two different charge numbers, 1 and 2. The mobilities and the diffusion coefficients, also given in Table I, were measured with the electrophoretic equipment as described in the Experimental Section. The measuring error, expressed by the relative standard deviation for 10 measurements, is 0.67% for the determination of the mobilities and about 6% for the diffusion coefficients.

It can be seen from Table I that the ratios  $u/D$ , obtained from the experimental data agree within a few percents with

**Table II. Dependence of the Plate Number,  $N$ , on the Electric Charge of Mono- and Divalent Anions at Two Different Voltages**

anion	charge no.	plate number $N$			
		8.84 kV		4.42 kV	
		theor <sup>a</sup>	exp	theor <sup>a</sup>	exp
benzene-1,3-di-sulfonate	2	344 000	233 000	172 000	126 000
1-naphthol-3,6-di-sulfonate	2	344 000	232 000	172 000	141 000
toluene-4-sulfonate	1	172 000	137 000	86 000	69 000
naphthalene-2-sulfonate	1	172 000	134 000	86 000	71 000
pyrocatechol violet	1	172 000	122 000	86 000	66 000

<sup>a</sup> According to eq 9.

the data theoretically derived from the physical constants  $e_0$ ,  $k$ , and  $T$ , according to eq 7.

The ratio  $u/D$  (eq 6), only depending on the charge number, is substituted in eq 3 for the plate height or in eq 4 for the plate number, thus obtaining the following expressions (4, 8, 9):

$$H_i = 2kT/z_i e_0 E = 2RT/z_i FE \quad (8)$$

$$N_i = z_i e_0 U / 2kT = z_i F U / 2RT \quad (9)$$

An analogous expression was discussed for the case that electroosmosis occurs (5) and for zone electrophoresis with gel-filled capillaries (6).

It can be seen from the equations given above, that the plate height as well as the plate number are not dependent on the individual diffusion coefficients or ionic mobilities of the ionic species but (under given experimental conditions) are dependent exclusively on the charge number  $z_i$  of the ions. This is the only individual quantity that is decisive for the peak dispersion, because the voltage (or field strength) and the temperature, occurring in these equations, are external parameters, being equal for all ionic species.

For the given experimental conditions, namely for an applied voltage of 10 kV (which leads to a potential drop of 8.84 kV along the migration distance) and for a temperature within the capillary of 25 °C, the plate number is given by  $N_i = 172000z_i$ . Thus, a maximum plate number of 172 000 can be expected for all monovalent ions with charge number 1 (independent of the particle), 344 000 plates can be expected for all divalent ions ( $z = 2$ ), etc. The plate number for different ions must linearly increase with the charge, according to eq 9. It must be mentioned that the plate number, given by eq 9, is obviously independent of the sign of the electric charge; for a given charge number, it is equal for anions as for cations. For neutrals, it is zero.

It can be seen from Table II, that the experimental values agree with those predicted by theory. For the sulfonic acids

under investigation with  $z = 1$ , between 122 000 and 137 000 plates are measured, and over 230 000 plates for substances with  $z = 2$ .

The deviations from the theoretical values (the values found are about 20–25% lower) can be explained by peak distortion caused by different conductivities of the sample zone and buffering electrolyte on the one hand and by Joule heating on the other hand.

The contribution of extracolumn effects to peak broadening can be neglected, because a very narrow input profile was generated due to injection of the samples from pure water as solvent. Compared to injection from buffer as solvent, a drastic peak sharpening is obtained in this way. Peak dispersion in the detector cell is also negligible, because the detector has an aperture of only 200  $\mu\text{m}$ , thus contributing much less than 1% to the total variance (10).

An even better result is found when the peak dispersion is determined as a function of the charge number at a lower voltage, namely 5 kV (4.42-kV effective voltage) and the same temperature of 25 °C. As the voltage is halved compared with the above given conditions, the plate number is also halved, leading to a theoretical value of 86 000 plates per charge number under this experimental realization. The resulting experimental values for the test substances given in Table II show the agreement with the theoretical values as discussed above.

The charge number must depend on the degree of dissociation,  $\alpha$ , which is given by the  $pK_a$  value of the substance and the pH of the buffering electrolyte. For this case, eqs 8 and 9 can be rearranged, taking into account that the effective charge number is then equal to  $\alpha$ , leading to the expressions

$$H = 2kT/\alpha e_0 E \quad (10)$$

$$N = \alpha e_0 U / 2kT \quad (11)$$

in the case of monofunctional acids and bases.

In order to prove this dependence of  $N$  on  $\alpha$ , the degree of dissociation of three weak electrolytes (substituted benzoic acids with  $pK_a$  values of 2.83, 3.53, and 4.58, respectively) was varied by varying the pH of the buffer in the range between 2.5 and 5.6, and the resulting peak dispersion was measured. The plate number, obtainable for the fully dissociated monobasic acids, has a maximum value of 172 000 under the given conditions. Due to experimental reasons (mainly peak distortion due to conductivity differences and Joule heating, as mentioned), values about 20% lower were found, being in the range of 140 000. Thus, for these monobasic acids it is expected that in practice the plate numbers should depend on the degree of dissociation by  $N = 140000\alpha$ .

The results of the measurements (obtained at a voltage of 10 kV) are given in Table III. It can be seen, that the degree of dissociation, and therefore the effective charge number, varies by a factor of about 5 from 0.22 to 1. The plate numbers at small  $\alpha$  are in fact significantly lower than 140 000, namely

**Table III. Dependence of the Plate Number,  $N$ , on the Net Charge, Corresponding to the Degree of Dissociation,  $\alpha$ , for Substituted Benzoic Acids, Using Buffering Electrolyte Systems of Different pHs**

pH	acid ( $pK_a$ )								
	2,3-dihydroxybenzoic acid (2.83)			2,3-dimethoxybenzoic acid (3.53)			2,4-dimethoxybenzoic acid (4.58)		
	$N$	$\alpha$	$N/\alpha$	$N$	$\alpha$	$N/\alpha$	$N$	$\alpha$	$N/\alpha$
2.5	39 000	0.30	130 000						
3.0	84 000	0.63	133 000	40 000	0.27	148 000			
3.3	97 000	0.74	132 000	49 000	0.37	132 000			
3.5	111 000	0.82	135 000	67 000	0.48	139 000			
4.0	139 000	0.94	148 000	105 000	0.77	136 000	33 000	0.22	149 000
4.5	142 000	0.98	144 000	121 000	0.92	132 000	66 000	0.47	140 000
5.0	130 000	0.99	131 000	124 000	0.97	128 000	94 000	0.72	130 000
5.6	139 000	1.00	139 000	140 000	1.00	140 000	130 000	0.90	144 000



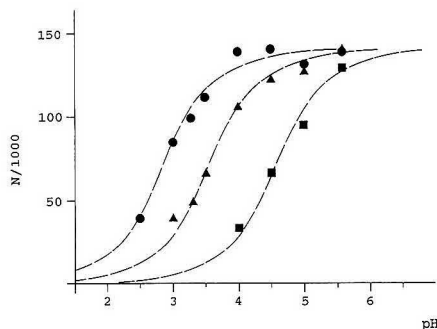


**Figure 1.** Dependence of the plate number,  $N$ , for different anions on the degree of dissociation via the pH of the buffering electrolyte. The net charge of the anions of the weak acids is determined by the degree of dissociation, depending on the  $pK_a$  of the acids and the pH of the electrolyte system. The broken curves indicate the theoretical dependence of the plate number on pH (see text). Experimental values for  $N$ : (●) 2,3-dihydroxybenzoic acid ( $pK_a$  2.83); (▲) 2,3-dimethoxybenzoic acid ( $pK_a$  3.53); (■) 2,4-dimethoxybenzoic acid ( $pK_a$  4.58).

between 30 000 and 40 000. They increase with increasing pH (and increasing  $\alpha$ ). At pH values where the acids are fully dissociated, about 140 000 plates are reached.

The experimentally found dependence of the plate number on  $\alpha$ , or pH, respectively, can be clearly seen from Figure 1, where the theoretical dependence of  $N$  on  $\alpha$  as given above, and the function of  $\alpha$  on pH, given by  $\alpha = 1/(1 + 10^{pK-pH})$ , is depicted by the dotted curves. The data points obtained experimentally are in excellent agreement with the theoretical curves, supporting again our basic presumption about the correlation of the plate number on the charge.

The validity of the relation between  $N$  and  $\alpha$  for the given experimental conditions can also be seen from the ratio  $N/\alpha$ , which should be 140 000. In fact, it can be seen from Table III that for all acids and all pH values this requirement is fulfilled.

Therefore it can be concluded, that under the limitations mentioned in the Introduction, the peak dispersion in capillary zone electrophoresis without electroosmotic flow depends

solely on, besides external parameters like temperature and voltage, the effective charge as the single individual property, but not on the diffusion coefficient or ionic mobility, although it is diffusion controlled.

This result is also important for the interpretation of the zone electropherograms, observed from nucleotides or proteins in gel-filled capillaries, where no electroosmosis occurs, too. Oligo- and polynucleotides, e.g., are separated according to their base number and are eluted with increasing charge number. Thus, it can be predicted from eq 9 that the plate number increases within the homologous series of the oligonucleotides. For a 100 mer, plate numbers in the order of 10 millions or more can therefore be reached theoretically.

In fact, it can be seen from published electropherograms (e.g. see refs 11–13) that the peak widths (which are based on time) remain about constant. Since the migration velocity decreases with increasing base number, and therefore the velocity of the components through the detector also decreases, it follows that the peak widths, based on length, are decreasing with increasing base number. This means, that according to eq 2, the plate height also decreases. Therefore, according to our presumption, an "efficiency gradient" can be observed within such an electropherogram, which is caused by the properties of the analytes, due to their increasing charge number, and is at least qualitatively in accordance with eq 9. A quantitative description of this effect is given in ref 6.

#### LITERATURE CITED

- Giddings, J. C. *Sep. Sci.* **1989**, *4*, 181.
- Jorgenson, J. W.; Lukacs, K. D. *HRC & CC, J. High Resolut. Chromatogr. Chromatogr. Commun.* **1981**, *4*, 230.
- Bockris, J. O'M.; Reddy, A. K. N. *Modern Electrochemistry*; Plenum Press: NY, 1970.
- Giddings, J. C. *J. Chromatogr.* **1989**, *480*, 21.
- Schwer, Ch.; Kenndler, E. *Chromatographia*, submitted for publication.
- Kenndler, E.; Schwer, Ch. *J. Chromatogr.*, submitted for publication.
- Hjerten, S. *Chromatogr. Rev.* **1967**, *9*, 122.
- Kenndler, E. *Chromatographia* **1990**, *30*, 713.
- Schwer, Ch.; Kenndler, E. *Chromatographia* **1990**, *30*, 546.
- Sternberg, J. C. In *Extracolumn Effects to Chromatographic Band Broadening*; Giddings, J. C.; Keller, R. A., Eds.; Advances in Chromatography; Marcel Dekker: NY, 1986; Vol. 2, pp 205–270.
- Cohen, A. S.; Karger, B. L. *J. Chromatogr.* **1987**, *397*, 409.
- Yin, H.-F.; Lux, J. A.; Schomburg, G. *J. High Resolut. Chromatogr.* **1990**, *13*, 625.
- Guttman, A.; Cohen, A. S.; Heiger, D. N.; Karger, B. L. *Anal. Chem.* **1990**, *62*, 137.

RECEIVED for review March 19, 1991. Accepted July 18, 1991.

# Migration Behavior of Cationic Solutes in Micellar Electrokinetic Capillary Chromatography

Joost K. Strasters and Morteza G. Khaledi\*

Department of Chemistry, North Carolina State University, P.O. Box 8204, Raleigh, North Carolina 27695

A phenomenological approach is presented to describe the migration of cationic solutes in micellar electrokinetic capillary chromatography (MECC). The migration behavior of an organic base is complicated by the presence of an acid-base equilibrium, the ion-pairing formation between the conjugated acid of the base and the monomer surfactants, and the interactions of both the base and its conjugated acid with the micellar pseudophase. An equation was derived that allows the calculation of the migration factor of a cationic solute in MECC with anionic micelles. Two limiting cases were considered: first the cationic solute completely associates with the anionic surfactant (ion-pair formation constant,  $K_{ip}$ , approaches infinity), and therefore there is no free charged species in the solution; second, the  $K_{ip} = 0$  and the free conjugated acid,  $BH^+$  migrates in the aqueous bulk solvent at its own electrophoretic velocity. An estimate for the ion-pair formation constant between cationic solutes and free surfactant can be obtained by using the model.

## INTRODUCTION

Capillary zone electrophoresis (CZE) is a powerful technique for the separation of charged compounds (1). For simultaneous separation of mixtures of charged and uncharged solutes, however, micellar electrokinetic capillary chromatography (MECC) is the method of choice. The main incentive in using micelles in the buffer solutions of CZE has been to extend the capabilities of this technique to separate neutral compounds (2-4). Terabe et al. have presented a quantitative treatment of the migration behavior of uncharged solutes in MECC based on the assumption that the separation mechanism is due to differential partitioning into micelles. As a result, MECC has been treated as a chromatographic technique. Like chromatography, the term capacity factor,  $k'$ , has been used to describe the "retention" of solutes. However, we agree with an anonymous reviewer of this manuscript that the term "migration" is more representative of the process occurring in MECC. Accordingly, the term migration factor,  $k_m$ , is used. This quantity is linearly related to the micelle concentration (which is proportional to the phase ratio) and this linear relationship can be effectively used in the optimization of separation of uncharged solutes in MECC (4, 5). The migration behavior of ionizable solutes in MECC, however, is more complicated than those of the neutral compounds due to two reasons. Firstly, in addition to partitioning into (or association with) micelles and moving at the velocity of micelles, ionizable compounds possess their own electrophoretic mobility. Second, the involvement of additional chemical equilibria (acid-base, ion-pairing) would further add to the complexity of the system. As a result, the number of experimental parameters that influence the separation would be rather extensive, some examples being pH, surfactant type and concentration, buffer concentration and type, etc. These additional equilibria, if optimized effectively and efficiently, would provide the analyst with additional tools to manipulate the selectivity and thus enhance separation. Although both CZE and MECC have been extensively discussed in the lit-

erature (6-11), the focus of most reports has been on specific applications. The complexity of the system and the large number of parameters would require a systematic approach to optimization of MECC separations in order to achieve the best results with a minimum amount of experimental effort.

Consequently, there is a need for more general and systematic methodologies. However, before the general validity of such approaches can be judged, it is essential to determine if and how the migration behavior (and separation selectivity) of solutes is influenced by these parameters. It can be expected that the concentration of surfactant (micelles) and pH are two of the major parameters in this respect. Although a fundamental physical model is always to be preferred, a semiempirical or phenomenological model can be used to derive meaningful relationships between the parameters and the observed migration behavior.

In a previous paper the migration behavior of acidic solutes in MECC and CZE was reported (12). Several mathematical models were derived to relate the migration parameters (migration factor and mobility) with pH and micelle concentration. It was shown that the migration behavior of acidic solutes in CZE and MECC can be accurately predicted on the basis of a few initial experiments. An acidic solute in an MECC system can migrate through its association with micelles as well as due to the electrophoretic mobility of the dissociated acid. Therefore, in order to accurately calculate the migration factors of acidic compounds in MECC, it is important to consider and correct for the electrophoretic mobility of the dissociated form (12). Interestingly, it was found that the variation of the two migration parameters with pH, i.e. migration factor (representing the chromatographic aspect) and mobility (representing the electrophoretic aspect) can be quite different for various solutes (12).

Here we are concerned with the second set of charged solutes, i.e. cationic and basic compounds. It can be expected that the observed migration will be more difficult to describe. This is due to the electrostatic interaction between the free surfactant ions in the mobile phase and the cations, which introduces an additional equilibrium (ion-pairing formation) into the equations. The following section will give a theoretical derivation taking this effect into account. The derived model will be tested using a set of catecholamines.

## THEORY

The various equilibria playing a role in the migration of a cationic solute in MECC are depicted in Figure 1. First, there will be a dissociation of the solute in the aqueous phase, represented by the equilibrium constant  $K_b$ , which also explains the major influence of the pH on the observed migration (12):

$$K_b = K^{aq}_b / [OH^-] = [BH^+] / [B] \quad (1)$$

where  $K^{aq}_b$  represents the base constant.

Both the base, B, and its conjugate acid,  $BH^+$ , will partition into (or associate with) the micellar phase, each according to its own distribution coefficient,  $P^{m}_{BH^+}$  or  $P^m_B$ , respectively:

$$P^{m}_{BH^+} = [BH^+]_{mc} / [BH^+]_{aq} \quad (2)$$

$$P^m_B = [B]_{mc} / [B]_{aq} \quad (3)$$

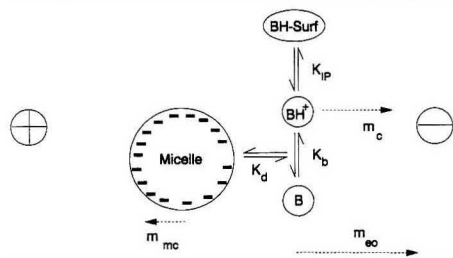


**Figure 1.** Schematic representation of the migration mechanism in the MECC of a cationic solute. Symbols are explained in the text.

Finally, there will be an interaction between the free ionized surfactant and the positively charged cations. This ion-pairing equilibrium is defined by the equilibrium constant  $K_{IP}$ . Since the concentration of free surfactant in micellar solutions is in first approximation constant and equal to the critical micelle concentration (cmc), we can define the constant  $K_I$ :

$$K_I = (\text{cmc})K_{IP} = [\text{BH}^+\text{S}^-]/[\text{BH}^+] \quad (4)$$

where  $[\text{BH}^+\text{S}^-]$  refers to the concentration of the surfactant-cation ion-pair.

As discussed in various publications (2, 12), the migration factor,  $k'$ , in MECC is expressed as the product of a distribution coefficient  $P_{mw}$ , relating the concentrations of the various species in the micellar and the aqueous phases and the phase ratio  $\Phi$ :

$$k' = P_{mw}\Phi = P_{mw}v([S] - \text{cmc}) \quad (5)$$

where  $v$  is the molar volume of micellar phase and  $[S]$  is the concentration of surfactant. In a similar fashion as described in ref 12, the following expression for  $P_{mw}$  can be derived. However, since the ion-pair complex is assumed to exist in the aqueous phase, the constant  $K_I$  will be introduced in the denominator:

$$P_{mw} = \frac{P_{\text{BH}^+\text{S}^-}K_b + P_{\text{B}}^m}{1 + K_b + K_I K_I} \quad (6)$$

Consequently, a linear relation between  $k'$  and the surfactant concentration will also be observed for cationic solutes (eq 5), with a pH dependence of  $P_{mw}$  due to  $K_b$ .

The following relations will define the relationship between the overall electrophoretic mobility of a cationic solute  $\mu$  (i.e. the observed migration corrected for the electroosmotic flow) and  $k'$ . Identical to the derivation presented in ref 12, the observed velocity of a solute will be a weighted sum of the velocities of the various species of the solute shown in Figure 1. The major difference with the anionic case is again the contribution of a fraction related to the ion-pair complex with a velocity equal to the velocity of the bulk aqueous phase. In addition, the observed velocity of the cationic solute in the absence of micelles cannot be used directly to derive the relation between the mobilities and the migration factor  $k'$ , since the added surfactant will also influence the overall velocity of the species in the aqueous phase. In this case it is more appropriate to derive the relation directly using the various fractions,  $\mu$ , and the electrophoretic mobility of the micellar phase  $\mu_{mc}$  and the electrophoretic mobility of the nonion-paired cationic species  $\mu_c$ . Rewriting the fractions in a similar fashion as presented in ref 12 results in the following equation:

$$\mu = \frac{K_b/(1 + K_b + K_b K_I)}{1 + k'} \mu_c + \frac{k'}{1 + k'} \mu_{mc} \quad (7)$$

Rewriting and solving for  $k'$  gives

$$k' = \frac{\mu - \left[ \frac{K_b}{1 + K_b + K_I K_I} \right] \mu_c}{\mu_{mc} - \mu} \quad (8)$$

$\mu_c$  can be related to the observed electrophoretic mobility in the absence of the micellar pseudophase,  $\mu_0$ :

$$\mu_c = \mu_0(1 + K_b)/K_b \quad (9)$$

Here the assumption was made that the electroosmotic flow is in first approximation independent of the surfactant concentration, which seems justified in view of earlier observations (12).

Combining eqs 8 and 9 finally results in

$$k' = \frac{\mu - \left[ \frac{1}{1 + K_I K_b/(1 + K_b)} \right] \mu_0}{\mu_{mc} - \mu} \quad (10)$$

In regard to eq 10 a number of observations are immediately apparent: (1) As in all calculations with respect to  $k'$  in MECC, this equation shows that  $k'$  will approach infinity if the observed relative mobility of the solute becomes equal to the mobility of the micelles, i.e. complete partitioning of all species of a solute into the micelles. This is directly linked with the limited migration range in MECC. (2) In the case of complete complexation of the cations with the surfactants (i.e.  $K_I$  approaches infinity), eq 10 will reduce to

$$k' = \frac{\mu}{\mu_{mc} - \mu} \quad (11)$$

which is identical to the relation derived for uncharged solutes (3, 12). This is in accordance with the expectations, since the cation-surfactant complex will not have an electrophoretic mobility of its own. (3) In the absence of complexation (i.e.  $K_I$  approaches zero) eq 10 reduces to

$$k' = \frac{\mu - \mu_0}{\mu_{mc} - \mu} \quad (12)$$

which is identical to the relation derived for anionic solutes (9, 12). The mobility is now completely defined by the mobility of the micellar phase and the mobility of the solute in the absence of micelles.

## EXPERIMENTAL SECTION

In order to examine the migration behavior of cationic solutes in MECC, a set of catecholamines and related substances was examined (Figure 2). The migration was measured at varying surfactant concentrations and voltages. In addition, the migration in the absence of the micellar phase was determined.

The CZE and MECC experiments were performed on a home-built system (after the description in ref 1), equipped with a 0-30-kV high-voltage power supply (series EH, Glassman High Voltage, Whitehouse Station, NJ) and a variable-wavelength UV detector (Linear Instruments, Reno, NV) operated at 254 nm. The capillary was 53  $\mu\text{m}$  i.d., 375  $\mu\text{m}$  o.d. (Polymicro Technologies, Phoenix, AZ). The total length measured 58 cm, and the detection was performed 44.5 cm downstream. The temperature of the capillary was controlled at 40  $^\circ\text{C}$  by jacketing in light mineral oil using a constant-temperature circulator bath (Type K2-R, Lauda, FRG). Data collection was performed by means of ChemResearch software (ISCO, Lincoln, NB) running on a Deskpro 286 (Compaq, TX).

For each new mobile phase, the capillary was flushed with a dilute solution of sodium hydroxide. After the capillary was filled with the new buffer, the system was allowed to stabilize for 30 min before starting the injections. The injections were performed by placing the upstream end of the capillary in the sample solution and raising this solution 5 cm for 20 s.

The MECC experiments were performed using solutions of 0.01, 0.02, 0.03, 0.04, and 0.05 M SDS in a phosphate buffer (pH 7, 0.05

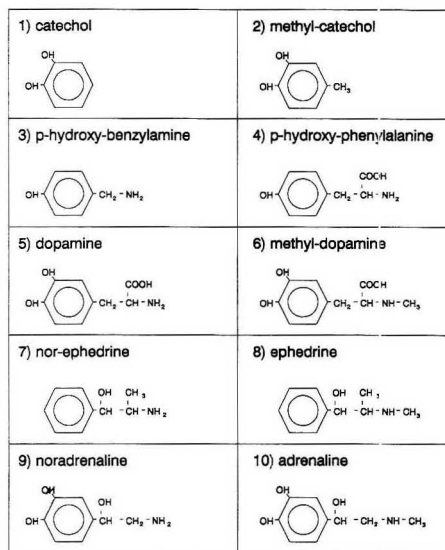


Figure 2. Examined set of catecholamines.

M ionic strength (in the absence of SDS), buffer capacity 0.005 at 25 °C). This (relatively low) pH was chosen because of a combination of good buffer capacity and more or less complete protonation of the weak bases. Before mixing, stock solutions of SDS and sodium monobasic phosphate (Fisher Scientific, Fair Lawn, NJ) were filtered over a 0.45- $\mu$ m filter. The sample solutions were prepared by diluting 20  $\mu$ L of stock solutions of the compounds (ca. 10 mg/mL in methanol) and 100  $\mu$ L of a saturated solution of Sudan III (in methanol) in 2 mL of the mobile phase. The disturbance in the baseline due to the methanol was used as the marker for the electroosmotic flow, while Sudan III was assumed to partition completely into the micellar pseudophase and was used as an indicator for the mobility of the micelle.

## RESULTS AND DISCUSSION

**CZE Experiments.** First, the migration of the cationic and neutral solutes were determined in the absence of a micellar pseudophase, i.e. in a series of CZE experiments. A subset of the data is displayed in Figure 3. In addition to the electrophoretic mobility, the relative mobility  $\mu'$ , relating the observed mobility to the electroosmotic mobility  $\mu_{eo}$  or the dead time  $t_0$ , is presented:

$$\mu' = \mu / \mu_{eo} = (t_0 / t) - 1 \quad (13)$$

Note however that all equations presented in the theoretical section can be derived using either relative or absolute mobilities. Catechol and methylcatechol are noncharged compounds, as can be determined both from the molecular structure (Figure 2) and a comparison of the migration of these compounds and the unretained compound methanol. As a consequence, both the mobility and relative mobility will be approximately 0. Cationic solutes like adrenaline and noradrenaline will be detected before methanol because the electrophoretic mobility will be directed toward the negative pole (defined as a positive electrophoretic mobility). By way of illustration, Figure 3 also includes the data of an anionic solute (2,4,5-trichlorophenol): since the electrophoretic mobility will be directed toward the positive pole, both  $\mu$  and  $\mu'$  will be negative.

Apparently, the amphoteric compounds *m*-dopamine and *p*-hydroxyphenylalanine are slightly charged at pH 7, since

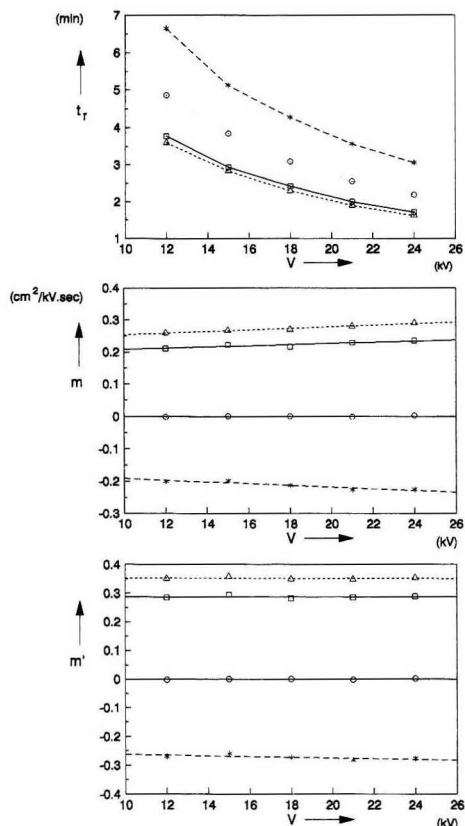


Figure 3. Observed migration  $t_r$ , mobility  $\mu$ , and relative mobility  $\mu'$  of a number of the catecholamines as a function of the voltage  $V$ . Displayed are the data related to the neutral solute methylcatechol (circle) and the cationic solutes adrenaline (square) and noradrenaline (triangle). For purposes of comparison, data related to an anionic solute, 2,4,5-trichlorophenol (asterisk), are included as well.

the mobility is only slightly smaller than 0, which is caused by a stronger dissociation of the carboxyl group as compared to the protonation of the amine group. Apart from the neutrals catechol and methylcatechol, the other compounds show cationic behavior due to the basic behavior of the amine group.

Theoretically, the calculated mobilities should be independent of the applied voltage. However, when the voltage over the capillary is varied, the current will change and the Joules heating will increase. This increase in temperature can result in a slight dependence of the mobility on the voltage as can be seen in Figure 3b (middle). However, since this phenomenon influences both the electrophoretic mobilities of the solutes and the electroosmotic flow in a more or less equal measure, the resulting relative mobility will be more stable (Figure 3c) (bottom). On the other hand, since  $\mu'$  is a result of a comparison of two measurements, the experimental error will increase and the scatter around an average value will be slightly more pronounced than the variation in  $\mu$  after correction for the linear dependence with  $V$ .

**MECC Experiments.** More scatter is observed, when the observed migration of the micelles, indicated by  $t_{me}$ , and the

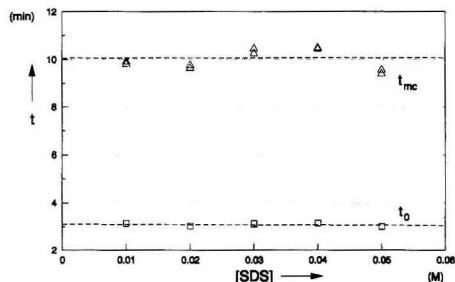


Figure 4. Observed migration times of the markers for the electroosmotic flow, methanol ( $t_0$ ), and for the micellar pseudophase, Sudan III ( $t_{mc}$ ), at various surfactant concentrations [SDS].

electroosmotic flow are compared with varying surfactant concentration at a fixed voltage (18 kV). These values are displayed in Figure 4. A clear trend could not be observed, indicating that the variation was a result of irreproducible changes in the characteristics of the capillary. These variations could not be avoided, despite a rigorous rinsing procedure indicated in the Experimental Section. This variation is partly compensated for in the calculation of the relative mobility, resulting in a more stable value of  $\mu'_{mc}$ : the relative standard deviation in  $t_0$  was 2.2%,  $t_{mc}$  4.1%, and  $\mu'_{mc}$  1.1%. A slight systematic variation might also be introduced in the calculated migration factors due to an increase in the current (and consequently in the Joule heating) with an increase in the surfactant concentration. However, the observed linearity in previous experiments (12) shows that this contribution can be neglected in a first approximation, indicating that the jacketing of the column is quite efficient.

Since migration factors represent a partition mechanism, a stronger dependence on temperature, and consequently on the voltage and current, can be expected (3). The results obtained at 18 kV were used to examine the proposed models. The plausibility of eqs 10–12 (and therefore the calculated  $k'$  values) can be demonstrated by examining the relationship indicated in eq 5: a plot of the  $k'$  values calculated using the appropriate equation, (10), (11), or (12), vs the surfactant concentration should result in a linear function in order for the relation to be a valid alternative. In addition, as shown by eq 5 and discussed earlier in refs 3 and 12, a linear regression of  $k'$  vs the surfactant concentration will result in values for the critical micelle concentration cmc (intersection with the x axis) and the distribution coefficient  $P_{mw}$  (assuming a molar volume of the micellar phase of 0.251 L/mol). A comparison between the calculated and expected value for the cmc can be used to further examine the plausibility of the proposed equations.

In a further analysis of the data, a distinction was made between four types of components. The calculated  $k'$  values for the first two groups, the neutrals (catechol and methylcatechol) and the anionics (*p*-hydroxyphenylalanine and methyl-dopamine), are displayed in Figure 5.

The  $k'$  of the neutrals was calculated using eq 11 (absence of electrophoretic mobility of the solutes in the aqueous phase). In this case values of 4.3 mM (catechol) and 4.0 mM (methylcatechol) were obtained for the cmc, which corresponds relatively well with values obtained experimentally by means of conductivity experiments. These values are lower than the literature value of 8 mM, which can be explained by the presence of the buffer system and consequently a higher ionic strength as well as the higher operating temperature in this study. The two components show some interaction with the micellar phase ( $P_{mw} = 28$  and 68 for catechol and methyl-

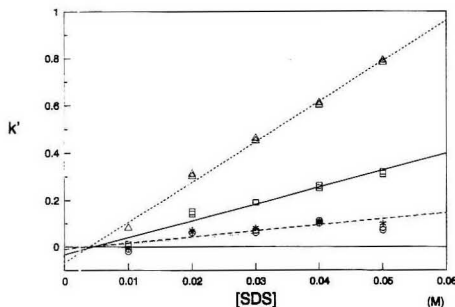


Figure 5. Migration factors  $k'$  calculated for catechol (square) and methylcatechol (triangle) using eq 11, and *p*-hydroxyphenylalanine (circle) and methyl-dopamine (asterisk) using eq 12 as a function of the surfactant concentration [SDS].

Table I. Critical Micelle Concentration and Distribution Ratio  $P_{mw}$  Values Derived from eqs 11 and 12

compd	cmc, (mM)	$P_{mw}$	eq
catechol	4.3	28	11
methylcatechol	4.0	68	11
<i>p</i> -hydroxyphenylalanine	4.2	9.0	12
methyl-dopamine	3.8	11	12
dopamine	3.7	520	11
<i>p</i> -hydroxybenzylamine	3.7	280	11
norephedrine	3.1	2200	11
ephedrine	1.3	2800	11
noradrenaline	9.2	110	11
noradrenaline	-1.6	150	12
adrenaline	5.1	180	11
adrenaline	-1.7	260	12

catechol, respectively) where the hydrophobic contribution of the methyl group is apparent from the increase in the  $P_{mw}$  value (Table I).

The  $k'$  values of the two anionic solutes were calculated using eq 12, to correct for the (slight) electrophoretic mobility of the ions in the aqueous phase. If this correction is not taken into consideration, the calculated values for the cmc are -4.7 and 1.7 mM for *p*-hydroxyphenylalanine and methyl-dopamine, respectively. Table I contains the values resulting from eq 12: 4.2 and 3.8 mM. However, due to the minor interaction between the two components and the micellar phase ( $P_{mw}$ 's of 9 and 11 respectively) the calculated intersection points have a larger uncertainty than those of the neutral solutes.

The  $k'$  values of a third set of compounds, dopamine, *p*-hydroxybenzylamine, norephedrine, and ephedrine were calculated using eq 11, i.e. by assuming a full complexation of the solutes in the aqueous phase with free surfactant molecules. In other words, it is assumed that the migration behavior follows the behavior observed for uncharged solutes. The corresponding regression lines are shown in Figure 6 for three of the components in the top frame. Both norephedrine and ephedrine (not shown) show a very strong interaction with the micellar phase ( $P_{mw} = 2200$  and 2800 respectively), due to a combination of the electrostatic interaction of a positively charged amine group with the negatively charged surfactant head groups and the hydrophobic contribution of the additional methyl group. In addition the peak shapes were very poor for these two compounds, especially at higher surfactant concentrations. The combination of this poor peak shape and the fact that the observed migration is very close to the migration of the micellar phase introduces a larger amount of uncertainty in the regression, although the cmc value calculated on the basis of norephedrine is still fairly close to the



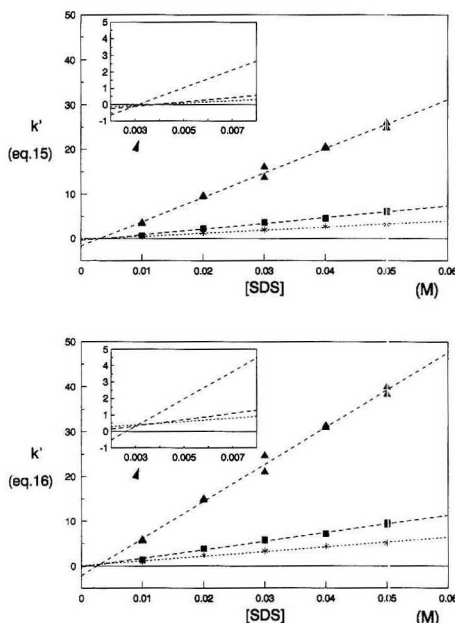


**Figure 6.** Migration factors  $k'$  calculated for dopamine (square), *p*-hydroxybenzylamine (asterisk), and norephedrine (triangle) using eq 11 (upper frame) or eq 12 (lower frame) as a function of the surfactant concentration [SDS]. The area of intersection with the  $x$  axis is shown further enlarged in the upper left corner of the frames.

values related to the other components.

When eq 12 is applied to calculate the migration factor, i.e. when it is assumed that there is no ion-pair formation between the cations and the anionic surfactant, the calculated cmc will deviate from the value observed for the neutral compounds. Since the second term in the numerator is negative (positive electrophoretic mobility of cations), the combination with the observed negative mobility of the solutes in the MECC experiments will result in higher values of  $k'$ , and consequently lower values of cmc (Figure 6, lower frame). The intersections with the  $x$  axis no longer coincide (1.3, -0.8, and 2.5 mM for dopamine, *p*-hydroxybenzylamine, and nor-ephedrine, respectively). The conclusion is that it is not possible to show the occurrence of free cationic solutes in the aqueous phase (as opposed to cations in ion pairs with the surfactant) and that the model based on the assumption of a strong interaction resulting in neutral behavior in the aqueous phase should be used to describe the migration factors for these solutes.

Finally, the  $k'$  values for the two remaining compounds in the test set, i.e. noradrenaline and adrenaline, were calculated according to the two limiting cases described by eqs 11 and 12, i.e. complete ion-pair formation or absence of ion-pair formation. Although a slight curvature can be observed in the data, which is not accounted for in the model relating the surfactant concentration and the migration factor, the behavior could be approximated by a linear relation, as shown in the Figure 7.

The top frame of Figure 7 refer to the situation where complete ion-pair formation is assumed (eq 11). The intersection with the  $x$  axis is higher than the values observed for the neutral solutes, especially for noradrenaline (cmc = 9.2 and 5.1 mM for noradrenaline and adrenaline respectively). This is due to the fact that the observed mobility is considered

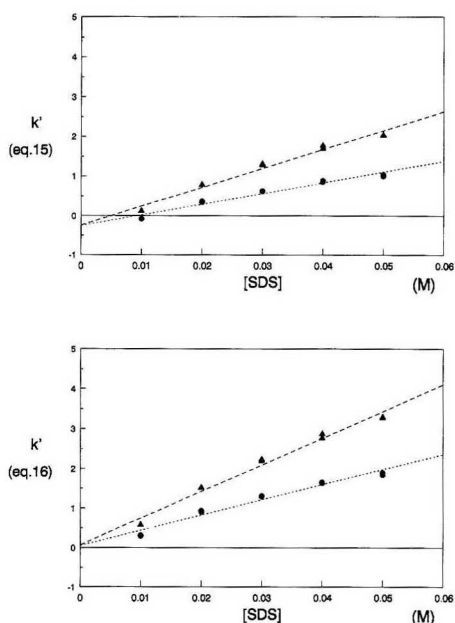


**Figure 7.** Migration factors  $k'$  calculated for noradrenaline (circle) and adrenaline (triangle) using eq 11 (upper frame) or eq 12 (lower frame) as a function of the surfactant concentration [SDS].

to be fully related to the interaction of the solutes with the micellar phase. However, at low surfactant concentrations, the observed migration time for noradrenaline is lower than  $t_0$ ; hence at least a fraction of the solute retains some of its own electrophoretic mobility.

However, if the analysis is performed assuming no ion-pair formation (eq 12, lower frame Figure 7), the calculated cmc values are too low (-1.6 and -1.7 mM for noradrenaline and adrenaline, respectively, values without physical meaning). If no ion-pair formation is taking place, lower migration values should be observed; hence some interaction between the cations and the free surfactant is taking place.

By application of eq 10, an estimate of this interaction can be obtained: by a variation of the factor  $1/(1 + K_p K_I / (K_b + 1))$  the results of the regression can be varied between the two extremes shown in Figure 7. When full dissociation of the solutes is assumed (a reasonable assumption at pH 7 for these catechol amines), this factor reduces to  $1/(K_I + 1)$ , which enables estimation of  $K_{IP}$ , the ion-pair formation constant as defined in eq 4. Under the assumption that correct value of cmc is approximately 4.15 mM (average of the values obtained with the neutral solutes), the ion-pair formation constant  $K_{IP}$  was estimated to be  $380 \text{ M}^{-1}$  for noradrenaline and  $2000 \text{ M}^{-1}$  for adrenaline.

## CONCLUSION

Although experimental errors in the migration times of the catecholamines, especially those showing a very strong interaction with the micellar pseudophase, introduce some variation in the data, the above discussion has shown the plausibility of the equations presented in the theoretical section.

For most cationic solutes, the behavior can be expressed by means of equations used to calculate the migration factor of neutral solutes. As a consequence the determined distri-

bution coefficients are related to the distribution of the ion pairs between the aqueous phase and the micellar pseudo-phase.

However, for two catecholamines in the examined set of cationic compounds it was shown that some fraction in the aqueous phase was not directly associated with the free surfactant ions, resulting in a slight electrophoretic mobility of the solute in the aqueous phase. By means of the presented equations it is possible to obtain an estimate of the ion-pair formation constant of these solutes under the assumption that the solutes were fully dissociated at the examined pH. A full evaluation of eq 10 will require a set of experiments at various pH values and a comparison of the resulting correction factors. A study is presently underway in this laboratory to examine the effect of different important parameters on selectivity of acidic and basic compounds.

In summary, it is possible to describe the observed migration and migration factors of solutes in MECC experiments with more or less linear relationships (eq 5), even in the case of charged (anionic or cationic) solutes, which reduces the number of experiments required in the method development stage.

## High-Speed Countercurrent Chromatography Used for Alkylbenzene Liquid-Liquid Partition Coefficient Determination

Alain Berthod\* and Madeleine Bully

Laboratoire des Sciences Analytiques, UA CNRS 435, Université de Lyon 1, 69622 Villeurbanne Cedex, France

Countercurrent chromatography (CCC) can be used to determine liquid-liquid partition coefficients. A hydrodynamic CCC apparatus was used to obtain methanol-water-heptane partition coefficients,  $P$ , of the homologous series of  $n$ -alkylbenzene from benzene to dodecylbenzene. The methanol-water compositions ranged from pure methanol to methanol 80%–water 20% v/v. They were used as liquid stationary phases. Heptane was the mobile phase. The partition coefficients ranged from  $8 \times 10^{-4}$  to 0.95, corresponding to heptane-methanol partition coefficients ranging from 1.05 to 1250. For every methanol-water stationary phase, the linear plots of  $\log P$  versus the atom carbon number,  $n_C$ , produced the free energy of transfer,  $\Delta G^\circ$ , for the methylene incremental group and the phenyl terminal group. Both  $\Delta G^\circ$  energies increased linearly with the water molar fraction which allowed development of an equation giving the methanol-heptane  $P$  value of an alkylbenzene ( $n_C \leq 12$ ) with water content  $\leq 20\%$  v/v.

Since the early Craig apparatus (1) for continuous extraction, countercurrent chromatography (CCC) was developed by Ito (2-4). Ito introduced high-speed CCC which allows separations within a few hours when classical CCC separations may need days (5). Today, high-speed CCC is moving from research laboratories to industrial laboratories (6).

CCC uses two nonmiscible liquid phases: one is the mobile phase, the other one is the stationary phase (3-7). The CCC column is most often a continuous open tube coiled on a centrifuge rotor. The centrifugal field is used to hold tightly

### ACKNOWLEDGMENT

We thank C. Quang for his assistance in performing some of the experiments.

### LITERATURE CITED

- (1) Jorgenson, J. W.; Lukacs, K. D. *Anal. Chem.* **1981**, *53*, 1298.
- (2) Terabe, S.; Otsuka, K.; Ichikawa, K.; Ando, T. *Anal. Chem.* **1984**, *56*, 111.
- (3) Terabe, S.; Otsuka, K.; Ando, T. *Anal. Chem.* **1985**, *57*, 834.
- (4) Foley, J. P. *Anal. Chem.* **1990**, *62*, 1302.
- (5) Ghowsi, K.; Foley, J. P.; Gale, R. J. *Anal. Chem.* **1990**, *62*, 2714.
- (6) Ewing, A. G.; Wallingford, R. A.; Olefirowicz, T. M. *Anal. Chem.* **1989**, *61*, 292A.
- (7) McCormick, R. M. *Anal. Chem.* **1988**, *60*, 2322.
- (8) Snopek, J.; Jelinek, I.; Smolkova-Keulemansova, E. *J. Chromatogr.* **1988**, *452*, 571.
- (9) Otsuka, K.; Terabe, S.; Ando, T. *J. Chromatogr.* **1985**, *348*, 39-47.
- (10) Cohen, A. S.; Terabe, S.; Smith, J. A.; Karger, B. L. *Anal. Chem.* **1987**, *59*, 1021.
- (11) Wallingford, R. A.; Ewing, A. G. *Anal. Chem.* **1988**, *60*, 258.
- (12) Khaleidi, M. G.; Smith, S. C.; Strasters, J. K. *Anal. Chem.* **1991**, *63*, 1820.

RECEIVED for review April 24, 1991. Revised manuscript received August 5, 1991. Accepted August 8, 1991. We gratefully acknowledge a research grant from the National Institutes of Health (FIRST Award, GM 38738).

the liquid stationary phase. CCC is mainly used in preparative separation and purification of samples.

The basic retention equation is (5, 6, 7)

$$V_R = V_o + PV_s \quad (1)$$

Unlike in HPLC, in CCC the total internal volume,  $V_T$ , can be used for partition process (5)

$$V_T = V_o + V_s \quad (2)$$

Equation 1 can be rewritten as

$$V_R = V_T + (P - 1)V_s \quad (3)$$

$V_o$ ,  $V_R$ ,  $V_T$ , and  $V_s$  are respectively the mobile phase volume, the solute retention volume, the internal volume of the apparatus, and the liquid stationary-phase volume inside the apparatus.  $P$  is the solute partition coefficient, i.e. the ratio of the solute concentration in the stationary phase to the solute concentration in the mobile phase. The retention volume,  $V_R$ , of a solute allows determination of its partition coefficient,  $P$ , in the biphasic liquid system used in the CCC apparatus.

Partition coefficient determination is a critical measurement in quantitative structure-activity relationship (QSAR) studies. The classical shake-flask method for  $P$  measurements has a tedious procedure including accurate weighing, dissolution of the compound in one phase,  $\sim 0.5$ -h shaking, centrifugation for several hours to separate the two liquid phases, and spectrophotometric analysis of both phases (8). It is critical to have a highly pure compound. CCC is able to produce reliable  $P$  values in a shorter time and with an easier operation that can separate impurities from the compound of interest during the run. Liquid chromatography on columns was used to obtain  $P$  values from capacity factors,  $k'$  (8). Linear regressions are used to correlate both  $\log k'$  and  $\log P$  param-

eters. The regression coefficients are significant. However, for a given compound, the log  $P$  value obtained from the log  $k'$  value of the compound can be off by 0.3 unit or more. The estimated  $P$  value can be 2 times higher or lower than the actual  $P$  value. CCC is better than HPLC since the partition coefficients are obtained with no approximation. The same two liquids used in the shake-flask method are also used in the CCC apparatus. For this reason, CCC is a promising technique for liquid-liquid partition coefficient determination.

Octanol-water partition coefficients,  $P_{\text{oct}}$  were measured directly by CCC over the range  $-2 < \log P_{\text{oct}} < 2.5$  (9). Hexane was added to octanol to decrease the viscosity. The partition coefficients, obtained by CCC with octanol-hexane-water biphasic mixtures, correlated well with the  $P_{\text{oct}}$  literature values (9, 10). Several technical improvements were used to extent the measurable  $P_{\text{oct}}$  range: use of an octanol mobile phase instead of a water mobile phase (11), dual-mode or back-flushing (12, 13), cocurrent mode in which both the mobile and the stationary phase move at different speeds (14), and use of modified apparatus (15).

CCC can measure liquid-liquid partition coefficients in any biphasic liquid system (4, 5, 6, 16). The goal of this work is to show that CCC can be used to measure accurately the liquid-liquid partition coefficients of the homologous series of  $n$ -alkylbenzenes, from benzene to dodecylbenzene, in the ternary biphasic liquid system heptane-methanol-water. The  $n$ -alkylbenzene homologous series is widely used in liquid chromatography to obtain information on solute-stationary-phase interaction and the structure-retention relationship (17-20). The heptane-methanol-water partition coefficients of alkylbenzenes, which are not found in the literature, could be useful in structure-retention studies with identical methanol-water mobile phases.

## EXPERIMENTAL SECTION

**Chemicals.** Benzene, toluene, ethylbenzene, butylbenzene, hexylbenzene, and dodecylbenzene were obtained from Merck, Shuchardt, Germany, and Aldrich, Steinheim, Germany. Methanol and heptane were obtained from Prolabo, Rhône-Poulenc, France. Heptane was used instead of hexane because its toxicity is lower. Water was deionized and distilled before use.

**Countercurrent Chromatograph.** The CCC apparatus was the Model CPHV 2000 from Société Française de Chromatologie (SFC), 93360 Neuilly-Plaisance, France. It is a coil planet centrifuge apparatus first designed by Ito (4). It contains three multilayer coils connected in series and spinning with a planetary motion around a central axis. The original design described by Ito contained 10 gears (21). It was simplified to obtain a similar motion with only 7 gears. Figure 1 shows the gear arrangement used to produce the planetary motion of the three spools without rotating seals. Each spool bears a gear (dotted) that meshes into the central stationary gear (hatched). The connecting tubing is twisted by the spool rotation. It is unwinded passing through the antitwisting connector that rotates in the opposite way (open gear). With such a gear arrangement, if the rotor makes one full rotation, each coiled spool makes two rotations. All rotation speeds given in the text correspond to rotor rotation.

Each spool was filled with 133 turns of PTFE tubing, i.d.  $\frac{5}{8}$  in. (1.6 mm), length 29 m, coiled in 7 layers of 19 turns. The Ito  $\beta$  value is the ratio of the coil radius,  $r$ , to the spool revolution radius,  $R$ . The  $\beta$  ratio was 0.37 for the inner first layer with  $r = 2.2$  cm and  $R = 6$  cm. It was 0.75 for the most outer visible layer with  $r = 4.5$  cm and  $R = 6$  cm. The average  $\beta$  value for this CCC apparatus was 0.56. The internal volume of one coiled spool was 58 mL. The three-coil apparatus had a total internal volume,  $V_T$ , of 175 mL. The total PTFE tube length was 87 m, with a total of 400 turns. The whole system was housed in an air-thermostated box. The temperature was regulated at  $22 \pm 0.5$  °C.

**Chromatograph Preparation.** The heptane-methanol-water system is a normal biphasic system. It means that the best stationary-phase retention in a CCC apparatus is obtained when the lighter mobile phase (heptane) is pushed through the denser

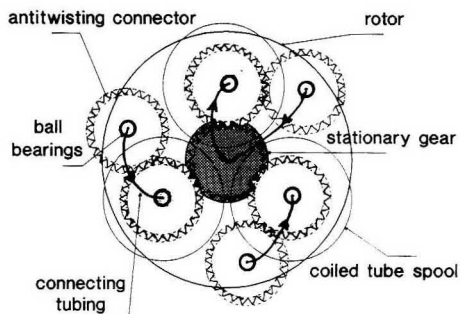


**Figure 1.** CCC three-coil gear arrangement. The seven gears are one central stationary gear (hatched), three gears coupled to the spool (dotted), and three gears used to unwind the connecting tube (open). The arrows indicate the mobile-phase motion when entering through the head of the apparatus.

stationary phase (methanol phase) entering through the tail of the apparatus (3-6).

The apparatus is first filled with the heptane-saturated methanol phase using a Model LC 6A Shimadzu pump. This takes about 25 min at a 8 mL/min flow rate. Then, the rotor is started and the rotation allowed to stabilize at the desired speed. The heptane phase is pushed through the methanol phase at the working flow rate of 2 mL/min, unless otherwise indicated, entering through the tail of the apparatus.

As long as the apparatus is not equilibrated, the methanol phase is pushed off, exiting by the head of the apparatus. The methanol phase displaced by the heptane phase is collected in a graduated cylinder. Once the heptane phase appears at the apparatus head, two liquid layers are seen in the graduated cylinder. The mobile-phase-stationary-phase equilibrium is reached. The CCC "column" is ready. The displaced methanol phase is measured. The volume is  $V_0$  (eq 1). The mixture of alkylbenzenes solubilized in heptane can be injected using an in-line Rheodyne 7125 valve with a 300- $\mu$ L sample loop. At a flow rate of 2 mL/min, the working pressure was always lower than 1 kg/cm<sup>2</sup> (<14 psi). Depending on the liquid system, it takes about 1 h to elute benzene, the most retained solute.

**Detection.** It was not possible to monitor continuously the heptane effluent. Microdroplets of the methanol stationary phase were always present in the heptane mobile phase producing a random turbidity and a large noise in UV detection. The stationary-phase carryover or "bleeding" was estimated to range between 1  $\mu$ L/min (methanol 80%-water 20% v/v stationary phase) to about 10  $\mu$ L/min (100% methanol stationary phase) at 1000 rpm rotation speed and 2 mL/min heptane flow rate. To stabilize the signal obtained with a Model SPD 6A Shimadzu UV detector, it was necessary to add 2-propanol as a postcolumn clarifying agent. A second pump was used to add 2-propanol at a flow rate of 0.2 mL/min (or 10% of the CCC flow rate) through a "T" and a 150- $\mu$ L mixing reactor made of 50 cm of 0.6 mm i.d. knitted Teflon tube. This arrangement allowed one to obtain a stable continuous UV detection at 254 nm without adding too much pressure in the CCC apparatus and with minimizing the extracolumn band-broadening.

**Partition Coefficient Determination.** The displaced methanol phase corresponded to  $V_0$ . The stationary phase volume,  $V_s$ , can be calculated as  $V_s = V_T - V_0$  (eq 2) (5-7). Equations 1 and 3 show that the retention volume,  $V_R$ , allows one to obtain the partition coefficient,  $P$

$$P = (V_R - V_0) / V_s = [(V_R - V_T) / V_s] + 1 \quad (4)$$

## RESULTS AND DISCUSSION

The phase diagram of the heptane-methanol-water system was recently published by Conway (6). The advantage of this system is that the heptane phase equilibrated with any methanol-water mixture contains a trace amount of methanol (less than 0.1%) and practically no water. The methanol

**Table I. Retention Volume and Partition Coefficients of Alkylbenzenes in Heptane-Methanol-Water Systems**

		methanol-water stationary phase, v/v						
		pure methanol	99-1	97-3	95-5	90-10	85-15	80-20
benzene	$V_R$	172.5	162	128.3	113	97	67.2	53
	$P$	0.95	0.89	0.68	0.58	0.49	0.30	0.22
toluene	$V_R$	163.5	138	106	87.5	71.8	49.2	38.3
	$P$	0.76	0.70	0.52	0.40	0.33	0.19	0.13
ethylbenzene	$V_R$	158.5	125	90.8	74	59.5	40.2	31.5
	$P$	0.66	0.59	0.415	0.31	0.25	0.13	0.087
butylbenzene	$V_R$	149	101.5	69	54	40.4	28.9	22.5
	$P$	0.46	0.39	0.26	0.175	0.13	0.056	0.030
hexylbenzene	$V_R$	142.5	85.5	55	43	30.9	24.2	20
	$P$	0.325	0.26	0.17	0.10	0.064	0.025	0.013
dodecylbenzene	$V_R$	132.5	64	37	31	22.6	20.6	18
	$P$	0.11	0.080	0.042	0.18	0.0083	0.0021	0.0008
$V_o$ , mL		127	54	31	28	21	20.3	17.9
$V_a$ , mL		48	121	144	147	154	154.7	157.1
retention, %		27	68	82	84	88	88.5	90

<sup>a</sup> All methanol-water stationary phases were saturated in heptane. Conditions: temperatures;  $22 \pm 0.5$  °C; rotation speed, 1000 rpm; flow rate, 2 mL/min heptane entering tail. The  $P$  values are the methanol-heptane partition coefficients; the heptane-methanol partition coefficients are the inverse.

**Table II. Slopes and Intercepts of the log  $P$  versus  $n_C$  Plots<sup>a</sup>**

mobile phase, vol %		$\chi$	slope	intercept	$r^2$	$\Delta G^\circ_\phi$ , kJ/mol	$\Delta G^\circ_{CH_2}$ , kJ/mol
methanol	water						
100	0	0	-0.0075	-0.018	0.998	-0.10	-0.43
99	1	0.022	-0.087	-0.058	0.997	-0.33	-0.50
97	3	0.065	-0.10	-0.180	0.999	-1.00	-0.57
95	5	0.106	-0.123	-0.257	0.999	-1.46	-0.70
90	10	0.200	-0.148	-0.307	0.999	-1.74	-0.85
85	15	0.284	-0.177	-0.535	0.999	-3.04	-1.00
80	20	0.360	-0.200	-0.660	0.999	-3.75	-1.14

<sup>a</sup> Temperature  $22 \pm 0.5$  °C.

phase contains the whole water volume and amounts of heptane decreasing dramatically with increasing water concentration. The methanol phase of the mixture pure methanol-heptane contains 30% heptane in volume at 22 °C (6). There is only 1.5% v/v heptane in the methanol phase of the system methanol 80%-water 20% v/v equilibrated with heptane.

The retention study of members of homologous series is commonly used in liquid chromatography to obtain information on solute-stationary-phase interactions (17-20). The capacity factor,  $k'$

$$k' = (V_R - V_o) / V_o = PV_s / V_o \quad (5)$$

is related to the solute free energy of retention,  $\Delta G^\circ$ , by (17, 19)

$$\ln k' = \Delta G^\circ / RT + \ln V_s / V_o \quad (6)$$

For members of a homologous series of solutes, eq 6 can be written as

$$\ln k' = \ln P + \ln V_s / V_o = \Delta G^\circ_\phi / RT + n_C \Delta G^\circ_{CH_2} / RT + \ln V_s / V_o \quad (7)$$

where the subscripts  $\phi$  and  $CH_2$  refer to the retention energy contribution of the end group (phenyl) and the incremental methylene group, respectively, and  $n_C$  is the number of methylene groups. Equation 7 gives

$$RT \ln P = n_C \Delta G^\circ_{CH_2} + \Delta G^\circ_\phi \quad (8)$$

**Alkylbenzene Partition Coefficients.** Table I lists the retention volumes and the corresponding methanol-heptane partition coefficients obtained for six alkylbenzenes and seven different methanol-water compositions. The listed values

**Table III. Slopes and Intercepts of log  $P$  versus Water Molar Fraction Plots<sup>a</sup>**

$\Delta C^\circ_{CH_2}$ $\Delta C^\circ_\phi$	slope		intercept		$r^2$
	A	B	C	D	
	-1.93	-0.45	-9.7	-0.19	0.994
					0.975
compd	slope		intercept		$r^2$
	exp	calc	exp	calc	
benzene	-1.7	-1.70	-0.029	-0.033	0.982
toluene	-2.1	-2.05	-0.13	-0.113	0.987
ethylbenzene	-2.4	-2.39	-0.20	-0.192	0.984
butylbenzene	-3.2	-3.07	-0.35	-0.350	0.988
hexylbenzene	-3.8	-3.77	-0.52	-0.509	0.991
dodecylbenzene	-5.8	-5.79	-1.00	-0.984	0.991

<sup>a</sup> The A, B, C, and D terms are used in eq 11. Equations 12 and 13 were used to obtain calculated slopes and intercepts.

corresponded to the first chromatogram obtained after a chromatograph preparation with a liquid system freshly prepared (see Experimental Section). Further chromatograms were obtained with the same "column". A slight increase in retention volumes due to the  $\mu$ L/min stationary phase carryover was always observed. However, the partition coefficients, obtained through eq 4 with the correct  $V_s$  value, were very reproducible (relative standard deviation 0.01).

The methanol-heptane partition coefficients range from  $8 \times 10^{-4}$  (dodecylbenzene and methanol 80%-water 20% v/v) to 0.95 (benzene and pure methanol phase, Table I). This corresponds to heptane-methanol partition coefficients ranging from 1.05 to 1250. The values of log  $P$  were plotted versus  $n_C$  according to eq 8. The excellent linearity of the resulting curves (regression coefficient higher than 0.997)

allowed the calculation and significant comparison of the  $\Delta G^{\circ}_{\text{CH}_2}$  and  $\Delta G^{\circ}_{\phi}$  (Table II).

Both the  $\Delta G^{\circ}_{\phi}$  values decreased linearly with the water molar fraction,  $\chi$  (Table III). The  $\Delta G^{\circ}_{\phi}$  slope was about 5 times higher than the  $\Delta G^{\circ}_{\text{CH}_2}$  slope. In the methanol-rich compositions of the heptane-methanol-water system, the hydrophobic contribution of the phenyl group of the alkylbenzene series roughly corresponded to five methylene groups (8).

The experiments showed that

$$\Delta G^{\circ}_{\text{CH}_2} = A\chi + B \quad (9)$$

$$\Delta G^{\circ}_{\phi} = C\chi + D \quad (10)$$

Combining eqs 8-10 yields

$$2.3RT \log P = (An_C + C)\chi + Bn_C + D \quad (11)$$

The log  $P$  value shall decrease linearly with the stationary-phase water content. Table III lists the slopes, intercepts, and regression coefficients of the log  $P$  versus  $\chi$  plots. The theoretical values

$$\text{slope} = (An_C + C)/2.3RT \quad (12)$$

$$\text{intercept} = (Bn_C + D)/2.3RT \quad (13)$$

are listed for comparison. The agreement is satisfactory.

It was previously reported for other compounds and differing liquid systems that log  $P$  could decrease linearly with the water molar fraction,  $\chi$  (6). However, this is not a general behavior. Most often the log  $P$  versus  $\chi$  plots present curvatures difficult to predict (6, 8, 22). In the heptane-methanol-water system, the partition coefficient,  $P$ , of members of the alkylbenzene series with  $n_C \leq 12$ , can be accurately predicted in methanol-rich composition ( $\chi \leq 36\%$ ) using eq 11 with the  $A$ ,  $B$ ,  $C$ , and  $D$  terms listed in Table III.

**CCC and Partition Coefficients.** *Precision of the Method.* The absolute error on CCC determination of partition coefficients is estimated by differentiating eq 4

$$dP = (\delta P/\delta V_R) dV_R + (\delta P/\delta V_S) dV_S \quad (14)$$

which produced, using eqs 1-3

$$\Delta P = \Delta V_R/V_S + P\Delta V_S/V_S + \Delta V_S/V_S \quad (15)$$

The relative error is

$$\Delta P/P = (\Delta V_R + \Delta V_S)/PV_S + \Delta V_S/V_S \quad (16)$$

Equation 16 shows that small partition coefficients are measured with a large error. The solute is little retained. It is difficult to determine the difference between the peak solute and the dead volume. We have shown that the minimum  $P$  value measurable with a given relative error depends on the stationary-phase volume (23). With a relative error of  $\pm 10\%$  and a stationary phase volume of 150 mL, the minimum  $P$  value was 0.003. The lowest accuracy for partition coefficients listed in Table I was obtained with dodecylbenzene.

The relative error on CCC partition coefficient determination critically depends on the stationary-phase volume,  $V_S$ . For example a 1% relative error on the stationary-phase volume,  $\Delta V_S/V_S$ , increases the relative error on  $P$  by the same amount (eq 16). So, it is essential to have a correct knowledge of  $V_S$ . In this work, we minimized the error on  $V_S$  by making the  $P$  measurements with newly equilibrated "columns". Since there is always a slight stationary-phase carryover, the  $V_R$  and  $V_0$  volumes change with time. However, the partition coefficient of a solute is a physicochemical parameter that does not depend on the  $V_R$  or  $V_0$  CCC volumes. A good method to know exactly the  $V_R$  and  $V_0$  volumes is to add to the injected solution a "tracer", which is a solute whose partition coefficient

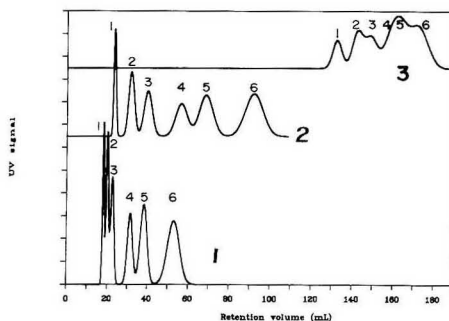


**Figure 2.** Effect of the stationary-phase water content on the alkylbenzene chromatograms: (1) methanol 80%–water 20% v/v; (2) methanol 90%–water 10%; (3) methanol 100%. Solutes: (1) dodecylbenzene (0.84 mg injected); (2) hexylbenzene (0.85 mg); (3) butylbenzene (0.85 mg); (4) ethylbenzene (0.86 mg); (5) toluene (1.3 mg); (6) benzene (1.7 mg). Conditions: injected volume, 300  $\mu$ L; detection, UV 254 nm after 0.2 mL/min 2-propanol postcolumn addition, 1.28 a.u.; rotation speed, 1000 rpm; flow rate; heptane 2 mL/min entering tail; temperature,  $22 \pm 0.5$   $^{\circ}$ C.

in the liquid system used is known (9). We used the tracer procedure to cipher the stationary-phase carryover flow rate. The tracers were the alkylbenzene solutes themselves that we injected 4 times in a row without reequilibration of the CCC apparatus.

*Retention.* Equation 1 shows that partition coefficients and retention volumes are directly related. Figure 2 shows the CCC chromatograms obtained with heptane mobile phases and three different stationary phases: pure methanol and 10% water and 20% water in methanol (v/v). In all cases dodecylbenzene eluted first and benzene eluted last. Table I shows a rapid retention volume and partition coefficient decrease when the water stationary-phase content increased. As far as analysis duration is concerned, the higher the water content (i.e. the stationary-phase polarity), the lower the solute retention.

Figure 2 also shows that the chromatographic resolution dramatically depends on the stationary-phase volume and the partition coefficients. The resolution factor of peaks 2 and 3 (hexyl- and butylbenzene, respectively) was 0.7 with 20% water in the stationary phase (low partition coefficients, high  $V_S$ ); it increased to 1.5 with 10% water in the stationary phase due to a 5-fold partition coefficient increase (Table I); it decreased to a mere 0.4 with pure methanol stationary phase. The further 3-fold increase in partition coefficients was offset by the stationary-phase volume decrease (Table I and Figure 2). The chromatographic figure of merit of CCC chromatograms will be studied in another paper in preparation.

## LITERATURE CITED

- (1) Craig, L. C.; Post, O. *Anal. Chem.* **1949**, *21*, 500–504.
- (2) Ito, Y.; Bowman, R. L. *Science* **1970**, *167*, 281–283.
- (3) Ito, Y. *CRC Crit. Rev. Anal. Chem.* **1986**, *17*, 65–143.
- (4) Mandava, N. B.; Ito, Y. *Countercurrent Chromatography*; Chromatography Sciences Series; Marcel Dekker: New York, 1988, Vol. 44.
- (5) Foucault, A. P. *Anal. Chem.* **1991**, *63*, 569A–579A.
- (6) Conway, W. D. *Countercurrent Chromatography*; VCH Publishers: Weinheim, Germany, 1990.
- (7) Berthod, A. *Eur. Chromatogr. Anal.* **1991**, Feb, 13–15.
- (8) Rekker, R. F. *The Hydrophobic Fragmental Constant*; Elsevier: Amsterdam, 1977.
- (9) Berthod, A.; Han, Y. I.; Armstrong, D. W. *J. Liq. Chromatogr.* **1988**, *11*, 1441–1456.
- (10) Terada, H.; Kosuge, Y.; Murayama, W.; Nakaya, N.; Yoshiaki, N.; Nunogaki, K. I. *J. Chromatogr.* **1987**, *400*, 343–352.
- (11) Vallat, P.; El Tayer, N.; Testa, B.; Slacanin, I.; Martson, A.; Hostettmann, K. *J. Chromatogr.* **1990**, *504*, 411–422.
- (12) Gluck, S. J.; Martin, E. J. *J. Liq. Chromatogr.* **1990**, *13*, 2529–2551.
- (13) Menges, R. A.; Bertrand, G. L.; Armstrong, D. W. *J. Liq. Chromatogr.* **1990**, *13*, 3061–3077.



- (14) Berthod, A. *Analisis* 1990, 18, 352-357.  
(15) Tsai, R. S.; El Tayar, N.; Testa, B.; Ito, Y. *J. Chromatogr.* 1991, 538, 119-123.  
(16) El Tayar, N.; Martson, A.; Bechalany, A.; Hosteltmann, K.; Testa, B. *J. Chromatogr.* 1989, 469, 91-99.  
(17) Guiochon, G. In *HPLC: Advances and Perspectives*; Horwath, Cs., Ed.; Academic Press: New York, 1989; Vol. 2.  
(18) Dorsey, J. G. *Chromatographic Quantitative Structure-Retention Relationships*. Presented at the Analytical Chemistry Symposium, 202nd National Meeting of the American Chemical Society, New York, Aug 25-30, 1991.  
(19) Melander, W. R.; Horwath, Cs. *Chromatographia* 1982, 15, 86-90.  
(20) Krafft, M. P.; Jeannaux, F.; Le Blanc, M.; Riess, J. G.; Berthod, A. *Anal. Chem.* 1988, 60, 1969-1972.  
(21) Ito, Y.; Oka, H.; Siemp, J. L. *J. Chromatogr.* 1989, 475, 219-227.  
(22) Mandava, N. B.; Ito, Y.; Ruth, J. M. *J. Liq. Chromatogr.* 1985, 8, 2221-2238.  
(23) Berthod, A.; Armstrong, D. W. *J. Liq. Chromatogr.* 1988, 11, 1187-1204.

RECEIVED for review May 13, 1991. Accepted August 8, 1991. This work was supported by the Centre National de la Recherche Scientifique, UA 435, J. M. Mermet. Additional funding was provided by TOTAL Raffinage Distribution, Grant No. 900918E29, J. Goupy, Levallois-Perret, which is gratefully acknowledged.

## Real-Time Principal Component Analysis Using Parallel Kalman Filter Networks for Peak Purity Analysis

Stephen J. Vanslyke and Peter D. Wentzell\*

*Trace Analysis Research Centre, Department of Chemistry, Dalhousie University, Halifax, Nova Scotia, Canada B3H 4J3*

**A new approach for performing principal component analysis (PCA) during data acquisition is described. The method is based on a network of multilinear models which are fit to data with the discrete Kalman filter. Application to absorbance matrices such as those obtained in chromatography with multiwavelength detection is considered. Multivariate data projected into two- and three-dimensional subspaces are fit with linear and planar models, respectively. Model deviations, detected using principles of adaptive Kalman filtering, are used to elucidate the rank of the data set. Principal component eigenvectors are then constructed from the individual models. Results of this initial work using simulated and experimental data demonstrate that extraction of the first two principal components is readily accomplished and eigenvectors obtained are in good agreement with traditional batch PCA results. Extension to more principal components should be possible although it will increase the number and complexity of models. Advantages of the new algorithm include its recursive implementation, parallel structure, and ability to indicate model errors as a function of time. The procedure should prove particularly useful for self-modeling curve resolution applications in chromatography.**

The increasing availability of analytical instruments capable of producing large amounts of multidimensional data has made the use of multivariate data analysis methods more commonplace. In the case of second-order bilinear instruments such as GC/MS or HPLC coupled to photodiode array UV-visible detection, one data analysis tool that is frequently used is principal component analysis (PCA), a type of factor analysis (1-4). This method is at the core of most algorithms designed for multicomponent curve resolution in chromatography. The problem of mathematically resolving overlapped chromatographic profiles is an old and difficult one in chemical analysis. It consists of essentially three steps: detection of peak overlap, identification of individual analytes, and quantitation of components. A variety of methods have been proposed for the first of these problems, the simplest involving the monitoring of response ratios at two detector

settings (e.g. absorbances at two wavelengths) (5). This approach, while straightforward, suffers from a number of disadvantages, including a susceptibility to a sloping background and the requirement of a preexisting knowledge of wavelengths to be used. Its biggest drawback, however, is that it does not identify the number and nature of coeluting analytes or provide quantitative results.

In recent years, a number of algorithms have been described for curve resolution in HPLC with UV-visible diode array detection (3, 4, 6-13). Most of these are based on the original method of Lawton and Sylvestre (6), which uses PCA coupled with nonnegativity constraints for the spectral and concentration domains. This approach requires no assumptions to be made regarding the number of components, or the shapes of component spectra or elution profiles. Additional information is often used to provide more exact solutions than can be provided by the algorithm alone, however. This self-modeling curve resolution approach has been very successful for two-component elution profiles, and commercial software is available. Numerous extensions to three or more components have been suggested (9, 10, 13), but effective use generally requires the availability of additional information.

One of the drawbacks of chromatographic curve resolution based on PCA is that calculations are generally performed after all of the data have been acquired. Chromatographic regions of interest must first be selected manually or automatically and subjected to PCA to determine the number of components. Thorough analysis requires interrogation of all chromatographic peaks. A simple peak purity test can be performed to screen particular areas of interest, but this suffers from the problems previously noted. A useful alternative would be the ability to carry out PCA recursively, i.e. while the data are being acquired. This would allow the determination of the number of coeluting components in real time and also act as a preprocessing step for self-modeling curve resolution. The development of a real-time PCA algorithm was the objective of this work.

The possibility of conducting recursive principal components analysis is made difficult by the fact that the usual PCA procedure is already iterative. To be capable of real-time implementation, a recursive procedure needs to maintain a static cycle time for each new data point obtained. One so-

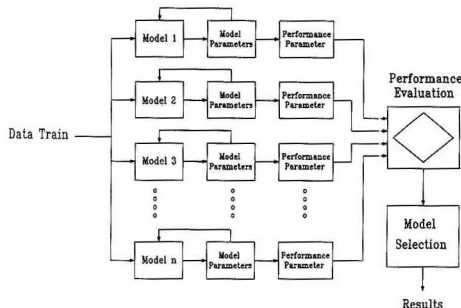


**Figure 1.** Strategy for implementation of parallel Kalman filter networks.

lution to the problem is to use the principles of adaptive Kalman filtering. The adaptive Kalman filter can be used as a recursive linear least-squares estimation procedure that has some built-in features to compensate for model errors. The strength of the adaptive Kalman filter is that it provides diagnostic information on model validity. If a parallel network of filters is employed, each with a different model, this information can be used to select the best model to fit experimental observations. This is the basis of the work described here, in which initial results for a recursive PCA method are presented. The use of parallel and block sequential Kalman filters for processing speech signals has been described in the engineering literature (14), but this is the first application of this type we have encountered. Currently, the recursive PCA procedure is limited to two-component models, but extension to higher dimensionality should be possible. Computer-simulated chromatographic profiles and experimental data from coeluting dyes are used to demonstrate the capabilities of the algorithm.

### THEORY

**Kalman Filter Algorithm.** Details of the Kalman filter have appeared elsewhere (15-18) and only a brief description will be given here. Most applications of the Kalman filter to chemical measurements have implemented the algorithm as a means for performing recursive ordinary least squares. This generally simplifies mathematical and computational aspects of the algorithm. The Kalman filter requires the definition of a linear model describing how the observations (measurements) change with one or more independent variables. The adjustable parameters of this model are known as state variables, or collectively as the state vector, and estimates of these are adjusted after each measurement, ultimately converging on the final estimate which can be represented as a point in state space. State variables may be dynamic or static. Most chemical applications have employed static models, which simplifies the algorithm somewhat since the identity matrix can be used to describe how the state vector propagates between measurements. The Kalman filter algorithm defines how estimates of the state vector and its associated covariance matrix evolve with measurements and includes compensation for four factors: (1) the current parameter estimates, (2) the difference between observed and predicted measurements, (3) the estimated error in the parameters (covariance matrix), and (4) the estimated error in the measurement. Certain restrictions regarding the modeled system apply (e.g. model linearity, model validity, Gaussian white noise), but under these conditions the Kalman filter will yield estimates which are optimal in the least-squares sense.

The use of parallel Kalman filter networks has been previously described for kinetic methods of analysis (19). The

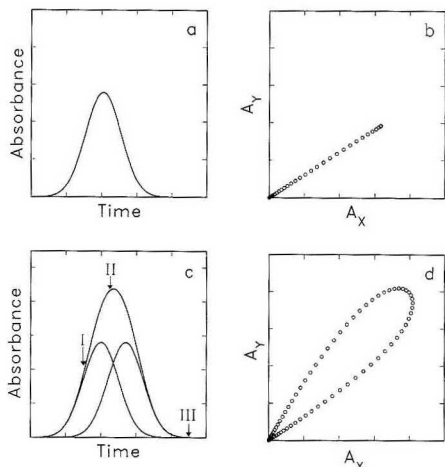


**Figure 2.** Chromatographic elution profiles and their projections into  $A^2$ -space: (a) and (b) one-component profile and its projection; (c) and (d) two-component profile and its projection.

general scheme is illustrated in Figure 1. The incoming data sequence is applied to the inputs of a number of Kalman filters, each with a different model. These models may be used to handle data from nonlinear systems by introducing small variations in nonlinear parameters between adjacent models (quasi-continuous case), or they may represent distinct alternatives (discrete case). The recursive PCA application described here employs the latter form. In either case, the application of each filter provides new estimates of the state parameters for the corresponding model. These parameters are used to evaluate the performance of each model in terms of its consistency with actual observations. A useful measure of the model performance is the innovations sequence which has been employed for adaptive Kalman filter algorithms (20, 21). The innovation is defined simply as the difference between the actual and predicted measurement (for multiple measurements in a single cycle, the innovation is a vector). The innovation differs from the residual normally used in modeling problems in that it is calculated after each measurement on the basis of current model parameters, whereas residuals are calculated in a batch procedure. The innovations sequence is particularly useful where model deviations are localized, since it indicates regions of model validity.

The application of the Kalman filter to chromatographic peak resolution has been previously described by Brown and co-workers (22, 23) and by Hayashi et al. (24), but these methods require a knowledge of individual component spectra or elution profiles and differ from the present work which seeks to function in the absence of this information. The principles of the recursive PCA approach are best illustrated with an example. Figure 2 shows synthetic chromatograms obtained for the elution of one- and two-component mixtures. For simplicity, Gaussian, noise-free peaks have been assumed, but this is not a requirement of the algorithm. It is also assumed that the two components are not completely overlapped and have sufficiently different spectral profiles. These are requirements of most curve resolution methods. Shown adjacent to the two representative chromatograms in Figure 2 are plots of absorbance measurements ( $A_x$  and  $A_y$ ) at two wavelengths for each sampled point. The wavelengths selected are the absorbance maxima of the two hypothetical components. Plots such as these will be referred to as  $A^2$  plots (also

known as biplots) and illustrate the principles of both the absorbance ratio and PCA methods for peak purity assessment. It is clear that the one-component mixture gives a constant  $A_y/A_x$ , while the two-component case does not. Methods based on PCA extend this principle further by recognizing that in an  $n$ -dimensional absorbance space ( $A^n$ ), the one-component case will always fit a linear model within experimental error. Likewise, a two-component chromatogram will fit a planar model in  $A^n$  space. Therefore, the minimum number of components in an overlapped region can be determined from the intrinsic dimensionality (i.e. rank) of multivariate absorbance data. Obviously, the PCA method is more general than simple absorbance ratio.

Two notable drawbacks of usual methods based on PCA are the need for batch processing of the data and difficulty of accurately determining the dimensionality of the data. The former problem has already been mentioned. The latter results from the difficulty of distinguishing residual eigenvectors arising from experimental error from those that represent true components. This problem is further complicated by experimental realities such as a sloping background that may appear as additional chromatographic components. Such features, while of interest in quantitation, can be misleading in the detection of peak overlap. Part of the difficulty in the determination of the true number of chromatographic components is that rank is normally assessed on the basis of one or more scalar quantities (1, 7, 8) that ignore information available in the temporal structure of the data. Clearly, deviations from an  $n$ -dimensional model due to the presence of additional components or a sloping background should exhibit characteristic patterns if the evolution of the model is examined. This behavior can be detected if PCA is performed recursively.

The principle of operation of recursive PCA is that an  $n$ -dimensional data set projected onto an  $n + 1$  dimensional space (or higher) should always give a fit to a multilinear function which is satisfactory within experimental error. Thus, the one-component data in Figure 2 will give a satisfactory fit to a straight line at any two wavelengths, but the fit for the two-component data should be unsatisfactory for at least certain pairs of wavelengths. Both data sets should give a good fit to a planar model in any  $A^3$  space, but a three-component data set should not. This strategy can be extended to higher dimensions, although visualization becomes more difficult. On this basis, the intrinsic dimensionality of the data set can be deduced by selecting a number of wavelengths and fitting data in lower subspaces comprised of various wavelength combinations. A one-component model should exhibit comparable residuals for both linear and planar models, but a two-component data set should exhibit excessive residuals for the linear model at certain wavelength combinations. Furthermore, the resulting models will serve as a means to construct good approximations to the principal component vectors. For example, the linear models should be projections of the first eigenvector, and the planar models should all contain the planes defined by the first two eigenvectors. The correspondence between the true eigenvectors and the reconstructed vectors may not be exact, since the multilinear least-squares models are generally constructed assuming no errors in the independent variable (25), but the correspondence should be close under the right conditions.

The use of multiple models of lower dimensionality offers no particular advantages over traditional PCA except when used in conjunction with the Kalman filter. The Kalman filter can be used to generate fits to linear and planar models recursively. This increases the potential for real-time implementation of the algorithm and observation of model evolution. Before the algorithm is initiated,  $n$  wavelengths at

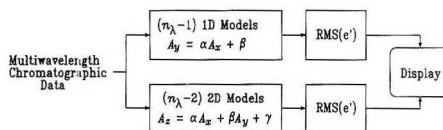


Figure 3. Parallel Kalman filter network for recursive PCA application.

conveniently spaced intervals are selected. For the one-component model, the absorbance at one wavelength (designated  $A_x$ ) is selected as the independent variable and a series of  $n - 1$  models of the form

$$\hat{A}_{ij} = \alpha_i A_{xj} + \beta_i \quad (1)$$

are used for the Kalman filter. In this equation,  $\hat{A}_{ij}$  represents the predicted absorbance at wavelength  $i$  for measurement  $j$ ,  $A_{xj}$  is the measured absorbance at the wavelength chosen as for the independent variable, and  $\alpha_i$  and  $\beta_i$  are parameters associated with the one-dimensional model. The parameter estimates evolve as each measurement is processed by the Kalman filter. The model may be limited to the trivial case of single parameter ( $\alpha_i$ ) if a zero intercept is assumed, but this will not always be the case. These models are used as  $n - 1$  elements of the parallel filter network. Likewise,  $n - 2$  two-dimensional (planar) models of the form

$$\hat{A}_{ij} = \alpha_i A_{xj} + \beta_i A_{yj} + \gamma_i \quad (2)$$

are also used. In this case, absorbances at two wavelengths (arbitrarily designated as  $A_x$  and  $A_y$ ) are needed as independent variables and three parameters are estimated. Models of higher dimensionality are also possible, but were not employed in this initial work. The  $2n - 3$  models described are sufficient to indicate one, two, or more than two coeluting components.

The strategy for implementation of the models in the parallel Kalman filter network is shown in Figure 3. As each set of absorbance values for a single chromatographic point is received, a set of innovations corresponding to the  $2n - 3$  models is calculated using predicted measurements according to

$$e_{ij} = \hat{A}_{ij} - A_{ij} \quad (3)$$

where  $e_{ij}$  is the innovation for measurement  $j$  at wavelength  $i$ , and  $\hat{A}_{ij}$  and  $A_{ij}$  are the predicted and measured absorbances, respectively. In each cycle, there are  $n - 1$  innovations calculated for the one-dimensional models and  $n - 2$  for the two-dimensional models. The magnitude of the innovations should be close to the measurement noise level if the correct model is used, but significant deviations should be observed otherwise. Thus, the absolute value of the innovations sequence can be used to indicate when the dimensionality of the data does not match the dimensionality of the model. Not all of the innovations will provide this information, however, since the wavelengths used in a particular model may not be appropriate for observing model variations (e.g. if there is no absorbance for the dependent variable). One way around this problem is to examine the maximum absolute innovation for each set of models, but this will be sensitive to outliers in the data. An alternative approach is to calculate the root mean square (rms) value of innovations for each set of models:

$$\text{rms}(e_k) = \sqrt{\frac{\sum e_k^2}{m_k}} \quad (4)$$

where the summation is over the number of models of dimension  $k$ ,  $m_k$  ( $m_k = n - k$ ). The rms values can be plotted in real time along with the chromatogram, and the sequence should remain fairly flat as long as the dimensionality of the

data is a subset of the model space.

A number of practical problems need to be addressed in implementing the above strategy. The first is the selection of wavelengths which will act as independent variables in the models. The selection is not entirely arbitrary since the independent variable will exhibit a certain amount of uncertainty along its axis. In the case of one-dimensional model, this means that if the wavelength selected for the  $x$  variable shows no absorbance for any component, the least-squares fit will result in a nearly vertical line ( $\alpha \rightarrow \infty$ ) for those models whose dependent variable is non-zero. Although this may result in a valid least-squares fit, the innovations (measured in the  $y$  direction) will be excessively large, leading an erroneous assessment of model validity through eq 4. One way to minimize this problem is to ensure that the wavelengths chosen as the independent variables in an  $n$ -dimensional model exhibit significant absorbance for some portion of the data. In practice, the wavelengths exhibiting the highest absorbance when the peak is first detected are used. This does not eliminate the problem entirely since the magnitude of the innovations will still increase with the slope of the line. In the two-dimensional case, the problem is compounded by the likelihood of high correlation between the independent variables. A more robust solution uses innovations measured orthogonally from the model rather than vertically. For the one-dimensional model, it can be shown that the orthogonal innovation is given by

$$e_{i,j}' = \frac{-\alpha_i A_{xj} + A_{ij} - \beta_j}{\sqrt{\alpha_i^2 + 1}} \quad (5)$$

where the prime denotes an orthogonal innovation. Likewise for a two-dimensional model

$$e_{i,j}' = \frac{-\alpha_i A_{xj} - \beta_j A_{yj} + A_{ij} - \gamma_j}{\sqrt{\alpha_i^2 + \beta_j^2 + 1}} \quad (6)$$

Extension to higher dimensions is straightforward. These modified innovations were used in place of the usual values for model evaluation (eq 4) since they should more accurately reflect the true model errors. The modified values were not used in the Kalman filter algorithm, however, since they underestimate the true innovations and lead to errors in the estimation of model parameters.

Another practical aspect of the implementation of the recursive PCA algorithm concerns its activation. In practice, the Kalman filter network is not activated until a peak is detected, although in principle the baseline region could be used if appropriate independent variables could be selected in advance. Once activated, the rms innovations for each model (eq 4) may exhibit high values for the first two or three points as the model converges on reasonable parameter estimates. Display of these points could be suppressed, but this was not done for the results presented here and is generally not necessary.

**Relationship to Principal Component Analysis.** In view of the importance of the connection drawn between PCA and the Kalman filter algorithm developed here, a more detailed discussion of this relationship is warranted. There are obvious computational differences between the traditional batch processing method for performing PCA and the multilinear approach presented here. This means that the resultant vectors are not necessarily identical, but the differences should be small enough to be inconsequential. It is known that the Kalman filter will provide model equations that are virtually identical to the traditional least-squares method as long as the diagonal elements of the covariance matrix are initially set to large values relative to estimated measurement error

(26, 27). In this work, a ratio of  $>10^{10}$  was normally used for the diagonal elements in order to achieve the least-squares solution (off-diagonal elements were initially set to zero).

The relationships between the PCA eigenvectors and the Kalman filter results are as follows. For the set of one-dimensional models given by eq 1, the vector resulting from the combination of all models into  $A^n$  space corresponds to the first eigenvector obtained by traditional PCA methods if the absorbance data were mean-centered at each wavelength. As this eliminates residual eigenvectors resulting from an offset at particular wavelengths, it is preferred for peak purity analysis. If mean-centering of the absorbance vectors is not carried out prior to batch PCA, the first eigenvector will correspond to the vector generated by the models in eq 1 of the  $\beta_j$ 's are forced to zero. In either case, the first eigenvector from the Kalman filter ( $E_1$ ) will be given by

$$E_1 = [\alpha_1 \quad \alpha_2 \quad \dots \quad \alpha_{n-1} \quad 1] / \sqrt{1 + \sum_{i=1}^{n-1} \alpha_i^2} \quad (7)$$

The first  $n-1$  components of the vector are the projections of the  $n-1$  dependent variables of the models, while the last represents the wavelength selected as the independent variable. The denominator simply serves to normalize the vector. To find the second eigenvector, both the one- and two-component models are required. This is because the two-component model only defines the plane containing the first two eigenvectors and not the vectors themselves. Generally, if it is known that two-components are present, a knowledge of the plane of the first two eigenvectors is sufficient to perform self-modeling curve resolution. Nevertheless one method of obtaining the actual eigenvectors is presented here. As in the case of the one-component models, omission of the offset parameter (in this case  $\gamma_j$ ) will lead to the PCA result for data which are not mean-centered for absorbance. The plane containing the first two eigenvectors will also contain the vectors  $V_1$  and  $V_2$ . The  $(n-1)$ th component of the vectors

$$V_1 = [\alpha_1 \quad \alpha_2 \quad \dots \quad \alpha_{n-2} \quad 1 \quad 0]$$

$$V_2 = [\beta_1 \quad \beta_2 \quad \dots \quad \beta_{n-2} \quad 0 \quad 1]$$

corresponds to the first independent variable and  $n$ th component to the second. These vectors correspond to the intersection of the planar model with the  $(n-1)$  dimensional subspaces along the axes of  $A_x$  and  $A_y$ . After normalization of  $V_1$  to  $N_1$ , a vector  $N_2$  which is orthogonal to  $N_1$  is determined by projection of  $V_2$  onto  $N_1$ , subtraction, and normalization. The vectors  $N_1$  and  $N_2$  are just one set of or-

$$N_1 = V_1 / |V_1| \quad (8)$$

$$P = V_2 - (V_1 \cdot V_2) V_1 \quad (9)$$

$$N_2 = P / |P| \quad (10)$$

thonormal vectors which can be used to define the plane. Ideally, the first eigenvector obtained from the one-dimensional models ( $E_1$ ) will lie on this plane, but in practice there may be a slight elevation due to minor computational differences for the two models. To ensure the integrity of the two-component plane, the first eigenvector is recalculated as its projection onto the plane defined by the orthonormal vectors ( $E_1'$ ). In all cases that we have checked, the difference

$$E_1' = (E_1 \cdot N_1) N_1 + (E_1 \cdot N_2) N_2 \quad (11)$$

between  $E_1$  and  $E_1'$  has been insignificant, but calculation of the projection is more robust in cases where a two-dimensional model is employed. Calculation of the second eigenvector,  $E_2$ , in the two-dimensional subspace is now trivial. Extension

$$E_2 = -(E_1' \cdot N_2) N_1 + (E_1' \cdot N_1) N_2 \quad (12)$$

of these principles to systems of higher dimensionality should

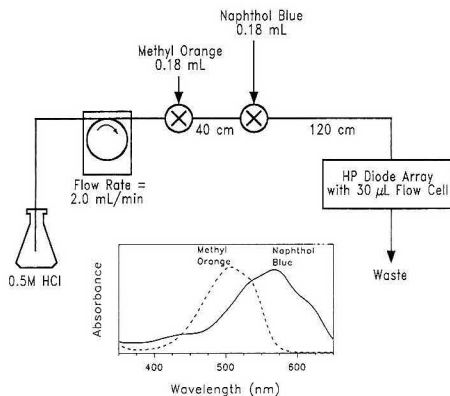


Figure 4. Merging zones continuous-flow apparatus for studies of dye coelution with spectra of dyes inset.

be straightforward, but will not be considered here.

#### EXPERIMENTAL SECTION

**Simulation Studies.** Generation of absorbance vs wavelength vs time data to test the Kalman filter algorithm was carried out with a program that allowed a variety of conditions to be simulated. For simplicity, Gaussian shapes were assumed for spectral and concentration profiles. Normally distributed random values were added to simulate measurement noise. Further details of conditions used accompany results presented in the Results and Discussion.

**Dye Coelution.** Experimental results for coeluting components were obtained using a continuous-flow system in a merging zones configuration, as shown in Figure 4. Dye solutions employed for the results presented here were 0.312  $\mu\text{M}$  methyl orange (acid orange 52, color index 13025; Fisher, Fair Lawn, NJ) and 1.17  $\mu\text{M}$  naphthol blue (Meldola's blue, basic blue 6, c.i. 51175; Pfaltz & Bauer, Waterbury, CT), both prepared in 0.5 M HCl. These concentrations were found to give a noise level suitable for testing the algorithm. The samples were injected simultaneously into the stream using two six-port two-way valves (Rheodyne Model 5020, Cotati, CA) with 180  $\mu\text{L}$  sample loops. The injected samples were transported to the detector through 0.8 mm i.d. PTFE tubing by an 8-roller Ismatec SA peristaltic pump (Cole-Parmer, Chicago, IL). A Hewlett-Packard Model 8452A photodiode array spectrometer (Hewlett-Packard, Palo Alto, CA) with a 30- $\mu\text{L}$  flow cell (Hellma Cells, Jamaica, NY) was used to acquire spectra at 1-s intervals for about 100 s after injection.

**Computational Aspects.** All calculations were carried out on a 16-MHz IBM PC/AT compatible computer with a math coprocessor. Programs were written in Microsoft QuickBASIC (Microsoft Corp., Redmond, WA). Implementation of the Kalman filter employed the standard algorithm (18) with double precision arithmetic. Principal components analysis was carried out using subroutines written in our laboratory and based on procedures outlined by Malinowski and Howerly (1). Three-dimensional displays of experimental data were generated with the program SURFER (Golden Software, Golden, CO).

#### RESULTS AND DISCUSSION

**Simulation Studies.** To provide an initial evaluation of the Kalman filter algorithm for recursive PCA, simulated chromatographic data were used. Because a large number of parameters will affect the performance of the algorithm (chromatographic peak shapes, spectral profiles, spectral and chromatographic resolution, number of components, component ratios, noise level, background absorbance, number of wavelengths used, etc.), only a limited subset of results is presented here to demonstrate the principles of the method. More complete studies to investigate the limitations of the algorithm are ongoing.

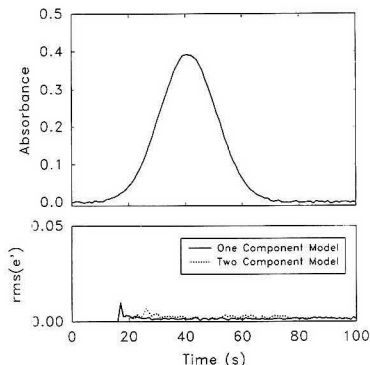


Figure 5. Results of the application of the Kalman filter PCA algorithm to a single-component elution profile (simulated). The top trace shows the chromatographic signal at the wavelength of maximum absorbance. The bottom trace shows the sequence of rms orthogonal innovations for each model type.

The simulated experimental data presented here utilized Gaussian profiles in both the chromatographic and spectral domains for simplicity. Component 1 was assigned a wavelength maximum of 400 nm and component 2 a maximum at 500 nm. The width of both spectral peaks was  $\sigma = 100$  nm, and equivalent molar absorptivities were assumed. The concentration ratio and chromatographic resolution of components were varied between studies. Chromatographic peak widths of  $\sigma = 10$  s were used with a simulated spectral sampling rate of 1 s. Chromatographic resolution was defined in the usual manner ( $R = \Delta t_R/4\sigma$ ). The noise level (typically 0.5% RSD) was computed as a percentage of the maximum of the entire absorbance matrix. For all of the results presented here, 10 wavelengths at equally spaced intervals were used.

Figure 5 shows typical results obtained with the parallel Kalman filter network for the elution of a single component. The top part of the figure shows the chromatographic trace at the absorbance maximum, while the bottom portion shows the rms orthogonal innovations for the one- and two-component models. Note that both models indicate acceptable performance, verifying that there is only one component present. In contrast, Figure 6 shows results for two eluting components (3:1 ratio, 0.35 resolution, 0.5% noise). Under these conditions, the two-component model gives a fairly flat innovations trace, while the trace for the one-component model indicates significant model deviations. Furthermore, the point at which the innovations sequence begins to diverge for the one-component model reveals where the second component begins to appear. This information is not provided with batch PCA and is significant because it allows a key set of factors to be identified for target transformation (7-9, 12). This could expedite the generation of component elution profiles considerably.

In order to illustrate how the Kalman filter network functions, the evolution of a single one-dimensional model for a two-component data set is shown in Figure 7. One  $A^2$  data space for the data in Figure 2c is shown. Lines in Figure 7 correspond to the one-dimensional model at various points throughout the elution of the peak and are labeled to correspond to points indicated in Figure 2c. Initially, when only one component is present, the linear model fits the observed data relatively well and the innovations are small (case I). As the second component introduces curvature into the data, the least-squares fit must accommodate this nonlinearity and the model begins to track the measurements more poorly, leading



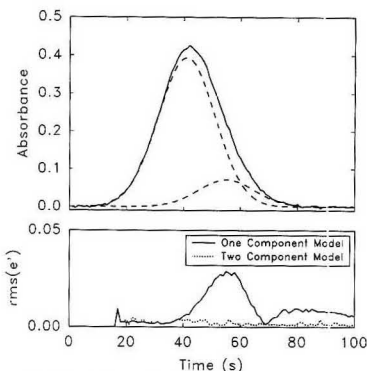


**Figure 6.** Results of the application of the Kalman filter algorithm to a simulated two-component elution profile.

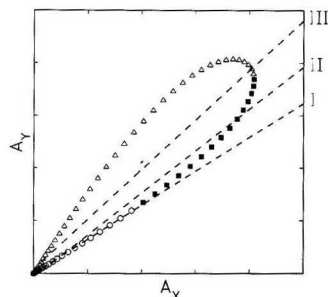


**Figure 7.** Evolution of the one-component model for the data in Figure 2c. The model equations (dashed lines) are shown at three stages: initial (after the open circles, I), intermediate (after the filled squares, II), and final (III). Corresponding points on the elution profile are indicated in Figure 2.

to larger innovations (case II). Although the model is no better when the signal returns to the baseline (case III) measurements near the origin do not exhibit large deviations and so the innovations return to their original level. Note that in this sense the innovations do not behave the same as a residual sum of squares.

As an indication of the limitations of the Kalman filter PCA method, Figure 8 shows results obtained with a 10:1 component ratio and a resolution of only 0.25. The second component can still be detected in this case. Although the statistical significance of the small perturbation to the one-dimensional model might be contested, the algorithm is intended mainly to provide an indication of the possibility of a second component, so this point will not be addressed here. The ability of the algorithm to detect minor components is very dependent on the noise level, as expected. Generally, it was found that when the recursive algorithm failed to distinguish a second component, visual inspection of the data in the plane resulting from the first two eigenvectors also suggested only one component. As anticipated, performance of the method also improves with chromatographic and spectral resolution and with the number of wavelengths used. The latter effect arises from the increased likelihood of selecting wavelengths with maximum discriminating ability, and smoother traces for the rms innovations. Improvements in results achieved by increasing the number of wavelengths are quickly limited by the spectral correlation of the two components, however. The order of component elution (i.e. minor component first

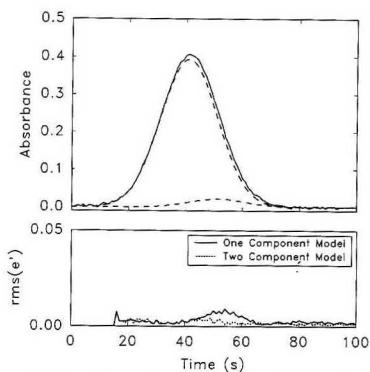


**Figure 8.** Results of the application of the Kalman filter algorithm to a simulated two-component elution profile near limiting conditions.

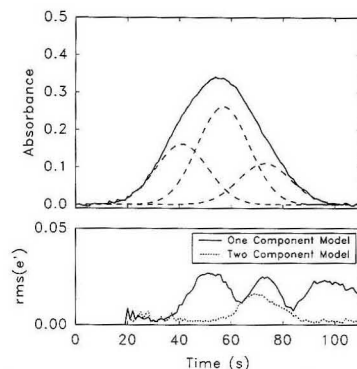


**Figure 9.** Results of the application of the Kalman filter algorithm to a simulated three-component elution profile.

or second) affects the shape of the innovations trace but does not significantly diminish the ability of the algorithm to determine the dimensionality of the data set in most cases. In some extreme cases, the rms innovations of the two-component model exhibit a small disturbance when the second component is detected (i.e. the reverse of the usual case) but this is due to the fact that the planar model "floats" around its primary axis until the necessary points are obtained to more rigidly define the second eigenvector. The shape of the elution profile should also affect the performance of the algorithm, but this aspect has not been investigated in detail.

An example of a simulated three-component mixture is shown in Figure 9. In this case, the third component was assigned a wavelength maximum of 300 nm with  $\sigma = 100$  nm. The concentration ratio ( $c_1:c_2:c_3$ ) is 1.3:1, and components elute in order with a resolution of 0.4 between adjacent peaks. Other conditions are as previously given. Note that the trace of rms innovations indicates the successive failure of the one- and two-component models. It should be pointed out, however, that failure of the two-component model was not always observed for three-component mixtures, depending on the relationships among spectra and elution profiles. It is believed that this problem has its roots in the correlation between wavelengths selected for independent variables. Solutions include a more careful selection of wavelengths or imposition of a complete set of models with all wavelength combinations. Other options also exist but may not be necessary as the

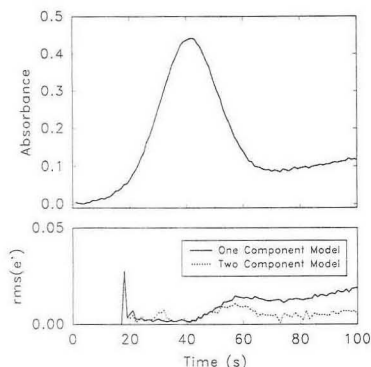


Figure 10. Effect of a sloping baseline on the Kalman filter algorithm.

pattern of the innovations for the one-dimensional model will indicate the presence of a third component in most cases.

As a final example, Figure 10 demonstrates the effect of a sloping background on the recursive PCA algorithm. Conditions used were the same as for Figure 5 (one component) but a gradient ramped up to 30% of the maximum absorbance was added at all wavelengths. A gradient of this type should show up as an additional component with batch PCA procedures with no indication of its source. With the Kalman filter method, deviations of the one-component model are also seen, but the divergence of the innovations trace is more gradual, indicating that the second component is due to changes in the background rather than coelution. Such information about the temporal structure of model variations is a particular advantage of the Kalman filter approach.

The computational performance of the parallel Kalman filter network is currently limited by its implementation in serial fashion but is still quite acceptable. Cycle times of about 0.1 s are not difficult to achieve with one- or two-component models at 10 wavelengths. This is in a range suitable for most chromatographic applications. The efficiency of the serial implementation will diminish as the models of higher dimensionality are added and the number of wavelengths is increased. The highly parallel nature of the algorithm can exploit trends in computing toward vector processing, however, and this should dramatically reduce computation time.

**Experimental Results.** Since simulated experimental data often imposes deterministic and stochastic characteristics which are not observed in practice (e.g. Gaussian profiles, uncorrelated noise), the recursive PCA algorithm was also applied to experimental data from the coelution of organic dyes. One of the data sets used in this study, obtained with the apparatus in Figure 4, is shown in Figure 11. Dye concentrations were reduced to a level which gave a relatively noisy signal (approximately 3% baseline noise relative to the absorbance maximum). It also appears from the figure that the noise exhibits some correlation, possibly due to pump pulsations. The ratio of peak heights (methyl orange to naphthol blue) was 2:1 and the resolution (determined by individual injection) was about 0.4. Ten wavelengths at equally spaced intervals were used. Results of the application of the Kalman filter are shown in Figure 12. The presence of two components in the elution profile is clearly indicated by the rms innovations sequence even though the noise level is quite high. The rms innovations are likely higher in this case than for simulated results due to the high correlation along the wavelength axis.

**Comparison with PCA Results.** A comparison between the eigenvectors computed by the usual batch PCA procedure

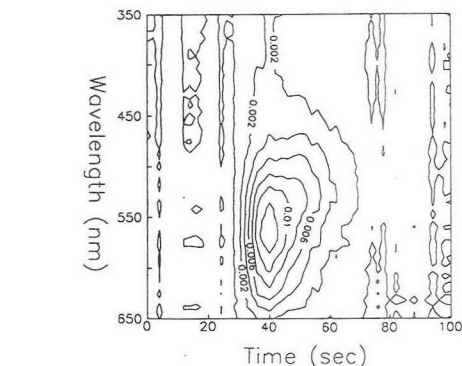
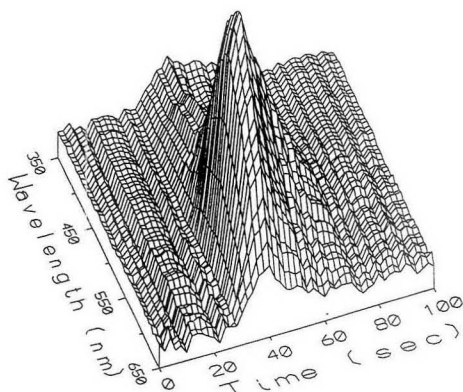


Figure 11. Absorbance matrix obtained from the coelution of organic dyes.

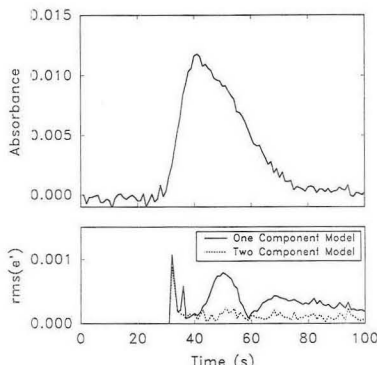


Figure 12. Results of the application of the recursive PCA algorithm to the data in Figure 11.

and those determined by the parallel Kalman filter network is given in Table I. The basis of the comparison is the angle between the eigenvectors calculated through the batch PCA procedure and the Kalman filter network. Results under various simulation conditions for a ten-dimensional space (ten wavelengths) are shown. The first eigenvector used from the

**Table I. Angles between Eigenvectors Produced by Traditional Principal Component Analysis and the Kalman Filter Method**

no. of components	concn ratio	resoln	noise level, %	angle between eigenvectors, deg	
				first eigenvector	second eigenvector
1			0.5	0.01	53.0
2	3:1	0.35	0.5	0.06	1.37
2	3:1	0.35	2.0	0.49	7.99
2	10:1	0.25	0.5	0.02	6.39
2	5:1	0.2	0.5	0.08	3.12
2	1:5	0.2	0.5	0.06	3.02

Kalman filter network was that obtained from the combination of one- and two-component models rather than from the one-component model alone, but differences were insignificant. Agreement between the two PCA methods, while not perfect, is very good in most cases. One exception is where an attempt is made to determine the second eigenvector for the one-component data set. In this case, the second eigenvector is defined purely by noise and is of no real consequence, however. Certainly, the agreement between batch and recursive procedures should be good enough to permit further calculations, such as self-modeling curve resolution, to be carried out.

The recursive PCA method does not directly provide eigenvalues or the row and column matrices associated with batch PCA, but these can be easily determined (if necessary) once the eigenvectors are assigned. Eigenvalues are not as essential for determination of rank with the recursive algorithm since this information is provided by the rms innovations sequence.

### CONCLUSIONS

The initial studies presented here have demonstrated the viability of performing principal components analysis recursively through the use of a parallel Kalman filter network. Application to the problem of chromatographic peak purity analysis has shown how the rank of a data matrix can be deduced while the data are being acquired. Although more extensive studies are required to fully explore the potential and limitations of this approach, several important advantages are apparent. First, because the algorithm is recursive and parallel with a fixed cycle time, it should be significantly faster than traditional PCA methods, especially when implemented on parallel computing architectures. The speed advantage does not result from a more computationally efficient algorithm, but rather because data analysis is performed while data are being acquired. A second advantage of the recursive approach is that it provides information on the temporal evolution of models. This is particularly useful in cases such as chromatography and titrimetry where certain types of behavior can be anticipated. To obtain equivalent information by batch PCA, numerous subsets of the data would have to be processed independently. The information provided by

recursive PCA should be particularly useful in resolving ternary component mixtures by evolutionary factor analysis (13) since it identifies regions in which certain models are valid. Furthermore, it can help diagnose model deviations arising from factors such as a sloping background. Absolute information on model deviations is readily provided by the rms innovations sequence, which should approximate measurement noise when the model is valid. Finally, the flexibility of the Kalman filter models allows for a variety of processing options to be exercised, simultaneously if desired. Inclusion of the offset term in the models, for example, will have the same effect as mean-centering the absorbance data prior to batch PCA. Unlike some approaches (3), however, the absorbance data are not normalized, so the measurement noise information is retained at its original magnitude (11).

In spite of these advantages, it is clear that the Kalman filter network will not be useful in those cases where real-time data processing is not required. It is also likely to become less useful as the number of factors to be extracted becomes large, since the number and complexity of models become more difficult to handle. Nevertheless, it may allow techniques such as self-modeling curve resolution to be more readily implemented in real time.

### LITERATURE CITED

- (1) Malinowski, E. R.; Howery, D. G. *Factor Analysis in Chemistry*; Wiley: New York, 1980.
- (2) Sharaf, M. A.; Kowalski, B. R. *Anal. Chem.* **1981**, *53*, 518-522.
- (3) Osten, D. W.; Kowalski, B. R. *Anal. Chem.* **1984**, *56*, 991-995.
- (4) Ramos, L. S. Ph. D. Thesis, University of Washington, Seattle, WA, 1988.
- (5) Yost, R.; Stoveken, J.; MacLean, W. J. *Chromatogr.* **1977**, *134*, 73-82.
- (6) Lawton, W. H.; Sylvestre, E. A. *Technometrics* **1971**, *13*, 617-633.
- (7) McCue, M.; Malinowski, E. R. *Appl. Spectrosc.* **1983**, *37*, 463-469.
- (8) Gemperline, P. J. *J. Chem. Inf. Comput. Sci.* **1984**, *24*, 206-212.
- (9) Vandeginste, B. G. M.; Derks, W.; Kateman, G. *Anal. Chim. Acta* **1985**, *173*, 253-264.
- (10) Vandeginste, B.; Essers, R.; Bosman, T.; Reijnen, J.; Kateman, G. *Anal. Chem.* **1985**, *57*, 971-985.
- (11) Lindberg, W.; Ohman, J.; Wold, S. *Anal. Chem.* **1986**, *58*, 299-303.
- (12) Gemperline, P. J. *Anal. Chem.* **1986**, *58*, 2656-2663.
- (13) Schostack, K. J.; Malinowski, E. R. *Chemom. Intell. Lab. Syst.* **1990**, *8*, 121-141.
- (14) Azimi-Sadjadi, M. R.; Lu, T.; Nebot, E. M. *IEEE Trans. Signal Process.* **1991**, *39*, 137-147.
- (15) Kalman, R. E. *J. Basic Eng.* **1960**, *181*, 35-45.
- (16) Brown, S. D. *Anal. Chim. Acta* **1986**, *181*, 1-26.
- (17) Rutan, S. C. *J. Chemomet.* **1987**, *1*, 7-18.
- (18) Wentzell, P. D.; Wade, A. P.; Crouch, S. R. *Anal. Chem.* **1988**, *60*, 905-911.
- (19) Wentzell, P. D.; Vanslyke, S. J. *Anal. Chim. Acta*, in press.
- (20) Brown, S. D.; Rutan, S. C. *Anal. Chim. Acta* **1984**, *160*, 99-119.
- (21) Brown, S. D.; Rutan, S. C. *J. Res. Natl. Bur. Stand. (U.S.)* **1985**, *90*, 403-407.
- (22) Barker, T.; Brown, S. D. *J. Chromatogr.* **1989**, *469*, 77-90.
- (23) Redmond, M.; Brown, S. D.; Wilk, H. R. *Anal. Lett.* **1989**, *22*, 963-979.
- (24) Hayashi, Y.; Yoshioka, S.; Takeda, Y. *Anal. Chim. Acta* **1988**, *212*, 81-94.
- (25) Williamson, J. H. *Can. J. Phys.* **1968**, *46*, 1845-1847.
- (26) Sorenson, H. W. *IEEE Spectrum* **1970**, *7*(7), 83-88.
- (27) Poulisse, H. N. *J. Anal. Chim. Acta* **1978**, *112*, 361-374.

RECEIVED for review May 30, 1991. Accepted August 14, 1991. We gratefully acknowledge the support of the Natural Sciences and Engineering Research Council of Canada.

# Concentration of Hydrophobic Organic Compounds and Extraction of Protein Using Alkylammoniosulfate Zwitterionic Surfactant Mediated Phase Separations (Cloud Point Extractions)

Tohru Saitoh<sup>1</sup> and Willie L. Hinze\*

Department of Chemistry, Laboratory for Analytical Micellar Chemistry, Wake Forest University, P.O. Box 7486, Winston-Salem, North Carolina 27109

The zwitterionic surfactants 3-[nonyl- (or decyl-) dimethylammonio]propyl sulfate, ( $C_9$ -APSO, or  $C_{10}$ -APSO<sub>4</sub>) were synthesized using Nilsson's procedure, and their phase separation behavior under different experimental conditions was evaluated. The results indicate that such zwitterionic surfactants can be utilized for the extraction/preconcentration of hydrophobic species in a manner akin to that previously reported for nonionic surfactants. This was demonstrated for several practical applications including the extraction/preconcentration of some steroidal hormones and vitamin E prior to high-performance liquid chromatography analysis. The zwitterionic surfactant mediated phase separation was also applied to the extraction of the hydrophobic membrane protein, bacteriorhodopsin, from the hydrophilic cytochrome *c* protein, both originally present in an aqueous phase. The concentration factors for this aqueous two-phase extraction technique using  $C_{10}$ -APSO<sub>4</sub> ranged from 26 to 35 with recoveries in the range 88 to >96%. Some comparative studies indicate that the use of zwitterionic surfactants in lieu of nonionic surfactants (e.g. polyoxyethylene(7.5) nonyl phenyl ether PONPE-7.5) in such an extraction method offers some significant advantages such as purer, homogeneous surfactant preparation, minimum background absorbance at UV detection wavelengths, the two-phase region occurring at lower temperatures, and greater extraction efficiencies/concentration factors among others.

## INTRODUCTION

Aqueous solutions of many nonionic surfactant micellar systems, when subjected to an increase in temperature, become turbid over a narrow temperature range, which is referred to as their cloud point (1-4). Above the cloud point temperature, such solutions separate into two isotropic phases. That is, the system will contain a surfactant-rich phase with a small amount of water (surfactant phase) which is separated from the bulk aqueous solution (aqueous phase) in which the surfactant concentration will be approximately equal to the critical micelle concentration (cmc) of the nonionic surfactant present. Figure 1 shows the typical phase diagram for such a nonionic surfactant system.

This cloud point behavior of nonionic surfactants has been utilized to design some efficient extraction systems akin to conventional liquid-liquid extractions (2, 5-13). That is, in an aqueous surfactant solution, any hydrophobic materials present will be solubilized and incorporated into the nonionic micellar assembly. As the surfactant micelle aggregates are condensed to an extremely small surfactant phase upon tem-

perature alteration due to the cloud point phenomenon, the hydrophobic species that are incorporated in the micellar surfactant are efficiently concentrated into this surfactant-rich phase. This extraction method using nonionic surfactant mediated phase separation (referred to as cloud point extraction) has been utilized to separate and concentrate metal ions based upon distribution of sparingly water soluble metal chelates into the nonionic surfactant, polyoxyethylene nonyl phenyl ether (PONPE-7.5), by Watanabe et al. (2, 5, 6). More recently, such cloud point extraction has been proposed and utilized for the preconcentration of organic compounds prior to gas or liquid chromatographic analysis (4, 8, 9). In addition, Bordier initially reported use of the cloud point technique with Triton X-114 as surfactant for the separation of hydrophobic membrane proteins from hydrophilic proteins (10, 11). This procedure has since found widespread use for the purification of membrane proteins (12, 13). In all of these applications, only nonionic surfactants of the Triton X or PONPE series have been employed.

Advantages cited, among others (2, 4), for the use of such nonionic cloud point extraction schemes include (i) ability to concentrate a variety of analytes (with high concentration factors), (ii) safety and cost benefits (only very small amounts of the relatively nonflammable and nonvolatile nonionic surfactant "extractant solvent" are required, which eliminates the need to use/handle the larger volumes of organic solvent typically required in traditional liquid-liquid extractions), (iii) easy disposal of the nonionic surfactant "extractant solvent" (it is reportedly easily burned in the presence of waste acetone or ethanol), (iv) the surfactant-rich phase compatibility with micellar (in micellar liquid chromatography) or hydroorganic (in reversed-phase LC) mobile phases, and (v) the possibility of enhanced detection due to the fact that the analyte(s) is(are) in the surfactant-rich micellar phase. Disadvantages include the fact that nonionic surfactants are not available as pure homogeneous preparations, they have a high background absorbance in the ultraviolet region due to the presence of the aromatic moiety in the surfactants employed to date, and thermally labile analytes can undergo degradation at the temperatures required for phase separation to occur with some of these surfactants.

Nilsson et al. (14) have reported that aqueous solutions of certain zwitterionic surfactants also exhibit critical phenomenon but that their behavior is different from that described for nonionic surfactants in that the zwitterionic systems display an upper (rather than lower) consolute boundary. That is, an isotropic two-phase system exists at temperatures below (rather than above) a certain critical temperature, as shown by the phase diagrams in Figure 2. Such systems should also be suitable for the extraction, concentration, and purification of hydrophobic organic or biomaterials based upon their phase separation behavior. In this study, we synthesized 3-(nonyl(dimethylammonio)propyl sulfate ( $C_9H_{19}(CH_3)_2N^+$ -

<sup>1</sup>Present address: Hokkaido University, Faculty of Engineering, Analytical Chemistry Laboratory, Sapporo, 060 Japan.

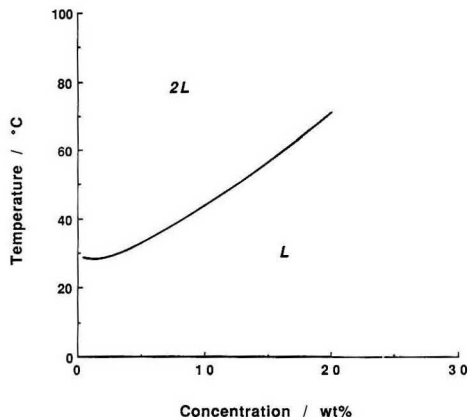


**Figure 1.** Typical phase diagram of an aqueous nonionic surfactant solution. L refers to the single isotropic solution region whereas 2L indicates the region where two isotropic phases coexist.

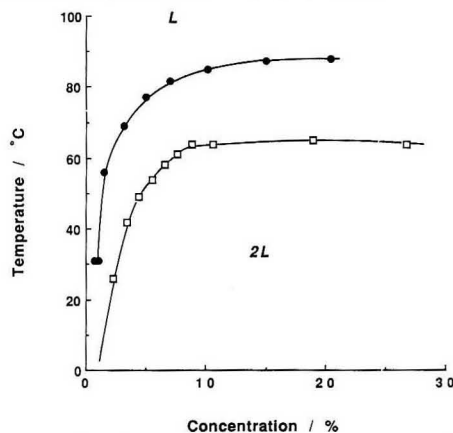


**Figure 2.** Phase diagram of the zwitterionic surfactants: (O)  $C_9$ -APSO<sub>4</sub> and (●)  $C_{10}$ -APSO<sub>4</sub>.

$(CH_2)_3OSO_3^-$ ,  $C_9$ -APSO<sub>4</sub>) and 3-(decyldimethylammonio)-propyl sulfate ( $C_{10}H_{21}(CH_3)_2N^+(CH_2)_3OSO_3^-$ ,  $C_{10}$ -APSO<sub>4</sub>) by Nilsson's method (14), characterized their phase behavior under a variety of experimental conditions, and examined the feasibility of utilizing such zwitterionic surfactant systems in extraction schemes. The phase separation behavior of such zwitterionic surfactants was successfully applied for the preconcentration of some biological compounds (i.e. steroid hormones, vitamins) for HPLC separation and the results were compared to that obtained using the conventional PONPE-7.5 nonionic surfactant system. In addition, the extraction of a hydrophobic membrane protein is demonstrated. The advantages and limitations of using zwitterionic instead of nonionic surfactants in such phase separation extraction/preconcentration schemes are compared and contrasted.

#### EXPERIMENTAL SECTION

**Materials. Zwitterionic Surfactants.** The zwitterionic surfactants,  $C_9$ -APSO<sub>4</sub> and  $C_{10}$ -APSO<sub>4</sub>, were prepared by mixing the appropriate alkyldimethylamine with trimethylene sulfate in dry acetone and heating gently as reported by Nilsson et al. (14). Following recrystallization, the surfactants were washed with

dry ether (Aldrich, 99+%) and dried in a vacuum desiccator over  $P_2O_5$ . The required alkyldimethylamines were not directly synthesized from the corresponding primary amines but rather prepared by lithium aluminum hydride (LiAlH<sub>4</sub>) reduction of the amides in THF in order to avoid the possibility of primary or secondary amine impurities. The specific synthesis of the intermediate materials required for preparation of the zwitterionic surfactants were as follows.

**Dimethylnonylamide.** A solution composed of 90.0 g (0.506 mol) nonanoyl chloride in dry benzene (1 + 1) was slowly added dropwise to 150 mL of an aqueous 40% (w/w) solution of dimethylamine with vigorous stirring at 0 °C. This mixture was stirred continuously for 1 h at 0 °C and then for an additional 1 h at room temperature. The benzene layer was collected after separation using a separation funnel and dried over magnesium sulfate for 1 day. Removal of the benzene by rotary evaporation followed by distillation at 98–100 °C at 1 mmHg yielded 85.9 g (90% yield) of the product, dimethylnonylamide.

**Dimethylnonylamine.** To a 250-mL two-necked flask fitted with a condenser and dropping funnel (with side tube) was added 6 g of LiAlH<sub>4</sub> powder followed by the slow dropwise addition of 100 mL of anhydrous THF with thorough mixing. Next, a dimethylnonylamide (18.5 g, 0.10 mol) solution in THF was slowly added dropwise to the flask. The resulting mixture was then heated under a gentle reflux with stirring for 5 h. After cooling, the excess LiAlH<sub>4</sub> and metallic complexes were decomposed by the careful addition of acetone to the well-stirred mixture. Next, about an equal volume of dry ether was added to the mixture followed by careful dropwise addition of about 10 mL of water, after which the mixture was filtered with suction and the solid residue washed with a 100-mL portion of ether. The collected solution was then dried over anhydrous sodium sulfate and the THF-ether solvent mixture removed by rotary evaporation. The product was distilled under reduced pressure (bp 86 °C at 30 mmHg) to yield 14.5 g (85% yield) of dimethylnonylamine.

**Dimethyldodecylamide and dimethyldodecylamine** were prepared in a similar fashion to that just outlined for the  $C_9$  nonyl analogues.

**Trimethyleneglycol Diacetate.** A 30.0-g portion of trimethyleneglycol (1,3-propanediol) was slowly added dropwise into 140 mL of gently refluxing acetic anhydride. The mixture was refluxed for an additional 2 h, and then the acetic acid was slowly removed by distillation. The resulting solution was then cooled, poured into ice water, and extracted with benzene. The benzene phase was neutralized with sodium bicarbonate and washed with water. After drying over anhydrous magnesium sulfate for 24 h, the benzene solvent was removed by rotary evaporation and the product distilled at reduced pressure (96–98 °C at 30 mmHg) to yield 39.3 g (62% yield) of trimethyleneglycol diacetate.

Trimethylene sulfate was prepared according to Brunken's method (15) by mixing trimethyleneglycol diacetate (32 g, 0.20 mol) with dimethyl sulfate (50 g) in a 100-mL round-bottom flask connected to a distillation system. The flask was immersed in a 130 °C oil bath and the methylacetate byproduct first slowly removed from the reaction mixture at slightly reduced pressure, after which the excess dimethyl sulfate was removed at 100–120 °C with reduced pressure (30 mmHg). The final product was obtained after high-vacuum distillation (140–160 °C, 1 mmHg) and yielded 15.5 g (56% yield) of trimethylene sulfate.

**Other Materials.** Steroid hormones (estrone,  $\beta$ -estradiol, estriol, and progesterone), vitamin E, proteins (bacteriorhodopsin, from *Halobacterium halobium*; cytochrome c, type III, from horse heart), and the nonionic surfactants (Triton X-114 and Brij-35) were all obtained from Sigma Chemical Co. (St. Louis, MO). Octyl  $\beta$ -D-glucoside was purchased from Boehringer Mannheim (Indianapolis, IN). Polyoxyethylene (7.5) nonyl phenyl ether (PONPE-7.5) was obtained from Tokyo Kasei Industries Co. (Tokyo, Japan). A premium standard coal sample (200 mesh) was kindly provided by Professor Fawzy S. Sadek (Winston-Salem State University, Winston-Salem, NC). All other reagents/solvents used were of the best commercial grade available.

**Procedures. Phase Diagrams and Phase Ratio Determinations.** The phase behavior for each surfactant system under different experimental conditions was determined by observing the temperature required for clarification of the solution upon heating or the onset of turbidity upon subsequent cooling of a 1.0-mL aqueous solution of the surfactant in a small sample tube



placed in a controlled temperature water bath (Haake, Berlin, Germany). The slope of the temperature change of the water bath was less than 1 °C/15 min.

The volumes of the respective surfactant and aqueous phases upon phase separation were measured using calibrated glass tubes. The surfactant solution was placed into the tube and the tube allowed to sit in a constant-temperature cold room (4 °C) for 1 week prior to measurement of the respective phase volumes. The results were the average of triplicate measurements.

**"Cloud Point" Extraction Prior to HPLC Analysis.** A 0.10-g portion of the zwitterionic surfactant was poured into 5.00 mL of the steroid hormone or vitamin-containing sample solutions. The solution was mixed for 5 min and centrifuged (1500 rpm, 10 min) in order to promote the phase separation. Aliquots (25 µL) of the surfactant-rich and aqueous phases were withdrawn using Hamilton microsyringes, and 10 µL of each phase was then injected into the high-performance liquid chromatographic system (Waters Model 510 HPLC pump, Model U6K injector, and Model 484 absorbance detector) for analysis. For comparison purposes, the cloud point extraction was also conducted in a similar manner using a nonionic surfactant system in which the sample was dissolved in a 2 g/L PONPE-7.5 aqueous solution.

**Coal Extraction.** A 0.05-g portion of coal (200 mesh) was poured into 10.0 mL of 0.05 g/mL C<sub>9</sub>-APSO<sub>4</sub> solution. The suspension was heated at 80 °C for 5 min and stirred during this period. Following filtration, the solution was cooled to room temperature and centrifuged at 1500 rpm for 10 min. A 20-µL aliquot of the surfactant-rich phase was then taken and injected for HPLC analysis.

**Protein Extraction.** A 0.20-g portion of C<sub>9</sub>-APSO<sub>4</sub> and 0.90 mL of 0.05 M MES, HEPES, or CHES buffer were placed into a 2.0-mL test tube. After the surfactant was dissolved, or the solution separated into two clear liquid phases, the tube was placed into an ice water bath for at least 10 min. Next, 0.10 mL of cytochrome c or bacteriorhodopsin solution was added to the test tube and the resulting solution gently stirred for 5 min, after which it was centrifuged for 10 min at 1500 rpm. A 0.50-mL aliquot of the aqueous phase was withdrawn and mixed with an equal volume of 1% (w/w) Brij-35 buffered solution. The absorbance of this solution was measured (Varian Cary Model 219 spectrophotometer) against a blank prepared in the same manner except that the proteins were absent. The extraction percentage of the proteins was calculated as a function of solution pH on the basis of the material balance of the proteins and the phase ratio of the surfactant-rich extraction and bulk aqueous phases.

## RESULTS AND DISCUSSION

**Phase Diagrams of Aqueous Zwitterionic Surfactant Solutions.** Figure 2 gives the phase diagrams, i.e. plots of the temperatures at which the two coexisting isotropic phases convert to a single isotropic solution as a function of the surfactant concentration of the solution, for the two zwitterionic surfactants, C<sub>9</sub>-APSO<sub>4</sub> and C<sub>10</sub>-APSO<sub>4</sub>, examined. The cloud points (i.e. upper critical temperatures) determined for these two zwitterionic surfactants in pure aqueous solution are 65 and 88 °C for C<sub>9</sub>-APSO<sub>4</sub> and C<sub>10</sub>-APSO<sub>4</sub>, respectively, which are in good agreement with values reported by Nilsson et al. (14). It was also observed that the cloud point of these zwitterionic surfactants did not change even if the solutions were heated for over 2 h at 80 °C. This indicates that the zwitterionic surfactants are quite stable in aqueous solutions even at relatively high temperatures. As previously mentioned, these zwitterionic surfactants exhibit a different type of phase separation behavior compared to that of nonionic surfactant solutions in that an upper (Figure 2) rather than lower (Figure 1) consolute boundary is present in the case of the zwitterionic system. Consequently, one can cause the phase separation behavior to occur and conduct extractions at much lower temperatures with zwitterionic surfactants compared to that possible with nonionics. For instance, the cloud points for aqueous 1.0% (w/v) solutions of the nonionic surfactants, Triton X-100 and Triton X-114, are 64 and ca. 23–27 °C, respectively.

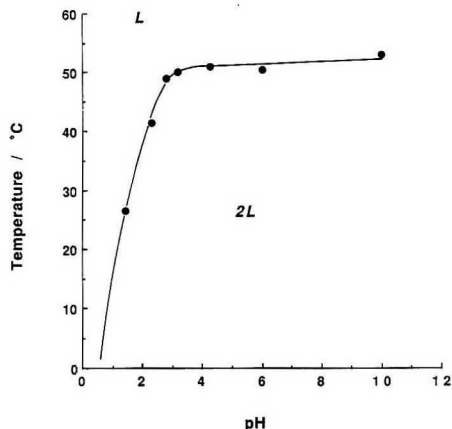


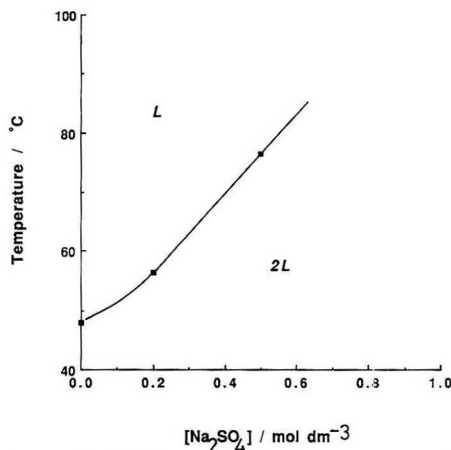
Figure 3. pH dependence of cloud point temperature of an aqueous 5% (w/w) C<sub>9</sub>-APSO<sub>4</sub> solution; total salt concentration = 0.05 M.

Since many analytical systems require pH control, the phase behavior was also determined as a function of pH. Figure 3 illustrates the pH dependence of the cloud point for a 5% (w/w) C<sub>9</sub>-APSO<sub>4</sub> solution. As can be seen, the cloud point remained relatively constant over the pH range 4–10. However, on the more acidic side, the cloud point of the solution dramatically decreased as the acidity was increased until a completely clear homogeneous solution resulted at pH = 0 at temperatures above 0 °C. Since the second dissociation constant of hydrosulfuric acid is reported by be 1.91 (16), it is thought that this behavior reflects the fact that the sulfate group of the zwitterionic C<sub>9</sub>-APSO<sub>4</sub> surfactant is being protonated as the pH is lowered. Thus, one is converting the zwitterionic surfactant to a cationic surfactant, C<sub>9</sub>H<sub>19</sub>N<sup>+</sup>(CH<sub>2</sub>)<sub>9</sub>OSO<sub>3</sub>H, in this region. This phenomenon will prove to be useful since it allows one to manipulate the pH following the zwitterionic phase separation extraction step in order to obtain a clear and nonviscous surfactant phase.

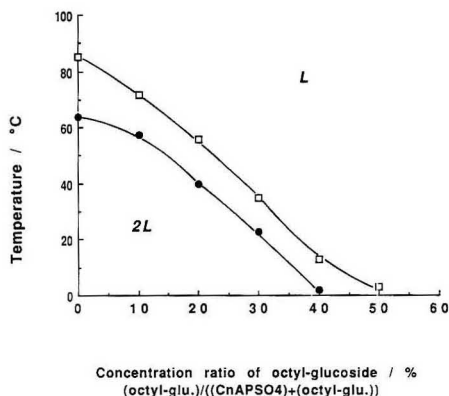
The ionic strength also can affect the cloud point. For nonionic surfactants, most added salts, such as sodium sulfate, cause a decrease in the cloud point compared to that observed in water alone. In contrast, as shown in Figure 4 for the zwitterionic surfactant C<sub>9</sub>-APSO<sub>4</sub>, the cloud point temperature increased with increases in added salt concentration. This is probably due to a salting-out type effect. The ability to use both the pH and ionic strength effects to alter the cloud point of these zwitterionic surfactants is important since it allows one to control the critical temperature.

Figure 5 shows the cloud point dependence as a function of composition for a mixed zwitterionic–nonionic surfactant system. As the concentration ratio of the nonionic surfactant, octyl glucoside, was increased, the cloud point temperature for the zwitterionic surfactant solutions decreased. In fact, the cloud point temperature was depressed to below 0 °C when the ratio of octyl glucoside present was greater than 40% (for C<sub>9</sub>-APSO<sub>4</sub>) or 50% (for C<sub>10</sub>-APSO<sub>4</sub>). Thus, the temperature required for phase separation can be predictably controlled by appropriate changes in the concentration or concentration ratio of zwitterionic and nonionic surfactants. This ability to lower the cloud point temperature will prove to be important in those instances where separation of thermally labile compounds (such as biomaterials) by the cloud point extraction technique is desired.

**Cloud Point Extraction as a Preconcentration Technique for HPLC.** Figures 6–8 each show the chromatographs



**Figure 4.** Plot of the dependence of the cloud point of an aqueous 5.0% (w/w)  $C_{10}$ -APSO<sub>4</sub> solution upon added salt (sodium sulfate) concentration.



**Figure 5.** Cloud point of an aqueous mixed solution of indicated zwitterionic surfactant, (●)  $C_{10}$ -APSO<sub>4</sub> or (□)  $C_{10}$ -APSO<sub>4</sub>, and octyl glucoside as a function of the total surfactant composition; total surfactant = 0.20 g; 1.00 mL of water.

of some steroid hormones and vitamin E prior to (reference chromatograph a in each figure for injection of the indicated analyte(s) originally present in surfactant solution) and after the cloud point extraction/preconcentration step after injection of the surfactant-rich phase of a nonionic surfactant, PONPE-7.5 (chromatograph b), or zwitterionic surfactant,  $C_{10}$ -APSO<sub>4</sub> (chromatograph c in each figure). As is evident from the figures, each analyte chromatographic peak height (or area) was considerably increased when the species was concentrated into the surfactant-rich extractant phase. The concentration factors achieved and percent recovery of the analytes are summarized in Table I. Good recoveries were obtained for both the nonionic and zwitterionic mediated cloud point extractions despite the fact that the volume ratio of the surfactant-rich phases was extremely small. Under the experimental conditions employed, the concentration factors obtained ranged from ca. 10 to 20 when the PONPE-7.5 nonionic surfactant was used compared to ca. 25–45 for the  $C_{10}$ -APSO<sub>4</sub> zwitterionic surfactant. In addition to these better

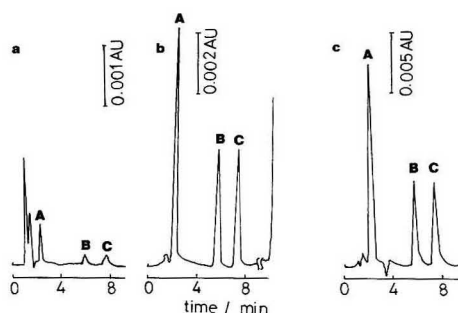


**Figure 6.** Chromatograms of the steroid hormones: (A) estriol, (B)  $\beta$ -estradiol, and (C) estrone following injection of sample in (a) 2 g/dL  $C_{10}$ -APSO<sub>4</sub> solution prior to phase separation extraction, and the surfactant-rich phase following a cloud point extraction using (b) the nonionic surfactant PONPE-7.5 or (c) zwitterionic surfactant  $C_{10}$ -APSO<sub>4</sub>. HPLC conditions: 10-cm  $C_{18}$  column; 40% (v/v) aqueous acetonitrile mobile phase; flow rate of 1.0 mL/min; detection at 280 nm.

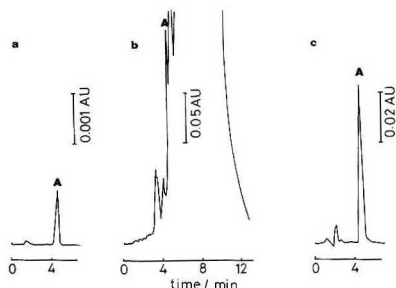


**Figure 7.** Chromatograms of progesterone (peak A) following injection of sample in (a) a reference 1% (w/w) Brij-35 surfactant solution not subjected to any cloud point extraction, and in the surfactant-rich phases following cloud point extraction with (b) PONPE-7.5 or (c) zwitterionic  $C_{10}$ -APSO<sub>4</sub>. The large peak in chromatogram b is that of the nonionic surfactant, PONPE-7.5. HPLC conditions: 10-cm  $C_{18}$  stationary phase; 60% (v/v) aqueous acetonitrile mobile phase; flow rate of 1.0 mL/min; detection at 260 nm.

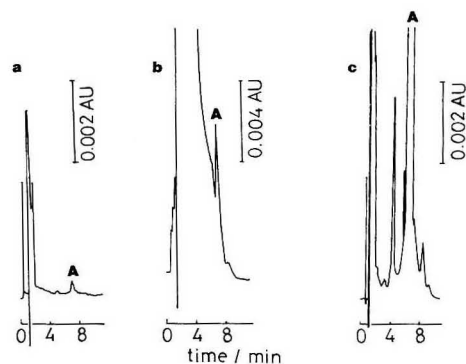


**Figure 8.** Chromatograms of vitamin E (peak A) following injection of samples in media a, b, and c as noted in Figure 7. The huge peak in chromatogram b is due to PONPE-7.5. The smaller peaks on either side of peak A in chromatogram c are due to decomposition products from vitamin E. HPLC conditions: 10-cm  $C_{18}$  stationary phase; 96% (v/v) aqueous acetonitrile mobile phase; flow rate of 2.0 mL/min; detection at 254 nm.

**Table I. Summary of Concentration Factors and Percent Recoveries Possible for Surfactant Mediated Phase Separations Using Zwitterionic and Nonionic Surfactant Systems**

surfactant system	component extracted	% recovery achieved	concn factor achieved
PONPE-7.5, 2 g/dL at 35 °C	estriol	67	12
	$\beta$ -estradiol	80	19
	estrone	82	19
	progesterone		11
$C_{10}$ -APSO <sub>4</sub> , 2 g/dL at 35 °C	estriol	90	26
	$\beta$ -estradiol	>96	35
	estrone	>96	35
	progesterone	88	29
PONPE-7.5, 2 g/dL at 30 °C <sup>a</sup>	vitamin E		dec <sup>b</sup>
$C_{10}$ -APSO <sub>4</sub> , 2 g/dL at 30 °C <sup>a</sup>	vitamin E		45 <sup>c</sup>

<sup>a</sup> 0.001 M 2-mercaptoethanol present. <sup>b</sup> Vitamin E decomposed. <sup>c</sup> Some decomposition of vitamin E occurred.

concentration factors, the use of the zwitterionic rather than the nonionic surfactant in the phase separation extraction procedure led to somewhat better recoveries for the analytes examined. The phase separation of the zwitterionic  $C_9$ -APSO<sub>4</sub> and  $C_{10}$ -APSO<sub>4</sub> systems was also faster than that of the nonionic PONPE-7.5 system. This fact suggests the possibility of applying this zwitterionic system to continuous-flow schemes such as multisolvent extraction or flow injection analysis.

Almost all of the economical commercially available nonionic surfactants, such as PONPE-7.5 or Triton X-114, which have a suitably low cloud point temperature (i.e. near room temperature) and have been previously employed in cloud point extractions, possess an aromatic ring. Thus, they exhibit an absorbance band at 254 nm, which is a popular detection wavelength for other aromatic organic compounds as well as many biological materials. Due to the fact that the surfactant-rich extractant phase contains considerable surfactant, a huge absorbance peak will result in the ultraviolet region of the spectrum when such nonionic surfactants are used. As illustrated in the figures (chromatograph b in each case), this causes problems when the nonionic PONPE-7.5 surfactant is used in the cloud point extraction. In the case of the steroid hormone separation (Figure 6), the start of a huge peak due to the elution of the nonionic PONPE-7.5 surfactant is observed after separation of the hormones and several hours time is required for its total elution. Furthermore, in the case of progesterone (Figure 7) and vitamin E (Figure 8), the huge PONPE-7.5 surfactant peak overlapped the chromatographic analyte peaks. Such problems were not encountered when the zwitterionic surfactants  $C_9$ - (or  $C_{10}$ )-APSO<sub>4</sub> were used since they only negligibly absorb near 254 nm. This fact should facilitate not only ultraviolet absorbance detection of analytes in the surfactant-rich phase but also fluorescence and phosphorescence detection as well.

Another advantageous property of the zwitterionic surfactant system is that they have their two-phase region at the lower temperature side, as previously described (Figure 2). Consequently, one does not have to heat the solution to cause the phase separation to occur. This is very important in attempting to extract thermally labile compounds or membrane proteins and yet minimizing their decomposition or degradation. In addition, studies have shown that zwitterionic detergents are good solubilization agents and their use in lieu of other charge-type surfactants can minimize decomposition of biological compounds or protein denaturation in many instances (17). This aspect is illustrated by the vitamin E data (Table I, Figure 8). As can be seen, the cloud point extraction using the nonionic surfactant resulted in substantial decomposition of vitamin E whereas its decomposition was much less extensive if the zwitterionic surfactant was used in the

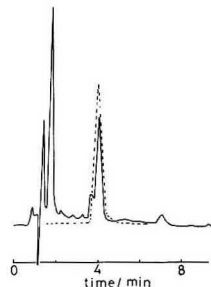


**Figure 9.** Chromatogram of the surfactant-rich extractant phase following cloud point extraction of a coal sample with  $C_9$ -APSO<sub>4</sub>. The dotted line represents the chromatogram obtained following injection of a standard anthracene solution. Chromatographic conditions: 10-cm  $C_{18}$  column; 70:10 (v/v) acetonitrile:water mobile phase; flow rate of 1.00 mL/min; detection at 254 nm.

extraction (both conducted at 30 °C). Essentially no vitamin E decomposition was observed if the zwitterionic extraction was done at 12.5 °C.

The fact that the zwitterionic surfactant system has its two-phase region at the lower temperature side could also prove to be important with respect to convenience in attempted extractions from solid matrices. The extraction of hydrophobic compounds from a solid sample often requires heating to improve mass transfer. For zwitterionic surfactant solutions, a clear homogeneous surfactant micellar solution will result at the required higher temperatures with phase separation subsequently occurring when the solution is cooled back to room temperature. Nonionic surfactant solutions would give the opposite behavior. In this regard, Figure 9 shows the chromatogram obtained for the surfactant-rich phase following the cloud point extraction of a coal sample using the zwitterionic surfactant  $C_9$ -APSO<sub>4</sub>. Although the extraction system was not optimized, it appears that some anthracene was extracted from the coal sample on the basis of a comparison of the retention times with pure standards. This ability to use zwitterionic surfactants for the extraction/preconcentration of hydrophobic species from solids may prove useful in such applications as pesticides in plants, polycyclic aromatic hydrocarbons in dusts or biomass, etc.

A potential problem with use of these zwitterionic surfactants in cloud point extractions stems from the fact that their critical micelle concentrations, cmc's [0.045 M (=1.4 wt %) for  $C_9$ -APSO<sub>4</sub> (14); greater than 0.50 wt % for  $C_{10}$ -APSO<sub>4</sub>], are much higher than those of nonionic surfactants [i.e. 0.20 and 0.35 mM for Triton X-100 and Triton X-114, respectively (4)]. This means that the surfactant "lost" to the aqueous phase in each extractive preconcentration step will be greater for the zwitterionic surfactants. However, the surfactant that has been lost to the aqueous phase can be recovered by the addition of a high concentration of salt.

A general problem encountered for both zwitterionic and nonionic surfactants in the cloud point extraction technique was that the surfactant-rich phase was almost too viscous for convenient sampling by a HPLC microsyringe. It required several minutes to accurately draw a sample from this phase. However, the addition of a small volume of methanol to the surfactant-rich phase after its initial removal from the aqueous-rich phase proved to be effective in decreasing the viscosity of the surfactant-rich phase.

**Cloud Point Extraction of Membrane Proteins.** The hydrophobic membrane protein, bacteriorhodopsin, was efficiently extracted into the zwitterionic  $C_9$ -APSO<sub>4</sub> surfactant phase at slightly acidic pHs (i.e. 5.5–6.5), while the hydrophilic

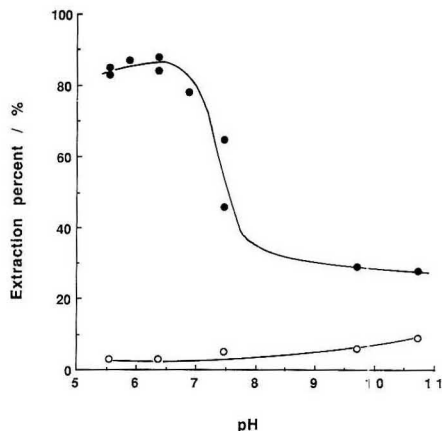


**Figure 10.** Percentage extraction of bacteriorhodopsin (●) and cytochrome *c* (○) as a function of solution pH for cloud point extraction with the zwitterionic surfactant C<sub>9</sub>-APSO<sub>4</sub> at 4 °C.

protein, cytochrome *c*, was not extracted, as shown in Figure 10. This demonstrates that the cloud point type of extraction using the zwitterionic surfactant mediated phase separation approach can also be utilized for the isolation/purification of integral membrane proteins, as had been previously reported only for the nonionic surfactant Triton X-114 (10–13). An advantage of the zwitterionic surfactant mediated extraction process compared to that with Triton X-114 is that the extraction can be carried out at much lower temperatures (at or below 0 °C). This is significant since use of lower extraction temperatures helps to prevent or minimize protein denaturation; particularly in view of the reported fact that there can be significant loss of activity for some enzymes in the highly concentrated Triton X-114 surfactant-rich phase (18). An additional attractive feature stemming from the use of zwitterionic surfactants in protein extraction/isolation schemes is that it will be much easier to subsequently separate the protein molecules from the zwitterionic surfactant-rich phase by dialysis. This stems from the fact that dialysis is most suitable for removal of the detergent from protein molecules in situations where the surfactant has a relatively high cmc value (i.e. > 1 mM) (19), which is the case for the zwitterionic surfactants examined in this work.

It should be noted that the surfactant mediated phase separation technique is similar to the aqueous polymer mediated phase separations, so-called "aqueous two-phase systems". Such aqueous two-phase systems have been widely employed for the extraction of macromolecules (20, 21). In fact, the general method is routinely applied for the separation/purification of a variety of biomaterials, i.e. DNAs, cells, proteins, etc. However, the general aqueous two-phase separation technique is reportedly not very effective for the separation of simpler, smaller organic species (20). Thus, the surfactant cloud point extraction technique described in this paper is more versatile since it can be applied to the separation of not only macromolecules but also smaller molecules/species, such as organic compounds, metal chelates, and oligomers. Also, according to a recent presentation, such cloud point extractions require less extractant material (i.e. the amount of surfactant required for the cloud point technique is much less than the amount of polymer materials required for

aqueous polymeric two-phase-based extractions) (22). In addition to the extraction of relatively hydrophobic species, as demonstrated in this paper, it is expected that use of appropriate affinity ligands in conjunction with the zwitterionic surfactant mediated phase separation technique will also allow for the extraction of more hydrophilic species, as has been reported for some aqueous two-phase systems (21, 23, 24).

#### ACKNOWLEDGMENT

We thank Dr. Fawzy S. Sadek (Winston-Salem State University) for providing the coal sample as well as lab space for conducting a portion of this work during which time our building was closed due to an asbestos crisis. We benefitted from helpful discussions with Dr. Edmondo Pramauro (University of Torino, Italy), Dr. Alain Berthod (University Claude Bernard, France), and Dr. Yasuzo Suzuki (Research Institute for Polymers and Textiles, Japan).

#### LITERATURE CITED

- (1) Laughlin, R. G. In *Advances in Liquid Crystals*; Brown, G. H., Ed.; Academic Press: New York, 1978; Vol. 3, pp 41, 76, 103.
- (2) Watanabe, H. In *Solution Behavior of Surfactants*; Mittal, K. L., Fendler, E. J., Eds.; Plenum Press: New York, 1982; Vol. 2, pp 1305–1313.
- (3) DeGiorgio, V. In *Physics of Amphiphiles: Micelles, Vesicles, and Microemulsions*; DeGiorgio, V., Corti, M., Eds.; North-Holland: Amsterdam, 1985; pp 303–335.
- (4) Hinze, W. L. In *Ordered Media in Chemical Separations*; Hinze, W. L., Armstrong, D. W., Eds.; American Chemical Society: Washington, DC, 1987; pp 48–55 (see also references therein).
- (5) Watanabe, H.; Tanaka, H. *Talanta* **1978**, *25*, 585.
- (6) Hoshino, H.; Saitoh, T.; Takeuchi, H.; Yotsuyanagi, T.; Watanabe, H.; Tachikawa, K. *Anal. Chim. Acta* **1983**, *147*, 339.
- (7) Pramauro, E.; Minero, C.; Pelizzetti, E. In *Ordered Media in Chemical Separations*; Hinze, W. L., Armstrong, D. W., Eds.; American Chemical Society: Washington, DC, 1987; pp 152–161.
- (8) Hinze, W. L.; Singh, H. N.; Fu, Z. S.; Williams, R. W.; Kippenberger, D. J.; Morris, M. D.; Sadek, F. S. In *Chemical Analysis of Polycyclic Aromatic Compounds*; Vo-Dinh, T., Ed.; John Wiley & Sons: New York, 1989; Chapter 5, pp 155–157.
- (9) Pramauro, E. *Ann. Chim. (Ital.)* **1990**, *80*, 101.
- (10) Bordier, C. *J. Biol. Chem.* **1981**, *256*, 1604.
- (11) Bouvier, T.; Elges, R. J.; Bordier, C. *J. Biol. Chem.* **1985**, *260*, 15504.
- (12) Ganong, B. R.; Delmore, J. P. *Anal. Biochem.* **1991**, *193*, 35.
- (13) Pryde, J. G. *Trends Biochem. Sci.* **1988**, *11*, 160–163.
- (14) Nilsson, P. G.; Lindman, B.; Laughlin, R. G. *J. Phys. Chem.* **1984**, *88*, 6357.
- (15) Brunken, J.; Glockner, G. German Domestic Republic Patent 15024, June 24, 1956.
- (16) *CRC Handbook of Chemistry and Physics*, 70th ed.; Weast, R. C., Lide, D. R., Astle, M. J., Beher, W. H., Eds.; CRC Press: Boca Raton, FL, 1989; p D-165.
- (17) Ernst, R. *J. Am. Oil Chem. Soc.* **1980**, *57*, 93.
- (18) Schulze, H. U.; Kanner, R.; Junker, B. *Biochim. Biophys. Acta* **1985**, *814*, 85.
- (19) Furth, A. J. *Methods Enzymol.* **1984**, *104*, 318.
- (20) Albertsson, P. A. *Partition of Cell Particles and Macromolecules*, 2nd ed.; John Wiley & Sons, Inc.: New York, 1971.
- (21) Kula, M. R. In *Protein Purification, Micro to Macro*; Burgess, R., Ed.; Alan R. Liss: New York, 1987; pp 99–115.
- (22) Liu, C. L.; Abbott, N. L.; Srivastava, T.; Nikas, Y.; Blankschtein, D. *Abstracts of Papers*, 65th Colloid and Surface Science Symposium, June 18, 1991; Abstr. No. 151.
- (23) Johansson, G. In *Partitioning in Aqueous Two-Phase Systems: Theory, Methods, Uses, and Applications to Biotechnology*; Walter, H., Brooks, D. E., Fisher, D., Eds.; Academic Press: Orlando, FL, 1985; p 161.
- (24) Muller, W. In ref 23, p 227.

RECEIVED for review June 11, 1991. Accepted August 19, 1991. W.L.H. gratefully acknowledges the financial support of the National Institute of General Medical Sciences through Grant BBCA (AHR-A) 1 R15 GM42076-01 and the University of North Carolina Water Resources Research Institute through Grant 70108. This paper was presented at the 52nd Symposium of Japanese Analytical Chemistry, Obihiro, Hokkaido, Japan, May 19, 1991, and the 65th Colloid and Surface Science Symposium, University of Oklahoma, Norman, OK, June 18, 1991.

## CORRESPONDENCE

### Quadrupole Fourier Transform Mass Spectrometry of Oligosaccharides

Sir: The investigation of bioorganic molecules in Fourier transform mass spectrometry (FTMS) has been greatly advanced by the addition of the external source (1-8). Separating the ion source from the analyzer allows the use of ion sources that generate pressures generally much higher than those necessary to operate the FTMS system (1-8). Thus, the use of liquid secondary ion mass spectrometry (LSIMS) (9) in the FTMS system has been made possible only with an external source (4, 10, 11). Hunt and McIver first showed the capability of liquid secondary ion mass spectrometry (LSIMS)/FTMS on peptides (11). A detection limit of 10 pmole and resolution as high as 20 000 for a peptide with a mass  $m/z$  1758 was obtained (11). Subsequent studies by Hunt and others show that peptides larger than  $m/z$  10 000 can be generated and observed (12). The trapped-ion technique has several inherent advantages. Collisionally induced dissociation can be performed without loss in resolution due to kinetic energy release (13). Ions are all simultaneously sampled during the analysis (1, 2). Photodissociation of trapped ions is far simpler, particularly with low duty time lasers such as excimers (14). Thus, the photodissociation of peptides has been performed in the FTMS system to yield useful sequence information (14-16). Photodissociation has been performed on a 30-pmole sample of a peptide derived from spinach chloroplasts, yielding full sequence information (15). A comparison of FAB fragmentation and photodissociation of peptides shows that photodissociation produces many of the ions found in FAB alone as well as other fragments not observed in the FAB spectra (16). The general performance of FTMS is also enhanced with an external source (4, 17). For example, masses as large as  $m/z$  31 830 corresponding to the cesium iodide cluster  $(CsI)_{122}Cs^+$  have been observed as well as resolution of 53 000 for  $m/z$  9746 corresponding to the cluster  $(CsI)_{37}Cs^+$  (4, 17).

Despite its general utility, QFTMS has been used with a relatively few classes of bioorganic compounds. We have begun the study of oligosaccharides using a QFTMS instrument recently built in our laboratory. No studies exist on LSIMS/FTMS of this class of compounds although the laser desorption/FTMS of oligosaccharides has been reported (18). In this report we show the ideal compatibility of these compounds with LSIMS/FTMS. In contrast to the lack of fragmentation, the presence of pseudomolecular peaks, and the overabundance of matrix ions reported for the FAB spectra of oligosaccharides in sector instruments, we find the spectra of these compounds to be very nearly free of matrix ions with large abundances of both parent and fragment ions (19).

#### EXPERIMENTAL SECTION

All experiments have been performed on the UC Davis QFTMS instrument, which has been described in an earlier publication (20). Ions are produced in a SIMS source fitted with an Antek  $Cs^+$  gun operating between 5 and 10 kV. The primary beam is pulsed and accelerated to a copper probe tip that contains the sample in a glycerol or glycerol/thioglycerol matrix. The resulting secondary ion beam is extracted and guided by a 119 cm long quadrupole ion guide into the analyzer cell contained in the homogeneous region of a superconducting 3-T magnet from Cryomagnetics Inc. The ion current has been monitored on the

rear trapping plate of the analyzer cell and is usually between 1 and 10 nA. The ion production/injection time is variable and is typically between 5 and 500 ms although pulses as narrow as 1 ms are sufficient to obtain signals. The quadrupole, operated in an rf-only mode, functions only as an ion guide with typical frequencies ranging between 0.5 and 1.5 MHz, depending on the mass range desired (21). Pulsing the trapping plate is not necessary to trap the ions. Ions can be collected linearly by increasing the length of the injection until saturation (space charge limit) is reached. Saturation can be anywhere between 100 and 1000 ms, depending on the strength of the signal.

To maintain differential pumping, a turbo pump with a pumping speed of 170 L/s operates on the source. Two APD cryopumps each with a pumping speed of 2000 L/s (for  $N_2$ ) operate on the ion transport region and on the analyzer region. Pressures in the source during an experiment are typically in the range  $10^{-4}$ - $10^{-6}$  Torr, while pressures in the analyzer region are maintained at  $10^{-9}$ - $10^{-10}$  Torr.

All the compounds used are commercially available (Sigma and Aldrich) and are used without further purification. For the low molecular weight oligosaccharides such as the di- and tri-saccharides, impurities of higher molecular weight oligosaccharides are observed. Sample preparation involves dissolving the oligosaccharide in water or dilute acid ( $CH_3CO_2H$  or  $HCl$ ) to form an approximately  $10^{-2}$  M solution. A 1-5- $\mu$ L portion of the solution is placed on a copper probe tip that contains 2  $\mu$ L of matrix material. For the disaccharides, pure glycerol is used. Mixtures of glycerol and thioglycerol are used for the larger oligomers. Before the sample is introduced into the ion source, it is briefly degassed to remove most of the water. When the sample probe is in place, it is grounded and bombarded by a  $Cs^+$  beam produced from an Antek ion gun with acceleration energies typically between 5 and 10 kV. A series of scans are accumulated for each spectra. The number of accumulated scans varies; for long ion injection time (e.g. 500 ms) only 10 scans are accumulated, while for the short (e.g. 5 ms) injection time up to 100 scans are accumulated. A routine analysis usually lasts several minutes.

#### RESULTS

Representative QFTMS spectra of several oligosaccharides are shown in Figures 1-4. Abundant protonated molecular ( $MH^+$ ) and fragment ions are observed with all the oligosaccharides we have investigated.  $\alpha$ -Lactose (4-O- $\beta$ -D-galactopyranosyl- $\alpha$ -D-glucose) and sucrose ( $\alpha$ -D-glucopyranosyl  $\beta$ -D-fructofuranoside) are representatives of the disaccharide samples.

The sucrose sample we obtained contained trisaccharide impurities, which are observed as a trio of peaks having  $m/z$  487, 505, and 523 (Figure 1). The protonated molecular parent of sucrose is readily identifiable, forming the base peak of the spectrum. An adduct of water ( $MH + H_2O$ ) $^+$  is observed for both the disaccharide ( $m/z$  361) and the trisaccharide impurity ( $m/z$  523). Major fragmentation due to the cleavage of the glycosidic bond is also observed ( $m/z$  163) as well as losses of water molecules from both the parent and the fragment ions. The cleavage of the glycosidic linkage ( $m/z$  163) is equivalent to that commonly reported in the mass spectrometry of oligosaccharides (19). Fragmentation to form the protonated monosaccharide ( $m/z$  181) is not observed. A matrix background corresponding to a peak at every mass unit is observed up to around  $m/z$  325. These signals are, however, small with intensities less than 10% and usually below 5% of the base peak. The largest matrix signal is due to pro-



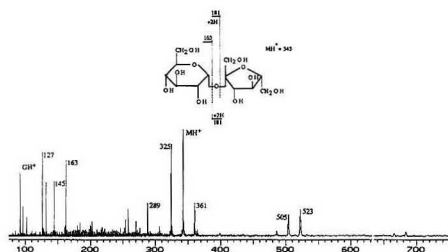


**Figure 1.** Liquid SIMS/FTMS of sucrose with glycerol matrix in broad-band mode. The base peak is the protonated molecular ion. Unidentifiable matrix ions are present at every mass unit with the largest matrix signal ( $m/z$  93) due to the protonated glycerol ion ( $G_1H^+$ ). Fragment ions of sucrose are labeled by their masses with the corresponding fragmentation illustrated in the structure above. The ions having  $m/z$  505 and 523 correspond to oligosaccharide impurities.

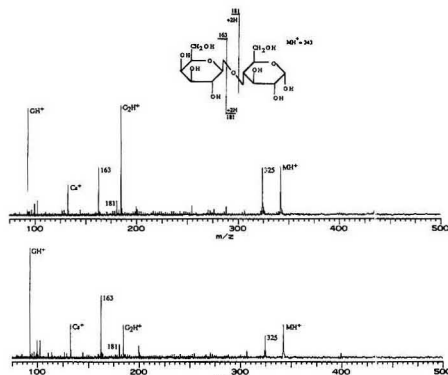


**Figure 2.** Liquid SIMS/FTMS of lactose with a 5-ms injection width and 1-ms detection delay (top spectrum) and a 5-ms injection width and 10-ms detection delay (bottom spectrum) in the broad-band mode. Two prominent matrix peaks are labeled corresponding to protonated glycerol ( $m/z$  92,  $G_1H^+$ ) and the protonated dimer ( $m/z$  185,  $G_2H^+$ ). The dimer decomposes at the longer detection delay time (bottom). Fragment ions are labeled by their masses with the corresponding fragmentation illustrated in the structure above. Both spectra are normalized to the protonated glycerol peak.

tonated glycerol ( $m/z$  93), which is 70% of the base peak.

A signal due to  $Cs^+$  ( $m/z$  133) is often present in the QFTMS spectrum.  $Cs^+$  from the cesium gun is sometimes extracted from the source and injected into the analyzer cell, albeit in small amounts. We find that the intensity of the  $Cs^+$  signal rises as a function of time the sample is in the instrument. Initially, very little or no  $Cs^+$  is observed and, as the sample becomes "old", the  $Cs^+$  intensity increases. This phenomenon may be due to the increase of reflecting collisions between the primary beam and the metal probe tip as the sample and the matrix are depleted. The gun is mounted  $45^\circ$  to the probe tip surface, with the extraction aperture forming an equivalent reflection angle to the  $Cs^+$  gun. When the sample is in place the primary beam is deflected away from the extraction aperture. As the sample is depleted and the metal surface of the probe becomes exposed, reflecting collisions direct the primary beam toward the extraction aperture. This is confirmed by the sole presence of  $Cs^+$  ions after the sample is nearly depleted.

Two spectra of the disaccharide lactose were obtained to illustrate the effects of varying the detection delay time on

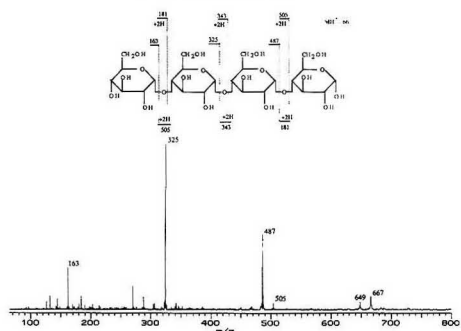


**Figure 3.** Liquid SIMS/FTMS of maltotetraose with glycerol/thioglycerol (1:1) matrix in the broad-band mode. Fragment ions are labeled by their masses. The corresponding fragmentation is illustrated in the structure above.

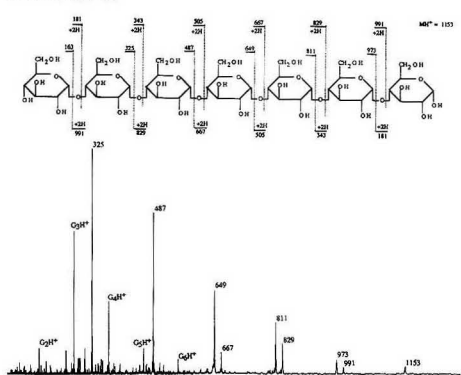


**Figure 4.** Liquid SIMS/FTMS of maltoheptaose with glycerol/thioglycerol (3:1) matrix in the broad-band mode. It is not always possible to totally eliminate matrix ions, but the oligosaccharide signals are clearly identifiable. Signals due to the matrix ions are labeled as  $G_nH^+$ . Fragment ions are labeled by their masses with the corresponding fragmentation illustrated in the structure above.

the general appearance of the spectrum. Figure 2 consists of spectra produced with an ion injection time of 5 ms with a detection delay time of 1 ms (top spectrum) and a detection delay time of 10 ms (bottom spectrum) after the ion injection. Large abundances of protonated glycerol ( $m/z$  93, 97% relative abundance) as well as the protonated dimer ( $m/z$  185, base peak) are observed at the shorter detection delay time. With the longer detection delay time the dimer ion abundance decreases relative to the protonated glycerol. The monoglycerol signal increases as the diglycerol cluster decreases but is not observed in this comparison because both spectra have been normalized to the protonated glycerol base peak. Interestingly, the intensity of the saccharide fragment ions also increases slightly with respect to the parent.

Weak abundances of background matrix ions are also observed with larger oligosaccharides (Figures 3 and 4). The spectrum for maltotetraose (Figure 3), for example, is nearly devoid of matrix ions. No attempts have been made in the experiments to filter out these ions using the quadrupole rods in any of the spectra shown. Although matrix ions can usually be minimized, it is not yet possible to totally eliminate them, as evidenced by the peaks labeled  $G_nH^+$  in the maltoheptaose spectrum. Both examples, maltotetraose and maltoheptaose

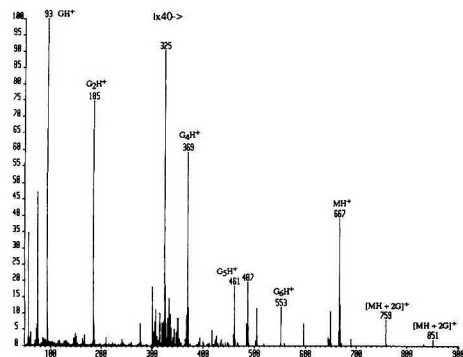


**Figure 5.** FABMS of maltotetraose using a glycerol matrix in a VG ZAB-2F instrument. Identifiable signals due to matrix and matrix/analyte complex ions are labeled accordingly (e.g.  $G_nH^+$  or  $[MH + G_n]^+$ ). A parent ion is obtained as well as two major fragment ions, which are also observed in the QFTMS spectra, i.e.  $m/z$  325 and 487, respectively.

yield large fragment ion abundances. The spectrum of maltotetraose is significant in that underivatized samples of this compound have been reported to produce little fragmentation in sector instruments (22). For comparison, we have obtained the spectrum of this compound using a VG ZAB-2F double-sector instrument (Figure 5). The prevalence of matrix ions in this spectrum is apparent as well as the formation of complexes between analyte and matrix molecules ( $M + G_n + H^+$ ) (23). Fragment ions are formed, however, corresponding to the loss of one and two glycoside units. The major fragment peak observed in both instruments corresponds to the same ionic species ( $m/z$  325). The relative abundance of the parent is greater in the sector than in the QFTMS instrument.

The large abundances of fragment ions as well as the lack of matrix and matrix/analyte clusters may be attributed to the significantly different time scales between the two MS methods. The time between ion production and ion detection for sector instruments is in the order of microseconds, while for the FTMS system it ranges from milliseconds to even minutes. We propose that sufficient internal energy is obtained by the ions during LSIMS and FAB ionization to produce the unimolecular fragmentation of both the oligosaccharide and matrix cluster ions. However, only the longer experimental time scale of FTMS allows the ions sufficient time to undergo a greater degree of fragmentation. This effect is somewhat illustrated by the two spectra of lactose, where the detection times are varied. It is further evidenced by the similarity in fragment ions observed in both the QFTMS and ZAB spectra. Thus, by varying the detection delay time with the QFTMS instrument, it is possible to vary the relative abundance of the parent and fragment ions (24). In sector instruments, derivatization is often used to increase the yields of fragmentation. However, derivatization significantly increases the mass of the compound and represents an added step (25). Other complications occur during derivatization such as noncompletion and even degradation of naturally occurring, partially derivatized oligosaccharides (26). Thus, in general, fragmentation without derivatization is clearly desirable.

By far the major cleavage reactions observed with all the oligosaccharides we have investigated in the QFTMS instrument correspond to the same as those observed for the disaccharides. These cleavages occur strictly along interglycosidic linkages, producing the fragments shown earlier. The fragmentation features of maltohexaose and malto-

heptaose differ slightly from those of smaller oligomers in that sequence peaks appear as doublets starting with the tetrasaccharide fragment ions of the larger oligomers up to the parent peak. The doublets correspond to dissociations occurring on both sides of the connecting oxygen atom (Figure 4).

A recent report has shown that surface-induced dissociation (SID) occurs when ions are transported by the quadrupole rods and collided with a 90% transmittance wire mesh, which forms the front trapping plate (i.e. the trapping plate closest to the quadrupole rods) of the analyzer cell (26). We must emphasize that the UCD instrument contains a solid stainless steel plate with a 2-mm aperture as a front trapping plate. Ions enter unhindered through the hole into the analyzer cell. SID may occur if the injected ions collide with a solid rear trapping plate of the analyzer cell. However, the rear trapping plate of our instrument has a 13-mm hole covered with a high-transmittance gold wire mesh (90% optical transmittance), which is used as part of the internal electron impact source. The trapping plate is maintained between 1.5 and 3.5 V, thus allowing high translational energy ions to go through the mesh and become lost. In addition, SID on metal surfaces is a low-efficiency process due to the competition with neutralization reactions so that the few back-scattered particles are most likely neutralized. It is, therefore, unlikely that SID occurs on the rear trapping plate of our instrument. Similar conclusions have been reported by Williams et al. on their QFTMS instrument (26). A source for vibrational excitation could be collisions between the ions and the background neutral either during ion transport or after the ions have been trapped in the analyzer cell. This mode of excitation is unlikely due to the low background pressure ( $6 \times 10^{-10}$  Torr) in the analyzer chamber during the experiments. Hence, we are fairly confident that ions acquire sufficient energy for decomposition during ion formation and decompose unimolecularly in the analyzer cell of the FTMS instrument. Further investigations are underway to probe the magnitude and the nature of the vibrational excitation.

Cleavages within the glycosidic rings are not observed with any of the oligosaccharides in the study. This means that no information on the linkage positions is obtainable. This result is not atypical for the FABMS of underivatized oligosaccharides. However, the CID of the trapped ions or better yet, the photodissociation, may yield fragmentation of the glycosidic ring, thus providing linkage information. The large fragment ion abundances and the low matrix background means that MS/MS experiments can also be performed on the daughter ions, yielding further structural information.

The detection limit of the instrument for oligosaccharides has been determined by using maltotriose. At least  $6 \mu\text{g}$  (12 nmol) of material is needed to obtain a spectrum complete with parent and fragment ions. With this amount of sample, a signal/noise ratio of roughly 4 is obtained for the parent ( $m/z$  505) and about 20 for the most abundant disaccharide fragment ( $m/z$  325). This limit corresponds well to those reported for sector instruments, which is between 1 and  $5 \mu\text{g}$  (27). Further optimization, however, is still being performed on the instrument.

Satisfactory agreement is obtained between the observed masses and exact mass for parent and fragment ions despite the large mass range. An average deviation of 56 ppm between exact mass and observed mass is obtained for the ions produced from maltohexaose. This mass range includes the smallest fragment with  $m/z$  163 to the protonated parent with  $m/z$  991. This kind of mass deviation is not yet at the best limit reported for FTMS instruments. Average mass deviation of less than 10 ppm has been reported for the laser desorption/FTMS of several oligosaccharides (28). The resulting

resolution at the high mass value is a limitation of the data system and can be corrected by using faster digitization rates.

Further work is in progress to increase the sensitivity and to determine the upper mass limit of the instrument for oligosaccharides. Laser photodissociation studies are currently in progress to produce fragmentation of the glycosidic ring to yield pos-

CONCLUSION

analysis of oligosaccharides. Extra abundances of fragment ions are observed. As with sector instruments, sensitivity is not good at high mass values. Oligosaccharides are clean without major interference from matrix ions. A methylation, acetylation is not necessary to

Further work is in progress to increase the sensitivity and to determine the upper mass limit of the instrument for oligosaccharides. Laser photodissociation studies are currently in progress to produce fragmentation of the glycosidic ring to yield pos-

34612-38-9; maltoheptaose, 34620-78-5.

LITERATURE CITED

(1) Comisarow, M. B.; Marshall, A. G. *Chem. Phys. Lett.* **1974**, *25*, 1-4.

(2) Comisarow, M. B.; Marshall, A. G. *Chem. Phys. Lett.* **1974**, *26*, 1-4.

(3) McIver, H. I., Jr.; Hunter, H. L.; Bowers, W. D. *Int. J. Mass Spectrom.* **1974**, *15*, 1-12.

(4) Lebrilla, C. B.; Amster, J. J.; McIver, H. I., Jr. *Int. J. Mass Spectrom.* **1975**, *18*, 1-12.

(5) Kotel, P.; Allemann, M.; Keilmann, H.; Wanczek, K. P. *Int. J. Mass Spectrom.* **1976**, *21*, 1-12.

(6) Kotel, P.; Allemann, M.; Keilmann, H.; Wanczek, K. P. *Int. J. Mass Spectrom.* **1976**, *22*, 1-12.

(7) Aiford, J. M.; Weiss, F. D.; Laaksonen, H. I.; Smailey, H. E. *J. Phys. Chem.* **1977**, *81*, 1-12.

(8) McManon, I. B. Proceedings of the 37th ASMS Conference on Mass Spectrometry and Allied Topics, 1987, 1-12.

(9) Kotel, P.; McManon, I. B. *Int. J. Mass Spectrom. Ion Processes* **1988**, *85*, 1-12.

(10) Barber, M.; Borzani, F. S.; Seagwick, R. D.; Byer, A. N. *J. Chem. Phys.* **1988**, *88*, 1-12.

(11) Lebrilla, C. B.; Williams, C. E. *Anal. Chem.* **1989**, *61*, 1-12.

(12) Lebrilla, C. B.; Williams, C. E.; Amster, J. J.; McIver, H. I., Jr. *Anal. Chem.* **1989**, *61*, 1-12.

(13) Lebrilla, C. B.; Williams, C. E. *Anal. Chem.* **1987**, *59*, 1-12.

(14) Lebrilla, C. B.; Williams, C. E. *Anal. Chem.* **1987**, *59*, 1-12.

(15) Lebrilla, C. B.; Williams, C. E. *Anal. Chem.* **1987**, *59*, 1-12.

(16) Lebrilla, C. B.; Williams, C. E. *Anal. Chem.* **1987**, *59*, 1-12.

(17) Lebrilla, C. B.; Williams, C. E. *Anal. Chem.* **1987**, *59*, 1-12.

(18) Lebrilla, C. B.; Williams, C. E. *Anal. Chem.* **1987**, *59*, 1-12.

(19) Lebrilla, C. B.; Williams, C. E. *Anal. Chem.* **1987**, *59*, 1-12.

(20) Lebrilla, C. B.; Williams, C. E. *Anal. Chem.* **1987**, *59*, 1-12.

(21) Lebrilla, C. B.; Williams, C. E. *Anal. Chem.* **1987**, *59*, 1-12.

(22) Lebrilla, C. B.; Williams, C. E. *Anal. Chem.* **1987**, *59*, 1-12.

(23) Lebrilla, C. B.; Williams, C. E. *Anal. Chem.* **1987**, *59*, 1-12.

(24) Lebrilla, C. B.; Williams, C. E. *Anal. Chem.* **1987**, *59*, 1-12.

(25) Dell, A.; Tiller, P. R. *Biochem. Biophys. Res. Commun.* **1986**, *135*, 1-12.

(26) Williams, E. R.; Henry, K. D.; McLafferty, F. W.; Shabanowitz, J.; Hunt, D. F. *J. Am. Chem. Soc.* **1986**, *108*, 1-12.

(27) Dell, A.; Oates, J. E.; Morris, H. R.; Eoac, H. *Int. J. Mass Spectrom.* **1986**, *80*, 1-12.

(28) Lam, Z.; Comisarow, M. B.; Dutton, G. G. S.; Parolis, H.; Parolis, L. A. *Anal. Chem.* **1986**, *58*, 1-12.

Lambert Neale  
Sesi McLaughlin

A Daniel Jones  
Carlito B. Lebrilla\*

Department of Chemistry  
Director for Advanced Instrumentation  
University of California

Presented at the Meeting of the American Chemical Society, Division of Analytical Chemistry, San Francisco, California, September 1990.

Financial support has been provided by the Chemistry Department of the University of California, Davis, a grant from the National Science Foundation (NSF) (CHE-8806011).

to thank the U. C. President's Undergraduate Fellowship Program for the award.

Separation and Determination of Copper, Zinc, Palladium, Iron, and Manganese with a New Tetra(4-Carboxyphenyl)porphyrin and Reversed-Phase HPLC on a Liquid Chromatography

Sir: Porphyrins are highly sensitive reagents for the spectrophotometric determination of trace amounts of metals. The metal complexes certainly interferes with the spectrophotometric determination of metals. Separation of these metal complexes is necessary for the determination of metals. Determined at one wavelength, thus the application of UDFC to the separation and determination of metalloporphyrins is highly sensitive and selective. The metalloporphyrins are: *meso*-tetraphenylporphyrin (TPP) (1, 2), *meso*-tetrakis(4-hydroxyphenyl)porphyrin (THPP) (3), and *meso*-tetrakis(4-

carboxyphenyl)porphyrin (TCPP) (4). In these porphyrin reagents only TPP and THPP have been applied to the determination of metals. TDD was used to determine Cu, Zn, and Ni in NRS human liver, and limits of detection (5 µL injected) were 125 pg for Cu and 9150 pg for Zn. We synthesized a new porphyrin reagent, *meso*-tetrakis(4-carboxyphenyl)porphyrin (TCPP) (4). The metalloporphyrins Fe(III), Zn(II), Pd(II), and Cu(II) were successfully separated by reversed-phase HPLC on a liquid chromatography. This method was applied to the determination of the metals in the peach leaves

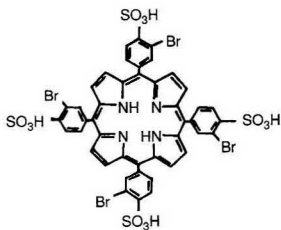


Figure 1. Structure of *meso*-BrTPPS<sub>4</sub>.

standard sample, and it is simple, convenient, and exact. Limits of detection (20  $\mu$ L injected) were 160 pg for Mn, 79 pg for Fe, 70 pg for Pd, 36 pg for Cu, and 31 pg for Zn. The number of simultaneous quantitative determinations of metals in this method is more and the limits of detection are lower than that in two reported papers (2, 5).

### EXPERIMENTAL SECTION

**Apparatus and Chemicals.** The high-performance liquid chromatography system (Model LC-6A, Shimadzu, Japan) consisted of an auto inject valve (20- $\mu$ L sample loop, Model SIL-6A, Shimadzu, Japan) and a UV-vis spectrophotometer (Model SPD-6AV, Shimadzu, Japan). A column packed with Lichrosorb RP-18 (particle size, 5  $\mu$ m; 200  $\times$  4.6 mm i.d.; E. Merck, West Germany) was used. A spectrophotometer (Model UV-3000, Shimadzu, Japan) was used.

The stock solutions of Mn(II), Fe(III), Zn(II), Pd(II), and Cu(II) (1.000 mg·mL<sup>-1</sup>) were prepared from "high pure" metals by dissolving the metal (purity > 99.99%, Shanghai Chemical Co., Shanghai, China) in 1:1 (v/v) nitric acid. Working standards were prepared by diluting the stock solutions. The chelating reagent *meso*-tetrakis(3-bromo-4-sulphophenyl)porphine and the other porphyrins were synthesized according to the method of Fleischer (7). The *meso*-BrTPPS<sub>4</sub> solution (1.5  $\times$  10<sup>-4</sup> mol·L<sup>-1</sup>) was prepared by dissolving *meso*-BrTPPS<sub>4</sub> in water. The ion-pair reagent was tetrabutylammonium bromide (TBABr, AR, Shanghai Chemical Co., Shanghai, China). Double-distilled water was used throughout. All other reagents and solvents were of analytical-grade reagent.

**Formation of Complexes.** *meso*-BrTPPS<sub>4</sub> (3 mL, 1.5  $\times$  10<sup>-4</sup> mol·L<sup>-1</sup>), 5.0 mL of 1.0 mol·L<sup>-1</sup> acetate buffer (pH 4.1), 1.0 mL of 0.01% (w/w) beryllon II (2-(3,6-disulfo-8-hydroxynaphthylazo)-1,8-dihydroxynaphthalene-3,6-disulfonic acid, tetrasodium salt), and 2.0  $\mu$ g of Hg(II) were added to a sample containing Cu(II), Zn(II), Pd(II), Mn(II), and Fe(III), and the mixture was diluted to about 15 mL. The solution was heated in boiling water for 45 min, cooled to room temperature, and then diluted to 25.00 mL for HPLC analysis and spectrophotometric analysis.

**Separation of the Complexes and Reagent.** For HPLC analysis, the 5- $\mu$ m ODS reversed phase was equilibrated with an aqueous mobile phase containing 45% acetonitrile and 55% water (v/v) (2.0 mmol·L<sup>-1</sup> TBABr and 10 mmol·L<sup>-1</sup> acetate buffer pH 5.0). A 20- $\mu$ L aliquot of the 25.00 mL of prepared solution was injected by the auto inject valve. The flow rate of the mobile phase was 1.0 mL·min<sup>-1</sup> and the detection wavelength was 420 nm. The sensitivity was set at 0.002 absorbance unit at full scale (AUFS). The amount of each metal was determined by measuring the peak areas.

### RESULTS AND DISCUSSION

**Selection of Porphine Reagent.** We synthesized a series of compounds of *meso*-tetrakis(4-sulphophenyl)porphine (TPPS<sub>4</sub>) derivatives of fluorine, chlorine, and bromine because the halogen substituents have obvious influence upon the retention behavior of compounds (8). It was found that each porphine reagent can form stable complexes with Mn(II), Fe(III), Zn(II), Pd(II), and Cu(II) in the conditions chosen in this paper, and the halogen substituents resulted in an obvious increase in retentions of TPPS<sub>4</sub> and their complexes (Tables I and II). The retention sequence of the porphyrins

Table I. Capacity Factors (*k'*) of Porphyrin Reagents on a C<sub>18</sub> Column<sup>a</sup>

	TPPS <sub>4</sub>	<i>meso</i> -FTPPS <sub>4</sub>	<i>meso</i> -ClTPPS <sub>4</sub>	<i>meso</i> -BrTPPS <sub>4</sub>
<i>k'</i>	2.10	5.67	9.48	15.19

<sup>a</sup> Conditions: column, 150  $\times$  5 mm i.d., 5- $\mu$ m YWG-C<sub>18</sub>; mobile phase, 40% acetonitrile, 60% H<sub>2</sub>O (pH 6.0) and 5 mmol·L<sup>-1</sup> TBA-Br; flow rate, 1.0 mL·min<sup>-1</sup>; detection, 420 nm, 0.02 AUFS.

Table II. Capacity Factors (*k'*) of Porphyrin Complexes on the C<sub>18</sub> Column

	Mn(II)	Fe(III)	Zn(II)	porphine	Pd(II)	Cu(II)
TPPS <sub>4</sub> <sup>a</sup>	1.82	2.40	10.24	11.15	11.15	13.72
<i>m</i> -BrTPPS <sub>4</sub> <sup>b</sup>	0.55	1.27	1.89	4.91	9.54	9.68

<sup>a</sup> Conditions: column, 200  $\times$  4.6 mm i.d., 5- $\mu$ m, Lichrosorb RP-18; mobile phase, acetonitrile-water (40:60, v/v) containing 8.0 mmol·L<sup>-1</sup> TBABr, pH 4.1; flow rate: 1.0 mL·min<sup>-1</sup>; detection: 420 nm, 0.002 AUFS. <sup>b</sup> Conditions: column, 200  $\times$  4.6 mm i.d., 5- $\mu$ m, Lichrosorb RP-18; mobile phase, acetonitrile-water (45:55, v/v) containing 2.0 mmol·L<sup>-1</sup> TBABr, pH 5.0; flow rate, 1.0 mL·min<sup>-1</sup>; detection, 420 nm, 0.002 AUFS.

is *meso*-BrTPPS<sub>4</sub> > *meso*-ClTPPS<sub>4</sub> > *meso*-FTPPS<sub>4</sub> > TPPS<sub>4</sub>. The values of *k'* for the porphyrins increased with the decrease of the electronegativities of the halogen substituents and with the increase of the size of porphine molecules. In the optimum conditions, TPPS<sub>4</sub> and its complex of Pd(II) are not separated but *meso*-BrTPPS<sub>4</sub> and its complexes of five metal ions are completely separated. Neither the complex of Pd(II) with *meso*-FTPPS<sub>4</sub> nor *meso*-ClTPPS<sub>4</sub> is completely separated, thus *meso*-BrTPPS<sub>4</sub> was selected for the further HPLC research to separate and determine more metal ions.

**Formation of Complexes.** Our experimental results showed that Fe(III) or Mn(II) complexes formed slowly with *meso*-BrTPPS<sub>4</sub>, thus Hg(II) (9) was used to catalyze the reaction of Mn(II) and *meso*-BrTPPS<sub>4</sub>. The 2.0- $\mu$ g amount of Hg(II) used in this experiment was enough. Beryllon II (10) was used to efficiently catalyze the reaction of Fe(III) and *meso*-BrTPPS<sub>4</sub>, but it had little influence upon the complex reaction of Mn(II), Zn(II), Pd(II), or Cu(II). The amount of beryllon II used in our studies was examined, and 1.0 mL of 0.01% (w/w) beryllon II solution was enough. Beryllon II has no absorbance at about 420 nm, so it has no influence upon the separation of the metal complexes. All peak areas of the complexes showed little change after 2 days. It was found that the pH change from 4 to 7 had little effect on the chelating reactions of Cu(II), Zn(II), Mn(II), and Pd(II) but the absorbance of Fe(III) decreased at pH > 4. The pH value of 4.1 was used in this paper. The 5-mL amount of 1.5  $\times$  10<sup>-4</sup> mol·L<sup>-1</sup> *meso*-BrTPPS<sub>4</sub> solution used in the experiments was enough. The UV-vis spectra of these complexes and the reagent are shown in Figure 2. The wavelength of 420 nm was chosen as the detection wavelength so that all the complexes could be detected simultaneously.

**HPLC Separation of Mn(II), Fe(III), Zn(II), Pd(II), and Cu(II) Complexes.** When a mixture of methanol-water (containing TBABr) was used as the mobile phase, the complexes and the reagent gave wide and tailing peaks. Acetonitrile-water (containing TBABr) mixture proved to be a very good mobile phase for this separation and was selected.

The effect of the concentration of CH<sub>3</sub>CN and TBABr on the capacity factors (*k'*) was examined (Figures 3 and 4). The retention and resolution decreased with increasing concentration of CH<sub>3</sub>CN and increased with increasing concentration of TBABr. The concentration of 45% (v/v) CH<sub>3</sub>CN and 2 mmol·L<sup>-1</sup> TBABr was adopted. The metalloporphyrin of

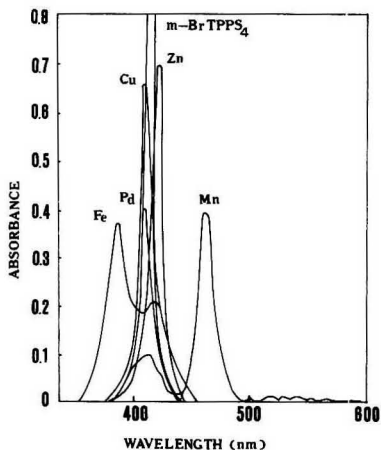


**Figure 2.** Absorption spectra of complexes and reagent. Experimental conditions: All the complexes and the reagent were dissolved in the chosen mobile phase and the concentrations were all  $3.0 \times 10^{-5}$  mol·L<sup>-1</sup>, pH 4.1; for the absorption spectra of complexes, the reference was the reagent blank; for the absorption spectra of *meso*-BrTPPS<sub>4</sub>, the reference was water.

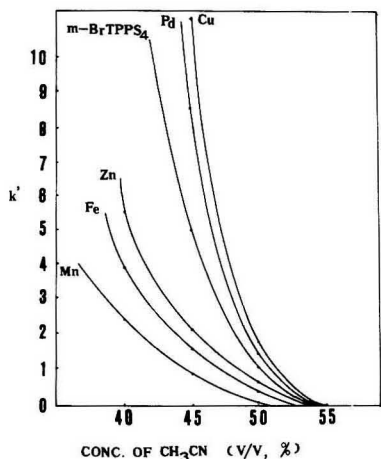


**Figure 3.** Effect of concentration of CH<sub>3</sub>CN on the capacity factor: 2 mM TBABr, pH 5.0, 1.0 mL·min<sup>-1</sup>.

Mn(II) exists in the form of Mn<sup>3+</sup>(*meso*-BrTPPS<sub>4</sub>)<sup>-</sup>(TBA<sup>+</sup>)<sub>4</sub> in the mobile phase because the metalloporphyrin of Mn(II) can be easily oxidized into the metalloporphyrin of Mn(III) (II). So the metalloporphyrin of Mn(III) was eluted before that of Fe(III).

The effect of pH in the mobile phase on the capacity factor and the peak area was studied (Table III). The higher the pH of the mobile phase, the shorter the retention time. The resolution of peaks decreased with increasing pH for these complexes, but the peak areas showed little change. The reason the retention time increased with a decrease in pH may be that the concentration of the acetate ion (Ac<sup>-</sup>) in the eluent decreased as pH decreased, thus the neutral ion pair TBA<sup>+</sup>Ac<sup>-</sup> decreased and the ion pairs of the metal complexes increased, to the retention time of the metal complexes increased. The

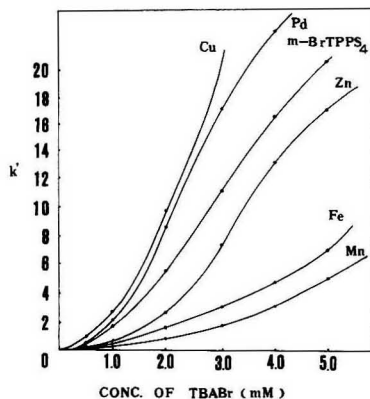


**Figure 4.** Effect of concentration of TBABr on the capacity factor: 45% CH<sub>3</sub>CN (v/v), pH 5.0, 1.0 mL·min<sup>-1</sup>.

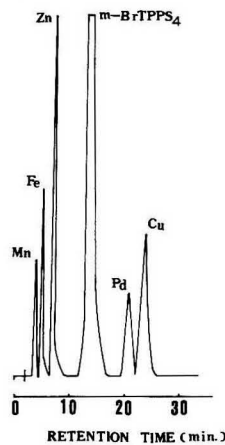


**Figure 5.** Separation of Mn(II), Fe(III), Zn(II), Pd(II), and Cu(II) *meso*-BrTPPS<sub>4</sub> complexes by HPLC: column, 200 × 4.6 mm 5- $\mu$ m Lichrosorb RP-18; mobile phase, 45% CH<sub>3</sub>CN (v/v), 55% H<sub>2</sub>O (v/v), 2 mM TBABr, and 10 mM acetate buffer (pH 5.0); flow rate, 1.0 mL·min<sup>-1</sup>; sample, 20  $\mu$ L containing 0.16  $\mu$ g·mL<sup>-1</sup> of every metal ion; detector, UV at 420 nm, 0.002 AUFS.

**Table III.** Effect of the pH of the Mobile Phase on the Capacity Factor and the Peak Area<sup>a</sup>

	<i>k'</i>				
	4.1	4.4	4.7	5.0	5.4
MnL	1.47	0.64	0.57	0.55	0.53
FeL	2.15	1.45	1.38	1.27	1.18
ZnL	14.60	5.03	3.75	1.89	0.73
PdL	25.88	17.80	12.29	8.54	4.92
CuL	29.94	20.54	14.13	9.68	5.52
L	14.06	10.09	7.10	4.91	1.59

<sup>a</sup> Experimental conditions: 45% CH<sub>3</sub>CN (v/v), 2 mM TBABr, 1.0 mL·min<sup>-1</sup>.

value of pH 5.0 was chosen in this paper. It was found that the concentration of acetate buffer also had some effect on the separation, and 10 mmol·L<sup>-1</sup> acetate buffer was suitable



Table IV. Result of Sample Analysis

element	ref value, $\mu\text{g}\cdot\text{g}^{-1}$	found, <sup>a</sup> $\mu\text{g}\cdot\text{g}^{-1}$	SD <sup>b</sup>	RSD <sup>c</sup>
Mn	75.4	71.9	1.88	2.61
Fe	431	439	22.98	5.24
Zn	22.8	23.4	0.27	1.17
Cu	10.4	10.1	0.18	1.78
Pd		not found		

<sup>a</sup> Average value of five determinations. <sup>b</sup> Standard deviation.  
<sup>c</sup> Relative standard deviation.

for the separation. When the concentration of acetate buffer is larger than  $10\text{ mmol}\cdot\text{L}^{-1}$ , the retention time of the metal complexes will decrease and this experimental result is also an evidence of the previous explanation for the effect of pH upon the retention time. In this paper,  $1.0\text{ mL}\cdot\text{min}^{-1}$  was used as the flow rate and a  $20\text{-}\mu\text{L}$  sample was injected. Chromatograms obtained under these conditions are shown in Figure 5.

**Calibration Curves.** The calibration curves for the determination of Mn(II), Fe(III), Pd(II), Cu(II), and Zn(II) were linear over the range  $(0.07\text{--}4.4) \times 10^{-6}\text{ M}$  for Mn,  $(0.07\text{--}4.3) \times 10^{-6}\text{ M}$  for Fe,  $(0.04\text{--}4.0) \times 10^{-6}\text{ M}$  for Pd,  $(0.06\text{--}5.0) \times 10^{-6}\text{ M}$  for Cu, and  $(0.06\text{--}5.0) \times 10^{-6}\text{ M}$  for Zn; Mn,  $C(\mu\text{g}\cdot\text{mL}^{-1}) = (7.80 \times 10^{-6}) \times \text{area}$ ; Fe,  $C(\mu\text{g}\cdot\text{mL}^{-1}) = (4.00 \times 10^{-6}) \times \text{area}$ ; Pd,  $C(\mu\text{g}\cdot\text{mL}^{-1}) = (3.43 \times 10^{-6}) \times \text{area}$ ; Cu,  $C(\mu\text{g}\cdot\text{mL}^{-1}) = (1.81 \times 10^{-6}) \times \text{area}$ ; and Zn,  $C(\mu\text{g}\cdot\text{mL}^{-1}) = (1.54 \times 10^{-6}) \times \text{area}$ . The following detection limits (at a signal-to-noise ratio of 2:1) for metals ( $20\text{ }\mu\text{L}$  injected) were achieved:  $160\text{ pg}$  of Mn,  $79\text{ pg}$  of Fe,  $70\text{ pg}$  of Pd,  $36\text{ pg}$  of Cu, and  $31\text{ pg}$  of Zn.

**Effect of Foreign Ions.** The effect of the presence of other ions on the determination of Mn(II), Fe(III), Zn(II), Pd(II), and Cu(II) was examined. It was found that metal ions such as Cd(II), Pb(II), Hg(II), Co(II), and Ni(II) which could react with *meso*-BrTPPS<sub>4</sub> would not interfere with the determination, because they did not form complexes with *meso*-

BrTPPS<sub>4</sub> or the formed metal complexes were not eluted.

**Sample Analysis.** The peach leaves standard sample (No. 08501) was provided by the Institute of Environmental Chemistry, Academia, Sinica, Beijing. The results are shown in Table IV. The contents of Mn, Fe, Zn, and Cu obtained are in good agreement with the reference values.

#### LITERATURE CITED

- (1) Saitoh, K.; Kobayashi, M.; Suzuki, N. *J. Chromatogr.* **1982**, *243*, 291-300.
- (2) Saitoh, K.; Suzuki, N. *Anal. Chim. Acta* **1985**, *178*, 169-177.
- (3) Kobayashi, M.; Saitoh, K.; Suzuki, N. *Chromatographia* **1985**, *20* (2), 72-74.
- (4) Igarashi, S.; Nakano, M.; Yotsuyanagi, T. *Bunseki Kagaku* **1983**, *32*, 67-68.
- (5) Igarashi, S.; Hashimoto, T.; Matsumoto, Y.; Yotsuyanagi, T. *Bunseki Kagaku* **1983**, *32*, 591-591.
- (6) Igarashi, S.; Obara, A.; Adachi, H.; Yotsuyanagi, T. *Bunseki Kagaku* **1983**, *35*, 829-831.
- (7) Fleischer, E. B.; Palmer, J. M.; Srivastava, T. S.; Chatterjee, A. *J. Am. Chem. Soc.* **1971**, *93* (13), 3182-3187.
- (8) Engelhart, H. *High-Performance Liquid Chromatography*; Springer Verlag: Berlin, 1979.
- (9) Tabata, M.; Tanaka, M. *Anal. Lett.* **1980**, *13* (A6), 427-438.
- (10) Zhang, C. Y.; Yao, X. D.; Cheng, J. K. *Chem. J. Chin. Univ.* **1985**, *6* (12), 1080-1082.
- (11) Dolphin, D., Ed. *The Porphyrins*; Academic: New York, 1978; Vol. 1, Chapter 10.

\* To whom correspondence should be addressed.

Xue-Jun Xu  
Hua-Shan Zhang  
Chuan-You Zhang  
Jie-Ke (Jai-Kai) Cheng\*

Department of Chemistry  
Wuhan University  
Wuhan 430072, China

RECEIVED for review January 15, 1991. Revised manuscript received July 26, 1991. Accepted July 31, 1991. This project was supported by the National Natural Science Foundation of China.

## TECHNICAL NOTES

### Determination of Total and Free Sulfur Dioxide in Wine by Flow Injection Analysis and Gas-Diffusion Using *p*-Aminoazobenzene as the Colorimetric Reagent

Jordi Bartroli,\* Manel Escalada, Cecilia Jimenez Jorquera, and Julian Alonso

Departament de Quimica, Universitat Autònoma de Barcelona, 08193 Eellaterra, Spain

#### INTRODUCTION

Sulfur dioxide is typically used as an antioxidant and antiseptic in winemaking. As a result, this substance occurs in two different forms in wine: free (aqueous SO<sub>2</sub> and HSO<sub>3</sub>, the actual active fraction) and bound to aldehyde and ketone groups (basically acetaldehyde, with which it forms hydroxysulfonates) (1). The total and free SO<sub>2</sub> contents of wine are key analytical parameters for must and wine quality control; the amounts added to wine should ensure adequate protection while complying with prevailing legislation. Processing of a large number of samples calls for the use of automated methods minimizing analytical times and costs in addition to providing major advantages over the typically laborious classical distillation methods (2, 3) and iodometries, which are subject to a number of interferences (2).

So far, sulfur dioxide has been determined by various FIA methods (4-6), even in environmental analysis (7-9). FIA methods for the determination of this compound in wine rely on colorimetric techniques based on the well-known *p*-rosaniline reaction (10-12) or on potentiometric (13, 14) or chemiluminescence detection (15). None of these methods allows total SO<sub>2</sub> to be determined, and only those including a gas-diffusion separation can be applied to colored wine. However, some commercially available continuous segmented-flow analyzers (SFA) allow the determination of total and free SO<sub>2</sub> in wine. All of them include a gas-diffusion module for sample treatment and use *p*-rosaniline as reagent.

The FIA methods reported herein involve a preliminary separation by means of a gas-permeable membrane, which makes it more selective and applicable to any type of wine,

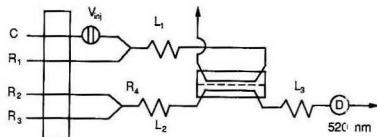


**Figure 1.** Scheme of the FIA configuration used for the determination of free  $\text{SO}_2$ . Conditions: flow rate of C,  $R_1$ ,  $R_2$ , and  $R_3$ , 0.58 mL/min;  $V_{m1} = 300 \mu\text{L}$ ;  $L_1$ , 30 cm  $\times$  0.5 mm i.d.;  $L_2$ , 200 cm  $\times$  0.7 mm i.d.;  $L_3$ , 250 cm  $\times$  0.5 mm i.d.; C and  $R_1$ , 0.6 M HCl;  $R_2$ , 1% HCHO in 0.2 M HCl;  $R_3$ , 0.004% PAAB.

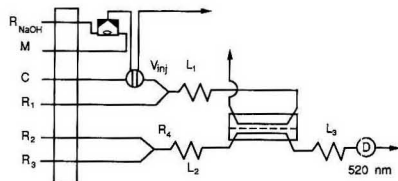


**Figure 2.** Scheme of the FIA configuration used for the determination of total  $\text{SO}_2$ . Conditions: flow rate of C,  $R_1$ ,  $R_2$ , and  $R_3$ , 0.83 mL/min; flow rate of  $R_{\text{NaOH}}$ , 0.6 mL/min;  $V_{m1} = 50 \mu\text{L}$ ; volume of mixing chamber, 1 mL;  $L_1$ , 30 cm  $\times$  0.5 mm i.d.;  $L_2$ , 200 cm  $\times$  0.7 mm i.d.;  $L_3$ , 200 cm  $\times$  0.8 mm i.d.; M, sample;  $R_{\text{NaOH}}$ , 4 M NaOH; C, 2 M HCl;  $R_1$ , 6 M HCl;  $R_2$ , 1% HCHO in 0.2 M HCl;  $R_3$ , 0.004% PAAB.

whatever its color. For the determination of total  $\text{SO}_2$ , the sample is continuously hydrolyzed within the FIA system prior to analysis in order to release all bound  $\text{SO}_2$ . Automation of this step will allow the sample manipulation process to be simplified and sample throughput to be increased with respect to the classical methods.

The analytical basis for the method is the reaction between  $\text{SO}_2$  and *p*-aminoazobenzene (PAAB) and formaldehyde in an acid medium, which is monitored colorimetrically. PAAB is chemically similar to *p*-rosaniline but containing only one amino group. Thus, we can assume that the reaction between PAAB and  $\text{SO}_2$  is similar to the *p*-rosaniline one which involves formation of an aminocarbonyl as the first intermediate, followed by nucleophilic substitution by bisulfite (16).

Unlike *p*-rosaniline, which is commercially unavailable in a pure state and must thus be purified quite often to prepare solutions (17, 18), PAAB had not yet been used for the determination of  $\text{SO}_2$  in wine, but only for the determination of  $\text{SO}_2$ , formaldehyde, and methanol in environmental samples (19–22).

## EXPERIMENTAL SECTION

**Reagents.** All reagents were prepared from analytical-reagent grade chemicals. The stock solution of PAAB (0.02% in 0.08 M HCl containing 4% ethanol) was found to be stable for at least 1 year. Aqueous solutions of formaldehyde were made daily.

Sulfur dioxide standards were prepared in deaerated water from a stock solution of sodium sulfite containing 500 ppm  $\text{SO}_2$  stabilized in 0.1 M NaOH with 5% glycerin as stabilizer (23), which was found to be superior to  $\text{Hg}_2\text{Cl}_4$  (18)—only a 1% loss was observed after 1 week's storage at 4 °C.

**Apparatus.** Figures 1 and 2 show the schemes of the proposed FIA configurations. They included a Gilson Minipuls-2 peristaltic pump, an Omnifit FIT-1106 six-way valve, and an LKB-Novaspec II spectrophotometer with a bandwidth of  $\pm 12$  nm and a precision of  $\pm 1$  mAU, equipped with a Hellma flow-cell (10 mm path length, 18  $\mu\text{L}$  inner volume). The diffusion module was a methacrylate block with a straight channel (7 cm long, 2 mm wide) provided with a Millipore GVHP 09050 polyvinylidene fluoride gas-permeable membrane. The well-stirred mixing chamber used was also made of methacrylate and had an inner volume of 1 mL.

**FIA System for the Determination of Free  $\text{SO}_2$ .** As can be seen from Figure 1, the sample (300  $\mu\text{L}$ ) was injected into

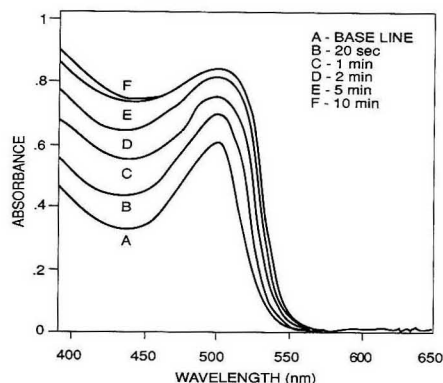


**Figure 3.** Absorption spectrum showing the course of the reaction between  $\text{SO}_2$ , PAAB and formaldehyde in an acid medium.

channel C and then merged with stream  $R_1$ , which provided a sufficiently acidic medium for the  $\text{SO}_2$  to diffuse across the membrane. Acceptor stream  $R_4$ , a mixture of PAAB and formaldehyde, collected the  $\text{SO}_2$  and transported the resulting reaction product formed in  $L_3$  to the detector, where its absorbance was measured at 520 nm.

**FIA System for the Determination of Total  $\text{SO}_2$ .** The configuration depicted in Figure 2 was constructed from that shown in Figure 1 by including a prehydrolysis unit consisting of a well-stirred chamber with two channel inlets and a net volume of 1 mL in which the sample (50  $\mu\text{L}$ ) was continuously mixed with a stream of 4 M NaOH. The flow rate was adjusted so that the residence time (1 min) was long enough for the reaction to complete.

The stream emerging from the chamber was used to fill the loop of the injection valve, and the sample was injected into a strongly acidic stream. After this point, the procedure involved the same steps as described above for the determination of free  $\text{SO}_2$ .

## RESULTS AND DISCUSSION

The kinetics of the reaction between  $\text{SO}_2$  and PAAB is rather slow: complete formation of the product takes about 10 min (Figure 3). This was a serious constraint to its implementation in an FIA system, where the time of contact between the analyte and the reagent is usually less than 1 min. We thus optimized the chemical and hydrodynamic parameters of the system in order to adapt it to the concentration range required by the method while minimizing analysis times.

**Optimization of Hydrodynamic Parameters.** Previously, in order to assure the robustness of the overall flow system, the carrier and reagent flow rates were set in such a way as to avoid overpressure on either side of the membrane and obtain analysis times of about 1 min. With this prefixed parameter, the others were performed by using the univariate approach.

Obviously, the length of  $L_3$  determined the extent to which the analytical reaction would take place. As can be seen from Figure 4, the behavior is inconsistent with what one would expect solely from dilution (24). The kinetic component prevailed at reactor lengths up to 250 cm, as the reaction rate was quite high at such a short reaction times (25). On the other hand, dispersion prevailed after the maximum of the curve. In such a way, the coil length for the total  $\text{SO}_2$  system proved to follow the same behavior.

Consequently, the injected volume was selected to obtain a proper linear working range for both systems.

**Optimization of Chemical Parameters.** According to Figure 5, the analytical reaction must have a complex kinetics

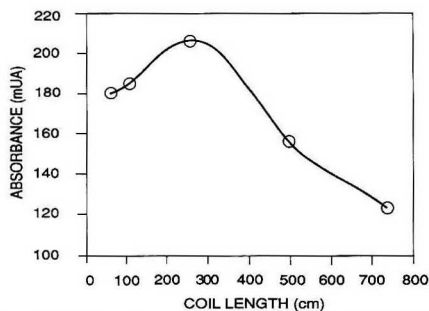


Figure 4. Variation of the response of the system for the determination of free  $\text{SO}_2$  as a function of the length of coil  $L_3$  (0.5 mm i.d.).

Table I. Results Obtained in the Analysis for Total  $\text{SO}_2$  from a Calibration with Aqueous Standards and by the Standard Addition Method<sup>a</sup>

	wine sample			
	white 1	white 2	rosé 1	red 1
direct method	63 ± 5	56 ± 5	45 ± 5	11 ± 6
std addition method	63 ± 2	57 ± 3	45 ± 4	9 ± 7

<sup>a</sup> All concentrations expressed in ppm.

Table II. Figures of Merit of the FIA Methods for the Determination of Total and Free  $\text{SO}_2$

	linear range, ppm	det limit, ppm	repeatability (rsd), %	sensitivity, mUA/ppm	sampling rate, samples/h
total $\text{SO}_2$	5-300	2	0.4	2.7 ± 0.1	20
free $\text{SO}_2$	2-35	0.2	0.4	24.2 ± 0.3	50

dependent on the PAAB, formaldehyde, and HCl concentrations. While an exhaustive study of the kinetics of this reaction was beyond the scope of this work, we believed it of interest to investigate the influence of the above chemical parameters in order to find the working conditions ensuring optimal performance of the FIA system.

Thus, we studied the effect of acidity by varying the HCl concentration in channel  $R_2$ . A concentration of about 0.2 M was found to result in the highest sensitivity and hence in the highest reaction rate. On the other hand, as can be seen from Figure 5, at a moderately low PAAB (0.004%) concentration minimizing baseline drifts, the reaction rate can be increased by increasing the formaldehyde concentration.

The optimal values of the different chemical parameters finally chosen for use with the two FIA configurations are reflected in Figures 1 and 2.

**Interferences.** The chemical complexity of the wine compelled us to check that their matrices would have no effect on the accuracy of the method in performing a calibration with aqueous  $\text{SO}_2$  standards. For this purpose, total  $\text{SO}_2$  was determined by FIA in various wines by using two different methods: direct determination by interpolation on a cali-

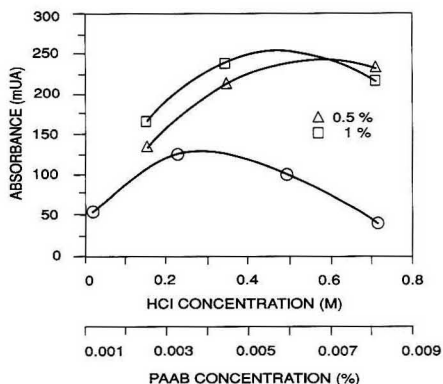


Figure 5. Variation of the response of the system for the determination of free  $\text{SO}_2$  as a function of (O) the HCl concentration in the formaldehyde solution ( $R_2$ ) and ( $\Delta$ ,  $\square$ ) the PAAB concentration at different formaldehyde concentrations.

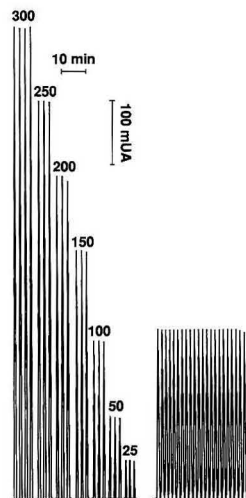


Figure 6. FIA recording showing the response of the system for the determination of total  $\text{SO}_2$  obtained by calibration with aqueous standards and the evaluation of repeatability with 20 injections of a 100 ppm standard. The numbers on the peaks are  $\text{SO}_2$  concentrations in ppm.

bration graph run from aqueous standards and by standard additions of different volumes of an  $\text{SO}_2$  standard at a constant sample volume. The results revealed the absence of interferences from the assayed samples (Table I).

Hydrogen sulfide was found to be the only gas species interfering with the reaction (16). However, its effect was only

Table III. Repeatability of the Calibration Graphs for the Determination of Total and Free  $\text{SO}_2$

day	total $\text{SO}_2$				day	free $\text{SO}_2$			
	slope, mUA/ppm	intercept, ppm	$r^2$	$n$		slope, mUA/ppm	intercept, ppm	$r^2$	$n$
1	2.7 ± 0.1	3 ± 13	0.9993	7	1	24.2 ± 0.3	1.0 ± 6.4	0.9998	7
2	2.6 ± 0.1	6 ± 13	0.9992	7	2	24.2 ± 0.5	-2 ± 7.7	0.9999	5
3	2.7 ± 0.1	8 ± 10	0.9997	6	3	24.1 ± 0.4	-2 ± 6.4	0.9999	5

**Table IV. Results of the Statistical Treatment Performed on the Pairs of Data Obtained by Using the Proposed FIA Systems and the INCAVI SFA System<sup>a</sup>**

	FIA linear regression versus SFA			student's <i>t</i>	
	slope	intercept	<i>r</i> <sup>2</sup>	<i>t</i> <sub>calc</sub>	<i>t</i> <sub>tab</sub>
total SO <sub>2</sub>	1.1 ± 0.1	-10 ± 15	0.9258	1.73	2.069
free SO <sub>2</sub>	1.0 ± 0.1	0.1 ± 0.5	0.9497	0.6	2.069

<sup>a</sup> Confidence limit = 95%; *N* = 24.

significant above 1 mM—the maximum tolerated concentration in wine is 10<sup>-5</sup> M (1).

**System Features.** The figures of merit of the FIA methods proposed for the determination of total and free SO<sub>2</sub> are summarized in Table II. While the total SO<sub>2</sub> analysis time was 1 min, adding the time required for the steady state to be reached in the mixing chamber gives a sample throughput of 20 samples/h.

As an example, Figure 6 shows the calibration graph of the FIA system for the determination of total SO<sub>2</sub> and an evaluation of repeatability. As can be seen from Table III, both methods proved to be highly reproducible over time. This allows calibrations to be more spaced in time and hence resulted in greater operativeness. In addition, the response was very stable, with no baseline drift.

Moreover, the two methods afford much higher precision than classical methods (±10 ppm), so they more than comply with the demands for methods used to control SO<sub>2</sub> levels in wine.

By the use of smaller injected volumes, the linear determination range could be extended to 400 ppm for total SO<sub>2</sub> and 200 ppm for free SO<sub>2</sub> in order to cover samples containing concentrations beyond the legal limits.

The results obtained by analyzing samples of different wines were compared with those provided by a continuous segmented-flow analyzer (SFA) used at an enological station (Institut Català de la Vinya i el Vi) for the routine analysis for total and free SO<sub>2</sub> in large numbers of samples. As can be seen from Table IV, which summarizes the results of the

statistical treatment applied to each pair of values, there were no significant differences between the two methods in this respect.

#### ACKNOWLEDGMENT

We thank the INCAVI for their cooperation. C.J.J. was supported by a research studentship from the FPI program (MEC).

Registry No. PAAB, 60-09-3; SO<sub>2</sub>, 7446-09-5.

#### LITERATURE CITED

- (1) Amerine, M. A.; Ough, C. S. *Methods for Analysis of Musts and Wines*; John Wiley & Sons: New York, 1980; p 201.
- (2) OIV. *Résumé des Méthodes Internationales d'Analyse des Vins*, 1969.
- (3) AOAC. *Official Methods of Analysis*, 10th ed.; AOAC: Washington, DC, 1965; p 486.
- (4) Williams, T. R.; McElvany, S. W.; Ighodalo, E. C. *Anal. Chim. Acta* **1981**, *123*, 351.
- (5) Marshall, G. B.; Midgley, D. *Analyst* **1983**, *108*, 701.
- (6) Masson, M.; Townshend, A. *Anal. Chim. Acta* **1986**, *179*, 339.
- (7) Ramasamy, S. M.; Mottola, H. A. *Anal. Chem.* **1982**, *54*, 283.
- (8) Yamada, M.; Nakada, T.; Suzuki, S. *Anal. Chim. Acta* **1983**, *147*, 401.
- (9) Rios, A.; Luque de Castro, M. D.; Valcárcel, M. *Anal. Chem.* **1987**, *59*, 660.
- (10) Ruzicka, J.; Hansen, E. H. *Anal. Chim. Acta* **1990**, *114*, 19.
- (11) Moller, J.; Winter, B. *Fresenius' Z. Anal. Chem.* **1985**, *320*, 451.
- (12) Linares, P.; Luque de Castro, M. D.; Valcárcel, M. *Anal. Chim. Acta* **1989**, *225*, 443.
- (13) Granados, M.; Maspoch, S.; Blanco, M. *Anal. Chim. Acta* **1986**, *179*, 445.
- (14) Matsumoto, K.; Matsubara, H.; Ukeda, H.; Osajima, Y. *Agric. Biol. Chem.* **1989**, *53* (9), 2347.
- (15) Burguera, J. L.; Burguera, M. *Anal. Chim. Acta* **1988**, *214*, 429.
- (16) Dasgupta, P. K.; DeCesare, K.; Ullrey, J. C. *Anal. Chem.* **1980**, *52*, 1912.
- (17) West, P. W.; Gaeke, G. C. *Anal. Chem.* **1956**, *28*, 1816.
- (18) Scaringelli, F. P.; Saltzman, B. E.; Frey, S. A. *Anal. Chem.* **1967**, *39*, 1709.
- (19) Kniseley, S. J.; Throop, L. J. *Anal. Chem.* **1966**, *38*, 1270.
- (20) Bhatt, A.; Gupta, V. K. *Analyst* **1983**, *108*, 374.
- (21) Verma, P.; Gupta, V. K. *Talanta* **1983**, *30*, 443.
- (22) Verma, P.; Gupta, V. K. *Talanta* **1984**, *31*, 394.
- (23) Urone, P. F.; Boggs, W. E. *Anal. Chem.* **1951**, *23*, 1517.
- (24) Ruzicka, J.; Hansen, E. H. *Flow Injection Analysis*; John Wiley & Sons: New York, 1981.
- (25) Vanderslice, J. T.; Beecher, G. R.; Rosenfeld, A. G. *Anal. Chem.* **1984**, *56*, 268.

RECEIVED for review January 30, 1991. Accepted July 1, 1991.

## Bulk-Electrolysis Flow-Cell System for UV-Visible and X-ray Absorption Spectroelectrochemical Analysis

David H. Igo,<sup>1</sup> R. C. Elder,\* and William R. Heineman\*

Department of Chemistry, University of Cincinnati, Cincinnati, Ohio 45221-0172

Howard D. Dewald

Department of Chemistry and Condensed Matter and Surface Science Program, Ohio University, Athens, Ohio 45701-2979

### INTRODUCTION

Recent studies have shown the utility of electrolysis as a practical alternative to chemical generation of specific oxidation states of metal complexes in solution for X-ray spectroelectrochemical analysis (1-6). Electrochemistry is an inherently clean process because the reducing or oxidizing agent is an inert electrode which provides or removes electrons without introducing possible interfering agents. For extended X-ray absorption fine structure (EXAFS) measurements,

potential control of a static solution may be necessary to maintain a specific oxidation state of the metal complex being observed. This is due to the highly reducing environment generated by secondary electrons produced by the intense synchrotron radiation.

Solution cells used in EXAFS analysis generally utilize a thin-layer configuration which enables rapid and exhaustive electrolysis of a specific analyte. Either gold minigridd (7) or reticulated vitreous carbon (RVC) (1) has served as the working electrode material, due to their transparency.

Recent efforts have focused on the development of a more versatile spectroelectrochemical system having an efficiency equivalent to that of the RVC cell previously developed (1).

\* To whom all correspondence should be addressed.

<sup>1</sup> Current address: Glaxo, Inc., Five Moore Drive, Research Triangle Park, NC 27709.

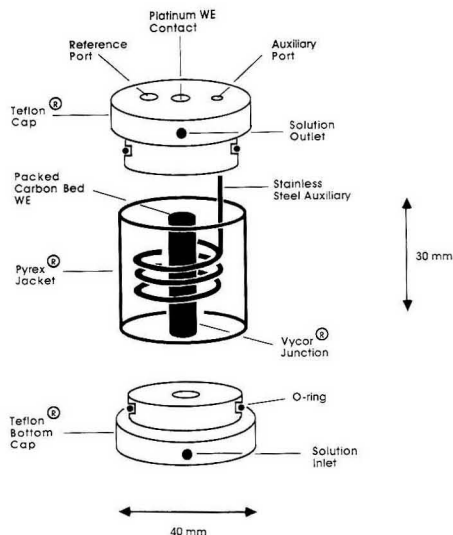


Figure 1. Exploded view of packed carbon-bed bulk-electrolysis cell.

The new electrochemical methodology uses a packed-carbon-bed bulk-electrolysis cell. The packed bed provides a high surface area to volume ratio, thus enabling rapid electrolysis of solutions having relatively high analyte concentrations.

The packed-carbon-bed electrolysis cell was first introduced by Blaedel and Strohl (8). A more recent cell by Clark and Evans (9) was used to electrochemically generate quinone radicals for subsequent analysis with infrared spectroscopy. Pinkerton and Mikelsons have used a similar electrolysis cell for the electrochemical synthesis of a series of technetium formate complexes (10).

Our bulk-electrolysis and flow-cell configuration was developed for UV-vis and X-ray spectroelectrochemical analysis. The characteristics of the bulk-electrolysis cell were evaluated by generation of the  $\text{Co}^{\text{II}}$  and  $\text{Co}^{\text{III}}$  oxidation states of a  $[\text{Co}(\text{2,2}'\text{-bipyridine})_3]^{2+}$  solution. The utility of the system in the analysis of an oxygen-sensitive compound, methyl viologen, was also examined.

#### EXPERIMENTAL SECTION

**Apparatus.** The bulk-electrolysis cell is a replica of a model designed by Bioanalytical Systems, Inc. (West Lafayette, IN) and is shown in Figure 1. The housing of the bulk-electrolysis cell consists of Teflon caps located at the top and bottom of the assembly. The Teflon bottom cap is tapped to provide a solution inlet, which accepts a standard HPLC fingertight connection of the tubing to the Teflon cap. An O-ring located within the channel at the top of the bottom cap enables a watertight connection to be made with the Pyrex body. An  $1/4$  in. outer diameter Vycor tube (Bioanalytical Systems), cut to the appropriate length, is retained by an inner O-ring seal. The seal is achieved when the O-rings, which reside in channels of both the top and bottom caps, fit tightly with the outside of the Vycor tube. Cotton wadding serves as the porous plug at the top and bottom of the Vycor tube, which is filled with  $200\text{-}\mu\text{m}$  carbon particles. The carbon particles were obtained by crushing a sheet of reticulated vitreous carbon or RVC (The Electrolysis Co., Inc., East Amherst, NY) and sieving the material to separate the  $200\text{-}\mu\text{m}$  diameter particles. The assembly is equipped with a coiled stainless steel auxiliary electrode, constructed from end-sealed,  $1/16$  in. outer-diameter HPLC tubing. The Teflon cap was then fitted with O-rings, which form the final seal with the Pyrex and carbon-filled Vycor tube.

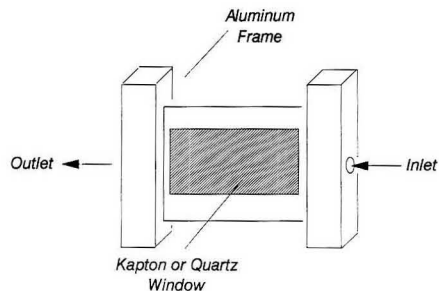


Figure 2. Aluminum spectrochemical flow-cell component of bulk electrolysis/flow cell system.

The Teflon top cap is drilled and tapped to provide the solution outlet. Ports were drilled into the top cap for Ag/AgCl reference and auxiliary electrodes. A fingertight fitting modified with a platinum wire, serves as the electrical contact to the packed carbon bed. The space between the Vycor and Pyrex body is filled with supporting electrolyte solution. The bulk-electrolysis system uses an ISCO, eight-cylinder peristaltic pump, which provides a continuous flow of analyte solution over the packed carbon bed. The pump was calibrated and set to deliver  $0.5\text{ mL}$  of analyte solution/min for all reported experiments.

The spectral flow cell that was developed for collection of UV-vis and X-ray spectra is a simple aluminum frame with a solution inlet and outlet port (Figure 2). The inlet and outlet connections are made by fingertight fittings. The solution flows through a rectangular channel, sandwiched between two quartz windows for UV-vis applications or  $0.1\text{ mm}$  thick Kapton (Du Pont Co.; Wilmington, DE) sheets for X-ray measurements. The window material is attached to the frame with a two-part Elmers (Borden, Inc. Columbus, OH) epoxy resin. The dimensions of the cell window are  $25\text{ mm}$  in length by  $5\text{ mm}$  in height by  $1\text{ mm}$  in width. The flow cell was connected to the bulk-electrolysis cell with  $5\text{ cm}$  of  $0.25\text{ mm}$  inner diameter Teflon tubing. A polyethylene jacket surrounds all of the connecting Teflon tubing and is purged with either helium or oxygen. The calculated volume of the tubing between the bulk-electrolysis and flow cell is on the order of  $0.03\text{ mL}$ . The travel time for solution exiting the electrolysis cell and arriving at the flow cell is less than  $4\text{ s}$ , for a flow rate of  $0.5\text{ mL}/\text{min}$ .

UV-vis absorption spectra were recorded on a Hewlett-Packard Model 8450A diode array spectrophotometer. A Lytle type fluorescence detector was used for the measurement of fluorescence X-ray spectra. A specialized flow cell positioner, which gives quick and accurate positioning of the flow cell in the X-ray beam, was machined out of aluminum (Custom Machining Inc., Mt. Sterling, KY). The positioner possesses a slot into which the flow cell is inserted. The positioner utilizes a set-screw configuration to fix the position of the flow cell.

**Reagents.**  $\text{Co}^{\text{II}}(\text{2,2}'\text{-bipyridine})_3\text{Cl}_2 \cdot 2\text{H}_2\text{O}$  was prepared as described in ref 11. Solutions of  $\text{Co}^{\text{II}}(\text{2,2}'\text{-bipyridine})_3\text{Cl}_2 \cdot 2\text{H}_2\text{O}$  were prepared by dissolving the solid in phosphate buffer,  $0.13\text{ M}$ , pH 7.

**Procedures.** X-ray spectral data were collected at the National Synchrotron Light Source, beamline X-19A, and processed in a manner previously described (12). A series of six fluorescence spectra was averaged for each oxidation state of the complex in solution and for the  $\text{Co}^{\text{II}}(\text{2,2}'\text{-bipyridine})_3\text{Cl}_2 \cdot 2\text{H}_2\text{O}$  solid model compound. Data reduction and optimization were performed with locally modified versions of XPAK, written by Robert A. Scott (University of Georgia, School of Chemical Sciences, Athens, GA).

Constant flow of the analyte/electrolyte was maintained during collection of both UV-vis and X-ray spectra. The volume of analyte solution analyzed was  $10\text{ mL}$ , and solution was recirculated during the course of the experiment.

#### RESULTS AND DISCUSSION

**Cyclic Voltammetry.** Cyclic voltammetry of  $[\text{Co}^{\text{II}}(\text{bpy})_3]^{2+}$  where  $\text{bpy} = 2,2'\text{-bipyridine}$ , in aqueous phosphate



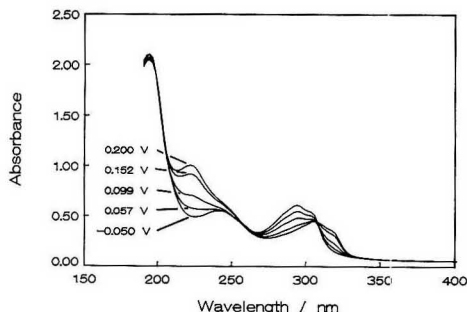
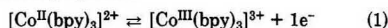


**Figure 3.** Spectropotentiostatic analysis of 0.1 mM  $\text{Co}^{\text{II}}(2,2'\text{-bipyridine})_3/\text{pH } 7.0$  phosphate buffer in flow cell. Spectra collected at designated potentials.

buffer at pH 7.0 was performed at a glassy-carbon disk electrode. A positive potential scan initiated at  $-0.20$  V at a scan rate of  $0.050$  V/s through the oxidation wave ( $E_{\text{pa}} = 0.120$  V), for the conversion of  $\text{Co}^{\text{II}}$  to  $\text{Co}^{\text{III}}$ . The scan direction was reversed at a potential of  $+0.50$  V and a reduction wave ( $E_{\text{pc}} = 0.056$  V), for the conversion of  $\text{Co}^{\text{III}}$  to  $\text{Co}^{\text{II}}$  was obtained on the reverse scan. By averaging of the peak potentials for  $\text{Co}^{\text{II}}$  oxidation and  $\text{Co}^{\text{III}}$  reduction, the formal redox potential is calculated to be  $+0.088$  V. The peak potential separation is  $0.065$  V. When set equal to the ratio  $0.059/n$  (13), an electron stoichiometry of 0.91 or approximately 1 is obtained. For a Nernstian wave with stable products, the ratio of peak currents for the anodic and its corresponding cathodic process should be equivalent to 1. A value of 0.99 was obtained for the  $\text{Co}(\text{bpy})_3$  II/III redox couple and was independent of the scan rate. The reversible one-electron process is represented by the following equation:



$[\text{Co}^{\text{II,III}}(\text{bpy})_3]^{2+,3+}$  was used as a representative electrochemically reversible couple to evaluate the UV-vis and X-ray spectroelectrochemical applications of the bulk-electrolysis/flow-cell system.

**UV-Visible Spectroelectrochemistry.** Spectroelectrochemical analysis was performed on a continuously flowing solution of  $0.1$  mM  $[\text{Co}^{\text{II}}(\text{bpy})_3]^{2+}$  in pH 7.0 phosphate buffer. Spectra were recorded at 12 potentials within the range of  $-0.050$  and  $+0.200$  V. The  $[\text{Co}^{\text{II}}(\text{bpy})_3]^{2+}$  spectrum possesses absorption maxima at 244, 308, and 332 nm while the maxima of the  $\text{Co}^{\text{III}}$  form are at 222, 306, and 318 nm. The results of the spectropotentiostatic experiment (five of the spectra are shown in Figure 3) reveal isosbestic points at 198, 258, 308, and 332 nm. The presence of isosbestic points indicates that stable redox products are formed with no long-lived intermediate or decomposition product.

A Nernstian plot was made by graphing the applied potentials versus their corresponding  $\log [\text{ox.}/[\text{red.}]]$  terms, which were calculated from the absorbance data at 222 nm (14). The values of  $n$  and  $E^\circ$  for  $[\text{Co}^{\text{II}}(\text{bpy})_3]^{2+}$  resulting from analysis of the Nernstian plot slope and intercept are 0.965 electrons and  $0.113$  V, respectively. The correlation coefficient of the data to a straight line fit is 0.996.

Analysis of the absorbance behavior of  $\text{Co}(\text{bpy})_3$  enables determination of the potentials at which essentially complete oxidation or reduction will occur. For the EXAFS spectroelectrochemical experiment, potentials of  $-0.300$  V were applied to generate and maintain  $[\text{Co}^{\text{II}}(\text{bpy})_3]^{2+}$  and  $+0.600$  V for  $[\text{Co}^{\text{III}}(\text{bpy})_3]^{3+}$ .

**X-ray Spectroelectrochemistry.** The tris(2,2'-bipyridine) complex of cobalt undergoes dramatic changes in cobalt-ni-

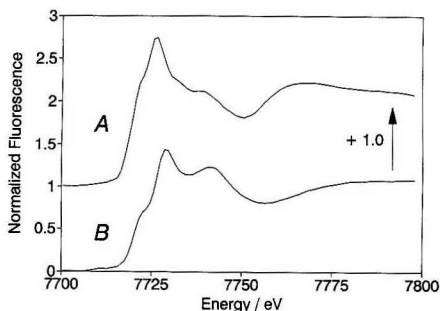


**Figure 4.** XANES comparison of (A)  $\text{Co}^{\text{II}}(2,2'\text{-bipyridine})_3$  and (B)  $\text{Co}^{\text{III}}(2,2'\text{-bipyridine})_3$ .

trogen bond length with changes in oxidation state. A difference in bond length of  $0.20$  Å is observed when the crystal structures of the  $\text{Co}^{\text{II}}$  (11) and the  $\text{Co}^{\text{III}}$  form (15) of the complex are compared. Bond length differences of  $0.02$  Å and greater are distinguishable with EXAFS spectroscopy (16). Since the structures for the solid forms of  $[\text{Co}^{\text{II}}(\text{bpy})_3]^{2+}$  and  $[\text{Co}^{\text{III}}(\text{bpy})_3]^{3+}$  are known, these compounds were used as structural standards for the X-ray spectroelectrochemical experiment.

The XANES region of the fluorescence spectra reveals information pertaining to the symmetry about the absorbing cobalt atom and its oxidation state while in solution (17). Changes in oxidation state are observable due to shifts in the energy required to ionize the metal atom. As seen in Figure 4, there is an obvious shift in the position of the first peak of the X-ray absorption spectra, XANES region. The shift to higher energy, from  $7726.9$  to  $7728.6$  eV, is indicative of a change in oxidation from  $\text{Co}^{\text{II}}$  to  $\text{Co}^{\text{III}}$ , due to the transition from a high-spin,  $d^7$ , to a low-spin,  $d^6$ , cobalt state.

The extracted EXAFS signals are presented in Figure 5 and are of relatively high quality. Fourier transforms of the raw EXAFS signals for the  $\text{Co}^{\text{II}}$  and  $\text{Co}^{\text{III}}$  states are presented in Figure 6. There is a noticeable shift in the position of the major peak in the pseudoradial distribution function (PRDF) of  $0.19$  Å. The coordination structure can be optimized by fitting the back-transform of the major PRDF peaks for the  $\text{Co}^{\text{II}}$  and  $\text{Co}^{\text{III}}$  solutions with parameters extracted from the  $\text{Co}^{\text{II}}(\text{bpy})_3 \cdot \text{Cl}_2 \cdot 2\text{H}_2\text{O}$  solid model compound.

The results of the  $\text{Co}^{\text{II}}$  and  $\text{Co}^{\text{III}}$  optimization are presented in Table I. The Co-N bond distance decreases as expected, when  $\text{Co}^{\text{II}}$  is oxidized to  $\text{Co}^{\text{III}}$ . The coordination number was essentially unchanged by electrochemical oxidation, within the limits of the EXAFS calculations.

**Conversion Rates.** The bulk-electrolysis cell can rapidly generate a specific oxidation state of a metal complex in solution. When a potential step experiment is performed, essentially instantaneous conversion of the  $\text{Co}^{\text{II}}$  species to the  $\text{Co}^{\text{III}}$  is achieved within the electrolysis cell. The limiting factor in collecting spectra of the  $\text{Co}^{\text{III}}$  form of the complex is the time it takes to flow the analyte from the bulk electrolysis cell to the flow cell, which is on the order of 3 min in our case. By comparison, thin-layer cells for EXAFS spectroelectrochemistry (1) required approximately 10 min for essentially complete conversion in a similar potential step experiment.

**Gas Saturation of Analyte Solution.** Another advantage of the bulk-electrolysis/flow-cell experimental setup includes the ability to saturate the analyte solution with a particular gas while the experiment is performed. This is accomplished by purging the polyethylene jacket surrounding the gas-permeable Teflon tubing, which is used to transport the solution, with either a reactive or inert gas. This feature was

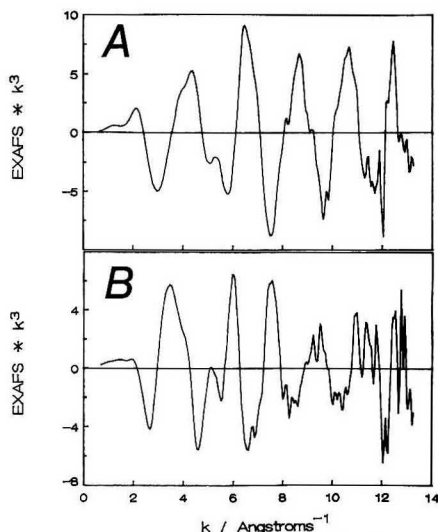


Figure 5. Extracted raw EXAFS spectra for (A)  $\text{Co}^{\text{III}}(2,2',\text{-bipyridine})_3$  and (B)  $\text{Co}^{\text{II}}(2,2',\text{-bipyridine})_3$ .

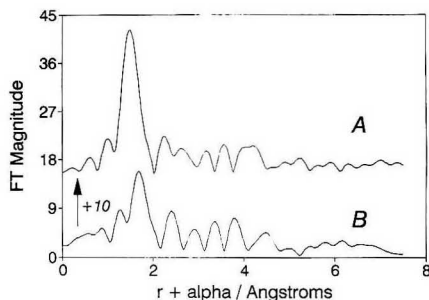
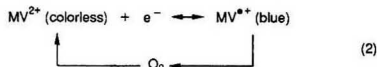


Figure 6. Forward Fourier transforms of raw EXAFS spectra for (A)  $\text{Co}^{\text{III}}(2,2',\text{-bipyridine})_3$  and (B)  $\text{Co}^{\text{II}}(2,2',\text{-bipyridine})_3$ .

tested with methyl viologen,  $\text{MV}^{2+}$ , which is known to undergo a reversible one-electron reduction to a radical species,  $\text{MV}^{\cdot+}$  (18). The radical species possesses an intense blue color and is easily monitored by its characteristic absorption band at 546 nm. Reaction of the radical species with  $\text{O}_2$  results in its oxidation back to  $\text{MV}^{2+}$  in accordance with eq 2.



The analyte solution was deoxygenated with helium prior to electrolysis. In addition to presaturation of the solution, helium was also circulated through the polyethylene jacket surrounding the Teflon transport tubing. A potential of  $-0.900$  V was applied to the packed-carbon bed, generating  $\text{MV}^{\cdot+}$ . As a result of the absence of oxygen and the application of a sufficiently reducing potential, there was no observed decrease in absorbance at 546 nm for a period of 2 h.

The ability to react the electrogenerated radical with oxygen was examined by electrochemically reducing a flowing stream of  $\text{MV}^{2+}$  and purging the polyethylene jacket surrounding the Teflon transport tube between the bulk-electrolysis cell and

Table I. Optimization Results for  $\text{Co}^{\text{II}}(2,2',\text{-bipyridine})_3$  and  $\text{Co}^{\text{III}}(2,2',\text{-bipyridine})_3$

information	$\text{Co}^{\text{II}}(\text{bpy})_3$	$\text{Co}^{\text{III}}(\text{bpy})_3$	change
from crystal structure <sup>a</sup>			
Co-N dist, Å	2.128	1.93	0.20
Co coord no.	6.00	6.00	0.00
from solid PRDF			
Co-N dist, Å	1.68	not collcd	
Co coord no.	6.00		
from solution PRDF			
Co-N dist, Å	1.69	1.50	0.19
refinement results <sup>b</sup>			
Co-N dist, Å	2.10	1.88	0.22
Debye-Waller factor, Å	0.054	0.022	
Co coord no.	6.17	6.60	0.43

<sup>a</sup>From ref 11. <sup>b</sup> $\text{Co}^{\text{II}}(\text{bpy})_3\text{Cl}_2 \cdot 2\text{H}_2\text{O}$  solid served as the model compound for both the  $[\text{Co}^{\text{II}}(\text{bpy})_3]^{2+}$  and  $[\text{Co}^{\text{III}}(\text{bpy})_3]^{3+}$  solutions. Parameters assigned to the model were Co-N = 2.128 Å, coordination no. = 6.00, and Debye-Waller factor = 0.07 Å.

flow cell with 98%  $\text{O}_2$ . Complete reaction of  $\text{MV}^{\cdot+}$  with  $\text{O}_2$  took place in 3 min, as revealed by a decay to background of the absorbance at 546 nm.

## CONCLUSIONS

The bulk-electrolysis/flow-cell assembly provides an effective means of controlling the oxidation state of the  $\text{Co}(\text{bpy})_3^{2+/3+}$  solution. The EXAFS optimization yielded coordination numbers and bond distances which are consistent with the reported crystal structures. When machined to a thickness of 1.0 mm, the flow cell and analyte were of adequate transparency to permit energy calibration. Calibration typically requires that the sample transmit approximately 30% of the total X-ray flux when the X-ray energy is above the absorption edge of interest.

The electrochemical conversion rate is greater than that achieved with the previous RVC spectroelectrochemical cell (1). The fast rate at which a particular oxidation state is generated is due to the high surface area of the packed-carbon-bed working electrode.

Another advantage is the ability to saturate the analyte solution with a particular gas while the experiment is performed. This is accomplished through the use of a helium- or oxygen-purged polyethylene jacket, surrounding the gas-permeable Teflon tubing which is used to transport the solution.

## LITERATURE CITED

- (1) Dewald, H. D.; Watkins, J. W., II; Elder, R. C.; Heineman, W. R. *Anal. Chem.* **1986**, *58*, 2968.
- (2) Tourillon, G.; Dexpert, H.; Lagarde, P. *J. Electrochem. Soc.* **1987**, *134*, 327.
- (3) White, J. H.; Abruña, H. D. *J. Phys. Chem.* **1988**, *92*, 7131.
- (4) McBrean, J.; O'Grady, W. E.; Pandya, K. I. *J. Power Sources* **1988**, *22*, 323.
- (5) Brunschwig, B. S.; Creutz, C.; Macartney, D. H.; Sharn, T.-K.; Sutin, N. *Faraday Discuss. Chem. Soc.* **1982**, *74*, 113.
- (6) Sharn, T.-K. *Acc. Chem. Res.* **1986**, *19*, 99.
- (7) Smith, D. A.; Elder, R. C.; Heineman, W. R. *Anal. Chem.* **1985**, *57*, 2361.
- (8) Blaedel, W. J.; Strohl, J. H. *Anal. Chem.* **1984**, *36*, 1245.
- (9) Clark, B. R.; Evans, D. H. *J. Electroanal. Chem. Interfacial Electrochem.* **1978**, *69*, 181.
- (10) Mikelsons, M. V.; Pinkerton, T. C. *Appl. Radiat. Isot.* **1986**, *37*, 991.
- (11) Szalda, D. J.; Creutz, C.; Mahajan, D.; Sutin, N. *Inorg. Chem.* **1983**, *22*, 2372.
- (12) Igo, D. H.; Elder, R. C.; Heineman, W. R. *J. Electroanal. Chem. Interfacial Electrochem.*, in press.
- (13) Kissinger, P. T.; Heineman, W. R. *J. Chem. Ed.* **1983**, *60*, 702.
- (14) DeAngelis, T. P.; Heineman, W. R. *J. Chem. Educ.* **1978**, *55*, 594.
- (15) Yanagi, K.; Ohashi, Y.; Sasada, Y.; Kaizu, Y.; Kobayashi, H. *Bull. Chem. Soc. Jpn.* **1981**, *54*, 118.
- (16) Teo, B. K. *EXAFS: Basic Principles and Data Analysis*; Springer-Verlag: Berlin, 1986.
- (17) Bianconi, A. *XANES Spectroscopy*. In *X-ray Absorption: Principles, Applications, Techniques of EXAFS, SEXAFS and XANES*, Koningsberger, D. C., Prins, R., Eds.; Wiley: New York, 1988; Vol. 92, p 573.

(18) Steckhan, E.; Kuwana, T. *Ber. Bunsen-Ges. Phys. Chem.* 1974, 78, 253.

RECEIVED for review May 6, 1991. Accepted August 12, 1991. Financial support was provided by the Air Force Office of

Scientific Research (Grant No. 88-0089). Research carried out in part at the National Synchrotron Light Source, Brookhaven National Laboratory, which is supported by the U.S. Department of Energy, Division of Materials Sciences and Division of Chemical Sciences.

## On-Line Preconcentration and Volatilization of Iodine for Inductively Coupled Plasma Atomic Emission Spectrometry

Scott P. Dolan, Scott A. Sinex,<sup>1</sup> and Stephen G. Capar

*Division of Contaminants Chemistry, Food and Drug Administration, Washington, D.C. 20204*

Akbar Montaser\* and Robert H. Clifford

*Department of Chemistry, George Washington University, Washington, D.C. 20052*

The Food and Drug Administration (FDA) monitors toxic and nutrient elements in the United States food supply through FDA's Total Diet Study. The quality of the food supply is assessed through analysis of foods and calculation of dietary intakes in representative diets based on nationwide food consumption surveys (1-6). Current method development at FDA for monitoring elements in foods consolidates elemental analysis into one multielement technique. Inductively coupled plasma atomic emission spectrometry (ICP-AES) is used for determination of many elements in foods by the FDA (7). Currently, iodine is determined by a spectrophotometric technique (8, 9) with a limit of detection ( $2\sigma$ ) of 0.1 ng/mL (10). In one-third of the foods tested in the FDA's Total Diet Study, iodine generally cannot be quantified by this method. Moreover, this method occasionally yields recoveries that are erratic and frequently low for foods high in starch or lipids (11). The conventional instrumental limit of detection (154  $\mu\text{g/mL}$ , 3  $\sigma$ ) for iodine by ICP-AES is also inadequate for determining iodine in most foods (12). Thus, it is desirable to improve the ICP-AES limit of detection for iodine by 1000-10 000-fold.

The limit of detection for iodine by ICP-AES may be improved by several approaches. A helium-argon mixed-gas plasma has been applied to the determination of iodine, and a 7-fold improvement has been reported by Caruso and associates (13). Treatment of test solutions has also been used to form the volatile molecular species of iodine ( $\text{I}_2$ ) before nebulization into the plasma (14, 15). Introducing a volatile analyte into the nebulizer increases the efficiency of analyte transport compared to conventional nebulization, which is only 1-2% efficient (16, 17). Flow injection analysis (FIA) has been used to preconcentrate metals (18-20) for determination by atomic spectrometric techniques.

Since the advent of FIA (21, 22), the development of on-line microcolumn preconcentration techniques for atomic spectrometry has received considerable interest (18-20). In general, on-line preconcentration is performed by passing a relatively large volume of test solution (e.g., 20 mL) through a microcolumn of chelating or ion-exchange material. The retained analytes are eluted by injecting a small volume (e.g., 200  $\mu\text{L}$ ) of eluent, which gives a nominal enrichment factor of 100, assuming quantitative deposition and elution for the analytes. The chelating, ion exchange, and adsorbent materials most often used include Chex 100, Muromac A-1, and activated alumina. Chex 100 (23) and Muromac A-1 (24) have been used for on-line, multielement preconcentration

of Ba, Be, Cd, Cr, Cu, Mn, Ni, and Pb, and of Al, Cr, Fe, Ti, and V, respectively. Activated alumina, an adsorbent (25), has been used in the determination of phosphate (26), chromium IV (27), and sulfate (28). For the present study, a commercial anion-exchange resin, with a strong affinity for iodide ion, was used for preconcentration of iodine as  $\text{I}^-$  and  $\text{IO}_3^-$ . The capability of this approach for improving the limit of detection for iodine was compared to on-line oxidation of iodine used in conjunction with Ar ICP-AES and He ICP-AES, as developed by Montaser and co-workers (29-37).

### EXPERIMENTAL SECTION

**On-Line Oxidation.** Details of experimental facilities and operating conditions are summarized in Tables I and II. Reagents [acidified test solution (5% (v/v)  $\text{H}_2\text{SO}_4$ , double distilled from Vycor, GFS Chemicals, Columbus, OH) and 30% hydrogen peroxide (Fisher Scientific, Fair Lawn, NJ)] were mixed with two peristaltic pumps (Minipulse 2, Gilson Medical Electronics, Middleton, WI, and Rabbit peristaltic pump, Rainin Instrument Co. Inc., Woburn, MA) connected via a Teflon tee (Swagelok Teflon union tee T-200-3, Washington Valve & Fitting Co., Rockville, MD) to the nebulizer with a 37-cm length of Teflon tubing having an i.d. of 0.5 mm (no mixing coil was used); see Figure 1a. To minimize memory effect, Teflon tubing was used from the point of mixing to the nebulizer and for the drain line connected to the spray chamber. Mixing ratios were set by varying pump speed (20-400 reading on the dial) and tubing size (0.030 and 0.045 in.).

**Preconcentration through Flow Injection.** A 25-mm membrane disk containing the AG1-X8 anion-exchange resin within a polypropylene housing (BIO-RAD Laboratories, Richmond, CA) was used for preconcentration of iodine as  $\text{I}^-$  and  $\text{IO}_3^-$ . The anion-exchange membrane is composed of resin permanently enmeshed in a polytetrafluoroethylene (PTFE) membrane. The polypropylene housing has a female Luer fitting with locking tab and a male Luer taper outlet fitting for easy connection. Preconcentration on the membrane disk was automated with flow injection equipment (see Figure 1b and Table I), which consisted of an autosampler, a valve for reagent selection, a variable-speed pump for flow rate control, and an injector valve with a mixing coil for on-line methods (not used for this work). The injector valve (and its mixing coil) was not used because concentrated  $\text{H}_2\text{SO}_4$  tended to deform the injector valve seals, thus causing leaks. Preconcentration was automated by using an IBM personal computer (PC) and a BASIC program written for this study. The FIA system was controlled by using ASCII character codes sent by an RS-232 communications interface to the flow injection microprocessor.

Preconcentration was performed by pumping 10 mL of test solution followed by double-deionized water at a rate of 5.5 mL/min from the autosampler through the membrane disk. The selector valve was subsequently switched to the counterion line ( $\text{HNO}_3$ , double distilled from Vycor, GFS Chemicals) and the flow rate was changed to 1.8 mL/min. A total volume of 7.7 mL of

\* To whom correspondence should be addressed.

<sup>1</sup> Present address: Department of Physical Sciences, Prince George's Community College, Largo, MD 20772-2199.

Table I. Experimental Facilities

radio frequency generator	A 2.5-kW, 27.12-MHz crystal-controlled generator (Henry Electronics, Los Angeles, CA) with auto power control was used. The automatic matching network is described elsewhere (36).	
ICP torches	An extended tangential flow torch with side arm (Applied Research Laboratories, Valencia, CA) and a 3.5-turn, shielded load coil was used for Ar ICP (37). A low gas flow torch (30) and a 4.5-turn, shielded load coil with the top turn grounded was used for He ICP (34). See Table II for operating conditions.	
sample introduction system	A concentric glass nebulizer for Ar (Model TR-30-A3, J. E. Meinhard Associates, Santa Ana, CA) and for He (Model TR-50-A1) with a conical, nonthermostated glass spray chamber (Applied Research Laboratories) was used.	
flow injection analysis system	A Model SHS-300 flow injection system and a Model SC-110 autosampler (FIAtron Systems Inc., Oconomowoc, WI) were used.	
spectrometer	It was equipped with a 1-m focal length direct-reader in a Paschen-Runge mounting (Model 3580, Applied Research Laboratories) with a 1080 groove/mm grating, and a 1 m focal length sequential spectrometer (Model 3580, Applied Research Laboratories), and 21- and 20- $\mu$ m entrance and exit slit widths, respectively. The slit height was 10 mm. A 1:1 image of the plasma was formed on the entrance slit.	
detection system	The current output from the photomultiplier (PMT R166, Hamamatsu Corp., Bridgewater, NJ), operated at 975 V for all measurements, was amplified by a linear current-to-voltage converter (Model 427, Keithley Instrument, Inc., Cleveland, OH). The data acquisition system consisted of a Labmaster ADC instrument (Tecmar, Inc., Cleveland, OH) installed on a IBM-PC microcomputer. ASYSTANT+ (Asyst Software Technologies, Inc., Rochester, NY) was used to acquire and analyze the data.	

Table II. Plasma Operating Conditions for Ar and He ICP Discharges

	Ar	He
forward power, W	1150	1500
reflected power, W	<5	<5
obsn height center, mm	15	25
outer gas flow rate, L/min	12	7
intermediate gas flow rate, L/min	0.8	N/A
injector gas flow rate, L/min	1	1
sample uptake rate, mL/min	2	2
integration time, s	10	10

counterion was used for peak elution (3.6 mL for I<sup>-</sup>, 1.35 mL for IO<sub>3</sub><sup>-</sup>) and cleaning of the membrane disk. During elution from the membrane disk, I<sup>-</sup> was also oxidized by the counterion. After the elution process, the system was rinsed with double-deionized water.

The data acquisition system for the ICP-AES spectrometer was not capable of collecting data rapidly enough for transient signals such as the type generated by chromatographic or flow injection applications. Therefore, the signal from the PMT (located in the simultaneous spectrometer for monitoring iodine at the 183.040-nm line) was amplified, digitized at a rate of 30 points/s, and stored as summarized in Table I. Analyte signal intensity was measured by peak area integration.

**Standard Solutions.** Stock solutions of iodide and iodate ions were prepared from potassium iodide and iodic acid (Fisher Scientific) in 1000  $\mu$ g of 1/mL concentrations with double-deionized 18 M $\Omega$ -cm (25  $^{\circ}$ C) water. Iodate standards were stored in dark bottles to prevent breakdown by ultraviolet light.

## RESULTS AND DISCUSSION

Oxidation of I<sup>-</sup> in acidified test solution to I<sub>2</sub> by using hydrogen peroxide both for Ar ICP-AES and He ICP-AES was evaluated. The batch method (14) suffered from two problems. First, I<sub>2</sub> was adsorbed onto the peristaltic PVC pump tubing and caused a memory effect. Second, mixed reagents were stable for only about 1 h. To minimize the memory effect in the batch method, the transfer line was rinsed with a 0.02% solution of sodium thiosulfate in an attempt to reduce I<sub>2</sub> (adsorbed on the transfer line) to I<sup>-</sup>. Although this procedure was effective in reducing the memory effect, its use in routine analysis was limited because of cross contamination and increased analysis time.

To eliminate the cited limitations in the batch method, reagents were mixed on-line in an all-Teflon line (except for peristaltic pump tubing). For an 8:1 H<sub>2</sub>SO<sub>4</sub>:H<sub>2</sub>O<sub>2</sub> mixing ratio, the iodine signal at 183.04 nm was enhanced by a factor of 33 and 100 for Ar ICP and He ICP. Limits of detection measured at 183.04 nm for Ar ICP and He ICP were 5 and 9 ng/mL, respectively, for on-line oxidation compared to 154

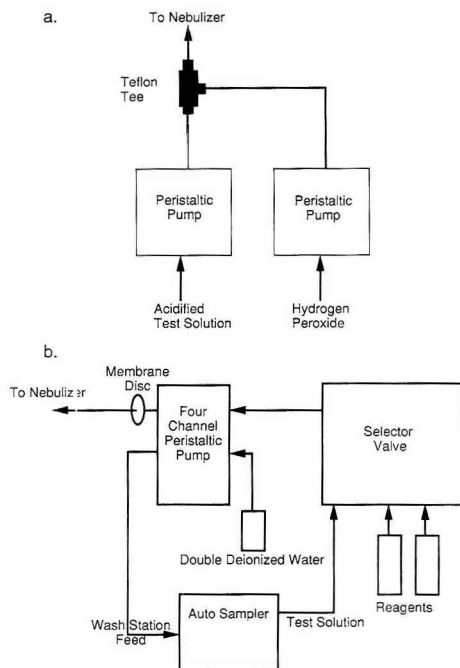


Figure 1. (a) Transfer line used for on-line oxidation of I<sup>-</sup>. (b) Schematic of the flow injection analysis system with the accompanying autosampler used in the preconcentration mode.

and 900 ng/mL for conventional nebulization. Slightly lower limits of detection (2 and 8 ng/mL for Ar ICP and He ICP, respectively) were measured at the 178.28-nm line, but this line is subject to spectral interference from P, a common element in most foods. Analysis of foods at this wavelength may be possible with preconcentration (see next paragraph) if phosphorus and iodine are not in the forms HPO<sub>4</sub><sup>-</sup> and IO<sub>3</sub><sup>-</sup> because they would coelute. The limits of detection for iodine for the He ICP were limited by the dark current of the PMT used in this work. Under the present conditions, the background level from the He ICP was approximately the same as the dark current. In contrast, background emission from Ar ICP was approximately 5 times that of the dark current.

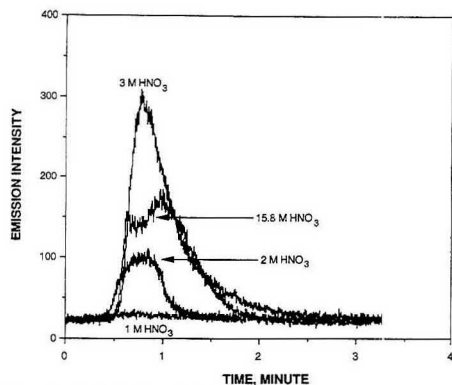


Figure 2. Typical effect of nitric acid on the preconcentration of  $I^-$ .

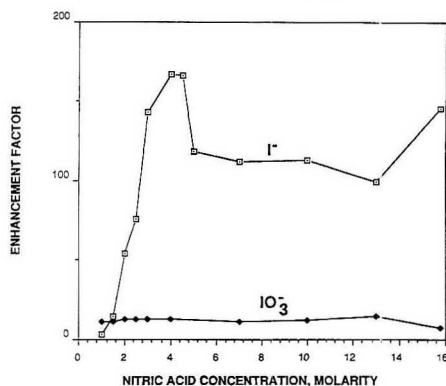


Figure 3. Typical effect of nitric acid concentration for preconcentration of  $I^-$  and  $IO_3^-$ . At the optimum acid concentrations ( $M = 4, 2$ ), the RSDs of measurement for  $I^-$  and  $IO_3^-$  determination were 2.5% and 1.5%, respectively.

Thus, a detector with a much lower dark current, such as a cooled PMT, cooled charge-coupled device or cooled charge injection detector, is needed to estimate the true detecting power of this He ICP compared to the Ar plasma.

A number of counterions were tested for the preconcentration of  $I^-$  and  $IO_3^-$ . The relative affinities of AG 1-X8 for selected anions are as follows: benzenesulfonate 500, salicylate 450, citrate 220,  $I^-$  175,  $HSO_4^-$  85,  $NO_3^-$  65,  $Br^-$  50,  $Cl^-$  2.2,  $HCO_3^-$  6.0,  $IO_3^-$  5.5,  $HPO_4^{2-}$  5.0,  $F^-$  1.6,  $OH^-$  1.0 (38). The high relative selectivity of  $I^-$  for the AG-1 resin precluded elution with the organic counterions because these counterion solubilities are limited to 1–2 M. Sulfuric and nitric acids were the best counterions for preconcentration of  $I^-$  because they could be obtained in high aqueous concentrations. Also, nitric acid acts as an oxidant in the conversion of  $I^-$  to  $I_2$  during elution. Iodate ion was eluted more readily than  $I^-$  because it has a low relative selectivity for the AG 1-X8 resin. Iodate ion was easily eluted with a 1–2 M solution of counterion exhibiting high relative selectivity, such as benzenesulfonate, sulfuric acid, or nitric acid. Elution volumes for  $I^-$  and  $IO_3^-$  were 3.60 and 1.35 mL, respectively, for the nitric acid counterion.

The effects of  $HNO_3$  concentration on preconcentration of  $I^-$  are shown in Figure 2. Both preconcentration of  $I^-$  and oxidation of  $I^-$  to  $I_2$  contributed to the intensity of iodine as

Table III. Summary of Analytical Results Measured at 183.04 nm for the FIA Ar ICP-AES Preconcentration  $I^-$  and  $IO_3^-$

	$I^-$	$IO_3^-$
bckgd area, counts <sup>a</sup>	90 355	32 555
net area, counts <sup>a</sup>	338 464	266 845
signal-to-background ratio	3.75	8.20
% RSD of bckgd	0.93	0.85
% RSD of signal	2.50	1.48
limit of detn, this work <sup>b</sup>	0.75	31
limit of detn, ARL 3580 <sup>c</sup>	154	472
improvement factor	207	15

<sup>a</sup>The peak widths for  $I^-$  and  $IO_3^-$  were 117 and 43 s, respectively. Areas are expressed in counts/1000. A signal of 1 V is equivalent to 50 kHz. <sup>b</sup>Limits of detection (ng/mL,  $3\sigma$ ) were calculated using  $3\sigma$  for 11 background measurements, with 100 ng/mL  $I^-$  and 10  $\mu\text{g/mL}$   $IO_3^-$  solutions. <sup>c</sup>For 10-s integration times using  $3\sigma$ .

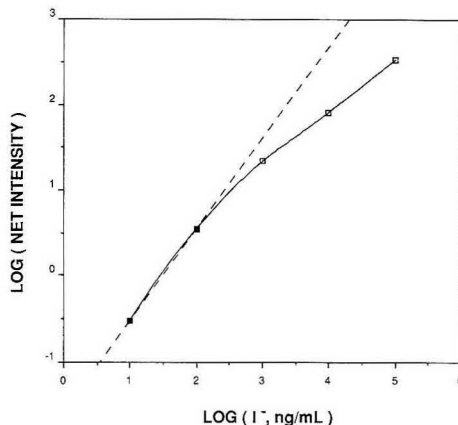


Figure 4. Linear range for preconcentration,  $I^-$ .

the concentration of  $HNO_3$  was changed. To elute  $I^-$  as a peak, the concentration of  $HNO_3$  had to be greater than 1 M; the optimum concentration was 4 M  $HNO_3$  (see Figure 3). Further increase in acid concentration enhanced the preconcentration factor but reduced the efficiency of  $I_2$  production because further oxidation converts  $I_2$  to  $IO_3^-$ . Consequently, a double peak was obtained at 15.8 M, as shown in Figure 2. In contrast, as shown in Figure 3, preconcentration of  $IO_3^-$  was independent of  $HNO_3$  concentration because the affinity of the resin for  $IO_3^-$  relative to  $HNO_3$  was low. At the optimum conditions ( $M = 4, 2$ ), detection limits of  $I^-$  and  $IO_3^-$  were improved (Table III) by a factor of 207 and 15, respectively, compared with those for continuous nebulization.

At optimum  $HNO_3$  concentration, the signal from  $I^-$  was linear below 0.1  $\mu\text{g/mL}$  but fell off at higher concentrations (see Figure 4). This nonlinearity is probably due to reduced membrane efficiency as iodine concentration is increased. The linear range might be extended by increasing the number of active sites (e.g. larger membrane disk) and/or increasing the interaction time between the analyte ion and active sites (e.g. slower flow rate during the preconcentration stage).

## CONCLUSIONS

Preconcentration was combined with oxidation to improve the atomic emission limit of detection for iodine by inductively coupled plasmas (ICPs) formed in argon and helium. The process was automated with the flow injection technique. Two ionic forms of iodine were studied:  $I^-$  and  $IO_3^-$ . The pre-



concentration medium was a membrane disk containing the AG1-X8 anion-exchange resin within a polypropylene housing. Preconcentration was coupled with chemical conversion of  $I^-$  to  $I_2$  to enhance analyte transport to the plasma. The combined technique improved the limit of detection of iodine as  $I^-$  and  $IO_3^-$  in aqueous solution by a factor of 207 (0.75 ng/mL) and 15 (31 ng/mL), respectively. Improvement factors for on-line oxidation of  $I^-$  were 33 and 100, respectively, for Ar and He ICP discharges. The limit of detection should be further improved by a factor of 8 to match the current spectrophotometric technique (10) used in the FDA Total Diet Study. With a suitable digestion procedure, preconcentration combined with oxidation would satisfy FDA needs.

#### ACKNOWLEDGMENT

We thank W. F. Syner of the Food and Drug Administration for his assistance in constructing the data acquisition system for this work.

#### LITERATURE CITED

- (1) Lombardo, P. *Environmental Epidemiology*; Kopley, F. C., Craun, G. F., Eds.; Lewis: Chelsea, MI, 1986; Chapter 11.
- (2) Pennington, J. A. T. *J. Assoc. Off. Anal. Chem.* **1987**, *70*, 772-782.
- (3) Pennington, J. A. T. *J. Am. Diet. Assoc.* **1983**, *82*, 166-173.
- (4) Pennington, J. A. T. *Documentation for the Revised Total Diet Study: Food List and Diets*; National Technical Information Service: Springfield, VA, 1981; Accession Number PB 82-192154.
- (5) Pennington, J. A. T.; Young, B. E.; Wilson, D. B. *J. Am. Diet. Assoc.* **1989**, *89*, 659-664.
- (6) Gunderson, E. L. *J. Assoc. Off. Anal. Chem.* **1988**, *71*, 1200-1209.
- (7) Capar, S. G. *Analytical Method Aspects of Assessing Dietary Intake of Trace Elements*. In *Biological Trace Elements Research*; Subramanian, K. S.; Iyengar, G. V.; Okamoto, K., Eds.; ACS Symposium Series No. 445; American Chemical Society: Washington, DC, 1991; Chapter 13.
- (8) Luchtefeld, R. G. *FDA Laboratory Information Bulletin 1678*; Food and Drug Administration, Division of Field Science: Rockville, MD 20857, 1974.
- (9) Sandell, E. B.; Kolthoff, I. M. *J. Am. Chem. Soc.* **1934**, *56*, 1426.
- (10) Fisher, P. W. F.; L'Abbé, M. R.; Giron, A. *J. Assoc. Off. Anal. Chem.* **1986**, *69*, 687-689.
- (11) Blaha, J. *J. FDA Laboratory Information Bulletin 3045*; Food and Drug Administration, Division of Field Science: Rockville, MD 20857, 1986.
- (12) *Inductively Coupled Plasma in Analytical Atomic Spectrometry*; Montaser, A.; Golightly, D. W., Eds.; VCH: New York, 1987; 660 pages.
- (13) Sheppard, B. S.; Caruso, J. A.; Wolnik, K. A.; Fricke, F. L. *Appl. Spectrosc.* **1990**, *44*, 712-715.
- (14) Nakahara, T.; Wasa, T. *Appl. Spectrosc.* **1987**, *41*, 1238-1242.
- (15) Cave, R. M.; Green, K. A. *J. Anal. At. Spectrom.* **1989**, *4*, 223-225.
- (16) *Inductively Coupled Plasma in Analytical Atomic Spectrometry*; Montaser, A.; Golightly, D. W., Eds.; VCH: New York, 1987; Chapter 11.
- (17) Browner, R. F. In *Inductively Coupled Plasma Emission Spectroscopy*; Boumans, P. W. J. M., Ed.; Wiley: New York, 1987; Part II, Chapter 8.
- (18) Christian, G. D.; Ruzicka, J. *Spectrochim. Acta* **1987**, *42B*, 157-167.
- (19) McLeod, C. W. *J. Anal. At. Spectrom.* **1987**, *2*, 549-552.
- (20) McLeod, C. W.; Zhang, Y.; Cook, I.; Cox, A.; Date, A. R.; Cheung, Y. *J. Res. Natl. Bur. Stand.* **1988**, *93*, 462-465.
- (21) Ruzicka, J.; Hansen, E. H. *Anal. Chim. Acta* **1975**, *78*, 145-157.
- (22) Ruzicka, J. *Flow Injection Analysis (Chemical Analysis Series)*; 2nd ed.; Wiley: New York, 1988.
- (23) Hartenstein, S. D.; Ruzicka, J.; Christian, G. D. *Anal. Chem.* **1985**, *57*, 21-25.
- (24) Hirata, S.; Umezaki, Y.; Ikeda, M. *Anal. Chem.* **1986**, *58*, 2502-2606.
- (25) Dean, J. A. *Chemical Separation Methods*; Van Nostrand Reinhold: New York, 1969; Chapter 7.
- (26) McLeod, C. W.; Cook, I. G.; Worsfold, P. J.; Davies, J. E.; Queay, J. *Spectrochim. Acta* **1985**, *40B*, 57-62.
- (27) Cox, A. G.; Cook, I. G.; McLeod, C. W. *Analyst* **1985**, *110*, 331-333.
- (28) Cox, A. G.; McLeod, C. W. *J. Anal. At. Spectrom.* **1987**, *2*, 553-555.
- (29) Chan, S.; Montaser, A. *Spectrochim. Acta* **1985**, *40B*, 1467-1472.
- (30) Chan, S.; Van Hoven, R. L.; Montaser, A. *Anal. Chem.* **1986**, *58*, 2342-2343.
- (31) Chan, S.; Montaser, A. *Spectrochim. Acta* **1987**, *42B*, 591-597.
- (32) Montaser, A.; Chan, S.; Koppenaal, D. W. *Anal. Chem.* **1987**, *59*, 1240-1242.
- (33) Montaser, A.; Van Hoven, R. L. *CRC Crit. Rev. Anal. Chem.* **1987**, *18*, 45-103.
- (34) Chan, S.; Tan, H.; Montaser, A. *Appl. Spectrosc.* **1989**, *43*, 92-95.
- (35) Chan, S.; Montaser, A. *Spectrochim. Acta* **1989**, *44B*, 175-184.
- (36) Montaser, A.; Ishii, I.; Clifford, R. H.; Sinex, S. A.; Capar, S. G. *Anal. Chem.* **1989**, *61*, 2589-2592.
- (37) Montaser, A.; Clifford, R. H.; Sinex, S. A.; Capar, S. G. *J. Anal. At. Spectrom.* **1989**, *4*, 499-503.
- (38) Personal communication, Anne Stevens, Bio-Rad Laboratories, 1414 Harbour Way South, Richmond, CA 94804.

RECEIVED for review May 7, 1991. Accepted August 12, 1991. This research was sponsored in part by the U.S. Department of Energy under Grant No. DE-FG05-87-ER-13659. Partial financial support for A.M. and R.H.C. and use of certain facilities was provided by the FDA.

## Determination of Small Amounts of Water in Dimethylformamide and Dimethylsulfoxide Using Luminescence Lifetime Measurements of Europium(III)

Stefan Lis<sup>1</sup> and Gregory R. Choppin\*

Department of Chemistry, The Florida State University, Tallahassee, Florida 32306-3006

#### INTRODUCTION

A linear dependence of the rate of luminescence decay on the degree of cation hydration has been observed for several trivalent lanthanides (1, 2). As a result, the luminescence decay rates have become valuable data in evaluating hydration in the primary coordination sphere of complexes of these cations (1-6). This correlation has been applied for Eu(III) and Tb(III) to the calculation of residual hydration numbers in complexes of these cations. Generally, the hydration numbers have been obtained by using the difference in the decay rate constants in  $H_2O$  and in  $D_2O$  solutions. However,  $k_{H_2O} \gg k_{D_2O}$  generally and  $k_{D_2O} \approx$  constant. As a result, a relationship was proposed in which the hydration number could be related more simply to the decay rate constant in water (7):

$$n_{H_2O} = Ak_{H_2O} + B \quad (1)$$

Knowledge of the residual hydration has been useful in interpreting the binding mode in biological systems as well the number of ligating functions in interactions with polydentate ligands (2-9).

We have measured the luminescence lifetimes of Eu(III) in mixtures of water (or deuterated water) and methanol (MeOH), ethanol (EtOH), tertiary butanol (*t*-BuOH), *N,N*-dimethylformamide (DMF), and dimethyl sulfoxide (DMSO). Our results agreed well with those of Tanaka et al. (10) for some of the same mixed solvent systems. In the alcohol-water solvents, Eu(III) was preferentially solvated by water whereas in the DMF and DMSO solutions, the organic solvents were favored over water. However, even at very low mole fractions of water, water molecules were present in the primary solvation sphere of Eu(III). The implications of the variation in the preferential solvation by the different organic solvents vs water is to be discussed in a subsequent publication. In the DMF

<sup>1</sup> On leave from the Faculty of Chemistry, Adam Mickiewicz University, Poznan, Poland.

**Table I. Water Content and the Luminescence Lifetime for Eu(III)**

mol % water		lifetime, <sup>a</sup> ms
added	measd	
A. DMF Solution		
0.050	0.046	1.579
0.10	0.10	1.528
0.20	0.20	1.457
0.50	0.50	1.286
1.00	1.00	1.023
B. DMSO Solution		
0.070	0.063	1.601
0.10	0.11	1.596
0.20	0.21	1.584
0.50	0.48	1.554
1.00	0.98	1.489
2.00	2.04	1.380
5.00	4.98	1.050

<sup>a</sup> Mean of at least seven measurements in each DMF sample and five measurements in each DMSO sample.

and DMSO mixtures, the luminescence lifetimes were found to be linearly dependent on the water concentration over ranges from 0.1 to 1 (DMF) and 0.1 to 5 (DMSO) mol %. This paper describes a method for the determination of small amounts of water in these solvents using Eu(III) luminescence lifetime measurements.

### EXPERIMENTAL SECTION

Europium perchlorate stock solutions were prepared by dissolving the oxide (Aldrich Chemical Co., Inc.) in perchloric acid. This solution was evaporated to dryness and the residue dissolved in either DMF or DMSO followed by evaporation to dryness again. The preparation can be done equally well with hydrochloric acid to avoid concerns over evaporation to dryness of perchlorate solutions. The process of solution and evaporation was repeated four times to eliminate water completely (<0.01 mol %). The dry samples of Eu(ClO<sub>4</sub>)<sub>3</sub> were dissolved in reagent grade DMF or DMSO (Fisher Scientific). The initial content of water in these solutions was determined to be 0.05 mol % in DMF and 0.07 mol % in DMSO from the dependence of the luminescence lifetimes on known amounts of water added to the original "dry" solution. The linearity of response indicated that this was as reliable as direct measurements of these low levels of H<sub>2</sub>O by conventional techniques such as Karl Fischer titrations. Moreover, these amounts of residual water are below the recommended ranges for the luminescence technique.

Working solutions were prepared by introducing measured amounts of water into the Eu(III)-DMF or Eu(III)-DMSO solutions. All tubes containing the samples were stoppered and wrapped tightly with parafilm to avoid the contents absorbing moisture by contact with the air.

The Eu(III) in the samples was excited to the <sup>5</sup>L<sub>6</sub> electronic level by a pulsed laser beam at 395 nm, and the subsequent emission from the <sup>5</sup>D<sub>0</sub> luminescent excited state to the ground <sup>7</sup>F manifold (<sup>7</sup>F<sub>0</sub>) was measured. The 395-nm beam was obtained with the pulsed (10 kHz) 532-nm second-harmonic output of a Quanta Ray DCR 2A Nd-YAG laser pumping Rhodamine 640 (Exciton Chemical) in methanolic solution in Quanta Ray PDL2 equipment. The beam from the dye laser was converted to 395 nm by frequency doubling and mixing with the 1064-nm fundamental in a Quanta Ray WEX-1 wavelength extender. The pulse energy was typically 2-3 mJ, and the pulse width was in the nanosecond range. The details for conducting the experiments and collecting the data have been described earlier (7).

The luminescence decay curves observed in this work could be analyzed by a single exponential relation; i.e., semilogarithmic plots of the luminescence intensity versus time were linear. These plots provided the decay constants reported in Table I. In some systems where the concentration of water in DMF exceeded 1 mol

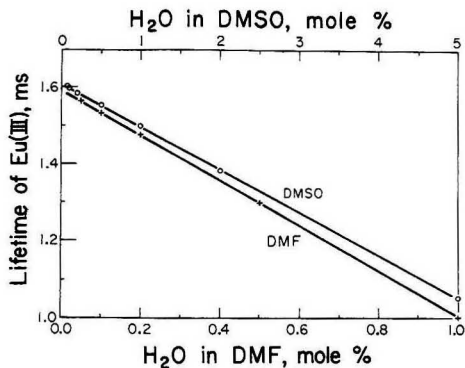


**Figure 1.** Dependence of the Eu(III) luminescence lifetime on the H<sub>2</sub>O concentration in DMF and DMSO.

% and in 5 mol % DMSO, the luminescence lifetimes for Eu(III) did not show a simple linear dependence on the H<sub>2</sub>O concentration. These concentrations, as a consequence, are used as the limits of applicability of the method for water analysis.

### RESULTS AND DISCUSSION

Normally, the degree of hydration of Eu(III) is calculated from the luminescence decay rate constants. However, the linearity of response to water concentration was equally good for the rate constants or the directly measured lifetimes, so we report the method in terms of the latter.

The luminescence lifetimes measured for Eu(III) in samples containing water in DMF and DMSO solutions are listed in Table I. The relative standard deviation for eight repeated measurements of a solution of DMF is 2.9% and, for six such measurements of a solution of DMSO, 1.7%. The plot of a calibration curve for Eu(III) versus water concentration in DMF and DMSO systems is shown in Figure 1. The data had a linear least-squares fit with a correlation coefficient of 0.999 for both solvents. The correlation gives the following equations for the calculation of the mole percent water in each solvent:

$$\text{DMF: mol \% H}_2\text{O} = [1.591 - t]/0.588 \quad (2)$$

$$\text{DMSO: mol \% H}_2\text{O} = [1.605 - t]/0.112 \quad (3)$$

where  $t$  is the fluorescence lifetime in milliseconds. The mole percent water content calculated from the measured lifetime values is listed in Table I along with the amount (in mole percent) known to be present from the added water.

### LITERATURE CITED

- (1) Kropp, J. L.; Windsor, M. W. *J. Chem. Phys.* **1965**, *42*, 1599; (b) **1966**, *45*, 761.
- (2) Horrocks, W. De W.; Studnick, D. R. *J. Am. Chem. Soc.* **1979**, *101*, 334.
- (3) Breen, P. J.; Horrocks, W. De W. *Inorg. Chem.* **1983**, *22*, 536.
- (4) Albin, M.; Farber, G. K.; Horrocks, W. De W. *Inorg. Chem.* **1984**, *23*, 1648.
- (5) Bryden, C. C.; Reilley, C. N. *Anal. Chem.* **1982**, *54*, 610.
- (6) Okamoto, Y.; Kido, J.; Brittain, H. G.; Paoletti, S. *J. Macromol. Sci.-Chem.* **1988**, *A25* (10&11), 1385.
- (7) Barthelemy, P. P.; Choppin, G. R. *Inorg. Chem.* **1989**, *28*, 3354.
- (8) Soini, E.; Lovgren, T. *CTC Crit. Rev. Anal. Chem.* **1987**, *18* (2), 105.
- (9) Richardson, F. R. *Chem. Rev.* **1982**, *82*, 541.
- (10) Tanaka, F.; Kawasaki, Y.; Yamashita, S. *J. Chem. Soc., Faraday Trans. 1*, **1988**, *84*, 1083.

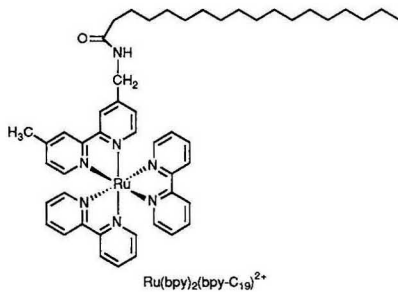
RECEIVED for review May 21, 1991. Accepted August 22, 1991. This research was supported by a grant from the USDOE-OBES, Division of Chemical Sciences.

CORRECTION *corrected 24-Dec-91*

**Horizontal Touch Voltammetric Analysis—Determination of Insoluble Electroactive Species in Films at the Air/Water Interface**

Cary J. Miller and Allen J. Bard (*Anal. Chem.* **1991**, *63*, 1707–1714).

The structure for  $\text{Ru}(\text{bpy})_2(\text{bpy-C}_{19})^{2+}$  in Figure 1 is incorrect. The correct structure is as follows:





# JANAF THERMOCHEMICAL TABLES

## Third Edition

A Major Supplement from JOURNAL OF PHYSICAL AND CHEMICAL  
REFERENCE DATA

Presenting Reliable Data Utilized by Chemists, Chemical Engineers, and Materials  
Scientists from Around the World for Over 25 Years

JOURNAL OF PHYSICAL AND CHEMICAL REFERENCE DATA is very pleased  
to publish the Third Edition of the JANAF THERMOCHEMICAL TABLES.

Since the first version appeared 25 years ago, the JANAF THERMOCHEMICAL  
TABLES have been among the most widely used data tables in science and engineering.

You'll find:

- Reliable tables of thermodynamic properties of substances of wide interest
- A highly professional approach with critical evaluations of the world's thermochemical and spectroscopic literature
- A concise and easy-to-use format

This Third Edition presents an extensive set of tables including thermodynamic properties of more than 1800 substances, expressed in SI units. The notation has been made consistent with current international recommendations.

There is no other reference source of thermodynamic data that satisfies the needs of such a broad base of users.

Order your 2-volume set of the JANAF THERMOCHEMICAL TABLES today! You'll get over 1890 pages of valuable information that is crucial to your research—in two hardback volumes.

#### SUBSCRIPTION INFORMATION

The JANAF THERMOCHEMICAL TABLES, THIRD EDITION is a two-volume supplement of *Journal of Physical and Chemical Reference Data*.

1896 pages, 2 volumes, hardcover  
ISBN 0-88318-473-7  
Supplement Number 1 to Volume 14, 1985

U.S. & Canada	\$130.00
All Other Countries	\$156.00

(Postage included.)

All orders for supplements must be prepaid.

Foreign payment must be made in U.S. currency by international money order, UNESCO coupons, U.S. bank draft, or order through your subscription agency. For rates in Japan, contact Maruzen Co., Ltd. Please allow four to six weeks for your copy to be mailed.

For more information, write American Chemical Society, Marketing Communications Department, 1155 Sixteenth Street, NW, Washington, DC 20036.

In a hurry? Call TOLL FREE **800-227-5558** and charge your order!



Published by the American Chemical Society and the American Institute of Physics for the National Institute of Standards and Technology

#### Editors:

M.W. Chase, Jr.  
National Institute of  
Standards and Technology

C.A. Davies  
Dow Chemical U.S.A.

J.R. Downey, Jr.  
Dow Chemical U.S.A.

D.J. Frurip  
Dow Chemical U.S.A.

R.A. McDonald  
Dow Chemical U.S.A.

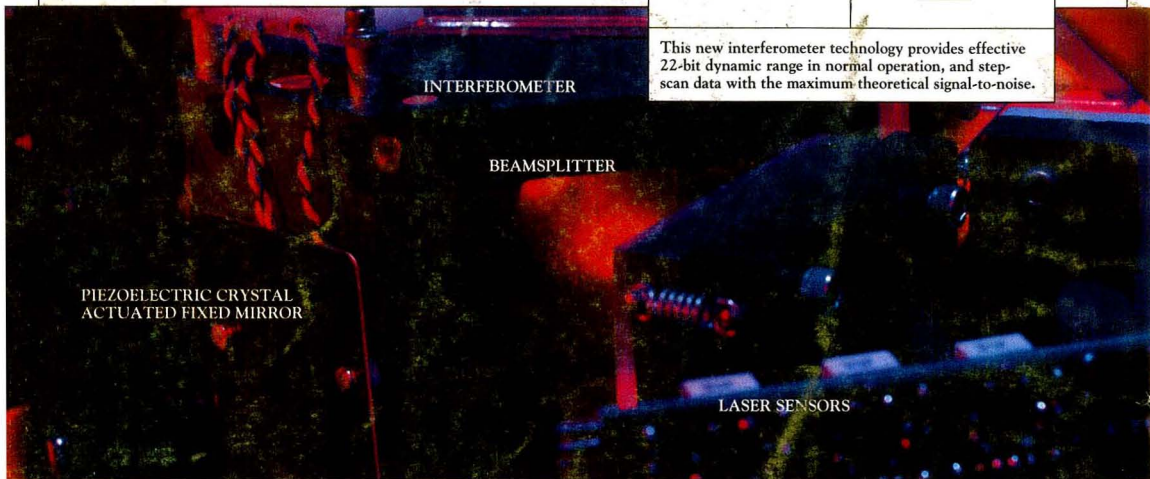
A.N. Syverud  
Dow Chemical U.S.A.

# FT-IR in the $\mu$ sec domain

Our new FT-IR spectrometer is a powerful new tool for spectroscopy and chemical physics. With its new 896 interferometer, it can operate in the step-scan mode at the rate of 0.25-800 steps/second and collect data at 5 $\mu$ s intervals.



This new interferometer technology provides effective 22-bit dynamic range in normal operation, and step-scan data with the maximum theoretical signal-to-noise.



INTERFEROMETER

BEAMSPLITTER

PIEZOELECTRIC CRYSTAL  
ACTUATED FIXED MIRROR

LASER SENSORS

The new 896 interferometer technology is comprised of the interferometer itself and a innovative, new generation of dynamic alignment, control and signal processing electronics (shown above).

The 896 interferometer technology, upon which our new chemical physics level FT-IR spectrometer is based, massively extends the application of FTS methods, and creates new horizons in such diverse areas of research as:

- Step scan spectroscopy of sample modulation experiments, e.g. polymer rheology (2D IR), photolysis studies and spectroelectrochemistry
- Time Resolved Spectroscopy (TRS) of fast repetitive events
- Double modulation experiments: e.g. LD, VCD, MCD
- Step scan FT-Raman
- Visible-uv emission studies, e.g. FT-ICP & laser-induced fluorescence
- Photoacoustic and photothermal beam deflection studies
- Surface and monolayer studies
- Trace component analyses

The capabilities offered by the new spectrometer include in-scan co-adding, giving step-scan data with the maximum possible signal-to-noise (by making optimum use of the available measurement

time), and the collection of rapid-scan data with an effective 22-bit dynamic range. This latter capability advances studies of weak absorbances where limited dynamic range is currently a problem.

In the step-scan mode, fast data collection (5 $\mu$ s resolution) may be used to support time resolved spectroscopy (TRS) of repetitive events. Variable speed phase modulation is available for photothermal and other studies. The large control bandwidth provided by the piezoelectric fixed mirror actuators means that all these studies can be performed in the normal laboratory environment, without special precautions. In addition, the control and signal processing electronics of the 896 interferometer support the use of lock-in amplifiers required

for multiple modulation experiments.

In kinetic scan mode the 896 interferometer can perform bidirectional data collection at 50+ scans/second for single events.

Finally, the 896 interferometer gives our new FT-IR spectrometer a nominal free-scanning spectral range of 0-63,000  $\text{cm}^{-1}$  (Nyquist frequency), with practical operation to beyond 230 nm. This avoids the traditional aliasing problems encountered in near-IR/visible/near-UV interferometry. It supports a resolution of up to 0.1  $\text{cm}^{-1}$  in the mid-IR, and a resolving power of up to 1 in  $10^5$  in the near-UV.

For more information on our new chemical physics level FT-IR spectrometer and its 896 interferometer technology, please call (617) 868-4330. Or write Bio-Rad Digilab Division, 237 Putnam Avenue, Cambridge, MA 02139.



**BIO-RAD** Digilab  
Division